# Geology, Geochemistry and Genesis of the Namosi Porphyry Cu-Au Deposits, Fiji

Evan A. Orovan
BSc (Honours)

Submitted in fulfillment of the requirements for the degree of
Doctor of Philosophy

May, 2016


UNIVERSITY
OF TASMANIA

CODES
ARC CENTRE OF EXCELLENCE IN ORE DEPOSITS

## Declaration of Originality

This thesis contains no materials which has been accepted for a degree or diploma by the University or and other institution, except by way of background information and duly acknowledged in the thesis, and to the best of my knowledge and belief, contains no material previously published or written by another person except where due acknowledgment is made in the text of the thesis.

Date: May 17, 2016

Signature:

## Authority of Access

Copying and communication of any part of this thesis is prohibited until November 2017 (1.5 years after acceptance); following that time, limited copying and communication is permitted in accordance with the Copyright Act 1968.

## Abstract

The porphyry Cu-Au(-Mo) deposits of the Namosi district are located 30 km west-northwest of Suva, southeastern Vitu Levu, Republic of Fiji. The district comprises three principal porphyry deposits (Wainaulo, Waisoi West, and Waisoi East) and several other peripheral porphyry, polymetallic vein, and skarn prospects. The combined Wainaulo, Waisoi West, and Waisoi East resources are in excess of 7.86 million tonnes of copper and 7.97 million ounces of gold.

The Namosi porphyry district formed after a major perturbation in the Australian-Pacific plate tectonic regime during the Late Miocene. The collision of the Melanesian Border Plateau with the Vitiaz Arc led to a localized reversal of arc polarity, wherein the South Fiji Basin began to subduct northeastward along the Matthew-Hunter Trench. This short-lived subduction system had a low-angle component beneath the Fiji Platform that may have triggered the generation of the Namosi district porphyry deposits. A north-dipping and locally flat-lying orphaned slab from the fossil subduction zone currently abuts the westward subducting Pacific plate ~ 350 km beneath the Fiji platform.

The Namosi district consists of a gently dipping, andesitic, volcanic and volcaniclastic succession ≥ 1 km thick (known as the Namosi Andesite Formation of the Medrausucu Group), which was deposited on the submerged flank of a shoaling seamount in the Late Miocene. The Namosi Andesite Formation unconformably overlies steeply dipping, low-K tholeiitic submarine basaltic andesite volcanic and volcaniclastic rocks of the Late Oligocene to Middle Miocene Wainimala Group. The Namosi porphyry deposits are temporally and genetically associated with a sequence of medium-K calc-alkalic porphyritic rocks that intruded both the Wainimala Group and Namosi Andesite Formation. Diorite plutons and a dike complex were emplaced at Wainaulo, quartz-diorite stocks were intruded at Waisoi West, and dacite stocks and dikes were emplaced at Waisoi East.

The high $^{143}Nd/^{144}Nd_i$ (~ 0.51304) and low $^{87}Sr/^{86}Sr_i$ (~ 0.7036) values of the Namosi district porphyries suggest a primitive mantle source with no crustal input. Neodymium isotopic compositions infer more primitive sources throughout the evolution of the Namosi district, interpreted to reflect the onset of rifting in the vicinity of the Fiji Platform in the Early Pliocene.

Two contrasting styles of porphyry deposits have been recognized within the Namosi district. The first style is a variation on the plutonic-hosted porphyry deposit model (Wainaulo and Wainaulo West), consisting of dike complexes emplaced into pre-mineralization porphyritic diorite plutons. The ore bodies are localized around dikes and are vertically attenuated (> 800 m). The second type are classic volcanic-hosted porphyry deposits (Waisoi West and Waisoi East), consisting of multiphasic porphyritic stocks that intruded the volcanic host sequence. The ore bodies are shallow and annular, occurring in and around the cupola of the porphyritic stocks.

Alteration assemblages at Wainaulo are mineralogically complex, but have well-constrained zonation patterns. A central zone of biotite – albite – magnetite – actinolite ± muscovite ± rutile and chalcopyrite ± molybdenite bearing veins is spatially and temporally associated with two early-mineralization diorite phases. Separating the central biotite-bearing assemblage from the peripheral chlorite – albite – epidote – calcite ± montmorillonite ± magnetite assemblage is a zone of actinolite – albite – chlorite – magnetite ± epidote ± rutile ± titanite alteration. Overprinting the central biotite-bearing assemblage are domains of chlorite – albite – quartz – actinolite – epidote alteration that are spatially and temporally associated with the main-stage quartz-diorites and abundant quartz – magnetite – bornite and quartz – sulfide veins. The last significant ore-bearing event at Wainaulo consists of epidote – sulfide – anhydrite – calcite – hematite veins with conspicuous K-feldspar – epidote – phengite vein halos that overprint the main-stage diorite and quartz-diorite complex. Structurally focused illite – muscovite – anhydrite – calcite – pyrite and kaolinite – montmorillonite – ankerite ± hematite, as well as ubiquitous chlorite – illite-smectite assemblages overprint the earlier alteration domains throughout the deposit.

The alteration assemblages at both Waisoi deposits consist of an inner biotite – albite – magnetite ± actinolite ± K-feldspar core that grades out to a peripheral chlorite – albite – magnetite ± calcite ± epidote domain. The bulk of the copper mineralization is hosted in a sulfide-bearing quartz stockwork that overprinted the earlier formed alteration assemblages. Paragonite – quartz – pyrite and chlorite – illite-smectite alteration is ubiquitous, but is most intensely developed overprinting the intrusions associated with mineralization at each deposit.

High-resolution CA-TIMS U–Pb dating on zircons and Re–Os dating on molybdenite from each of the principal deposits has revealed that mineralization in the Namosi district occurred

rapidly over a span of ≤ 520,000 years from the Late Miocene to Early Pliocene. Re–Os ages overlap with U–Pb ages of interpreted causative intrusions at Wainaulo (5.690 ± 0.023 Ma) and Waisoi West (5.473 ± 0.022 Ma), whereas at Waisoi East molybdenum mineralization post-dates the interpreted source intrusion by ≥ 2000 years (5.248 ± 0.022 Ma). These strong correlations demonstrate the genetic link between mineralization and intrusive activity at each deposit.

The sulfur isotopic compositions at Wainaulo indicate sulfides precipitated from a redox neutral to $SO_4^{2-}$-dominant exsolved magmatic fluid that had probably mixed with seawater. There is a zonation of sulfur isotopic compositions at Wainaulo (i.e., $\delta^{34}S_{sulfide}$ values range from > 1 ‰ within and directly above the deposit core to < -3 ‰ at the deposit periphery; $\delta^{34}S_{sulfate}$ values vary from > 11.5 ‰ in the core of the deposit to < 11.5 ‰ distally), whereas at the progressively more reduced deposits at Waisoi West ($\delta^{34}S_{sulfide}$ from -2.9 to +0.6 ‰; mean = -1.4 ‰) and Waisoi East ($\delta^{34}S_{pyrite}$ from +1.8 to +3.4 ‰; mean = +2.4 ‰), no sulfur isotopic zonation was discernible. The calculated $\delta^{18}O$ and $\delta D$ composition of water in isotopic equilibrium with gangue minerals from Wainaulo, Waisoi West and Waisoi East reflect the involvement of three different fluid sources during the evolution of the Namosi district porphyry deposits: exsolved magmatic fluid, Late Miocene seawater and a local meteoric component. Results from a Sr isotopic study on Namosi district epidote separates confirm the minor involvement of seawater during hydrothermal alteration.

The Namosi district records a rapid evolution of contrasting porphyry deposit styles (low tonnage-high grade to large tonnage-low grade) within a time period of ≤ 520,000 years. These findings have significant implications to porphyry exploration strategies that need to be considered when working at a district scale. Geology, hydrothermal alteration, geochemistry, structural trends, mechanisms for ore concentration, deposit footprints and deposit size can vary significantly over a short period of time and within a confined space. The rapid evolution of the Namosi district reflects the dynamic tectonic setting during ore-formation. The recognition of tectonic environments that reflect arc fragmentation and rotation can be valuable targets for identifying new metallogenic belts worldwide.

## Acknowledgments

Thanks go to my primary supervisor, David Cooke, for supporting me through the entire thesis process. I am grateful for your guidance, advice, and encouragements. You always had my back. To Anthony Harris, my external supervisor at Newcrest Mining Limited, thank you for making this project possible. Your involvement, input and expertise are greatly appreciated.

Financial and logistical support was provided by Newcrest Mining Limited, CODES and the SEG Foundation. Big thanks goes to Ben Ackerman who was always willing to share ideas and provide guidance, even though he was always super busy. Fraser MacCorquodale and John Holliday are also thanked for their time and guidance. Thank you to the NJV staff at Waisoi Camp who were always very helpful and accommodating. Thanks to Prachant, Jarrod, Nick, Will, Jimmy, Gito, Negishi, Fukasawa and Ben from NJV and Newcrest Mining Limited for all of their support.

I have benefited greatly from the tutelage of world-class experts at CODES and the Earth Sciences department at the University of Tasmania. Thanks to Jocelyn McPhie, David Selley and Patrick Quilty for their generous insights into my volcanic, sedimentary and fossiliferous rock samples, to Tony Crawford and Peter Hollings for all of their help with my igneous geochemistry, to Garry Davidson for providing very useful discussions on isotopic tracing, to Sebastien Meffre for guidance with my particularly tricky igneous geochronology, and to Noel White for sitting through my midterm review and giving valuable feedback and suggestions. I would like thank a variety of University of Tasmania staff for their administrative and technical support throughout my candidature, in particular: Anya Reading, Rose Pongratz, Karen Mollross, Deborah Macklin, Jane Higgins, Helen Scott, Chris Evans, Keith Dobson, Karsten Goemann, Katie McGoldrick, Al Cuison, Christine Cook, Izzy Von Lichtan, Ian Little and Peter Cornish.

I would like to thank the friends and colleagues that I met during my time at CODES: Marc and Angela, Nic, Nathan, Josh, Ange, Steph, and many more. I would like to thank my Ma, Pa and sibling back in Canada who have always believed in me. Finally, I would like to thank my de facto partner Erin. Erin always supported me whenever I needed it, and provided lots of laughs and encouragement. I couldn't have done it without her.

# Table of Contents

# List of Figures

**Chapter 1**



**Chapter 2**



**Chapter 3**

## Chapter 4



## Chapter 5

## Chapter 6

## Chapter 7

# List of Tables

# CHAPTER 1

# Introduction

## 1.1 Introduction

Magmatic-hydrothermal porphyry Cu deposits are among the largest repositories of Cu in the world, containing about 60 percent of the known resources (John et al., 2010). Their large size (commonly tens of millions to billions of metric tons), long mine lives and high production rates combine to make these deposits valuable exploration targets for the mineral exploration industry, despite their typically low grade (0.2 – 1.5 % Cu, < 0.01 – 0.03 % Mo, < 0.4 g/t Au; Sillitoe, 1993). As a result of their economic importance, porphyry Cu deposits have been researched extensively and are well understood in regards to many aspects of their genesis (e.g., Lowell and Guilbert, 1970; Richards, 2003; Cooke et al., 2005; Seedorff et al., 2005; Sillitoe, 2010).

Porphyry Cu deposits are genetically, temporally and spatially associated with porphyritic intrusive complexes that are emplaced in the upper 4 km of the crust (rarely deeper than 6 km; Seedorff et al., 2005). These intrusive complexes include stocks, dikes and breccia pipes, that are most commonly derived from medium-K calc-alkaline melts of felsic to intermediate composition from depths of 5 to 15 km (Sillitoe, 2010). Multiple stages of intrusions can introduce volatiles and fluids before, during and after mineralization and/or alteration events. These fluids metasomatize the surrounding country rock, forming lateral and vertical alteration zonation patterns that are centered on the composite porphyry complex. The alteration assemblages are commonly referred to as sodic, calc-sodic, potassic, propylitic, phyllic, intermediate argillic and advanced argillic and can define footprints up to several kilometers away from the deposit center. Detailed reviews of porphyry Cu deposit characteristics are provided by Sillitoe (1997, 2010), Hedenquist and Richards (1998), Cooke et al. (2005) and Seedorff et al. (2005).

At the district scale, porphyry Cu systems tend to occur in clusters (broadly equidimensional groups of deposits) or as alignments (linear deposit arrays that are either oriented parallel or transverse to their associated magmatic arcs; Sillitoe, 2010). Individual porphyry deposits in a district can range from 100s to 1000s of meters apart. Their surface distribution is interpreted to reflect the extent of an underlying parental pluton, and the orientation of faults that localized intrusive activity (Sillitoe and Gappe, 1984; Sillitoe, 2010). Porphyry deposits within a district usually display a wide variety of characteristics (e.g., grade, tonnage, alteration footprint), in part due to their protracted magmatic history (e.g., Batu Hijau, Indonesia ~ 2.2 m.y.: Garwin, 2002; Escondida, Chile ≤ 5.2 m.y.: Padilla-Garza et al., 2004; Boulder batholith, USA ~ 13 m.y.: Lund et al., 2002). Porphyry districts may contain a diversity of deposit types ranging from skarn to carbonate-replacement to sediment-hosted gold deposits (with increasing distance from the porphyry center) and superjacent high- and intermediate-sulfidation epithermal deposits. District-scale studies in Bingham, USA (Babcock et al., 1995), Potrerillos, Chile (Olson, 1984; Marsh et al., 1997), Yerington, USA (Dilles, 1987; Dilles and Einaudi, 1992; Dilles and Proffett, 1995), Cadia, Australia (Wilson, 2003; Wilson et al., 2007), Batu Hijau, Indonesia (Garwin, 2000, Garwin, 2002) and Baguio district, Philippines (Cooke and Bloom, 1990; Cooke et al., 2011) are key studies documenting the geological framework and evolution of hydrothermal systems in porphyry copper districts.

This PhD thesis is a study of the Late Miocene – Early Pliocene porphyry Cu-Au(-Mo) deposits of the Namosi district in the Republic of the Fiji Islands (Fig. 1.1). Fiji is located in an unusual tectonic environment, far from a continent, and separated from active subduction by two flanking backarc basins. The complex tectono-magmatic history has resulted in overlapping and proximal terranes of different geochemical affinities (tholeiitic, calc-alkalic and shoshonitic), and consequently the juxtaposition of incongruent deposit styles (e.g., low-sulfidation epithermal Au, calc-alkalic porphyry Cu-Au(-Mo) and volcanogenic massive sulfide). The close spatial and temporal overlap of these mineralized systems provides a valuable opportunity to investigate the genetic and tectonic links that have resulted in these juxtapositions. Outcomes of this research have global significance in providing a modern analogue to ancient terranes (e.g., Stikine and Quesnel,

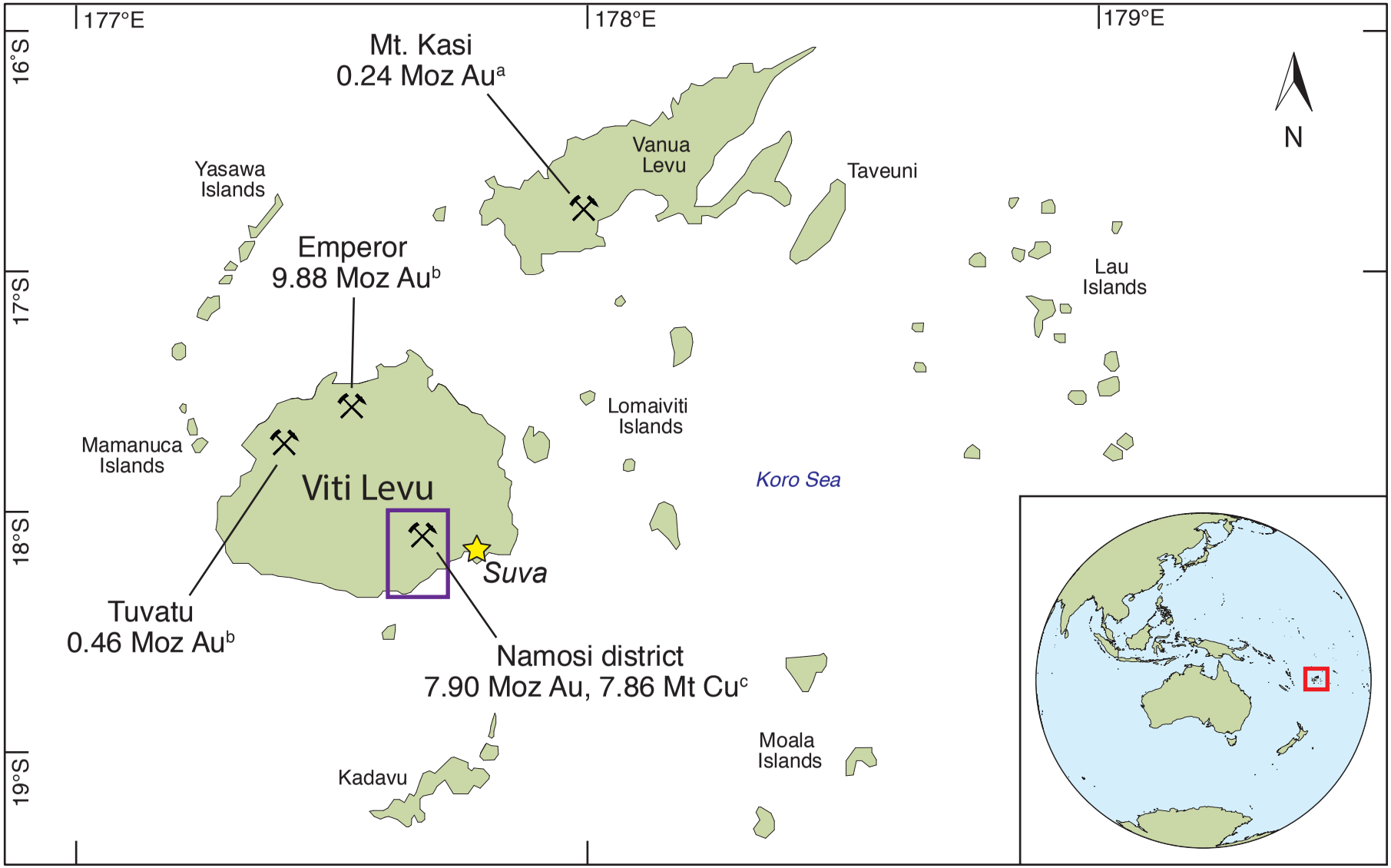


**Figure 1.1:** Map of the Fijian Archipelago showing the location of the Namosi district and other major mineral deposits. The purple box outlines Special Prospecting License area SPL1420, the field of view for Fig. 1.2. [a]Burkedin Pacific Ltd. (2005), [b]Scherbarth and Spry (2006), [c]Newcrest Mining Ltd. (2013).

British Columbia; Macquarie Arc, New South Wales), establishing constraints on the timespan of a porphyry district in a transient tectonic environment and providing exploration vectors within a complex geological setting.

The host sequence of the Namosi district porphyry deposits (Namosi Andesite Formation; NAF) was first analyzed by Taylor et al. (1969) and became the original 'andesite model' for the origin of continental crust. Following this model, Green (1972) and Green and Ringwood (1968) performed high-pressure experiments on these rocks to determine the origin of andesite by partial melting of subducted ocean floor basalts. Gill (1974) then used NAF rocks to demonstrate that such a process cannot explain suites of andesite. Furthermore, NAF rocks were amongst the first arc rocks analyzed isotopically (Gill and Compston, 1973) and were the first analyzed for all of Sr, Nd, and Pb isotopes (Gill, 1984). This thesis adds a detailed geological study of the NAF rocks and provides a revised depositional model, as well as documents the significant Cu, Au and Mo mineralization and hydrothermal alteration within the formation.

The largest deposits in the Namosi district are the Waisoi East and Waisoi West Cu-Au(-Mo) porphyry deposits (Fig. 1.2). Resource drilling shows that the Waisoi deposits can be classified as a giant (Singer, 1995) world class deposit, with a combined total resource of 2.1 Gt at 0.35 % Cu and 0.11 g/t Au (Newcrest Mining Limited, 2015). A smaller, and higher grade Cu-Au porphyry deposit occurs at Wainaulo in the Waivaka Corridor, a 5 km-long ENE-trending alignment of porphyry mineralization (Fig. 1.2). Wainaulo has an inferred resource of 94 Mt at 0.72 % Cu and 0.12 g/t Au (Newcrest Mining Limited, 2015). Another Cu-Au porphyry prospect at Wainabama (Fig. 1.2) has a probable resource of 22.9 Mt at 0.53 % Cu and 0.32 g/t Au (Morita et al., 2002). Epithermal Au-Ag-Pb-Zn veins, Fe-skarns, and many smaller Cu(-Au) porphyry prospects also occur within the district (Fig. 1.2). Currently, the Special Prospecting License for exploration in the Namosi district (SPL1420; Figs. 1.1 and 1.2) is owned by the Namosi Joint Venture (NJV), an unincorporated joint venture between Nittetsu Mining Company Limited, Mitsubishi Materials Corporation and Newcrest (Fiji) Limited (Newcrest Mining Limited). This project has been partly funded by Newcrest Min-

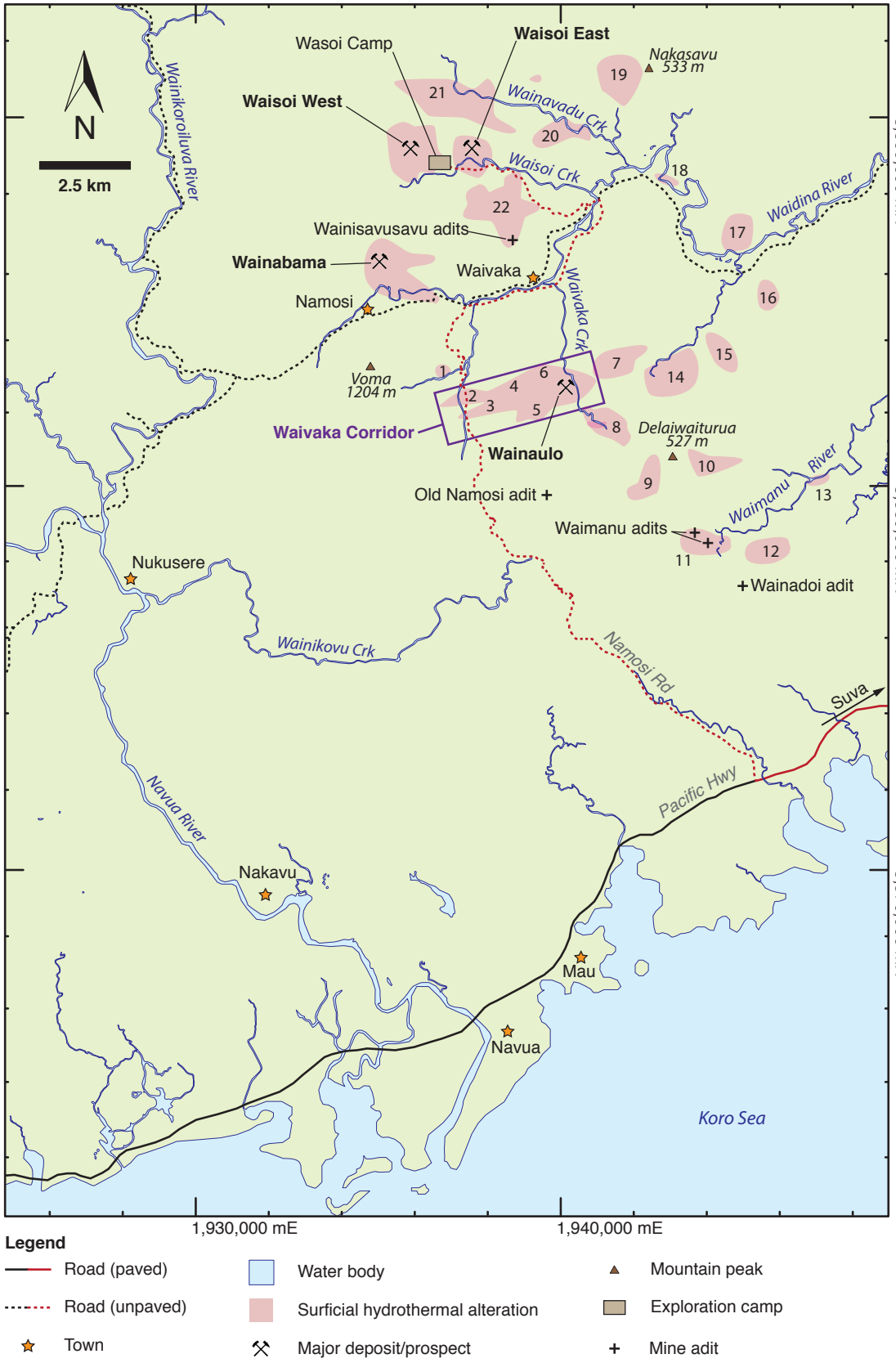


**Figure 1.2:** Location of porphyry Cu-Au(-Mo) deposits (Waisoi West, Waisoi East and Wainaulo) and ore prospects in the Namosi district. Field of view is equivalent to the area of Special Prospecting License SPL1420. Streams, roads, zones of hydrothermal alteration and the location of prospects and adits are from the Newcrest database. The access route to Waisoi exploration camp is highlighted in red. 1 = Wainitinikadua; 2 = Waivaka West; 3 = Wainkatama; 4 = Wainivisowaqa; 5 = Wainavuga; 6 = Wainaulo West; 7 = Wainikana; 8 = Waivaka South; 9 = Upper Waimanu and Delaiwaiturua; 10 = Waiturua; 11 = Wainiwi-Wainabau; 12 = Wainadoi Northeast; 13 = Waimanu Alluvials; 14 = Waisomo West; 15 = Waisomo Central; 16 = Waisomo East; 17 = Nowai; 18 = Naseuvou; 19 = Wainimoli; 20 = Waininiu; 21 = Wainavadu; 22 = Wainibavatu.

ing Limited, whose interest in the joint venture is 69.94 %.

## 1.2 Location and access

The Namosi district is located in the Namosi and Naitasiri provinces of southeastern Viti Levu, Republic of Fiji, approximately 30 kilometers west-northwest of the capital city of Suva (approximate coordinates are 18°00'S latitude and 178°10'E longitude; Fig. 1.1). Just 70 km northwest of Namosi is the Tavua Goldfield (Emperor), an epithermal Au-Ag deposit containing 27 Mt at 9.90 g/t Au (Mutschler et al., 1999). To the northeast is the Mt. Kasi high-sulfidation epithermal Au-Cu deposit (3.4 Mt at 2.2 g/t Au; Burdekin Pacific Ltd., 2005; Fig. 1.1).

Namosi has a tropical climate with temperatures ranging from 15 to 35°C and an annual rainfall of ~ 5500 mm per year. Most of the area is uninhabited and undeveloped and is covered by dense tropical rainforest. The jagged north-trending Korobasabasaga Ranges (Fig. 1.3A) transect the Namosi district and connect with the north-trending Nakauvadra Range further north. These mountains contain several peaks above 900 m, including Tomanivi (1,324 m) in northern Viti Levu and Mount Voma (1,204 m) in the Namosi area, which are the first and the third highest mountains in Fiji, respectively. Several major braided river systems have their headwaters in these central mountains, including the Navua and Waidina Rivers, which drain into the Koro Sea to the south. The Namosi district is centered on the upper reaches of the Waidina River and its tributaries.

Exploration in the Namosi district is based out of Namosi Joint Venture's Waisoi camp (Fig. 1.3B), which is about a two-hour drive from Suva airport (Fig. 1.2). The Waisoi camp is accessed from Suva by driving 25 km west-southwest along the Pacific Highway, then for 22 km to the north along Namosi Road (unpaved). At the end of Namosi Road, an unpaved road heads east along the southern bank of the Waidina River for about 6 km. After crossing the Waidina River, the Serea Laselevu Road (unpaved) leads to the Waisoi camp, on the northwestern bank of Waisoi Creek (Fig. 1.2).


**Figure 1.3:** Photographs of the Namosi area. **A.** Photo of four geologists admiring the Korobasabasaga Ranges and discussing the local geology. From left to right: Anthony Harris, Evan Orovan, Jarrod Fair and Mike Erceg. **B.** Photo of Waisoi exploration camp taken by the on-site helicopter pilot (photo: http://scottandkathieadventures.blogspot.com.au).

## 1.3 Previous work

Previous work in the Namosi district has been undertaken mainly for the purposes of mineral exploration. There have been several scientific studies that focuses on the Namosi district Cu porphyry deposits, including an MEconGeol (Master of Economic Geology) thesis by Ellis (1996), an MSc thesis by Egashira (2009), three peer-reviewed journal articles (Leggo, 1977; Imai, 2007; Tanaka et al., 2010), and a few additional journal articles that are untranslated from the original Japanese (Morita et al. 2002; Tanaka et al., 2003, 2004, 2006). The Mineral Resources Department (MRD) of Fiji has mapped the Namosi district at various scales and has provided descriptions of

the surficial geology and regional stratigraphy. Several of the MRD reports (e.g., Hirst, 1965; Rodda, 1966; Rodda and Band 1967; Band, 1968) mention occurrences of exposed metallic deposits in the area.

## 1.4 Thesis aims

The aims of this study are to:

1. Describe and discuss the lithology and geochemistry of the host sequence and mineralized intrusions of the Namosi district to constrain the tectonic setting of ore formation;

2. Document the spatial and temporal distribution of porphyry intrusions, hydrothermal alteration and Cu(-Au-Mo) mineralization;

3. Determine the absolute age of magmatism, alteration events and sulfide deposition within the Namosi district;

4. Constrain the physicochemical environment of ore deposition and related hydrothermal alteration; and

5. Synthesize results into a genetic model for the Namosi district and highlight aspects that may aid in exploration for calc-alkalic porphyry deposits in the southwest Pacific.

## 1.5 Methods

This PhD study included three field seasons in the Namosi district totaling twelve weeks (February 2011; May 2012; September 2013). Fieldwork consisted of detailed graphic logging of drill core from the Wainaulo, Wainaulo West, Waisoi East, Waisoi West, Waivaka West, Wainavuga and Wainabama porphyry deposits and exploration targets, surface geological mapping in the Waivaka Corridor, and sample collection. A principal objective of the fieldwork was the construction of representative cross sections through Waisoi East, Waisoi West, Wainaulo and Wainaulo

West, that document the geometry of the host stratigraphy, and the spatial distribution of porphyry intrusions, hydrothermal alteration and mineralization. In total, approximately 20 km of drill core was logged from 21 drill holes; details are summarized in Appendix A. Drill core logging followed the combined methods described in McPhie et al. (1993), Einaudi (1997), and Gifkins et al. (2005). Where possible, chip samples were collected at 5 m intervals during core logging for hyperspectral analyses. Representative samples of lithotypes, alteration and mineralization were also collected, both from drill core and at surface.

Extensive laboratory work was conducted on the collected samples in order to further characterize the lithotypes, and vein and alteration styles of the Namosi porphyry deposits. Detailed examination and photography of 150 polished thin sections was undertaken at CODES, University of Tasmania using transmitted and reflected light microscopy. Systematic staining for both potassium and calcium feldspars from polished rock slabs, thin section offcuts and drill core chip samples was also conducted at CODES, University of Tasmania. Quantitative X-ray diffraction (QXRD) analysis of 27 drill core samples was carried out at the University of Ballarat by Stafford McKnight. Over 500 SWIR spectra from chip and core samples were measured using a TerraSpec Hi-Res Mineral Spectrometer at CODES, University of Tasmania. The spectra were interpreted using The Spectral Geologist (TSG™) mineral library to aid in the differentiation of fine-grained phyllosilicates and the recognition of sulfates, carbonates and various other fine-grained and/or amorphous hydrous minerals (e.g., amphibole).

In order to constrain the tectonic setting of ore formation, studies of the whole-rock geochemistry and Sr–Nd isotope systematics of the host sequence and mineralized intrusive rocks of the Namosi district were undertaken. In total, 52 core and surface samples were analyzed by X-ray fluorescence (XRF) and inductively-coupled plasma mass spectrometry (ICP-MS) at Acme Analytical Laboratories Ltd. in Vancouver, Canada. Strontium–neodymium isotope analyses were conducted at the University of Melbourne, Australia, by Dr. Roland Maas.

Geochronological studies were undertaken in order to determine the absolute age of magmatism, alteration events and sulfide deposition. Uranium–lead dating of zircon was performed

using two different methods: 1) excimer laser ablation inductively-coupled plasma mass spectrometry (ELA-ICP-MS; Research School of Earth Sciences, Australian National University, Dr. Charlotte Allen), and 2) chemical ablation thermal ionization mass spectrometry (CA-TIMS; Pacific Centre for Isotopic and Geochemical Research, University of British Columbia; Dr. Richard Friedman). Re–Os age determinations of molybdenite were conducted at the Radiogenic Isotope Facility, University of Alberta, by Dr. Robert Creaser.

Stable and radiogenic isotope analyses were conducted in order to constrain the physicochemical environment of ore deposition and related hydrothermal alteration. Sulfur isotope analyses were performed at the Central Science Laboratory (CSL), University of Tasmania, Australia. Oxygen and deuterium isotope analyses were carried out at GNS Stable Isotope Laboratory, New Zealand. Strontium isotope analyses were conducted at the University of Melbourne, Australia, by Dr. Roland Maas.

### 1.6 Thesis Organization

This thesis comprises seven chapters. They are structured as follows:

**Chapter 2 (Regional geology)** provides an introduction to the regional geology and tectonic setting of the Namosi district and proposes a new tectono-metallogenic model for the Fijian calc-alkalic and alkalic porphyry-epithermal deposits. Components of this chapter were incorporated into an Economic Geology Special Publication research paper titled "Volcanotectonic setting of world-class alkalic porphyry and epithermal Au ± Cu deposits of the southwest Pacific" (Harris et al., 2013).

**Chapter 3 (Geology and geochronology)** documents the geology of the Namosi district, based on fieldwork completed by the author. Detailed descriptions of the host volcano-sedimentary succession (twelve lithofacies) and intrusive rocks (fourteen phases) are provided, and interpretations of the geometric relationships amongst the rock units are presented on two new geological maps and on four new geological cross sections. This is followed by an interpretation

of the paleoenvironment and geological evolution of the district before and during the period of porphyry ore formation. Geochronological constraints on the absolute timing of magmatism (five CA-TIMS U–Pb ages and four ELA-ICP-MS U–Pb ages) associated with the Wainaulo, Waisoi West and Waisoi East porphyry deposits are used to discuss the temporal relationships of ore-related magmatic activity, the absolute duration of magmatic-hydrothermal events, and the geological evolution of the district.

**Chapter 4 (Igneous geochemistry)** describes and discusses the whole-rock geochemistry and isotope composition of the volcanic and igneous rocks in the Namosi district, based on the results of 52 new whole-rock geochemical analyses and five whole-rock Sr–Nd isotope analyses. The results are compared with regional igneous geochemical datasets for the southwest Pacific area in order to place additional constraints on the tectonic setting of Namosi and the possible sources of magma for igneous activity in the district over time.

**Chapter 5 (Alteration and mineralization)** documents the paragenesis and absolute timing of hydrothermal alteration and mineralization associated with the principal deposits in the Namosi district. In total, twelve alteration types and thirteen vein stages were identified and documented for Wainaulo, six alteration types and eight vein stages were identified and documented for Waisoi West, and nine alteration types and eight vein stages were identified and documented for Waisoi East. These alteration and vein stages are summarized in comprehensive space-time plots. Vein and alteration distribution sections are presented, which were compiled using systematic hand specimen and thin section observations, feldspar staining, quantitative XRD, SWIR and Corescan hyperspectral core imaging. This chapter also presents three new Re–Os age dates for molybdenite associated with mineralizing events, which provide additional evidence for a genetic link between mineralization and progenitor intrusions. Components of this chapter were included in an extended abstract for the PACRIM 2015 Congress titled “Mineral Footprints to Porphyry Cu-Au Deposits – Enhanced Ore Deposit Models Using High-resolution VNIR-SWIR Core Logging” (Harris et al., 2015).

**Chapter 6 (Hydrothermal geochemistry)** documents the stable and radiogenic isotope compositions of the Namosi district porphyry deposits and uses this data to infer the physicochemical environment of ore deposition and hydrothermal alteration. The evolution of the fluid chemistry with time and its relation to fluid sources is discussed. For Waisoi East, one oxygen–deuterium isotope analysis for zeolite, two oxygen–deuterium analyses for illite, and ten sulfur isotope analyses for pyrite are presented. For Waisoi West, thirteen sulfur isotope analyses on sulfides [pyrite (n = 6), chalcopyrite (n = 3) and bornite (n = 1)] and two sulfur isotope analyses on sulfate (anhydrite) are presented. For Wainaulo, nine oxygen–deuterium analyses for epidote, one oxygen isotope analysis for anhydrite, 24 sulfur isotope analyses on sulfides (pyrite (n = 18), chalcopyrite (n = 5) and bornite (n = 1)) and 22 sulfur isotope analyses on sulfates (gypsum (n = 8) and anhydrite (n = 14)), and five Sr isotope analyses on talc-phlogopite (n = 1), epidote (n = 3) and anhydrite (n = 1), are presented.

**Chapter 7 (Genetic model and conclusions)** presents a synthesis of the preceding chapters and proposes deposit- and district-scale genetic models for the formation of the Namosi porphyry deposits. This is followed by a discussion of the implications of this study for exploration of calc-alkalic deposits in the southwest Pacific and recommendations for future research.

# CHAPTER 2

# Regional geology

## 2.1 Introduction

This chapter introduces the tectonic and geological setting of the Namosi porphyry district. It provides a regional framework for geology and geochronology (Chapter 3), igneous geochemistry (Chapter 4), and genetic interpretations of the Namosi district porphyry deposits (Chapter 7). The Namosi district is located on Viti Levu Island within the Fiji Platform (Fig. 2.1C), a curvilinear belt of thickened crust (15 – 25 km thick; Hamburger et al., 1988) that has created a zone of relatively shallow water (< 2 km deep; Taylor et al., 2000) surrounding the islands of the Fijian Archipelago (Figs. 2.1C and D).

## 2.2 Geological history of Viti Levu

During the Middle Eocene (~ 43 Ma) there was a change in the direction of absolute Pacific Plate motion from northwards to westwards (Clague and Dalrymple, 1989). This resulted in the creation of new subduction zones along the western margin of the Pacific Plate (Hilde et al., 1977; Kroenke, 1984). South of the equator, west- to southwest-dipping subduction of the Pacific Plate beneath the Indo-Australian Plate generated the Outer Melanesian Arc, which included the New Guinea-Manus-Kilinailau-North Solomon Arc to the north and the Solomon-Vanuatu-Fiji-Tonga Arc (Vitiaz Arc) to the south (Fig. 2.1A). Remnants from the early stages of Vitiaz Arc formation can be found as basement rocks in Fiji and Tonga and in clasts of Late Oligocene sediments in Vanuatu (Ewart and Bryan, 1972; Coleman and Packham, 1976; Gill, 1976; Carney and Macfarlane, 1978; Gill, 1987; Hathway and Colley, 1994; Tappin and Ballance, 1994). Within Fiji, early Vitiaz Arc rocks comprise reef limestones (Late Eocene; Hathway, 1994), tholeiitic and boninitic pillows, dikes and lava flows (32 – 29 Ma; Whalen et al., 1985; Todd, 2011) and tonalite-trondh-

jemite stocks of the Yavuna Group (~ 37 to 31 Ma; Fig. 2.2; Whalen et al., 1985; Rodda, 1994; Wharton et al., 1995). At ~ 35 Ma the Vitiaz Arc began to rift along its length south of Fiji forming the South Fiji Basin (Weissel, 1981; Davey, 1982; Malahoff et al., 1982; Crawford et al., 2003; Sdrolias et al., 2003; Todd, 2011). Backarc spreading in the South Fiji Basin ceased at ~ 25 Ma (Whalen et al., 1985; Crawford et al., 2003; Sdrolias et al., 2003).

After 28 Ma, relative movement of the Pacific and Indo-Australian Plates became more obliquely convergent (Neall and Trewick, 2008), which resulted in the generation of low- to medium-K arc tholeiitic pillow basalt lavas, dacites, subvolcanic intrusions, volcaniclastics and tuffs of the Wainimala Group (Gill, 1987). The Wainimala Group unconformably overlies the Yavuna Group and is exposed in southern and western Viti Levu as well as on a number of the surrounding smaller islands, including the Mamanuca, Lau and Yasawa Islands (Fig. 2.2). Volcanics and sediments of the Wainimala Group built up a segment of the Vitiaz Arc that is referred to as the Wainimala Arc (Rodda, 1994). Wharton et al. (1995) reported two K–Ar dates from Kawa Formation andesite clasts (basal Wainimala Group) of 28.1 ± 0.6 Ma and 23.6 ± 0.5 Ma. The youngest Wainimala Group rocks are 12.0 ± 0.1 Ma hornblende andesite dikes that occur near Nadi (Rodda, 1994). The Sigatoka Group rocks, exposed in southwestern Viti Levu, were deposited synchronously with the Wainimala Group volcanics, in the forearc basin to the north of the developing Wainimala Arc (Fig. 2.2; Hathway and Colley, 1994; Johnson, 1994). The Savura Group overlies the Wainimala Group volcanics in southeast Viti Levu (Rodda, 1967). These rocks have a similar magmatic affinity (low-K tholeiitic), isotopic signature (Sr, Nd) and age (~ 15 Ma) as the Wainimala Group volcanics; however, they consist of mainly felsic volcano-sedimentary rocks with subordinate andesites and basalts (Crawford, 2011).

In the Late Oligocene to Middle Miocene, two large igneous provinces—the Ontong Java Plateau and the Melanesian Border Plateau (aka. the North Melanesian Borderlands; Fig. 2.1)—collided with the Vitiaz Trench, slowly locking up the subduction margin north of the Fiji Platform. The precise timings of the collisions are uncertain. Kroenke (1972, 1984), Bruns et al. (1989), Petterson et al. (1997) and Crawford et al. (2003) suggested that the Ontong Java Plateau – Solomon

Trench collision may have commenced as early as 25 – 20 Ma; whereas, the Melanesian Border Plateau may have collided with the Vitiaz Trench closer to ~ 10 Ma (Wortel et al., 2009). The effects of blocking and compression resulting from the collisions were not prominent in Fiji until ~ 10 Ma (Wessel and Kroenke, 2000; Crawford et al., 2003) and included the cessation of Wainimala Group volcanism, compressional deformation (Colo Orogeny; Colley and Greenbaum, 1980) and synorogenic plutonism (Colo Plutonic Suite; Rodda, 1967; Band, 1968; Rodda and Kroenke, 1984). The Colo Orogeny folded the strata of the Yavuna, Wainimala, Sigatoka and Savura Groups into an arcuate, east-northeast-striking anticlinorium known as the Wainimala Oroclinal Flexure (Fig. 2.2; Colley and Greenbaum, 1980). Colo Plutonic Suite (CPS) plutonism was focused along the axis of the Wainimala Arc and intruded along the cores of anticlines resulting in elongate plutonic bodies that approximate the axial trace of the Wainimala Oroclinal Flexure (Fig. 2.2). The CPS plutons can be divided into two main suites, a low-K suite ranging in composition from noritic gabbro to diorite (~12 – 10 Ma) and a medium-K suite that consists of tonalite-trondhjemite intrusions (~ 9 – 7 Ma; Whalen et al., 1985; Crawford, 2011).

Continued convergence across the choked Vitiaz Trench north of Fiji eventually resulted in a reversal of arc polarity. The west-southwest-directed component of Pacific Plate subduction terminated and an arcuate, mainly northeast-directed subduction zone was initiated (~ 12 – 10 Ma; Figs. 2.1A and B; Hamburger and Isacks, 1988; Auzende et al., 1995). This subduction zone extended along the western margin of the Vanuatu Arc and continued along an arcuate path to the southeastern margin of the Fiji Platform, occupying the area that is now known as the Hunter Fracture Zone (Figs. 2.1B and C; Auzende et al., 1995; Crawford, 2003; Martin, 2013). Westward-directed subduction continued along the Tonga – Kermadec Trench from the Tonga Arc to New Zealand (Fig. 2.1).

After the subduction polarity inversion, seafloor spreading was initiated in the backarc to the newly formed, curvilinear Vanuatu – Fiji Trench, near the junction between the Vanuatu Arc and Fiji Platform (Fig. 2.1). Seafloor spreading propagated northeast and northwest, parallel to the arcs, separating them from the fossil Vitiaz Trench (Fig. 2.1B). These conjugate branches of sea-

floor spreading opened in a fan shape towards the south, resulting in inward and opposite rotations of the Vanuatu Arc (clockwise) and Fiji Platform (counterclockwise; e.g., Falvey, 1978; Malahoff et al., 1982; Inokuchi et al., 1992; Musgrave and Firth, 1999; Taylor et al., 2000; Crawford, 2003; Martin, 2013). The fan-shaped seafloor spreading developed in response to slab rollback at the maximum point of curvature along the arcuate Vanuatu – Fiji Trench (Martin, 2013, 2014). The geometry of the fanning, arc-parallel spreading centers necessitated the development of a third, north-trending (arc perpendicular) spreading center at their point of intersection. This new spreading center propagated to the north and south, exaggerating the curvature of the concave-north Vanuatu – Fiji subduction zone (Figs. 2.1B and C; Martin, 2013). As seafloor spreading continued, the backarc region expanded into a large triangular area of oceanic crust, known as the North Fiji Basin (Figs. 2.1C and D).

Continued counterclockwise rotation of the Fiji Platform corresponded with medium-K, calc-alkalic volcanism of the Medrausucu Group (specifically, the Namosi Andesite Formation) in southeastern Viti Levu (~ 6.0 Ma; Fig. 2.2; Gill et al., 1984). It has been argued that Namosi Andesite Formation (NAF) volcanism was geographically separated from active subduction during the Late Miocene (e.g., Gill, 1984; Crawford, 2011); however, NAF rocks have been shown to have the geochemical characteristics of subduction-related volcanism (e.g., Gill, 1981; Pearce, 1982; Gill et al., 1984). Some authors argue that continued convergence across the Fiji portion of the Vitiaz Arc generated these arc-like calc-alkalic magmas in Fiji (Gill et al., 1984; Rodda and Kroenke, 1984; Gill and Whelan, 1989a). The NAF rocks occur in an area of about 200 km$^2$, consisting of breccias and tuffs and approximately 30 km$^2$ of lavas (Gill, 1987). The thickest part of the sequence is up to 1.5 km thick (Rodda, 1976). Volcanism may have occurred in a shallow sub-

**Figure 2.1 (opposite):** Tectonic history of Fiji. **A.** Tectonic reconstruction of the Fiji area during the Eocene to Middle Miocene, showing the location of the low-K tholeiitic Vitiaz Arc (aka. Wainimala Arc in Fiji), which formed during westward subduction of the Pacific Plate beneath the Indo-Australian Plate. **B.** Tectonic reconstruction at ~ 5.5 Ma, after the Melanesian Border Plateau had collided with the Vitiaz Trench, which lead to a reversal in arc polarity north of Fiji and the opening of the North Fiji Basin. The Namosi porphyry Cu-Au(-Mo) deposits were emplaced at this time coincident with the onset of shoshonitic volcanism in the north of Viti Levu. **C.** Present-day tectonic setting of Fiji, Vanuatu and Tonga. The light blue shaded areas represent submarine depths of less than 2 km. Diagrams A, B and C are modified from Gill and Whelan (1989b), Hathway (1993), Hawkins (1995), Auzende et al. (1996), and Schellart et al. (2006). **D.** Map showing the location of the Fiji Islands along the western Pacific Rim, which can be traced by seismic activity. Seismic data show westward subduction of the Pacific Plate along the Tonga-Kermadec Trench east and southeast of Fiji, and eastward subduction of the Indo-Australian Plate along the New Hebrides (Vanuatu) Trench west, southwest and northwest of Fiji. This map was produced using GeoMapApp (geomapapp.org) with topography data from Ryan et al. (2009) and seismic data from the International Seismological Centre (2009). The magnitude of the earthquakes shown range from 5 to 9 and the data were collected during the years from 1964 – 1995. Green data points correspond to hypocenter depths < 50 km, yellow data points correspond to hypocenter depths from 50 – 250 km, and red data points correspond to hypocenter depths > 250 km. Abbreviations: FP = Fiji Platform, HFZ = Hunter Fracture Zone, LCR = Lau-Colville Ridge, MBP = Melanesian Border Plateau, MHR = Matthew-Hunter Ridge, NHR = New Hebrides Ridge, TKR = Tonga-Kermadec Ridge.

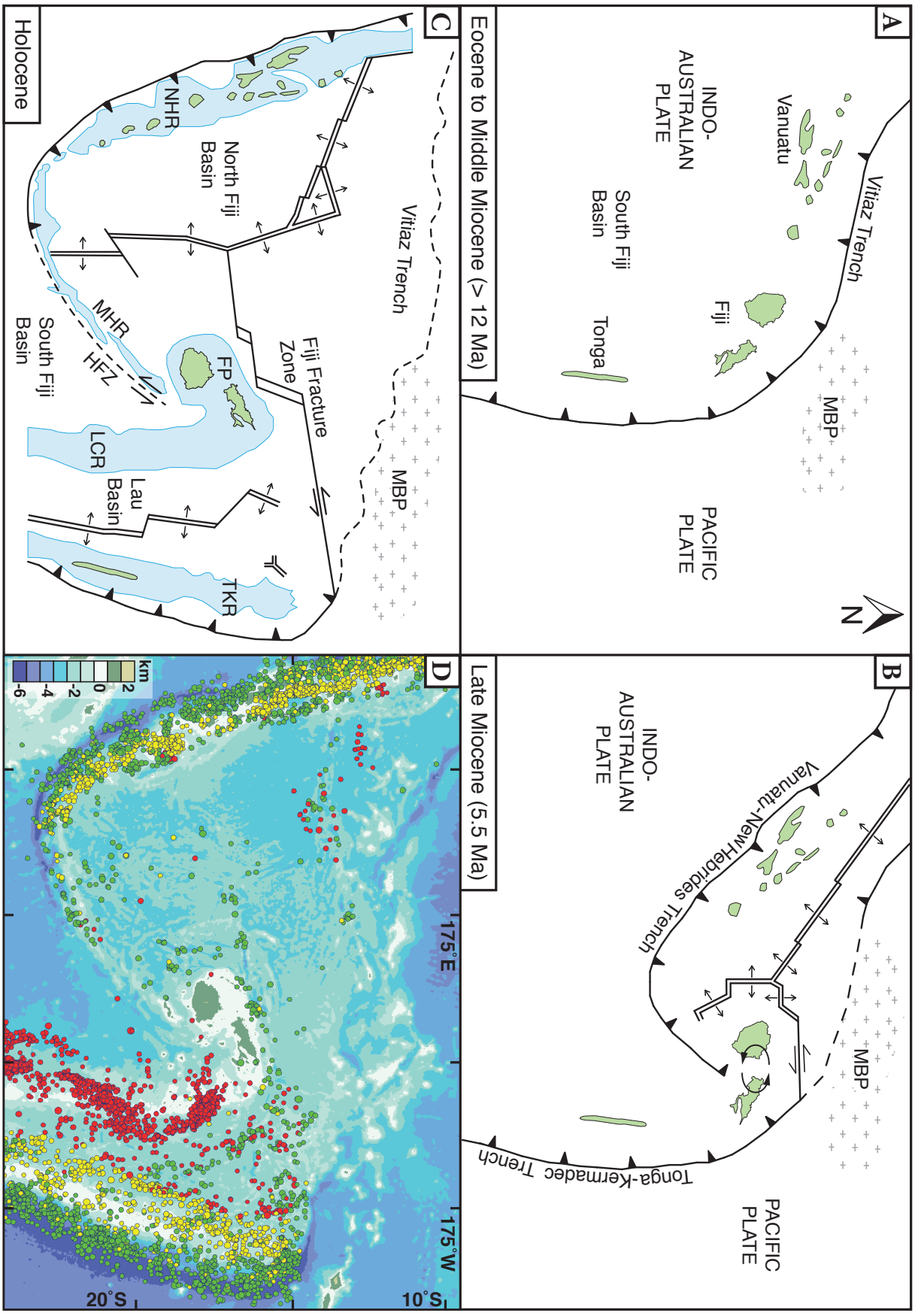
A
Eocene to Middle Miocene (> 12 Ma)
Vitiaz Trench
Vanuatu
Fiji
Tonga
South Fiji Basin
INDO-AUSTRALIAN PLATE
PACIFIC PLATE
MBP
N
B
Late Miocene (5.5 Ma)
Vanuatu-New Hebrides Trench
Tonga-Kermadec Trench
INDO-AUSTRALIAN PLATE
PACIFIC PLATE
MBP
C
Holocene
Vitiaz Trench
North Fiji Basin
NHR
MHR
HFZ
South Fiji Basin
Fiji Fracture Zone
FP
LCR
Lau Basin
TKR
MBP
D
175°E
175°W
20°S
10°S
km
2
0
-2
-4
-6

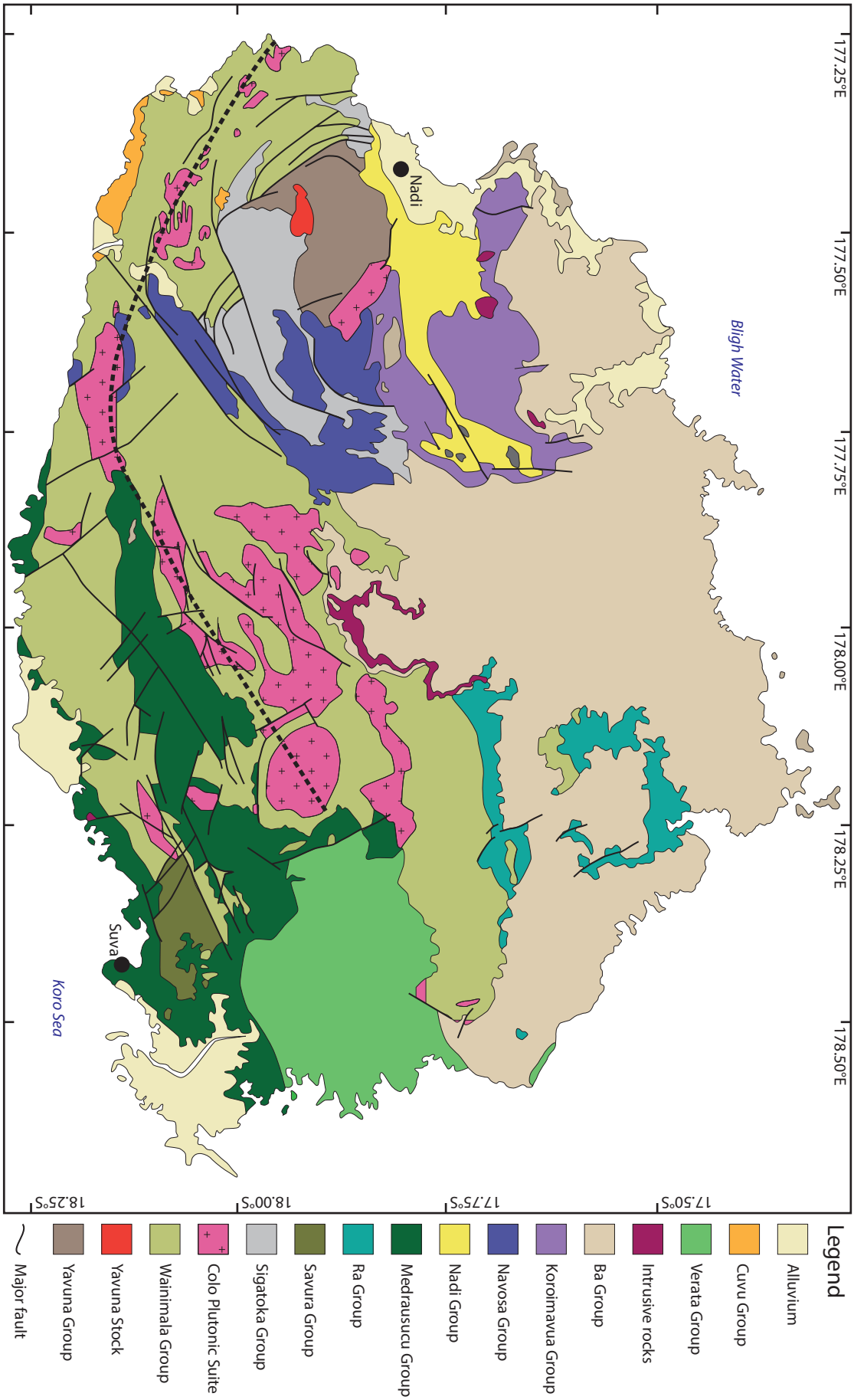


**Figure 2.2:** Simplified geological map of Viti Levu, Fiji. Modified from Rodda (1967). Black dashed line is the trace of the Wainimala Orocline Flexure.

marine to subaerial environment based on the gradual facies changes from lavas to marine volcaniclastics and the high breccia to lava ratio (Gill, 1987). Contemporaneous with the Late Miocene volcanism was widespread sedimentation. The NAF sediments were deposited in predominantly elongate basins, which formed as a result of strike-slip faulting related to the rotation of the Fiji Platform (Hathway, 1993; Hathway and Colley, 1994; Johnson, 1994). The onshore expression of these basins are the Navosa, Verata and Medrausucu Group sediments of the Nadi, Sovi and Navua basins in Viti Levu (Fig. 2.2; Hathway, 1993).

At ~ 5.5 Ma, there was a transition from medium-K calc-alkalic magmatism in southeastern Viti Levu to high-K calc-alkalic and shoshonitic volcanism (Koroimavua and Ba Groups) in northern Viti Levu (Fig. 2.2; McDougall, 1963; Gill and McDougall, 1973; Whalen et al., 1985). The widespread shoshonitic volcanism occurred during the opening of the Lau backarc basin to the east of Fiji (e.g., Hawkins, 1995) and maximum rotation of the Fiji Platform (e.g., Begg and Gray, 2002). The north-trending Lau Basin split the northern edge of the Tonga Arc into two segments: Lau-Colville Ridge to the west and Tonga-Kermadec Ridge to the east (Fig. 2.1C). Active rifting of the Fijian lithosphere behind the Lau-Colville Ridge has been occurring since the Pliocene, producing a complex of spreading centers, triple junctions, and diffuse left-lateral transform faults (Fig. 2.1C; Crawford et al., 2003). At 3 Ma, the Lau backarc basin shifted from rifting to active spreading, leaving Fiji as part of a remnant arc (Gill and Whelan, 1989b).

Rotation of the Fiji Platform totaled greater than 100° before it abruptly ceased at 1.56 Ma, when the Fiji Platform collided with the Lau Ridge (Malahoff et al., 1982; Taylor, 2000; Crawford, 2011; Martin, 2013). When the Fiji Platform stopped rotating, north-northwest-directed subduction ceased south of Fiji and transform motion initiated along the Hunter Fracture Zone (Martin, 2013). Since then the sinistral Hunter Fracture Zone has acted as a subduction transform edge propagator (cf. Pelletier et al., 2001; Ruellan and Lagabrielle, 2005; Govers and Wortel, 2005; Martin, 2013), connecting the southern Vanuatu and northern Tonga subduction zones. The Vanuatu Arc has rotated ≥ 40° clockwise according to paleomagnetic data interpreted by Musgrave and Firth (1999), and is continuing to rotate in a clockwise direction today (Calmant et al., 1995,

2003; Taylor et al., 1995). The Vanuatu Arc collided with the D'Entrecasteaux Ridge from 3.0 to 1.7 Ma and with West Torres Platform from 0.7 Ma to present-day (Collot et al., 1992; Greene and Collot, 1994; Meffre and Crawford, 2001; Schellart et al., 2002), slowing but not stopping rotation of the Vanuatu Arc (Martin, 2013).

The eruption of alkalic OIB-type rocks marked the final dissociation of the Fiji Islands from active subduction. The transition in volcanic activity to a non-arc intraplate variety may have occurred in response to rapid backarc spreading in the Lau Basin that promoted decompression melting of upwelling asthenosphere (Leslie, 2004). Alternatively, the alkali OIB-type rocks may reflect the migration of sub-Pacific mantle sourced from the Samoa Hot Spot to Fiji, Lau and North Fiji Basins (Gill and Whalen, 1989b). The OIB-type rocks of the Fiji Platform crop out on the Lau Islands and on Vanua Levu (Crawford, 2011). The oldest known Fijian alkali OIB-type rocks are from Seatura Volcano on Vanua Levu (~ 3.3 Ma; Whelan et al., 1985), and the most recent activity has occurred on Taveuni Island ~ 2,050 ± 150 years ago (Kroenke, 1984).

### 2.3 Current tectonic configuration of the Fiji area

Currently the Fiji Islands are situated at the northern tip of the 2,400 km-long submarine Lau-Colville Ridge and are comprised of two main islands, Viti Levu and Vanua Levu, which are encircled by smaller islands of the Kadavu Island Group, the Lomaiviti Group and the Lau Island Group, as well as other emergent features including atolls and seamounts (Fig. 2.1). The Fiji Islands are flanked by two extensional backarc basins: the North Fiji Basin to the west and the Lau Basin to the east. These basins, along with a complex series of transform faults (North Fiji and Hunter Fracture Zones), separate Fiji from two opposing convergent zones: the Tonga – Kermadec and Vanuatu arc-trench systems (Figs. 2.1 and 2.3). Seismic activity related to the Tonga – Kermadec subduction zone can be traced to a depth of 700 km and has a moderate (~ 45 – 50°) dip to the west-northwest (section C – D; Fig. 2.3). The Tongan seismogenic zone abruptly ends north of the Fiji Platform (section E – F and plan section; Fig. 2.3) where the Melanesian Border Plateau collided with the Vitiaz Trench (Fig. 2.1). The Vanuatu subduction zone is associated with

shallow seismicity (< 350 km depth) and steep (~ 55 – 70°) dips to the east-northeast. The Vanuatu seismogenic zone becomes shallow (< 100 km) southwest of Fiji at the intersection of the active Vanuatu and fossil Hunter subduction systems (section A – B; Fig. 2.3).

Evidence for short-lived north-directed subduction of a concave Indo-Australian slab south of Fiji includes the distribution of earthquake hypocenters (e.g., Chen and Brudzinski, 2001), slices from a tomographic model at 200 km and 320 km depth (Hall and Spakman, 2002), Vp/Vs tomographic images at depths from 100 to 250 km (Conder and Wiens, 2006) and the intra-oceanic island arc geochemical signature of the submarine Matthew-Hunter Ridge (Fig. 2.1C; Crawford and Verbeeten, 2000; Crawford et al., 2003; Danyushevsky et al., 2008; Crawford, 2011). The seismic data presented in Figure 2.3 can be interpreted to show this detached semi-concave north slab abutting the downgoing Tonga slab at ~ 350 – 400 km depth. I propose that the slab has a low-angle (25°) dip component to the north-northwest at its eastern extent (section E – F; seismic anomalies are visible as deep as 400 km; Fig. 2.3), where the slab would have underlain the Fiji Platform in the Late Miocene (Fig. 2.1C). This low-angle subduction may have been an important driver in the generation of porphyry deposits of the Namosi district (cf. Cooke et al., 2005) and NAF magmatism. Previous models relate NAF magmatism to southwest-directed subduction of the Pacific Plate along the Vitiaz Trench (e.g., Gill et al., 1984; Rodda and Kroenke, 1984; Gill and Whelan, 1989a) or to intraplate processes (e.g., Gill, 1984; Crawford, 2011). The dip of the slab steepens to the west-southwest, where seismic anomalies are visible as deep as 600 km, likely reflecting the increasing influence of slab rollback towards the point of maximum curvature in the fossil Vanuatu – Fiji Platform Trench (section G – H; Fig. 2.3).

It has long been recognized that there is a seismic anomaly beneath the North Fiji Basin consisting of a flat cluster of deep (~ 550 – 650 km) earthquake hypocenters (e.g., Sykes, 1964; Dubois et al., 1973; Hanus and Vanek, 1981, 1983; Hamburger and Isacks, 1985; Cooper and Kroenke, 1994; Brudzinski and Chen, 2003; Richards, 2011). Most authors conclude that the seismic anomaly relates to a foundered, detached slab from either the fossil Vitiaz or active Vanuatu subduction systems. Based on the plan section for depths > 550 km (Fig. 2.3), the seismic anomaly

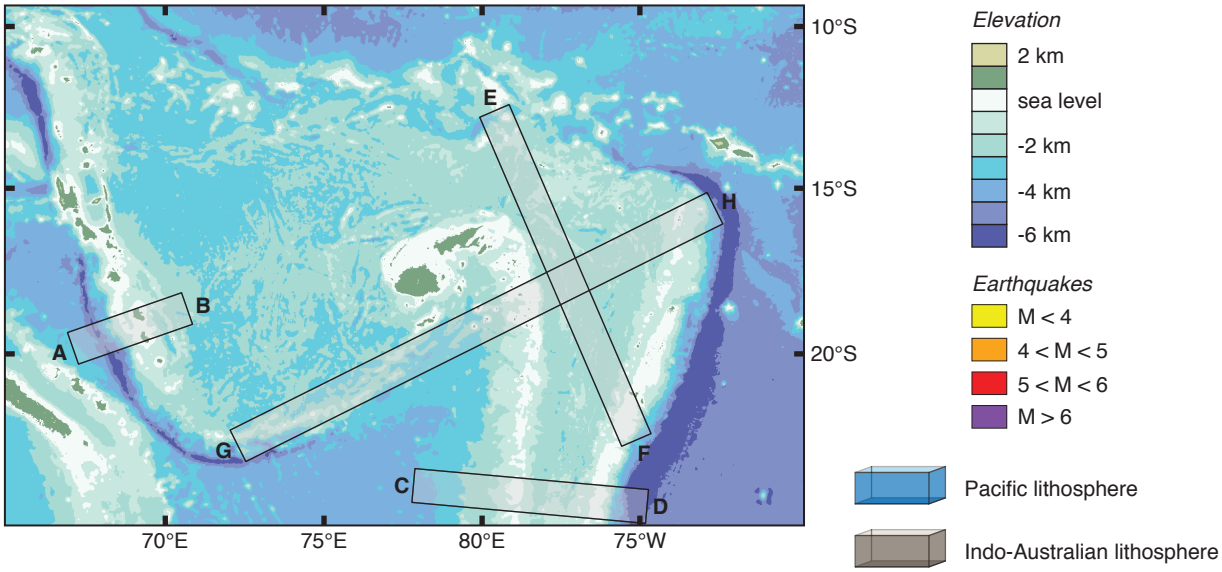
10°S
15°S
20°S
70°E
75°E
80°E
75°W
A
B
C
D
E
F
G
H
Elevation
2 km
sea level
-2 km
-4 km
-6 km
Earthquakes
M < 4
4 < M < 5
5 < M < 6
M > 6
Pacific lithosphere
Indo-Australian lithosphere

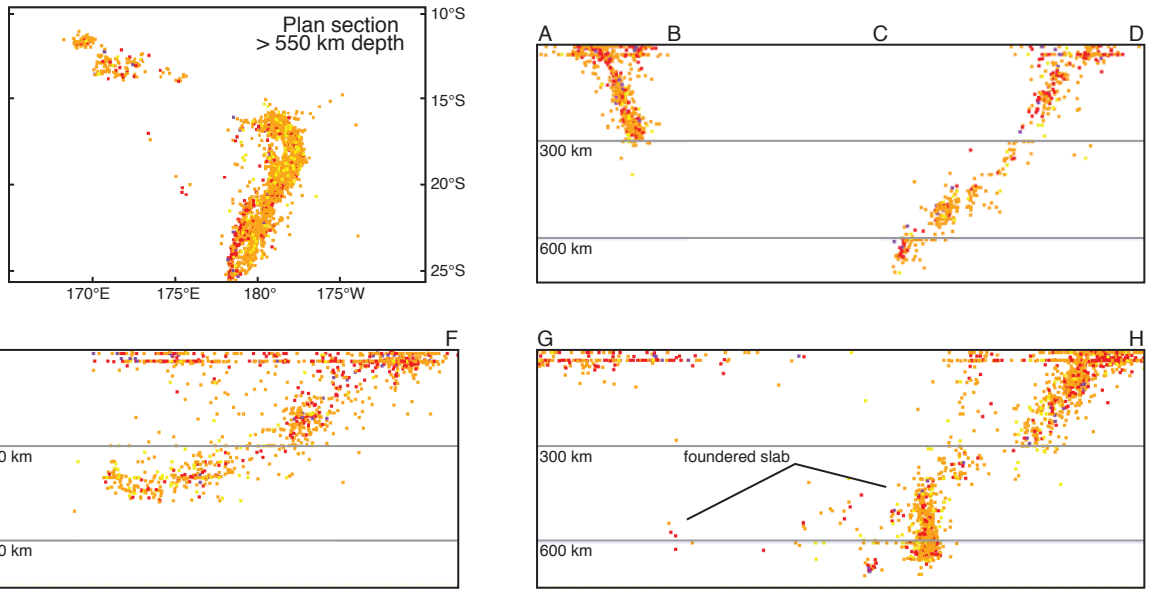
Plan section
> 550 km depth
10°S
15°S
20°S
25°S
170°E
175°E
180°
175°W
A
B
C
D
300 km
600 km
E
F
G
H
foundered slab

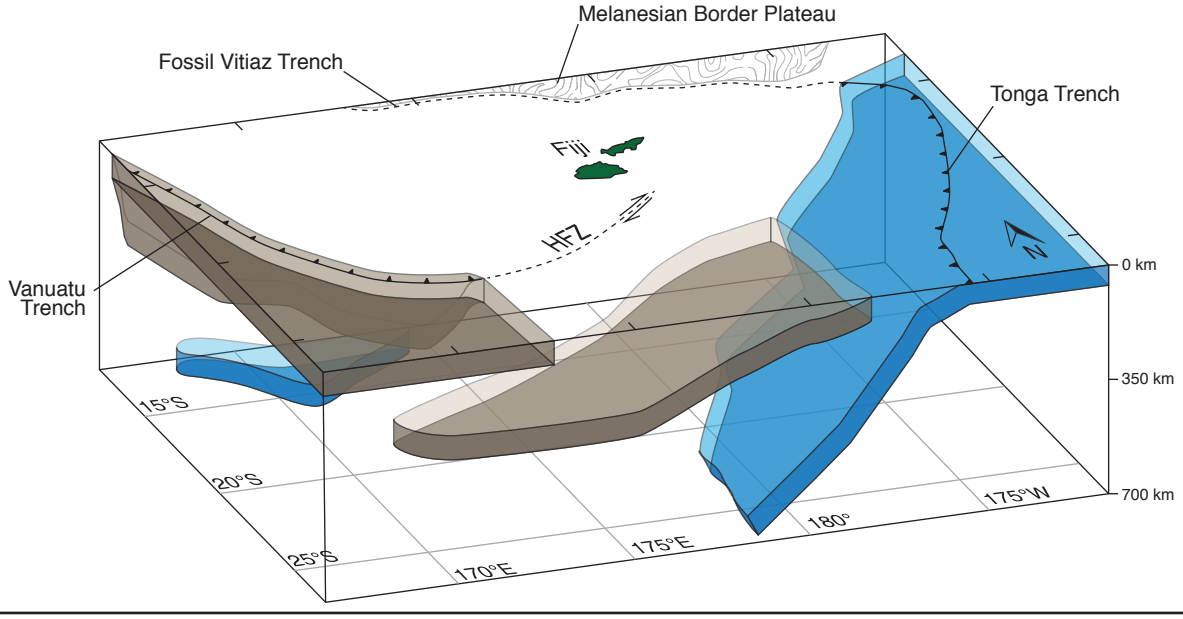
Melanesian Border Plateau
Fossil Vitiaz Trench
Tonga Trench
Fiji
HFZ
Vanuatu
Trench
0 km
350 km
700 km
15°S
20°S
25°S
170°E
175°E
180°
175°W

**Figure 2.3 (opposite):** Four representative seismicity sections and a 3D block model illustrating the subduction geometry in the Fiji area. The seismic data show two oppositely and steeply dipping active subduction zones on either side of Fiji: the east-northeast-dipping Vanuatu subduction zone (A – B) and the west-northwest-dipping Tonga subduction zone (C – D). The Tongan seismogenic domain abruptly ends north of the Fiji Platform, below the fossil Vitiaz Trench (E – F). Also interpreted from the seismic data is an orphaned concave-north slab of South Fiji Basin (Indo-Australian) lithosphere (G – H) that has a low-angle northwestward dip and flat-slab component adjacent to the westward-dipping Pacific Plate (E – F). A cluster of deep earthquake hypocenters (550 – 650 km) near 13°S and 170°E are interpreted to delineate a foundered, detached segment of the Pacific Plate associated with the currently inactive Vitiaz subduction system (see plan-view seismicity section). Earthquake hypocenters are from the USGS catalogue (from the years 1950 to 2010 and all magnitudes). The bathymetric map was produced using GeoMapApp (geomapapp.org), using topography data from Ryan et al. (2009). Some components of the block model are modified after Brudzinki and Chen, 2003. Abbreviations: M = earthquake magnitude.

appears to represent a detached slab from the south-southwest-directed fossil Vitiaz subduction system that originated near the western margin of the region where the Melanesian Border Plateau – Vitiaz trench collision occurred.

## 2.4 Structural geology of southeastern Viti Levu

Rahiman and Pettinga (2008) completed a structural study of southeastern Viti Levu, in which they compared interpretations made from remote sensing images (i.e., side-looking airborne radar maps, a digital terrain model, aeromagnetic maps and vertical aerial photographs) with mapped surface faults that were identified during Fiji Geological Survey field mapping campaigns between 1960 and 1970 (Ibbotson, 1960; Houtz, 1960, 1962; Rodda and Band, 1966; Band, 1967a, 1967b, 1967c; Hirst, 1967; Rodda, 1970). The study reported six major fault zones in southeastern Viti Levu: 1) Sovi Fault Zone, 2) Yarawa Fault Zone, 3) Mavuva Fault Zone, 4) WWW Fault Zone, 5) Mauivuso Fault Zone, and 6) Suva Fault zone (Fig. 2.4). The WWW Fault Zone is inferred here to be equivalent to the Waimanu – Wainivakindau – Wainiveisolekau fault system reported by Band (1968). Rahiman and Pettinga (2008) identified a positive statistical correlation between the trends of the lineaments interpreted from remote sensing images and the trends of faults and fractures that were mapped in the field.

The Namosi district porphyry deposits occur within a zone of overlap between the WWW and Mauivuso Fault Zones (Fig. 2.4). In particular, the Waivaka Corridor porphyry deposits (e.g., Wainaulo, Wainivuga and Waivaka West) lie along major steeply-dipping, ENE-trending faults of the WWW Fault Zone and their alteration footprints are elongated along a similar orientation (~ 075°; Fig. 2.4). Waisoi East, Waisoi West and Wainabama occur close to major NW-trending faults of the Mauivuso Fault Zone (Fig. 2.4). Sense of shear data for faults in southeastern Viti

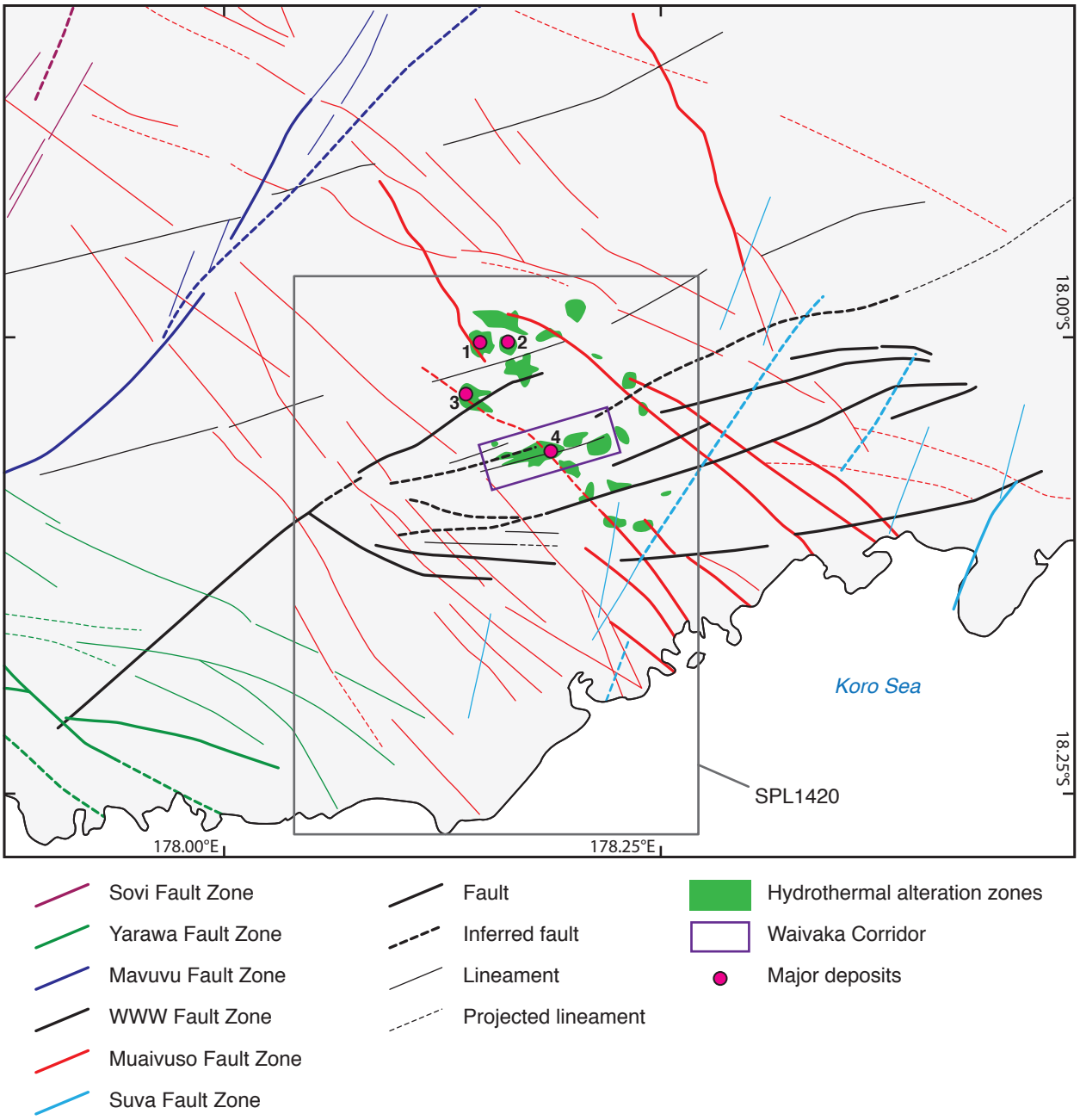


**Figure 2.4:** Map of faults and other structural lineaments in southeastern Viti Levu and distribution of Namosi district hydrothermal alteration. Structures are mostly from Rahiman and Pettinga (2008). 1 = Waisoi West, 2 = Waisoi East, 3 = Wainabama, 4 = Wainaulo.

Levu indicate strike-slip to oblique-normal strike-slip and normal-slip movement along fault zones (Rahiman and Pettinga, 2008). In strike-slip structural domains it is common for near-surface manifestations of the fault system to occur as zones of upwardly-flaring splays that merge at depth into a more competent basement fault (e.g., Sylvester, 1988). These root zones may have played an important role in the focusing of magmatic-hydrothermal activity in the Namosi district.

## 2.5 Mineral deposits of Viti Levu

Magmatism and precious and base metal mineralization occurred episodically throughout the evolution of the Fiji Platform. The oldest mineral occurrences were emplaced during the early arc stage of the Vitiaz Arc (Early to Middle Miocene) and are hosted within low-K tholeiitic volcanics of the Wainimala Group. These mineral occurrences are predominantly base-metal rich volcanogenic massive sulfide (VMS) deposits (e.g., Colo-i-Suva, Nakoro, Wainaleka and Wainivesi) that are concentrated in southeastern Viti Levu (Fig. 2.5B). Manganese deposits were also emplaced during the early arc phase. The economically most important manganese deposits (e.g., Nabu, Vunamoli and Nasaucoko) are located along fault zones within well-bedded volcano-sedimentary sequences and hemipelagic sediments of the Early Miocene Sigatoka Group in southwestern Viti Levu (Figs. 2.2 and 2.5). Polymetallic base metal mineralization also occurs in the area and may be genetically related (Colley and Flint, 1995). In the mature arc stage of the Vitiaz Arc (Late Miocene), low-K tholeiitic to calc-alkalic gabbros, tonalites and trondhjemites of the Colo Plutonic Suite intruded the Wainimala Group rocks. These intrusions were associated with small occurrences of base and precious metal veins, and minor porphyry and skarn-type mineralization throughout the Wainimala – Colo Plutonic Suite belt (e.g., Rama Creek, Namoli, Liwa Creek, Wainivau and Nuku; Colley and Greenbaum, 1980; Fig. 2.5).

In the early rifting stage of the Fiji Platform (Late Miocene to Pliocene), calc-alkalic porphyry copper-gold-molybdenum deposits (e.g., Waisoi East, Waisoi West and Wainaulo), epithermal Au-Ag-Pb-Zn veins (Wainikovu), and a Cu-Fe skarn (Wainikana) were emplaced in association with diorite, quartz-diorite and dacite intrusions in the Namosi district (e.g., Tanaka et al., 2010; Fig. 2.5B). The Namosi deposits may have been generated during the short-lived subduction of the north-directed concave South Fiji Basin slab (Indo-Australian Plate) in the Late Miocene. A component of low-angle subduction from the orphaned slab is still visible in the seismic data (Fig. 2.3) and is the likely trigger for the generation of these deposits (cf. Cooke et al., 2005; Rinne, 2015).

In the Latest Miocene to Pliocene (~ 5.5 – 3.0 Ma), igneous activity in the Fiji Platform

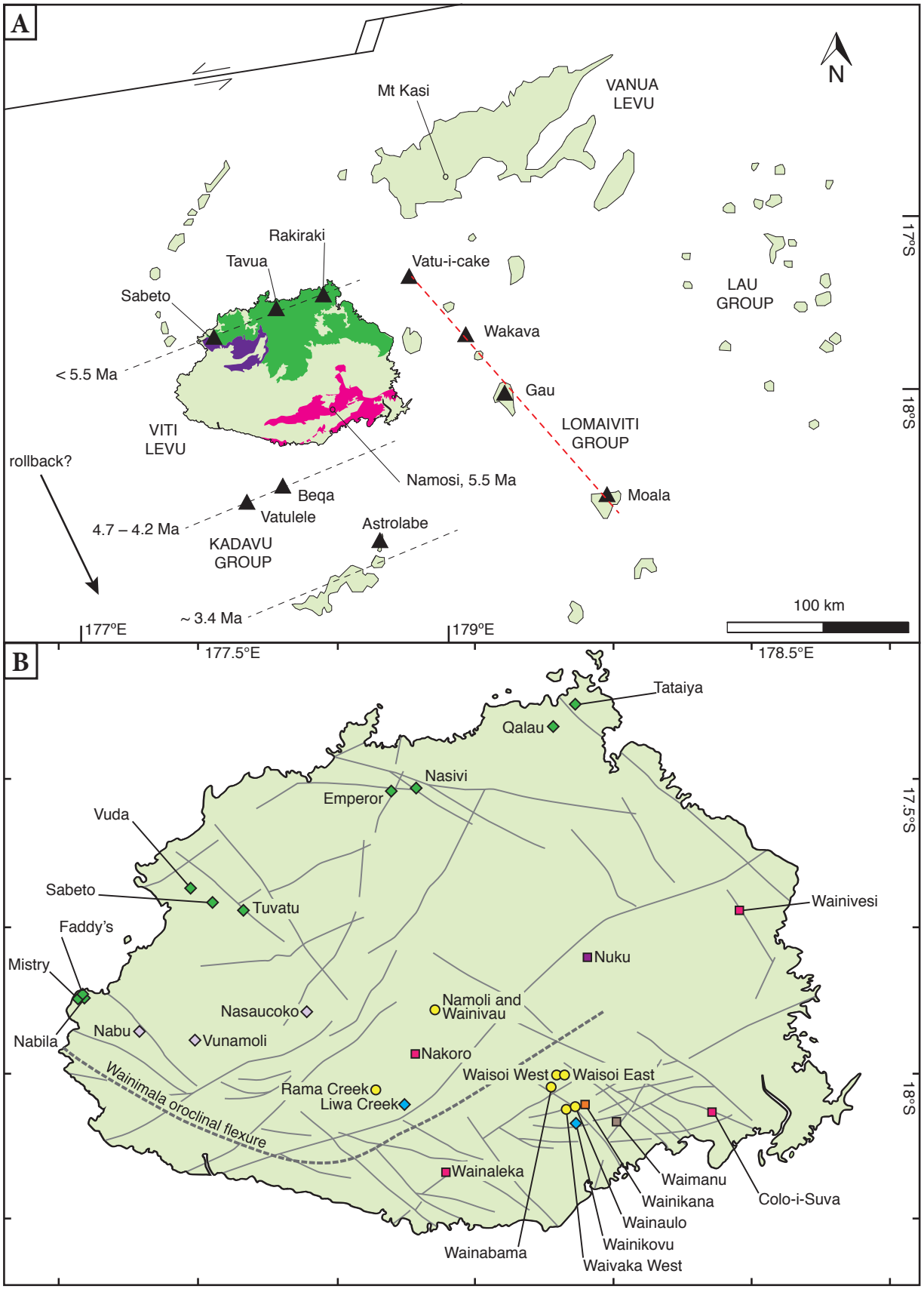
A
N
Mt Kasi
VANUA LEVU
Rakiraki
Tavua
Sabeto
Vatu-i-cake
Wakava
Gau
LOMAIVITI GROUP
LAU GROUP
< 5.5 Ma
VITI LEVU
rollback?
Namosi, 5.5 Ma
Beqa
Vatulele
Moala
4.7 – 4.2 Ma
KADAVU GROUP
Astrolabe
~ 3.4 Ma
100 km
177°E
179°E
17°S
18°S
B
177.5°E
178.5°E
17.5°S
18°S
Tataiya
Qalau
Nasivi
Emperor
Vuda
Sabeto
Tuvatu
Faddy's
Mistry
Nabila
Nabu
Vunamoli
Nasaucoko
Namoli and Wainivau
Nuku
Wainivesi
Nakoro
Waisoi West
Waisoi East
Rama Creek
Liwa Creek
Wainimala oroclinal flexure
Wainaleka
Waimanu
Wainikana
Wainaulo
Wainikovu
Waivaka West
Wainabama
Colo-i-Suva
Calc-alkalic Cu-Au porphry
Au-Zn-Cu skarn
Alkalic Au porphyry-epithermal
Faults
Fe-Cu skarn
Zn-Cu-Ag VMS
Alluvial Au
Shoshonitic volcanos
Calc-alkalic Au epithermal
Mn

**Figure 2.5 (opposite):** Metallogenesis of the Fiji Islands. **A.** Map of the Fiji Islands, showing the distribution of Pleistocene shoshonitic centers and the location of the Namosi district. The Sabeto, Tavua and Rakiraki shoshonitic centers are all associated with significant Au-rich porphyry-epithermal mineralization. The Medrausucu Group rocks, which host the Namosi porphyry Cu-Au(-Mo) deposits and prospects, are shown in pink. Shoshonitic rocks, which host the Tuvatu and Emperor deposits on Viti Levu, are represented by the dark green (Ba Volcanic Group) and dark purple (Koroimavua Group) polygons. The northwest – southeast red dashed line illustrates a shoshonitic volcanic trend unrelated to rollback along the Fiji – Vanuatu subduction system. **B.** Early arc stage mineralization consists of Zn-Cu-Ag VMS deposits and prospects in southeastern Viti Levu. Mature arc stage mineralization consists of calc-alkalic porphyry, epithermal and skarn deposits along the Wainimala Oroclinal Flexure. Early rifting stage consists of calc-alkalic Cu-Au(-Mo) porphyry deposits of the Namosi district and alkalic Au-Ag porphyry-epithermal deposits and prospects along a 250 km-long corridor in northern Viti Levu.

evolved in composition to mafic and intermediate high-K calc-alkalic and shoshonitic affinities (Whalen et al., 1985; Gill and Whelan, 1989b). Shoshonitic volcanics erupted along three broad east-northeast trends (Hathway, 1993; Fig. 2.5A). Intrusions emplaced along these shoshonitic belts are mostly monzonites and monzodiorites and are locally associated with porphyry-epithermal gold mineralization (Eaton and Setterfield, 1993; Spry and Scherbarth, 2006). The largest of the Late Miocene – Pliocene shoshonitic volcanic centers is the Tavua Caldera. This collapsed volcanic edifice hosts the 3.89 ± 0.05 Ma (Begg and Gray, 2002) high-grade Au-Ag telluride veins of the Emperor alkalic low-sulfidation epithermal Au deposit (14.7 Mt @ 8.1 g/t Au; Jensen and Barton, 2000; Fig. 2.5) and a number of peripheral prospects (e.g., Korovou Hill, Nasivi, Waikatakata and Balata). The Emperor deposit has been studied in detail by Forsythe (1971), Ahmad et al. (1987a,b), Anderson et al. (1987), Ahmad and Walshe (1990), Anderson and Eaton (1990), Kwak (1990), Eaton and Setterfield (1993), Begg (1996) and Begg and Gray (2002). The host rocks are 4.8 million-year-old, oxidized alkaline mafic volcanics (absarokite, shoshonite and banakite) of the Ba Volcanic Group, that were intruded by monzonite stocks and associated low-grade porphyry mineralization (Eaton and Setterfield, 1993, Begg and Gray, 2002). Gill et al. (1984) and Gill and Whelan (1989b) proposed that these intrusions were not related to active subduction, but rather to a period of arc lithospheric extension in response to far-field stresses associated with the opening of the North Fiji and Lau Basins. However, there is an arc-parallel southward younging of shoshonitic volcanism from the Sabeto – Tavua – Rakiraki trend in northern Viti Levu to the younger Vatulele – Beqa trend south of Viti Levu and then to the youngest shoshonitic center at the Astrolabe volcano in the Kadavu Island Group (Fig. 2.5A; e.g., Nunn, 1998). Therefore, I propose that shoshonitic volcanism in the Fiji Platform may instead be associated with a southward migrating locus of backarc alkalic volcanism caused by progressive slab rollback of the concave downgoing South Fiji Basin slab (Indo-Australian Plate) southwest of the Fiji Platform (Figs.

2.1 and 2.5A). Other Au deposits and prospects hosted in alkalic igneous rocks on Viti Levu are Tuvatu, Rakiraki (Tataiya and Qalau), Vuda, Sabeto, Faddy's, Mistry and Nabila, all of which are spatially associated with the Viti Levu east-northeast alkaline volcanic trend (Figs. 2.1 and 2.5).

In the Fiji Platform, porphyry copper mineralization was absent from earliest stage tholeiitic magmatism and became more important in successively younger stages of arc evolution prior to dissociation from active subduction in the Pliocene (cf. Panamanian Arc; Kesler et al., 2006). It is estimated that ~ 75 % of porphyry-epithermal deposits in Fiji were generated during the early rifting stage and the latter part of the mature arc stage (Colley and Flint, 1995). The youngest prospect noted in Viti Levu is the Pliocene to Recent placer-type Au that was deposited at Waimanu within the Namosi district (Fig. 2.5B).

**2.6 Summary**

The Fiji Platform records the complex history of an intra-oceanic subduction zone, including a reversal of arc polarity, arc fragmentation, rapid rotation, and development of flanking backarc basins. This tectonic history is paralleled by a complicated magmatic evolution that progressed from low-K tholeiitic to medium-K calc-alkalic to shoshonitic to alkali OIB magmatic affinities.

The Namosi porphyry deposits were generated during northwest-directed subduction of the South Fiji Basin lithosphere in the Late Miocene. Deeply penetrating strike-slip faults associated with rotation of the Fiji Platform controlled the emplacement of the magmatic-hydrothermal activity associated with mineralization. Slab rollback of the downgoing concave South Fiji Basin lithosphere in the Pliocene may have led to the southeast migration of backarc-related alkalic volcanism and porphyry-epithermal mineralization.

# CHAPTER 3

# Geology and geochronology of the Namosi district

## 3.1 Introduction

This chapter presents the geology of the Namosi porphyry deposits in the context of the district-scale geological framework. The principal aim is to determine the geological evolution leading to ore formation. New U–Pb geochronology results constrain the timing of emplacement of the Namosi intrusive complexes.

## 3.2 Methods

District-scale geological relationships are based on mapping by Newcrest Mining Limited (Johanssen, 2011) and by early geological mapping completed by the MRD, Fiji (Band, 1968). Lithofacies and deposit-scale geological relationships have been interpreted from cross sections constructed by the author as part of this thesis. The geological cross sections were created based on observations made by the author during detailed graphic logging of ~ 20 km of drill core across the Namosi district. A new cross section through each principal deposit within the district was constructed (Wainaulo, Waisoi West and Waisoi East) as well as through one of the peripheral prospects (Wainaulo West). Interpretations were also made based on photo-logging of the remaining drill holes off-section using the Namosi Joint Venture (NJV) drill core photo library.

Thin section petrography was used to help identify structures and textures, as well as to evaluate the modal mineral abundances within intrusive and lava units. To supplement this process, X-ray diffraction traces were collected from three least-altered hand samples from the study area to aid with mineral identification and quantification. The sample powders were analyzed by Staf-

ford McKnight at the University of Ballarat. Siemens D500 and D501 diffractometers were used with Fe-filtered CoKα X-rays at 36 kV and 30 mA. The XRD profiles (diffractograms) were collected by step scans with a starting angle of 5° 2θ, at conventional scan rates (1° or 2θ per minute), and ending at 76° 2θ. SiroQuant 3.0 software was used to identify and quantify the relative proportions of minerals in each sample. The XRD results are provided in Appendix B.

Five drill core samples of intrusive rocks that are interpreted to be related to Cu-Au(-Mo) mineralization at Wainaulo, Waisoi West and Waisoi East were sent to Dr. Richard Friedman at PCIGR, University of British Columbia, Canada for CA-TIMS U–Pb age determinations on zircons. Zircons from four drill core samples were also analyzed by Dr. Charlotte Allen at the Australian National University, Canberra, using ELA-ICP-MS techniques. Detailed results and methods are provided in Appendix C.

### 3.3 Volcanic framework of the Namosi district

The Namosi porphyry deposits are located in southeastern Viti Levu, Fiji, and define a mineralized district within an area of about 40 $km^2$ (Colley and Greenbaum, 1980; Fig. 3.1). Two mountain ranges dominate the physiography and bound the Namosi porphyry deposits to the east and to the west. To the east are the southwest trending Medrausucu ranges and to the west are the south-southeast trending Korobasabasaga ranges. Compressional tectonics has led to uplift of these ranges to elevations exceeding 1000 masl since the Late Miocene (Rodda, 1967). The principal deposits and peripheral prospects are exposed in topographic depressions that are infilled with a thin veneer of overburden (Fig. 3.1).

The local basement in the Namosi district is composed of Late Oligocene to Middle Miocene intra-oceanic island arc volcanic and volcano-sedimentary rocks of the Wainimala Group, which have been uplifted, tilted and regionally metamorphosed (Band, 1968; Rodda, 1994). The Wainimala Group comprise the majority of basement rocks throughout Viti Levu, with the exception of the Late Eocene to Early Oligocene Yavuna Group submarine volcanics that are localized in western Viti Levu (Wharton et al., 1985; Rodda, 1994; Fig. 2.2). Wainimala Group rocks are ex-

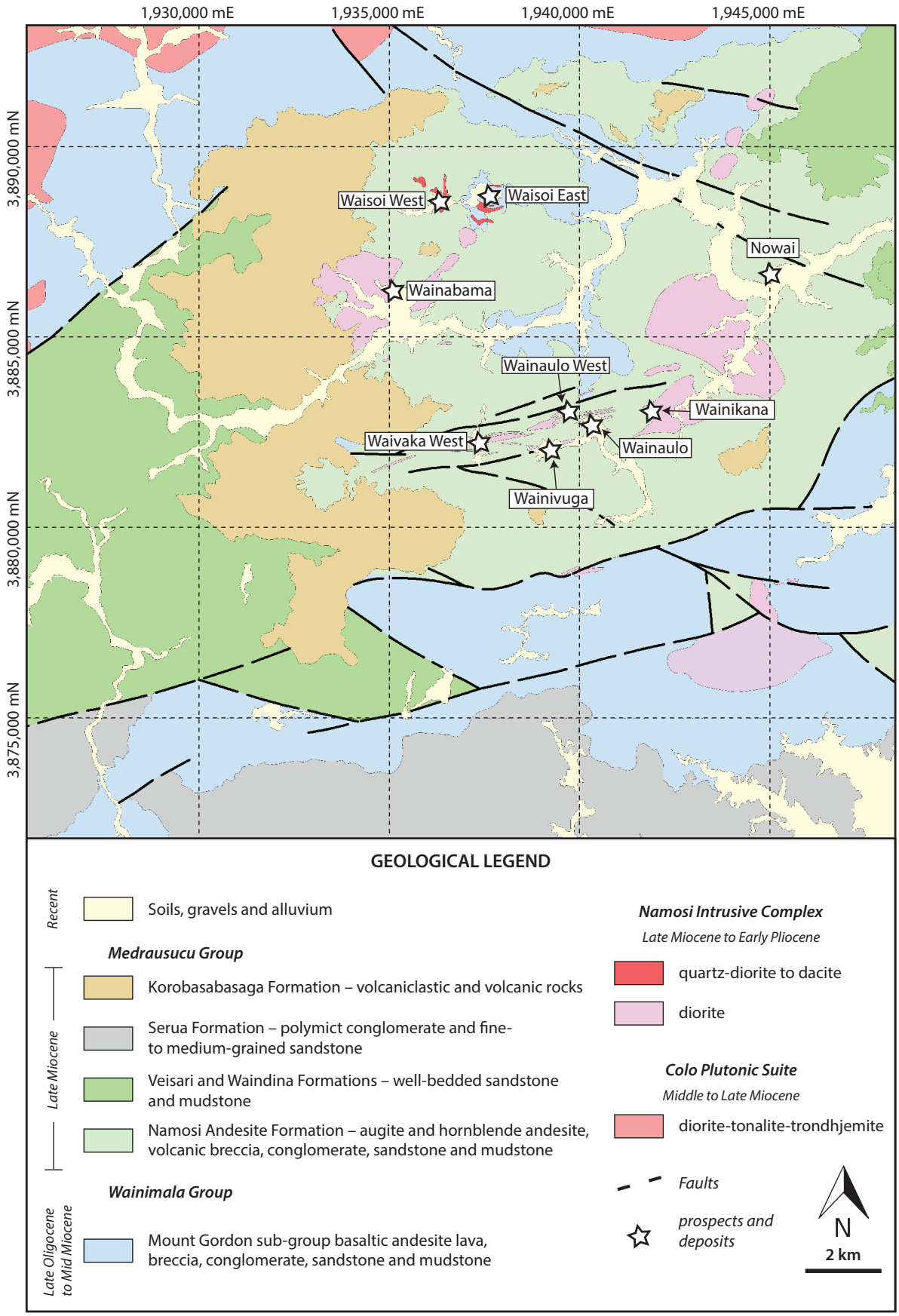


**Figure 3.1:** Geological map of the Namosi district. This map is based on unpublished mapping by Newcrest Mining Limited (Johanssen, 2011) and mapping by the MRD, Fiji (Band, 1968). The location of selected porphyry related deposits and prospects are indicated and labeled. The Fiji Map Grid (WGS72) was used.

posed along a broad anticlinorium that is concave up towards the northeast and extends across the island (Rodda, 1967; Fig. 2.2). Olivine-augite gabbro and diorite-tonalite-trondhjemite stocks of the Middle to Late Miocene Colo Plutonic Suite have intruded the core of the anticlinal structures within the Wainimala Group basement (Fig. 2.2). The arcuate and elongate distribution of the Wainimala Group and Colo Plutonic Suite is considered to represent the magmatic axis of Miocene volcanism (Rodda, 1994). In the vicinity of the Namosi district, the Wainimala Group can be subdivided into two broad tectono-stratigraphic packages: the Mount Gordon and Matailombau sub-groups (Rodda and Band, 1967; Band, 1968). The Matailombau sub-group consists of a < 1 km-thick package of well-bedded greywacke and occurs to the east and south of the study area (Band, 1968). The Nubuonaboto Formation of the Mount Gordon sub-group is the dominant package of Wainimala Group rocks that occurs within the Namosi district. The formation consists of a > 6 km-thick package of basalt lavas, volcanic conglomerates and breccias, pillow breccias, and volcaniclastics (Band, 1968; Rodda, 1994).

The Nubuonaboto Formation is unconformably overlain by the Namosi Andesite Formation (NAF) of the Medrausucu Group, which comprises volcanic and volcanogenic sedimentary rocks (Rodda, 1967). Both the Wainimala Group and NAF sequences have been crosscut by several phases of Late Miocene to Early Pliocene intrusions associated with porphyry-style mineralization that range from mafic to felsic compositions (i.e., from diorite to quartz-diorite to dacite stocks, pipes and dikes). The stratigraphic and intrusive units of the Namosi district encountered during this study are illustrated in comparative stratigraphic columns (Fig. 3.2) and a series of cross sections (Figs. 3.4, 3.5, 3.7 and 3.8; cross section locations are shown on Figs 3.3 and 3.6).

### *3.3.1 Wainimala Group*

The Wainimala Group crops out in the Namosi district to the north of Wainaulo and within the Waisoi East area (Figs. 3.1 and 3.6). Light and dark gray, well-laminated to thinly bedded volcanic mudstone and sandstone of the Wainimala Group are exposed ~ 500 m north of the NVD019 collar (FMG 1940200 E 3883615 N) and show steep north-dipping beds (G. Johanssen, pers. comm., 2011). At Wainaulo and Wainaulo West the Wainimala Group has been intersected

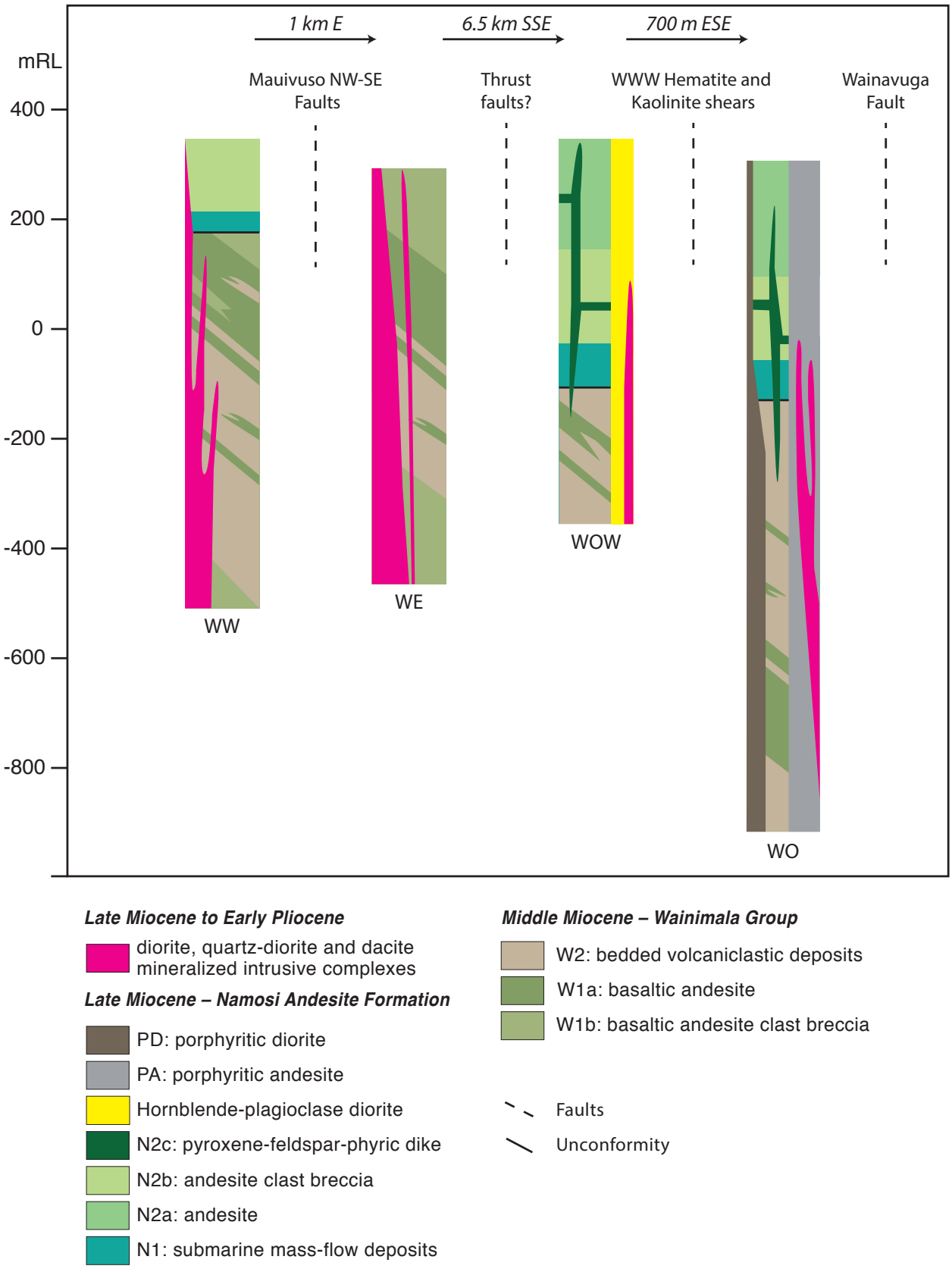


**Figure 3.2:** Schematic comparative stratigraphy across the Namosi district, from Waisoi West (WW) to Waisoi East (WE) to Wainaulo West (WOW) to Wainaulo (WO). Both of the Namosi Andesite Formation and Wainimala Group rocks are exposed in the Waisoi area, whereas in the Wainaulo area only Namosi Andesite Formation crops out. The N1 submarine mass-flow deposit is a useful marker horizon for the district.

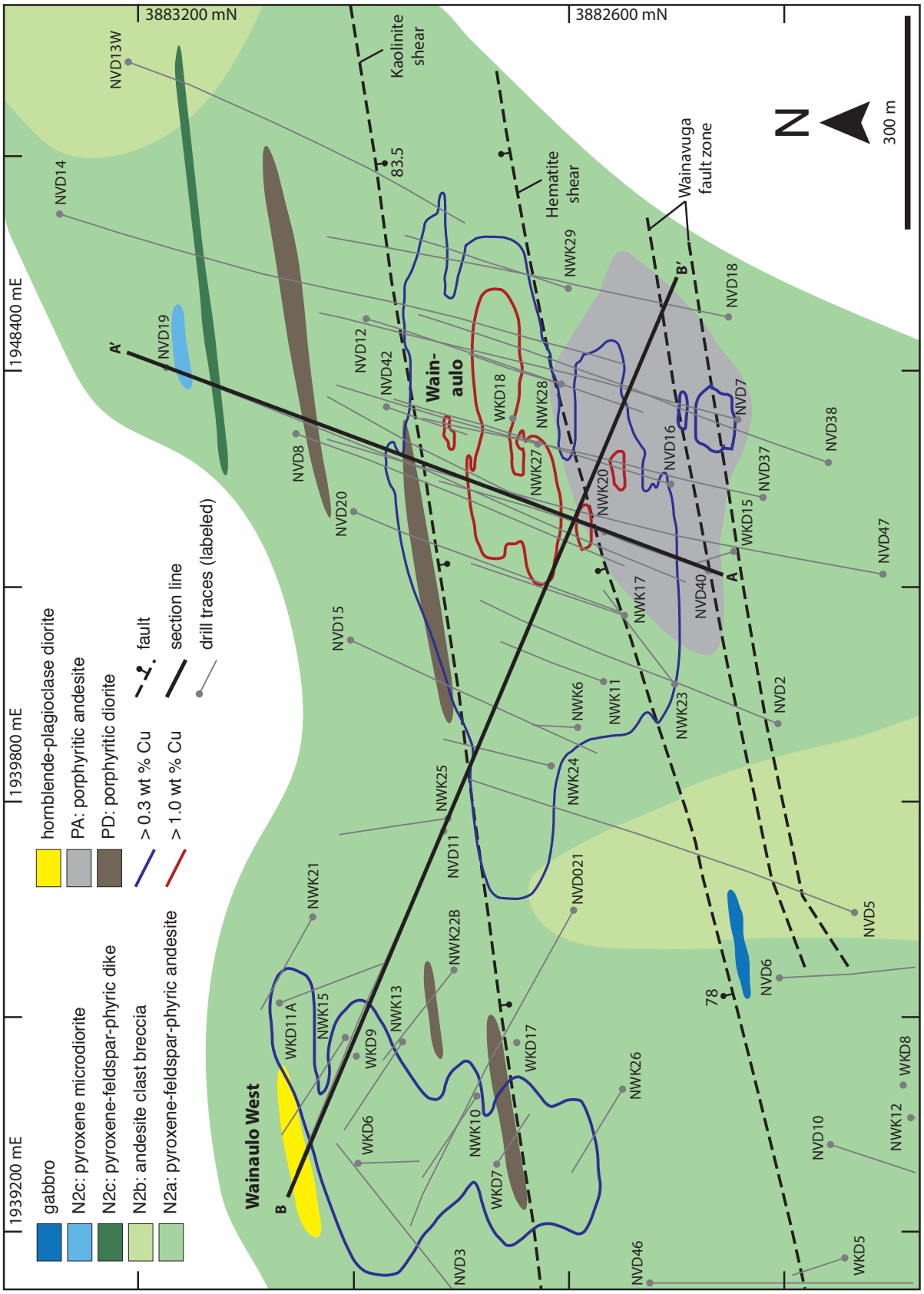


**Figure 3.3:** Simplified plan view geology map of the Wainaulo and Wainaulo West areas, looking below overburden and the oxidized zone. The geology map is based on interpretations made by the author after drill core logging of the cross sections indicated on the map, as well as photo-logging the remaining drill holes using the NJV drill core photo library. The location and shape of the gabbro outcrop is from Johanssen (2011) and the Wainavuga fault zone is from Newcrest Mining Ltd. (2010). Copper grades are contoured from the first 500 m below the present-day surface. High copper grades (> 1.0 wt % Cu) appear to be controlled by oppositely dipping shear zones.

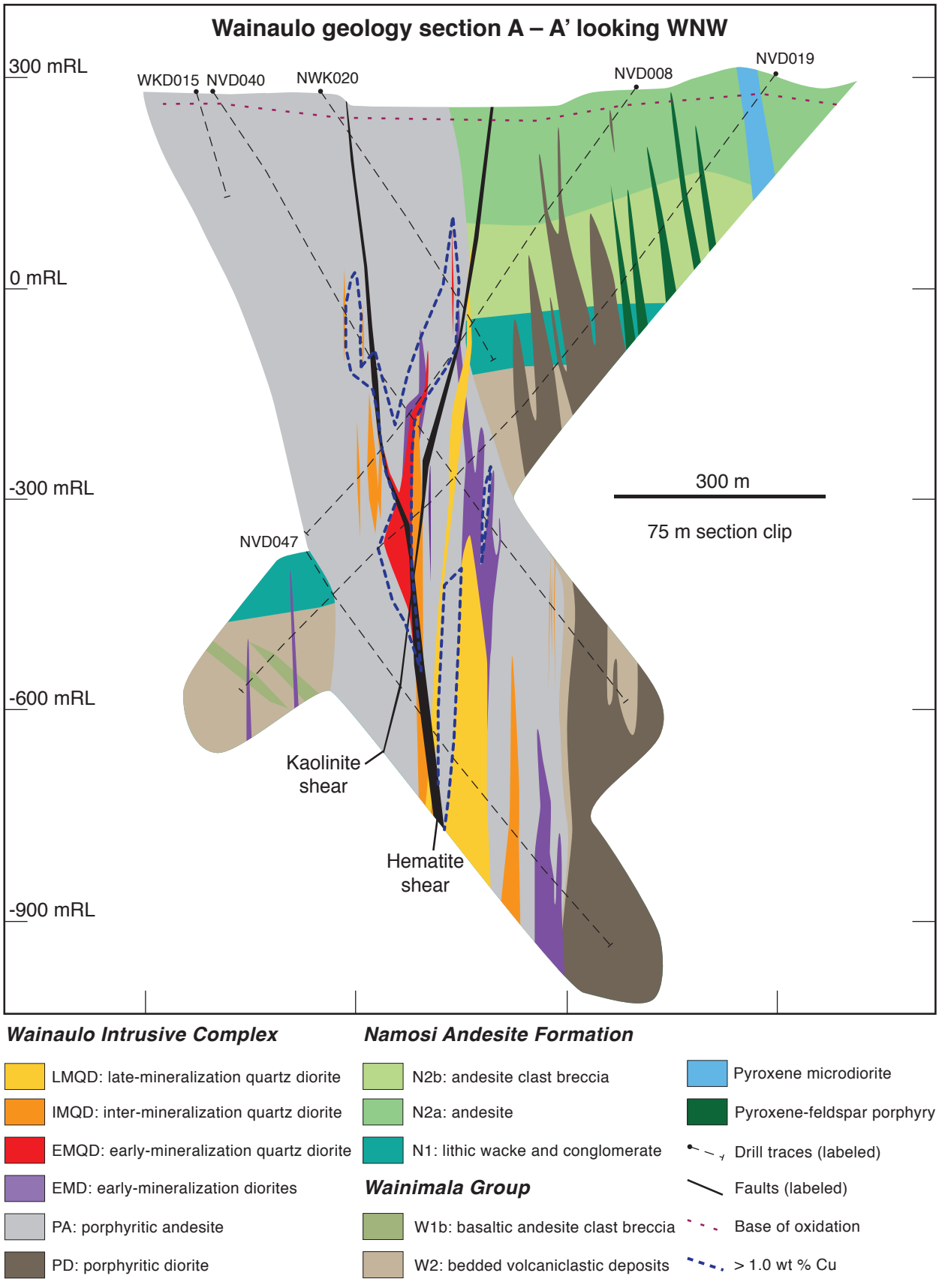


**Figure 3.4:** Geology section A – A' at Wainaulo showing distribution of copper mineralization. Location of the cross section is shown in Fig. 3.3.

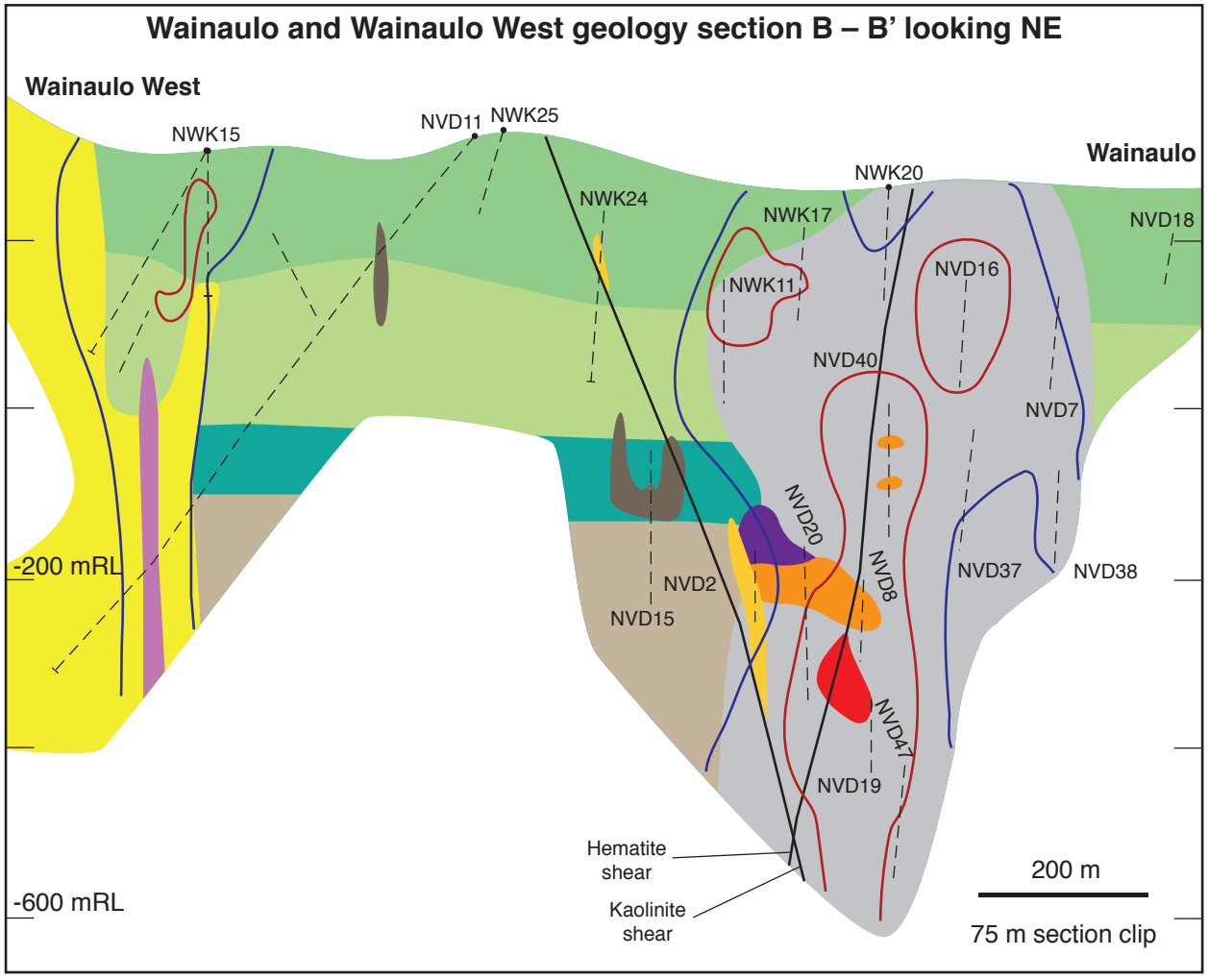


***Wainaulo Intrusive Complex***

- LMQD: late-mineralization quartz-diorite
- IMQD: inter-mineralization quartz-diorite
- EMQD: early-mineralization quartz-diorite
- EMD: early-mineralization diorites
- PA: porphyritic andesite
- PD: porphyritic diorite

***Wainaulo West Intrusive Complex***

- Quartz-plagioclase-phyric diorite
- Hornblende-plagioclase diorite

***Namosi Andesite Formation***

- N2b: andesite clast breccia
- N2a: andesite
- N1: submarine mass-flow deposits

***Wainimala Group***

- W2: bedded volcaniclastic deposits
- Drill traces (labeled)
- Faults (labeled)
- > 0.3 wt % Cu
- > 0.7 wt % Cu

**Figure 3.5:** Geology section B – B' at Wainaulo West and Wainaulo showing distribution of copper mineralization. Location of the cross section is shown in Fig. 3.3.

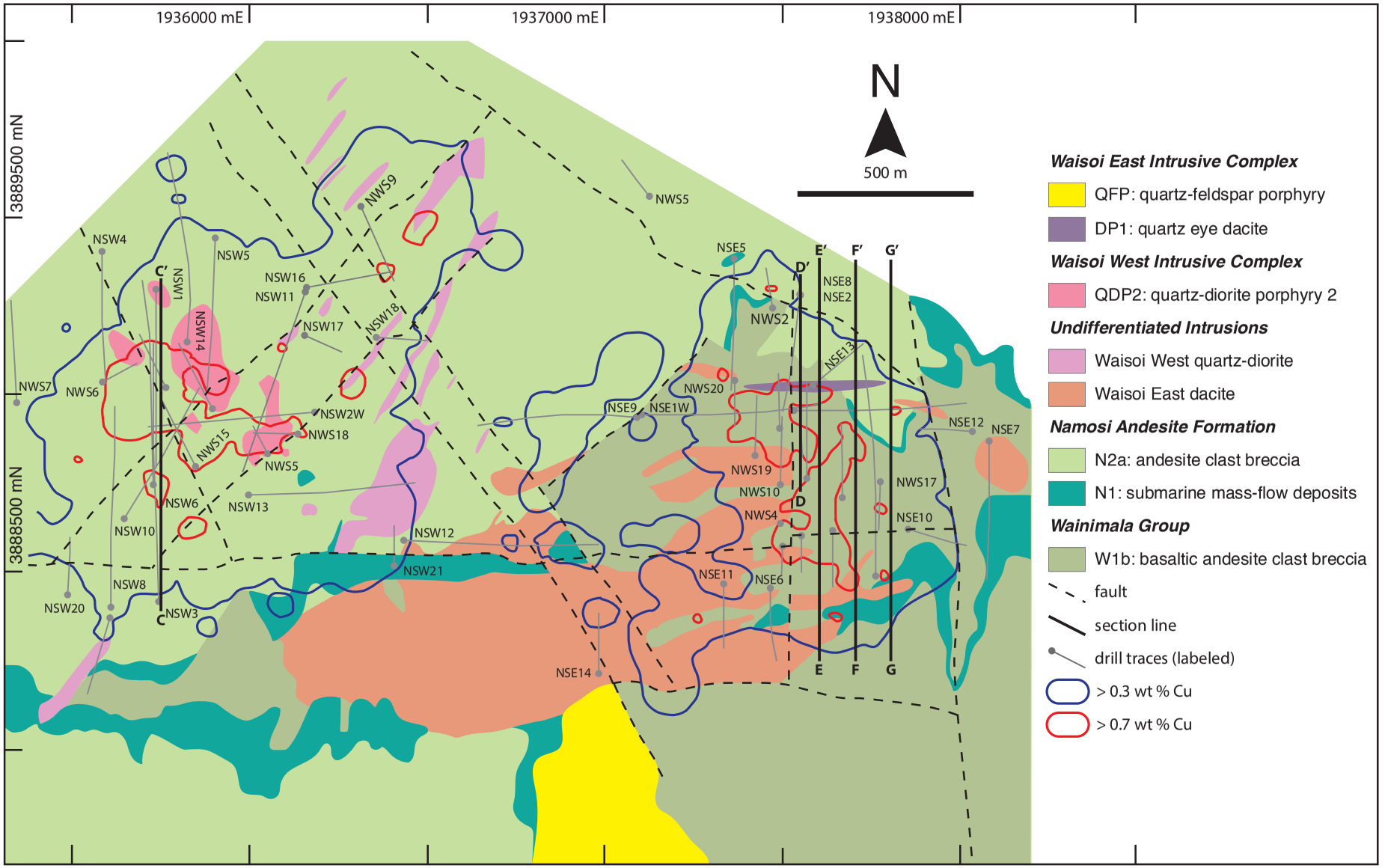


**Figure 3.6:** Simplified plan view geology map of the Waisoi West and Waisoi East areas, looking below overburden and the oxidized zone. The geology map and faults are after Ellis (1996) with additions made based on interpretations by the author after drill core logging of the cross-sections indicated on the map, as well as photo-logging the remaining drill holes using the NJV drill core photo library. Copper grades are contoured from the first 500 m below the present-day surface.

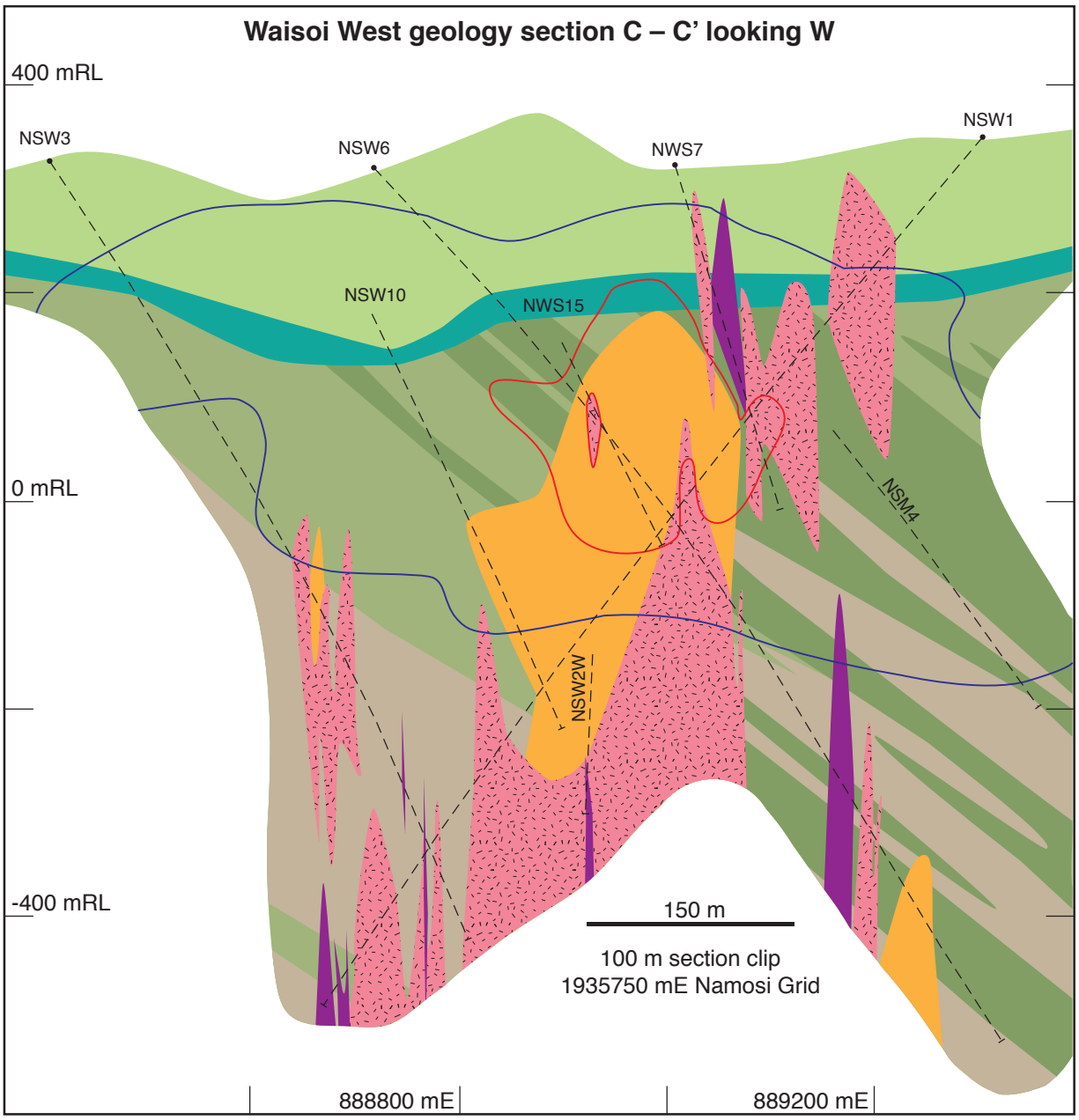


**Figure 3.7:** Geology section C – C' at Waisoi West, showing distribution of copper mineralization. Location of the cross section is shows in Fig. 3.6.

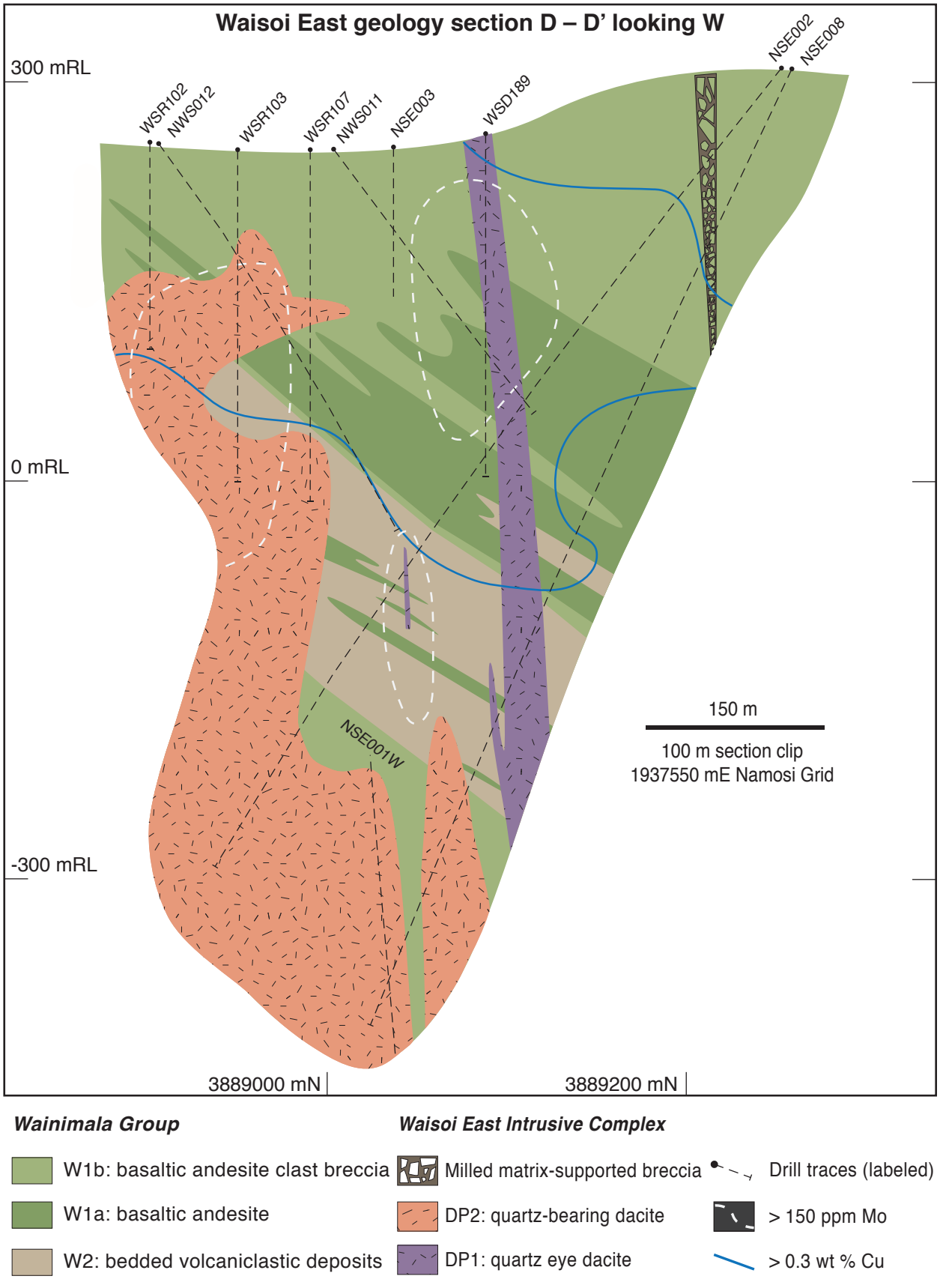


**Figure 3.8:** Geology section D – D' at Waisoi East, showing distribution of copper and molybdenum mineralization. Location of the cross section is shown in Fig. 3.6.

in drill core below -100 mRL and have a minimum vertical extent of 900 m (Figs. 3.2, 3.4 and 3.5). At Waisoi West the Wainimala Group occurs below ~ 200 mRL (Figs. 3.2 and 3.7) and at Waisoi East is exposed at surface (~ 300 mRL; Figs. 3.2, 3.6 and 3.8).

Two Wainimala Group members have been identified and defined within the vicinity of the principal deposits of the Namosi district during this study. These Wainimala Group rocks comprise pyroxene-feldspar-phyric basaltic andesite lavas and breccias that are locally amygdaloidal and laminated siltstone and volcanic sandstone with interbedded polymict breccias.

#### *3.3.1.1 Pyroxene-feldspar-phyric basaltic andesite and associated breccia (W1)*

The W1 member consists of compositionally related pyroxene-feldspar-phyric basaltic andesite and monomict, pyroxene-feldspar-phyric basaltic andesite breccia. W1 rocks have been intersected in drill core at Wainaulo, Wainaulo West, Waisoi West and Waisoi East (Figs. 3.2, 3.4, 3.5, 3.7 and 3.8), and have a lateral continuity that can be traced across several drill holes (Fig. 3.7).

##### *Pyroxene-feldspar-phyric basaltic andesite (W1a)*

The basaltic andesite (W1a) is typically dark gray to black and homogeneous (no significant layering, banding, or mineral alignment). Individual unit thicknesses can range from a few meters to 150 m (e.g., Ellis, 1996; Fig. 3.2). W1a is characterized by a population of evenly distributed albite-altered plagioclase phenocrysts (0.5 – 4.0 mm; 10 – 30 %), and another population of plagioclase phenocrysts with a glomerophyric texture, and subordinate blocky chlorite-altered pyroxene phenocrysts (0.3 – 1.0 mm; < 5 %; Figs. 3.9B and C). The formerly glassy groundmass is strongly chlorite-altered and has abundant anhedral magnetite and felted plagioclase microlites (< 0.2 mm; Fig. 3.9C). Relict perlitic fractures are preserved locally (e.g., Fig 3.12E). Quartz-filled

**Figure 3.9 (opposite):** Examples of Wainimala Group rocks in the Namosi district. **A.** Hand sample of typical amygdaloidal and porphyritic basaltic andesite (W1a). Sample: NSW014 367 m. **B.** Hand sample of basaltic andesite (W1a) featuring glomerophyric plagioclase textures. Sample: NVD014 595 m. **C.** Photomicrograph of basaltic andesite (W1a) illustrating plagioclase phenocrysts, plagioclase glomerocrysts and quartz-filled amygdales in a fine-grained groundmass that consists of magnetite and felted plagioclase microlites. Sample: WSD219 217 m. **D.** Hand sample of monomict basaltic andesite breccia (W1b). Sample: NSW006 522 m. **E.** Core box photograph of polymict, pumice-rich volcaniclastic breccia (W2a), illustrating the distribution and angular nature of the basaltic andesite clasts. Sample: NVD014 538.60 – 541.05 m. **F.** Hand sample of polymict, pumice-rich volcaniclastic breccia (W2a), illustrating chlorite-altered, flattened tube pumice (F) and lithic fragments (L). Sample: NVD014 540 m. **G.** Hand sample of normally graded coarse sandstone to siltstone (W2b). Sample: NSW014 514 m. **H.** Hand sample of very thinly laminated mudstone (W2c). Sample: NSW014 723 m. Abbreviations: A = amygdales, F = flattened pumice, G = glomerophyric plagioclase, L = lithic clast, pl = plagioclase.

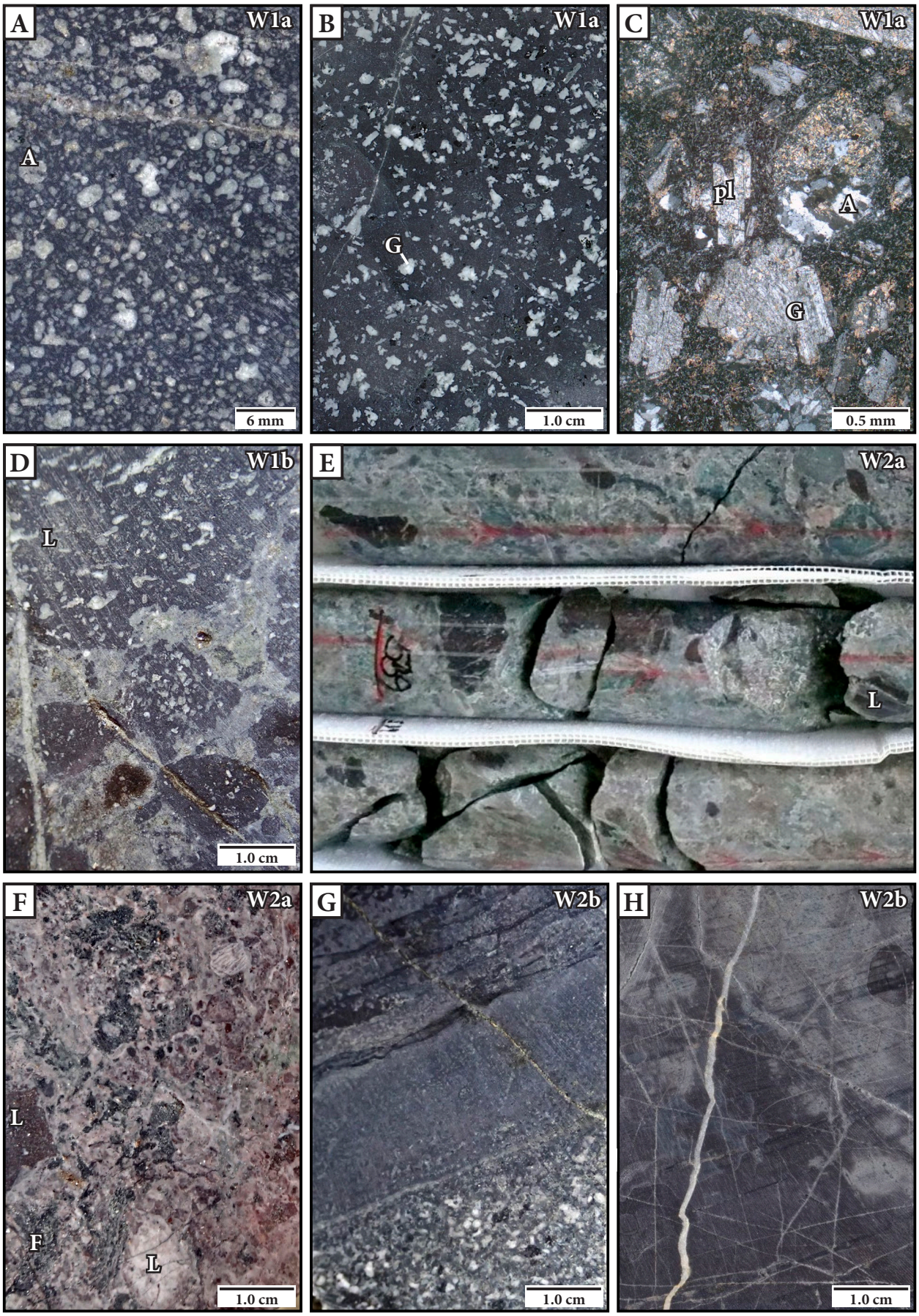
A
W1a
A
6 mm
B
W1a
G
1.0 cm
C
W1a
pl
A
G
0.5 mm
D
W1b
L
1.0 cm
E
W2a
L
F
W2a
L
F
L
1.0 cm
G
W2b
1.0 cm
H
W2b
1.0 cm

amygdules are locally present and can be abundant (< 50 vol %; Figs. 3.9A and C). W1a locally has lower peperitic contacts with sandstone (e.g., Skilling et al., 2002). The peperite typically displays a closely packed to widely dispersed clast concentration that is poorly sorted. The clasts consist of blocky basaltic andesite and irregular sandstone (Fig. 3.10A).

*Monomict, pyroxene-feldspar-phyric basaltic andesite breccia (W1b)*

Monomict, pyroxene-feldspar-phyric basaltic andesite breccia (W1b) is a massive, clast- to matrix-supported, jigsaw-fit to chaotic breccia with granule- to boulder-sized clasts. W1b is volumetrically more significant than W1a, and locally can be > 150 m thick (Fig. 3.2). The clasts in W1b are composed of amygdaloidal pyroxene-feldspar-phyric basaltic andesite with ragged to cuspate margins (Fig. 3.9D). Rounded, fragmented, pillow shapes are preserved locally (Ellis, 1996).

*Interpretation of W1:*

The W1 member is composed of coherent basaltic andesite and spatially and compositionally related basaltic andesite clast breccia with blocky and irregularly shaped clasts in a matrix-poor, clast-supported arrangement. Due to ubiquitous hydrothermal alteration within the Namosi area, it is not clear if the breccia is a hyaloclastite or autobreccia facies that is related to the coherent pyroxene-feldspar-phyric basaltic andesite (e.g., McPhie et al., 1993). The lack of bedforms, angular clast shapes, monomict clast population and jigsaw-fit organization indicate little post-fragmentation transport (e.g., McPhie et al., 1993).

Peperite is a common component of mixed sedimentary-volcanic sequences that occur in subaqueous settings (Skilling et al., 2002). The local presence of peperite along the bottom contacts of the basaltic andesite unit suggests emplacement within or above unconsolidated wet sediment. Since peperitic contacts were not observed above or along the sides of the coherent basaltic andesite, it is not possible to conclude whether the basaltic andesite was a sill, intrusive feeder dike or an extrusive lava flow or dome.

The presence of relict perlite in the basaltic andesite indicates hydration (or quenching) of constituent volcanic glass, a texture typical of lavas that have either erupted into or within a subaqueous environment (McPhie et al., 1993; McPhie and Orth, 1999). The local occurrence of pillowed lava fragments provides further evidence that the basaltic andesite was deposited subaqueously (e.g., Snyder and Fraser, 1963; Cas and Wright, 1987; McPhie et al., 1993). However, these features do not provide enough evidence to exclude the possibility that the lava was subaerial and had flowed into the sea (e.g., Tribble, 1991).

Given this evidence and the regional context that the Wainimala group is submarine (Colley and Flint, 1995; Wharton et al., 1995), the pyroxene-feldspar-phyric basaltic andesite and associated breccias (W1) are interpreted to be the coherent and clastic components of submarine lavas and possibly shallow submarine intrusions.

#### *3.3.1.2 Bedded volcaniclastic deposits (W2)*

##### *Polymict, pumice-rich volcaniclastic lithic breccia (W2a)*

The polymict, pumice-rich volcaniclastic lithic breccia (W2a) is a matrix-supported, poorly sorted, weakly reverse graded, thickly bedded breccia (Fig. 3.9E) that is < 50 m thick and has a widespread distribution across the Namosi district (e.g., W2 distribution in Fig. 3.2, 3.4, 3.5, 3.7 and 3.8). This breccia has been intersected by diamond drilling at Wainaulo, Waisoi East and Waisoi West. Irregular-shaped, angular fragments of basaltic andesite (granule to cobble sized; < 15 vol %; locally with chlorite-altered formerly glassy rims) and chlorite-altered, variably compacted relict tube pumice (coarse ash to lapilli sized; 15 – 40 vol %) are the dominant clast types (Fig. 3.9F). Subordinate clast types consist of subrounded quartz-feldspar-phyric dacite clasts and irregular-shaped mudstone clasts. The matrix is strongly and pervasively altered to an albite – chlorite – hematite assemblage and is composed of cuspate and platy fragments of relict glass, sand-sized feldspar crystals and lithic fragments (Fig. 3.9F).

*Normally graded, very coarse sandstone to laminated siltstone (W2b)*

W2b consists of thin to medium beds of laminated to massive siltstone, sandstone and very coarse sandstone with interbedded polymict volcaniclastic lithic breccia (W2a). Laminated or thinly bedded lenses are less than 10 m thick. The thickest beds are normally graded sandstone with volcanic lithic and crystal (plagioclase, pyroxene) components (Fig. 3.9G). Laminated siltstone caps the sequence (Fig. 3.9G).

*Laminated mudstone (W2c)*

Very thinly laminated to thinly bedded mudstone occurs in intervals less than 30 m thick and has planar, even and continuous laminations and beds with no evidence of tractional structures. Individual laminations and beds range between < 1 and 10 mm in thickness and show localized variations in grain size that help define the distinct laminations (Fig. 3.9H). W2c has an unknown lateral continuity and has not been correlated across drill holes, except as being considered part of the W2 package as a whole (e.g., Figs. 3.7 and 3.8). No fossils have been reported from this lithofacies, precluding any relative age determinations.

*Interpretation of W2:*

Due to the moderate to strong alteration affecting most of this unit, interpretation is limited and based only on a few least-altered samples.

The absence of current and wave ripples and the distinctly fine-grained, laminated nature of the mudstone (W2c) suggests that deposition occurred in a low-energy, below-wave-base environment by direct suspension settling of volcanic derived material (e.g., Walker, 1984). The normally graded sandstone to laminated mudstone (W2b) is interbedded with the polymict, pumice-rich volcaniclastic lithic breccia (W2a). The sequence of normally graded sandstone, topped by graded, laminated mudstone to siltstone is common in many turbidite systems (Stow, 2005).

The extent and thickness of the polymict, pumice-rich volcaniclastic lithic breccia (W2a) is consistent with a syn-eruptive origin (e.g., Orton, 1996). The wispy character of the chlorite-altered relict basaltic andesite tube pumice clasts suggests they are likely to be juvenile. The dense, ragged and blocky (non-pumiceous) basaltic andesite clasts may also be juvenile. The high abundance of fine matrix and relict pumice clasts suggest that the eruption was explosive (e.g., Cas and Wright, 1987). Macroscopically, the former pumice clasts show no consistent evidence of compaction. Locally, the more ragged basaltic andesite clasts have chlorite-altered, quenched rims, consistent with hot emplacement. They may have been erupted from an active vent seated in a basaltic andesite dome or lava (e.g., White, 2000). Submarine welded pyroclastic facies such as these are extremely rare.

The normally graded to massive internal organization of the W2c breccia, interbedded with marine mudstones and sandstones (W2b and W2c), suggests deposition from syn-eruptive, pumice-rich gravity currents (e.g., Bull and McPhie, 2007). Therefore, the W2 facies association can be interpreted as an accumulation of one or more explosive-eruption-fed submarine mass-flow deposits (e.g., White, 2000).

### *3.3.2 Namosi Andesite Formation*

The Namosi Andesite Formation has the widest distribution of any rock unit in the Namosi district. The NAF has an inferred total thickness of < 1500 m and a lateral extent > 16 km (Fig. 3.1). Band (1968) identified five major stratigraphic members during his geological mapping

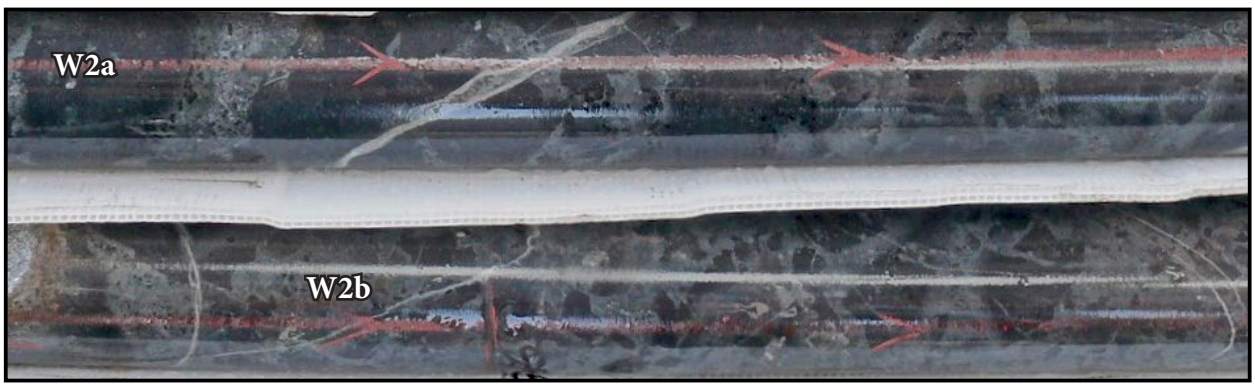


**Figure 3.10:** Core box photograph of the peperitic contact between basaltic andesite (W1a) and sandstone (W2b). Core tray: NVD014 589.30 – 591.90 m.

campaign of southern Viti Levu, which are, from oldest to youngest: (i) sandstones and conglomerates; (ii) augite andesite flows; (iii) augite andesite volcanic conglomerates; (iv) hornblende andesite volcanic conglomerates and (v) hornblende andesite flows. The current study has identified and defined two mappable lithofacies associations that occur in and around the principal porphyry deposits of the Namosi district: (i) mixed-provenance sedimentary and (ii) primary volcanic facies associations. Descriptions of the facies are based on observations made during logging of drill core from the deposits and prospects across the district.

#### *3.3.2.1 Mixed-provenance submarine mass-flow deposits (N1)*

##### *Calcareous sandstone and siltstone (N1a)*

The calcareous sandstone and siltstone unit is laterally discontinuous and locally forms the basal portion of the Namosi Andesite Formation. This lithofacies is characterized by thinly bedded calcareous sandstone comprising moderate- to well-sorted, fine- to medium-grained calcite and feldspar crystals with lesser pyroxene. Individual beds are < 5 cm thick and form part of a package up to 4 m thick. Thinly bedded (< 5 cm thick) calcareous and siliceous siltstone is interbedded locally with the sandstone (Fig. 3.11). The calcareous sandstone unconformably overlies the Wainimala basement and occurs subjacent to the polymict conglomerates and pebble-bearing wackes (N1b) of the Namosi Andesite Formation. Locally, the calcareous sandstones are replaced by a calc-silicate mineral assemblage of garnet, epidote, actinolite and chlorite that has imparted a distinctive mottled green, white, black and red coloration (Fig. 3.11). The sandstones locally con-


**Figure 3.11:** Hand sample photograph of calcareous sandstone (N1a). Pale fine-grained sandstone to siltstone with medium grained calcareous feldspathic sandstone forming dark green beds. Sample is intruded by small finger of the EMD intrusion. Sample: NWK020 403 m. Abbreviations: act = actinolite, EMD = early mineralization diorite.

tain rounded coral fragments and small mollusca (e.g., Band, 1968). Most notably they contain *Cycloclypeus indopacificus* foraminifera.

*Very-thickly bedded, polymict conglomerate and pebble-bearing wacke (N1b)*

Facies N1b consists of a poorly to very poorly sorted, polymict, sand matrix-supported, weakly graded and diffusely bedded pebble conglomerate (Fig. 3.12C) and pebble-bearing wacke (Fig. 3.12B). The lower part of the unit locally displays weak reverse grading. This package overlies an angular unconformity with steeply-dipping basaltic andesite lavas and breccias of the Wainimala group (Fig. 3.2) and locally overlies facies N1a. The individual beds range from 3 to > 20 m thick and the package has an overall thickness of up to 70 m. Unit N1b is laterally extensive (> 6.5 km; occurs at ~ -100 mRL at Wainaulo and ~ 200 mRL at Waisoi West). It maintains a relatively uniform thickness across the district and is a useful marker horizon (Fig. 3.3).

The conglomerate consists of subrounded, granule to very large pebble-sized clasts (outsized to boulders) of chert, mudstone, andesite, dacite, Wainimala basaltic andesite, and Colo Plutonic Suite intrusives. Mauve, thermally oxidized quartz-feldspar-phyric dacite clasts occur locally (e.g., Fig. 3.12C). Near the base of the unit, clasts derived from the Wainimala basement become increasingly abundant. The clasts are supported by a matrix of granule-sized lithic fragments and sand-sized broken crystals of plagioclase and pyroxene (Figs. 3.12D and E).

The pebble-bearing wacke consists of granule- to pebble-sized clasts (~ 5 vol %) of quartz and undifferentiated lithic fragments. Medium to coarse sand-sized broken feldspar and pyroxene crystal fragments are supported in a mud- to fine sand-sized matrix (~ 20 vol %). The pebble-bearing wacke is the most abundant rock type of the N1 facies association.

*Very thinly interbedded mudstone and fine-grained sandstone (N1c)*

Facies N1c is a relatively thin package (< 70 cm) of moderately well to well-stratified, very thinly bedded, lithic-bearing volcaniclastic mudstone and interbedded fine-grained sand-

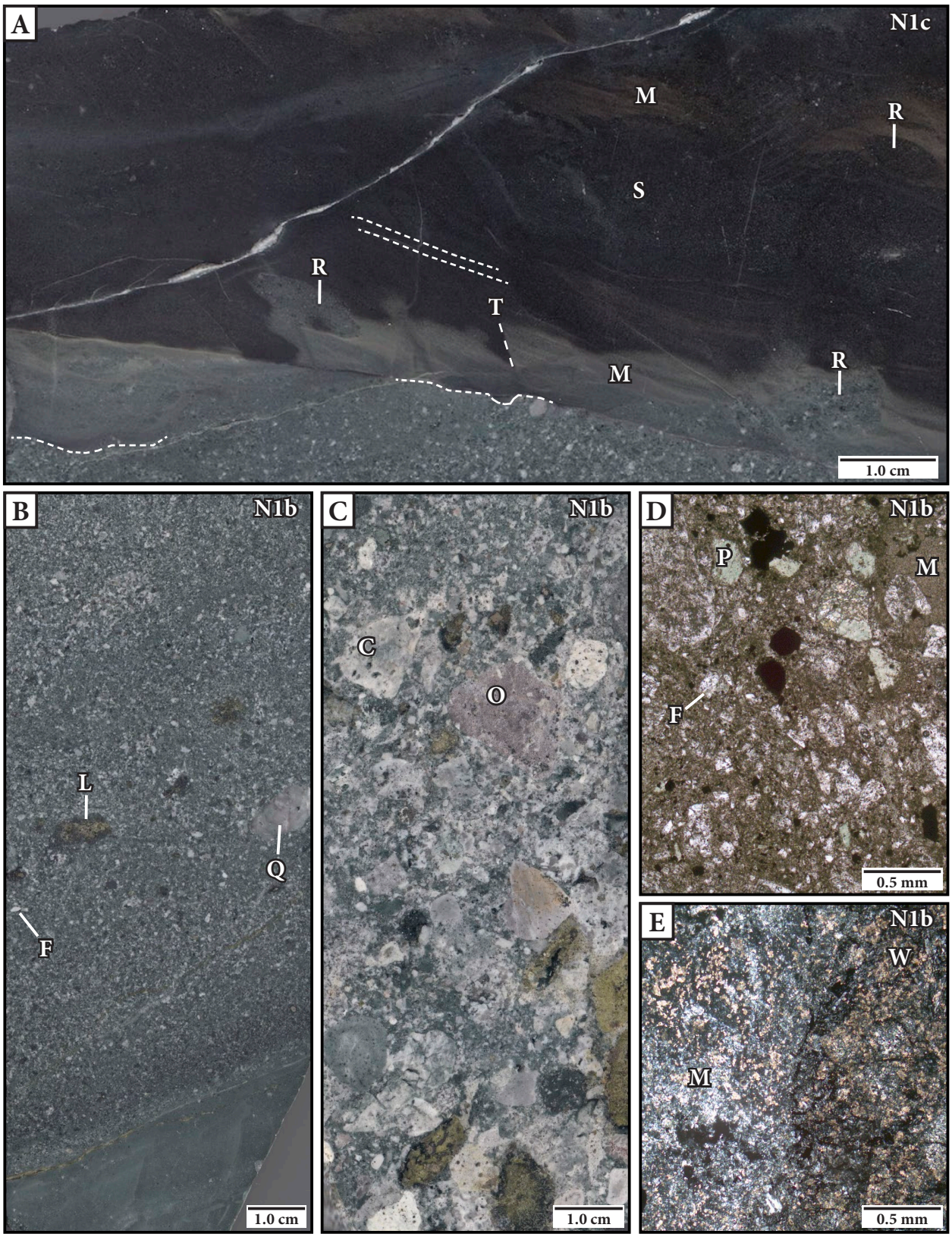


**Figure 3.12:** Representative photographs of facies N1b and N1c. **A.** Interbedded mudstone and sandstone unit showing erosive lower contact, sandstone rip-up clasts, disrupted laminations and planar laminations. Sample: NVD014 499 m. **B.** Pebble-bearing wacke showing quartz, lithic and feldspar fragments. Sample: NVD014 498 m. **C.** Polymict conglomerate showing thermally oxidized rhyolite clast. Sample: NVD014 514 m. **D.** Plane polarized photomicrograph of pebble-bearing wacke showing abundance of mud to fine sand-sized matrix with mudstone clasts and broken feldspar and augite crystals. Sample: NVD014 498 m. **E.** Cross polarized photomicrograph of pebbly conglomerate showing mud matrix and perlitic Wainimala clast. Sample: WSD214 205 m. Abbreviations: C = chert, F = feldspar crystal fragment, L = lithic, M = mudstone, O = thermally oxidized, P = pyroxene crystal fragment, Q = quartz, R= rip-up clast, S = sandstone, T = thrust, W = Wainimala clast.

stone. The mudstone is buff gray to dark brown and has an erosive contact with the underlying pebble-bearing wacke (N1b; Fig. 3.12A and C). At the base of the facies, discontinuous, wavy, non-parallel laminations are disrupted by cm-scale faults (Fig. 3.12A). Local scours and sandstone rip-up clasts also occur (Fig. 3.12A). Further up the package, laminations become discontinuous and planar parallel subjacent to the interbedded sandstone (Fig. 3.12A). The sandstone is dark brown, fine-grained, moderately well sorted and locally displays normal grading. Rip-up clasts of the sandstone occur within the overlying wavy-laminated mudstone beds (Fig. 3.12A).

*Interpretation of N1:*

The N1 facies association is dominated by polymict conglomerate and pebble-bearing wacke, reflecting proximity to a source of coarse clasts. Massive, graded, or internal planar stratified, tabular beds within all N1 facies suggest emplacement by mass-flow processes in a setting below storm-wave-base (e.g., McPhie, 1995). The high percentage of matrix to clasts suggests a debris flow origin (e.g., Swarbick and Naylor, 1980). Very thinly interbedded mudstone and fine-grained sandstone comprise only a minor proportion of the sequence (< 5 %) and lack well-developed current-generated sedimentary structures typical of shoreline marine environments such as cross-stratified sediments (e.g., Elliot, 1986). The mudstone (N1c) may have been deposited by a dilute turbidity current, rather than by the debris flow and may have been created by mud-water mixing at the debris flow snout (e.g., Hampton, 1972).

The presence of incomplete *Cycloclypeus indopacificus* foraminifera fossils within the calcareous sandstone (N1a) suggests a tropical shallow marine source for the sediments and a maximum Middle to Late Miocene age. Typically, these organisms lived in shallow platform reef banks or reef slopes defined by the 200 m isobath (Koba, 1978; Hallock and Glenn, 1986). This suggests that the site of deposition was at least 200 m deep. The presence of thermally oxidized clasts suggests that subaerially-derived, weathered volcanic clasts were incorporated into the debris flows, and similarly imply a near-shore setting. Therefore, the N1 lithofacies association is interpreted as one or more shallow submarine debris flow-turbidite couplets.

### *3.3.2.2 Crowded pyroxene-plagioclase-phyric andesite and associated breccia (N2)*

#### *Crowded pyroxene-plagioclase-phyric andesite (N2a)*

The crowded pyroxene-plagioclase-phyric andesite is typically massive, fine to coarse grained, phenocryst-crowded with a hypocrystalline groundmass. Locally, the groundmass contains very faint round shapes with internal subdivisions (Fig. 3.13B). These features delineate cuspate, dark brown apparent shard shapes (false vitriclastic texture) commonly found in altered perlite (e.g., McPhie et al., 1993; Fig. 3.13B). The dominant phenocryst phase is stubby to tabular, subhedral to euhedral, albite-twinned and normally-zoned plagioclase that are 0.5 to 2.0 mm and have a modal abundance up to 40 % (Figs. 3.13A and C). Less abundant clinopyroxene occurs as dark brown to black, blocky, euhedral phenocrysts that are 0.5 to 3.0 mm (outsized to 6.0 mm) and have a modal abundance up to 10 % (Figs. 3.13A and C). Accessory magnetite and Fe-Ti oxides are fine-grained and sparse and are enclosed by murky brown glass (Fig. 3.13B).

The crowded pyroxene-plagioclase-phyric andesite occurs as a massive, tabular body, locally > 150 m thick, laterally extensive (> 750 m) and open to the north. It occurs around the Wainaulo and Wainaulo West deposits where it forms the dominant outcropping unit in the area (Figs. 3.3, 3.4 and 3.5). Unit N2a is poorly constrained elsewhere. The top and bottom of the unit have a gradational contact with the monomict breccia facies (N2b), however it is typically obscured by the effects of hydrothermal alteration.

#### *Monomict, in situ to clast-rotated andesite breccia (N2b)*

The monomict, *in situ* to clast-rotated andesite breccia is characterized by jigsaw-fit to clast-rotated, crowded pyroxene-plagioclase-phyric andesite (N2a) clasts in an apparent sand-

**Figure 3.13 (opposite):** Examples of Namosi Andesite Formation andesite and andesite breccia (N2). **A.** Hand sample of float from the NVD019 collar area illustrating outsized pyroxene phenocrysts in the N2a andesite. **B.** Photomicrograph of andesite (N2a) illustrating false vitriclastic texture (dark brown concavo-convex shapes) and perlitic fractures defined by illite-smectite alteration. Sample: NVD047 240 m **C.** Hand sample of characteristic N2a pyroxene-feldspar-phyric andesite. Sample: NVD047 240 m. **D.** Hand sample of monomict andesite breccia (N2b) showing perlitic fractures in an andesite clast. Sample: NVD014 215 m. **E.** Sample of N2b showing clast-selective epidote alteration where the formerly glassy clast edges have been completely altered to chlorite and are surrounded by a domain of albite alteration with closely packed jigsaw-fit breccia textures. Sample NVD019 224 m. **F.** Photomicrograph of the pyroxene-microdiorite (N2c) illustrating a fine-grained equigranular texture. Sample: NVD019 361 m. Abbreviations: ab = albite, aug = augite, C = clast, chl = chlorite, ep = epidote, fv = false vitriclastic texture, Mx = matrix, P = relict perlitic texture, pl = plagioclase.

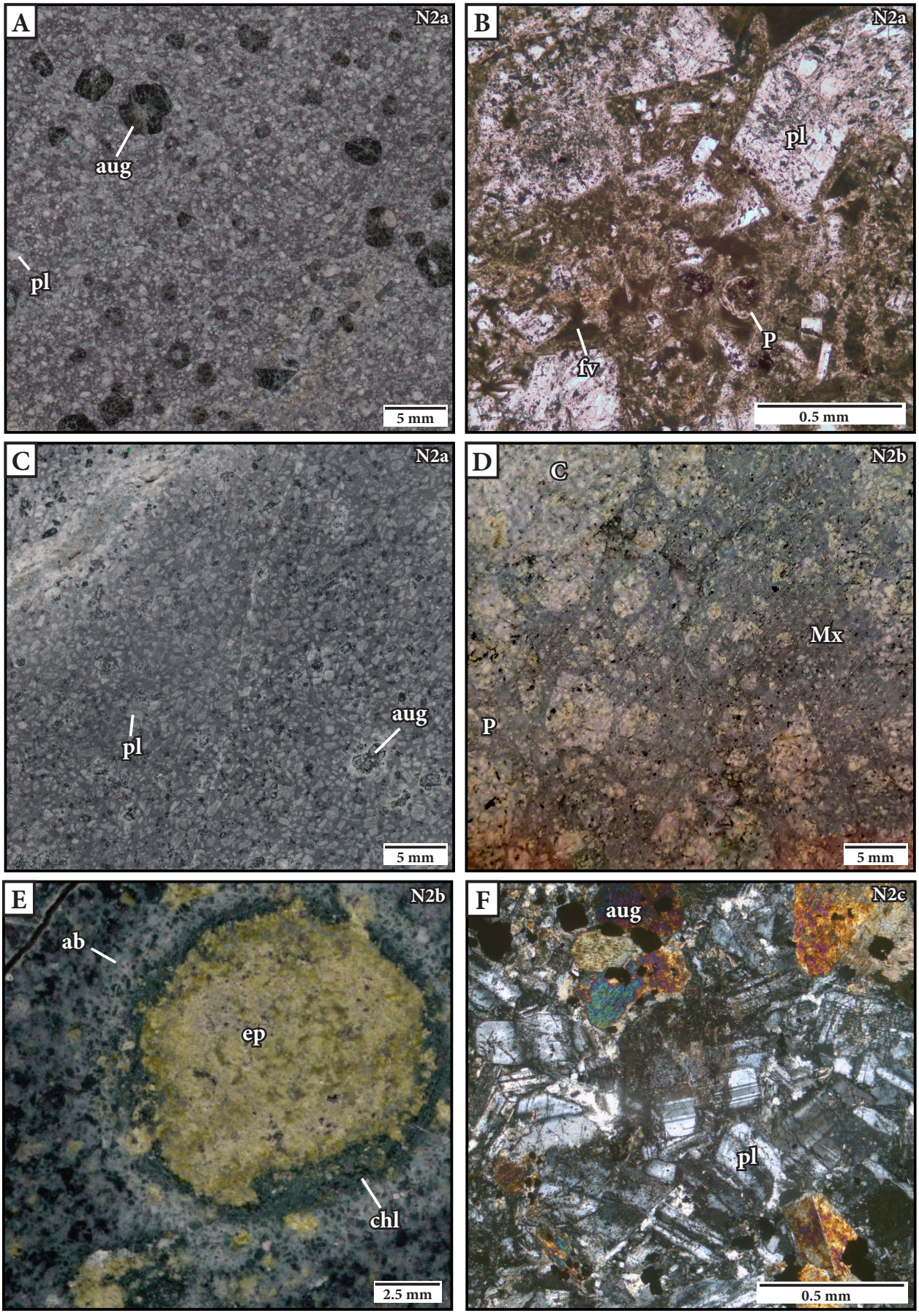
A
N2a
aug
pl
5 mm
B
N2a
pl
P
fv
0.5 mm
C
N2a
pl
aug
5 mm
D
N2b
C
Mx
P
5 mm
E
N2b
ab
ep
chl
2.5 mm
F
N2c
aug
pl
0.5 mm

sized matrix. This unit is up to 200 m thick and is laterally extensive (> 750 m; Figs. 3.3, 3.4 and 3.5). It has gradational upper and lower contacts with the crowded pyroxene-plagioclase-phyric andesite (N2a) and sharp lower contacts with the very-thickly bedded, polymict conglomerate and pebble-bearing wacke (N1b) and locally with pyroxene-microdiorite. The breccia is predominantly massive and poorly sorted. It contains well-defined blocky and splintery clasts of perlitic crystal-crowded pyroxene-plagioclase-phyric andesite (5 mm to 40 cm; 40 to 90 % of the rock; Fig. 3.13D). A network of smaller splintery clasts (millimeter to centimeter scale) of identical composition occurs interstitial to the larger clasts, giving an apparent matrix-supported texture locally, whereby the clasts appear to have a gradational contact with the matrix (Fig. 3.13E). Where clasts are better defined, their margins are intensely chlorite altered (formerly glassy?) and are surrounded by a narrow zone (< 1 cm) of albite alteration and a closely packed jigsaw-fit texture (Fig. 3.13E).

*Pyroxene-feldspar-phyric microdiorite (N2c)*

The pyroxene-feldspar-phyric microdiorite consists of 5 to 20 m-thick bodies with an unknown vertical extent and length (Figs. 3.2 and 3.4). N2c has an equigranular to strongly porphyritic texture and is fine to medium grained (Fig. 3.13F). Primary plagioclase are euhedral to subhedral, blocky to stubby, turbid, locally zoned, and have a modal abundance up to 75 % (Fig. 3.13F). Subordinate primary clinopyroxene has commonly been completely pseudomorphed by secondary actinolite ± chlorite and can be difficult to identify (Fig. 3.13F). Where unambiguously identifiable, the clinopyroxene occurs as black, blocky, euhedral crystals with up to 20 % modality and outsized phenocrysts up to 4 mm.

N2c has sharp contacts with N1, N2a and N2b, that are discordant with the sedimentary layering. N2c is most abundant in the northern portion of Wainaulo (Figs. 3.3 and 3.4).

*Interpretation of N2:*

The monomict, *in situ* to clast-rotated andesite breccia (N2b) occurs superjacent and subja-

cent to the crowded pyroxene-plagioclase-phyric andesite (N2a). This relationship is observable in drill core from Wainaulo and Wainaulo West areas. The monomict breccia (N2b) is interpreted to be an autoclastic facies, likely part of a hyaloclastite sequence (e.g., Smith and Batiza, 1989). The clasts within the monomict breccia show jigsaw-fit to clast-rotated internal organization with sharp, irregular and blocky shapes signifying brittle fragmentation, probably from quench fragmentation (e.g., Cas and Wright, 1987). The lack of bed forms, abundant blocky clast shapes with curviplanar surfaces, jigsaw-fit organization, and monomict clast population is consistent with minimal post-fragmentation transport (Maicher et al., 2000). The clast composition of the monomict breccia is mineralogically and texturally identical to the crowded pyroxene-plagioclase-phyric andesite (N2b) and is interpreted to be its autoclastic facies (e.g., McPhie et al., 1993). The pyroxene-feldspar-phyric andesite is concordant with sedimentary layering, contains quenched glassy textures and is surrounded by *in situ* andesite hyaloclastite. These features are consistent with a subaqueous lava flow (e.g., McPhie et al., 1993).

The pyroxene-microdiorite is highly porphyritic to equigranular and has discordant contacts with sedimentary layering, which suggest a shallow dike-like intrusive origin. The N2c dikes have locally intruded the crowded pyroxene-plagioclase-phyric andesite and the monomict, *in situ* to clast-rotated andesite breccia within the Wainaulo area. These dikes may be feeder dikes associated with the crowded pyroxene-plagioclase-phyric andesite (e.g., Kano, 1989).

The crowded pyroxene-plagioclase-phyric andesite and breccia are interpreted to be the coherent and hyaloclastite components of subaqueous lavas and hypabyssal intrusions (e.g., Mcphie et al., 1993).

### *3.3.3 Korobasabasaga Formation*

Field relationships between the NAF and the Korobasabasaga Formation (KF) are not well constrained and contacts were not observed during this study. Ellis (1996) reported that the two formations have a faulted contact and that KF has a post-mineralization timing. The KF forms a thick (> 1000 m), predominantly volcaniclastic sequence that weathers to form steep cliffs west

of the Waisoi area (Fig. 3.1; Ellis, 1996). The KF varies from very coarse sandstone near its base, to coarse sandstone and minor basaltic trachyandesite flows near its top. Where encountered in this study, the KF presents as a polymict, matrix-supported breccia with a chaotic clast organization. The unit it typified by angular to subangular, moderately to poorly sorted, granule- to cobble-sized clasts set in a crystal-rich matrix. The clasts are grey to orange (thermally oxidized) and have a K-feldspar-phyric trachyandesite to basaltic trachyandesite composition. Pale pumice fiamme define a weak to strong foliation locally. Crawford (2011) interpreted the KF to be part of the extensive Pliocene Ba Group, which include the stratovolcanoes at Raki Raki, Tavua and Tuvatu in northern Viti Levu.

## 3.4 Intrusive rocks of the Namosi district

### *3.4.1 Introduction*

In this section, three Late Miocene to Early Pliocene intrusive complexes that are associated with copper-gold mineralization are described (Table 3.1). The intrusive complexes are separated by up to 6.5 km, but are interpreted to be apophyses from the same source pluton at depth (e.g., Dilles et al., 2000). These complexes have intruded the NAF and Wainimala Group rocks. The Wainaulo intrusive complex (WIC) consists of two pre-mineralization plutons, stocks and dikes that locally crop out at ~ 250 mRL in the Wainaulo area (Figs. 3.2, 3.3 and 3.4). The interpreted mineralizing dikes are not exposed at surface, and their tops are as shallow as ~ 250 m depth (~ 0 mRL; Fig. 3.4). The dikes are almost entirely hosted within the pre-mineralization intrusions. The Waisoi West intrusive complex (WWIC) occurs ~ 6.5 km to the northeast of the WIC and locally crops out at ~ 200 mRL within NAF host rocks (Figs. 3.1, 3.2, 3.6 and 3.7). The Waisoi East intrusive complex (WEIC) occurs < 2 km directly east of the WWIC. The WEIC crops out at ~ 250 mRL within Wainimala Group rocks (Figs. 3.1, 3.2 and 3.6).

### *3.4.2 Wainaulo intrusive complex*

The Wainaulo intrusive complex is spatially and temporally associated with the hydrothermal

**Table 3.1**: Characteristics of the intrusive complexes of the Namosi district

| Intrusive phase | Textures and distinctive features | Phenocryst assemblage: | Phenocryst % | Mafics % | Plagioclase (mm) | Hornblende (mm) | Groundmass | Cu (%)/ Au (ppm)[a] | Age (Ma) |
|---|---|---|---|---|---|---|---|---|---|
| Wainaulo intrusive complex (WIC) | | | | | | | | | |
| PD | Dosemic | pl, hbl, mag, qtz, aug | 60 – 65 | 20 | 1 – 4; outsized to 7 | 1 – 4; outsized to 8 | Hypidiomorphic granular; pl, qtz > mag, ap; 0.05 – 0.10 mm | Passive host | 5.99 ± 0.46[2] |
| PA | Sempatic; dark gray-green pl | pl, hbl, mag | 50 – 55 | 7 – 10 | 1 – 3; outsized to 8 | 1 – 3; outsized to 8 | Hypidiomorphic granular; fsp, qtz; < 0.02 mm | Passive host | 6.0 ± 0.3[4] |
| EMD | Sempatic; stubby (rounded) pl; EMD2: bt - qtz miarolitic cavities | pl, hbl, mag | 45 – 50 | 5 – 7 | 1 – 4; outsized to 10 | 1 – 4; outsized to 10 | Seriate; pl, hbl, or > qtz, mag, ap; < 0.05 to 0.30 mm | 0.61/ 0.03 | 5.654 ± 0.095[1] 5.31 ± 0.43[2] |
| EMQD | Sempatic; act - ep - ccp miarolitic cavities; USTs; subophitic | pl, hbl, or, aug, mag, qtz, ap | 40 – 45 | ~ 12 | 0.2 – 2.0 | 0.1 – 2.0 | Hypidiomorphic granular; qtz, fsp > hbl, ap; < 0.05 mm | 2.86/ 0.74 | 5.554 ± 0.054[1] 5.46 ± 0.90[2] |
| IMQD | Sempatic; EMQD xenoliths; subophitic | pl, hbl, or, aug, mag, qtz, ap | 40 – 45 | ~ 15 | 0.2 – 2.0 | 0.1 – 3.0; outsized to 5 | Hypidiomorphic granular; qtz, fsp > hbl, ap; < 0.05 mm | 0.58/ 0.11 | 5.4 ± 0.3[3] |
| LMQD | Sempatic; PA and mafic xenoliths; subophitic | pl, hbl, or, aug, mag, qtz, ap | 40 – 45 | ~ 17 | 0.2 – 2.0 | 0.1 – 3.0; outsized to 10 | Hypidiomorphic granular; qtz, fsp > hbl, ap; < 0.05 mm | 0.05/ < 0.01 | 5.33 ± 0.22[2] |
| Waisoi West intrusive complex (WWIC) | | | | | | | | | |
| QDP1 | Sempatic; USTs; dense qtz vein stockwork; green to rust ill-altered pl | pl, or, hbl | 40 – 43 | 3 – 5 | 0.5 – 3.0 | 0.5 – 3.0 | Creamy white; intensely altered; fsp, qtz, mag; < 0.2 mm | 0.94/ 0.34 | 5.492 ± 0.043[1] |
| QDP2 | Sempatic; QDP1 and qtz-vn xenoliths; ghosted gray pl; glomerophyric pl; bipyramidal qtz-eyes | pl, hbl, or, qtz, mag | 40 – 43 | 5 – 7 | 0.3 – 2.0 | 0.3 – 3.0 | Hypidiomorphic granular; pl, qtz, or, hbl, mag; < 0.2 mm | 0.48/ 0.20 | 5.0 ± 0.3[3] |
| QDP3 | Dopatic; anh miarolitic cavities; translucent white glomerophyric pl with interstitial anh | pl, hbl, aug, mag, or, qtz, ttn | 37 – 40 | 5 – 7 | < 4; outsized to 8 | 0.3 – 2.0 | Hypidiomorphic granular; pl, qtz, or, hbl, rt; 0.01 – 0.20 mm | 0.06/ 0.02 | |
| Waisoi East intrusive complex (WEIC) | | | | | | | | | |
| DP1 | Dopatic; abundant amoeboid and subhedral bipyramidal qtz phenocrysts; qtz - ccp - py miarolitic cavities; glomerophyric pl and or | pl, qtz, or, hbl, mag | 35 – 40 | 3 – 5 | 1 – 4 | 0.2 – 3.0 | Hypidiomorphic granular; or, pl, qtz, hbl, ttn, mag; < 0.02 mm | 0.43/ 0.11 | 5.432 ± 0.031[1] |
| DP2 | Dopatic; qtz-vn xenoliths | pl, qtz, or, hbl, mag | 35 – 40 | 3 – 5 | < 4 | < 5 | Hypidiomorphic granular; or, pl, qtz, hbl, ttn, mag; < 0.02 mm | 0.01/ 0.01 | 5.297 ± 0.025[1] |
| DP3 | Dopatic; rare qtz compared with DP1 and DP2; conspicuous hbl | pl, qtz, or, hbl, mag | 35 – 40 | 5 – 7 | 1 – 6 | 0.5 – 2.0; outsized to 7 | Hypidiomorphic granular; or, pl, qtz, hbl, ttn, mag; 0.03 – 0.40 mm | 0.23/ 0.03 | |
| QFP | Dosemic; bimodal phenocryst grain size; conspicuous coarse grained fsp and qtz | pl, or, qtz, hbl, mag | 65 – 70 | 3 – 5 | 0.5 to 3.0; 5 to 20 | 0.5 to 2.0 | Hypidiomorphic granular; fsp, qtz, hbl, rt, ttn, mag; < 0.01 mm | 0.00/ 0.00[b] | Pleistocene[5] |

Metal grades: [a]Copper, gold and molybdenum grades based on averages of assay results from the NJV database over intervals of that intrusion logged by the author, [b]Copper and gold grades from whole-rock analysis of a grab sample of the QFP intrusion (Appendix D). Geochronology methods and data sources: [1]CA-TIMS (This study), [2]ELA-ICP-MS (This study), [3]ELA-ICP-MS (Harris, 2009a), [4]K–Ar (Tanaka et al., 2010), [5]Relative age estimate based on post-mineralization timing. Abbreviations: act = actinolite, anh = anhydrite, ap = apatite, aug = augite, bt = biotite, ccp = chalcopyrite, DP1 = quartz-eye dacite, DP2 = quartz-bearing dacite, DP3 = dacite porphyry, EMD = early-mineralization diorite, EMQD = early-mineralization quartz-diorite, ep = epidote, fsp = feldspar, hbl = hornblende, ill = illite, IMQD = inter-mineralization quartz-diorite, LMQD = late-mineralization quartz-diorite, mag = magnetite, or = orthoclase, PA = porphyritic andesite, PD = porphyritic diorite, pl = plagioclase, py = pyrite, QDP1 = quartz-diorite porphyry 1, QDP2 = quartz-diorite porphyry 2, QDP3 = quartz-diorite porphyry 3, QFP = quartz-feldspar porphyry, qtz = quartz, qtz-vn = quartz-vein, rt = rutile, ttn = titanite, UST = unidirectional solidification texture.

system that formed the Wainaulo copper-gold orebody (Figs. 3.4 and 3.14). The results from drill core logging and cross-section construction during this study revealed that mineralization and alteration span multiple intrusive events at Wainaulo. This is typical of porphyry Cu systems worldwide (e.g., El Salvador, Chile: Gustafson and Hunt, 1975; Ridgeway, Australia: Wilson et al., 2003; Bingham Canyon, USA: Redmond and Einaudi, 2010).

Two texturally distinctive porphyritic stocks, dikes and plutons characterize the earliest phases of magmatism at Wainaulo (PA: porphyritic andesite; PD: porphyritic diorite). The low quartz vein abundances, absence of refractory quartz-vein xenoliths and their position with respect to mineralization and alteration is interpreted to indicate a pre-mineralization age (Fig. 3.14).

Five different intrusive phases related to Cu-Au ± Mo mineralization at Wainaulo have been identified during this study (EMD1, EMD2, EMQD, IMQD and LMQD). These porphyry phases are petrographically similar and therefore were distinguished on the basis of igneous textures, crosscutting relationships, chilled contacts, abrupt changes in copper and gold tenor, types and styles of associated hydrothermal alteration, and the presence of vein xenoliths (cf. Sillitoe, 2010).

### *3.4.2.1 Pre-mineralization diorites (PA and PD)*

*Porphyritic diorite (PD)*

Age: 5.99 ± 0.46 Ma (ELA-ICP-MS U–Pb on zircons; this study)

The PD intrusion occurs on the northern side of the Wainaulo orebody (Figs. 3.3 and 3.4) as a subvertical, tabular stock and dikes (up to 40 m wide) with an east-northeast elongation. The PD stock measures 125 m north-south and has a vertical extent > 1 km (Fig. 3.4). It has a length along strike > 350 m, but its limits are poorly defined. Field relationships indicate that the PD

**Figure 3.14 (opposite):** Partial summary log of NVD019, showing lithotype, alteration, copper and gold grades. High copper and gold grades coincide with chlorite – albite – actinolite – epidote alteration in the EMQD and adjacent PA host rock. Copper grades decrease gradually over 30 meters away from the EMQD and PA contact. Gold grades decrease substantially outside of the EMQD intrusion. Moderate copper and low gold grades are coincident with the EMD1 and EMD2 intrusions. Copper grades gradually decline from 50 to 100 m away from the EMD1 contact within the PA host rock. Moderate copper grades coincide with the andradite – actinolite – magnetite alteration at ~ 540 m depth. The Hematite and Kaolinite shears and associated kaolinite – montmorillonite alteration had a negative effect on copper and especially gold grades. The intrusion of LMQD also had a negative effect on copper and gold grades. LMQD is almost Cu and Au barren.

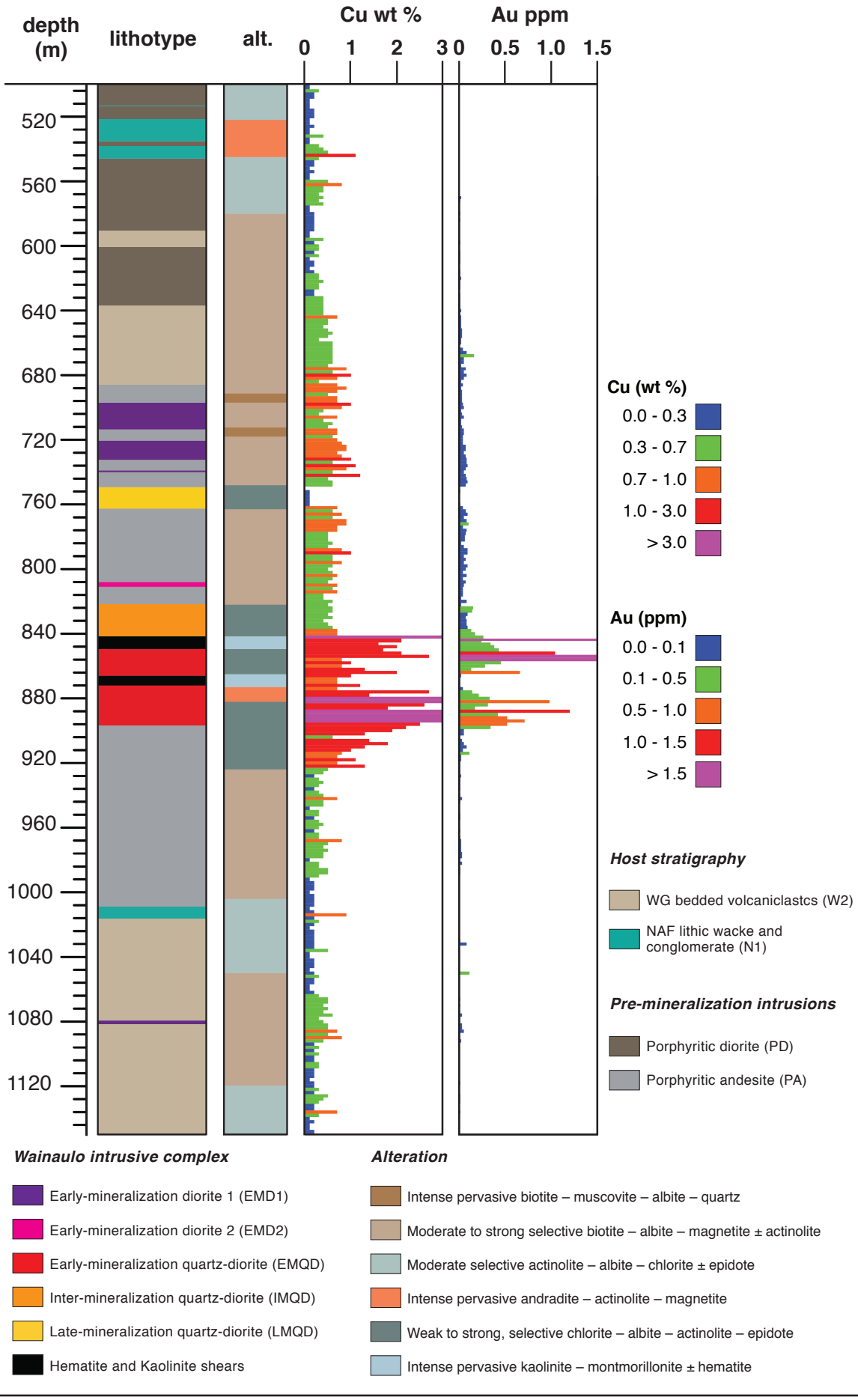
depth (m)
lithotype
alt.
Cu wt %
0
1
2
3
Au ppm
0
0.5
1.0
1.5
520
560
600
640
680
720
760
800
840
880
920
960
1000
1040
1080
1120
Cu (wt %)
0.0 - 0.3
0.3 - 0.7
0.7 - 1.0
1.0 - 3.0
> 3.0
Au (ppm)
0.0 - 0.1
0.1 - 0.5
0.5 - 1.0
1.0 - 1.5
> 1.5
Host stratigraphy
WG bedded volcaniclastcs (W2)
NAF lithic wacke and conglomerate (N1)
Pre-mineralization intrusions
Porphyritic diorite (PD)
Porphyritic andesite (PA)
Wainaulo intrusive complex
Early-mineralization diorite 1 (EMD1)
Early-mineralization diorite 2 (EMD2)
Early-mineralization quartz-diorite (EMQD)
Inter-mineralization quartz-diorite (IMQD)
Late-mineralization quartz-diorite (LMQD)
Hematite and Kaolinite shears
Alteration
Intense pervasive biotite – muscovite – albite – quartz
Moderate to strong selective biotite – albite – magnetite ± actinolite
Moderate selective actinolite – albite – chlorite ± epidote
Intense pervasive andradite – actinolite – magnetite
Weak to strong, selective chlorite – albite – actinolite – epidote
Intense pervasive kaolinite – montmorillonite ± hematite

intruded the NAF hyaloclastite sequence and the sedimentary facies, and has no direct contact relationships with any other intrusions (Figs. 3.4 and 3.14). The PD is spatially coincident with a magnetite-cemented breccia that occurs in NVD019 at 440 m depth (described in Chapter 5). Copper and gold grades, as well as alteration domains, cut across the PD intrusion (Figs. 3.4 and 3.14). Therefore, it is interpreted to be a passive host to mineralization.

The PD has a massive, dosemic ($1/7 < {}^{a}/_{b} < 3/5$ | a = groundmass %, b = phenocryst %; Cross et al., 1906) texture that comprises medium- to coarse-grained, subhedral to euhedral, blocky plagioclase phenocrysts (1 – 4 mm, outsized to 7 mm; 38 – 40 %), euhedral to subhedral, prismatic to blocky hornblende (1 – 4 mm, outsized to 8 mm; 20 %), subequant magnetite (< 2 mm; < 4 %) and resorbed quartz eyes (< 3 mm; trace – 3 %; Figs. 3.15A, B and C). Rare pyroxene occurs as an accessory phase. The medium gray, hypidiomorphic granular groundmass (0.05 – 0.20 mm; 35 – 40 %) consists of a mosaic of fine-grained anhedral plagioclase and lesser quartz, locally with magnetite and apatite (Figs. 3.15A and B). Plagioclase phenocrysts are typically turbid with ghosted edges in hand sample due to albite alteration, and exhibit normal and oscillatory zoning in thin section. Hornblende crystals are either altered to chlorite ± actinolite (Fig. 3.15B) or biotite ± magnetite ± actinolite (Figs. 3.15A).

*Porphyritic andesite (PA)*

Age: 6.0 ± 0.3 Ma (K–Ar on bulk samples; Tanaka et al., 2010; inferred as PA)

The PA is an east-northeast striking, subvertical body with horizontal dimensions of 250 x 500 m and a vertical extent of > 1 km (Fig. 3.4). The PA hosts the mineralizing intrusions and orebody at Wainaulo (Figs. 3.4 and 3.14) and crops out along the southern margin of the Wainaulo deposit (Fig. 3.3). It commonly has xenoliths of NAF sedimentary rocks (Fig. 3.15F).

**Figure 3.15 (opposite):** Pre-mineralization diorite intrusive phases at Wainaulo. **A.** Hand sample photograph of PD intrusion illustrating the abundance of hornblende, plagioclase and quartz phenocrysts. Sample: NVD019 627 m. **B.** Cross-polarized photomicrograph of PD intrusion illustrating the distribution of plagioclase and hornblende phenocrysts in the aplitic groundmass. Sample: NVD019 512 m. **C.** Feldspar-stained hand sample of PD intrusion showing that the feldspar phenocrysts and feldspathic groundmass have been altered to albite (no stain). Sample: NVD019 512 m. **D.** Cross-polarized photomicrograph of PA intrusion illustrating the contrast in phenocryst abundance and groundmass grain size with the PD intrusion in Fig. 3.14B. Sample: NVD008 720 m. **E.** Hand sample photograph of PA intrusion. Sample: NVD008 750 m. **F.** Hand sample photograph of PA intrusion with a NAF mudstone xenolith. Sample: NVD037 269 m. Abbreviations: hbl = hornblende, mag = magnetite, NAF = Namosi Andesite Formation, pl = plagioclase, PA = porphyritic andesite, PD = porphyritic diorite, qtz = quartz.

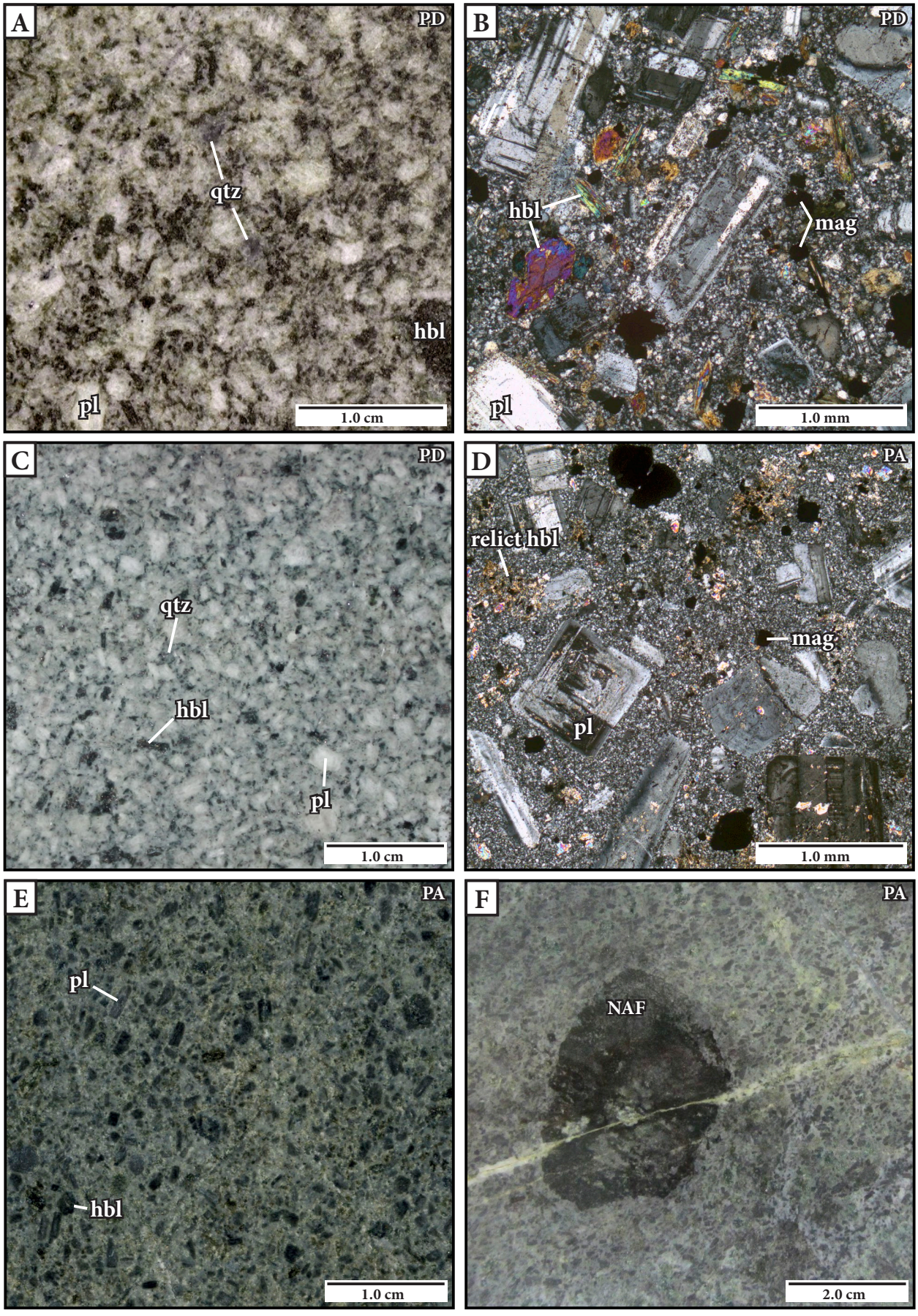
A
PD
qtz
hbl
pl
1.0 cm
B
PD
hbl
mag
pl
1.0 mm
C
PD
qtz
hbl
pl
1.0 cm
D
PA
relict hbl
mag
pl
1.0 mm
E
PA
pl
hbl
1.0 cm
F
PA
NAF
2.0 cm

The PA has a massive, sempatic (⅗ < ⅘ < ⅚ | a = groundmass %, b = phenocryst %; Cross et al., 1906) texture that consists of medium- to coarse-grained phenocrysts in a very fine-grained (< 0.02 mm) grayish-green groundmass (Fig. 3.15D). Dark greenish-gray, blocky to tabular plagioclase (1 – 3 mm, outsized to 8 mm; 40 – 43 %), relict hornblende (1 – 3 mm, outsized to 8 mm; 7 – 10 %) and medium-grained magnetite (0.2 – 1 .0 mm; 1 – 2 %) are the only phenocryst phases present (Figs. 3.15D and E). The groundmass grain size and abundance, presence of dark greenish-gray plagioclase phenocrysts, sparse hornblende, and lack of quartz eyes distinguish this unit from the PD intrusion (Fig. 3.15).

*3.4.2.2 Early-mineralization diorite complex (EMD1 and EMD2)*

Age EMD1: 5.654 ± 0.095 Ma (CA-TIMS U–Pb on zircons; this study)
Age EMD1: 5.31 ± 0.43 Ma (ELA-ICP-MS U–Pb on zircons; this study)

Early-mineralization diorites 1 and 2 (EMD1 and EMD2) occur as < 50 m-thick, subvertical, branching dikes that intrude the PA pluton below 0 mRL (Fig. 3.4). They also occur as thin (< 5 m-thick) dikes that intrude the volcano-sedimentary stratigraphy to the south of the Hematite and Kaolinite shears (Fig. 3.4). The spatial association with quartz veins, biotite alteration and moderate Cu grades (Fig. 3.14), and the absence of vein-quartz xenoliths in the EMD1 and EMD2 suggests that they are the oldest phases of magmatism genetically associated with Cu-Au mineralization at Wainaulo. Chilled margins within the EMD1 intrusions in contact with PA, suggest that EMD1 is younger (Fig. 3.16C). EMD2 can be distinguished from EMD1 by the occurrence of biotite – quartz miarolitic cavities and veins (Fig. 3.16D).

The EMD intrusions have a massive, sempatic texture (45 – 50 % phenocrysts) that comprises medium- to coarse-grained, subhedral to euhedral, stubby to blocky plagioclase phenocrysts (1 – 4 mm, outsized to 10 mm; ~ 40 %), euhedral to subhedral, prismatic hornblende (1 – 4 mm, outsized to 10 mm; 5 – 7 %) and magnetite (< 0.3 mm; < 2 %). The fine-grained, gray-green, holocrystalline, seriate-textured (0.05 – 0.30 mm) groundmass consists of subhedral to euhedral plagioclase, hornblende, orthoclase and rare quartz, magnetite and apatite (Figs. 3.16B). Plagioclase phenocrysts are turbid in hand sample due to albite alteration, and exhibit oscillatory

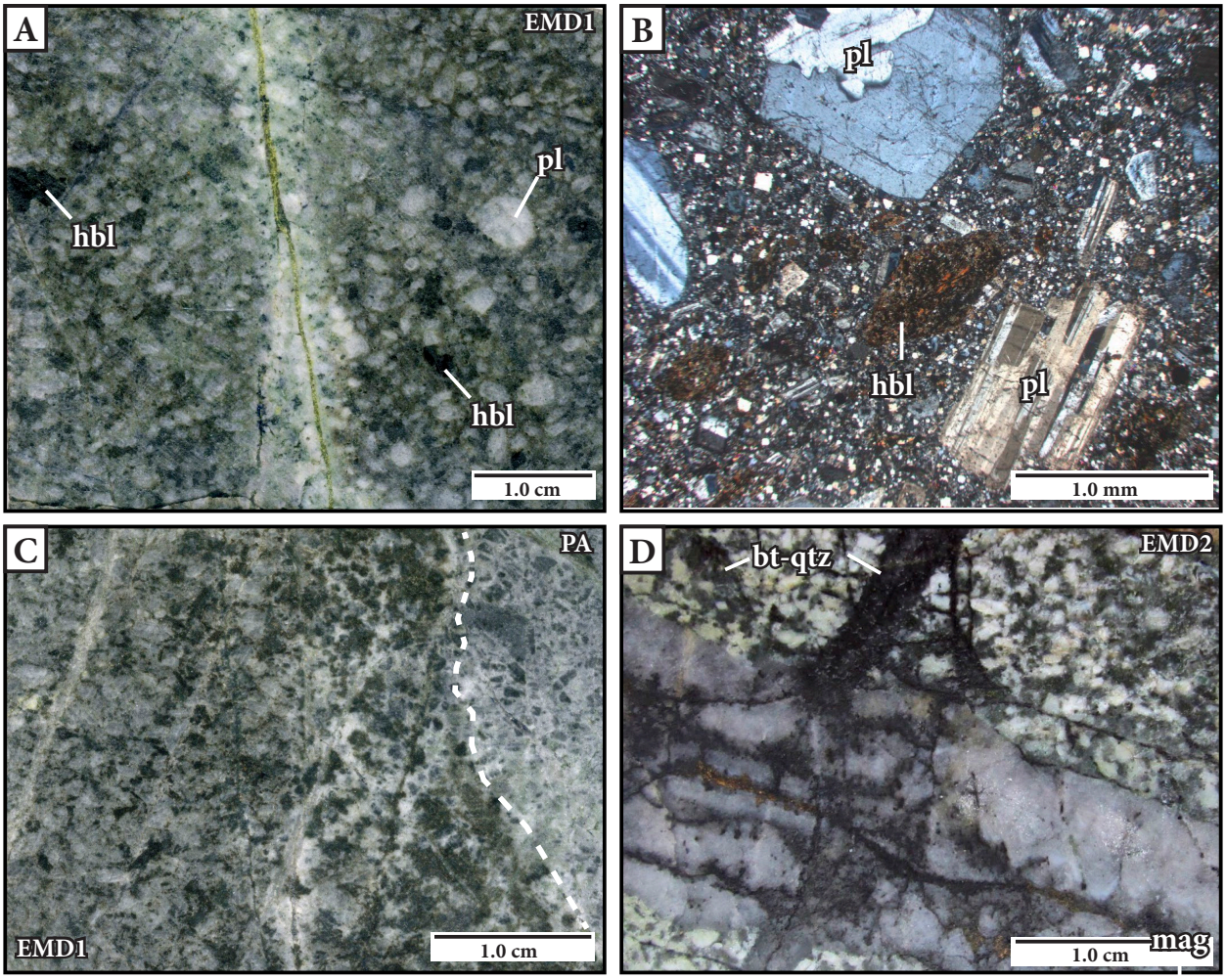


**Figure 3.16:** Representative photographs of the EMD1 and EMD2 intrusions at Wainaulo. **A.** Hand sample photograph of the EMD1 intrusion illustrating the outsized hornblende and plagioclase phenocrysts. Sample: NVD019 705 m. **B.** Cross-polarized photomicrograph of EMD1 illustrating the distribution of plagioclase and hornblende phenocrysts in the seriate-textured groundmass. Sample: NVD019 1081 m. **C.** Hand sample photograph of the contact between strongly altered EMD1 and moderately altered PA intrusions. Sample: NVD019 728 m. **D.** Hand sample photograph of the EMD2 intrusion containing biotite – quartz filled miarolitic cavities and veins. Sample: NVD019 852 m. Abbreviations: bt = biotite, EMD1 = early-mineralization diorite 1, EMD2 = early-mineralization diorite 2, hbl = hornblende, mag = magnetite, pl = plagioclase, PA = porphyritic andesite, qtz = quartz.

zoning, as well as albite and Carlsbad twinning in thin section. Hornblende crystals are partially or completely altered to secondary biotite ± actinolite (Figs. 3.16A and B).

### *3.4.2.3 Syn-mineralization quartz-diorite complex (EMQD, IMQD and LMQD)*

Age EMQD: 5.554 ± 0.054 Ma (CA-TIMS U–Pb on zircons; this study)
Age EMQD: 5.46 ± 0.90 Ma (ELA-ICP-MS U–Pb on zircons; this study)

Age IMQD: 5.4 ± 0.3 Ma (ELA-ICP-MS U–Pb on zircons; Harris, 2009a; inferred as IMQD)

Age LMQD: 5.33 ± 0.22 Ma (ELA-ICP-MS U–Pb on zircons; this study)

At Wainaulo, closely spaced, augite-bearing, orthoclase-, hornblende- and plagioclase-phyric

quartz-diorite dikes that are interpreted to be related to albite – chlorite – actinolite – epidote alteration and Cu-Au mineralization were emplaced during three phases of magmatism (Figs. 3.4, 3.14 and 3.17). The oldest of the ore-related intrusions, and the most strongly mineralized, is the early-mineralization quartz-diorite (EMQD). This was followed by the emplacement of the inter-mineralization quartz-diorite (IMQD) and then the late-mineralization quartz-diorite (LMQD) intrusions. All of the syn-mineralization quartz-diorites were emplaced as thin (< 30 m-thick), tabular dikes that strike ~ 275° – 280°, parallel to the orientation of the Hematite and Kaolinite shears, and are hosted entirely within the PA stock below ~ 100 mRL (Figs. 3.4 and 3.14). None of the syn-mineralization quartz-diorites crop out in the Wainaulo area (Fig. 3.5).

The syn-mineralization quartz-diorites have similar compositions and textures to each other (Figs. 3.17A to F). Each of the intrusions have a sempatic (40 – 45 % phenocrysts) porphyritic texture and a hypidiomorphic granular, fine-grained (< 0.05 mm) quartzofeldspathic groundmass containing accessory hornblende and apatite (Figs. 3.17B, D and F). Phenocrystic phases include medium- to coarse-grained plagioclase (0.2 – 2.0 mm; ~ 20 %), hornblende (0.1 – 3.0 mm-long; outsized to 10 mm long; 10 – 15 %; ), orthoclase (0.2 – 3.0 mm; 5 %), augite (0.2 – 5.0 mm; 2 %), magnetite (0.1 – 0.3 mm; 2 %), quartz (0.1 – 0.5 mm; ~ 1 %) and apatite (trace). Feldspars are typically translucent and white in hand specimen, and can only be differentiated petrographically or through chemical feldspar staining. In thin section, plagioclase phenocrysts display oscillatory zoning and albite twinning, while orthoclase phenocrysts display well-developed Carlsbad and simple twinning (Figs. 3.17B, D and F). Locally, elongate chadocrysts of plagioclase are partially enclosed and penetrate outsized augite oikocrysts in each of the syn-mineralization intrusions,

**Figure 3.17 (following two pages):** Representative images of the syn-mineralization quartz-diorite intrusions at Wainaulo. **A. C. and E.** Hand sample photographs of the EMQD, IMQD and LMQD intrusions, respectively, illustrating prominent augite phenocrysts as well as hornblende, plagioclase and orthoclase phenocrysts set in a creamy white fine-grained groundmass. Note the subtle increasing modal abundance of hornblende in EMQD through LMQD. Outsized augite oikocrysts partially enclose plagioclase chadocrysts, defining a subophitic texture. Sample A: NVD008 537 m. Sample C: NVD019 840 m. Sample E: NVD019 761 m. **B. D. and F.** Cross-polarized photomicrographs of the EMQD, IMQD and LMQD intrusions, respectively, illustrating the petrographic similarities between the three intrusive phases and their fine-grained, hypidiomorphic, granular quartzofeldspathic groundmasses. Sample B: NVD040 533 m. Sample D: NVD019 835. Sample F: NVD019 761 m. **G.** Hand sample photograph of the IMQD intrusion containing UST- and epidote – chalcopyrite vein-bearing EMQD xenoliths. Sample: NVD037 653 m. **H.** Hand sample photograph of the LMQD intrusion containing PA xenoliths. The xenoliths have truncated quartz and magnetite – chalcopyrite veins that are associated with the EMD1 intrusion. Sample: NVD040 620 m. **I.** Hand sample photograph of the LMQD intrusion containing a trapezoidal mafic xenolith. Sample: NVD040 633 m. **J.** Hand sample photograph of EMQD intrusion highlighting a miarolitic cavity infilled with coarse-grained actinolite, epidote and chalcopyrite, situated at the margin of a quartz UST. Sample: NVD037 619 m. **K. and L.** Hand sample photographs of the EMQD intrusion containing contorted bands of quartz and copper sulfide minerals, interpreted to be USTs. Sample K: NVD007 543 m. Sample L: NVD040 533 m. Abbreviations: act = actinolite, aug = augite, bn = bornite, ccp = chalcopyrite, EMD1 = early-mineralization diorite 1, EMQD = early-mineralization quartz-diorite, ep = epidote, hbl = hornblende, IMQD = inter-mineralization quartz-diorite, LMQD = late-mineralization quartz-diorite, mag = magnetite, or = orthoclase, PA = porphyritic andesite, pl = plagioclase, py = pyrite, qtz = quartz, UST = unidirectional solidification texture.

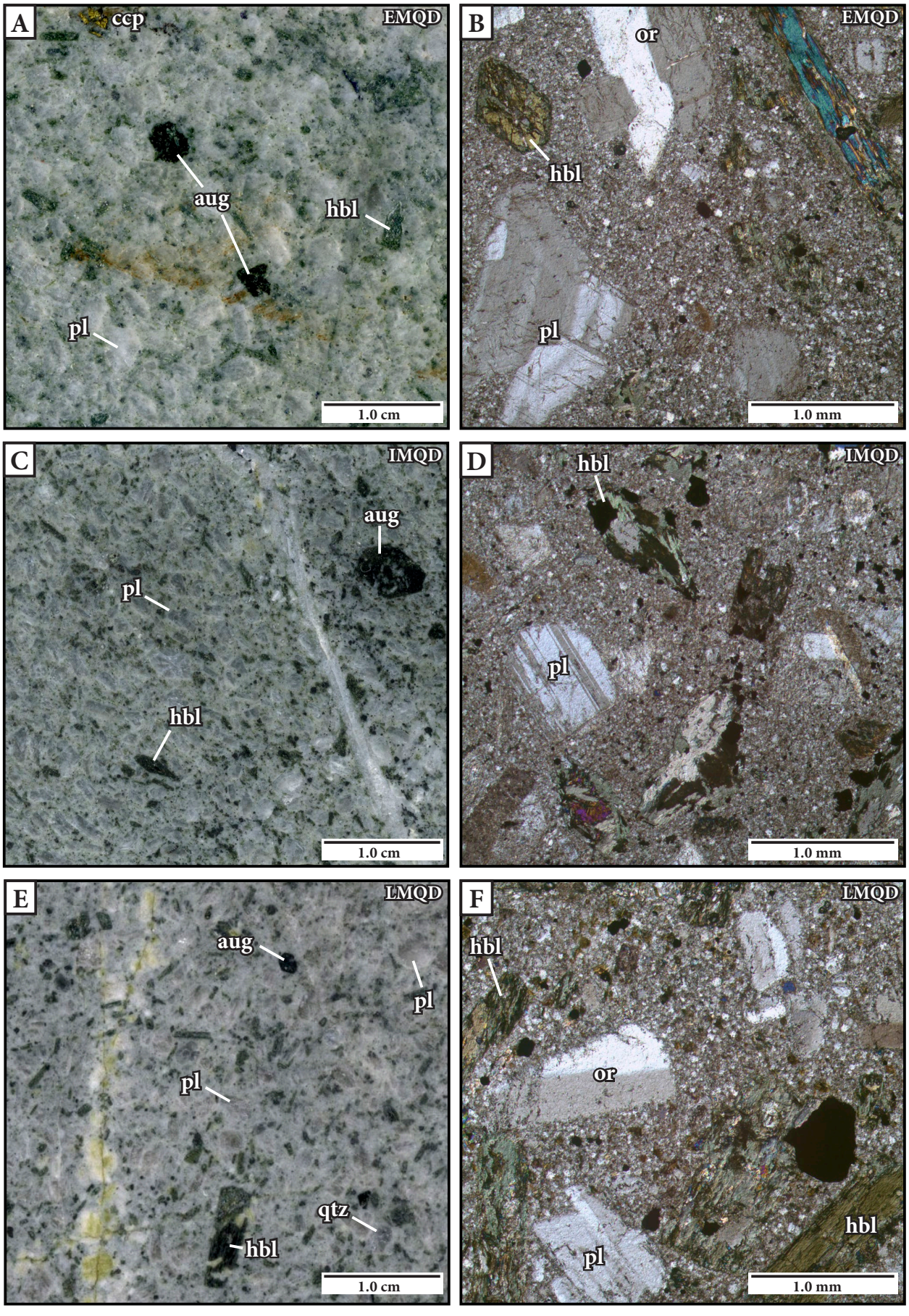
A
ccp
EMQD
aug
hbl
pl
1.0 cm
B
or
EMQD
hbl
pl
1.0 mm
C
IMQD
aug
pl
hbl
1.0 cm
D
hbl
IMQD
pl
1.0 mm
E
LMQD
aug
pl
pl
qtz
hbl
1.0 cm
F
LMQD
hbl
or
hbl
pl
1.0 mm

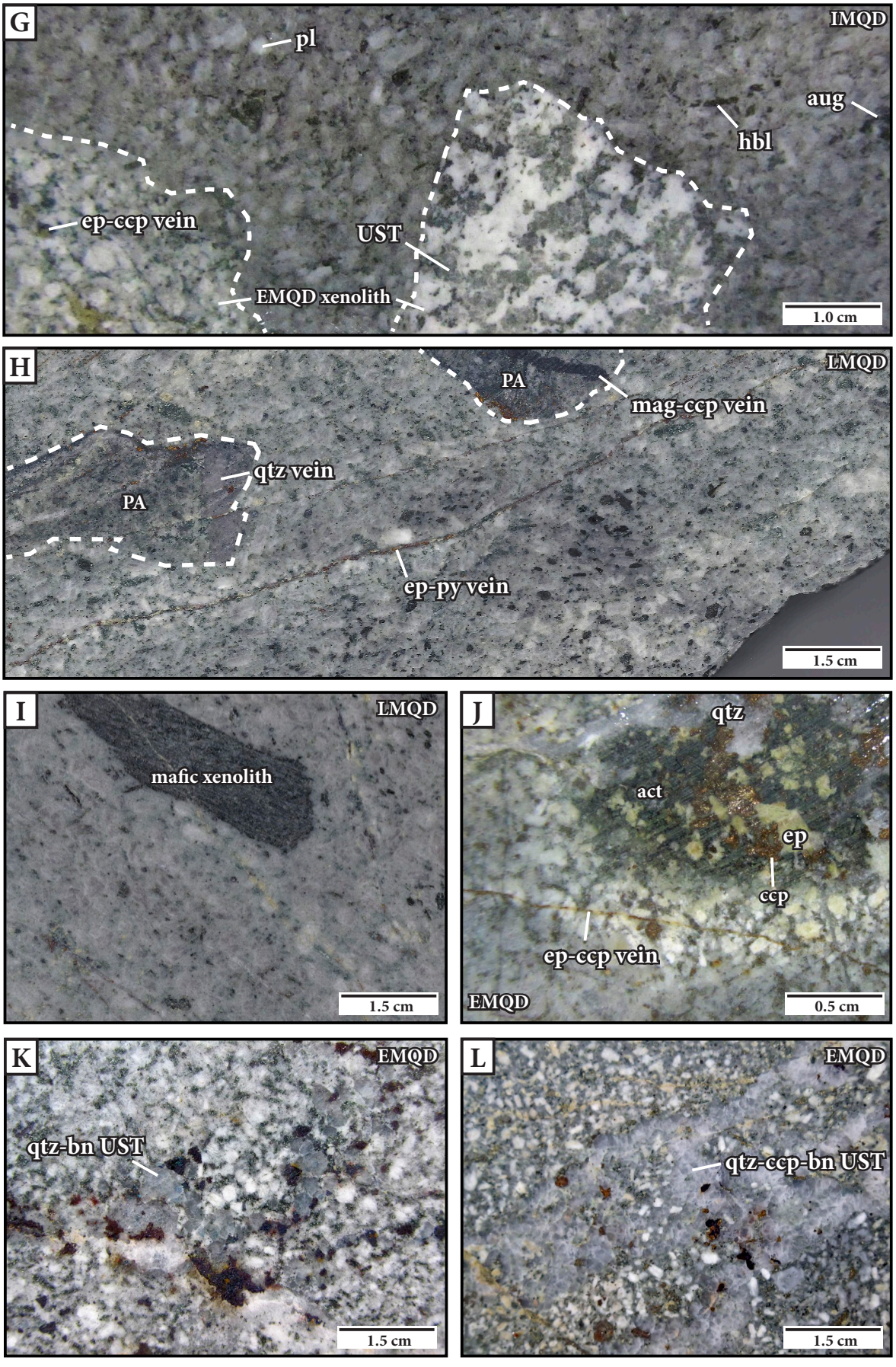
G
IMQD
pl
aug
hbl
ep-ccp vein
UST
EMQD xenolith
1.0 cm
H
LMQD
PA
mag-ccp vein
qtz vein
PA
ep-py vein
1.5 cm
I
LMQD
mafic xenolith
1.5 cm
J
qtz
act
ep
ccp
ep-ccp vein
EMQD
0.5 cm
K
EMQD
qtz-bn UST
1.5 cm
L
EMQD
qtz-ccp-bn UST
1.5 cm

defining a subophitic texture (Fig. 3.17C). Hornblende phenocrysts are prismatic and simple twinned and are typically dark green due to chlorite ± actinolite alteration (Fig. 3.17A). The modal abundance of hornblende increases from 10 % in the EMQD intrusions to 15 % in the LMQD intrusions. The syn-mineralization quartz-diorites can be distinguished from the early mineralization diorites by the presence of quartz as sparse amoeboid phenocrysts and as a major constituent of the groundmass, by the presence of coarse-grained augite phenocrysts and by the lack of biotite alteration affecting mafic minerals.

Early-, inter- and late-mineralization diorite porphyries (EMQD, IMQD, and LMQD) host progressively lower copper and gold grades (EMQD: ~ 2.86 wt % Cu, ~ 0.74 g/t Au; IMQD: ~ 0.58 wt % Cu, ~ 0.11 g/t Au; LMQD: ~ 0.05 wt % Cu, < 0.01 g/t Au; values are averaged over intervals intersected in NVD019 using NJV assay data; Fig. 3.14). The EMQD intrusions are the only quartz-diorite intrusions that contain unidirectional solidification textures (USTs)—asymmetric, contorted chains of quartz and Cu-Fe sulfides inter-layered with aplitic igneous material (Figs. 3.17K and L)—and actinolite – epidote – chalcopyrite-filled miarolitic cavities (Fig. 3.17J). IMQD intrusions contain small EMQD xenoliths with truncated USTs and epidote – chalcopyrite veins, giving strong evidence for their later relative timing of emplacement. LMQD intrusions contain sparse blocky to tabular mafic and PA xenoliths (< 5 cm in diameter) that have truncated quartz and magnetite – chalcopyrite veins. The xenoliths are not surrounded by reaction halos. The mafic xenoliths are composed of fine grained chlorite – magnetite-altered biotite and pyroxene and trace apatite (Fig. 3.17I) and are mineralogically distinct from the NAF mudstone xenoliths found sporadically within the PA (e.g., Fig. 3.15F).

Egashira (2009) distinguished four intrusive phases at Wainaulo: 'fine-grained diorite porphyry', 'andesite porphyry breccia', 'augite-hornblende diorite porphyry' and a diorite phase with a clotted texture, termed 'clotted diorite porphyry'. The 'augite-hornblende diorite porphyry' and the 'andesite porphyry breccia' are interpreted to be equivalent to the NAF andesite lava (N2a) and associated monomict andesite breccia (N2b). The 'fine-grained diorite porphyry' is interpreted to be equivalent to the syn-mineralization quartz-diorite intrusions. During this study a

clotted texture was observed; however, the texture is interpreted here to be caused by secondary chlorite ± magnetite ± epidote and biotite ± magnetite clots that have nucleated on the margins of fine- to medium-grained mafic components of porphyritic andesite (PA) and porphyritic diorite (PD), as well as pyroxene-feldspar-phyric dikes (N2c) and pyroxene-feldspar-phyric lavas (N2a; Fig. 3.18). Because the clotted alteration texture has affected multiple phases, it does not define a separate intrusive phase, and is described further in Chapter 5.

### *3.4.3 Waisoi West intrusive complex*

The Waisoi West intrusive complex (WWIC) is a roughly cylindrical composite stock comprising sub-vertical, steeply north plunging quartz-diorite intrusions that have an unconstrained vertical continuity (at least 600 m) and a stock thickness of < 200 m east to west (Fig. 3.7). Several distinct intrusions based on texture, presence and abundance of veins and the presence of mineralized refractory quartz xenoliths have been identified during this study. However, the relative

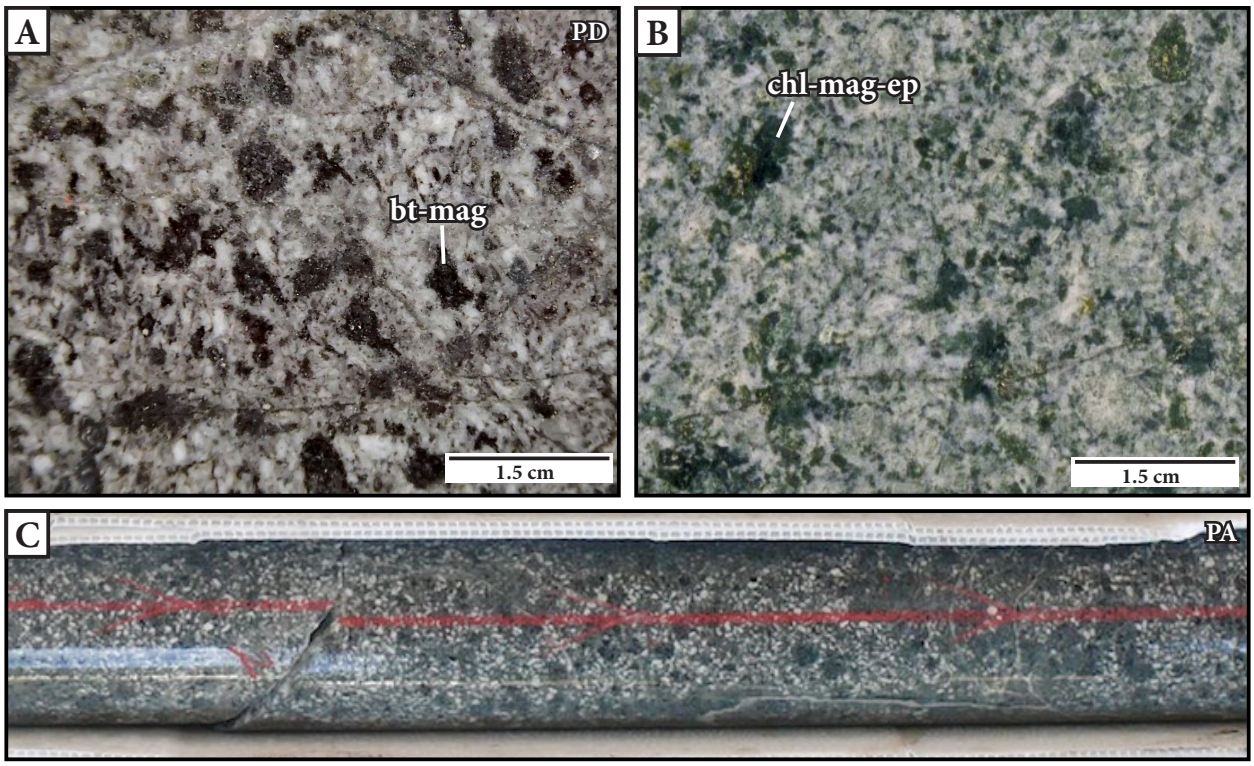


**Figure 3.18:** Clotted alteration texture within various intrusive phases at Wainaulo. **A.** Hand sample of porphyritic diorite illustrating clotted texture caused by biotite – magnetite alteration of hornblende minerals. Sample: NVD037 809 m. **B.** Hand sample of feldspar-pyroxene-phyric dike illustrating clotted texture caused by chlorite – magnetite – epidote alteration of primary pyroxene phenocrysts. Sample: NVD019 361 m. **C.** Chlorite clotted texture in porphyritic andesite. NVD037 Tray 180 (384.7 – 385.6 m) Abbreviations: bt = biotite, chl = chlorite, ep = epidote, mag = magnetite, PA = porphyritic andesite, PD = porphyritic diorite.

ages of individual intrusions at Waisoi West are not always well constrained and therefore have been grouped into three composite intrusions, termed the QDP1, QDP2 and QDP3 (quartz-diorite porphyry 1, quartz-diorite porphyry 2, quartz-diorite porphyry 3).

*Quartz-diorite porphyry 1 (QDP1)*

Age: 5.492 ± 0.043 Ma (CA-TIMS U–Pb on zircons; this study)

The QDP1 is a large (< 150 m in diameter) hornblende-plagioclase-phyric quartz-diorite stock that is associated with relatively high Cu and Au grades at its apical portion and a dense and barren quartz-vein stockwork at its core (Figs. 3.7, 3.19A and B). Distinctive, contorted quartz banding occurs near the QDP1 margins (interpreted as USTs; Fig. 3.19B). The QDP1 is typically strongly to intensely kaolinite – illite-smectite- and illite – chlorite-altered, which has obscured many of its primary features and imparted a white to buff coloration to the groundmass (Figs. 3.19A and B). Plagioclase occurs as subhedral, tabular crystals (< 3 mm; ~ 35 %) and orthoclase occurs as rare tabular crystals (< 1 mm; < 2 %). Relict primary hornblende (< 2 mm; 3 – 5 %) are typically obscured by biotite – magnetite ± chalcopyrite ± rutile alteration (Fig. 3.19A). The groundmass comprises fine-grained (< 0.3 mm) feldspar and quartz and accessory magnetite.

*Quartz-diorite porphyry 2 (QDP2)*

Age: 5.0 ± 0.3 Ma (ELA-ICP-MS U–Pb on zircons; Harris, 2009a; inferred as QDP2)

The QDP2 intrusion is a large (< 200 m diameter), sempatic (40 – 43 vol % phenocrysts), quartz-hornblende-plagioclase-phyric quartz-diorite stock that truncated the QDP1 intrusion at depth (Fig. 3.7). The QDP2 intrusion contains quartz-vein stockwork-bearing xenoliths of QDP1 and fragments of refractory quartz veins (Fig. 3.19D). Quartz veins and Cu and Au mineralization are associated with this intrusion, however to a much lesser degree than QDP1 (Table 3.1; Figs. 3.7. 3.19C and D). Therefore, this intrusive phase is considered to be an inter-mineralization quartz-diorite porphyry stock. Phenocryst phases in the QDP2 intrusion include blocky, euhe-

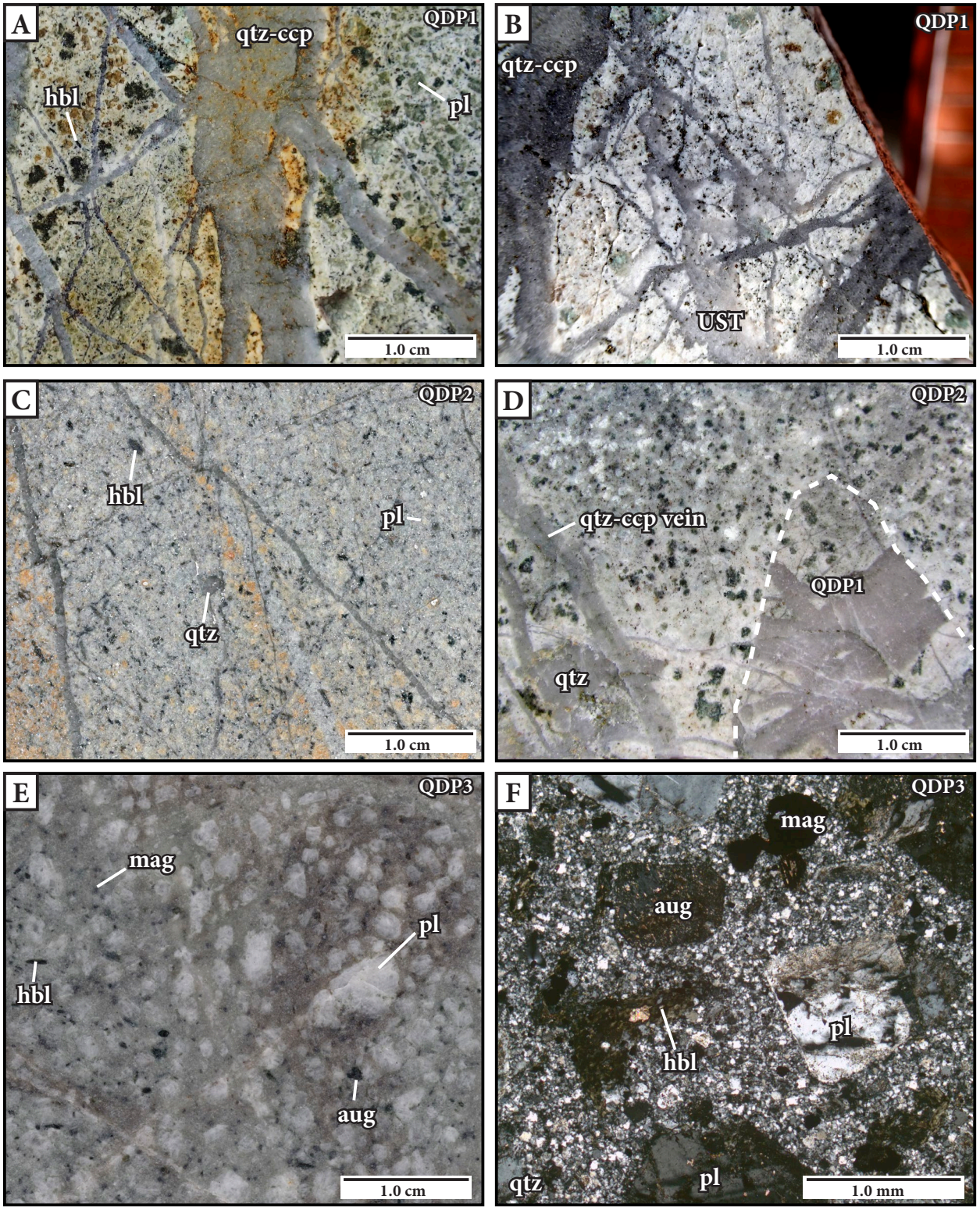


**Figure 3.19:** Representative images of the Waisoi West intrusive complex. **A.** Hand sample photograph of QDP1 showing rust to green, strongly altered plagioclase phenocrysts set in a cream to buff groundmass. The sample is crosscut by quartz – chalcopyrite ± magnetite veins. Sample: NSW006 336 m. **B.** Hand sample photograph of QDP1 showing irregular quartz veins and quartz USTs. Sample: NSW006 366 m. **C.** Hand sample photograph of QDP2 illustrating the distribution of ghosted plagioclase, prismatic to acicular hornblende and quartz phenocrysts. Sample: NSW006 490 m. **D.** Hand sample photograph of the QDP2 intrusion highlighting a QDP1 xenolith with truncated quartz-vein stockwork and a refractory quartz vein xenolith, both of which are truncated by quartz – chalcopyrite veins. Sample: NSW010 583 m. **E.** Hand sample photograph of the QDP3 intrusion showing the distribution of translucent white and glomerophyric plagioclase, augite, hornblende and magnetite phenocrysts set in a brown to gray fine-grained groundmass. Sample: NSW001 1020 m. **F.** Photomicrograph of the QDP3 intrusion showing albite-altered plagioclase, biotite-rutile-magnetite-altered hornblende and augite, and magnetite (opaque) set in a hypidiomorphic granular groundmass of mainly quartz and feldspar. Sample: NSW006 727 m. Abbreviations: aug = augite, ccp = chalcopyrite, hbl = hornblende, mag = magnetite, pl = plagioclase, QDP1 = quartz-diorite porphyry 1, QDP2 = quartz-diorite porphyry 2, QDP3 = quartz-diorite porphyry 3, qtz = quartz, UST = unidirectional solidification texture.

dral and glomerophyric plagioclase (< 2 mm; ~ 30 %), prismatic to acicular hornblende (< 2 mm; 5 – 7 %), tabular and euhedral orthoclase (3 %; < 3 mm) and bipyramidal quartz (0.5 – 2.0 mm; 2 %). Accessory minerals include titanite and magnetite. Locally, plagioclase phenocrysts are ghosted, giving the QDP2 intrusion a fine-grained equigranular appearance. The groundmass is fine-grained (< 0.3 mm) and gray to white and consists of mainly quartz and feldspar.

*Quartz-diorite porphyry 3 (QDP3)*

The youngest phase of magmatism at Waisoi West consists of narrow (< 1 to 30 m), subvertical, dopatic (⅔ < ᵃ⁄ᵦ < ⁷⁄₁ | a = groundmass %, b = phenocryst %; Cross et al., 1906) magnetite- and augite-bearing, hornblende-feldspar-phyric quartz-diorite dikes that have a late-mineralization timing. They have crosscut the QDP2 intrusion at NSW002W below -200 mRL (Fig. 3.7). These dikes have been affected by weak biotite – albite ± actinolite and chlorite – illite-smectite alteration and have been crosscut by a low volume of quartz veins (typically < 5 vol %) and have low copper grades (< 0.1 wt % Cu). The dominant phenocryst phases within the QDP3 intrusions are stubby to tabular, subhedral to euhedral, glomerophyric plagioclase (< 4 mm; outsized to 8 mm; composite crystal clusters up to 8 mm; 30 %), subhedral to euhedral prismatic hornblende (up to 3 mm long; 5 – 7 %), tabular, euhedral orthoclase (< 3 mm; 3 – 5 %) stubby, euhedral augite (< 3 mm; ~ 3 %) and magnetite (< 0.5 mm; < 2 %; Fig. 3.19E). Accessory fine- to medium-grained quartz and titanite occur locally. The QDP3 has a hypidiomorphic granular groundmass consisting of fine-grained (0.01 – 0.20 mm) plagioclase, quartz, orthoclase, hornblende and rutile (Fig. 3.19F). Anhydrite occurs as an interstitial phase to coarser plagioclase phenocrysts and as infill to miarolitic cavities (Harris, 2009b).

### *3.4.4 Waisoi East intrusive complex*

*Quartz-eye dacite (DP1)*

Age: 5.432 ± 0.031 Ma (CA-TIMS U–Pb on zircons; this study)

The DP1 intrusion is a near vertical and east-striking tabular dike (~ 350 m east-west; < 50 m north-south; Figs. 3.6 and 3.8) with small (< 10 m-wide) branches at its southern periphery. The intrusion crops out in the north of the Waisoi area (~ 1937500 mE and 3889000 mN; Fig. 3.6). The apical portions of the DP1 dikes are spatially associated with zones of Cu-Au-Mo mineralization (> 150 ppm Mo and > 0.3 wt % Cu; Fig. 3.8). The quartz-eye dacite has a dopatic texture (35 – 40 % phenocrysts) with distinctive amoeboid and subhedral bipyramidal quartz eyes (< 3 mm; 7 – 10 %), some of which are mantled by magmatic chalcopyrite ± pyrite and are interpreted as infill to miarolitic cavities (Fig. 3.20B). Phenocrystic phases include stubby to blocky glomerophyric plagioclase (1 – 4 mm; crystal clusters up to 5 mm; 20 – 25 %), glomerophyric orthoclase (< 3 mm; < 5 %), prismatic to acicular hornblende (0.2 – 3.0 mm; 3 – 5 %) and fine-grained accessory magnetite. The hypidiomorphic granular groundmass consists of fine-grained (< 0.02 mm) orthoclase, plagioclase, quartz, relict hornblende, titanite and magnetite. Due to strong to intense hydrothermal alteration the DP1 intrusion has a conspicuous, white (Fig. 3.20A) appearance and ghosted plagioclase phenocrysts.

*Quartz-bearing dacite (DP2)*

Age: 5.297 ± 0.025 Ma (CA-TIMS U–Pb on zircons; this study)

The quartz-bearing dacite (DP2) is a large (< 600 m north-south and > 400 m east-west), roughly east-striking, irregular porphyritic stock that intruded the Wainimala host sequence (up to 300 mRL on section NSE002; Fig. 3.8) in the Waisoi East area. No crosscutting relationship with DP1 was observed; however, the DP2 intrusion contains quartz-vein xenoliths suggesting that it was emplaced after the initiation of the magmatic-hydrothermal system (Fig. 3.20 C). The

**Figure 3.20 (opposite):** Representative images of the Waisoi East intrusive complex. **A.** Hand sample photograph of the DP1 intrusion showing abundant amoeboid and bipyramidal quartz eyes. Feldspar and hornblende phenocrysts are obscured by strong kaolinite – illite-smectite and illite alteration. Sample: NSE002 339 m. **B.** Reflected light photomicrograph of the DP1 intrusion showing a quartz eye that has been mantled by magmatic chalcopyrite and pyrite and interpreted as a miarolitic cavity. The sample contains disseminated magnetite and chalcopyrite. Sample: NSE002 366 m. **C.** Hand sample photograph of the DP2 intrusion with abundant quartz vein xenoliths as well as quartz and plagioclase phenocrysts. Sample: NSE002 697 m. **D.** Hand sample photograph of the QFP intrusion showing the bimodal grain sizes of quartz and feldspar phenocrysts. Note the euhedral, prismatic orthoclase phenocryst in the bottom left corner of the photograph. Grab sample from south of Waisoi Camp. **E.** Hand sample photograph of the DP3 intrusion showing prominent hornblende phenocrysts and quartz eyes. Sample: NSE006 635 m. **F.** Photomicrograph of the DP3 intrusion showing a quartz eye surrounded by a hypidiomorphic granular groundmass of quartz, feldspar, hornblende and magnetite. Sample: NSE006 695 m. Abbreviations: ccp = chalcopyrite, DP1 = quartz-eye dacite, DP2 = quartz-bearing dacite, DP3 = dacite porphyry, hbl = hornblende, fsp = feldspar, mag = magnetite, or = orthoclase, pl = plagioclase, py = pyrite, QFP = quartz-feldspar porphyry, qtz = quartz, qtz-vn = quartz vein.

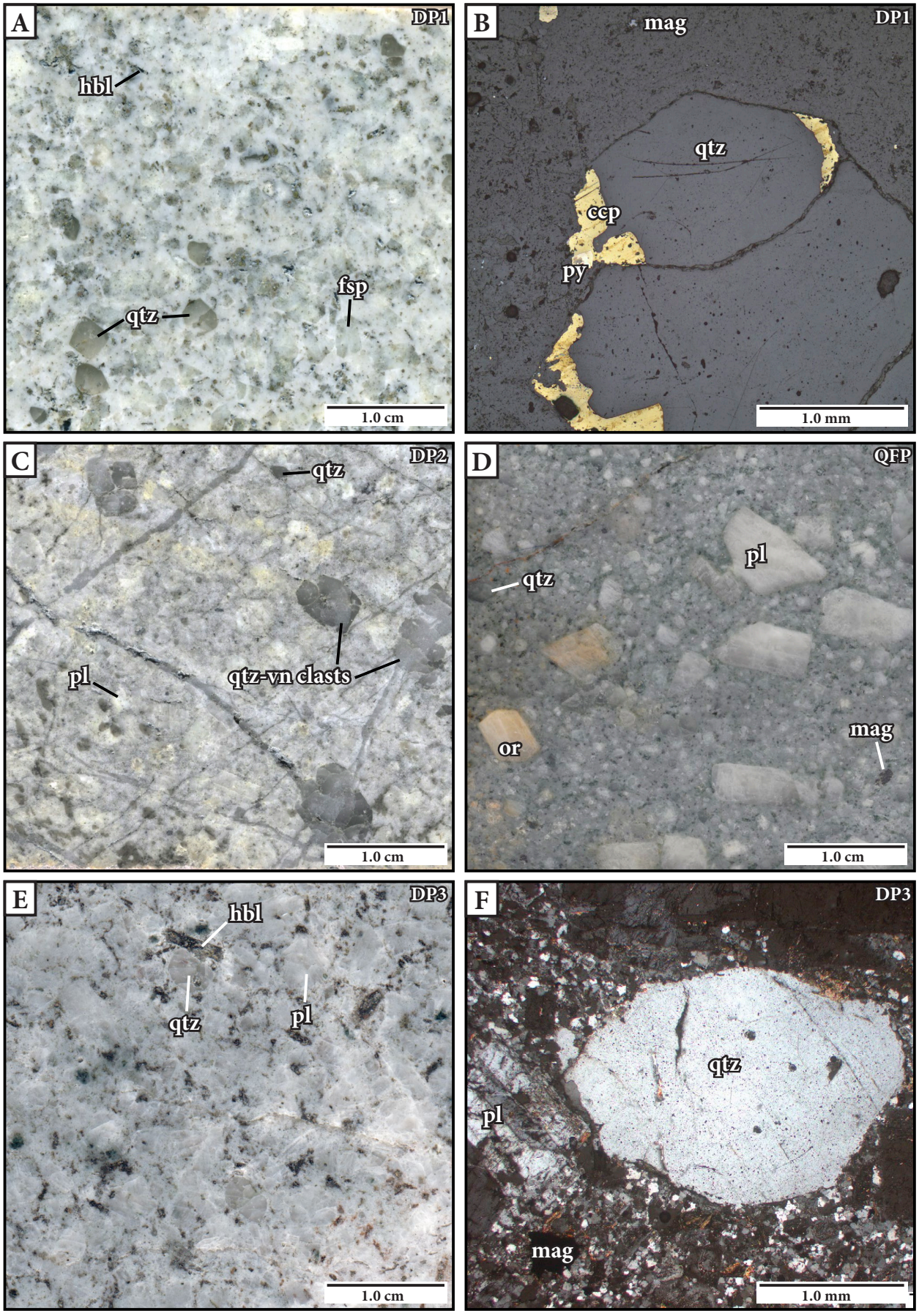
A
DP1
hbl
fsp
qtz
1.0 cm
B
mag
DP1
qtz
ccp
py
1.0 mm
C
DP2
qtz
pl
qtz-vn clasts
1.0 cm
D
QFP
pl
qtz
or
mag
1.0 cm
E
DP3
hbl
qtz
pl
1.0 cm
F
DP3
qtz
pl
mag
1.0 mm

bulk of Cu-Au-Mo mineralization at Waisoi East is superjacent to the DP2 intrusion, with some mineralization intersecting its apical portion. DP2 has a dense Cu-Au barren quartz-vein stockwork with a thick (< 40 m) zone of quartz defining its contact to the north with the Wainimala host sequence. The quartz-bearing dacite has a dopatic texture (35 – 40 % phenocrysts), consisting of euhedral, tabular plagioclase (< 4 mm; ~ 30 %), anhedral quartz (< 3 mm; < 2 %), stubby, glomerophyric orthoclase (2 mm; 2 – 3 %), hornblende (< 5 mm; 3 – 5 %) and accessory magnetite, set in a mottled gray to white, fine-grained (< 0.02 mm) groundmass. In thin-section the groundmass has a hypidiomorphic granular texture consisting of orthoclase, plagioclase, quartz, hornblende, titanite, and magnetite.

*Dacite porphyry (DP3)*

The dacite porphyry (DP3) is an east-west elongate porphyry stock. The dimensions of DP3 are poorly defined; however, it was intersected in drill core to the south of the Waisoi East deposit (i.e., in NSE006 from 30 – 303.2 m and from 328 to 712.3 m). The dacite porphyry has sparse quartz veins, moderate alteration intensity and low Cu-Au and Mo grades and is therefore considered to have a late-mineralization timing. This intrusion has a dopatic texture (35 – 40 % phenocrysts) and generally has larger phenocrysts and a higher percentage of mafic minerals than the earlier dacitic porphyry intrusions at Waisoi East (Table 3.1). The phenocryst phases include blocky to tabular plagioclase (1 – 6 mm; ~ 25 %), rounded quartz (1 – 5 mm; 3 – 5 %), stubby orthoclase (0.5 – 3.0 mm; ~ 3 %), conspicuous dark brown prismatic hornblende (0.5 – 2.0 mm; outsized to 7.0 mm; 5 – 7 %) and accessory magnetite (Fig. 3.20E). The DP3 has a coarser groundmass than DP1 and DP2 (0.03 – 0.40 mm). The groundmass has a hypidiomorphic granular texture and is composed of orthoclase, plagioclase, quartz, hornblende, titanite and magnetite (Fig. 3.20F).

*Quartz feldspar porphyry (QFP)*

The quartz feldspar porphyry (QFP) is a quartz-, plagioclase- and orthoclase-phyric intrusion that crops out south of the Waisoi Camp, ~ 700 m southwest of the Waisoi East deposit (Fig. 1.2).

It has an aerial extent of ~ 500 $m^2$ (Fig. 3.6) and has not been intersected by diamond drilling. The QFP is very fresh, has a dosemic texture (65 – 70 % phenocrysts), and has a distinctive bimodal population of phenocryst grain sizes (Table 3.1; Fig. 3.20D). Large, conspicuous, coarse-grained (5 – 20 mm), euhedral phenocrysts include plagioclase (10 %), orthoclase (2 %) and quartz (2 %). The medium-grained population of phenocrysts include plagioclase (0.5 – 3.0 mm; 40 %), orthoclase (< 3 mm; 5 %), quartz (0.5 – 4 mm; 2 – 5 %), hornblende (0.5 – 2.0 mm; 3 – 5 %) and accessory magnetite (Fig. 3.20D). The QFP has a fine-grained (< 0.01 mm) hypidiomorphic granular groundmass consisting of feldspar, quartz, hornblende, rutile, titanite and magnetite.

### *3.4.5 Timing of magmatism in the Namosi district*

Igneous geochronology results for the Namosi district intrusions are presented in Table 3.1 and Appendix C. Due to the low Pb (1.2 – 2.7 ppm) and U (median = 71.5 ppm; cf. 125 – 500 ppm for average zircons, Chiaradia et al., 2013) in Namosi district magmatic zircons, the ELA-ICP-MS results have relatively large errors (0.22 – 0.90 My) and high MSWD values (mean = 2.1; Appendix C). The minimum error of the ELA-ICP-MS ages (440 ky) spans the entire productive history of the Namosi district (~ 400 ky), based on CA-TIMS U–Pb and Re–Os results (discussed in Chapter 5). Therefore, geochronology results determined by ELA-ICP-MS for the Namosi district igneous rocks are interpreted with caution.

From the CA-TIMS U–Pb geochronology results (Table 3.1; Appendix C), it can be concluded that there were four brief and temporally distinct magmatic periods in the Namosi district, three of which are associated with porphyry Cu–Au(-Mo) ore formation. The first magmatic period involved the intrusion of pre-mineralization diorites at Wainaulo (PA and PD), and marked the cessation of submarine volcanism and associated sedimentation of the Namosi Andesite Formation at ~ 6.0 Ma (Table 3.1). The second period produced diorite and quartz-diorite intrusions from 5.749 – 5.500 Ma (Late Miocene) and was related to Cu-Au mineralization at Wainaulo. The third magmatic period produced quartz-diorite intrusions from 5.535 – 5.449 Ma (Late Miocene) and was related to Cu-Au mineralization at Waisoi West. The final period produced dacitic intrusions from 5.463 – 5.272 Ma (Late Miocene to Early Pliocene) and was related to Cu-Au-Mo mineral-

ization at Waisoi East. The emplacement of calc-alkalic intrusions at Waisoi East coincided with a period of maximum rotation of the Fiji Platform (e.g., Begg and Gray, 2002) and the onset of alkalic volcanism in northern Viti Levu (60 – 70 km northeast of the Namosi district; Section 2.5).

Previous workers had speculated that the Waisoi magmatic-hydrothermal system might be older than Wainaulo, based on K–Ar ages and stratigraphic exposure levels at each deposit (e.g., Ellis, 1996; Corbett, 2011). The current study provides strong evidence that Wainaulo is older than both Waisoi East and Waisoi West and that each deposit was emplaced at a different stratigraphic level. The diorite- to quartz-diorite-related Wainaulo Cu-Au deposit was emplaced higher in the stratigraphy, the more felsic Waisoi West Cu-Au deposit was emplaced at an intermediate level, and the felsic dacite Waisoi East Cu-Au-Mo deposit was emplaced at the deepest relative level within the stratigraphic sequence (Fig. 3.2).

### 3.5 Late Miocene structures

In the Wainaulo area, two steeply dipping ENE-striking fault zones—the Hematite and Kaolinite shears—crosscut and offset the volcano-sedimentary stratigraphy. These faults appear to have localized the emplacement of the Wainaulo intrusive complex and associated porphyry Cu-Au mineralization (Figs. 3.3 and 3.4). The Hematite shear, which was previously recognized by NJV geologists, has been modeled as a part of this study. Based on this model, the Hematite shear is oriented 076° and dips 78° to the NNW (Fig. 3.3). The Kaolinite shear trends 082°/83.5° SSE (Fig. 3.3) and coalesces with the Hematite shear at depth (below -450 mRL; Fig. 3.4). The Kaolinite – Hematite fault system has a minimum overall vertical displacement of approximately 300 m based on correlative offset of the polymict conglomerate and pebble-bearing wacke (N1b) marker horizon at the interface between the Wainimala Group and Namosi Andesite Formation (Fig. 3.4). Based on the orientation and location of the Kaolinite – Hematite fault system, they are likely associated with the strike-slip to normal-slip faults of the WWW Fault Zone in southeast Viti Levu (Section 2.4). No lateral fault displacements on the Kaolinite or Hematite shears were identified during this study.

## 3.6 Summary and conclusions

Within the vicinity of the principal porphyry deposits of the Namosi district, the host stratigraphy is made up of a thick sequence of submarine volcano-sedimentary rocks of the Late Oligocene to Middle Miocene Nubuonaboto Formation (Mount Gordon sub-Group, Wainimala Group) and Late Miocene Namosi Andesite Formation (Medrausucu Group). The Namosi Andesite Formation comprises a gently dipping sequence of andesite hyaloclastites (with local perlitic fractures), turbidites, and other subaqueous sediment gravity flow deposits. This volcano-sedimentary sequence is interpreted to have been deposited in a below-storm-wave-base submarine environment (i.e., below 10 – 200 m depth; e.g., Johnson and Baldwin, 1996), on the submerged flank of a shoaling andesitic seamount (e.g., Houghton and Landis, 1989). The original surface morphology of the volcano is no longer preserved. The Namosi Andesite Formation unconformably overlies the Wainimala Group, which comprises basaltic andesite hyaloclastite (with relict perlitic fractures and local pillow lava fragments) and submarine welded pyroclastic facies interbedded with marine mudstones and sandstones. The Wainimala Group is interpreted to have been deposited on the submerged slope of an explosive, active volcanic vent (e.g., White, 2000).

The Wainimala Group and Namosi Andesite Formation sequences were crosscut by intermediate, calc-alkalic ore-related intrusive complexes in the Late Miocene to Early Pliocene. Absolute age estimates indicate that the Wainaulo diorite and quartz-diorite dikes were intruded from 5.749 – 5.500 Ma. The dikes intruded along steeply dipping, ENE-striking faults of the WWW Fault Zone. Quartz-diorite stocks were emplaced at Waisoi West from 5.535 – 5.449 Ma, followed by the emplacement of dacite stocks at Waisoi East from 5.463 – 5.272 Ma.

# CHAPTER 4

# Igneous geochemistry of the Namosi district

## 4.1 Introduction

This chapter presents the results of whole-rock geochemical analyses of least-altered intrusive and volcanic rocks from the Namosi district. Whole-rock Sr–Nd of mineralized intrusions are also presented. The results are compared with data compiled from previous work on the geochemistry of igneous rocks in Fiji and the surrounding areas. Interpretations from the data are used to constrain the tectonic setting and petrogenesis of igneous rocks from the Namosi district.

## 4.2 Whole-rock geochemistry

### *4.2.1 Previous work*

Only limited whole-rock geochemical studies have been published for Tertiary arc-related igneous rocks of the Namosi district. Imai et al. (2007) published XRF data on six samples of intrusive rocks from Waisoi East and Waisoi West. They demonstrated that all analyzed samples plotted within the adakite domain of the Sr/Y–Y diagram of Defant and Drummond (1990); however, no further discussion was provided. Tanaka et al. (2010) published results for samples of intrusive rocks from regional outcrops and drill core from various prospects and deposits in the Namosi area (N = 50). Their sample suite includes rocks from Waisoi (n = 14), Waivaka Corridor (n = 21), Waisomo (n = 9), Wailutelevu (n = 2) and Wainabama (n = 4). The study characterized the samples as magnetite-series granitic intrusions that have a calc-alkaline magmatic affinity. Tanaka et al. (2010) used trace element compositions to show that these rocks were derived from mantle magmas that may have been contaminated with crustal material. The Waisoi samples were

shown to have less continental crustal contamination and higher Au contents than the Waivaka Corridor samples. The study concluded that the lower crustal contamination and higher $SiO_2$ contents of the Waisoi samples are associated with Au-rich porphyry Cu mineralization, while a higher degree of crustal contamination is correlated with Au-poor porphyry Cu mineralization in the Waivaka Corridor.

An unpublished MSc thesis (Ellis, 1996) reported ten analyses of volcanic rocks from the Namosi area in order to comment on their magmatic affinity. The author concluded that the "Wainimala Agglomerates" (Wainimala Group) are island-arc tholeiitic basaltic andesites, the "Namosi Andesites" (Namosi Andesite Formation) are calc-alkalic dacites and the "Korobasabasaga Pyroclastics" (Korobasabasaga Formation) are of island-arc tholeiitic affinity. Ellis (1996) surmised that the "Korobasabasaga Pyroclastics" might be related to the Nakobalevu Basalts of southeast Viti Levu and the Korobasaga Volcanics from the Lau Islands.

An internal, unpublished study for Newcrest Mining Limited (Crawford, 2011) provided a regional-scale fertility assessment of igneous rocks across southeastern Viti Levu, specifically within the Namosi district. The report included whole-rock geochemistry for rocks from the Wainimala Group (n = 22), Savura Group (n = 23), Colo Plutonic Suite (n = 69), Namosi Andesite Formation (n = 53), Namosi Diorite (n = 12), Namosi porphyries (n = 29) and Korobasabasaga Formation (n = 3). Following the methodology of Rohrlach and Loucks (2005), Crawford (2011) used bivariate plots (e.g., Sr–Y and MnO–$SiO_2$) and discriminant ratio plots (e.g., Sr/Y–Sr/MnO) to discriminate the Namosi porphyries and Namosi Andesite Formation hornblende andesite as "fertile" (i.e., $SiO_2$ > 57 wt %, MnO < 0.2 wt %, Sr/Y > 30, Sr/MnO > 5000, etc.) and the regional Colo Plutonic Suite intrusives as "barren".

### *4.2.2 Methods*

A total of 52 intrusive and volcanic rocks from the Namosi area were selected for whole-rock geochemical analysis in this study (Appendix D). Each of these samples has been analyzed for their major and trace element compositions at Acme Analytical Laboratories Ltd. in Vancouver,

Canada. Samples were crushed to 85 %, passing 200 mesh (74 μm) in an Essa standard stainless steel mill. A small quantity (0.2 g) of each powdered sample was fused in a crucible with 1.5 g of $LiBO_2/LiB_4O_7$ flux and then dissolved in American Chemical Society (ACS) Reagent Grade $HNO_3$. Major elements were determined using a Spectro ARCOS inductively coupled plasma emission spectrometer (ICP-ES). Trace elements were analyzed using a Perkin-Elmer ELAN 9000 inductively coupled plasma mass spectrometer (ICP-MS). For both major and trace elements, calibration standards and reagent blanks were included in the sample sequence. Reported detection limits for the major elements are 0.01 wt % and < 0.5 ppm for the majority of the trace elements, but < 0.1 ppm for the rare earth elements (REE). For comparative purposes, the sample

**Table 4.1:** Samples used for whole-rock geochemical study—pre-screening (N = 190)

| Lithotype | Deposit/areas | References | # of samples |
|---|---|---|---|
| Wainimala Group | | | |
| Lower Wainimala, Nubuonaboto Volcanics: pyroxene-feldspar-phyric basaltic andesite (W1a); basaltic andesite breccia clasts (W1b); and others | Waisoi, regional | Ellis (1996)<br>Crawford (2011)<br>This study | n = 4<br>n = 22<br>n = 5 |
| Namosi Andesite Formation | | | |
| Crowded pyroxene-plagioclase-phyric andesite (N2a) | Wainaulo, Wainaulo West | This study | n = 4 |
| Monomict, in-situ to clast-rotated andesite breccia clasts (N2b) | Wainaulo, Wainaulo West, Waisoi West | This study | n = 7 |
| Pyroxene-feldspar-phyric microdiorite (N2c) | Wainaulo | This study | n = 4 |
| Pyroxene andesite | Regional | Gill (1987)<br>Ellis (1996)<br>Crawford (2011) | n = 4<br>n = 3<br>n = 39 |
| Hornblende andesite | Regional | Gill (1987)<br>Crawford (2011) | n = 3<br>n = 14 |
| Namosi area intrusions | | | |
| Namosi diorite | Regional | Tanaka et al. (2010)<br>Crawford (2011) | n = 12<br>n = 12 |
| Pre-mineralization diorite stocks (PD, PA) | Wainaulo | This study | n = 6 |
| Early-mineralization diorite (EMD1) | Wainaulo | This study | n = 4 |
| Syn-mineralization quartz-diorites (EMQD, IMQD, LMQD) | Wainaulo | This study | n = 7 |
| Wainaulo West quartz-diorite | Wainaulo West | This study | n = 1 |
| Waisoi West quartz-diorites (QDP1, QDP2, QDP3) | Waisoi West | Royle et al. (1979)<br>Tanaka et al. (2010)<br>This study | n = 4<br>n = 11<br>n = 9 |
| Waisoi East dacites (DP1, DP2, DP3) | Waisoi East | Royle et al., 1979<br>Tanaka et al. (2010)<br>This study | n = 2<br>n = 3<br>n = 4 |
| Korobasabasaga Formation | | | |
| Basaltic trachyandesite and trachyandesite | | Ellis (1996)<br>Crawford (2011)<br>This study | n = 1<br>n = 3<br>n = 1 |
| Quartz feldspar porphyry (QFP) | Waisoi Divide | This study | n = 1 |

Note: The regional pyroxene andesite samples from Gill (1987) and Crawford (2011) may be equivalent to the crowded pyroxene-feldspar-phyric andesite (N2a) described in this study; however, hand samples or thin sections were not available for direct comparison. Abbreviations: DP1 = quartz eye dacite, DP2 = quartz-bearing dacite, DP3 = dacite porphyry, EMD1 = early mineralization diorite 1, EMQD = early mineralization quartz-diorite, IMQD = inter-mineralization quartz-diorite, LMQD = late mineralization quartz-diorite, PA = porphyritic andesite, PD = porphyritic diorite, QDP1 = quartz-diorite porphyry 1, QDP2 = quartz-diorite porphyry 2, QDP3 = quartz-diorite porphyry 3, QFP = quartz feldspar porphyry.

suite has been supplemented with data from previous work (Table 4.1), comprising 132 major and trace element XRF analyses, of which 44 include trace element solution ICP-MS analyses.

The petrographic screening process to determine the level of alteration in each sample was assisted by feldspar staining and short wave infrared (SWIR) analysis. Thin sections were prepared at the Earth Sciences Lapidary, University of Tasmania, Australia, and petrography was conducted using a Nikon Labophot-2® Pol standard polarizing microscope featuring an Olympus ColorView imaging system. A TerraSpec 4 Hi Res Mineral Spectrometer was used to measure the SWIR spectral signature of thin section offcuts (Appendix F). Feldspar staining of thin-section offcuts was conducted in order to determine modal abundance of potassic and plagioclase feldspar. Samples that had a > 10 % modal mineralogy of secondary K-feldspar + clay + mica minerals were excluded for this igneous geochemical study.

### *4.2.3 Hydrothermal alteration effects*

An effort was made to select least-altered outcrop and drill core samples; however, all selected samples show at least a weak degree of hydrothermal alteration. The effects of hydrothermal alteration on whole-rock geochemical compositions have been assessed using a combination of petrography and bivariate plots (Fig. 4.1).

Loss on ignition (LOI) can be used as a proxy for the degree of hydrothermal alteration (hydration, sulfide and/or carbonate alteration of mafic minerals) on a sample (Lechler and Desilets, 1987). The higher the LOI concentration, the stronger the effects of alteration. Weathering can also cause an increase in LOI, but weathered material was avoided in this sampling program. In order to screen samples for the effects of alteration, samples from this study and previous work were plotted on an alteration box plot diagram (e.g.,. Large et al., 2001) and a mobile-element total alkali–silica diagram (e.g., Le Maitre, 1989), with symbol sizes scaled based on LOI (Fig. 4.1). The gray domains indicate the population of samples that were considered weakly altered (at most) during petrographic inspection. Since thin sections were not available for the 132 samples from previous studies, the samples that lie outside of the gray domains were excluded from the

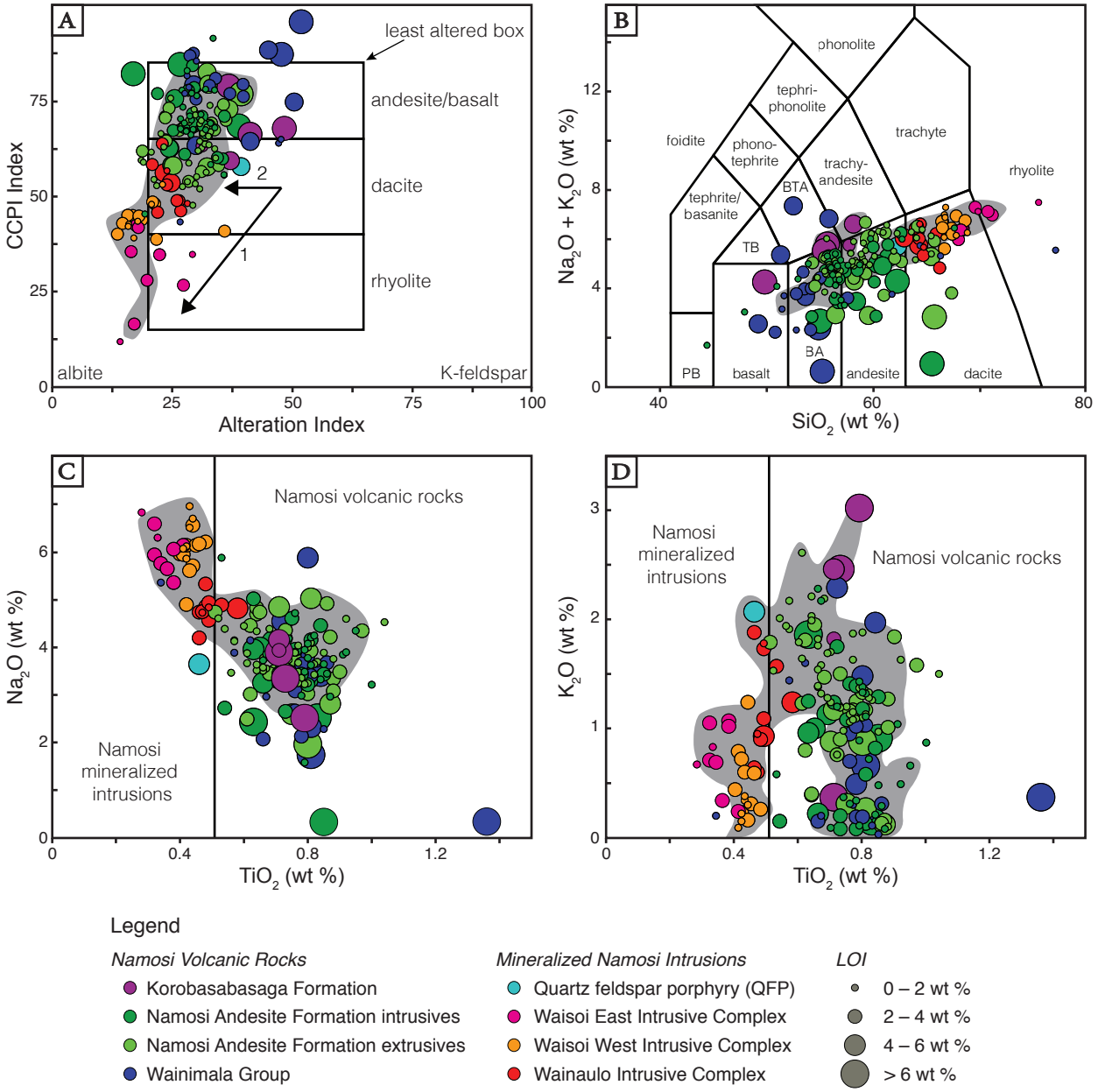


**Figure 4.1:** Assessment of the effects of hydrothermal alteration on the igneous geochemistry of intrusive and volcanic rocks from the Namosi district. **A.** Alteration box plot (cf. Large et al., 2001). Arrows indicate albite – chlorite (1) and epidote – calcite ± albite (2) alteration trends. **B.** Total alkali–silica classification diagram (cf. Le Maitre, 1989). **C.** and **D.** Bivariate plots of $TiO_2$ versus $Na_2O$ and $K_2O$, relative to LOI. The plots can be divided into least-altered Namosi intrusions and Namosi volcanic rocks. Note: Gray fields indicate the compositional range of weakly altered samples as determined by petrographic inspection. The Korobasabasaga Formation samples all have high LOI (> 4 wt %) but were determined to be unaltered in thin section. The high LOI is considered to be related to the presence of volcanic glass in the samples. Abbreviations: BA = basaltic andesite, BTA = basaltic trachyandesite, CCPI = chlorite-carbonate-pyrite index, PB = picrobasalt, TB = trachybasalt.

dataset for analysis of primary igneous rock compositions and interpretations of geodynamic environments.

The samples plotted on the alteration box plot diagram display moderate albite – chlorite (1) and weak epidote – calcite ± albite (2) alteration trends; however, the majority of the samples do

not significantly deviate from the least-altered box (Fig. 4.1A). Within the total alkali–silica (TAS) diagram (Fig. 4.1B), samples plot within compositional fields that are consistent with lithotype interpretations made in Chapter 3. The plotted samples display a broad linear trend from basalt to rhyolite. Only a small percentage of the samples deviate from the broad linear trend, suggesting that some remobilization of alkali elements occurred in a few samples. The majority of samples that deviate from the trend have a high LOI (> 4 wt %) and have been excluded from the dataset. Although the least-altered Wainimala Group samples (blue dots) follow the trend in Figure 4.1B, they are not considered to be cogenetic with the NAF or the Namosi intrusive complexes. The Wainimala basement samples are the oldest in the Namosi district and have been affected by the longest history of hydrothermal alteration and low-grade metamorphism (Ellis, 1996). Any interpretations from these data are to be made with caution.

Bivariate plots of immobile-mobile pairs ($K_2O$ and $Na_2O$ versus $TiO_2$), relative to LOI, were used in an attempt to identify samples that had experienced a significant degree of K or Na alteration (Figs. 4.1C and D); however, no correlation was found between increasing $K_2O$ or $Na_2O$ and the degree of feldspar alteration observed in thin section. During petrographic screening, samples with low $Na_2O$ (< 2.2 wt %) were determined to have been at least moderately altered and have been excluded from the dataset.

Overall, samples with S > 1.15 wt %, Cu > 2000 ppm, $Na_2O$ < 2.2 wt % and LOI > 5 wt % account for the majority of the samples that lie outside the gray domains and were eliminated from the dataset. An exception was made for five samples that had Cu values > 2000 ppm (Wainimala Group: NSW006-206, 2164.74 ppm Cu; EMD1: NVD019-708, 2653.48 ppm Cu and NVD019-728, 3247.79 ppm Cu; DP1: NSW003-201.3, 2987.00 ppm Cu and NSE002-362, 4241.61 ppm Cu) since they were the least-altered samples of their rock-type and their inclusion in the dataset still allowed for minimal scatter in the variation diagrams. The above screening process excluded 66 samples, and the following description and discussion is based on the remaining 124 samples, of which 29 are from this study (Tables 4.2, 4.3 and 4.4; see Appendix D for the full dataset).

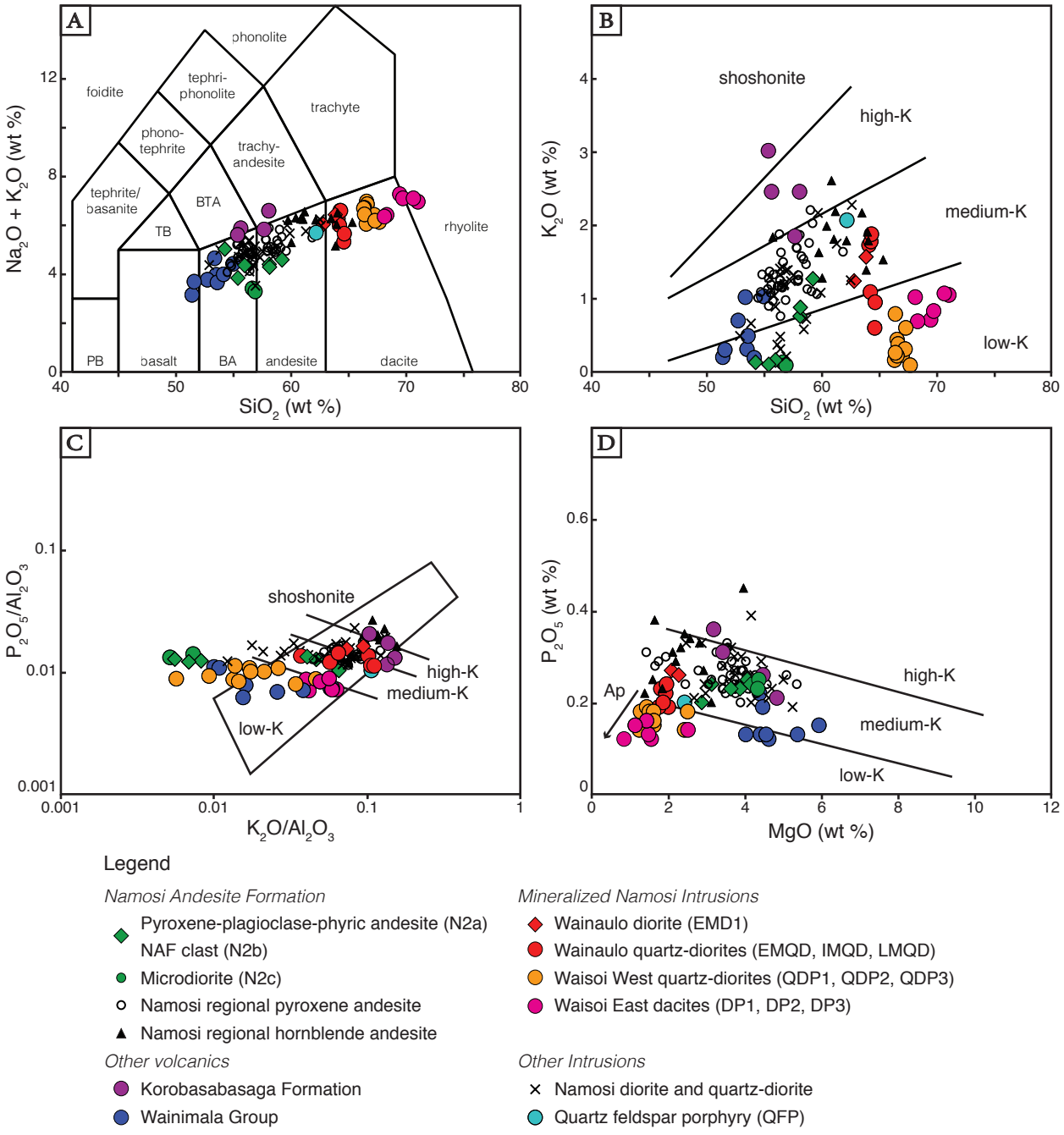


**Figure 4.2:** Major element discrimination diagrams for samples from the Namosi district. **A.** Total alkali–silica diagram (TAS). Fields from Le Maitre et al. (1989). **B.** $K_2O$ vs. $SiO_2$ diagram with fields for low-, medium- and high-K calc-alkaline rocks and shoshonites from Peccerillo and Taylor (1976) and Rickwood (1989). **C.** $P_2O_5/Al_2O_3$ vs. $K_2O/Al_2O_3$ plot with fields from Crawford et al. (2007). **D.** $P_2O_5$ vs. MgO with vector (Ap) showing effect of fractionation involving apatite; compositional fields defined by modern lavas from the Vanuatu and Sunda arcs from Crawford et al. (2007). Abbreviations: Ap = apatite, BA = basaltic andesite, BTA = basaltic trachyandesite, NAF = Namosi Andesite Formation, PB = picrobasalt, TB = trachybasalt.

## *4.2.4 Results*

### *4.2.4.1 Major element geochemistry*

The major element geochemistry for Namosi area rocks is summarized in Figures 4.2 and 4.3.

**Table 4.2:** Least-altered whole-rock geochemistry results for volcanic rocks used in this study

| Formation | Wainimala Group | | | Namosi Andesite Formation | | | | | | | | KF |
|---|---|---|---|---|---|---|---|---|---|---|---|---|
| Lithotype | W1a: basaltic andesite | | | N2a: pyroxene andesite | | | N2b: pyroxene andesite clast | | | N2c: microdiorite | | BT |
| Sample ID | NSE002-254 | NSW006-209a | NSW006-209b | NVD047-216 | NVD019-109 | NVD011-072.9 | NSW006-122 | NSW006-122b | NVD014-361 | NVD014-531 | NVD019-361 | KORO |
| $SiO_2$ | 53.54 | 52.77 | 53.63 | 56.02 | 59.28 | 55.43 | 58.16 | 58.19 | 54.29 | 56.68 | 56.93 | 57.71 |
| $TiO_2$ | 0.86 | 0.76 | 0.78 | 0.87 | 0.88 | 0.88 | 0.72 | 0.70 | 0.86 | 0.81 | 0.70 | 0.71 |
| $Al_2O_3$ | 19.32 | 18.41 | 19.00 | 19.52 | 19.49 | 18.11 | 18.80 | 18.98 | 19.08 | 17.89 | 17.53 | 17.63 |
| $Fe_2O_3$* | 10.35 | 12.87 | 11.02 | 9.69 | 8.67 | 9.00 | 8.28 | 8.18 | 9.35 | 8.98 | 8.01 | 7.43 |
| MnO | 0.09 | 0.10 | 0.12 | 0.14 | 0.10 | 0.21 | 0.07 | 0.07 | 0.20 | 0.20 | 0.20 | 0.14 |
| MgO | 5.93 | 4.40 | 4.02 | 3.13 | 2.87 | 3.87 | 4.06 | 4.14 | 3.63 | 4.36 | 4.33 | 3.18 |
| CaO | 5.76 | 6.79 | 7.60 | 6.01 | 3.95 | 8.36 | 5.27 | 5.17 | 7.29 | 7.39 | 8.70 | 7.06 |
| $K_2O$ | 0.31 | 0.70 | 0.49 | 0.16 | 1.27 | 0.10 | 0.76 | 0.88 | 0.13 | 0.13 | 0.09 | 1.82 |
| $Na_2O$ | 3.67 | 3.08 | 3.18 | 4.21 | 3.33 | 3.75 | 3.65 | 3.42 | 4.91 | 3.29 | 3.21 | 3.93 |
| $P_2O_5$ | 0.15 | 0.13 | 0.13 | 0.24 | 0.20 | 0.23 | 0.25 | 0.24 | 0.23 | 0.25 | 0.23 | 0.36 |
| Total C | 0.20 | 0.40 | 0.42 | 0.18 | 0.01 | 0.02 | 0.31 | 0.36 | 0.17 | 0.05 | 0.19 | 0.03 |
| Total S | 0.09 | 0.15 | 0.21 | 0.01 | 0.01 | 0.01 | 0.24 | 0.25 | 0.01 | 0.18 | 0.08 | 0.01 |
| Mg# | 38.90 | 27.53 | 28.85 | 26.42 | 26.89 | 32.34 | 35.27 | 36.00 | 30.14 | 35.05 | 37.53 | 32.23 |
| LOI | 3.40 | 3.70 | 4.40 | 3.50 | 2.80 | 1.80 | 3.70 | 4.20 | 3.10 | 2.10 | 1.90 | 2.50 |
| Sum | 99.98 | 100.00 | 99.97 | 99.98 | 100.03 | 99.95 | 100.02 | 99.98 | 99.97 | 99.99 | 99.95 | 99.97 |
| Cr | 20.53 | 13.68 | 34.21 | 6.84 | 6.84 | 6.84 | 13.68 | 6.84 | 6.84 | 27.37 | 20.53 | 13.68 |
| Co | 10.90 | 17.20 | 13.20 | 20.20 | 21.80 | 8.40 | 11.80 | 11.70 | 15.30 | 10.90 | 8.90 | 8.00 |
| Ni | 9.30 | 9.20 | 7.40 | 4.00 | 5.10 | 3.20 | 7.60 | 6.70 | 4.60 | 5.80 | 5.50 | 2.10 |
| Rb | 4.80 | 10.50 | 7.50 | 1.50 | 21.80 | 0.50 | 9.60 | 11.10 | 1.20 | 0.90 | 0.70 | 41.10 |
| Sr | 191.00 | 182.90 | 184.70 | 583.40 | 462.40 | 573.70 | 307.30 | 283.40 | 548.10 | 558.20 | 590.10 | 887.00 |
| Cs | 0.90 | 0.30 | 0.05 | 0.05 | 0.40 | 0.05 | 0.30 | 0.30 | 0.05 | 0.10 | 0.10 | 0.80 |
| Ba | 14.00 | 71.00 | 69.00 | 145.00 | 318.00 | 177.00 | 75.00 | 79.00 | 96.00 | 112.00 | 128.00 | 565.00 |
| Sc | 33.00 | 32.00 | 33.00 | 20.00 | 22.00 | 20.00 | 18.00 | 18.00 | 20.00 | 22.00 | 24.00 | 15.00 |
| V | 275.00 | 322.00 | 296.00 | 233.00 | 267.00 | 240.00 | 184.00 | 181.00 | 238.00 | 229.00 | 280.00 | 215.00 |
| Ta | 0.05 | 0.05 | 0.05 | 0.20 | 0.10 | 0.05 | 0.05 | 0.05 | 0.10 | 0.20 | 0.30 | 0.30 |
| Nb | 1.30 | 0.50 | 0.20 | 1.90 | 2.50 | 2.10 | 1.90 | 2.00 | 1.70 | 3.40 | 4.90 | 3.40 |
| Zr | 48.70 | 34.80 | 33.10 | 92.50 | 95.80 | 84.70 | 94.10 | 91.80 | 90.80 | 95.90 | 94.40 | 117.80 |
| Hf | 1.20 | 1.00 | 0.90 | 2.40 | 2.70 | 2.40 | 2.70 | 2.90 | 2.60 | 2.70 | 2.40 | 3.10 |
| Th | 0.40 | 0.20 | 0.30 | 1.60 | 1.80 | 1.60 | 1.40 | 1.40 | 1.50 | 1.90 | 1.90 | 2.40 |
| U | 0.20 | 0.05 | 0.05 | 0.60 | 0.70 | 0.50 | 0.60 | 0.50 | 0.50 | 0.70 | 0.70 | 0.90 |
| Y | 17.10 | 15.60 | 14.70 | 19.30 | 23.00 | 17.20 | 15.90 | 16.80 | 16.30 | 15.50 | 14.80 | 16.60 |
| La | 3.00 | 2.40 | 2.10 | 13.90 | 12.00 | 11.40 | 11.40 | 11.20 | 10.60 | 13.50 | 12.30 | 17.80 |
| Ce | 8.10 | 6.30 | 5.40 | 28.90 | 27.80 | 23.40 | 23.80 | 24.20 | 23.00 | 28.30 | 27.50 | 37.30 |
| Pr | 1.15 | 0.96 | 0.92 | 3.63 | 3.58 | 3.01 | 3.03 | 3.08 | 2.97 | 3.83 | 3.39 | 4.61 |
| Nd | 5.70 | 5.70 | 4.60 | 15.50 | 16.40 | 14.00 | 12.60 | 14.40 | 12.80 | 16.50 | 13.80 | 18.50 |
| Sm | 1.90 | 1.58 | 1.49 | 3.58 | 3.36 | 3.17 | 2.85 | 2.94 | 3.00 | 3.48 | 3.02 | 3.91 |
| Eu | 0.82 | 0.64 | 0.61 | 1.29 | 1.26 | 1.07 | 0.83 | 0.83 | 0.99 | 1.09 | 0.95 | 1.24 |
| Gd | 2.31 | 2.02 | 2.08 | 3.62 | 3.74 | 3.15 | 2.73 | 2.83 | 3.10 | 3.33 | 2.92 | 3.44 |
| Tb | 0.47 | 0.42 | 0.41 | 0.60 | 0.63 | 0.55 | 0.49 | 0.49 | 0.50 | 0.53 | 0.46 | 0.56 |
| Dy | 2.84 | 2.58 | 2.66 | 3.36 | 3.55 | 3.11 | 2.86 | 2.68 | 3.13 | 3.06 | 2.57 | 3.04 |
| Ho | 0.66 | 0.61 | 0.58 | 0.70 | 0.86 | 0.68 | 0.59 | 0.57 | 0.56 | 0.60 | 0.57 | 0.62 |
| Er | 2.11 | 1.85 | 1.80 | 2.08 | 2.29 | 1.88 | 1.90 | 2.07 | 1.90 | 1.80 | 1.69 | 1.71 |
| Tm | 0.32 | 0.26 | 0.27 | 0.34 | 0.36 | 0.28 | 0.28 | 0.30 | 0.28 | 0.26 | 0.23 | 0.25 |
| Yb | 2.00 | 1.76 | 1.64 | 2.04 | 2.62 | 1.66 | 1.94 | 1.81 | 1.84 | 1.74 | 1.49 | 1.87 |
| Lu | 0.33 | 0.27 | 0.26 | 0.29 | 0.38 | 0.32 | 0.29 | 0.30 | 0.29 | 0.25 | 0.29 | 0.29 |
| Cu | 824.81 | 2164.74 | 839.18 | 8.23 | 13.78 | 7.12 | 1207.04 | 1381.56 | 71.10 | 375.71 | 189.09 | 23.09 |
| Zn | 16.00 | 16.30 | 16.30 | 129.80 | 47.60 | 33.80 | 43.30 | 39.20 | 123.20 | 47.40 | 37.20 | 43.20 |
| Pb | 0.25 | 0.07 | 0.90 | 2.08 | 0.80 | 0.54 | 1.39 | 1.08 | 0.88 | 1.00 | 1.14 | 1.29 |
| Mo | 54.19 | 2.71 | 1.76 | 0.06 | 0.70 | 0.71 | 8.63 | 9.51 | 0.41 | 0.58 | 1.78 | 0.08 |
| Sn | 0.50 | 0.50 | 0.50 | 0.50 | 0.50 | 0.50 | 0.50 | 0.50 | 0.50 | 0.50 | 0.50 | 0.50 |
| W | 0.50 | 0.80 | 0.25 | 0.25 | 1.30 | 1.10 | 1.00 | 1.50 | 0.25 | 0.25 | 2.30 | 0.25 |
| Au | 17.80 | 62.10 | 14.10 | 0.50 | 0.10 | 0.10 | 17.50 | 15.80 | 2.40 | 1.90 | 1.20 | 1.50 |
| Ag | 101.00 | 326.00 | 110.00 | 9.00 | 4.00 | 11.00 | 352.00 | 345.00 | 23.00 | 103.00 | 57.00 | 7.00 |
| Pd | 5.00 | 5.00 | 5.00 | 5.00 | 5.00 | 5.00 | 5.00 | 5.00 | 5.00 | 5.00 | 5.00 | 5.00 |
| Pt | 1.00 | 1.00 | 1.00 | 1.00 | 1.00 | 1.00 | 1.00 | 1.00 | 1.00 | 1.00 | 1.00 | 1.00 |
| Re | 98.00 | 5.00 | 0.50 | 0.50 | 3.00 | 0.50 | 12.00 | 21.00 | 0.50 | 0.50 | 0.50 | 0.50 |

Major elements normalized to 100 % on a volatile free basis. *$Fe_2O_3$ is total Fe. Major elements, S and C are reported as wt %. Trace elements and REEs are reported as ppm. Noble metals are reported as ppb. Abbreviations: BT = basaltic trachyandesite, KF = Korobasabasaga Formation.

**Table 4.3:** Least-altered whole-rock geochemistry results for intrusive rocks from Wainaulo

| Lithotype | EMD1 | | EMQD | IMQD | | LMQD | | |
|---|---|---|---|---|---|---|---|---|
| Sample ID | NVD019-708 | NVD019-728 | NVD040 -531 | NVD019-834 | NVD040-405 | NVD008-443 | NVD016-558 | NVD047-1136 |
| $SiO_2$ | 63.91 | 62.87 | 64.70 | 64.66 | 64.28 | 64.16 | 64.33 | 64.38 |
| $TiO_2$ | 0.53 | 0.58 | 0.47 | 0.47 | 0.49 | 0.49 | 0.49 | 0.46 |
| $Al_2O_3$ | 16.68 | 16.88 | 16.68 | 16.32 | 16.86 | 17.05 | 16.88 | 16.96 |
| $Fe_2O_3$* | 4.53 | 5.21 | 6.16 | 6.15 | 5.36 | 4.67 | 4.58 | 4.34 |
| MnO | 0.03 | 0.03 | 0.05 | 0.04 | 0.02 | 0.06 | 0.08 | 0.08 |
| MgO | 2.08 | 2.27 | 1.86 | 1.93 | 1.95 | 1.80 | 2.00 | 1.75 |
| CaO | 5.51 | 5.83 | 4.22 | 4.87 | 4.76 | 5.27 | 4.80 | 5.19 |
| $K_2O$ | 1.57 | 1.24 | 0.95 | 0.60 | 1.09 | 1.73 | 1.78 | 1.88 |
| $Na_2O$ | 4.88 | 4.81 | 4.72 | 4.74 | 4.93 | 4.56 | 4.83 | 4.73 |
| $P_2O_5$ | 0.27 | 0.26 | 0.20 | 0.22 | 0.24 | 0.23 | 0.19 | 0.19 |
| Total C | 0.03 | 0.03 | 0.07 | 0.14 | 0.07 | 0.27 | 0.03 | 0.18 |
| Total S | 1.05 | 1.13 | 0.18 | 0.35 | 0.43 | 0.28 | 0.30 | 0.15 |
| Mg# | 33.79 | 32.62 | 25.13 | 25.86 | 28.79 | 29.99 | 32.67 | 30.95 |
| LOI | 3.20 | 4.20 | 1.80 | 2.60 | 2.80 | 2.30 | 1.70 | 2.10 |
| Sum | 99.99 | 99.98 | 100.02 | 99.99 | 100.01 | 100.02 | 99.96 | 99.98 |
| Cr | 6.84 | 6.84 | 6.84 | 6.84 | 123.16 | 6.84 | 6.84 | 13.68 |
| Co | 8.10 | 9.00 | 9.30 | 9.80 | 7.90 | 7.00 | 7.20 | 6.60 |
| Ni | 3.30 | 3.60 | 3.70 | 4.30 | 4.30 | 4.40 | 6.50 | 3.40 |
| Rb | 25.00 | 20.80 | 12.40 | 6.30 | 12.20 | 15.30 | 26.00 | 23.40 |
| Sr | 785.80 | 761.60 | 704.40 | 677.70 | 756.30 | 710.20 | 654.70 | 720.90 |
| Cs | 0.05 | 0.10 | 0.20 | 0.05 | 0.05 | 0.20 | 0.20 | 0.30 |
| Ba | 420.00 | 292.00 | 405.00 | 259.00 | 322.00 | 490.00 | 495.00 | 616.00 |
| Sc | 9.00 | 9.00 | 8.00 | 9.00 | 9.00 | 8.00 | 9.00 | 8.00 |
| V | 137.00 | 146.00 | 111.00 | 110.00 | 111.00 | 105.00 | 115.00 | 106.00 |
| Ta | 0.20 | 0.20 | 0.20 | 0.10 | 0.20 | 0.20 | 0.10 | 0.30 |
| Nb | 4.10 | 2.90 | 2.30 | 2.20 | 2.60 | 3.30 | 4.30 | 2.60 |
| Zr | 130.70 | 117.10 | 123.00 | 124.50 | 120.00 | 116.60 | 111.40 | 124.70 |
| Hf | 2.50 | 3.00 | 3.10 | 3.20 | 3.00 | 3.50 | 3.80 | 3.30 |
| Th | 2.20 | 2.10 | 1.80 | 1.80 | 1.90 | 1.70 | 1.50 | 2.20 |
| U | 0.70 | 0.60 | 0.30 | 0.30 | 0.60 | 0.30 | 0.50 | 1.00 |
| Y | 14.60 | 13.20 | 8.20 | 10.50 | 13.10 | 13.70 | 13.90 | 12.40 |
| La | 13.70 | 11.40 | 6.10 | 7.10 | 9.90 | 10.30 | 10.60 | 12.90 |
| Ce | 29.60 | 24.90 | 12.80 | 15.50 | 20.80 | 22.50 | 23.60 | 26.80 |
| Pr | 3.62 | 3.24 | 1.62 | 2.10 | 2.76 | 2.87 | 2.95 | 3.29 |
| Nd | 15.70 | 13.50 | 7.10 | 9.20 | 12.00 | 13.40 | 14.70 | 12.90 |
| Sm | 2.71 | 2.79 | 1.44 | 1.94 | 2.47 | 2.68 | 2.72 | 2.73 |
| Eu | 0.85 | 0.92 | 0.62 | 0.68 | 0.79 | 0.89 | 0.76 | 0.88 |
| Gd | 2.72 | 2.78 | 1.54 | 1.94 | 2.62 | 2.26 | 2.38 | 2.66 |
| Tb | 0.44 | 0.43 | 0.24 | 0.32 | 0.40 | 0.38 | 0.41 | 0.40 |
| Dy | 2.57 | 2.36 | 1.18 | 1.96 | 2.18 | 1.95 | 2.21 | 2.24 |
| Ho | 0.49 | 0.48 | 0.27 | 0.37 | 0.44 | 0.50 | 0.48 | 0.45 |
| Er | 1.46 | 1.52 | 0.85 | 1.11 | 1.38 | 1.41 | 1.41 | 1.36 |
| Tm | 0.24 | 0.21 | 0.13 | 0.16 | 0.20 | 0.20 | 0.22 | 0.22 |
| Yb | 1.48 | 1.47 | 0.89 | 1.07 | 1.51 | 1.22 | 1.45 | 1.48 |
| Lu | 0.27 | 0.25 | 0.15 | 0.19 | 0.23 | 0.22 | 0.25 | 0.23 |
| Cu | 2653.48 | 3247.79 | 1570.18 | 1331.80 | 433.04 | 668.10 | 123.56 | 33.56 |
| Zn | 33.00 | 44.00 | 41.40 | 34.70 | 27.50 | 22.50 | 30.20 | 20.10 |
| Pb | 1.10 | 1.23 | 1.13 | 0.65 | 0.46 | 0.09 | 0.42 | 0.42 |
| Mo | 2.33 | 5.45 | 2.04 | 2.66 | 0.96 | 2.07 | 1.04 | 1.01 |
| Sn | 1.00 | 0.50 | 0.50 | 0.50 | 0.50 | 0.50 | 0.50 | 0.50 |
| W | 2.00 | 0.25 | 0.25 | 0.25 | 0.25 | 1.30 | 2.70 | 0.25 |
| Au | 13.60 | 27.30 | 52.20 | 25.80 | 2.90 | 6.60 | 3.00 | 1.50 |
| Ag | 452.00 | 604.00 | 346.00 | 349.00 | 64.00 | 170.00 | 51.00 | 20.00 |
| Pd | 5.00 | 5.00 | 5.00 | 5.00 | 5.00 | 5.00 | 5.00 | 5.00 |
| Pt | 1.00 | 3.00 | 2.00 | 1.00 | 1.00 | 1.00 | 1.00 | 1.00 |
| Re | 4.00 | 6.00 | 4.00 | 0.50 | 1.00 | 1.00 | 2.00 | 0.50 |

Major elements normalized to 100 % on a volatile free basis. *$Fe_2O_3$ is total Fe. Major element, S and C values are reported as wt %. Trace element and REE values are reported as ppm. Noble metal values are reported as ppb. Abbreviations: EMD1 = early mineralization diorite 1, EMQD = early mineralization quartz-diorite, IMQD = inter-mineralization quartz-diorite, LMQD = late mineralization quartz-diorite.

**Table 4.4:** Least-altered whole-rock geochemistry results for intrusive rocks from Waisoi

| Deposit/Area | Waisoi West | | | | | Waisoi East | | | Waisoi |
|---|---|---|---|---|---|---|---|---|---|
| Lithotype | QDP1 | QDP1 | QDP2 | QDP2 | QDP3 | DP1 | DP2 | DP3 | QFP |
| Sample ID | NSW006-310 | NSW006-435 | NSW001-273 | NSW001-295 | NSW001-1042 | NSE002-362 | NSE002-767 | NSE006-635 | WD |
| $SiO_2$ | 66.46 | 67.07 | 66.64 | 66.70 | 66.61 | 69.53 | 71.12 | 68.40 | 62.24 |
| $TiO_2$ | 0.41 | 0.42 | 0.44 | 0.43 | 0.40 | 0.32 | 0.32 | 0.34 | 0.46 |
| $Al_2O_3$ | 17.17 | 17.32 | 17.67 | 17.94 | 16.81 | 17.12 | 16.71 | 17.34 | 19.50 |
| $Fe_2O_3$* | 5.29 | 3.97 | 4.19 | 4.20 | 3.34 | 1.42 | 0.60 | 2.68 | 5.98 |
| MnO | 0.02 | 0.02 | 0.02 | 0.01 | 0.03 | 0.01 | 0.02 | 0.02 | 0.17 |
| MgO | 1.45 | 1.62 | 1.43 | 1.50 | 1.27 | 1.55 | 0.84 | 1.13 | 2.42 |
| CaO | 2.31 | 3.07 | 2.44 | 2.18 | 4.94 | 2.60 | 3.25 | 3.51 | 3.27 |
| $K_2O$ | 0.79 | 0.23 | 0.30 | 0.38 | 0.44 | 0.71 | 1.05 | 0.69 | 2.07 |
| $Na_2O$ | 5.94 | 6.13 | 6.69 | 6.50 | 5.95 | 6.58 | 5.93 | 5.75 | 3.64 |
| $P_2O_5$ | 0.15 | 0.15 | 0.19 | 0.18 | 0.18 | 0.12 | 0.12 | 0.15 | 0.20 |
| Total C | 0.31 | 0.14 | 0.01 | 0.02 | 0.05 | 0.24 | 0.47 | 0.14 | 0.05 |
| Total S | 0.20 | 0.12 | 0.09 | 0.08 | 0.69 | 0.48 | 0.10 | 0.18 | 0.01 |
| Mg# | 23.35 | 31.20 | 27.50 | 28.41 | 29.71 | 54.81 | 60.87 | 31.91 | 31.02 |
| LOI | 2.90 | 2.20 | 1.50 | 1.90 | 2.50 | 2.10 | 3.10 | 2.10 | 4.10 |
| Sum | 99.99 | 99.99 | 100.01 | 100.02 | 99.98 | 99.96 | 99.96 | 100.02 | 99.94 |
| Cr | 6.84 | 6.84 | 6.84 | 6.84 | 6.84 | 6.84 | 6.84 | 6.84 | 6.84 |
| Co | 4.40 | 3.60 | 2.80 | 2.90 | 4.40 | 3.70 | 1.20 | 3.70 | 7.40 |
| Ni | 5.00 | 6.70 | 5.10 | 5.30 | 5.70 | 4.20 | 5.00 | 4.50 | 1.40 |
| Rb | 10.20 | 1.90 | 3.70 | 4.80 | 5.10 | 11.70 | 13.70 | 9.00 | 30.60 |
| Sr | 219.50 | 554.00 | 553.40 | 548.90 | 692.20 | 393.50 | 300.00 | 566.40 | 484.00 |
| Cs | 0.40 | 0.10 | 0.05 | 0.05 | 0.05 | 0.20 | 0.30 | 0.30 | 0.05 |
| Ba | 98.00 | 140.00 | 140.00 | 131.00 | 179.00 | 77.00 | 107.00 | 160.00 | 335.00 |
| Sc | 6.00 | 5.00 | 5.00 | 5.00 | 5.00 | 4.00 | 4.00 | 4.00 | 8.00 |
| V | 194.00 | 125.00 | 116.00 | 100.00 | 131.00 | 93.00 | 123.00 | 83.00 | 96.00 |
| Ta | 0.05 | 0.05 | 0.05 | 0.05 | 0.05 | 0.10 | 0.05 | 0.05 | 0.05 |
| Nb | 1.40 | 1.30 | 1.60 | 1.60 | 1.30 | 1.10 | 1.70 | 1.00 | 1.70 |
| Zr | 98.40 | 103.80 | 103.20 | 96.50 | 88.50 | 82.20 | 78.00 | 85.90 | 88.50 |
| Hf | 3.10 | 2.60 | 3.10 | 2.90 | 2.60 | 2.20 | 2.30 | 2.40 | 2.30 |
| Th | 0.50 | 0.80 | 0.80 | 0.80 | 0.60 | 0.60 | 0.60 | 0.70 | 1.30 |
| U | 0.20 | 0.30 | 0.40 | 0.30 | 0.20 | 0.20 | 0.20 | 0.40 | 0.50 |
| Y | 7.10 | 8.10 | 10.90 | 10.90 | 9.50 | 8.90 | 6.70 | 8.50 | 17.60 |
| La | 3.50 | 5.80 | 8.10 | 8.10 | 6.40 | 4.30 | 3.50 | 5.40 | 11.00 |
| Ce | 8.70 | 13.10 | 17.50 | 18.50 | 14.80 | 10.00 | 8.70 | 12.00 | 22.30 |
| Pr | 1.20 | 1.68 | 2.32 | 2.33 | 1.99 | 1.23 | 1.17 | 1.59 | 3.10 |
| Nd | 4.50 | 7.70 | 11.30 | 11.20 | 9.20 | 7.60 | 4.40 | 6.30 | 13.10 |
| Sm | 1.20 | 1.57 | 2.14 | 1.93 | 1.92 | 1.25 | 1.12 | 1.42 | 3.00 |
| Eu | 0.47 | 0.59 | 0.69 | 0.75 | 0.65 | 0.51 | 0.43 | 0.52 | 1.09 |
| Gd | 1.27 | 1.33 | 1.91 | 1.87 | 1.70 | 1.29 | 1.07 | 1.41 | 3.24 |
| Tb | 0.20 | 0.24 | 0.32 | 0.31 | 0.27 | 0.24 | 0.20 | 0.23 | 0.51 |
| Dy | 1.15 | 1.38 | 1.60 | 1.76 | 1.61 | 1.33 | 1.10 | 1.47 | 3.16 |
| Ho | 0.23 | 0.28 | 0.39 | 0.36 | 0.35 | 0.30 | 0.23 | 0.27 | 0.67 |
| Er | 0.75 | 0.87 | 1.08 | 1.18 | 0.98 | 0.86 | 0.65 | 0.98 | 2.04 |
| Tm | 0.13 | 0.14 | 0.19 | 0.18 | 0.16 | 0.16 | 0.12 | 0.15 | 0.33 |
| Yb | 0.73 | 0.81 | 1.29 | 1.20 | 1.04 | 1.01 | 0.82 | 1.01 | 2.13 |
| Lu | 0.13 | 0.15 | 0.21 | 0.21 | 0.17 | 0.18 | 0.15 | 0.18 | 0.33 |
| Cu | 1832.55 | 1283.80 | 1275.57 | 996.54 | 140.33 | 4241.61 | 865.96 | 935.76 | 28.55 |
| Zn | 6.70 | 9.70 | 14.40 | 11.70 | 14.10 | 6.00 | 7.40 | 8.40 | 60.80 |
| Pb | 0.15 | 0.01 | 0.03 | 0.08 | 0.01 | 0.28 | 0.60 | 0.44 | 3.09 |
| Mo | 11.12 | 3.88 | 9.07 | 4.77 | 3.15 | 17.04 | 46.79 | 2.67 | 0.06 |
| Sn | 0.50 | 0.50 | 0.50 | 0.50 | 0.50 | 1.00 | 0.50 | 0.50 | 0.50 |
| W | 1.60 | 1.90 | 1.90 | 0.90 | 1.10 | 2.60 | 5.10 | 2.10 | 0.25 |
| Au | 53.80 | 63.60 | 22.10 | 21.60 | 7.10 | 115.20 | 40.70 | 20.10 | 1.90 |
| Ag | 131.00 | 109.00 | 111.00 | 110.00 | 47.00 | 474.00 | 252.00 | 89.00 | 24.00 |
| Pd | 13.00 | 10.00 | 5.00 | 5.00 | 5.00 | 5.00 | 13.00 | 5.00 | 5.00 |
| Pt | 1.00 | 1.00 | 1.00 | 1.00 | 1.00 | 1.00 | 1.00 | 1.00 | 1.00 |
| Re | 20.00 | 8.00 | 25.00 | 19.00 | 1.00 | 49.00 | 115.00 | 3.00 | 0.50 |

Major elements normalized to 100 % on a volatile free basis. *$Fe_2O_3$ is total Fe. Major element, S and C values are reported as wt %. Trace element and REE values are reported as ppm. Noble metal values are reported as ppb. Abbreviations: DP1 = quartz eye dacite, DP2 = quartz-bearing dacite, DP3 = dacite porphyry, QDP1 = quartz-diorite porphyry 1, QDP2 = quartz-diorite porphyry 2, QDP3 = quartz-diorite porphyry 3.

On a total alkali–silica diagram (TAS; Fig. 4.2A) samples from the Namosi district range from basaltic to rhyolitic, with only a few samples plotting in the basaltic trachyandesite and trachyandesite fields. Wainimala Group rocks are predominantly basaltic andesite, whereas NAF rocks range from basaltic andesite to dacite. The NAF pyroxene andesite, including the pyroxene-plagioclase-phyric andesite (N2a) and pyroxene-phyric microdiorite (N2c), plot in the basaltic andesite to andesite fields. The NAF hornblende andesite and Namosi diorite are more evolved and plot in the andesite to dacite fields. The ore-related Namosi intrusive samples become increasingly more evolved from Wainaulo diorites to Wainaulo quartz-diorites to Waisoi West quartz-diorites to Waisoi East dacites and are more fractionated than the pre-mineralization Namosi diorite samples. The post-mineralization quartz feldspar porphyry (QFP) does not follow this fractionation trend; instead, it plots in the andesite field. The Korobasabasaga Formation (KF) samples are characterized by elevated alkali contents and mostly lie within the basaltic trachyandesite to trachyandesite fields (Fig. 4.2A).

Similarly, in the $K_2O$ versus $SiO_2$ diagram (Fig. 4.2B), the KF samples plot within the high-K and shoshonite fields, whereas the rest of the Namosi area samples are scattered across the medium- to low-K fields. The regional NAF pyroxene and hornblende andesite samples predominantly plot within the medium-K field; however, the N2a–c and the ore-related Namosi intrusions trend downwards from the medium- to low-K fields. These trends could be a result of K mobility due to hydrothermal alteration, since all of these samples were taken in proximity to the Namosi ore deposits. Crawford et al. (2007) proposed that plots of $P_2O_5/Al_2O_3$–$K_2O/Al_2O_3$ and MgO–$P_2O_5$ can be used to overcome this element mobility issue. In Figure 4.2C the Namosi area samples plot within similar fields as in the $K_2O$–$SiO_2$ diagram. Only a few samples exhibit a slight deviation towards the right side of the diagram, suggesting that there was not a significant addition of K due to hydrothermal alteration. Therefore, the KF samples can be considered to have a high-K calc-alkaline magmatic affinity. The Wainimala Group samples plot in the low-K field, which is consistent with interpretations made by Gill (1987) and Wharton et al. (1995) for Wainimala Group rocks elsewhere in Viti Levu. The N2a–c and Waisoi West quartz-diorite samples plot on a trend towards the left side of the diagram (Fig. 4.2C), sug-

gesting that these samples experienced K loss due to hydrothermal alteration. This K loss explains the downward trend of the plotted N2a–c samples on the $K_2O$–$SiO_2$ diagram in Figure 4.2B. On a $P_2O_5$ vs. MgO diagram (Fig. 4.2D), the N2a–c samples plot in the medium-K field, which is interpreted to reflect their true magmatic affinity. This diagram cannot be used for the Namosi intrusive complex samples, which have < 3 wt % MgO and for which apatite is a fractionating phase (e.g., they follow the Ap vector on Fig. 4.2D). In all three diagrams (Figs. 4.2B, C and D), the Wainaulo diorite samples plot in the medium-K field and the Waisoi East dacite samples plot in the low-K field.

The Namosi district samples were plotted on Harker diagrams (Fig. 4.3). Even though a majority of the NAF and ore-related Namosi intrusion samples are porphyritic, the major elements are well correlated (i.e., display minimal scatter) and show the characteristically smooth trend of $TiO_2$, $Fe_2O_3$ and CaO depletion with fractionation, which is typical in comagmatic calc-alkaline suites (e.g., Ewart, 1982). MgO and MnO also display this antithetic relationship with $SiO_2$. The Wainimala basaltic andesite, Korobasabasaga basaltic trachyandesite and quartz feldspar porphyry (QFP) samples do not neatly conform to the dominant trends on some of the major element plots (Fig. 4.3). This is consistent with the interpretation that these rocks are not comagmatic with the NAF or the Namosi ore-related intrusions. A plot of $SiO_2$ versus the relatively mobile $K_2O$ shows considerable scatter (Fig. 4.2B); however, $Na_2O$ shows relatively less scatter (Fig. 4.3G) and has a sympathetic relationship with $SiO_2$. The ore-related Namosi intrusions appear to continue the fractionation trends associated with the NAF samples (Fig. 4.3). Plots of $Al_2O_3$ and $P_2O_5$ versus $SiO_2$ are the exception, showing a greater complexity. In these plots, NAF samples have relatively constant $Al_2O_3$ and $P_2O_5$ with increasing $SiO_2$. Contrarily, the ore-related Namosi intrusions display a sympathetic relationship between $SiO_2$ and $Al_2O_3$ and an antithetic relationship between $SiO_2$ and $P_2O_5$.

*4.2.4.2 Trace element geochemistry*

Figure 4.4 shows trace element variation plots for the volcanic and intrusive rocks of the Namosi district. With increasing fractionation, the ore-related Namosi mineralized intrusions show

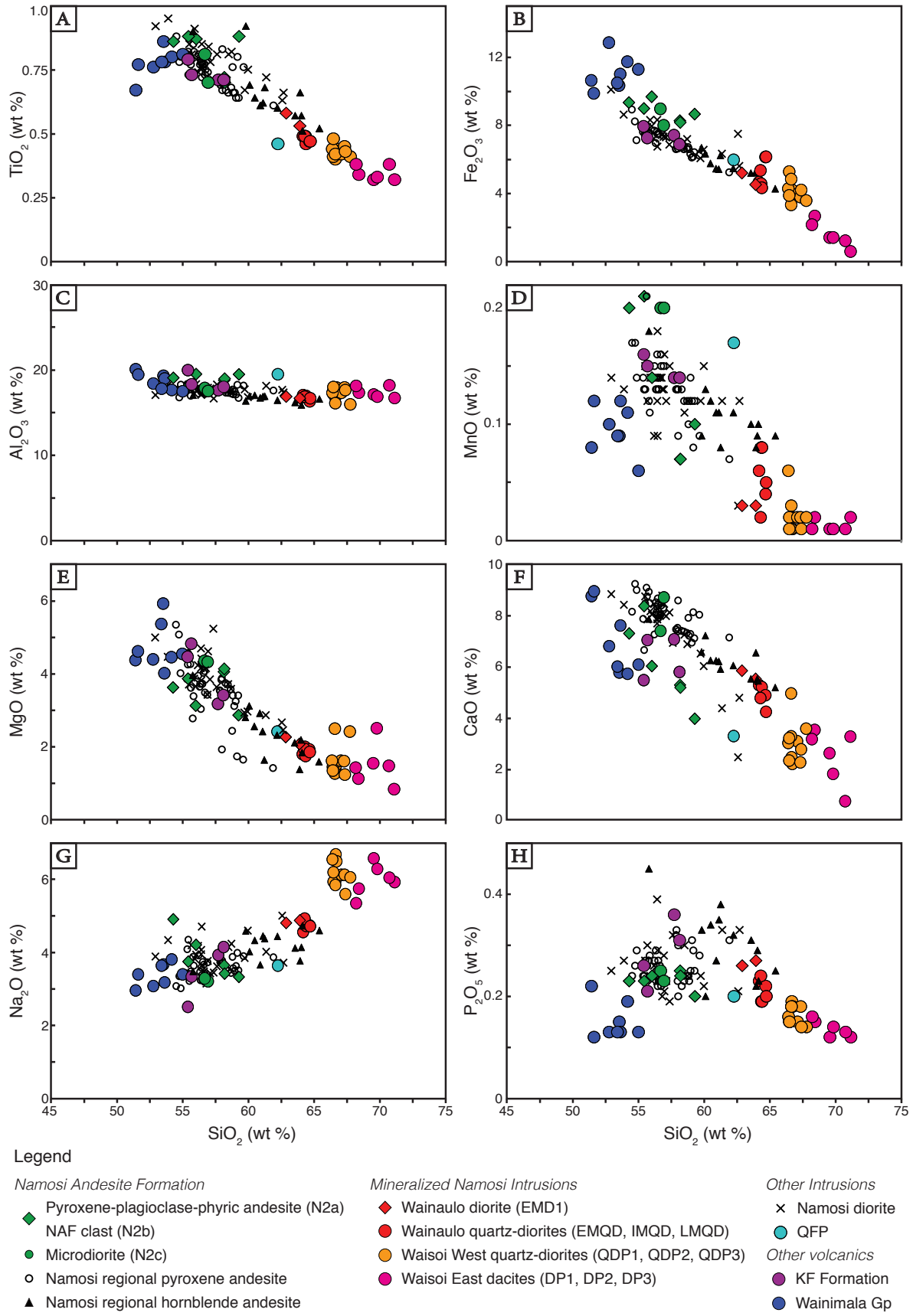


**Figure 4.3:** Harker diagrams for Namosi district volcanic and intrusive rocks. Abbreviations: DP1 = quartz-eye dacite, DP2 = quartz-bearing dacite, DP3 = dacite porphyry, EMD1 = early mineralization diorite 1, EMQD = early mineralization quartz-diorite, Gp = Group, IMQD = inter-mineralization quartz-diorite, Korobasabasaga Formation, LMQD = late mineralization quartz-diorite. QDP1 = quartz-diorite porphyry 1, QDP2 = quartz-diorite porphyry 2, QDP3 = quartz-diorite porphyry 3.

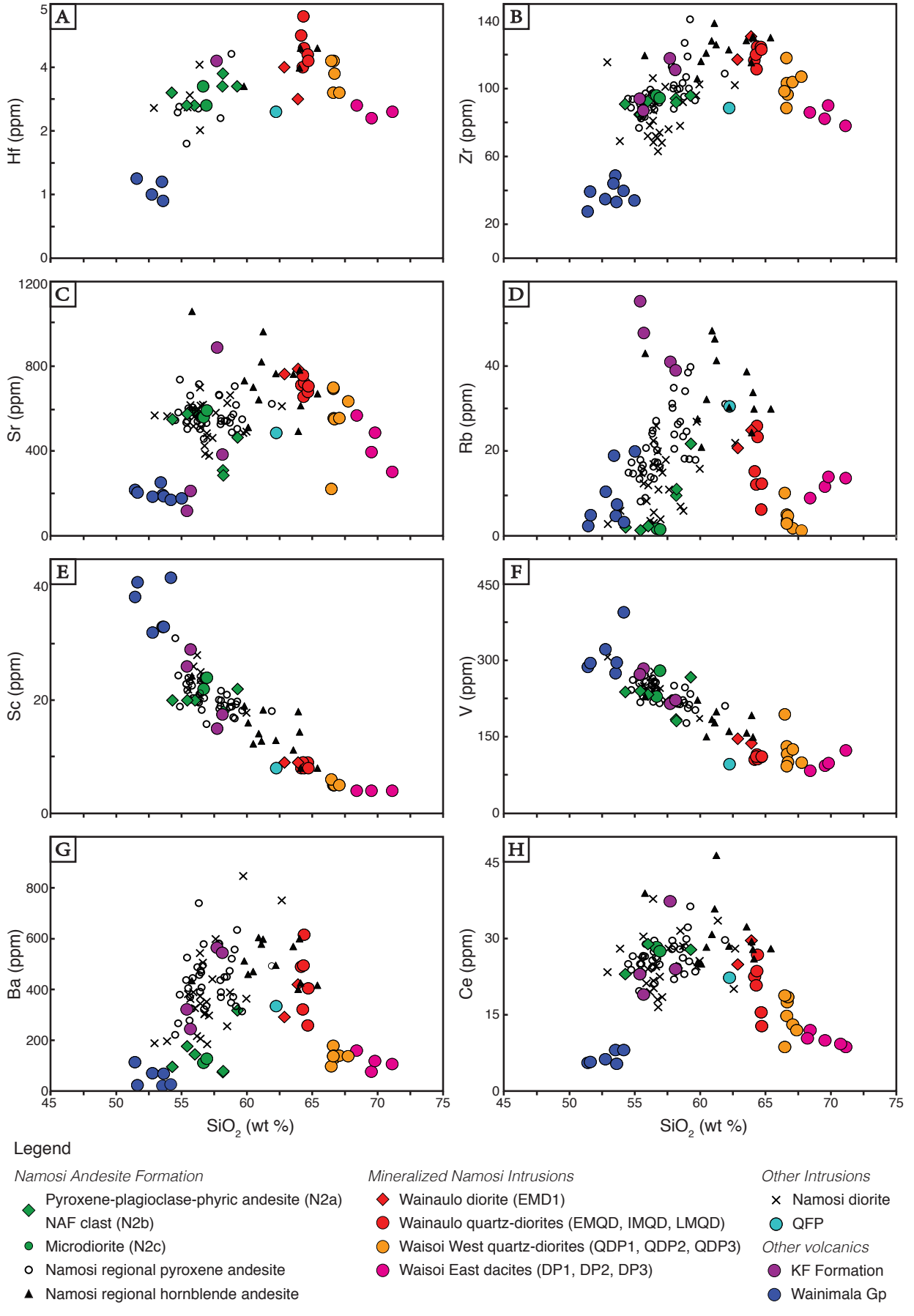


**Figure 4.4:** Trace element variation diagrams for Namosi district volcanic and intrusive rocks. Abbreviations are the same as in Figure 4.3.

decreasing concentrations of high field strength (HFS) cations (e.g., Sc, V, Zr, Hf and Ti) and lanthanides (e.g., Ce; Figs. 4.3 and 4.4). A similar antithetic relationship is shown between the large ion lithophile (LIL) elements (e.g., Rb, Ba and Sr) and $SiO_2$ (Fig. 4.4). These mobile LIL elements show considerably more scatter than the HFS cations, which is expected since LIL elements are more sensitive to secondary processes.

The volcanic rocks and pre-mineralization intrusions show a weak positive correlation between LIL elements and increasing $SiO_2$. Some of the HFS cations show a similar relationship (e.g., Hf, Zr and Ce); however, the first row series transition metals (e.g., Sc, Ti, V, Mn and Fe) show an antithetic relationship with increasing fractionation (Figs. 4.3 and 4.4). This relationship can be explained by the compatibility of these elements during the early stages of fractionation, which results in the enrichment of mafic minerals. Therefore, elevated values of these elements are indicative of more mafic rocks and should have a negative correlation with increasing fractionation.

The Wainimala Group basaltic andesite samples can be discriminated from the NAF samples by the absolute values of several HFS cations (e.g., Zr, Hf, Sc and Ce). Least-altered Wainimala Group samples have Hf < 1.3 ppm, Zr < 50 ppm, Ce < 10 ppm and Sc > 30 ppm; whereas, least-altered NAF samples have Hf > 1.7 ppm, Zr > 75 ppm, Ce > 19 and Sc < 25 ppm (Fig. 4.4).

Figure 4.5 shows primitive mantle-normalized spidergrams for the Namosi district volcanic and intrusive rocks. As expected, the samples show greater depletion in Sc and V with increasing fractionation (i.e., weak negative Sc and V anomalies for the Wainimala Group samples, moderate negative anomalies for NAF samples, and strong negative anomalies for Namosi mineralized intrusions; Fig. 4.5). Wainimala Group basaltic andesite is characterized by a flat primitive mantle-normalized pattern and a moderate negative Nb anomaly (Table 4.5; Fig. 4.5; $La/Yb_{cn}$ = 0.92 – 1.08; Nb/Nb* = 0.24 – 0.40). The NAF volcanic rocks are characterized by a LREE-enriched primitive mantle-normalized pattern and a strong negative Nb anomaly (Table 4.5; Figs 4.5D and F; $La/Sm_{cn}$ = 2.28 – 2.58; Nb/Nb* = 0.14 – 0.18). The NAF pyroxene andesites have a moderate negative Ti anomaly; whereas, the NAF horn-

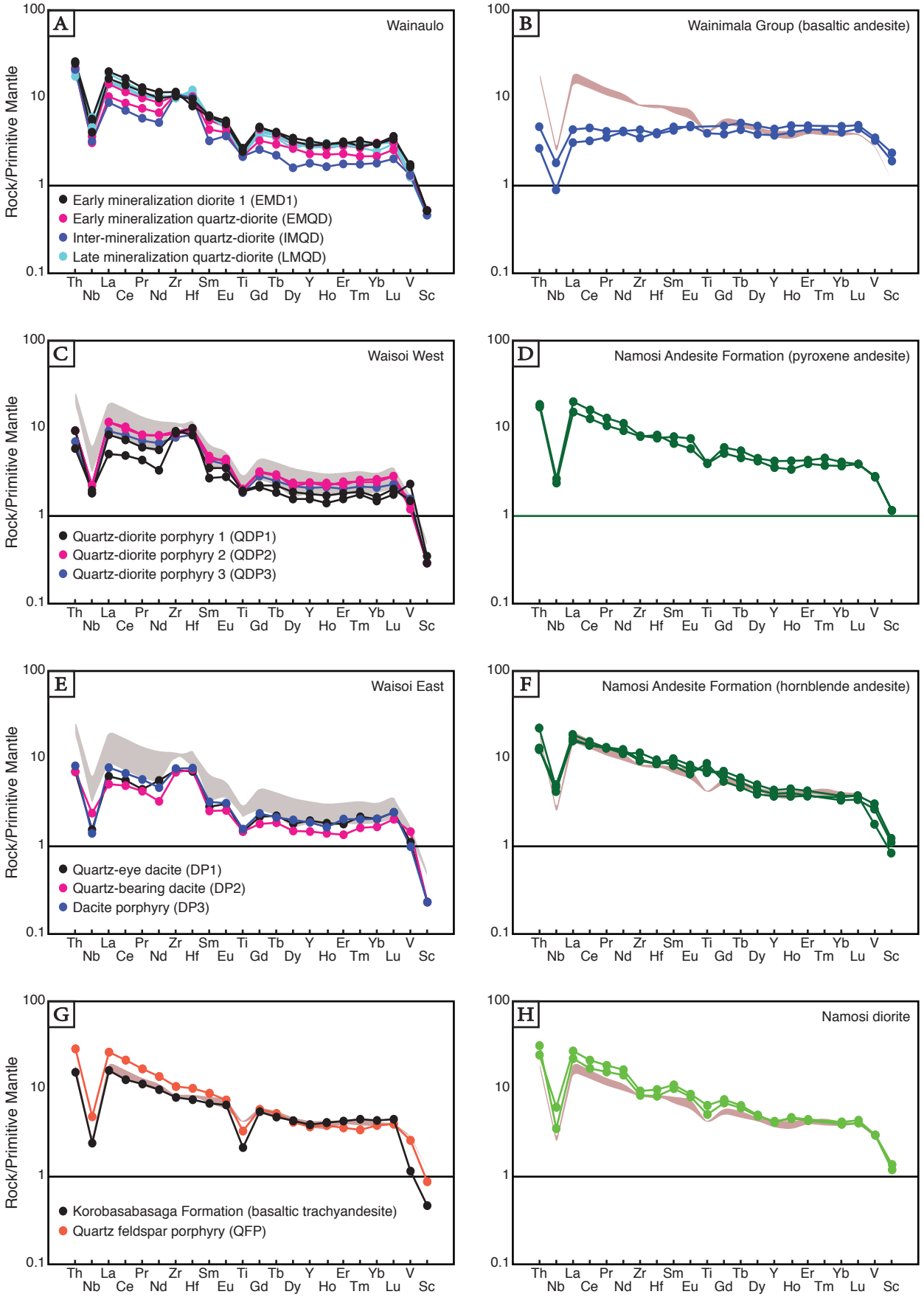


**Figure 4.5:** Representative primitive mantle-normalized diagrams for samples from the Namosi district. Normalizing values are from Sun and McDonough (1989). The gray and rose-gold shaded areas show the range in compositions of Wainaulo and pyroxene andesite samples, respectively.

**Table 4.5:** Chondrite-normalized REE ratios for Namosi district volcanic and intrusive samples analyzed in this study; normalizing values are from Sun and McDonough (1989)

| Lithotype | Sample ID | $(La/Sm)_{cn}$ | $(La/Yb)_{cn}$ | $(Gd/Yb)_{cn}$ | Nb/Nb* | Eu/Eu* |
|---|---|---|---|---|---|---|
| Wainimala Group | | | | | | |
| Basaltic andesite (W1a) | NSE002-254 | 1.02 | 1.08 | 0.96 | 0.40 | 1.20 |
| | NSW006-209a | 0.98 | 0.98 | 0.95 | 0.24 | 0.35 |
| | NSW006-209b | 0.91 | 0.92 | 1.05 | 0.08 | 0.33 |
| Namosi Andesite Formation | | | | | | |
| Pyroxene andesite (N2a) | NVD047-216 | 2.51 | 4.89 | 1.47 | 0.14 | 0.26 |
| | NVD019-109 | 2.31 | 3.29 | 1.18 | 0.18 | 0.25 |
| | NVD011-072.9 | 2.32 | 4.93 | 1.57 | 0.17 | 0.26 |
| Pyroxene andesite clast (N2b) | NSW006-122 | 2.58 | 4.22 | 1.16 | 0.16 | 0.25 |
| | NSW006-122b | 2.46 | 4.44 | 1.29 | 0.17 | 0.24 |
| | NVD014-361 | 2.28 | 4.13 | 1.39 | 0.14 | 0.26 |
| Microdiorite (N2c) | NVD014-531 | 2.50 | 5.57 | 1.58 | 0.23 | 0.24 |
| | NVD019-361 | 2.63 | 5.92 | 1.62 | 0.34 | 0.26 |
| Wainaulo intrusive complex | | | | | | |
| Early mineralization diorite (EMD1) | NVD019-708 | 3.26 | 6.64 | 1.52 | 0.25 | 0.26 |
| | NVD019-728 | 2.64 | 5.56 | 1.56 | 0.20 | 0.27 |
| Early mineralization quartz-diorite (EMQD) | NVD040-531 | 2.73 | 4.92 | 1.43 | 0.21 | 0.46 |
| Inter-mineralization quartz-diorite (IMQD) | NVD019-834 | 2.36 | 4.76 | 1.50 | 0.19 | 0.35 |
| | NVD040-405 | 2.59 | 4.70 | 1.44 | 0.20 | 0.27 |
| Late mineralization quartz-diorite (LMQD) | NVD008-443 | 2.48 | 6.06 | 1.53 | 0.26 | 0.33 |
| | NVD016-558 | 2.52 | 5.24 | 1.36 | 0.36 | 0.27 |
| | NVD047-1136 | 3.05 | 6.25 | 1.49 | 0.16 | 0.28 |
| Waisoi West intrusive complex | | | | | | |
| Quartz-diorite porphyry 1 (QDP1) | NSW006-310 | 1.88 | 3.44 | 1.44 | 0.36 | 0.47 |
| | NSW006-435 | 2.38 | 5.14 | 1.36 | 0.20 | 0.49 |
| Quartz-diorite porphyry 2 (QDP2) | NSW001-273 | 2.44 | 4.50 | 1.22 | 0.21 | 0.34 |
| | NSW001-295 | 2.71 | 4.84 | 1.29 | 0.21 | 0.40 |
| Quartz-diorite porphyry 3 (QDP3) | NSW001-1042 | 2.15 | 4.41 | 1.35 | 0.22 | 0.38 |
| Waisoi East intrusive complex | | | | | | |
| Quartz-eye dacite (DP1) | NSE002-362 | 2.22 | 3.05 | 1.06 | 0.23 | 0.49 |
| Quartz-bearing dacite (DP2) | NSE002-767 | 2.02 | 3.06 | 1.08 | 0.39 | 0.53 |
| Dacite porphyry (DP3) | NSE006-635 | 2.45 | 3.84 | 1.15 | 0.17 | 0.43 |
| Post-mineralization lithotypes | | | | | | |
| Korobasabasaga Fm - basaltic trachyandesite | KORO | 2.94 | 6.83 | 1.52 | 0.18 | 0.25 |
| Quartz feldspar porphyry (QFP) | WD | 2.37 | 3.70 | 1.26 | 0.15 | 0.27 |

blende andesites have a weak positive Ti anomaly. The Namosi diorite has a LREE-enriched primitive mantle-normalized pattern (Fig. 4.5H) with negative HFS cation anomalies (i.e., Hf, Zr and Ti). All of the ore-related Namosi mineralized intrusions have very similar primitive mantle-normalized patterns and are characterized by moderate

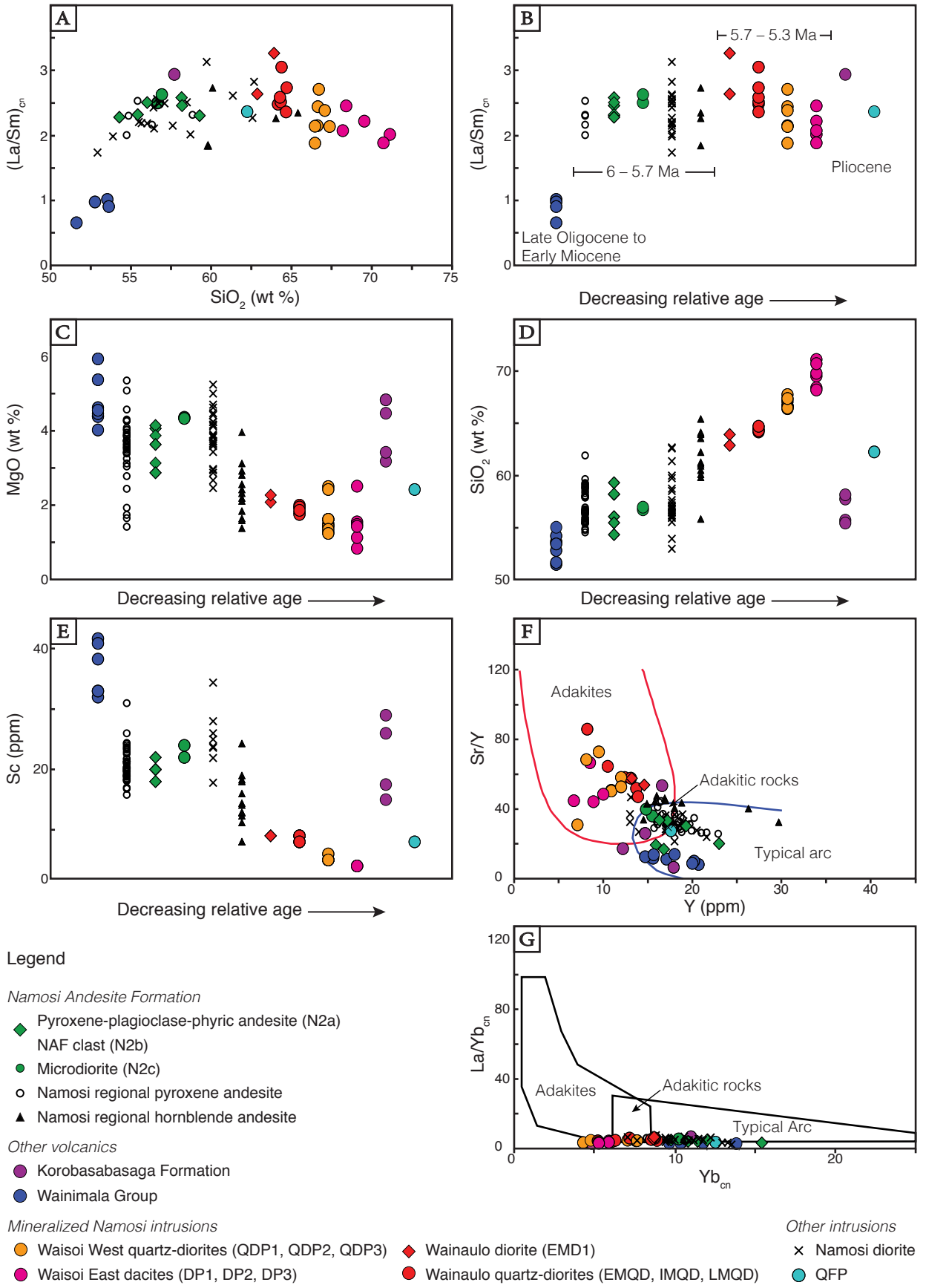


**Figure 4.6: A.** Plot of $La/Sm_{cn}$ vs. $SiO_2$. **B.** Plot of $La/Sm_{cn}$ vs. relative age. **C.** Plot of MgO vs. relative age. **D.** Plot of $SiO_2$ vs. relative age. **E.** Plot of Sc vs. relative age. **F.** Plot of Sr/Y vs. Y with fields from Drummond and Defant (1990). **G.** Plot of $La/Yb_{cn}$ vs. $Yb_{cn}$ with fields from Martin (1986). Normalizing values are from Sun and McDonough (1989). Abbreviations are the same as in Figure 4.3.

LREE enrichment with flat to weakly fractionated HREE (Table 4.5; Figs. 4.5A, C and E; $La/Sm_{cn}$ = 1.88 – 3.26; $Gd/Yb_{cn}$ = 1.06 – 1.56). The $Gd/Yb_{cn}$ ratios become closer to one (i.e., flatter) with increasing $SiO_2$ (average Wainaulo intrusive complex: $SiO_2$ = 64.16, $Gd/Yb_{cn}$ = 1.48; average Waisoi West intrusive complex: $SiO_2$ = 66.70, $Gd/Yb_{cn}$ = 1.33; average Waisoi East intrusive complex: $SiO_2$ = 69.68, $Gd/Yb_{cn}$ = 1.10). The ore-related intrusions all have relative Hf and Zr enrichment; however, the slight jagged progression from Zr to Hf (Figs. 4.5A, C and E) may be a result of incomplete dissolution of zircon during analysis. The primitive mantle-normalized patterns for the Korobasabasaga Formation basaltic trachyandesite and the quartz feldspar porphyry (QFP) are similar and display simple LREE-enriched patterns with moderate to weak HREE fractionation and strong negative Nb and Ti anomalies (Table 4.5; Fig. 4.5G; $La/Sm_{cn}$ = 2.37 – 2.94, $Gd/Yb_{cn}$ = 1.26 – 1.52, Nb/Nb* = 0.15 – 0.18).

### *4.2.5 Discussion*

#### *4.2.5.1 Petrogenesis*

The geochemical data show that there was an evolution in magmatic composition within the Namosi district from the Late Oligocene Wainimala Group to the Early Pliocene Korobasabasaga Formation. The Wainimala Group formed in the Vitiaz intra-oceanic island arc above the westward subducting Pacific plate (Hathway, 1993). The thickness of the Wainimala Group volcanics across Fiji is estimated to be > 11 km (Hirst, 1965; Band, 1968; Rodda, 1976), and there are noted compositional variations within its component sub-groups and formations (Wharton et al., 1995). In the Namosi district the Wainimala Group volcanics consist of a > 6 km-thick sequence (Rodda, 1976) of Late Oligocene to Middle Miocene (K–Ar: 28 – 12 Ma; Rodda, 1994; Wharton et al., 1995) basaltic andesites and correlatives of the Nubuonaboto Volcanics that have undergone greenschist facies metamorphism (e.g., Ellis, 1996; Crawford, 2011). In this study, the least-altered Wainimala Group basaltic andesite samples were found to have a low-K tholeiitic magmatic affinity (Fig. 4.2), which is consistent with interpretations made by previous workers (e.g., Gill, 1970; Rodda, 1976; Wharton et al., 1995 and Crawford, 2011). The LREE-depleted and flat HREE pro-

files (Fig. 4.5) of these Wainimala Group rocks indicate that they have been derived from shallow partial melting of the depleted Indo-Australian mantle wedge peridotite.

The oldest intrusions in the Namosi district are the Colo Plutonic Suite (CPS) diorite-to-nalite-trondhjemite and lesser olivine-augite gabbro stocks (Rodda, 1994) that were emplaced within Wainimala Group rocks north of the study area. CPS intrusive rocks were not encountered during this study, but their geochemistry has been documented previously and interpreted by Gill (1970), Gill and Stork (1979) and Crawford (2011). The CPS stocks have a transitional low-K tholeiitic to medium-K calc-alkaline magmatic affinity (Crawford, 2011). There are two reported U–Pb zircon ages of 11.1 ± 0.7 Ma and 10.4 ± 1.6 Ma for low-K CPS intrusions and two U–Pb zircon ages of 8.1 ± 1.2 Ma and 7.3 ± 0.9 Ma for medium-K CPS intrusions (Crawford, 2011). These U–Pb zircon ages are similar to K–Ar radiometric ages (12.5 – 7.5 Ma) for CPS stocks determined by Whelan et al. (1985).

Unconformably overlying the Wainimala Group rocks are the Late Miocene Namosi Andesite Formation volcanics (K–Ar: ~ 5.6 – 6.1 Ma for the hornblende andesite member; Gill and McDougall, 1973). These volcanics have been crosscut by the NAF pre-mineralization intrusions (i.e., Namosi diorites; K–Ar: 6.1 ± 0.5 Ma, Tanaka et al., 2010; U–Pb: 5.59 ± 0.35 Ma, Crawford, 2011). The depletion of Nb, Ti, V and Sc and the enrichment of LREE in the NAF and Namosi diorite, as demonstrated on the primitive mantle-normalized spidergrams (Fig. 4.5), is characteristic of emplacement within a typical suprasubduction zone tectonic setting (Wilson, 1989; e.g., Baguio district; Hollings et al., 2011). The low Ni (< 8 ppm), Cr (< 30 ppm) and MgO (< 4.5 wt %) concentrations as well the low Mg# (< 38) for the Namosi diorites (Table 4.2) indicate that their source underwent significant fractionation prior to emplacement. The pre-mineralization porphyritic diorite (PD) and porphyritic andesite (PA) are inferred to have been emplaced within the NAF after the intrusion of the Namosi diorites, and are the host rocks to the Wainaulo porphyry Cu-Au deposit. The whole-rock analyses for the PA and PD intrusive stocks were deemed too altered for consideration in this study, unfortunately (Appendix D).

The next phase of magmatism in the Namosi district consisted of the Late Miocene to Ear-

ly Pliocene Namosi intrusive complex (U–Pb: ~ 5.7 – 5.3 Ma; Chapter 3). The similar geochemical characteristics (e.g., coherent linear trends on Harker diagrams, Fig. 4.3; congruent trends on primitive mantle-normalized spidergrams, Fig. 4.5) of the Namosi Andesite Formation and ore-related intrusions, suggests that they have a comagmatic relationship. Based on their whole-rock geochemistry, these two magmatic suites are interpreted to have a medium-K calc-alkaline affinity (Fig. 4.2). The Late Miocene NAF volcanics have $La/Sm_{cn}$ ratios that are higher than that of the Wainimala Group (Fig. 4.6B). There is a trend to increasing LREE prior to mineralization in the Namosi district (cf. La/Yb ratios; Hollings et al., 2005; Table 4.5; Fig. 4.6B). The $La/Sm_{cn}$ ratios are highest for the Wainaulo early mineralization diorites (oldest of the Namosi mineralizing intrusions) and then decrease both with increasing $SiO_2$ (Fig. 4.6A) and time (Fig. 4.6B) throughout the evolution of the Namosi mineralized magmatic suite. This is interpreted to reflect increasing crustal thickness and a change from a pyroxene- to an amphibole-dominated lower crustal mineral assemblage up until the time of mineralization, and finally a change related to crustal thinning with initiation of backarc rifting in the Fiji Platform area. This change in stress regime is supported by the onset of high-K calc-alkalic and shoshonitic volcanism 60 km north of the Namosi district, starting at ~ 5.2 Ma (Begg and Gray, 2002). The shift to shoshonitic volcanism coincides with rifting and fragmentation of the Fijian arc lithosphere during a time of maximum rotation of the Fiji Platform and flanking backarc spreading in the North Fiji and Lau Basins. The decrease in LREE observed in the Waisoi West and Waisoi East intrusive rocks (e.g., Ce in Fig. 4.4H) may instead be attributed to the effects of hydrothermal alteration and mineralization and not related to changes in crustal thickness as suggested above. The La/Sm and La/Yb ratios from the Waisoi West and Waisoi East intrusive rocks are similar to those found in the Wainimala host rocks (Fig. 4.4), which supports this interpretation.

The similarities in the Wainaulo, Waisoi West and Waisoi East intrusive complex spidergrams indicate that they probably evolved along similar lines of liquid descent and underwent fractional crystallization to derive the increasingly felsic compositions for ore-related intrusions over time (e.g., Laramide magmatic complex, Arizona; Lang and Titley, 1998; Fig. 4.6). There is a change from smooth HREE primitive mantle-normalized patterns in barren, pre- and post-mineraliza-

tion intrusions to the "saggy", convex HREE profile in productive Namosi mineralized intrusions (e.g., Lang and Titley, 1998). The convex HREE profile is indicative of extensive fractionation of hornblende in a very hydrous parent magma (Rohrlach and Loucks, 2005), which is generally a prerequisite for mineralization in arc magmas (Loucks, 2014). Hand sample evidence that supports a more hydrous composition of the Namosi mineralized intrusions includes the presence of hornblende as a phenocrystic phase and localized accumulations of volatile components, including USTs and miarolitic cavities in several of the interpreted mineralizing phases (Chapter 3).

The coherent antithetic relationships between various elements (MgO, CaO, $TiO_2$, $Fe_2O_3$, V and Sc) and $SiO_2$ and the sympathetic relationship between $Na_2O$ and $SiO_2$ in both the NAF and mineralized intrusive samples (Figs. 4.3 and 4.4) indicate that clinopyroxene and Fe-Ti oxides were fractionating from basaltic compositions. A change from positive to negative slopes for the linear trends between $SiO_2$ and several incompatible element concentrations (e.g., $P_2O_5$, Sr, Ba, Ce, Hf, and Zr) occurs at ~ 62 wt % $SiO_2$ (Figs. 4.3 and 4.4). This inflection may suggest effective retention of apatite (which takes up $PO_4$), calcic plagioclase (in which Sr may substitute for Ca), titanite or rutile (in which Ce, Zr and Hf may substitute for Ti), and a potassic phase such as K-feldspar, biotite or hornblende (in which Ba and Sr may substitute for K) in the magma chamber beyond dacitic compositions. Apatite fractionation in the Namosi mineralized intrusions is also indicated by the trend towards low MgO and low $P_2O_5$ (Ap vector) in Figure 4.2D (e.g., Crawford et al., 2007). Fractionation and removal of K-feldspar, biotite or hornblende beyond dacitic compositions is also signified by a change from positive to negative trends for $K_2O$ and Rb versus $SiO_2$ at ~ 62 wt % $SiO_2$. However, the variation diagrams for $K_2O$ and Rb show strongly segmented trends, with another switch to a positive slope at 68 wt % $SiO_2$. This suggests a reincorporation of a potassic phase (likely alkali feldspar based on petrographic inspection) into the melt that crystallized to form the Waisoi East dacites.

The youngest volcanic unit in the Namosi district is the Korobasabasaga Formation (KF). Ellis (1996) suggested that there may be a faulted contact between the NAF and KF and that the KF appears to have been deposited after porphyry mineralization. Although the direct relationship

between NAF and KF was not observed in this study, the results of petrographic inspection are consistent with a post-ore emplacement (i.e., the KF sample did not contain secondary hydrothermal alteration minerals). Ellis (1996) analyzed a basalt fragment from the "Korobasabasaga Pyroclastics" and reported that it shows affinities of island arc tholeiitic rocks; however, this study demonstrated that the Korobasabasaga Formation consists of high-K basaltic trachyandesite lavas and volcaniclastics (consistent with interpretations made by Crawford, 2011). The Korobasabasaga Formation volcanics have higher concentrations of LREE than the NAF volcanics and Namosi mineralized intrusions, which precludes a comagmatic relationship with these Late Miocene rocks (Table 4.5 and Fig. 4.6B). The Korobasabasaga Formation has instead been correlated with the Pliocene, Ba and Medrausucu Groups (Crawford, 2011). The lavas have variable magmatic affinities, ranging from primitive- to low-MgO shoshonitic basalts of the Tavua stratovolcano to high-K calc-alkaline basalts and andesites of the Raki Raki stratovolcano (Crawford, 2011). They are interpreted to have been emplaced during the early rifting stage of the Fiji Platform tecto-no-magmatic history (Gill, 1989).

The QFP was interpreted by Ellis (1996) to have a pre-mineralization timing based on an observed contact relationship with the "Basal Namosi Conglomerate" (i.e., boulders similar to the QFP were identified in the conglomerate). However, this contact relationship is suspect, as the QFP was also shown to have intruded the conglomerate (Ellis, 1996). It is more likely that the QFP was emplaced post-mineralization. Ellis (1996) defined a pyrite – chalcopyrite zone that extends up to 1000 m from the Waisoi porphyry margin, where Cu values are ~ 100 – 200 ppm at its furthest extent. The QFP sample, which was collected less than 500 m from the Waisoi East mineralized porphyry intrusions, was found to have Cu < 30 ppm and S < 0.01 wt % (Table 4.2), suggesting that it was not overprinted by Cu porphyry mineralization or alteration. There was also a distinct lack of sulfides, veins and secondary alteration minerals observed in the QFP sample. The QFP has a primitive mantle-normalized pattern that is very similar to that of the Korobasabasaga Formation basaltic trachyandesite (Fig. 4.5G), and is interpreted to have been emplaced in a comparable tectonic environment.

*4.2.5.2 Adakite signature in Namosi district rocks?*

Adakites are intermediate to felsic volcanic rocks that typically have the following geochemical characteristics: $SiO_2 \geq 56$ wt %, $Al_2O_3 \geq 15$ wt %, MgO < 3 wt %, Sr ≥ 400 ppm, Y ≤ 18 ppm, Yb ≤ 1.9 ppm, Ni ≥ 20 ppm, Cr ≥ 30 ppm, and La/Yb ≥ 20 (Defant and Drummond, 1990; Drummond and Defant, 1990). The unusual petrochemistry of these rocks is derived from either partial melting of subducting oceanic crust (Defant and Drummond, 1990) or fractional crystallization of mantle-derived basaltic magmas underplating the arc crust (Drehler et al., 2005). Adakitic magmatism has been linked with porphyry-style and epithermal Cu or Cu-Au-Mo ore deposits around the world (e.g., Oyarzun et al., 2001; Rohrlach and Loucks, 2005; Richards and Kerrich, 2007; Chiaradia, 2009; Chiaradia et al., 2009; Richards, 2011; Loucks, 2014).

Previous studies have interpreted the Namosi district intrusive rocks to have an adakitic signature (e.g., Tanaka et al., 2010). In a plot of Sr/Y–Y (Fig. 4.6F), all Namosi ore-related intrusions clearly lie within the adakite field of Drummond and Defant (1990), which is consistent with the interpretation made by Imai et al. (2007) that mineralization in the Namosi district is associated with intrusions that have an adakitic signature. The Wainimala Group samples all plot in the typical arc field, and the NAF samples, including the pre-mineralization Namosi diorite, plot as adakitic and/or typical arc rocks. Figure 4.4C demonstrates that Sr has considerable scatter when plotted against $SiO_2$, suggesting that it may have been mobilized during hydrothermal alteration. Therefore, the Sr/Y–Y diagram is deemed unreliable, and a plot based on less mobile elements is required to assess if there are in fact rocks with an adakitic signature in the Namosi district. Martin (1986) proposed a plot of $La/Yb_{cn}$ versus $Yb_{cn}$ to distinguish adakites from normal arc rocks. The Namosi ore-related intrusions, which plotted as adakites in Figure 4.4C, plot below the adakite field in the $La/Yb_{cn}$ versus $Yb_{cn}$ diagram (Fig. 4.4D). This may indicate that the Namosi ore-related intrusions are sourced from primitive mantle-derived melts and not slab-derived melts as was previously interpreted. This result is consistent with the relatively unfractionated HREE patterns for the samples plotted in the spidergrams in Figure 4.5, which implies that partial melting occurred at a level that was above the garnet stability field, a level that would be more

shallow than a subducting slab. True adakites have been identified in the Fiji area, for example the high-Mg adakites from the Kadavu Island Group south of Viti Levu documented by Verbeeten (1996). These adakites have low abundances of Y (15.6 – 19.6 ppm), high Sr concentrations (553 – 1667 ppm), high Sr/Y (79.2 – 88.9) and strongly fractionated REE patterns (La/Yb= 17 – 26; Verbeeten, 1996). The Kadavu adakites were generated during rotation of the Fiji Platform over the last 3 My by fractionation of partial melts of a mantle wedge that was contaminated by slab-derived melts during the short lived subduction of the South Fiji Basin crust beneath the young and hot North Fiji Basin.

## 4.3 Strontium and neodymium isotopes

### *4.3.1 Previous work*

Only a few studies have published Sr–Nd isotopic values for island arc-related igneous rocks from Viti Levu, Fiji. Rogers and Setterfield (1994) provided eleven $^{87}Sr/^{86}Sr$ and nine $^{143}Nd/^{144}Nd$ analyses on shoshonitic volcanic and intrusive rocks from the Ba Volcanic Group. Results of this study indicate that Ba Volcanic Group rocks have a narrow range of $^{87}Sr/^{86}Sr$ (0.703558 to 0.704015) and $^{143}Nd/^{144}Nd$ (0.512945 to 0.513043) values. These ratios have been interpreted to suggest derivation from a depleted mantle source (i.e., $^{87}Sr/^{86}Sr < 0.7045$; Kesler et al., 1975). Gill (1984) presented results from a Fiji-wide Sr–Nd and Pb isotopic survey that fingerprinted arc-related rocks from the four tectono-magmatic stages of the Fiji Platform (cf. Chapter 2). The study included two Nd and three Sr isotopic analyses from Namosi district rocks (Namosi Andesite Formation, n = 2; Wainimala Group, n = 1). The Namosi Andesite Formation samples were found to have primitive $^{87}Sr/^{86}Sr$ values of 0.70357 and 0.70359 (hornblende andesite and pyroxene andesite, respectively) and an εNd of +7.6 for the hornblende andesite. The Wainimala Group sample was reported to have a lower Sr isotope concentration ($^{87}Sr/^{86}Sr = 0.70305$) and a higher εNd (+8.6) value than the Namosi Andesite Formation samples. These results were found to be consistent with an increase in LIL elements and La/Yb ratios from the early-arc Wainimala Group to the mature-arc Namosi Andesite Formation. This was interpreted to reflect an early N-MORB-like source for the island arc tholeiitic rocks evolving to an

OIB-like source for the medium-K calc-alkaline rocks (Gill, 1984). Additionally, Crawford (2011) conducted an unpublished study that included Sr–Nd analyses on twenty samples from southeastern Viti Levu, Fiji (Wainimala Group, n = 3; Namosi Andesite Formation, n = 4, Namosi diorite, n= 2; Namosi porphyry, n =1; Colo Plutonic Suite, n = 7; and Savura Group, n = 3). Results from this study show that the island arc rocks of southeastern Viti Levu, Fiji have strontium isotopic ratios that range from 0.703028 to 0.703999 and neodymium isotopic ratios that range from 0.512945 to 0.513079. Crawford (2011) concluded that the radiogenic isotopic data reflects a significant change in mantle source components between the end of the Colo Plutonic Suite magmatism and that of the medium-K calc-alkaline Namosi Andesite Formation. All previous results (including Crawford's unpublished 2011 data) have been recalculated according to methods outlined in section 4.3.2.

### *4.3.2 Methods and results*

Four whole-rock Sr–Nd isotopic compositions for Late Miocene – Early Pliocene ore-related intrusions of the Namosi district and one Early Pliocene basaltic trachyandesite from the Korobasabasaga Formation were analyzed at the University of Melbourne for this study (Table 4.6). Least-altered samples were chosen from each principal deposit within the district and from the post-mineralization volcanic suite. To correct for fractionation, $^{87}Sr/^{86}Sr$ isotope ratios were normalized to $^{86}Sr/^{88}Sr = 0.11940$ and $^{143}Nd/^{144}Nd$ ratios were normalized to $^{146}Nd/^{144}Nd = 0.72190$.

**Table 4.6:** Sr–Nd radiogenic isotope data for Namosi district rocks

| Lithotype | LMQD | QDP1 | DP1 | DP2 | Korobasabasaga Fm |
|---|---|---|---|---|---|
| Deposit | Wainaulo | Waisoi West | Waisoi East | Waisoi East | Post-Mineralization |
| Age (Ma) | 5.5 | 5.5 | 5.4 | 5.3 | ~ 5.0 |
| Sample | NVD008-443 | NSW006-310 | NSE002-362 | NSE002-682 | KORO |
| $^{147}Sm/^{144}Nd$ | 0.1210 | 0.1613 | 0.0995 | 0.1946 | 0.1308 |
| $^{87}Rb/^{86}Sr$ | 0.062 | 0.134 | 0.086 | 0.151 | 0.151 |
| $^{143}Nd/^{144}Nd$ | 0.513015 (6) | 0.513048 (8) | 0.513055 (6) | 0.513065 (7) | 0.513013 (8) |
| $\varepsilon_{Nd}$ | 7.5 | 8.1 | 8.3 | 8.4 | 7.4 |
| $^{143}Nd/^{144}Nd_i$ | 0.513011 | 0.513042 | 0.513052 | 0.513058 | 0.513008 |
| $\varepsilon_{Nd_i}$ | 7.5 | 8.1 | 8.3 | 8.4 | 7.4 |
| $^{87}Sr/^{86}Sr$ | 0.703581 (23) | 0.703633 (12) | 0.703585 (17) | 0.703576 (17) | 0.703501 (16) |
| $^{87}Sr/^{86}Sr_i$ | 0.70358 | 0.70362 | 0.70358 | 0.70357 | 0.70349 |

Absolute uncertainties (in parentheses) are shown at the 2σ level for the last digit indicated. Initial $^{87}Sr/^{86}Sr$ and $^{143}Nd/^{144}Nd$ ratios have been calculated based on the ages reported in this table. εNd and $\varepsilon Nd_i$ values were calculated using $^{143}Nd/^{144}Nd_{CHUR} = 0.512638$ from Zindler and Hart (1986) and equations from DePaulo and Wasserburg (1976). Abbreviations: DP1 = quartz-eye dacite, DP2 = quartz-bearing dacite, Fm = formation, LMQD = late-mineralization quartz-diorite, QDP1 = quartz-diorite porphyry 1.

The standards NIST SRM987 ($^{87}Sr/^{86}Sr$ = 0.710230) and La Jolla ($^{143}Nd/^{144}Nd$ = 0.511848) were used. The $\varepsilon_{Nd}$ and $\varepsilon_{Nd_i}$ values were calculated using a present-day chondrite uniform reservoir (CHUR) value of 0.512638 (Zindler and Hart, 1986) and by using the equations from DePaulo and Wasserburg (1976). The initial $^{87}Sr/^{86}Sr$ ratios for the samples vary from 0.70349 to 0.70362 and the initial $^{143}Nd/^{144}Nd$ range from 0.513009 to 0.513058. These calculated ratios were found to have a negligible deviation from the corrected ratios (Table 4.6). The calculated $\varepsilon_{Nd}$ values are indistinguishable from the $\varepsilon_{Nd_i}$ values (Table 4.6), as can be expected in rather young arc-related rocks.

### *4.3.3 Discussion*

The initial $^{87}Sr/^{86}Sr$ ratios determined for this study fall within the range for Fiji Platform rocks (0.703028 – 0.704015; the low value is for a low-K CPS stock from Wainanubu and the high value is for a Ba Volcanic Group monzonite; Fig. 4.7B) and are higher than the range for Pacific MORB (0.70240 – 0.70256; Saunders et al., 1988). All Namosi rocks have $\varepsilon_{Nd} > 0$ and $^{87}Sr/^{86}Sr < 0.705$ (Table 4.6; Appendix E), which implies that they were derived from a source region with relatively low Rb/Sr and high Sm/Nd ratios (Rollinson, 1993), and have a depleted mantle source.

Five Wainimala Group Sr–Nd isotopic values from Gill (1984) and Crawford (2011) were plotted on Figure 4.7B. Crawford (2011) interpreted that the samples have typical intra-oceanic Sr–Nd isotopic values, reflecting depleted upper mantle Nd with the addition of Sr-rich crustal material during subduction. The samples plot between the Pacific MORB and some unknown enriched component (probably Pacific pelagic sediments), with some overlap with the Tonga-Kermadec arc field (Fig. 4.7B). This enrichment trend (vector b in Figure 4.7B) coincides with the three plotted low-K Savura Group samples and the three plotted medium-K CPS samples, suggesting that they were also likely derived from similar depleted sources that had been metasomatized by a crustal sediment component of a downgoing slab (Crawford, 2011). The low-K CPS samples, however, have much lower $^{87}Sr/^{86}Sr$ values and were likely derived from a source with long-term depletion in $^{143}Nd/^{144}Nd$, with no subducted sediment input.

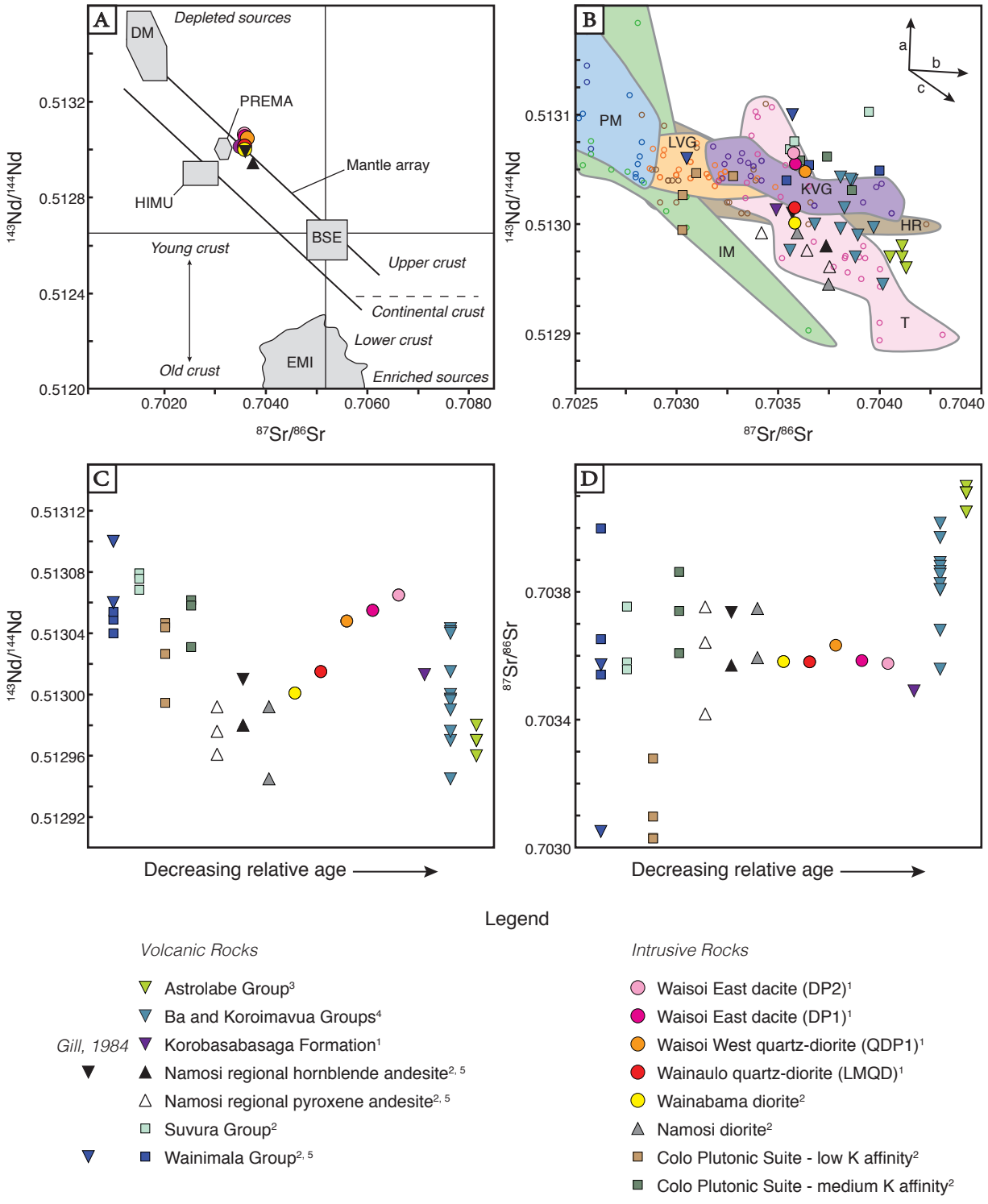


**Figure 4.7: A.** Plot of $^{143}Nd/^{144}Nd$ vs. $^{87}Sr/^{86}Sr$ for Namosi data showing the major oceanic mantle reservoirs from Rollinson (1993) and DePaulo and Wasserburg (1979). **B.** Plot of $^{143}Nd/^{144}Nd$ vs. $^{87}Sr/^{86}Sr$ showing Fiji area data. Fields are defined based on data from various studies, specifically: HR (Gill, 1984; Verbeeten, 1996), IM (Pyle et al., 1992), KVG (Cole et al., 1990; Hergt and Woodhead, 2007), LVG (Cole et al., 1990; Hergt and Woodhead, 2007), PM (Ito et al., 1987), and T (Jenner et al., 1987; Turner et al., 1997; Ewart et al., 1998). **C.** Plot of $^{143}Nd/^{144}Nd$ vs. relative age for Namosi and select Fiji Platform samples. **D.** Plot of $^{87}Sr/^{86}Sr$ vs. relative age for Namosi and select Fiji Platform samples. Plotted data sources: [1]This study, [2]Crawford (2011), [3]Verbeeten (1996), [4]Rogers and Setterfield (1994), [5]Gill (1984). Abbreviations: BSE = bulk silicate earth, DM = depleted mantle, EMI = enriched mantle, HIMU = mantle with high U/Pb, HR = Hunter Ridge, IM = Indian mantle, KVG = Korobasaga Volcanic Group, LVG = Lau Volcanic Group. PM = primitive mantle, PREMA = frequently observed prevalent mantle composition, T = Tofua arc.

The Sr–Nd isotopic data for the Namosi Andesite Formation (pyroxene andesite, hornblende andesite and Namosi diorite; Crawford, 2011) lies along the mantle array of Zindler and Hart (1986), which is a mixing line between depleted mantle and upper continental crust (Fig. 4.7A). The NAF Sr–Nd isotopic compositions are similar to primitive oceanic island arc rocks from the Tofua Arc (part of the Tonga-Kermadec arc that formed post-initiation of seafloor spreading in the Lau Basin; Fig. 4.7B; Hergt and Woodhead, 2007). The isotopic shift towards more radiogenic Sr and less radiogenic Nd in NAF samples implies that there was an increasing component of subduction input (Ewart et al., 1998).

The Namosi ore-related porphyry intrusions have a $^{87}Sr/^{86}Sr$ range from 0.70358 to 0.70362, which precludes the presence of a significant amount of continental crust as a source and implies the Namosi arc was entirely intra-oceanic (Kesler et al, 1985). Elevated $^{143}Nd/^{144}Nd$ values for ore-related Namosi intrusions compared to the Late Miocene NAF samples suggests a more primitive mantle source with recharge of the subarc mantle (Fig. 4.7). The increase in $^{143}Nd/^{144}Nd$ in these ore-related intrusions over time, from 0.513001 at ~ 5.7 Ma to 0.513058 at ~ 5.3 Ma (Table 4.6; Fig. 4.7C), records a shift towards a less contaminated and more primitive source. This shift is interpreted to reflect the migration of the Namosi arc away from the active subduction front due to the rapid rotation of the Fiji Platform that was occurring during this time. Therefore, the effect of continental material in the source region became successively less pronounced throughout the emplacement of the early NAF country rocks through to the emplacement of the more evolved Waisoi East dacitic intrusions.

The vertical Nd trend displayed in the Waisoi intrusive rocks data (Fig. 4.7) may be better explained by the leaching and transportation of more radiogenic Nd from the surrounding Wainimala basement rocks (e.g., Todd et al., 2012). This interpretation is consistent with the Wainaulo intrusive complex samples having a similar Nd signature to the Namosi Andesite Formation (the dominant host rock) and the Waisoi intrusive complex samples having a similar Nd signature to the Wainimala Group rocks (Fig. 4.7). The Nd variations may also be explained by random differences in the amount of slab component in the mantle source (the difference in Nd values lie with-

in an acceptable range found in individual Quaternary arc volcanos), amount of differentiation, or even external analytical uncertainty.

### 4.4 Summary

The geochemical data show that there was an evolution in magmatic composition within the Namosi district from the Late Oligocene Wainimala Group to the Early Pliocene Korobasabasaga Formation:

**Nubuonaboto Volcanics (Wainimala Group)**

- These Late Oligocene to Early Miocene basaltic andesite lavas and associated volcaniclastic rocks have a low-K tholeiitic magmatic affinity
- They were generated by shallow partial melting of the depleted Indo-Australian mantle wedge peridotite during westward-directed subduction of the Pacific plate beneath the Indo-Australian plate (Crawford, 2011)
- They formed in the Vitiaz intra-oceanic island arc (Hathway, 1994)

**Namosi Andesite Formation (Medrausucu Group)**

- These are Late Miocene medium-K calc-alkalic basaltic andesite to dacite lavas and associated volcaniclastic rocks; major subdivisions consist of pyroxene andesite and hornblende andesite
- They have been crosscut by the pre-mineralization Namosi diorite and formed after a reversal in arc polarity,
- They consist of normal primitive arc magmas interpreted to have been derived from partial melting of the North Fiji Basin (Pacific) mantle wedge overlying the descending Sou Fiji Basin (Indo-Australian) slab

**Namosi mineralized intrusions**

- These Late Miocene to Early Pliocene intrusions have medium-K calc-alkalic affinities
- They are comagmatic with the Namosi Andesite Formation
- Compositions evolved from diorite and quartz-diorite (Wainaulo) to quartz-diorite (Waisoi West) to dacite (Waisoi East) through fractional crystallization
- Prior to the onset of mineralization, there was an increase in $La/Sm_{cn}$ that may be associated with thickening of the Fijian lithosphere; over the course of mineralization, a shift towards increasingly more primitive mantle source signatures reflect the onset of rifting in the Fiji Platform vicinity

**Korobasabasaga Formation and quartz feldspar porphyry (QFP)**

- These are high-K calc-alkalic basaltic trachyandesite to trachyandesite and associated volcaniclastics
- The Korobasabasaga Formation and QFP are interpreted to be comagmatic; both are interpreted to postdate mineralization and are not considered to be geochemically related to the Namosi Andesite Formation or Namosi mineralized intrusions
- They have an inferred Late Pliocene age, and are correlated here with the Ba Group volcanics in northern Viti Levu
- They are inferred to have been emplaced during the early stages of Late Pliocene rifting of the Fiji Platform (e.g., Gill and Whalen, 1989a).

The high $^{143}Nd/^{144}Nd$ and low $^{87}Sr/^{86}Sr$ ratios of the Namosi Andesite Formation are consistent with a primitive mantle source with no crustal input. The overall elevated $^{143}Nd/^{144}Nd$ values and systematic increase in $^{143}Nd/^{144}Nd$ with time for the Namosi intrusive complex records a shift towards a less contaminated and even more primitive mantle source at the time of mineralization. This shift is interpreted to reflect the migration of the Namosi Arc away from the active subduction front due to the rapid rotation of the Fiji Platform from ~ 5.7 to 5.3 Ma.

# CHAPTER 5

# Alteration and mineralization of the Namosi district

## 5.1 Introduction

This chapter documents the hydrothermal alteration and vein paragenesis of three porphyry copper-gold-(molybdenum) deposits from the Namosi district (Wainaulo, Waisoi West and Waisoi East; abbreviated as WO, WW and WE, respectively). Three alteration cross sections through Wainaulo (NVD019; Fig. 5.1), Waisoi West (NSW006; Fig. 5.15) and Waisoi East (NSE002; Fig. 5.22) were constructed and are used as the primary framework for this study. Spatio-temporal relationships of hydrothermal alteration assemblages are described within the framework of the intrusive history at each deposit. Molybdenite grains from quartz – sulfide veins from Wainaulo, Waisoi West and Waisoi East were selected for Re–Os analysis in order to resolve the absolute age of mineralization for each deposit studied.

## 5.2 Paragenesis

### *5.2.1 Methods*

Detailed graphic logging of 20 km of drill core from the Namosi district has facilitated sample collection within a well-constrained spatio-temporal framework. Petrographic analyses of 150 polished thin sections and 35 polished slabs were carried out to observe primary and hydrothermal mineral assemblages and textures. This information has been supplemented by NJV drill core logs and data from the Namosi Joint Venture (NJV) acQuire database.

Hydrothermal K-feldspar and Na-rich plagioclase proved to be important minerals to identify

in the Namosi district. They are typically accompanied by paragonitic- to phengitic-illite, obscuring their characteristic features and making them difficult to identify while core logging. Systematic chemical feldspar staining of thin section offcuts and polished slabs was therefore conducted at CODES, University of Tasmania, Australia, in order to estimate the modal abundances of K-feldspar and plagioclase and to aid in textural analysis. Each sample was etched with hydrofluoric acid and then half was brushed with barium chloride solution, followed by a treatment of potassium rhodizonate, which stains Ca-plagioclase red. The second half of the sample was treated with sodium cobaltinitrate, $Na_3Co(NO_2)_6$, which stains K-feldspar yellow. Pure Na-feldspar (An < 3) does not stain using either technique (Gabriel and Cox, 1929; Bailey and Stevens, 1960).

Fine-grained alteration minerals such as kaolinite, montmorillonite, illite-smectite, illite and muscovite are difficult to identify during drill core logging. In thin-section, talc and muscovite appear very similar and usually cannot be reliably distinguished based on optical characteristics alone. It is therefore useful to use short-wave infrared (SWIR) spectroscopy to aid in the identification of fine-grained minerals within clay- and mica-bearing assemblages. Chip samples from drill core were analyzed using a Terraspec ASD spectrometer at 5 m intervals to evaluate the fine-grained minerals at Wainaulo. For Waisoi East and Waisoi West, a roaming sample interval was used, preferably targeting bleached or light colored rock chips. A spectrum average of 100 s and a white reference of 200 s was used, except in the case of dark-colored samples that were analyzed for twice as long. Spectral mineral identification was done by manually analyzing each spectral signature rather than by using The Spectral Assistant (TSA™) software. Shifts in the Fe-OH absorption band (2240 – 2260 nm) and the Mg-OH absorption band (2320 – 2360 nm) can be used to identify Fe- and Mg-rich chlorite (Pontual et al., 1997; Jones et al., 2005). In this study, only the Fe-OH absorption band is used to identify chlorite composition, due to the Mg-OH absorption band being poorly defined in most samples. Fe-OH values < 2248 nm indicate Mg-rich chlorite, whereas values > 2252 nm indicate Fe-rich chlorite, and all values in between indicate Fe-Mg chlorite (2248 to 2252 nm). SWIR results are provided in Appendix F.

X-ray diffraction (XRD) traces were collected from 28 drill core samples from the study area

to compliment petrographic analysis. The sample powders were analyzed by Stafford McKnight at the University of Ballarat. Siemens D500 and D501 diffractometers were used with Fe-filtered CoKα X-rays at 36 kV and 30 mA; the diffractograms/XRD profiles were collected by step-scan with a starting angle of 5° 2θ, at conventional scan rates (1° or 2θ per minute), and ending at 76° 2θ. SiroQuant 3.0 software was used to identify and estimate the relative proportions of minerals in each sample. Smectite-bearing samples were air-dried and glycolated in order to better resolve clay contents. Quantitative XRD results are provided in Appendix B.

The alteration terminology used in this chapter is based on Titley (1982) and Gifkins et al. (2005). Definitions of terms used in this study to describe various alteration assemblages and mineralization features are listed in Table 5.1.

**Table 5.1:** Definitions of alteration and mineralization terminology used in this study; based on Titley (1982) and Gifkins et al. (2005)

| Term | Definition |
|---|---|
| Pervasive alteration | Alteration that affects all primary minerals; this type of alteration is typically strong or intense and is texturally destructive |
| Selective alteration | Alteration in which specific minerals in the host rock and/or porphyry intrusion have been altered; alteration of this type usually preserves or enhances primary rock textures |
| Domainal alteration | A type of selective alteration that refers to the alteration of patches, clots, or groups of clasts |
| Vein | A fracture ≥ 5 mm wide that is partially or totally infilled by hydrothermal precipitates |
| Veinlet | A fracture < 5 mm wide that is partially or totally infilled by hydrothermal precipitates |
| Cement | Minerals precipitated *in situ* from a fluid that bind together clast ± matrix components of a breccia, either as infill of void space or as replacement of clasts or matrix |
| Stringer | Wavy veinlets (≤ 5 mm), occurring in a discontinuous sub-parallel pattern that is partially or totally infilled by hydrothermal precipitates |
| Multi-stage vein | A vein that has undergone one or more stages of fracturing and infill by hydrothermal precipitates; examples of this style of vein include centerline veins and breccia veins in which fragments of early vein material are cemented by later stages of hydrothermal infill |
| Centerline vein | A multi-stage vein in which fracturing and hydrothermal mineral infill occurs along a line of symmetry through the center of the vein; typical of reactivated, symmetrical comb quartz veins that become infilled with sulfide minerals |
| Vein halo | Alteration (pervasive or selective) that occurs in the wall rock immediately adjacent to a vein or veinlet |
| Ghosted | Primary phenocrysts that are rimmed by alteration minerals causing them to blend in with the surrounding groundmass |
| Weak alteration | Alteration in which most crystal edges are visible; crystal cores are typically replaced; this degree of alteration intensity does not modify primary rock textures |
| Moderate alteration | Alteration in which most crystal edges are visible and some crystal margins are ghosted; crystal cores are commonly replaced; this degree of alteration intensity partially obscures primary rock textures |
| Strong alteration | Alteration in which most crystal edges are ghosted; all primary minerals are almost completely replaced; this degree of alteration intensity partially obscures primary rock textures |
| Intense alteration | Alteration in which all primary minerals have been completely recrystallized or replaced by secondary minerals; this degree of alteration intensity obliterates primary rock textures |

*5.2.2 Previous work*

Several studies have documented various aspects of Namosi district alteration and mineralization, most notably: two MSc theses (Ellis, 1996; Egashira, 2009), one paper published in the Journal of Geochemical Exploration (Leggo, 1977) and one in Resource Geology (Tanaka et al., 2010), and several internal unpublished reports to Newcrest Mining Limited. Comprehensive studies of the Emperor and Tuvatu alkalic Au deposits located 60 km northwest of the Namosi district, are available for comparative purposes (e.g., Ahmed et al., 1987; Begg, 1996; Pals et al., 2003; Scherbarth and Spry, 2006; Spry and Scherbarth, 2006). The most comprehensive study on alteration and mineralization came from Ellis (1996), who documented hydrothermal and mineralization characteristics of the Waisoi Cu-Au(-Mo) deposits (Table 5.2). He defined eight stages of alteration and veining at Waisoi East and Waisoi West, of which six were related to composite quartz-diorite and dacite porphyry stocks. Ellis (1996) used a mixture of genetic-based terminology and assemblage names to categorize hydrothermal alteration assemblages observed at the Waisoi deposits. Early, pervasive albite and albite – biotite – chlorite – actinolite alteration were interpreted to pre-date the emplacement of the Waisoi mineralized intrusions. These alteration mineral assemblages were interpreted to be related to regional burial metamorphism. Early porphyry-related alteration and mineralization consisted of weak to strong, pervasive sericite – quartz – pyrite ('sericitization') and weak to intense, pervasive quartz – chlorite ± K-feldspar ('silicification') assemblages. The core of the deposits preserved main-stage, weak to strong, pervasive, disseminated and vein-style quartz – biotite – magnetite ± K-feldspar ('potassic') alteration. On the periphery of the deposits, the sericitic and silicic assemblages were overprinted by vein-style and vein-halo quartz – chlorite – sericite ('propylitic') alteration. Finally, late-stage vein-style and vein-halo calcite – quartz – chlorite alteration were interpreted to have overprinted all earlier stages of alteration and veins. No attempt at resolving spatial zonation of alteration mineral assemblages was carried out by Ellis (1996). A zonation of sulfides was identified, comprising a core of bornite, that grades outwards through a chalcopyrite-dominant zone to a peripheral pyrite-dominant zone. Leggo (1977), Egashira (2009), and Tanaka et al. (2010) only provided cursory discussions and descriptions of alteration and mineralization in the Namosi district.

**Table 5.2:** Hydrothermal alteration and mineralization characteristics of the Waisoi deposits, from Ellis (1996)

| Alteration stage | Gangue minerals | Sulfide minerals | Alteration style and intensity | Distribution and characteristics | Relationship to mineralization |
|---|---|---|---|---|---|
| Albitization | Albite, quartz | | Weak to intense, pervasive alteration; vein-style | Exclusive to Wainimala basement rocks; plagioclase is either completely replaced by albite or is rimmed by albite; fine-grained quartz – albite veinlets are rare | Pre-mineralization |
| Regional burial metamorphism | Albite, biotite, chlorite, actinolite, quartz, epidote, magnetite | py | Weak to strong, pervasive alteration; disseminated and vein-style | Occurs in Wainimala basement rocks and clasts within the basal Namosi Andesite Formation rocks; magnetite and pyrite are disseminated throughout groundmass; veinlets of chlorite – actinolite ± biotite are common | Pre-mineralization |
| Sericitization | Sericite, quartz | py | Weak to strong, patchy and pervasive; disseminated, vein-style and vein halo | Earliest alteration found in Namosi Andesite Formation; overprints metamorphism in Wainimala basement; abundant disseminated pyrite; veinlets of quartz – sericite ± pyrite with < 40 cm vein halos of sericite – quartz | Early-stage mineralization |
| Silicification | Quartz, chlorite, K-feldspar, magnetite | py, ccp | Weak to intense, patchy and pervasive; vein-style and vein halo | Occurs in quartz diorite stocks as abundant quartz – K-feldspar ± sericite stockwork veins (up to 90%); elsewhere, it occurs as intense, pervasive quartz – chlorite ± magnetite vein halos surrounding quartz ± chlorite ± pyrite ± chalcopyrite veins and veinlets; locally occurs as intense, pervasive patches of quartz alteration within the Wainimala basement and as diffuse zones of weak quartz – chlorite alteration within the Namosi Andesite Formation | Early-stage mineralization |
| Potassic | Quartz, biotite, magnetite, K-feldspar, chlorite, clay, sericite | bn, ccp, py, cc, cv, dg, cbn | Weak to strong, pervasive; disseminated; vein-style and vein halo | All rock types; common veinlets of quartz – biotite – bornite – magnetite with pervasive, zoned quartz – biotite, K-feldspar – chlorite and sericite – clay vein halos; disseminations of fine-grained chalcopyrite – magnetite ± pyrite; local zones of weak quartz – chlorite – K-feldspar ± hematite alteration | Main-stage mineralization |
| Propylitic | Quartz, chlorite, sericite | ccp, py | Vein-style and pervasive vein halo | Occurs in Wainimala basement and Namosi Andesite Formation; common quartz – chlorite ± chalcopyrite ± pyrite veins and veinlets surrounded by <20 cm vein halos of chlorite – sericite | Main-stage mineralization |
| Early carbonate | Calcite, quartz, chlorite | ccp, py | Vein-style and vein halo | Quartz – calcite ± chalcopyrite ± pyrite veins with calcite – quartz vein halo alteration | Late-stage mineralization |
| Late carbonate | Calcite, quartz, chlorite, epidote, analcime | py | Vein-style and vein halo | Calcite ± quartz ± pyrite ± analcime veins and veinlets with pervasive calcite ± chlorite ± epidote ± quartz vein halo alteration | Late-stage mineralization |

Abbreviations: bn = bornite, cbn = cubanite, cc = chalcocite, ccp = chalcopyrite, cv = covellite, dg = digenite, py = pyrite.

### 5.2.3 Wainaulo Cu-Au porphyry deposit

The Wainaulo Cu-Au porphyry deposit is centered on a sub-vertical, east-northeast-striking porphyry dike complex that is parallel to major, district-scale, faults and shears of the WWW Fault Zone that trend ~ 80° (Figs 2.4 and 5.1A). The Cu orebody, defined by the 1.0 wt % Cu gradeshell, has a narrow and elongate, dike-like geometry (100 x 300 m; open at depth) and is tilted steeply to the north (Fig. 5.1A). The top of the orebody occurs about 250 m below the present-day surface. The high-grade ore is associated with quartz – sulfide and epidote – sulfide

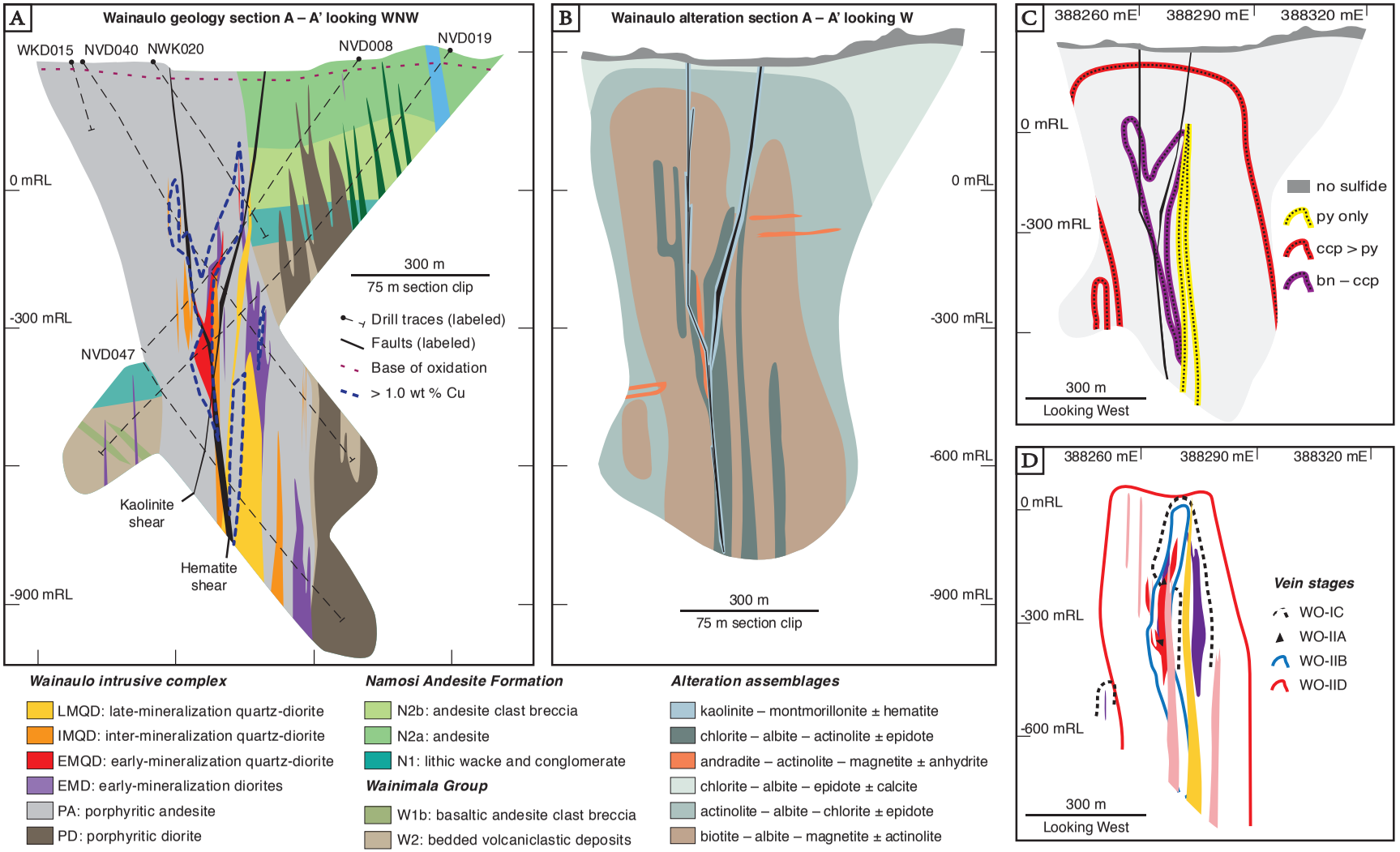


**Figure 5.1:** Section NVD019, Wainaulo **A.** Interpreted geology of section NVD019, with distribution of copper mineralization. Refer to Figure 3.3 for section location. **B.** Distribution of selected alteration assemblages observed on section NVD019. **C.** Sulfide zonation of section NVD019. **D.** Spatial distribution of selected vein stages relative to the Wainaulo Intrusive Complex. Stage WO-IC monomineralic magnetite stringers and veins appear to have a spatial association with EMD intrusions. Stage WO-IIA unidirectional solidification textures are restricted to the inside margin of EMQD intrusions. Stage WO-IIC laminated quartz – magnetite – bornite veins occur in a narrow zone within and just outboard of the EMQD intrusions and are not observed in any of the later intrusions (inter- and late-mineralization quartz-diorites). Stage WO-IIC roughly corresponds with the > 1 % Cu gradeshell. Stage WO-IIE epidote – sulfide – anhydrite veins have a broad distribution surrounding the Wainaulo Intrusive Complex. Paragenetic stages are summarized in Tables 5.3 and 5.4 and Fig. 5.2. Abbreviations: bn = bornite, ccp = chalcopyrite, py = pyrite.

vein stockworks concentrated within and proximal to porphyritic intrusions. The mineralizing intrusive complex was emplaced almost entirely within a pre-mineralization hornblende-feldspar-phyric andesite stock (PA) that had intruded the mixed-provenance sedimentary and primary volcanic facies associations of the Namosi Andesite Formation (Fig 5.1A).

Twelve hydrothermal alteration mineral assemblages (Table 5.3) and fourteen vein types (Table 5.4) have been identified at Wainaulo during this study. A relative paragenesis has been constructed based on crosscutting and overprinting relationships observed during detailed graphic drill core logging and petrographic analysis (Fig. 5.2).

There are five intrusive phases at Wainaulo that are intimately associated with hydrothermal alteration and mineralization. The two early-stage mineralized diorites (EMD1 and EMD2) are the earliest phases and host all vein stages found at Wainaulo. These porphyry phases are spatially associated with biotite – albite – magnetite ± actinolite alteration and early, disseminated and vein-style copper mineralization (chalcopyrite). They host medium copper grades and low gold grades (~ 0.61 wt % Cu, ~ 0.03 g/t Au; values are averaged over intervals intersected in NVD019 using NJV assay data). Early-, inter- and late-mineralization diorite porphyries (EMQD, IMQD, and LMQD) evolved from high to low copper and gold grades (~ 2.86 wt % Cu, ~ 0.74 g/t Au; ~ 0.58 wt % Cu, ~ 0.11 g/t Au; ~ 0.05 wt % Cu, < 0.01 g/t Au). This is attributed to a decreasing volume of quartz and epidote veins and a change from bornite- to chalcopyrite- to pyrite-dominant sulfide assemblages within the EMQD, IMQD and LMQD, respectively (Fig. 5.3).

*5.2.3.1 Sulfide zonation*

Sulfide zonation at Wainaulo exhibits a similar pattern to other SW Pacific porphyry deposits, e.g., Golpu, Papua New Guinea (Rinne, 2015), Batu Hijau, Indonesia (Arif and Baker, 2004), and Ridgeway, Australia (Wilson et al., 2003), with an inner core of chalcopyrite – bornite progressing outward to chalcopyrite – pyrite and an outer shell of pyrite. Deep drilling (> 1000 m) has established a vertical continuity of mineralization (Fig. 5.1C). The chalcopyrite – bornite-rich core is associated with sheeted, laminated quartz – magnetite – sulfide veins (WO-IIC) and related chlo-

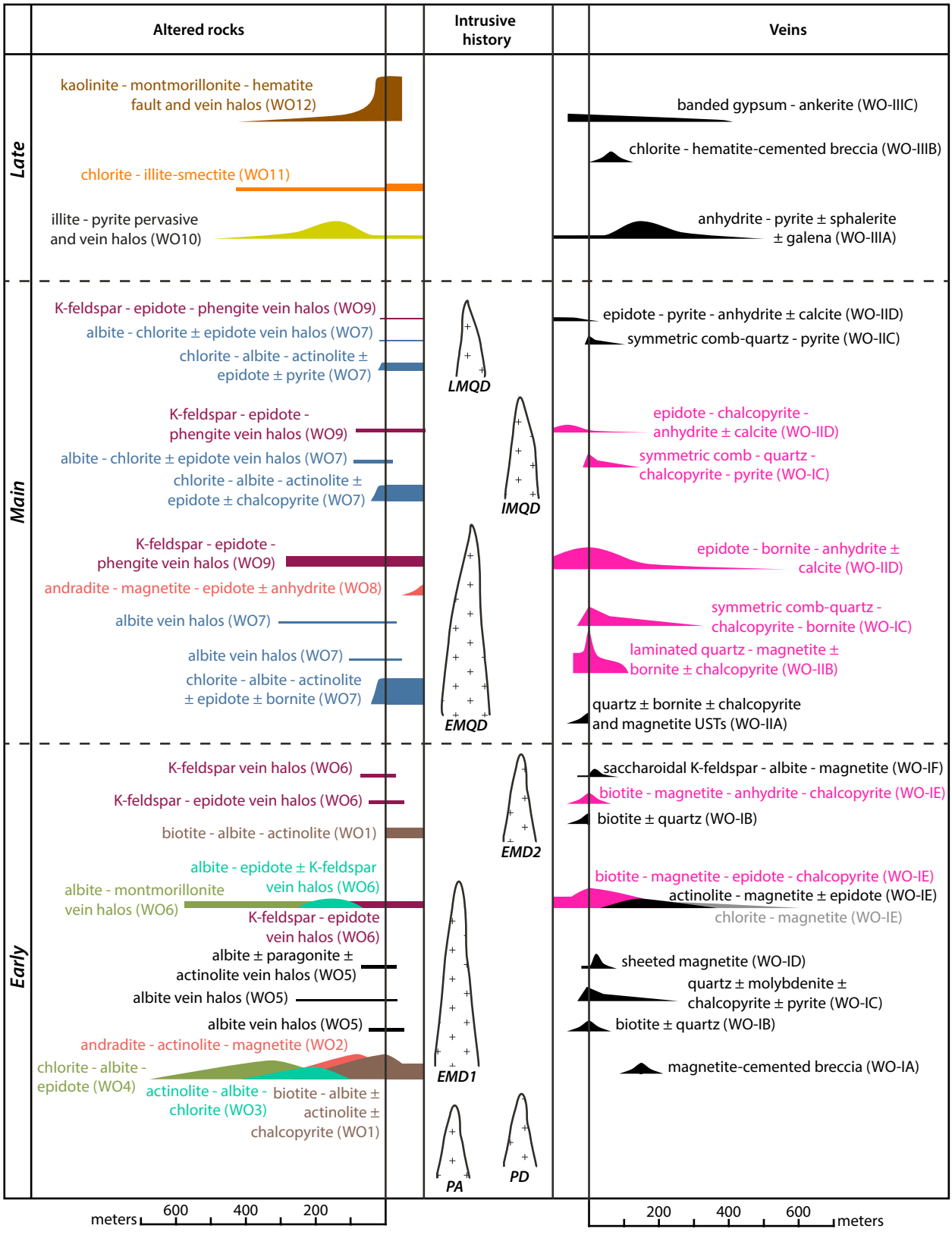


**Figure 5.2:** Schematic space-time plot showing the alteration and vein paragenesis at Wainaulo. The diagram depicts the oldest events at the bottom of the figure and the youngest at the top. The lateral extent of each colored bar indicates the distribution of the vein or alteration type observed in drill core relative to the related intrusive margin. The vertical bars directly adjacent to the intrusive history column indicate distribution within the porphyry intrusion. The characters within parentheses following the mineralogical components in the veins and alteration columns are the associated stages as described in Tables 5.3 and 5.4. Abbreviations: PA = porphyritic andesite, PD = porphyritic diorite, EMD1 = early-mineralization diorite 1, EMD2 = early-mineralization diorite 2, EMQD = early-mineralization quartz-diorite, IMQD = inter-mineralization quartz-diorite, LMQD = late-mineralization quartz-diorite.

**Table 5.3**: Styles and spatial and temporal distribution of alteration assemblages at Wainaulo

| Stage | Gangue minerals | Sulfide minerals | Alteration texture and intensity | Spatial and temporal distribution | Related veins |
|---|---|---|---|---|---|
| WO1 | Biotite, albite, magnetite, actinolite, muscovite, rutile | ccp, bn | Intense, pervasive alteration presented as fine-grained decussate biotite - muscovite and granoblastic quartz-albite surrounded by strong, selective biotite - magnetite ± actinolite alteration of ferromagnesian minerals and albite alteration of plagioclase | Intense alteration is well developed up to 5 m from EMD1 intrusion within the PA and NAF wall rocks; grades outward to selective alteration up to 150 m from EMD1 contact; occurs within EMD2; does not occur in EMQD, IMQD or LMQD | |
| WO2 | Andradite, actinolite, magnetite, anhydrite, calcite, chlorite | ccp, py | Strong to intense, pervasive, fine-grained andradite (partially altered to epidote - chlorite) intergrown with magnetite and actinolite | Hosted by reactive calcareous beds within NAF; proximal to EMD1; sub-horizontal (bedding-parallel) morphology | |
| WO3 | Actinolite, albite, chlorite, magnetite, rutile, epidote, titanite | ccp, py, bn | Weak to moderate intensity, selective alteration of ferromagnesian minerals to actinolite ± chlorite and primary feldspar to albite | Occurs as a halo surrounding WO1 alteration; temporally related to EMD1 intrusion with alteration up to 400 m from its contact; does not occur in EMQD, IMQD or LMQD | WO-IA |
| WO4 | Chlorite, albite, epidote, calcite, montmorillonite | py | Weak to moderate intensity, selective alteration of mafic minerals to chlorite ± epidote; plagioclase phenocrysts are selectively altered to epidote - albite or are stable; clast-selective epidote alteration with albite - chlorite halos | Occurs as a shell around the WO3 alteration domain; related to the EMD1 intrusion; does not occur in EMQD, IMQD or LMQD | |
| WO5 | Albite, actinolite, paragonite | | Strong intensity, pervasive albite ± actinolite ± paragonite vein-halo alteration | Surrounds early-stage veins and veinlets; overprints stage WO1 and WO2 alteration; overprinted by stage WO6 vein-halo alteration and is crosscut by stage WO-IE and WO-IF veins | WO-IB<br>WO-IC<br>WO-ID |
| WO6 | K-feldspar, epidote, actinolite, albite | | Moderate to strong intensity, selective to pervasive K-feldspar - epidote ± actinolite or albite vein-halo alteration | Surrounds early-stage veins; overprints stage WO1 to WO5 alteration; does not occur in EMQD, IMQD or LMQD | WO-IE<br>WO-IF |
| WO7 | Chlorite, albite, quartz, actinolite, epidote | bn, ccp | Moderate to strong intensity, selective alteration of ferromagnesian minerals to chlorite - actinolite; primary plagioclase are selectively altered to albite ± epidote | Occurs within and up to 15 m away from EMQD, IMQD and LMQD intrusions | WO-IIB<br>WO-IIC |
| WO8 | Andradite, epidote, magnetite, calcite | ccp | Intense, pervasive alteration presented as fine-grained andradite intergrown with epidote and magnetite | Structurally controlled; occurs within the EMQD intrusion adjacent to a major structural zone | |
| WO9 | K-feldspar, epidote, phengite, calcite, anhydrite | bn, ccp, py | Moderate intensity, selective vein- and alteration-clot-halos; plagioclase are selectively altered to K-feldspar - epidote - phengite ± calcite | Overprints all Wainaulo intrusions; best developed within and adjacent to EMQD intrusions | WO-IID |
| W10 | Illite, chlorite, quartz, anhydrite | py, sp | Occurs as moderate intensity, pervasive pyrite - illite - chlorite alteration and as texturally-destructive selective vein-halo alteration | Overprints WO-IA at the transition from WO3 to WO4; broad distribution as vein halos | WO-IIIA |
| W11 | Chlorite, illite, illite-smectite | | Weak, selective chlorite - illite-smectite alteration of ferromagnesian minerals and illite-smectite alteration of primary plagioclase; weak to strong, pervasive chlorite - illite-smectite alteration of PA, imparting a dark green color | Best developed overprinting intrusions at Wainaulo; broad, upwardly-flaring distribution | |
| W12 | Kaolinite, montmorillonite, hematite, ankerite, gypsum | | Intense, pervasive, texturally destructive bleaching of wall rock adjacent to and within steeply dipping fault zones; pervasive vein-halo alteration surrounding WO-IIIC veins | Structurally controlled; overprints all alteration styles and the EMQD and IMQD intrusions within the core of the deposit; occurs as vein-halo alteration throughout the deposit | WO-IIIC |

Abbreviations: bn = bornite, ccp = chalcopyrite, EMD1 = early-mineralization diorite 1, EMD2 = early-mineralization diorite 2, EMQD = early-mineralization quartz-diorite, IMQD = inter-mineralization quartz-diorite, LMQD = late-mineralization quartz-diorite, gn = galena, NAF = Namosi Andesite Formation, PA = porphyritic andesite, py = pyrite, sp = sphalerite.

**Table 5.4:** Vein stages of the Wainaulo deposit

| Vein Stage | Gangue minerals | Sulfide minerals | Form, styles and textures | Spatial and temporal distribution and associated intrusions | Envelope |
|---|---|---|---|---|---|
| WO-IA | Magnetite | | Monomict and locally polymict; poorly sorted; grades from clast-rotated to chaotic; granule to cobble clasts within a fine-grained magnetite cement; planar, parallel fabric defined by alignment of tabular and splintery clasts; pseudo-rounding of clasts | Irregular to tabular morphology; pinches out to form magnetite veins; steeply inclined; tens of meters across; occurs in NVD019 from 420 – 440 m; no observed association with intrusions | None |
| WO-IB | Quartz | mo, py | Discontinuous to continuous; wavy to straight-walled; sheeted or discrete; euhedral medium-grained quartz, locally intergrown with molybdenite; veinlets and veins | Occurs along the margins and within 250 m of EMD1 intrusion; crosscut by stage WO-IC and WO-IE | ab - act (WO5); φ < 4 mm |
| WO-IC | Magnetite | | Discontinuous; locally sheeted; irregular and diffuse wall rock contacts; monomineralic stringers, veinlets and chains | Abundant in PA stock within 70 m of contact with EMD1 | ab (WO5); φ < 2 mm |
| WO-ID | Biotite, quartz | | Two styles: veins and miarolitic cavities; veins are thin (< 5 mm), discontinuous and irregular with biotite ± quartz infill; miarolitic cavities consist of euhedral biotite and quartz in cavities < 20 mm wide | Veins occur within EMD1 and EMD2 intrusions and up to 50 m from their margins; miarolitic cavities only occur in EMD2 | ab (WO5); φ < 5 mm |
| WO-IE | Actinolite, magnetite, epidote, biotite, anhydrite, chlorite | ccp, py, bn | Continuous to discontinuous, with diffuse walls and irregular shapes; locally wispy with non-parallel vein walls; can occur as fibrous bands | Abundant in EMD1, EMD2, PA, pyroxene-feldspar-phyric dikes and hyaloclastite sequence; does not occur in EMQD, IMQD or LMQD | kfs - ep ± act or ab (WO6); φ < 10 mm |
| WO-IF | K-feldspar, quartz, albite, magnetite | ccp, bn | Saccharoidal-textured, fine-grained vein; discontinuous; cream to pink color; wavy and irregular morphology | Occurs within EMD2 and PA up to 20 m from contact with EMD2 | kfs (WO6); φ < 2 mm |
| WO-IIA | Quartz or magnetite | bn, ccp | Quartz or magnetite layers with interstitial bornite; euhedral coarse quartz crystals terminate perpendicular to layering | Only occurs at the margins and top of the EMQD | None |
| WO-IIB | Quartz, magnetite | bn, ccp | Continuous, sharp vein walls; magnetite ± bornite laminations parallel to vein walls | Well developed in apical portions and margins of the EMQD and adjacent PA wall rock < 30 m from the contact | ab (WO5); φ < 2 mm |
| WO-IIC | Quartz | bn, ccp, py, mo | Continuous and sharp-edged; comb-quartz with centerline; comb-quartz crystals radiating inward from vein margins; bornite ± chalcopyrite or pyrite ± chalcopyrite mineralization exploits fractures within quartz and is commonly found in central seam of comb-quartz veins | Well developed within EMQD and surrounding PA wall rock; sequentially less developed in IMQD and LMQD | ab (WO5); φ < 2 mm |
| WO-IID | Epidote, calcite anhydrite, magnetite | bn, ccp, py | Continuous to discontinuous, wavy, diffuse wall-rock contacts; commonly exploits fractures within all previous quartz veins; can have > 80 % bn; coarse-grained epidote forms sprays locally | Spatially associated with EMQD, IMQD and LMQD; extends up to 100 m from WIC | kfs - ep (WO7); φ < 10 mm |
| WO-IIIA | Anhydrite, chlorite, calcite | py, sp, gn, ccp | Continuous, straight-walled, planar anhydrite veins; pyrite, sphalerite and galena aggregates occur locally; pyrite commonly occupies central seam within the vein | Broadly distributed and overprints all intrusions | ill - py (WO8); φ < 10 mm |
| WO-IIIB | Chlorite, hematite, calcite, epidote | py, ccp | Occurs as straight-sided veinlets and cement within < 20 cm-wide breccia zones; breccia zones consist of tabular chlorite-hematite-altered clasts with a clast-rotated internal organization | Occurs in the upper portions of the Wainaulo deposit; contains PA clasts | None |
| WO-IIIC | Gypsum, ankerite, montmorillonite | py | Continuous, straight-walled, planar veins and fracture coatings (< 3 mm to > 20 cm vein-aperture); sharp contacts | Occurs in all rock types; most common peripheral to Hematite and Kaolinite shears | kln - mnt (WO10); φ < 5 cm |

Abbreviations: φ = vein-halo width, ab = albite, act = actinolite, bn = bornite, ccp = chalcopyrite, EMD1 = early-mineralization diorite 1, EMD2 = early-mineralization diorite 2, EMQD = early-mineralization quartz-diorite, ep = epidote, gn = galena, ill = illite, IMQD = inter-mineralization quartz-diorite, kfs = K-feldspar, kln = kaolinite, LMQD = late-mineralization quartz-diorite, mag = magnetite, mnt = montmorillonite, mo = molybdenite, PA = porphyritic andesite, py = pyrite, qtz = quartz, sp = sphalerite, WIC = Wainaulo intrusive complex.

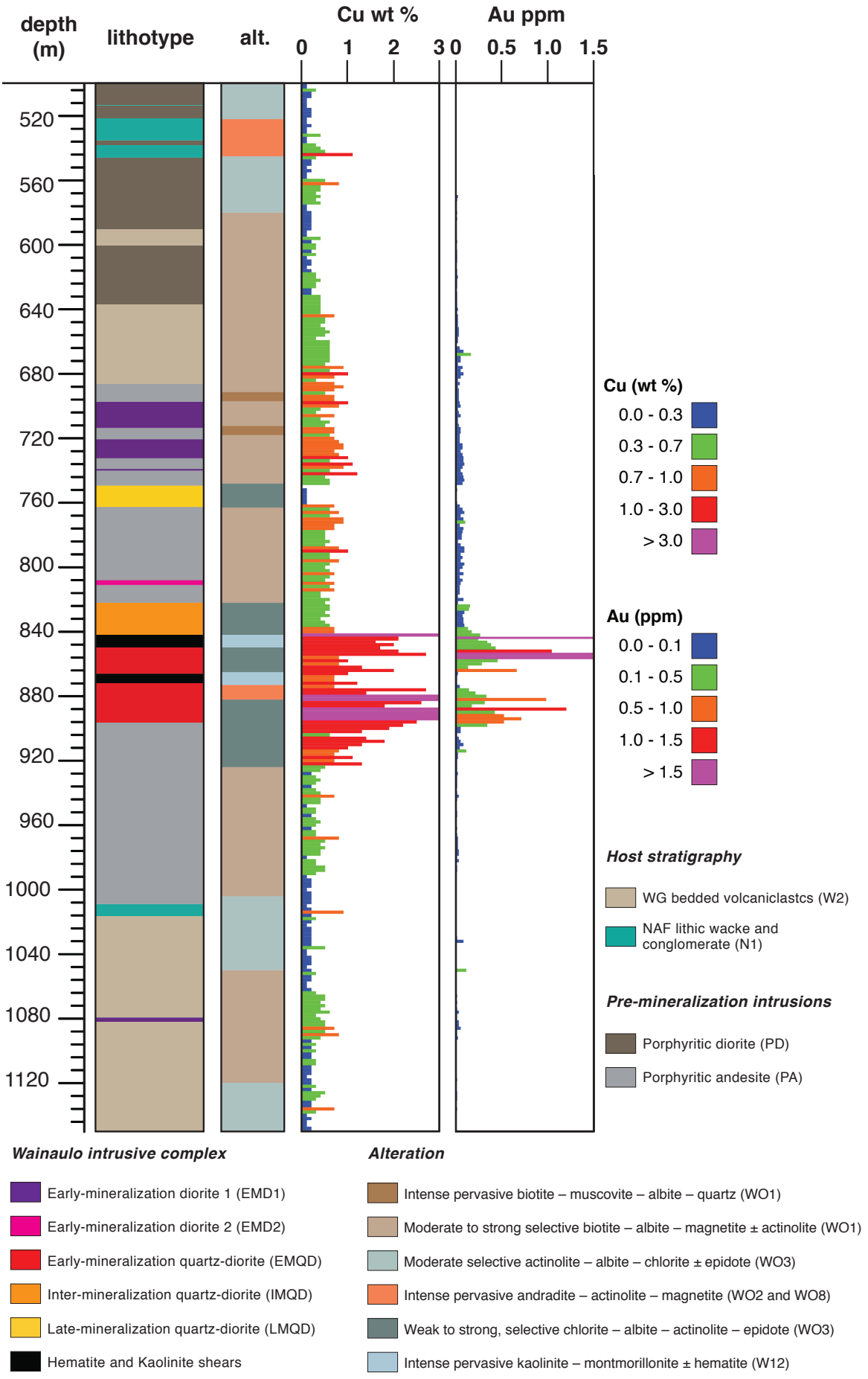
depth (m)
lithotype
alt.
Cu wt %
0
1
2
3
Au ppm
0
0.5
1.0
1.5
520
560
600
640
680
720
760
800
840
880
920
960
1000
1040
1080
1120
Cu (wt %)
0.0 - 0.3
0.3 - 0.7
0.7 - 1.0
1.0 - 3.0
> 3.0
Au (ppm)
0.0 - 0.1
0.1 - 0.5
0.5 - 1.0
1.0 - 1.5
> 1.5
Host stratigraphy
WG bedded volcaniclastcs (W2)
NAF lithic wacke and conglomerate (N1)
Pre-mineralization intrusions
Porphyritic diorite (PD)
Porphyritic andesite (PA)
Wainaulo intrusive complex
Early-mineralization diorite 1 (EMD1)
Early-mineralization diorite 2 (EMD2)
Early-mineralization quartz-diorite (EMQD)
Inter-mineralization quartz-diorite (IMQD)
Late-mineralization quartz-diorite (LMQD)
Hematite and Kaolinite shears
Alteration
Intense pervasive biotite – muscovite – albite – quartz (WO1)
Moderate to strong selective biotite – albite – magnetite ± actinolite (WO1)
Moderate selective actinolite – albite – chlorite ± epidote (WO3)
Intense pervasive andradite – actinolite – magnetite (WO2 and WO8)
Weak to strong, selective chlorite – albite – actinolite – epidote (WO3)
Intense pervasive kaolinite – montmorillonite ± hematite (W12)

**Figure 5.3 (previous page):** Partial summary log of NVD019, showing lithotype, alteration, copper and gold grades. High copper and gold grades coincide with chlorite – albite – actinolite – epidote alteration (WO3) in the EMQD intrusion and adjacent PA host rock. Copper grades decrease gradually over 30 meters away from the EMQD and PA contact. Gold grades decrease substantially outside of the EMQD intrusion. Moderate copper and low gold grades are coincident with the EMD1 and EMD2 intrusions. Copper grades gradually decline from 50 to 100 m away from the EMD1 contact within the PA host rock. Moderate copper grades coincide with the andradite – actinolite – magnetite alteration (WO2) at ~ 540 m. The Hematite and Kaolinite shears and associated kaolinite – montmorillonite alteration (W12) had a negative effect on copper and especially gold grades. The intrusion of LMQD also had a negative effect on copper and gold grades. LMQD is almost barren.

rite – albite – actinolite alteration (WO7) as well as epidote – sulfide – anhydrite veins (WO-IIE) and related K-feldspar – epidote – phengite vein-halo alteration (WO9). The bornite distribution is roughly coincident with the > 1 wt % Cu grade shell (Figs. 5.1A and C). The surrounding chalcopyrite – pyrite-dominant zone spans the biotite-bearing alteration domain (WO1) and extends just beyond the > 0.3 wt % Cu grade shell (Fig. 5.1A and C). An annular pyrite domain emulates the outer chlorite – albite – epidote alteration (WO4) distribution. Within the core of the deposit, a pyrite-rich zone corresponds with the late-mineralization quartz-diorite (Figs. 5.1A and C).

#### *5.2.3.2 Early-stage mineralization, alteration and veins (WO-I)*

Early-stage mineralization at Wainaulo is concentrically distributed around the EMD1 and EMD2 intrusions (Figs. 5.1, 5.2 and 5.3). The early alteration assemblages are characterized by abundant Na-rich plagioclase (ranging from pure albite to oligoclase); referred to collectively hereafter as albite. Six generations of veins and breccias are interpreted to have formed during the early-mineralization stage. These vein types are best developed within and/or proximal to EMD1 and EMD2 and do not occur in later intrusive phases (EMQD, IMQD and LMQD). Vein and vein-halo mineralogy changes with distance from the source intrusion.

*Biotite – albite – magnetite ± actinolite ± muscovite alteration (WO1)*

Texturally destructive, intense, pervasive alteration comprising fine-grained intergrowths of secondary decussate biotite ± muscovite with granoblastic quartz – albite (Table 5.3; Figs. 5.4A and B) and disseminated chalcopyrite extends up to 5 m from the EMD1 margin (Figs. 5.3 and 5.4). Biotite and quartz alteration produced a conspicuous, indurated, black wash that has obliterated primary textures in the PA host rock (Figs. 5.4A and B). The intense biotite alteration transitions outwards to moderate to strong, selective biotite – albite alteration that extends up to 150 m

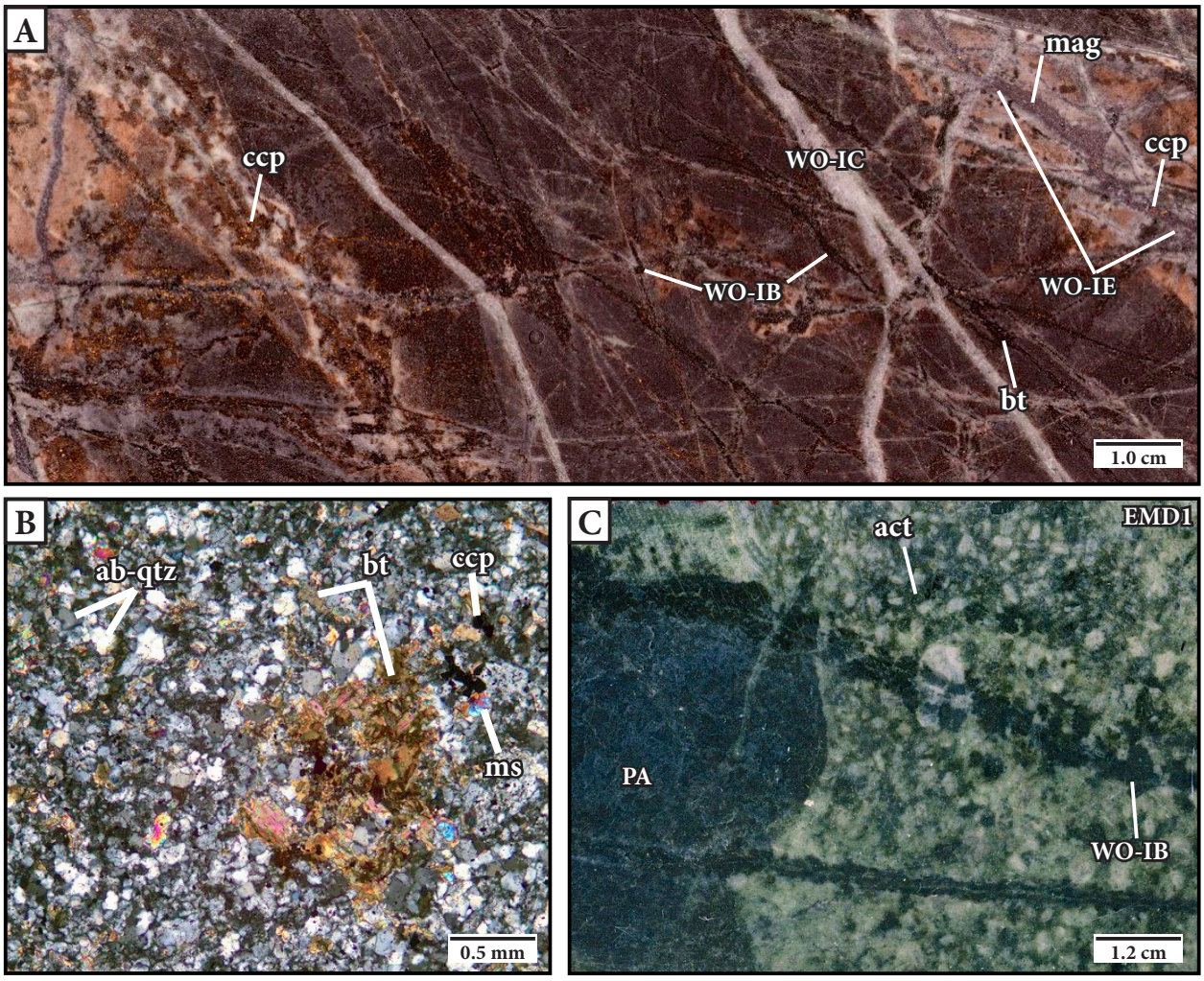


**Figure 5.4:** Examples of fine-grained biotite – muscovite – quartz – albite (WO1) alteration. **A.** Intense, pervasive biotite-altered PA wall rock within two meters of its contact with EMD1. The sample has been crosscut by stage WO-IB biotite veins that have been crosscut by stage WO-IC quartz veins. The quartz veins have been crosscut by stage WO-IE magnetite – chalcopyrite veins and spots with grayish-white and pink albite alteration halos. Sample: NVD019 717 m. **B.** Cross-polarized photomicrograph illustrating granoblastic quartz – albite and decussate biotite – muscovite textures. Sample NVD019 717 m. **C.** Contact of EMD1 with strongly biotite – muscovite – quartz – albite-altered PA. Sample: NVD019 697 m. Abbreviations: ab = albite, bt = biotite, ccp = chalcopyrite, EMD1 = early-mineralization diorite 1, ms = muscovite, PA = porphyritic andesite, qtz = quartz.

laterally from the porphyry margin, and from 100 m below the present-day surface to > 1000 m depth (Fig 5.1B). Magmatic ferromagnesian minerals (most likely hornblende) have been altered to fine-grained, shreddy, secondary biotite with magnetite ± actinolite ± chalcopyrite ± rutile (Figs. 5.5B and C), whereas magmatic plagioclase crystals are either stable or altered to secondary albite ± calcite ± biotite. Locally, within the core of the alteration zone, biotite – actinolite – magnetite clots (lenses and pods) are rimmed by pervasive albite alteration (Fig. 5.5A). These clots may have nucleated on the margins of primary hornblende phenocrysts. Distal to EMD1, domainal biotite – albite – muscovite – actinolite alteration has produced irregular patches with diffuse margins, including sprays and fibrous mats of actinolite (Figs. 5.5D and F). The biotite – al-

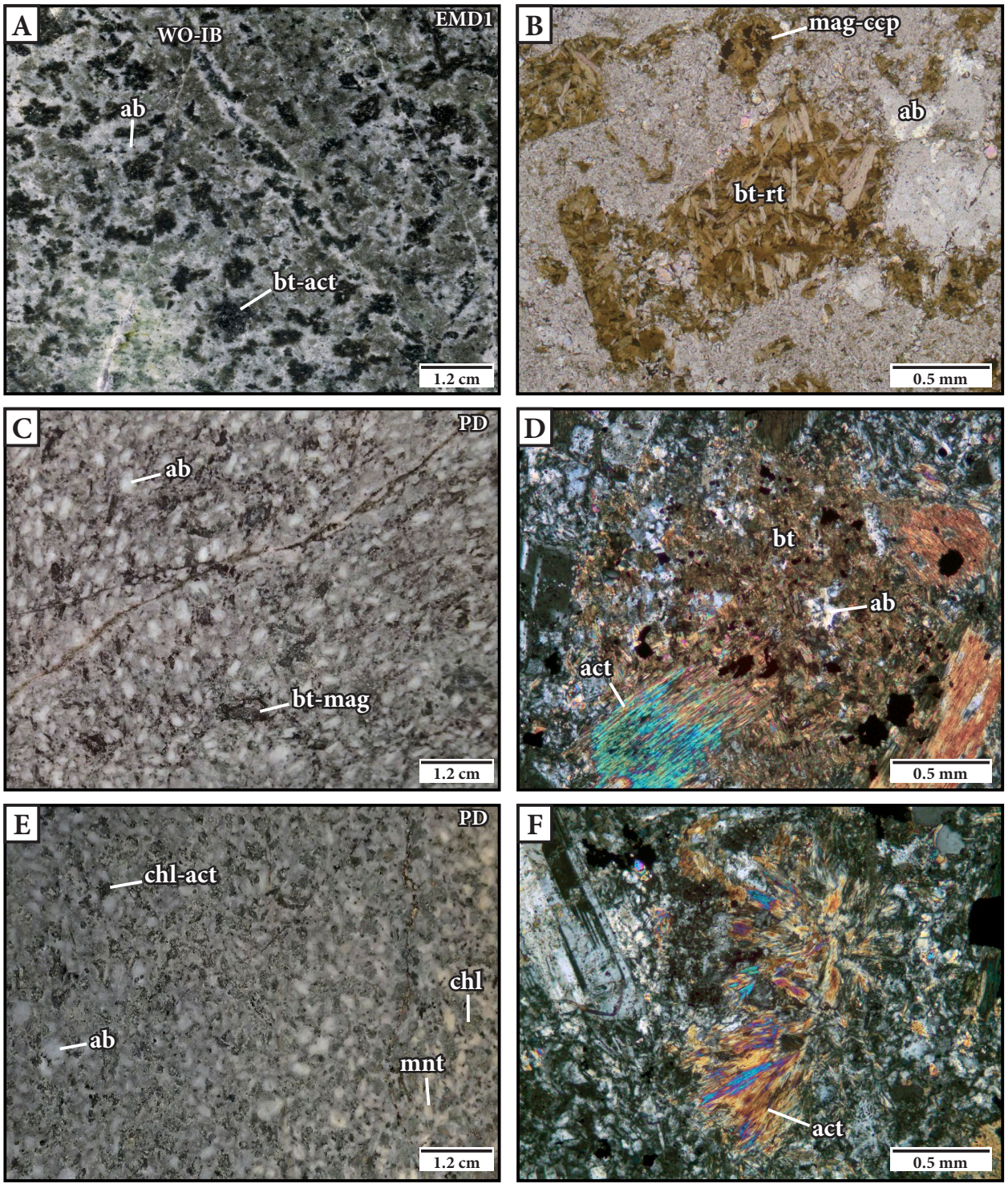


**Figure 5.5:** Examples of biotite – albite (WO1) and actinolite – albite (WO3) alteration. **A.** Clots of biotite – actinolite alteration rimmed by secondary, white albite within EMD1. Sample: NVD019 700 m. **B.** Plane-polarized photomicrograph of porphyritic andesite, illustrating primary hornblende that has been completely replaced by shreddy biotite, fine-grained rutile, magnetite and chalcopyrite. Sample NVD019 640 m. **C.** Selective biotite – magnetite alteration of hornblende, and albite alteration of plagioclase within PD. Sample: NVD019 582 m. **D.** Cross-polarized photomicrograph illustrating an irregular patch of biotite – albite – actinolite alteration including a fibrous mat of secondary actinolite within PD. Sample: NVD019 627 m. **E.** Selective chlorite – actinolite alteration of magmatic hornblende and albite alteration of primary plagioclase within PD 3 meters from the sample in Fig. 5.5C, illustrating the sharp transition between biotite- and actinolite-dominant alteration assemblages. The sample has been overprinted by selective cream and beige montmorillonite alteration of albite-altered plagioclase and chlorite – chalcopyrite alteration of actinolite-altered ferromagnesian minerals (right hand side). Sample: NVD019 579 m. **F.** Cross-polarized photomicrograph of a sub-radiating prism of actinolite within the biotite – albite alteration domain within PD. Sample NVD019 627 m. Abbreviations: ab = albite, act = actinolite, bt = biotite, ccp = chalcopyrite, chl = chlorite, EMD1 = early-mineralization diorite 1, mag = magnetite, mnt = montmorillonite, ms = muscovite, PD = porphyritic diorite, qtz = quartz, rt = rutile.

bite alteration has overprinted both EMD1 and EMD2 but has been truncated by EMQD, IMQD and LMQD intrusions and therefore is interpreted to pre-date main-stage mineralization (Figs. 5.2 and 5.3).

*Andradite – actinolite – magnetite – anhydrite alteration (WO2)*

A prograde calc-silicate alteration assemblage has locally replaced permeable, reactive carbonate-bearing beds within the calcareous sandstone (N1a) and polymict conglomerate (N1b) of the Namosi Andesite Formation (Table 5.3). Calc-silicate alteration minerals (and magnetite) are noted < 150 m from the interpreted source intrusion (EMD1). This alteration style presents as strong to intense, pervasive andradite – magnetite – actinolite – anhydrite ± chalcopyrite alteration of narrow, (meter-wide) calcareous horizons. Fine-grained, reddish-brown andradite occurs in patchy, irregular domains and is intergrown with pale to dark green actinolite and blueish-

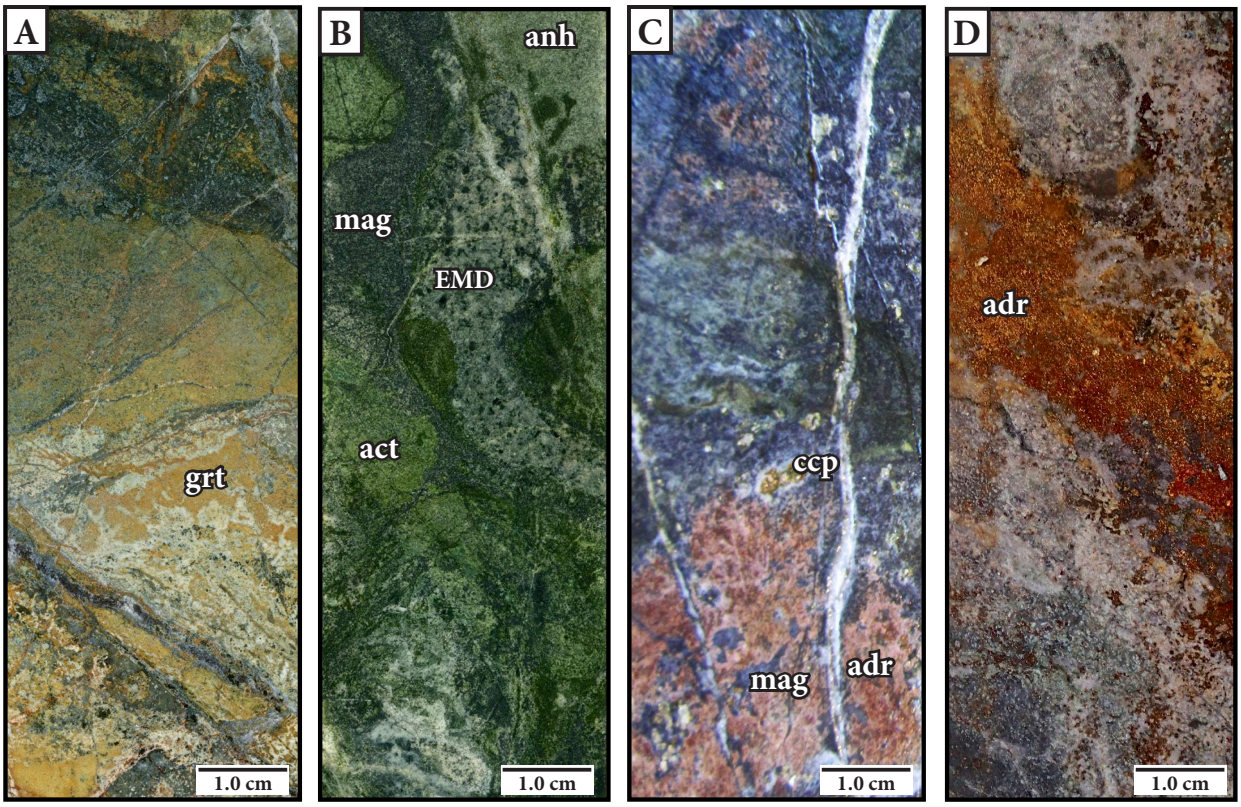


**Figure 5.6:** Examples of calc-silicate (WO2) alteration at Wainaulo. **A.** Intense garnet – anhydrite – magnetite-altered interval of NAF with abundant disseminated chalcopyrite. Sample: NVD019 544 m. **B.** Irregular bands of actinolite – chlorite – magnetite – anhydrite with trace chalcopyrite. The host rock is fine to medium-grained calcareous sandstone of the NAF surrounding a small interval of EMD1. Sample: NWK020 422 m. **C.** Intense andradite – actinolite – magnetite – chalcopyrite-altered NAF calcareous sandstone. Sample: NVD019 545 m. **D.** Band of andradite – anhydrite alteration within a calcareous horizon of the NAF. Sample: NVD014 619.5 m. Abbreviations: act = actinolite, adr = andradite, anh = anhydrite, ccp = chalcopyrite, EMD = early-mineralization diorite, grt = garnet, mag = magnetite.

black magnetite (Figs. 5.6A and B). Calc-silicate-altered zones are moderately Cu-mineralized at Wainaulo, however typically not exceeding 0.5 wt % Cu (Fig. 5.3). A genetic link is inferred with the EMD1 intrusion, since garnet-actinolite-rich calc-silicate alteration assemblages in porphyry-skarn districts are typically proximal to the causative intrusion (Meinert, 1997).

*Actinolite – albite – chlorite ± epidote alteration (WO3)*

Early actinolite – albite – chlorite ± epidote-altered rocks surround the central WO1 alteration domain in a zone less than 250 m wide (Table 5.3, Fig. 5.1B). The inner limit of this alteration style forms a sharp and distinct transition with the outer portion of the biotite-altered zone (Figs. 5.5C and E). This sharp transition is observed within the PD intrusion suggesting that lithology is not the primary control of this alteration type. Secondary actinolite – chlorite ± magnetite ± titanite ± rutile have pseudomorphed primary ferromagnesian minerals (Figs. 5.7A and B). Primary feldspar minerals have been replaced by hydrothermal albite ± chlorite ± paragonitic-illite (Figs. 5.7A and C; Appendix F). Epidote is notably rare in this alteration zone. Moderate, selective alteration of primary mafic minerals to chlorite – magnetite ± epidote with an albite halo marks the transition to the outer chlorite – epidote – albite alteration assemblages (Fig. 5.7C).

*Chlorite – albite – epidote ± calcite ± magnetite alteration (WO4)*

A distal chlorite – albite – epidote ± calcite ± magnetite alteration assemblage occurs outboard of the actinolite-bearing assemblages (Table 5.3, Fig. 5.1B). Moderate, pervasive albite – chlorite alteration formed a halo around intense clast-selecitve epidote – chlorite – calcite ± pyrite alteration within andesite clasts and mafic xenoliths from 250 to 400 m outside the 0.3 wt % Cu grade contour (Figs. 5.1B, 5.7D and E). Outboard of this alteration domain, ferromagnesian minerals are typically pseudomorphed by chlorite ± magnetite, and primary plagioclase is stable or weakly altered to albite – illite-smectite ± calcite ± epidote (Figs 5.7C and F). The chlorite – magnetite alteration assemblage appears to extend beyond the limits of observation (i.e. > 600 m from the Wainaulo intrusive complex; Figs. 5.1B and 5.2).

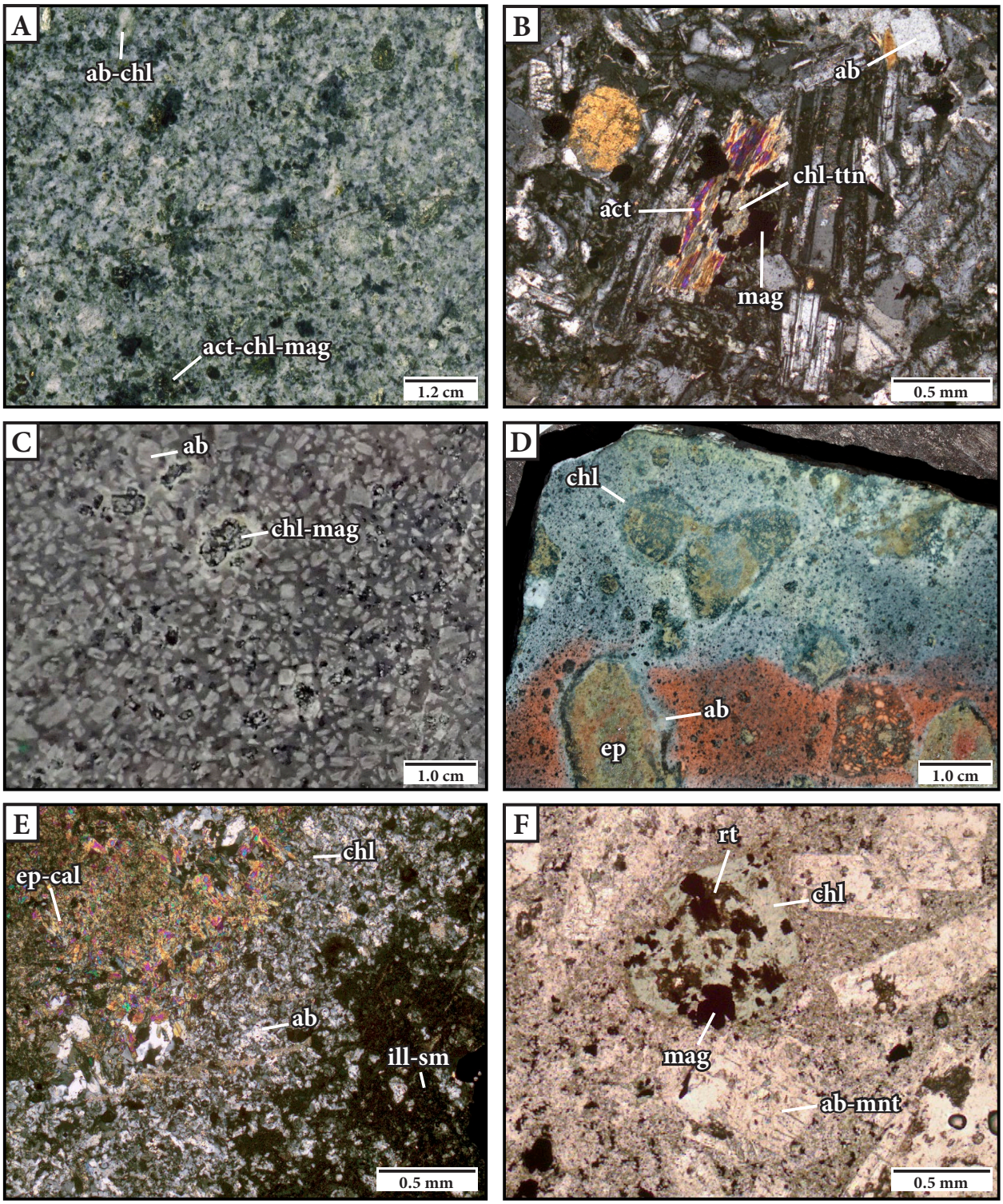


**Figure 5.7:** Examples of actinolite – albite (WO3) and epidote – albite (WO4) alteration at Wainaulo. **A.** Interval of a pyroxene-feldspar-phyric dike with selective alteration of primary ferromagnesian minerals to actinolite – chlorite and plagioclase to albite. Sample: NVD019 361 m. **B.** Cross-polarized photomicrograph illustrating selective actinolite – chlorite – magnetite – titanite alteration of a primary ferromagnesian mineral and albite alteration of plagioclase phenocrysts. Same sample as Fig. 5.7A. Sample: NVD019 361 m. **C.** Interval of pyroxene-feldspar-phyric andesite with moderate intensity, selective alteration of primary pyroxene to chlorite – magnetite and plagioclase to albite. Sample: NVD047 94 m. **D.** Interval of andesite-clast breccia with intense clast-selective epidote – calcite ± pyrite alteration with albite – chlorite alteration halos. Sample has been treated with chemical feldspar staining revealing Ca-plagioclase-rich groundmass (red) and distinct albite alteration rinds (no color) around clasts. Sample: NVD019 306 m. **E.** Cross-polarized photomicrograph illustrating intense epidote – calcite alteration of a volcanic clast surrounded by pervasive albite – chlorite alteration in a murky-brown illite-smectite-altered glassy matrix (bottom right of photomicrograph). Same sample as Fig. 5.7D. Sample: NVD019 306 m. **F.** Plane-polarized photomicrograph illustrating pyroxene that has been totally replaced by chlorite – magnetite – rutile alteration and plagioclase that has been altered to albite – montmorillonite. Sample: NVD019 71 m. Abbreviations: ab = albite, act = actinolite, cal = calcite, chl = chlorite, ep = epidote, ill-sm = illite-smectite, mag = magnetite, mnt = montmorillonite, rt = rutile, ttn = titanite.

*Magnetite-cemented breccia (WO-IA)*

The oldest observed vein style is a magnetite-cemented breccia (WO-IA). It is located near the transition from actinolite-dominant to chlorite-dominant alteration in NVD019 (Table 5.4; Fig. 5.1B). Drill intervals indicate a chaotic to clast-rotated breccia zone of less than 40 m (true width). The breccia contains tabular and splintery, granule to cobble sized, locally derived clasts of PD and rare mudstone (Fig. 5.8). These clasts define a planar, parallel fabric within a fine-grained magnetite cement (locally up to 60 % magnetite; Fig. 5.8A). Pervasive albite ± actinolite ± chlorite alteration of the clasts and wall rocks has been overprinted by pervasive and vein-style anhydrite – pyrite – illite alteration (Fig. 5.8). The breccia body is poorly defined, but is observed to have an irregular to tabular, sub-vertical morphology. Contacts are gradational into veined and fractured wall rock (Fig. 5.8B).

*Albite ± actinolite ± paragonite vein halos (WO5)*

Stage WO5 consists of albite and lesser actinolite and paragonite and occurs as thin (< 5 mm), pervasive alteration halos surrounding stages WO-IB to WO-ID veins and veinlets (Fig. 5.9A). Stage WO5 has the same distribution as stages WO-IB to WO-ID veins (Figs. 5.1D and 5.2).

*Biotite ± quartz veinlets and miarolitic cavity infill (WO-IB)*

There are two styles of stage WO-IB biotite – quartz infill: veins and miarolitic cavities (Table

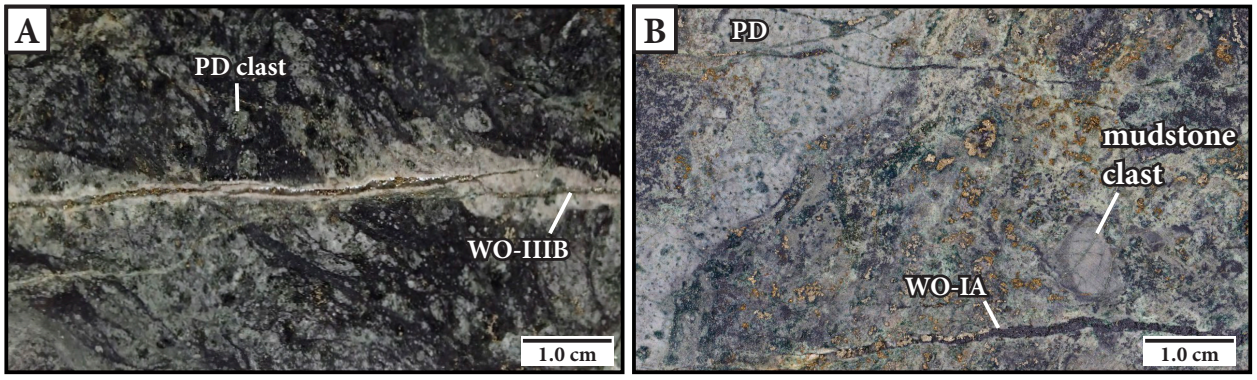


**Figure 5.8:** Examples of early-stage magnetite-cemented breccia at Wainaulo. **A.** Magnetite-cemented breccia containing PD clasts and crosscut by stage WO-IIIB anhydrite – pyrite veins with an illite – muscovite – pyrite alteration halo. Sample: NVD019 440 m. **B.** Magnetite-cemented breccia at the lower contact with PD containing a rare mudstone clast and vein-style magnetite. The magnetite is overprinted by stage WO8 pervasive pyrite – illite alteration. Sample: NVD019 460 m. Abbreviations: PD = porphyritic diorite.

5.4; Figs. 5.4A and 5.9B). Stage WO-IB veins are characterized by thin (< 5 mm) discontinuous, irregular biotite infill with a variable (0 – 60 %) proportion of quartz, and lack internal texture. Biotite also occurs as selvages and as disseminations within quartz (Fig. 5.4C). Veins that are biotite-only have thin (< 5 mm) stage WO5 albite alteration halos (Figs. 5.4A and 5.9B). The second style of WO-IB biotite and quartz presents as miarolitic cavities. This style consists of euhedral quartz and biotite with no alteration halos (Fig. 5.9B). Stage WO-IB veins crosscut both the EMD1 and EMD2 intrusions and occur up to 50 m from their margins within the PA intrusion (Figs. 5.2, 5.4C and 5.9B). Stage WO-IB miarolitic cavities only occur within the EMD2 intrusion. Stage WO-IB features have not been observed in the main-stage mineralization intrusions (i.e., EMQD, IMQD and LMQD), suggesting that they pre-date these intrusions (Figs. 5.2 and 5.3).

*Quartz stringers and veins (WO-IC)*

The second vein-stage at Wainaulo consists of wispy to straight-sided, continuous to discontinuous quartz veins and stringers with diffuse to sharp wall-rock contacts (Table 5.4; Figs. 5.9A, D and E). The quartz is typically clear, vitreous and granular. Stage WO-IC veins and stringers lack internal symmetry. Thin (up to 4 mm-wide), white and pervasive stage WO5 albite alteration halos are developed locally (Fig. 5.9A). In some cases, these veins have been reopened by later actinolite – magnetite veins (stage WO-IE; Fig. 5.9E). Stage WO-IC veins have not been observed crosscutting any other vein stage, indicating they are probably an early-stage vein (Fig. 5.2). Stage WO-IC have been documented up to 250 m from the margin of the EMD1 intrusion (Fig. 5.2). Rare molybdenite has been observed in the distal expression of these veins.

*Magnetite veinlets and stringers (Stage WO-ID)*

Stage WO-ID is characterized by thin, discontinuous and sheeted monomineralic magnetite veinlets and stringers that have diffuse and irregular vein walls and no internal symmetry (Table 5.4; Fig. 5.9A). Thin (up to 2 mm-wide), white and pervasive stage WO5 albite alteration halos are developed locally (Fig. 5.9A). Sulfides are rare to absent from this stage. Stage WO-ID veinlets are most densely concentrated in and around EMD1 (up to 70 m from its contact with PA;

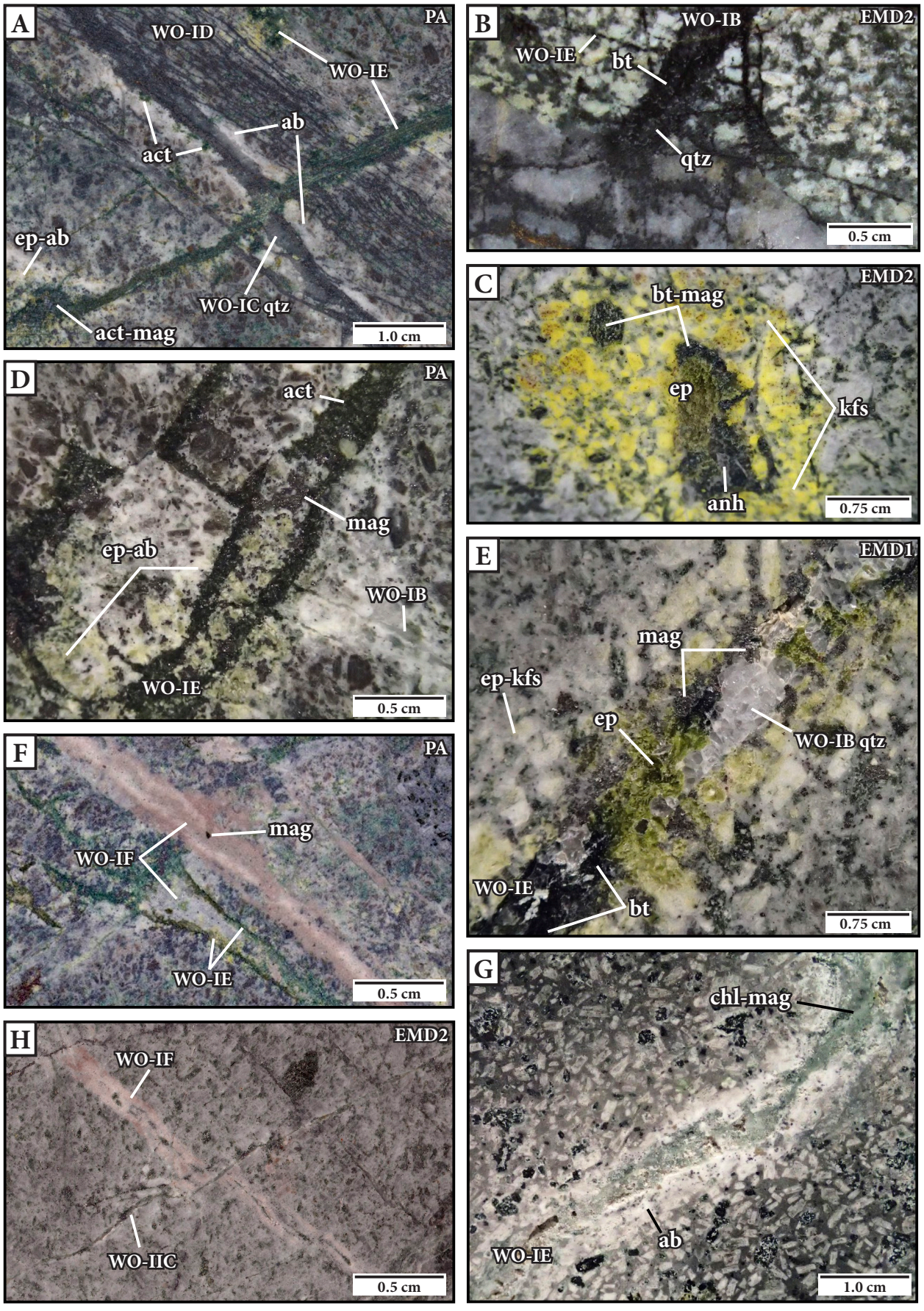
A
PA
WO-ID
WO-IE
ab
act
ep-ab
WO-IC qtz
act-mag
1.0 cm
B
WO-IB
EMD2
WO-IE
bt
qtz
0.5 cm
C
EMD2
bt-mag
ep
kfs
anh
0.75 cm
D
PA
act
mag
ep-ab
WO-IB
WO-IE
0.5 cm
E
EMD1
mag
ep-kfs
ep
WO-IB qtz
WO-IE
bt
0.75 cm
F
PA
mag
WO-IF
WO-IE
0.5 cm
G
chl-mag
ab
WO-IE
1.0 cm
H
EMD2
WO-IF
WO-IIC
0.5 cm

**Figure 5.9 (opposite):** Examples of early-stage veins and vein halo alteration at Wainaulo. **A.** Biotite – albite-altered PA that has been crosscut by magnetite stringers (stage WO-ID) with thin (< 1 mm) albite alteration halos. Stage WO-ID veins have crosscut early quartz veins and stringers (WO-IC) with thin (< 4 mm) albite – actinolite alteration halos. Stages WO-IC and WO-ID veins have been crosscut by actinolite – magnetite veins (WO-IE) with albite – epidote alteration halos. Sample: NVD019 745 m. **B.** Interval of EMD2 with a stage WO-IB miarolitic cavity filled with biotite and quartz and biotite veinlets with albite alteration halos. The stage WO-IB veins have been crosscut by a stage WO-IE actinolite vein with an epidote – K-feldspar vein halo. Sample: NVD019 852 m. **C.** EMD2 containing a clot of epidote – biotite – magnetite – anhydrite with a selective K-feldspar alteration envelope (yellow stain). Sample: NVD019 808 m. **D.** Interval of PA that has been crosscut by stage WO-IE actinolite – magnetite veins with an epidote – albite alteration halo (< 5 mm wide). The stage WO-IE vein has crosscut early quartz veins (WO-IB). Sample: NVD019 745 m. **E.** Stage WO-IE biotite – epidote vein with a selective K-feldspar – epidote alteration halo. The stage WO-IE vein has invaded an early stage WO-IB quartz vein. Sample: NVD019 708 m. **F.** Sample of PA that has been crosscut by a fine-grained, saccharoidal-textured quartz – K-feldspar vein (WO-IF) that has disseminated bornite and magnetite throughout. The stage WO-IF vein has crosscut stage WO-IE actinolite veins. Sample: NVD019 745 m. **G.** Distal stage WO-IE chlorite – magnetite vein with an albite alteration halo within the pyroxene-feldspar-phyric andesite. Sample: NVD047 94 m. **H.** EMD2 that has been crosscut by a stage WO-IF fine-grained, saccharoidal-textured K-feldspar – quartz vein. The stage WO-IF vein has been crosscut by main-stage WO-IIC comb-quartz – sulfide veins. Abbreviations: ab = albite, act = actinolite, anh = anhydrite, bt = biotite, chl = chlorite, EMD1 = early-mineralization diorite 1, EMD2 = early-mineralization diorite 2, ep = epidote, kfs = K-feldspar, mag = magnetite, PA = porphyritic andesite, qtz = quartz.

Fig. 5.1D). Stage WO-ID veinlets have been truncated by later actinolite – magnetite veins (stage WO-IE; Fig. 5.9A) and have crosscut earlier quartz veins and stringers (stage WO-IC; Fig. 5.9A). Stage WO-ID is absent from, truncated by and occurs as refractory xenoliths within main-stage mineralization intrusions (i.e., EMQD, IMQD and LMQD; Fig. 5.10I), indicating that these veins formed early in the history of hydrothermal activity at Wainaulo.

*K-feldspar – epidote ± actinolite and albite vein halos (WO6)*

Stage WO6 marks the first transition from albite-dominant to K-feldspar-dominant alteration assemblages. Stage WO6 is composed of K-feldspar – epidote ± actinolite near the core of Wainaulo and of albite at the deposit periphery, where it overprints stage WO4 alteration (Table 5.3; Figs. 5.2, 5.9D and G). Stage WO6 vein halos range in thickness from 3 – 15 mm (Figs. 5.9C and G). Stage WO6 vein-halo alteration has the same distribution as stage WO-IE and WO-IF veins and veinlets (Fig. 5.2).

*Magnetite ± actinolite ± biotite ± chlorite ± chalcopyrite veins (Stage WO-IE)*

Stage WO-IE veins and veinlets are composed of variable quantities of magnetite, actinolite, biotite, epidote, chlorite and chalcopyrite and have well-developed stage WO6 alteration halos consisting of K-feldspar – epidote ± actinolite or albite up to 15 mm wide (Table 5.4). Stage WO-IE veins and veinlets are sparsely distributed within WO1, WO3 and WO4 alteration domains, and their specific vein mineralogies reflect the alteration domains that they occur in. Within the WO1 alteration zone, stage WO-IE veins typically consist of biotite – magnetite – epidote ± ac-

tinolite with an alteration halo of K-feldspar – epidote (Figs. 5.4A and 5.9E). Stage WO-IE veins found within the WO3 alteration zone consist of actinolite – magnetite ± epidote with albite – epidote alteration halos (Figs. 5.9A and D). Within the WO4 alteration domain, stage WO-IE veins are largely composed of chlorite ± magnetite with a conspicuous albite alteration halo (Fig. 5.9G). The morphology of the veins ranges from diffuse and irregularly shaped to straight-sided with sharp vein walls (Figs. 5.9D, E and G). Crosscutting relationships between stages WO-IF, WO-IE, WO-ID WO-IC and WO-IB veins (Figs. 5.4A, 5.9A, D, E and F) indicate that stage WO-IE veins post-date the sheeted magnetite and quartz stringers as well as biotite ± quartz veins, whereas they formed prior to the fine-grained saccharoidal-textured K-feldspar – quartz – albite – magnetite veins. Within the EMD1 and EMD2 intrusions, stage WO-IE locally presents as clots of biotite – magnetite – epidote – anhydrite ± sulfides with K-feldspar alteration halos (Fig. 5.9C). Stage WO-IE veins and veinlets are best developed within the EMD1 and EMD2 intrusions, as well as the surrounding PA wall rock and within the Namosi Andesite Formation hyaloclastite sequence (Fig. 5.2). They are notably absent from the central quartz-diorite intrusive complex (i.e., EMQD, IMQD and LMQD), indicating that stage WO-IE veins pre-date these intrusive phases.

*Fine-grained, saccharoidal-textured K-feldspar – quartz – albite veins (WO-IF)*

Stage WO-IF are thin (5 – 20 mm) veins that are composed of fine-grained saccharoidal-textured K-feldspar – quartz ± albite with disseminations of magnetite ± chalcopyrite ± bornite (Table 5.4; Figs. 5.9F and H). The vein walls are typically irregular and diffuse, but are locally sharp and straight-sided. Crosscutting relationships indicate that WO-IF veins are younger than stage WO-IE actinolite veins (Fig. 5.9F) but older than stage WO-IIC comb-quartz veins (Fig. 5.9H). Stage WO-IF has not been observed to crosscut the EMQD, IMQD or LMQD intrusions.

*5.2.3.3 Main-stage mineralization, alteration and veins (WO-II)*

At Wainaulo, high-grade Cu-Au mineralization is associated with stage WO-II veins. This stage comprises a zone of moderate to strong chlorite – albite – actinolite – epidote ± quartz alteration that is spatially and temporally associated with the EMQD, IMQD and LMQD intrusions

(Figs. 5.1, 5.2 and 5.3). Sulfide-bearing epidote – anhydrite veins with selective K-feldspar – epidote – phengite alteration halos crosscut and overprint the chlorite – albite mineral assemblage.

*Asymmetric comb-quartz ± bornite layers and massive crenulated magnetite bands (WO-IIA)*

Although stage WO-IIA comb-quartz ± bornite layers and magnetite bands are technically not veins, they have a clear paragenetic relationship with main-stage mineralization at Wainaulo and are therefore described in this section. Stage WO-IIA comb-quartz layers and magnetite bands have been observed within the inside margin of EMQD at Wainaulo. Stage WO-IIA is most commonly composed of undulose and crenulate layers of coarse-grained, euhedral comb-quartz crystals that are intergrown with bornite (Table 5.4; Figs. 5.10E, F and G). Quartz layers range in thickness from 5 to 30 mm, are irregular to planar on one side, and have euhedral terminations of quartz crystals on the other side. The quartz crystals generally point towards the center of the intrusion. The magnetite bands exhibit alternating layers of coarse-grained (< 20 mm) magnetite with irregular fine-grained feldspar-quartz-aplite (Fig. 5.10H). These structures are interpreted to be examples of unidirectional solidification textures (USTs; e.g., Shannon et al., 1982; Kirkham and Sinclair, 1988).

*Chlorite – albite – actinolite – epidote ± quartz alteration (WO7)*

The oldest stage WO-II alteration assemblage is characterized by moderate to strong, selective chlorite – albite – actinolite – epidote ± quartz alteration. Stage WO7 is spatially restricted to the EMQD, IMQD and LMQD intrusions and has a limited occurrence in the wall rocks (Table 5.3, Fig. 5.1B). Stage WO7 affected the core of Wainaulo, overprinting biotite – albite (WO1) alteration up to 30 m from the Wainaulo quartz-diorite intrusive complex margin (Figs. 5.1, 5.2 and 5.3). Ferromagnesian minerals that occur as phenocrysts and in the groundmass of the EMQD, IMQD and LMQD intrusions have been altered to fine-grained aggregates of chlorite – actinolite – epidote ± bornite ± chalcopyrite ± magnetite ± rutile (Figs. 5.10A, B, C and D). Plagioclase phenocrysts are either stable or have been altered to albite ± illite (Figs. 5.10A and B). Stage WO5 alteration is spatially associated with all WO-II quartz-bearing veins (Fig. 5.3). These veins lack

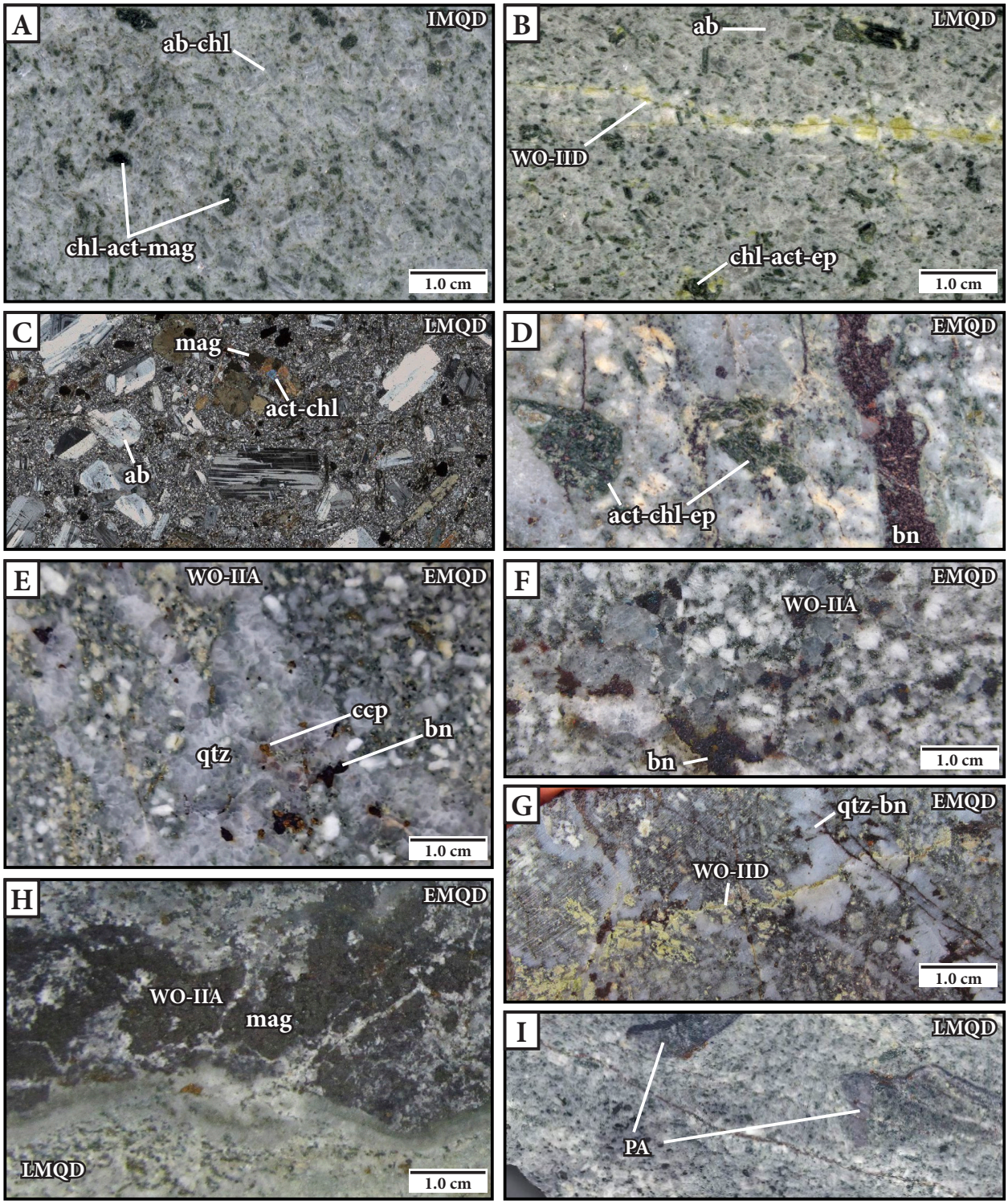


**Figure 5.10:** Examples of main-stage chlorite – albite – actinolite – epidote (WO7) alteration and stage WO-IIA layers **A.** IMQD with selective alteration of primary hornblende to chlorite – actinolite – magnetite and plagioclase to albite ± chlorite. Sample: NVD019 840 m. **B.** Interval of LMQD with selective alteration of primary hornblende to chlorite – actinolite – epidote and plagioclase to albite. The sample has been crosscut by epidote – pyrite – anhydrite veins (WO-IID) with epidote – K-feldspar vein-halo (WO9) alteration. Sample: NVD019 761 m. **C.** Cross-polarized photomicrograph of LMQD illustrating weak – moderate selective actinolite – chlorite – magnetite alteration of primary hornblende and albite alteration of primary plagioclase. Sample: NVD019 761 m. **D.** EMQD with selective alteration of hornblende to actinolite – chlorite. Sample: NVD040 533 m. **E.** Sample of EMQD with several layers of euhedral quartz crystals with interstitial bornite. Quartz crystals terminate perpendicular to the plane of layering. Sample: NVD040 533 m. **F.** EMQD with a discrete and discontinuous crenulate layer of euhedral quartz crystals and interstitial bornite. Sample: NVD007 543 m. **G.** EMQD with crenulate layers of quartz – bornite that have been crosscut by epidote – bornite veins (WO-IID). Sample: NVD019 887 m. **H.** Magnetite-rich bands adjacent to veined-contact between EMQD and LMQD. Sample: NVD037 720 m. **I.** LMQD containing magnetite- and quartz-vein-bearing PA xenoliths. NVD040 632 m. Abbreviations: ab = albite, act = actinolite, bn = bornite, ccp = chalcopyrite, chl = chlorite, EMQD = early-mineralization quartz-diorite, ep = epidote, IMQD = inter-mineralization quartz-diorite, LMQD = late-mineralization quartz-diorite, mag = magnetite, qtz = quartz, PA = porphyritic andesite.

obvious alteration halos, suggesting that the fluids responsible for their formation may have been in, or close to, chemical equilibrium with the surrounding altered wall rocks.

*Laminated quartz – magnetite ± bornite ± chalcopyrite veins (WO-IIB)*

Stage WO-IIB veins are composed of anhedral dark-gray quartz with laminations (< 1 mm) of intergrown sulfides ± magnetite (Table 5.4). Laminations are oriented sub-parallel to the long-axis of the vein (Fig. 5.11A). WO-IIB vein walls are sharp. Where crosscutting relationships have been observed, WO-IIB veins are truncated by stage WO-IID quartz – sulfide veins (Fig. 5.11A). Stage WO-IIB veins are most intensely developed within and immediately adjacent to the EMQD intrusions and extend up to 15 m away from the intrusive contact with surrounding PA wall rock (Fig. 5.1B). Stage WO-IIB veins have not been observed in the IMQD or LMQD intrusions, suggesting that they formed prior to the emplacement of these intrusive phases (Fig. 5.2).

*Symmetric comb-quartz – sulfide veins (WO-IIC)*

Stage WO-IIC veins are composed of discrete or stockwork, subhedral to euhedral, white quartz – sulfide veins associated with the EMQD, IMQD and LMQD intrusions (Table 5.4). Stage WO-IIC veins typically have a concordant central seam that is occupied by sulfide minerals (Figs. 5.9H, 5.11A, B and C). WO-IIC veins either lack alteration halos or locally have a narrow albite vein halo. The dominant sulfide species in WO-IIC veins changes with respect to lithotype and distance from the center of the orebody. Chalcopyrite and bornite are the dominant sulfides occupying the central seams of WO-IIC veins in the core of the deposit and in the EMQD intrusions (Figs. 5.1A, C and 5.11B). Grading outward from IMQD to LMQD, chalcopyrite then pyrite are the dominant sulfides present in stage WO-IIC veins (Figs. 5.1A, C and 5.11C).

*Andradite – magnetite ± epidote ± calcite alteration (WO8)*

Stage WO8 is characterized by intense and pervasive andradite – magnetite ± epidote ± chlorite ± actinolite ± calcite ± anhydrite alteration of the EMQD intrusions that are proximal to ma-

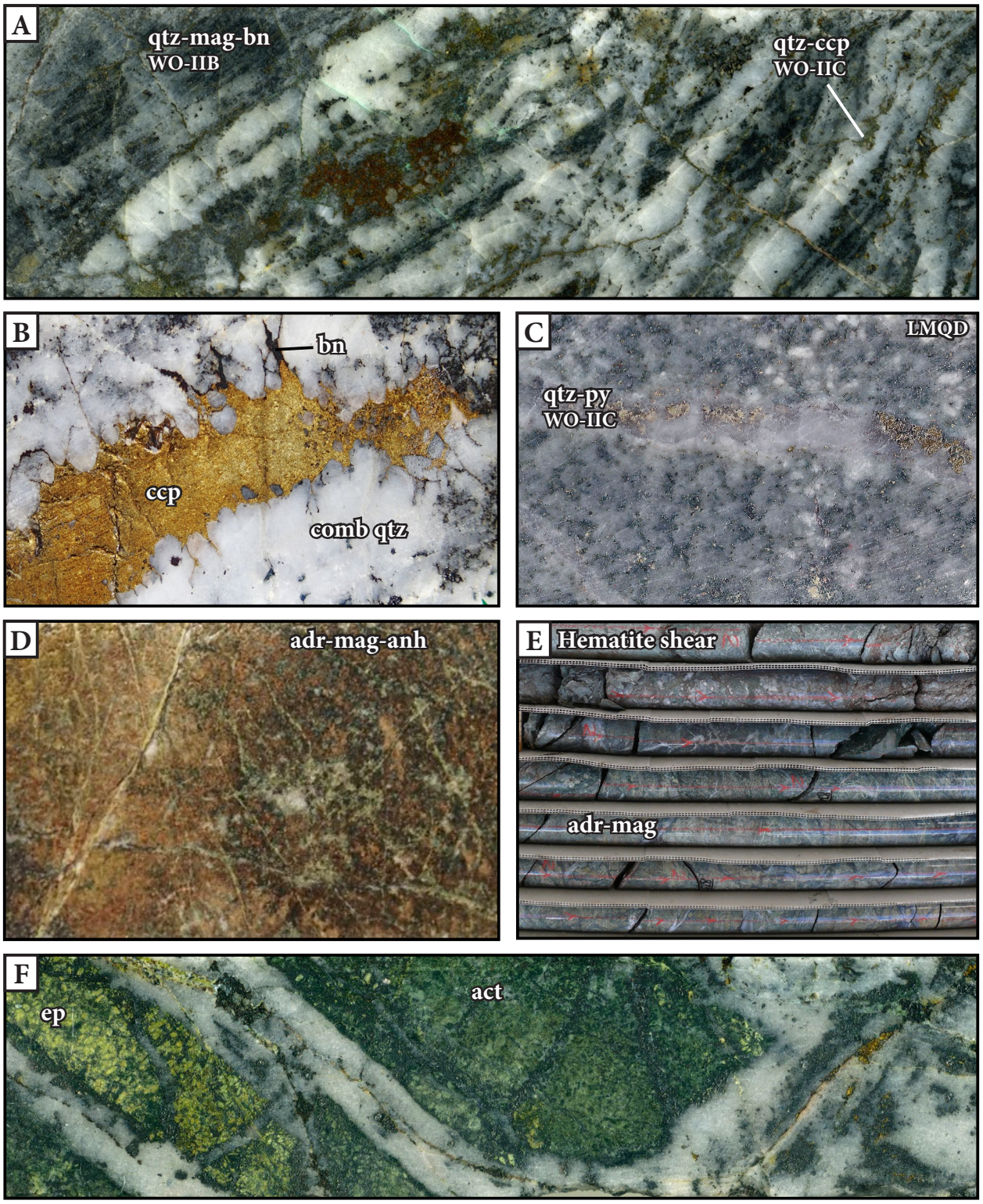


**Figure 5.11:** Examples of main-stage veins and andradite – magnetite (WO8) alteration at Wainaulo. **A.** Interval of PA adjacent to the EMQD intrusion that has been crosscut by stage WO-IIB laminated quartz – magnetite – bornite veins. Stage WO-IIB has been crosscut by stage WO-IIC quartz – chalcopyrite – bornite veins. This sample is from a three meter interval containing 4.7 wt % Cu and 1.2 g/t Au. Sample: NVD019 890 m. **B.** Interval of PA hosting a symmetric comb-quartz – chalcopyrite – bornite vein (WO-IIC). Chalcopyrite has exploited the central seam in this vein, whereas bornite has infiltrated cracks and fractures along the margins of the euhedral quartz. Sample: NVD047 1090 m. **C.** Interval of LMQD that has been crosscut by a quartz – pyrite vein (WO-IIC). Sample: NVD047 1122 m. **D.** Interval of intense andradite – magnetite – anhydrite alteration interpreted to be overprinting the EMQD intrusion. Sample: NVD019 873 m. **E.** Intense pervasive kaolinite – montmorillonite alteration associated with the Hematite shear adjacent to intense, pervasive andradite – magnetite alteration interpreted to be endoskarn. NVD019 Tray 375 (871.95 to 875.90 m). F. Hand sample photograph of PA with strong epidote – actinolite (distal WO8) alteration. Sample: NWK020 330 m. Abbreviations: act = actinolite, adr = andradite, anh = anhydrite, bn = bornite, ccp = chalcopyrite, EMQD = early-mineralization quartz-diorite, ep = epidote, LMQD = late-mineralization quartz-diorite, mag = magnetite, PA = porphyritic andesite, py = pyrite, qtz = quartz.

jor east-northeast trending fault zones (Table 5.3; Figs. 5.1B and 5.11E). WO8 presents as texturally destructive, pale red, massive andradite and magnetite (Figs. 5.11D and E) adjacent to fault zones and grades laterally into massive epidote – actinolite – calcite – magnetite alteration greater than 5 m from the fault (Fig. 5.11F).

*K-feldspar – epidote – phengite alteration (WO9)*

The assemblage of K-feldspar – epidote – phengite is restricted to vein-halo alteration surrounding stage WO-IID epidote – sulfide – anhydrite veins (Table 5.3). Stage WO9 alteration is best-developed in the high-grade Cu-Au core of the deposit and in the EMQD intrusions and adjacent wall rock (Figs. 5.12E and G). The intensity and width of the vein-halo alteration is minimized in the LMQD intrusions (Fig. 5.10B). White K-feldspar alteration could easily be confused with albite alteration in the field, but has been identified unambiguously by the application of sodium cobaltinitrate solution (stains K-feldspar yellow) and in thin section (Figs. 5.12B and C).

*Epidote – sulfide – anhydrite veins (WO-IID)*

Epidote – sulfide – anhydrite ± calcite ± magnetite veins with K-feldspar – epidote – phengite vein-halo alteration (stage WO9) have crosscut all intrusive phases and invaded all previous vein stages at Wainaulo (Table 5.4; Figs. 5.1D, 5.10B and G, and 5.12). Sulfides are intimately intergrown with subhedral to euhedral epidote and lesser anhydrite (Figs. 5.12C and D). Radiating sprays of 'watermelon epidote' have been observed locally (Fig. 5.12A). The core of the spray consists of pink piemontite grading outward to pale and then dark green pistacite (Fig. 5.12A). The sulfide mineralogy of WO-IID veins is related to its position within the Wainaulo orebody. Within the core of the deposit WO-IID veins can have > 80 vol % bornite and contribute the highest gold and copper grades within the deposit (Fig. 5.12E). Chalcopyrite-rich WO-IID veins occur in the IMQD intrusion (Fig. 5.12B) and pyrite-rich WO-IID veins are hosted in the LMQD intrusion (Fig. 5.10B) and at the deposit periphery (Fig. 5.12G).

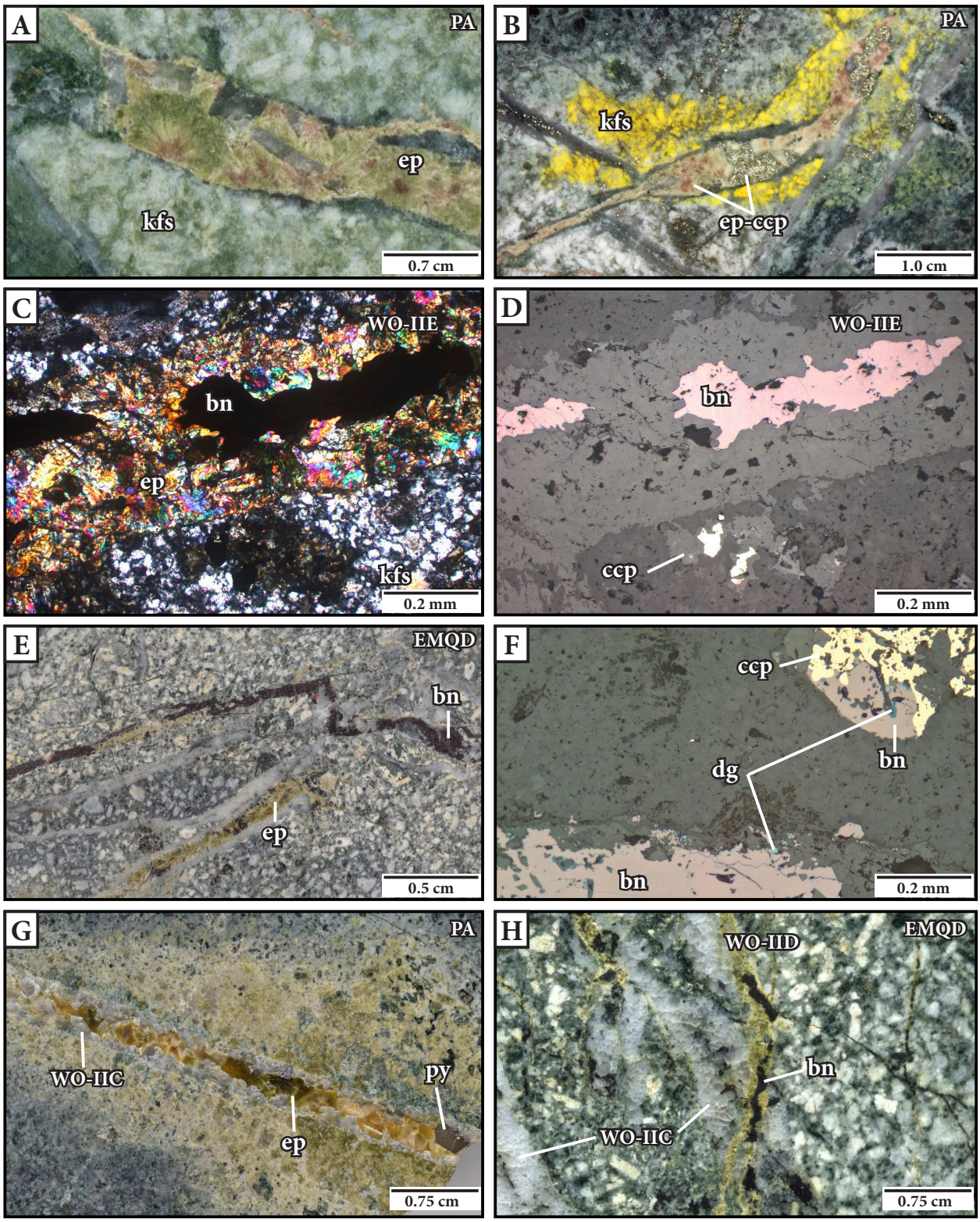


**Figure 5.12:** Examples of main-stage mineralization WO-IID veins at Wainaulo. **A.** Example of 'watermelon epidote' in an epidote – chalcopyrite – anhydrite vein that has exploited the central seam of an earlier quartz vein. The core of the epidote spray is piemontite that grades out radially to pale epidote and then dark green pistacite. Sample: NVD019 775 m. **B.** Epidote – chalcopyrite vein that has been treated with chemical feldspar stain and illustrates that K-feldspar (yellow) is localized around the vein. Sample: NVD019 785 m. **C.** and **D.** Photomicrograph (xpl) and (RL) of an epidote – bornite vein (WO-IID). The bornite is intergrown with epidote in the central portion of the vein. K-feldspar has altered plagioclase in the vein-halo. Sample: NVD008 545 m. **E.** Interval of EMQD that has been crosscut by bornite – epidote veins (WO-IID). Bornite can have > 80 vol % of WO-IID veins locally. This sample is from a two meter interval containing 6.9 wt % Cu and 1.69 g/t Au (NVD040 533 m). **F.** Photomicrograph (RL) of epidote – bornite vein (WO-IID). Bornite has replaced chalcopyrite and digenite has replaced the margins of bornite. Sample: NVD040 533 m. **G.** Stage WO-IID epidote – pyrite vein that has invaded the central seam of a stage WO-IIC comb-quartz vein. **H.** EMQD containing stage WO-IID epidote veins that have crosscut stage WO-IIC comb-quartz veins. Abbreviations: bn = bornite, ccp = chalcopyrite, dg = digenite, EMQD = early-mineralization quartz-diorite, ep = epidote, kfs = K-feldspar, PA = porphyritic andesite, py = pyrite.

*5.2.3.4 Late-stage alteration and veins (WO-III)*

Overprinting and crosscutting relationships have revealed several alteration and vein stages that postdate the main-stage mineralization and alteration events (Tables 5.3 and 5.4). Late-stage alteration includes a domain of pervasive pyrite – illite ± chlorite-altered rocks. Illite – pyrite ± chlorite also occur together as vein-halo alteration surrounding late pyrite-bearing veins. A widespread, weak, selective chlorite – illite-smectite alteration assemblage has overprinted all previous alteration assemblages across Wainaulo. The youngest stage of alteration at Wainaulo consists of kaolinite – montmorillonite – hematite associated with steeply dipping faults that have crosscut the core of Wainaulo and gypsum – ankerite and chlorite – hematite veins and breccias.

*Pyrite – illite ± chlorite (WO10)*

A narrow zone (50 to 100 m) of moderate intensity, pervasive pyrite – illite ± chlorite alteration, rims the early actinolite-bearing WO3 alteration zone (Table 5.3; Figs. 5.1B, 5.8A and B). It has overprinted the magnetite-cemented breccia (WO-IA), presenting as bleached zones of illite – pyrite that partially obscure previously-developed textures (Fig. 5.8A). Stage WO10 alteration also commonly presents as selective, texturally-destructive illite – pyrite ± chlorite alteration halos surrounding late-stage base metal- and pyrite-bearing anhydrite veins (Figs. 5.13A and B). Pyrite occurs as fine disseminations where it has partially replaced secondary magnetite and ferromagnesian minerals (Fig. 5.13A), whereas white illite has replaced all feldspathic components (Fig. 5.13A). These veins have a widespread spatial distribution throughout Wainaulo.

*Anhydrite – pyrite ± sphalerite veins (WO-IIIA)*

Stage WO-IIIA anhydrite – pyrite ± sphalerite ± galena veins have a widespread distribution at Wainaulo (Table 5.4; Fig. 5.2). Euhedral pyrite occurs as discrete aggregates with subordinate sphalerite and galena intergrown with anhydrite (Fig. 5.13B). Pyrite also occupies central bands within anhydrite veins (Fig. 5.13A). The relative proportions of anhydrite and pyrite is variable, but commonly anhydrite is the most abundant mineral by volume. Where crosscutting relation-

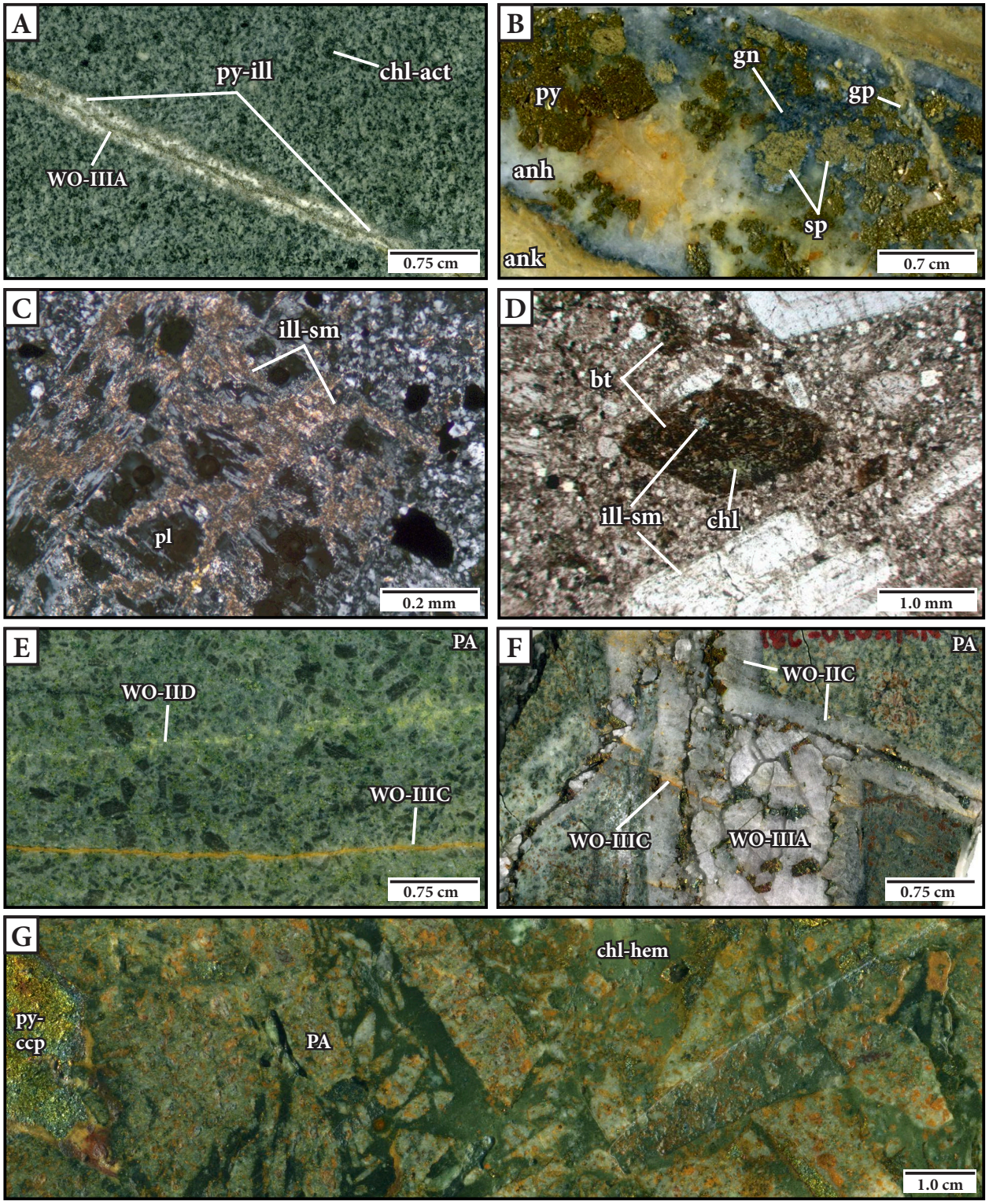


**Figure 5.13:** Examples of late-stage alteration and veins at Wainaulo. **A.** Interval of chlorite – actinolite – albite-altered microdiorite that has been crosscut by an anhydrite – pyrite vein (WO-IIIA) with a 4 mm-wide illite – pyrite alteration halo. Sample: NVD019 299 m. **B.** Interval of an anhydrite – pyrite – sphalerite – galena vein (WO-IIIA) crosscut by a gypsum – ankerite vein (WO-IIIC). Sample: NWK020 404 m. **C.** Cross-polarized photomicrograph showing illite-smectite replacement along fractures within an albite-altered plagioclase phenocryst. Sample: NVD040 533 m. **D.** Plane-polarized photomicrograph of a biotite-altered hornblende that is partially replaced by chlorite – illite-smectite (WO11). Sample: NVD019 1081 m. **E.** Interval of chlorite – illite-smectite-altered PA that has been crosscut by a stage WO-IIIC ankerite – gypsum veinlet. Sample: NWK020 313 m. **F.** Interval of PA crosscut by stage WO-IIC symmetric comb-quartz – sulfide veins that have been crosscut by stage WO-IIIA anhydrite – pyrite veins that are crosscut by stage WO-IIIC gypsum – ankerite veins. Sample: NWK020 281 m. **G.** Interval of chlorite – hematite-cemented breccia illustrating the tabular clasts of PA in a clast-rotated internal organization. Sample: NWK020 303 m. Abbreviations: act = actinolite, anh = anhydrite, ank = ankerite, bt = biotite, ccp = chalcopyrite, chl = chlorite, gn = galena, gp = gypsum, hem = hematite, ill = illite, ill-sm = illite-smectite, pl = plagioclase, PA = porphyritic andesite, py = pyrite, sp = sphalerite.

ships are observed, stage WO-IIIA veins have crosscut the early-stage magnetite-cemented breccia (WO-IA; Fig. 5.8A) and main-stage symmetric comb-quartz – sulfide veins (WO-IID; Fig. 5.13F) and have been crosscut by late-stage gypsum – ankerite veins (WO-IIIC; Fig. 5.13B).

*Illite – chlorite ± illite-smectite alteration (WO11)*

A widespread, weak, selective hydrothermal alteration assemblage of illite – chlorite ± illite-smectite has overprinted all previous alteration assemblages (Table 5.3). WO11 alteration consists of weak illite and illite-smectite dusting, or partial replacement along fracture surfaces within albite-altered plagioclase phenocrysts (Fig 5.13C). Ferromagnesian minerals have been weakly altered to chlorite ± illite-smectite (Fig 5.13D). The PA intrusion has been weakly- to strongly-altered to pervasive chlorite – illite-smectite alteration, imparting a dark-green color to the groundmass and plagioclase phenocrysts (Fig. 5.13E).

*Chlorite – hematite veins and breccias (WO-IIIB)*

Stage WO-IIIB chlorite-hematite-bearing veins occur locally in the upper portions of Wainaulo. These veins contain chlorite, hematite, calcite and pyrite with subordinate chalcopyrite and epidote (Table 5.4). Stage WO-IIIB formed as both veins and most commonly as cement to breccias occupying zones of brittle deformation up to 20 cm-wide (Fig. 5.13G). The breccias are comprised of predominantly tabular, weakly to strongly chlorite – hematite-altered PA clasts with a clast-rotated internal organization (Fig. 5.13G).

*Kaolinite – montmorillonite ± hematite alteration (WO12)*

Intense, pervasive kaolinite – montmorillonite ± hematite ± ankerite ± gypsum alteration is concentrated in and around steeply-dipping, east-northeast-trending faults (Table 5.3; Figs. 5.1A, B and 5.14A). Due to the local abundance of hematite defined by asymmetric foliations (Fig. 5.14B), the fault zones are referred to by NJV geologists as the “Hematite shear”. Stage WO12 alteration is constrained to < 40 m-wide, near-vertical, sheet-like and curviplanar zones that have

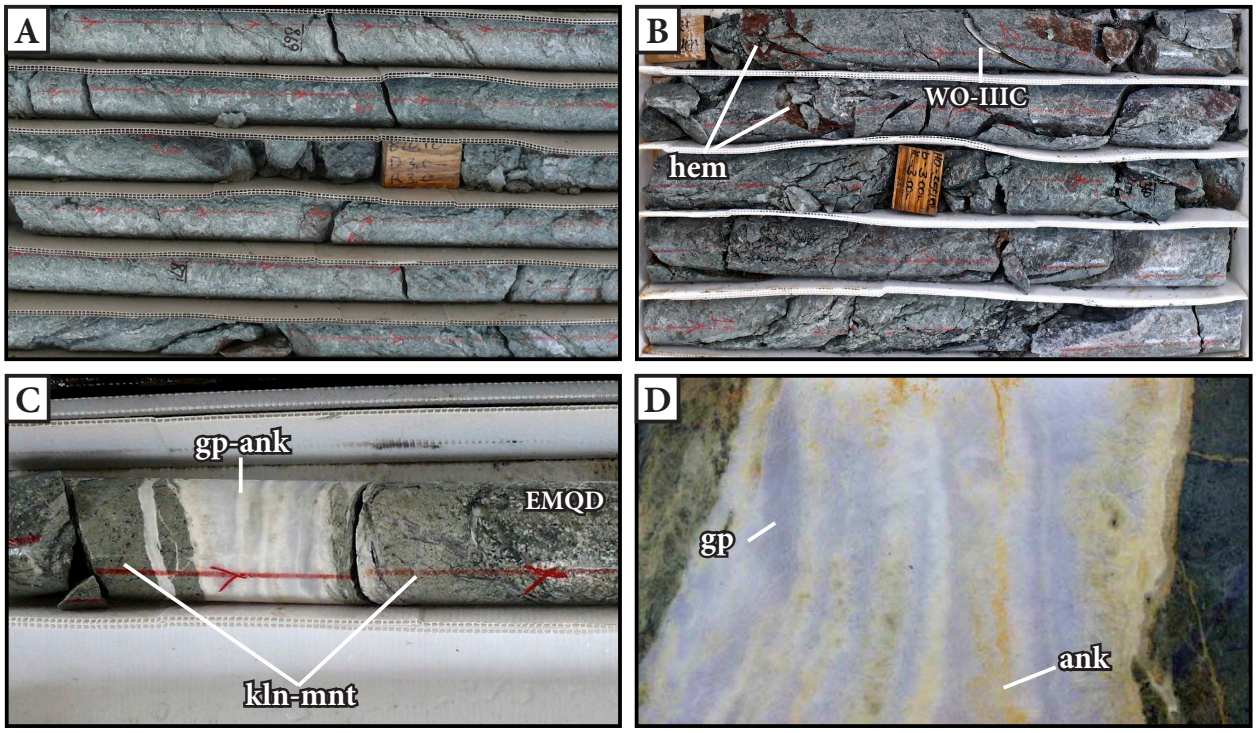


**Figure 5.14:** Examples of late-stage WO12 alteration and WO-IIIC veins. **A.** Intense, pervasive kaolinite – montmorillonite alteration associated with the steeply dipping Hematite shear. NVD019 Tray 374 (868.30 m to 871.95 m; HQ-sized drill core). **B.** Intense, pervasive kaolinite – montmorillonite alteration with brick-red hematite associated with the steeply dipping Hematite shear. NVD016 Tray 151 (358.60 m to 301.20 m; NQ-sized drill core). **C.** Interval of EMQD that has been crosscut by a banded gypsum – ankerite vein with a 5 cm-wide, intense, pervasive kaolinite – montmorillonite alteration halo. NVD019 Tray 367 (844.50 m to 845.00 m); HQ-sized drill core. **D.** Interval of stage WO-IIIC banded gypsum – ankerite vein. Sample: NVD019 844.6 m. Abbreviations: ank = ankerite, EMQD = early-mineralization quartz-diorite, gp = gypsum, hem = hematite, kln = kaolinite, mnt = montmorillonite.

truncated the mineralized intrusions and veins at Wainaulo (Fig. 5.1). These faults extend from depth (below 600 mRL) to the present-day surface (~ 300 mRL). Pervasive kaolinite – montmorillonite alteration of the wall rock occurs up to 10 m around the fault zones.

*Gypsum – ankerite – montmorillonite ± pyrite veins (WO-IIIC)*

WO-IIIC is the youngest vein-stage recognized at Wainaulo and crosscuts all earlier alteration assemblages and veins (Fig. 5.2). Stage WO-IIIC veins comprise bands of gypsum and ankerite with patches of montmorillonite and euhedral crystals of pyrite locally (Table 5.4; Figs 5.13E and F, 5.14C and D). These veins are broadly distributed throughout the Wainaulo deposit (Fig. 5.2). Stage WO-IIIC veins occur as fracture coatings (< 3 mm in vein-aperture; Fig. 5.14B) and as straight-walled, planar veins that can be > 20 cm-wide. Strong, pervasive kaolinite – montmorillonite-altered vein-halos surround stage WO-IIIC veins (up to 5 cm from the vein margin; Fig. 5.15C), suggesting they may be associated with the late-stage WO12 alteration and faults.

### 5.2.4 Waisoi West Cu-Au porphyry deposit

The Waisoi West Cu-Au porphyry deposit is located immediately west of Waisoi East and about 6.5 km northwest of Wainaulo (Fig. 3.1). Drilling has constrained the > 0.7 wt % copper grade shell from 200 mRL down to -100 mRL (less than 400 m below the present-day surface; Fig. 5.15A). The > 0.7 wt % copper grade shell is elongate (3:2 aspect ratio; long axis = 400 m) and has a shallow plunge towards the north-northwest (25/050°). Copper-gold mineralization is concentrated proximal to and within the Waisoi West quartz-diorite intrusive complex (WWIC) and is commonly hosted in quartz – sulfide veins and as sulfide disseminations. The intrusive complex was emplaced within Wainimala basement volcanics and within the basal portion of the Namosi Andesite Formation (Fig 5.15A).

The Waisoi West intrusive complex is a composite stock comprising sub-vertical, steeply north plunging quartz-diorite intrusions that have an unconstrained vertical continuity (at least 600 m; Fig. 5.15A). Several distinct intrusions based on texture, presence and abundance of veins and the presence of mineralized refractory quartz xenoliths have been identified during this study. However, the relative ages of individual intrusions at Waisoi West are not always well constrained and therefore have been grouped into three composite intrusions, termed the quartz-diorite porphyry 1 (QDP1), quartz-diorite porphyry 2 (QDP2) and quartz-diorite porphyry 3 (QDP3). The alteration and mineralization paragenesis of Waisoi West is presented within the framework of the NSW006 section (Fig. 5.15), and is summarized in Tables 5.5 and 5.6, respectively.

#### *5.2.4.1 Sulfide zonation*

Bornite, chalcopyrite, and pyrite are the principal sulfide minerals at Waisoi West. The dominant sulfide species changes in a zonal arrangement outward from the core of the deposit to its periphery. At the core of Waisoi West is a small zone (400 m N-S) characterized by the presence

**Figure 5.15 (following two pages):** Section NSW006 (1935750 mE), Waisoi West. **A (opposite).** Geology of section NSW006, with distribution of copper and gold mineralization. **B (opposite).** Alteration zonation of section NSW006, with distribution of selected vein stages relative to the Waisoi West quartz-diorite intrusions. **C (page 146).** Diagram of the distribution of sulfide species illustrating the outward transition from bornite > 0.1 vol % to chalcopyrite > 1 vol % to an annular halo of pyrite > 1 vol %. Volume estimates include disseminated and vein-hosted sulfide.

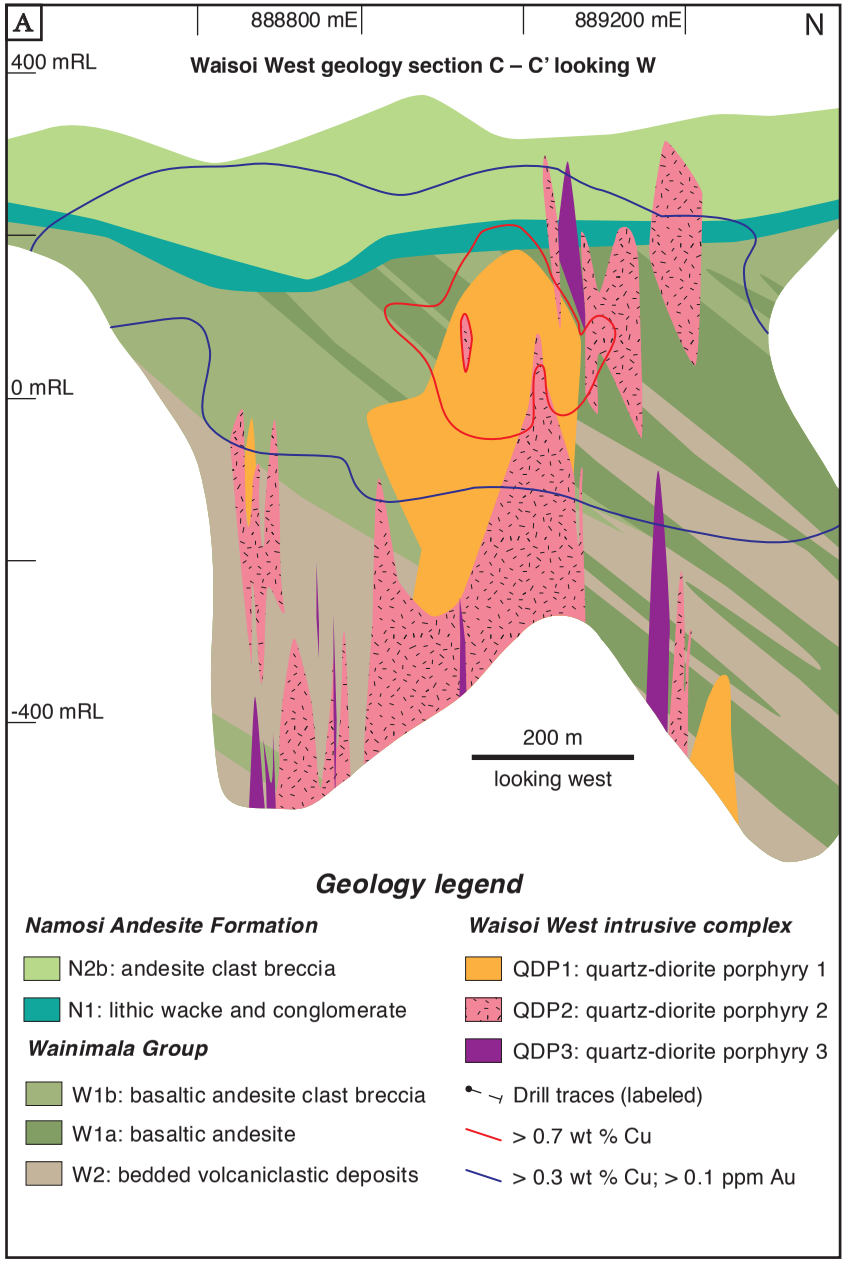
A
888800 mE
889200 mE
N
400 mRL
Waisoi West geology section C – C' looking W
0 mRL
-400 mRL
200 m
looking west
Geology legend
Namosi Andesite Formation
N2b: andesite clast breccia
N1: lithic wacke and conglomerate
Wainimala Group
W1b: basaltic andesite clast breccia
W1a: basaltic andesite
W2: bedded volcaniclastic deposits
Waisoi West intrusive complex
QDP1: quartz-diorite porphyry 1
QDP2: quartz-diorite porphyry 2
QDP3: quartz-diorite porphyry 3
Drill traces (labeled)
> 0.7 wt % Cu
> 0.3 wt % Cu; > 0.1 ppm Au

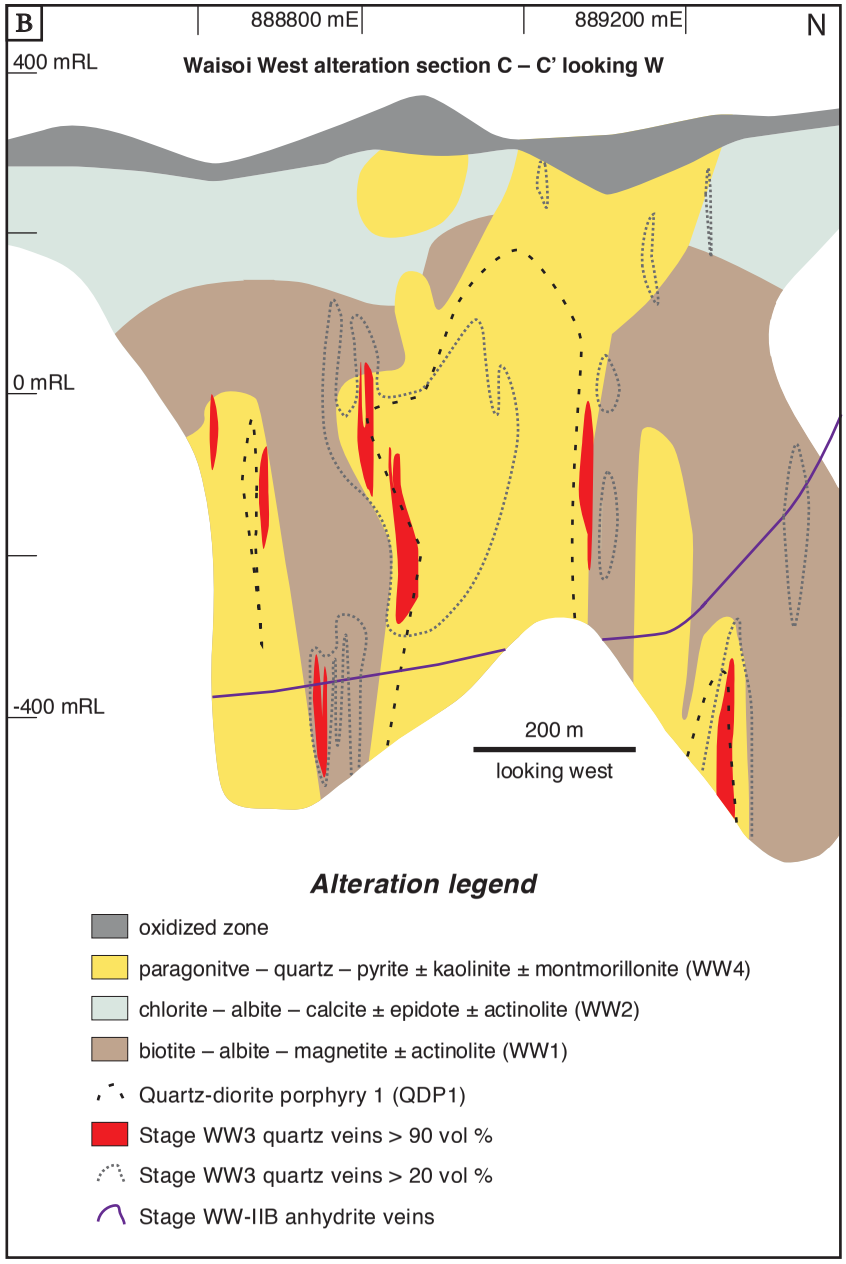
B
888800 mE
889200 mE
N
400 mRL
Waisoi West alteration section C – C' looking W
0 mRL
-400 mRL
200 m
looking west
Alteration legend
oxidized zone
paragonitve – quartz – pyrite ± kaolinite ± montmorillonite (WW4)
chlorite – albite – calcite ± epidote ± actinolite (WW2)
biotite – albite – magnetite ± actinolite (WW1)
Quartz-diorite porphyry 1 (QDP1)
Stage WW3 quartz veins > 90 vol %
Stage WW3 quartz veins > 20 vol %
Stage WW-IIB anhydrite veins

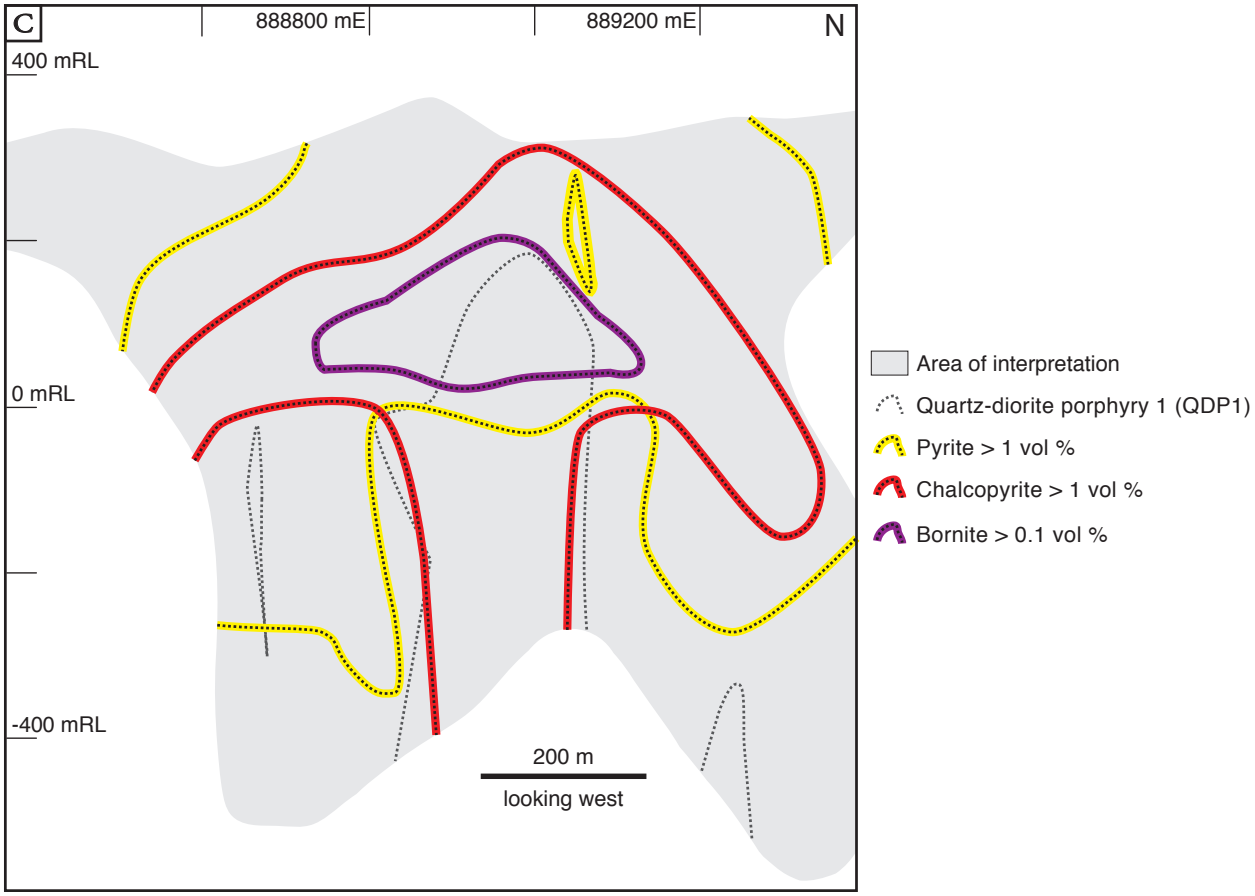


of bornite in quantities > 0.1 vol %. This zone is coincident with the top of the QDP1 intrusion. Surrounding and including the bornite zone, is a mushroom-shaped volume delimiting the extent that chalcopyrite is > 1 vol %. There is an outermost shell of pyrite > 1 vol % (Fig. 5.15C).

*5.2.4.2 Main-stage mineralization, alteration and veins (WW-I)*

Three hydrothermal alteration mineral assemblages are associated with main-stage mineralization at Waisoi West (Table 5.5). The oldest alteration event produced a central zone of biotite – albite – magnetite-altered rocks (WW1) that grade outward to a chlorite – albite – magnetite alteration assemblage (WW2). These alteration zones have been overprinted by albite ± K-feldspar vein-halo alteration (WW3) associated with main-stage veins. On the basis of texture and vein composition, four different stages of veins have been grouped with stage WW3 (Table 5.6).

The composition of feldspar alteration minerals, as phenocrysts and as components within groundmass, were determined using chemical feldspar staining during this study. Within the

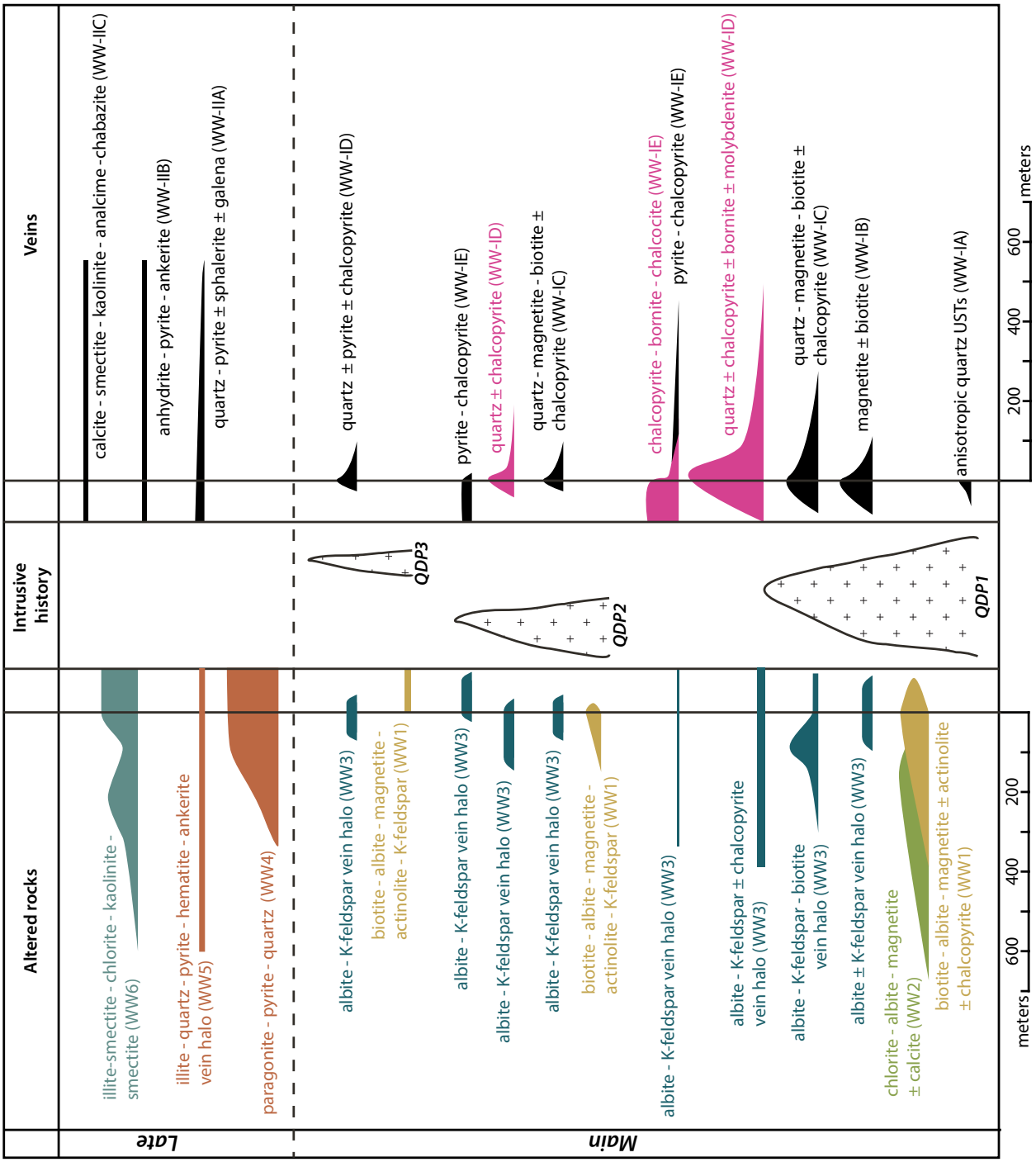


**Figure 5.16:** Schematic space-time diagram illustrating the hydrothermal alteration and vein paragenesis in the Waisoi West Cu-Au porphyry deposit. The relative age of the events are in order of oldest to youngest from the bottom to the top of the diagram. Hydrothermal alteration and veins observed within the mineralized intrusions are illustrated by the colored polygons within the columns immediately adjacent to the intrusive history column. The distribution of each event relative to the mineralized intrusions is depicted by the horizontal component of its colored polygon. The relative intensity of each event is depicted by the vertical component of its respective colored polygon. Abbreviations: QDP1 = quartz-diorite porphyry 1, QDP2 = quartz-diorite porphyry 2, QDP3 = quartz-diorite porphyry 3.

Waisoi West deposit, hydrothermal Na-rich feldspar occurs in association with all main-stage alteration events. Minor K-feldspar occurs with Na-rich feldspar in main-stage vein-halo alteration.

**Table 5.5**: Styles and spatial and temporal distribution of alteration assemblages at the Waisoi West deposit

| Stage | Gangue minerals | Sulfide minerals | Alteration texture and intensity | Spatial and temporal distribution | Related veins |
|---|---|---|---|---|---|
| WW1 | Biotite, albite, magnetite, K-feldspar, actinolite | ccp, bn | Strong, pervasive biotite - albite alteration of Wainimala bedded volcaniclastics (W2); moderate intensity, selective alteration of plagioclase phenocrysts to albite ± K-feldspar and ferromagnesian minerals to biotite - actinolite ± magnetite in the WWIC and Wainimala basaltic andesite-clast breccia; local patchy domains of intense biotite - albite ± chalcopyrite alteration in Wainimala basaltic andesite clast groundmass; local biotite - chalcopyrite alteration spots with strong intensity, pervasive albite alteration rinds within the QDP1 | Pre-dates high-grade copper-gold mineralization associated with quartz veins; occurs within the Wainimala host sequence and within the WWIC; occurs from 100 mRL to below -300 mRL and is > 800 m N–S (other dimensions are undefined) | None |
| WW2 | Chlorite, albite, magnetite, calcite, epidote | py, ccp | Weak to moderate intensity, selective alteration of plagioclase phenocrysts to albite ± calcite and ferromagnesian minerals to chlorite - magnetite; alteration spots of chlorite - albite - calcite or magnetite - albite with intense, pervasive albite alteration rinds occur in the NAF rocks; magnetite - pyrite alteration spots with intense, pervasive albite - chlorite alteration rinds occur in the Wainimala Group | Peripheral and outboard to stage WW1 biotite alteration; the outer limits of this alteration zone have not been defined; restricted to Wainimala and NAF host sequence; overprinted by vein-halo alteration associated with main-stage veins | None |
| WW3 | Albite, K-feldspar, biotite, epidote, calcite, chlorite | ccp | Most commonly presents as strong, pervasive, pale white to cream vein-halo alteration, < 1 to 20 mm thick; vein halos are best developed surrounding stages WW-IC and WW-ID veins and weakly developed surrounding stages WW-IB and WW-IE veinlets and stringers; within the NAF and WW2 alteration domain, WW3 alteration presents as intense, selective albite ± epidote - calcite alteration of plagioclase phenocrysts and feldspathic components of the groundmass; within the WWIC, main-stage veins are surrounded by strong intensity, selective albite ± K-feldspar ± biotite alteration envelopes | Spatially associated with main-stage quartz, magnetite and sulfide veins; overprinted early-formed biotite - albite (WW1) and chlorite - albite (WW2) alteration | WW-IB<br>WW-IC<br>WW-ID<br>WW-IE |
| WW4 | Paragonite, quartz, chlorite, hematite | py | Intense, selective alteration of stage WW1-altered plagioclase to green illite - calcite ± pyrite and weak, partial replacement of ferromagnesian minerals to quartz - chlorite | Preferentially developed in the WWIC; overprints early-formed WW1, WW2 and WW3 alteration assemblages | None |
| WW5 | Illite, quartz, hematite, ankerite | py | Intense, pervasive, white illite - quartz alteration envelopes surrounding stage WW-IIA veins; moderate to strong intensity, selective green illite - hematite alteration of albitized plagioclase phenocrysts within the alteration envelope | Spatially associated with stage WW-IIA veins; widespread distribution; crosscuts WWIC, and the NAF and Wainimala host sequence; overprints early-formed WW1 and WW2 alteration | WW-IIA<br>WW-IIB |
| WW6 | Illite, chlorite, illite-smectite, montmorillonite, kaolinite | py, ccp | Subtle to weak, selective alteration of plagioclase minerals and feldspathic groundmass components to illite ± illite-smectite and ferromagnesian minerals and groundmass components to chlorite | Widespread distribution across the Waisoi West deposit; occurs in all rock types; overprinted all earlier-formed alteration assemblages | WW-IIC |

Abbreviations: bn = bornite, ccp = chalcopyrite, NAF = Namosi Andesite Formation, py = pyrite, QDP1 = quartz-diorite porphyry 1; WWIC = Waisoi West intrusive complex.

**Table 5.6:** Vein stages of the Waisoi West deposit

| Vein Stage | Gangue minerals | Sulfide minerals | Form, associations and textures | Spatial and temporal distribution | Envelope |
|---|---|---|---|---|---|
| WW-IA | Quartz | ccp, bn | Discontinuous, anisotropic, irregular chains of crenulate prismatic quartz layers; diffuse and irregular quartz on one side and euhedral quartz terminating on the other side (with the c-axis at a high angle to the attitude of the layer); aplitic dacite is inter-layered with the quartz bands; disseminated chalcopyrite - bornite occurs within the quartz and aplite layers; interpreted to be USTs; 3 –10 mm layer-aperture | Restricted to margins and apical portions of the QDP1 intrusions; earliest formed hydrothermal feature at Waisoi West | None |
| WW-IB | Magnetite, biotite | ccp | Discontinuous and wispy; diffuse vein walls; both magnetite and biotite veinlets; presents as rare 1 cm-wide clots or miarolitic cavities of biotite - chalcopyrite within the QDP1; < 2 to 4 mm vein aperture | Occurs in the WWIC intrusions as well as the surrounding Wainimala basaltic andesite-clast breccia (up to 100 m from the WWIC margin); crosscut by stage WW-IC and WW-ID veins | ab ± kfs ± bt; φ < 2 mm |
| WW-IC | Quartz, magnetite, biotite | ccp, py | Irregular; saccharoidal-textured anhedral quartz with disseminated magnetite or biotite; magnetite also occurs within a concordant seam along the center of the vein | Occurs in the WWIC intrusions as well as the surrounding Wainimala basaltic andesite-clast breccia (up to 300 m from the WWIC margin); crosscut by stage WW-ID veins; crosscuts stage WW-IB veinlets and stringers | ab-bt-ccp ± kfs; φ < 10 mm |
| WW-ID | Quartz, chlorite | ccp, bn, cc, mo, dg, cv, tn, py | Irregular; saccharoidal-textured anhedral quartz commonly with concordant central seams or distinctive, concordant ribbon-textured banding; central seams are most commonly infilled with sulfide ± chlorite | Volumetrically most significant vein stage at Waisoi West; commonly crosscut by discordant sulfide chains (WW-IE?); crosscuts stage WW-IB and WW-IC magnetite and quartz veins | ab ± kfs ± ccp; φ < 20 mm |
| WW-IE | | ccp, bn, cc, py | Discontinuous and irregularly shaped sulfide-only veinlets and stringers with non-parallel vein walls; < 5 mm vein-aperture | Occurs within QDP1 and QDP2 intrusions; crosscuts stage WW-ID veins | ab ± kfs; φ < 2 mm |
| WW-IIA | Quartz, chlorite | py, ccp, sp, gn | Continuous and straight-sided; sharp and parallel vein walls; gray quartz with brassy pyrite occupies the central seam; surrounded by conspicuous illite - quartz - pyrite vein-halo alteration; 3 – 10 mm vein-aperture | Widely distributed throughout Waisoi West; crosscut by stage WW-IIC veins | ill-qtz-py ± hem; φ = 3 – 10 mm |
| WW-IIB | Anhydrite, ankerite | py | Continuous and straight-sided with sharp parallel margins; ankerite occurs within the vein selvage; pyrite occurs along center of the vein; < 10 mm vein-aperture | Crosscuts QDP2 intrusion; no other crosscutting relationships were observed | None |
| WW-IIC | Calcite, smectite, kaolinite, analcime, chabazite | py | Continuous to discontinuous, red-dish-brown veinlets; straight-sided and sharp-walled; locally occurring as tectonic breccia cement; < 5 mm vein-aperture; < 5 cm breccia zones | Crosscuts all previous vein stages at Waisoi West | None |

Abbreviations: φ = vein-halo width, ab = albite, bn = bornite, bt = biotite, cc = chalcocite, ccp = chalcopyrite, cv = covellite, dg = digenite, gn = galena, hem = hematite, ill = illite, kfs = K-feldspar, mo = molybdenite, py = pyrite, QDP1 = quartz-diorite porphyry 1, QDP2 = quartz-diorite porphyry 2, qtz = quartz, sp = sphalerite, tn = tennantite, UST = unidirectional solidification texture, WWIC = Waisoi West intrusive complex.

*Biotite – albite – magnetite ± actinolite ± K-feldspar alteration (WW1)*

The first stage of hydrothermal alteration at Waisoi West (Table 5.5; Fig. 5.16) affected the WWIC and Wainimala host sequence from approximately 200 mRL to below -450 mRL in a broad zone (> 800 m-wide; Figs. 5.15A, B and 5.16). Stage WW1 produced biotite, albite, magnetite, actinolite and lesser K-feldspar. Hydrothermal biotite ± actinolite occurs as moderate intensity, selective replacements of primary ferromagnesian phenocrysts in both the WWIC and the surrounding Wainimala host sequence (Fig. 5.17E). Within 400 m of the WWIC contacts and below 0 mRL, the Wainimala bedded volcaniclastics (W2) have been pervasively altered to biotite and albite (Fig. 5.17B). Biotite and albite also occur intergrown with chalcopyrite within the QDP1 intrusions, where they present as miarolitic cavities or as biotite – chalcopyrite alteration clots that have pervasive albite-altered halos (Figs. 5.17A and C). Patchy domains of biotite – albite – magnetite have altered the groundmass of the Wainimala basaltic andesite clasts, locally resulting in > 25 vol % biotite in the altered rock (Fig. 5.17D; Appendix B). Ellis (1996) interpreted the first porphyry-related hydrothermal alteration event at Waisoi to be a 'sericitization' consisting of a sericite – quartz ± pyrite mineral assemblage (Table 5.2). There was no evidence encountered during this study to suggest that a sericite – quartz ± pyrite alteration assemblage occurred prior to stage WW1. However, based on crosscutting and overprinting relationships there is evidence to suggest that illite – pyrite – quartz alteration assemblages (WW4 and WW5) and their associated veins (WW-IIA and WW-IIB) post-date the early-stage biotite – albite – magnetite assemblage (described in Tables 5.5 and 5.6).

*Chlorite – albite – magnetite alteration (WW2)*

Chlorite – albite – magnetite alteration (WW2; Table 5.5) occurs on the margins of the biotite – albite – magnetite alteration zone (WW1) and extends beyond the limit of available drilling (> 1 km from the WWIC margin; Figs. 5.15B and 5.16). Stage WW2 is characterized by weak to moderate intensity, selective alteration of the Namosi Andesite Formation and Wainimala host sequence to chlorite, albite, magnetite, calcite, epidote and pyrite (Figs. 5.17F, G and J). Primary magnetite is preserved in this alteration zone. Primary ferromagnesian minerals have been

altered to chlorite ± magnetite and plagioclase phenocrysts have been altered to albite ± calcite (Fig. 5.17J). Alteration clots consisting of chlorite – albite – calcite and clast-selective magnetite – albite alteration with pervasive albite halos occurs within the Namosi Andesite Formation above 200 mRL (Figs. 5.15B, 5.17F and J). Within the Wainimala basaltic andesite-clast breccia, secondary magnetite forms clumps surrounding amygdules and albite-altered plagioclase phenocrysts (Fig. 5.17H). Alteration clots consisting of magnetite – pyrite ± chalcopyrite with albite – chlorite halos occurs in increasing abundance toward the WW1 alteration zone (Fig. 5.17G).

*Anisotropic quartz layers (WW-IA)*

The earliest formed quartz-bearing hydrothermal features at Waisoi West are crenulate-textured quartz layers (Table 5.6). The bands are typically discontinuous, anisotropic, irregular and contorted chains of prismatic quartz that are crosscut by all other vein stages at Waisoi West (Figs. 5.16, 5.18A, and 5.20A). They are similar to the anisotropic "partial brain rock" features documented at the E26 porphyry Cu-Au deposit (cf., Lickfold et al., 2003). The layers are irregular and diffuse on one side, with euhedral quartz terminating on the opposite side (Fig. 5.20A). Plagioclase – quartz aplite fills the gaps between the apex of terminated quartz crystals, and is also inter-layered between separate quartz bands. These anisotropic features can be interpreted as unidirectional solidification textures (USTs; e.g., Shannon et al., 1982). These USTs are concordant with the contact of the QDP1 stock and surrounding Wainimala wall rock.

**Figure 5.17 (opposite):** Styles of main-stage biotite – albite – magnetite (WW1) and chlorite – albite – magnetite (WW2) alteration at Waisoi West. **A.** Interval of QDP1 that has been treated with chemical feldspar staining. Diffuse albite alteration rims (white) surround biotite – chalcopyrite alteration spots. The QDP1 has been crosscut by stage WW-ID quartz veins that have a halo of K-feldspar – albite (orange-yellow). Sample: NSW006 316 m. **B.** Characteristic sample of Wainimala sandstone illustrating strong biotite and albite alteration domains. Sample: NSW014 534 m. **C.** Closeup view of an alteration clot of biotite – chalcopyrite from Fig. 5.17A that is surrounded by an albite ± K-feldspar alteration rim. Sample: NSW006 316 m. **D.** Cross-polarized photomicrograph of Wainimala basaltic andesite-clast breccia illustrating patchy domains of biotite – albite alteration. Albite has replaced the rims of primary plagioclase minerals. Sample: WSD212 195.8 m. **E.** Cross-polarized photomicrograph of a primary ferromagnesian mineral that has been totally replaced by biotite – actinolite. Sample: WSD212 195 m. **F.** Characteristic interval of Namosi Andesite Formation andesite-clast breccia with a chlorite – albite – calcite alteration clot. Sample: NSW001 84 m. **G.** Characteristic interval of Wainimala amygdaloidal basaltic andesite with a magnetite – pyrite – chalcopyrite alteration clot that is surrounded by an albite – chlorite alteration rim. Sample: NSW014 420 m. **H.** Cross-polarized photomicrograph illustrating disseminated magnetite throughout the Wainimala basaltic andesite groundmass and clumps of magnetite that have surrounded amygdules and primary feldspar phenocrysts. Sample: WSD212 355.3 m. **I.** Interval of Namosi Andesite Formation andesite-clast breccia that has been crosscut by stage WW-ID quartz veins with discordant chlorite – pyrite chains and veinlets that have a halo of albite – epidote alteration. Sample: NSW006 78 m. **J.** Interval of Namosi Andesite Formation andesite-clast breccia with an andesite clast that has been partially replaced by magnetite and has a halo of albite alteration. Primary ferromagnesian minerals have been totally replaced by chlorite – magnetite. Sample: NSW006 39 m. Abbreviations: ab = albite, act = actinolite, am = amygdule, bt = biotite, cal = calcite, ccp = chalcopyrite, chl = chlorite, ep = epidote, kfs = K-feldspar, mag = magnetite, pl = plagioclase, py = pyrite, QDP1 = quartz-diorite porphyry 1.

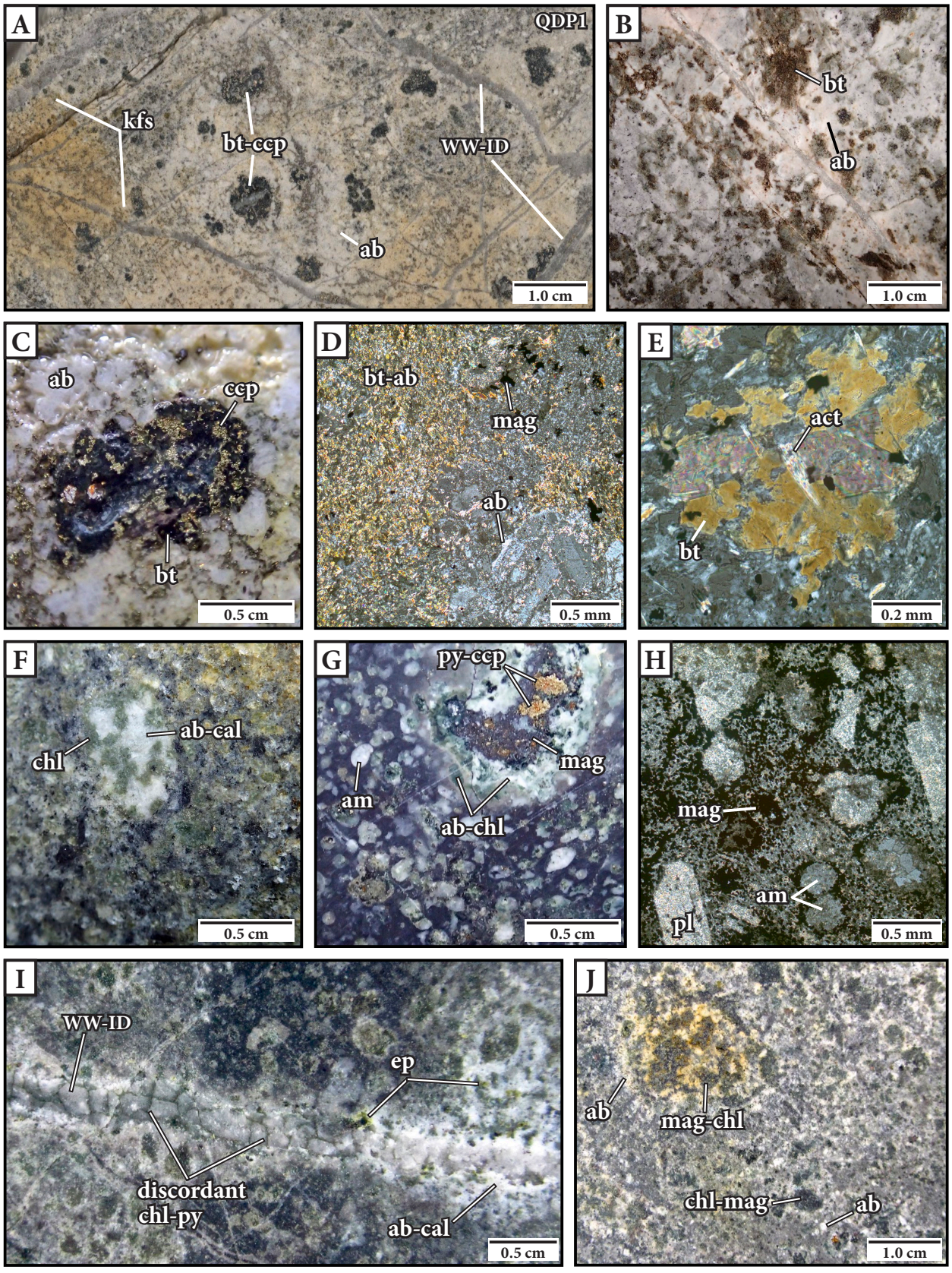
A
QDP1
kfs
bt-ccp
WW-ID
ab
1.0 cm
B
bt
ab
1.0 cm
C
ab
ccp
bt
0.5 cm
D
bt-ab
mag
ab
0.5 mm
E
act
bt
0.2 mm
F
chl
ab-cal
0.5 cm
G
py-ccp
mag
am
ab-chl
0.5 cm
H
mag
am
pl
0.5 mm
I
WW-ID
ep
discordant
chl-py
ab-cal
0.5 cm
J
ab
mag-chl
chl-mag
ab
1.0 cm

*Albite ± K-feldspar ± biotite ± epidote ± calcite vein-halo alteration (WW3)*

Albite, K-feldspar, biotite, epidote and calcite locally occur as a pervasive to selective vein-halo alteration assemblage surrounding main-stage magnetite and quartz veins (WW-IB, WW-IC and WW-ID; Table 5.5; Figs. 5.18, 5.19 and 5.20). The distribution of this alteration style is equivalent to the distribution of main-stage veins (Fig. 5.16). The veins occur in the central portion of the deposit and extend from depth to within 50 m of the present-day surface. Although the distribution of stage WW3 is widespread, the alteration envelopes surrounding main-stage veins are highly variable, ranging from < 1 to 20 mm from the vein margins. Stage WW3 alteration envelopes that overprinted the Namosi Andesite Formation within the WW2 alteration domain consist of selective alteration of plagioclase to white albite ± epidote and calcite (Fig. 5.17I). Stage WW3 vein-halo alteration within the WWIC comprises a weakly developed, selective alteration of albitized plagioclase to albite ± K-feldspar and ferromagnesian minerals to biotite (Figs. 5.18E and 5.19A). WW3 vein-halo alteration is magnetite-destructive.

*Magnetite and biotite veinlets (WW-IB)*

Stage WW-IB (Table 5.6) is characterized by thin (< 2 to 4 mm), discontinuous veinlets and stringers of magnetite or biotite with narrow (< 3 mm), white albite ± K-feldspar alteration halos (WW3; Figs. 5.18B, D and 5.20C). The vein walls are diffuse and non-parallel and the vein shapes are irregular. Stage WW-IB veinlets are most commonly found in the QDP1 and QDP2 intrusions, but can be found in a substantially decreased abundance within the QDP3 intrusions and the surrounding Wainimala host sequence (up to 100 m away from the WWIC margin; Fig. 5.16). Stage WW-IB veins are crosscut by stage WW-IC and WW-ID quartz veins (Figs. 5.18B, D and 5.20C).

*Quartz ± magnetite ± biotite veins (WW-IC)*

The earliest observed multimineralic quartz veins at Waisoi West (Table 5.6) are composed of variable quantities of quartz, magnetite, biotite and chalcopyrite. The quartz in stage WW-IC

veins is gray, anhedral, has a variable grain size and has a distinctive sugary texture (Figs. 5.18C, E and F). Magnetite occupies the interstices of coarser-grained quartz, while biotite and chalcopyrite occurs disseminated throughout the veins and within the alteration halo (Figs. 5.18E and F). Stage WW-IC veins commonly display concordant magnetite banding, although they occasionally have no internal texture. The veins are variable in width (1 – 20 mm), discontinuous, have an irregular form and have a variable thickness (< 1 to 10 mm) of moderate to strong albite ± biotite ± K-feldspar alteration halos (WW3; Figs. 5.18C and E). These veins are most commonly found within the QDP1 and QDP2 intrusions, although they also occur in less abundance within QDP3 and the Wainimala host sequence (up to 300 m from the WWIC margin; Fig. 5.16). These veins typically crosscut stage WW-IB quartz veins and have been crosscut by stage WW-ID quartz veins (Figs. 5.18C, D and 5.20C).

*Saccharoidal-textured quartz veins (WW-ID)*

Stage WW-ID is the most significant vein stage by volume at Waisoi West and typically occurs as quartz-vein stockworks (Table 5.5; Fig. 5.20D). Locally, stage WW-ID laminated quartz-vein stockworks comprise > 90 % of the drill core by volume (Figs. 5.20D and E). Stage WW-ID quartz veins are similar to stage WW-IC quartz veins in texture, however, they lack magnetite and biotite and commonly contain sulfide minerals. Stage WW-ID veins are continuous, straight-sided to wavy and typically have sharp and parallel vein walls. Stage WW-ID veins most commonly occur as massive anhedral quartz veins that are crosscut by discordant chalcopyrite, bornite, chlorite, and pyrite hairline veinlets. Some of these veins display distinctive concordant banding (e.g., Figs. 5.18A and C). The second style of WW-ID quartz veins contains a concordant central cavity that is commonly filled by sulfide minerals (Fig. 5.19A). Within the QDP1 intrusions, sulfide infill consists of chalcopyrite after bornite that is intergrown with chalcocite and digenite and is partially replaced by covellite locally (Figs. 5.19A, C and D). Where present, molybdenite occurs within the central seam of the quartz veins (Fig. 5.19E). Albite ± K-feldspar ± chalcopyrite vein-halo alteration is strongly developed surrounding this vein type (< 10 mm; Fig. 5.20C).

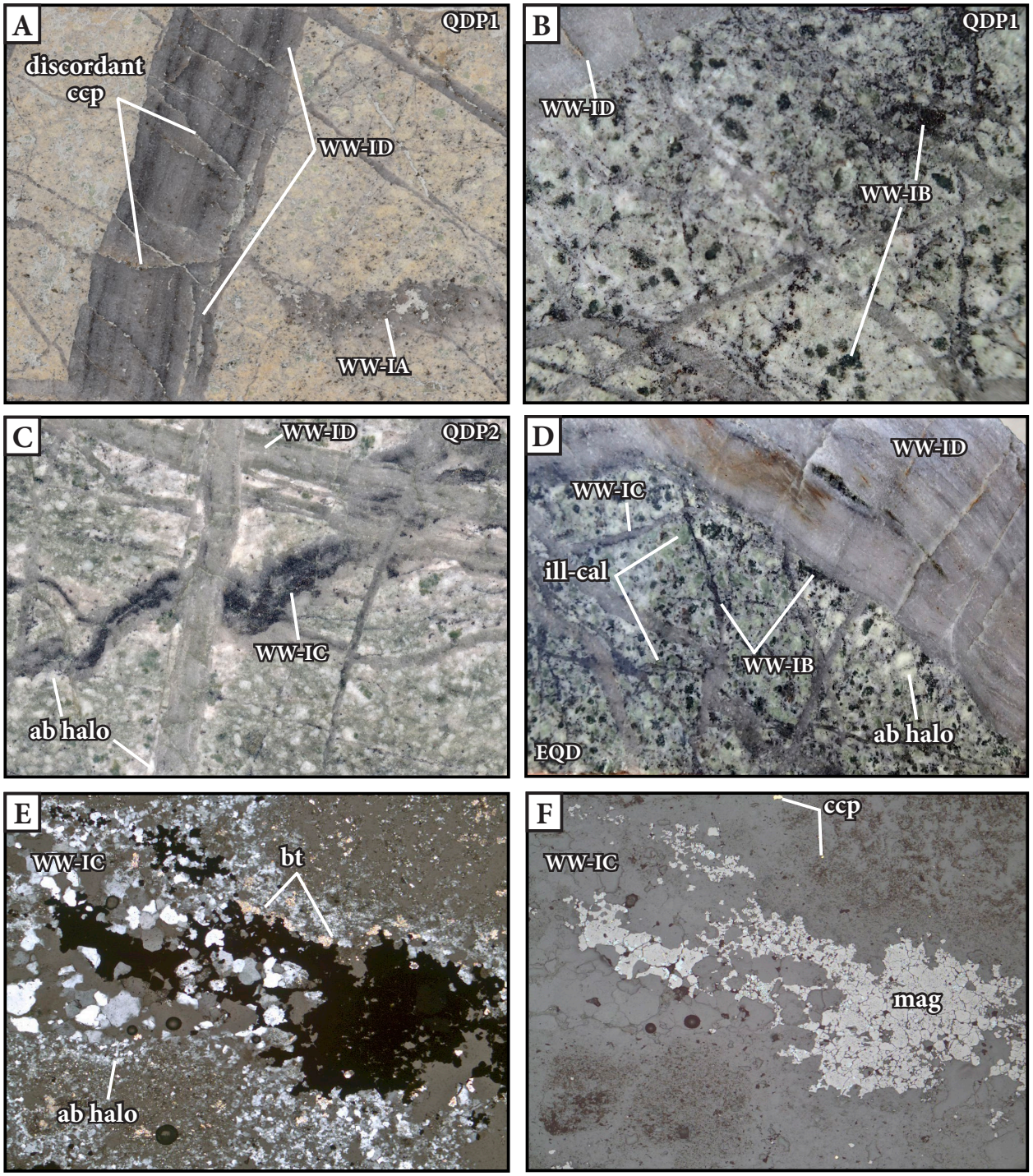


**Figure 5.18:** Examples of main-stage vein styles at Waisoi West. **A.** Interval of QDP1 containing stage WW-IA comb quartz USTs and finely banded stage WW-ID quartz with discordant chalcopyrite chains and veinlets. Sample: NSW006 355 m. **B.** Interval of intensely albite – illite-altered QDP1 that has been crosscut by stage WW-IB magnetite veinlets. Magnetite veinlets have been crosscut by stage WW-ID quartz veins that contain discordant chalcopyrite veinlets. Sample: NSW001 646 m. **C.** Interval of albite – illite-altered QDP2 crosscut by stage WW-IC quartz – magnetite – biotite veins with albite vein-halos. Quartz – magnetite – biotite veins have been crosscut by finely laminated stage WW-ID quartz veins with albite vein halos. Sample: NSW001 940 m. **D.** Interval of intense green illite – albite-altered QDP1 crosscut by stage WW-IB magnetite – biotite veinlets. Magnetite veinlets have been crosscut by stage WW-IC quartz – magnetite veins. Magnetite-bearing veins have been crosscut by finely laminated stage WW-ID quartz veins. Sample: NSW001 634 m. **E.** Cross-polarized photomicrograph of Wainimala basaltic andesite-clast breccia containing a stage WW-IC quartz – magnetite – biotite vein. Magnetite occupies the coarser-grained quartz interstices and biotite occurs as fine-grained disseminations throughout the vein and vein halo. Weakly developed albite – biotite vein-halo alteration surrounds the stage WW-IC vein. Sample: NSW006 271 m. **F.** Reflected light photomicrograph illustrating that the opaque minerals in Fig. 5.18E are magnetite and lesser chalcopyrite. Sample: NSW006 271 m. Abbreviations: ab = albite, bt = biotite, cal = calcite, ccp = chalcopyrite, ill = illite, mag = magnetite, QDP1 = quartz-diorite porphyry1, QDP2 = quartz-diorite porphyry 2.

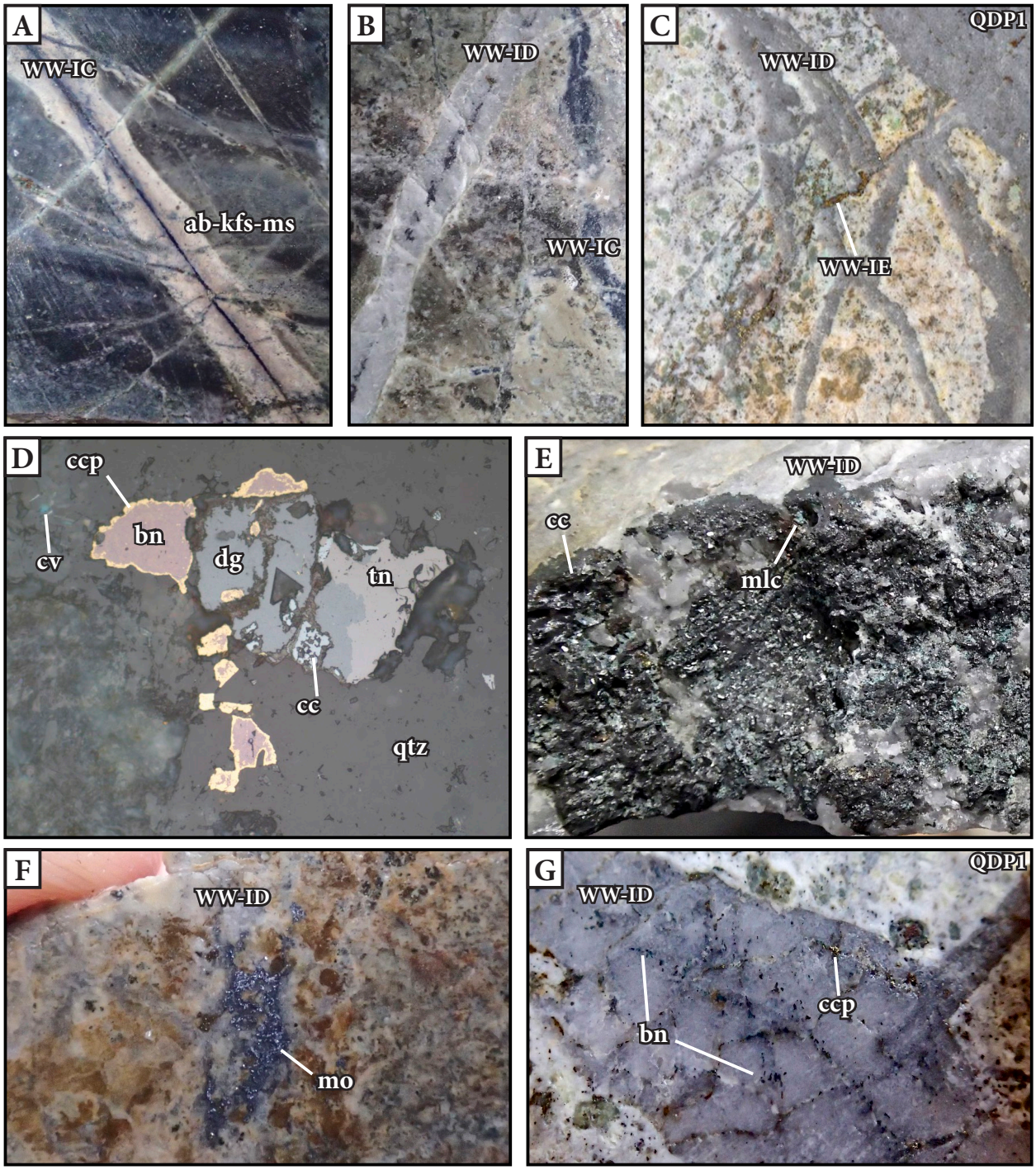


**Figure 5.19:** Examples of main-stage vein styles and the character of copper sulfide and molybdenite mineralization at Waisoi West. **A.** Interval of Wainimala mudstone that has been crosscut by stage WW-IC veins with conspicuous albite – K-feldspar – muscovite alteration halos. Sample: NSW014 637 m. **B.** Interval of Wainimala sandstone that has been crosscut by a stage WW-IC quartz – magnetite vein. The stage WW-IC vein has been crosscut by a stage WW-ID quartz – sulfide vein. Sample: NSW014 645 m. **C.** Interval of intense albite – illite – K-feldspar-altered QDP1 that has been crosscut by stage WW-ID quartz veins. Quartz veins have been crosscut by stage WW-IE copper sulfide veins. Green color surrounding WW-IE veins is caused by malachite in weathered albite – K-feldspar vein halos. The sample was treated with chemical feldspar staining revealing the distribution of albite (no color change) and K-feldspar (orange-yellow color). Sample: NSW006 365 m. **D.** Reflected light photomicrograph of chalcopyrite after bornite and digenite and chalcocite that has replaced chalcopyrite and tennantite. Fine-grained covellite has locally replaced the margins of chalcopyrite. The copper minerals occur within stage WW-ID open-space quartz veins along its central seam in the QDP1 intrusion. Sample: NSW006 342 m. **E.** Interval of QDP1 crosscut by stage WW-ID open-space quartz veins with chalcocite, malachite and chalcopyrite occupying the central seam. This sample belongs to a two meter composite interval that has 2.82 wt % Cu and 1.72 g/t Au. Sample: NSW006 351 m. **F.** Interval of Wainimala sandstone crosscut by stage WW-ID open-space quartz veins with molybdenite occupying the open spaces. NSW014 472 m. **G.** Interval of QDP1 crosscut by stage WW-ID quartz veins with discordant bornite and chalcopyrite chains and veinlets. Sample: NSW001 324 m. Abbreviations: ab = albite, bn = bornite, cc = chalcocite, ccp = chalcopyrite, cv = covellite, dg = digenite, kfs = K-feldspar, mlc = malachite, mo = molybdenite, ms = muscovite, QDP1 = quartz-diorite porphyry 1, qtz = quartz, tn = tennantite.

*Sulfide veinlets and stringers (WW-IE)*

The final vein style associated with main-stage WW3 vein-halo alteration is stage WW-IE sulfide veinlets and stringers (Table 5.6). Within the QDP1 intrusions, these veinlets are principally composed of chalcopyrite – bornite ± chalcocite (Fig. 5.19B). Within the Namosi Andesite Formation and Wainimala Group rocks, stage WW-IE veinlets are composed of pyrite – chalcopyrite. The sulfide-only veinlets are primarily < 4 mm in vein aperture and have rare, thin (< 1 to 3 mm), weakly developed, pervasive albite ± K-feldspar alteration halos (Fig. 5.29B).

*5.2.4.3 Late-stage alteration and veins (WW-II)*

Several alteration and vein types postdate main-stage mineralization and alteration at Waisoi West. The late timing of these veins and alteration stages have been constrained by crosscutting and overprinting relationships identified during drill core logging and thin-section petrography. Most of the late-stage alteration assemblages and veins contain variable amounts of carbonate, paragonite, and illite-smectite, and the dominant sulfide mineral is pyrite.

*Paragonite – quartz – pyrite ± calcite alteration (WW4)*

Late-stage WW4 paragonite – quartz – pyrite alteration is comprised of a white to pale green paragonite, calcite, quartz, hematite, and pyrite alteration assemblage that has variably overprinted all earlier-formed alteration assemblages (Table 5.5). Stage WW4 alteration is preferentially developed in the WWIC and becomes progressively more intense upwards and outwards, causing strong alteration of stage WW1-altered plagioclase to paragonite – calcite ± pyrite (Figs. 5.18D and 5.21A) and weak, partial replacement of ferromagnesian minerals to chlorite – quartz. Stage WW3-altered plagioclase crystals that have been overprinted by stage WW4 illite – pyrite alteration typically retain their white to cream color (Figs. 5.18C and D).

*Illite – pyrite ± carbonate alteration (WW5)*

A second style of illite – pyrite alteration, comprising green to white illite, quartz, hematite,

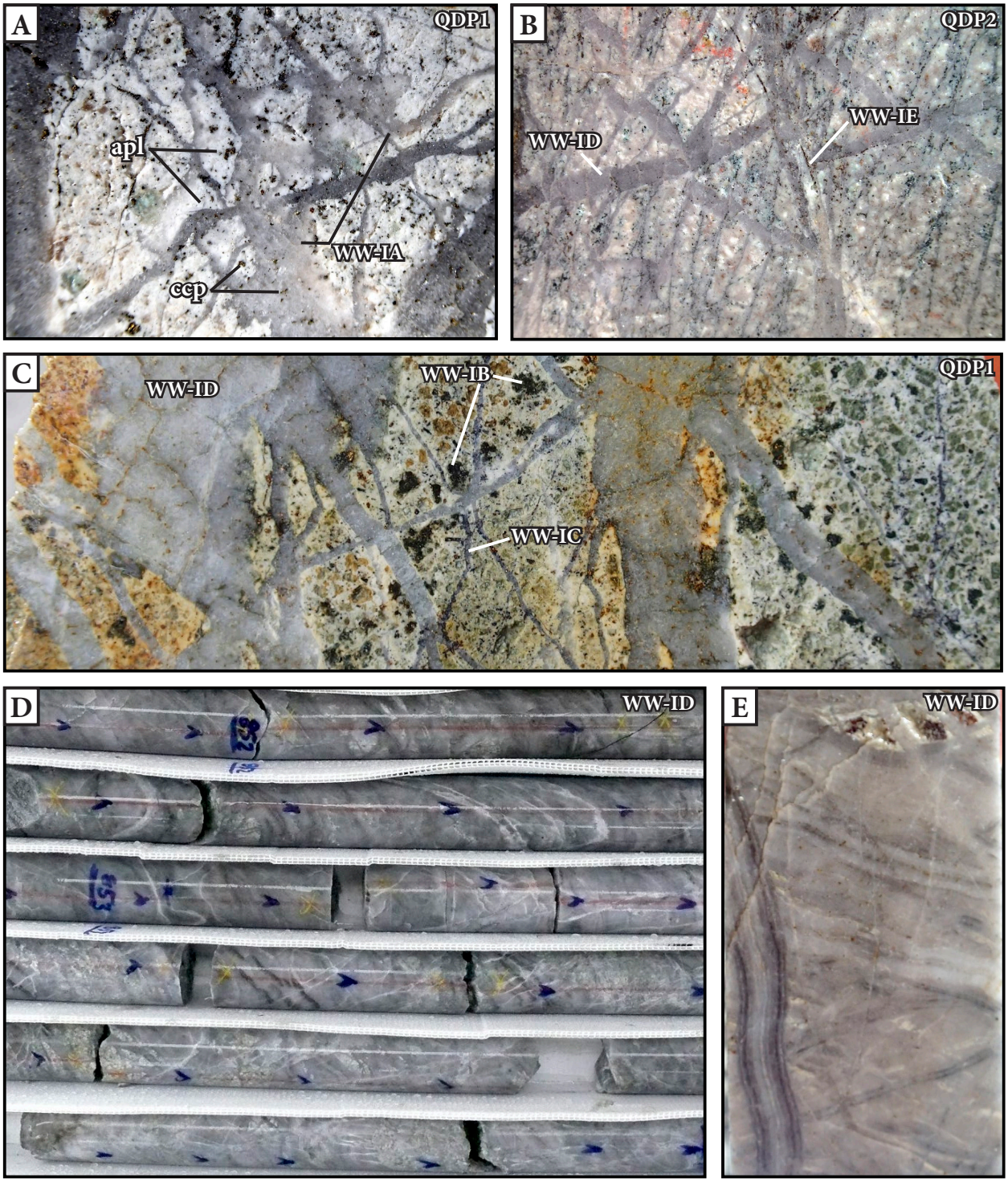


**Figure 5.20:** Examples of main-stage veins at Waisoi West. **A.** QDP1 containing stage WW-IA crenulate quartz layers that are inter-layered with plagioclase > quartz aplite. Chalcopyrite and bornite are disseminated throughout the layers. Sample: NSW006 366 m. **B.** Interval of QDP2 that is crosscut by stage WW-ID quartz veins. The quartz veins are crosscut by stage WW-IE chalcopyrite veinlets. Sample: NSW006 484 m. **C.** Interval of QDP1 crosscut by stage WW-IB biotite veins. The biotite veins have been crosscut by stage WW-IC quartz – magnetite veins. The quartz – magnetite veins have been crosscut by stage WW-ID quartz veins with discordant chalcopyrite chains and veinlets. Sample: NSW006 336 m. **C.** Core box photograph of stage WW-ID laminated quartz vein stockwork. The stockwork comprises > 90 % of the rock by volume over a 10 m interval. (NSW006 852 – 855 m). **E.** Stage WW-ID laminated quartz vein stockwork. Sample: NSW006 844 m. Abbreviations: apl = aplite, ccp = chalcopyrite, QDP1 = quartz-diorite porphyry 1, QDP2 = quartz-diorite porphyry 2.

pyrite and carbonate, is restricted to vein-halo alteration surrounding late-stage WW-IIA veins (Table 5.5; Figs. 5.21B, D and F). Strong to intense, pervasive, white illite – quartz alteration has surrounded stage WW-IIA quartz – pyrite veins up to 15 mm from their vein margins (Figs. 5.21B, D and F). Locally, selective green illite and hematite has altered plagioclase phenocrysts within the vein-halo alteration domain (Figs. 5.21B).

*Quartz – pyrite veins (WW-IIA)*

Stage WW-IIA quartz – pyrite veins have a widespread distribution at Waisoi West (Table 5.6; Fig. 5.16). These veins are composed of gray quartz and brassy pyrite with minor amounts of sphalerite, galena and chalcopyrite (Figs. 5.21B, D, and F). Stage WW-IIA veins are continuous and straight-sided, with sharp and parallel vein walls. Typically pyrite occurs along the center of the quartz veins and as disseminations throughout the alteration envelope. Stage WW-IIA veins are commonly discrete with a variable vein aperture (5 to 20 mm-wide) and have a conspicuous illite – pyrite – quartz ± carbonate ± hematite alteration envelope (WW5; Fig. 5.21D).

*Anhydrite – pyrite veins (WW-IIB)*

Rare WW-IIB veins (Table 5.6) crosscut all intrusive phases at Waisoi West and are most abundant below -100 mRL. These veins are characterized by medium-grained anhydrite with interstitial pyrite and commonly have an ankerite vein selvage (Fig. 5.21C). Stage WW-IIB veins have a vein aperture that is consistently < 10 mm. No vein-halo alteration has been observed surrounding these anhydrite veins. Due to the sparse distribution of stage WW-IIB veins, crosscut-

**Figure 5.21 (opposite):** Styles of late-stage paragonite – quartz – pyrite (WW4 and WW5) and chlorite – illite-smectite (WW6) alteration and their associated veins at Waisoi West. **A.** Cross-polarized photomicrograph of illite, calcite and pyrite that has replaced the core of a primary plagioclase phenocryst within an interval of basaltic andesite-clast breccia. Sample: NSW006 202 m. **B.** QDP1 that has been crosscut by stage WW-IIA quartz – pyrite veins with a distinct illite and hematite alteration halo. Sample: NSW006 271 m. **C.** Wainimala sandstone that has been crosscut by a stage WW-IIB anhydrite – pyrite vein with a selvage of ankerite. Sample: NSW014 450 m. **D.** QDP2 that has been crosscut by a stage WW-ID quartz vein. A narrow (< 5 mm-wide) pyrite – chalcopyrite veinlet with an intense white illite – quartz alteration halo has crosscut the older quartz vein stage. Sample: NSW006 276 m. **E.** QDP2 that has been crosscut by a stage WW-IIA pyrite – quartz vein with pyrite – ankerite vein-halo alteration. Sample: NSW006 271 m. **F.** QDP2 that has been crosscut by a stage WW-IIA quartz – pyrite vein with illite vein-halo alteration. The quartz – pyrite vein has been crosscut by a stage WW-IIC calcite vein. Sample: NSW006 514 m. **G.** Cross-polarized photomicrograph showing partial illite replacement of primary plagioclase phenocrysts. Sample: NSW006 624 m. **H.** Cross-polarized photomicrograph showing partial replacement of hydrothermal biotite by chlorite. Sample: NSW006 271 m. **I.** Interval of QDP2 that has been crosscut by stage WW-ID quartz veins. The quartz veins have been crosscut by a stage WW-IIC calcite vein. Sample: NSW006 884 m. **J.** Interval of QDP2 that has been crosscut and brecciated by stage WW-IIC. Stage WW-IIC fracture zones are typically brittle and contain angular wall rock clasts with no evidence of transportation or milling. Sample: NSW010 622 m. **K.** Stage WW-IIC montmorillonite – kaolinite – calcite – zeolite vein with coarse-grained euhedral analcime and chabazite. Sample: WSD215 204 m. Abbreviations: anh = anhydrite, ank = ankerite, anl = analcime, bt = biotite, cal = calcite, cbz = chabazite, ccp = chalcopyrite, chl = chlorite, hem = hematite, ill = illite, pl = plagioclase, py = pyrite, qtz = quartz.

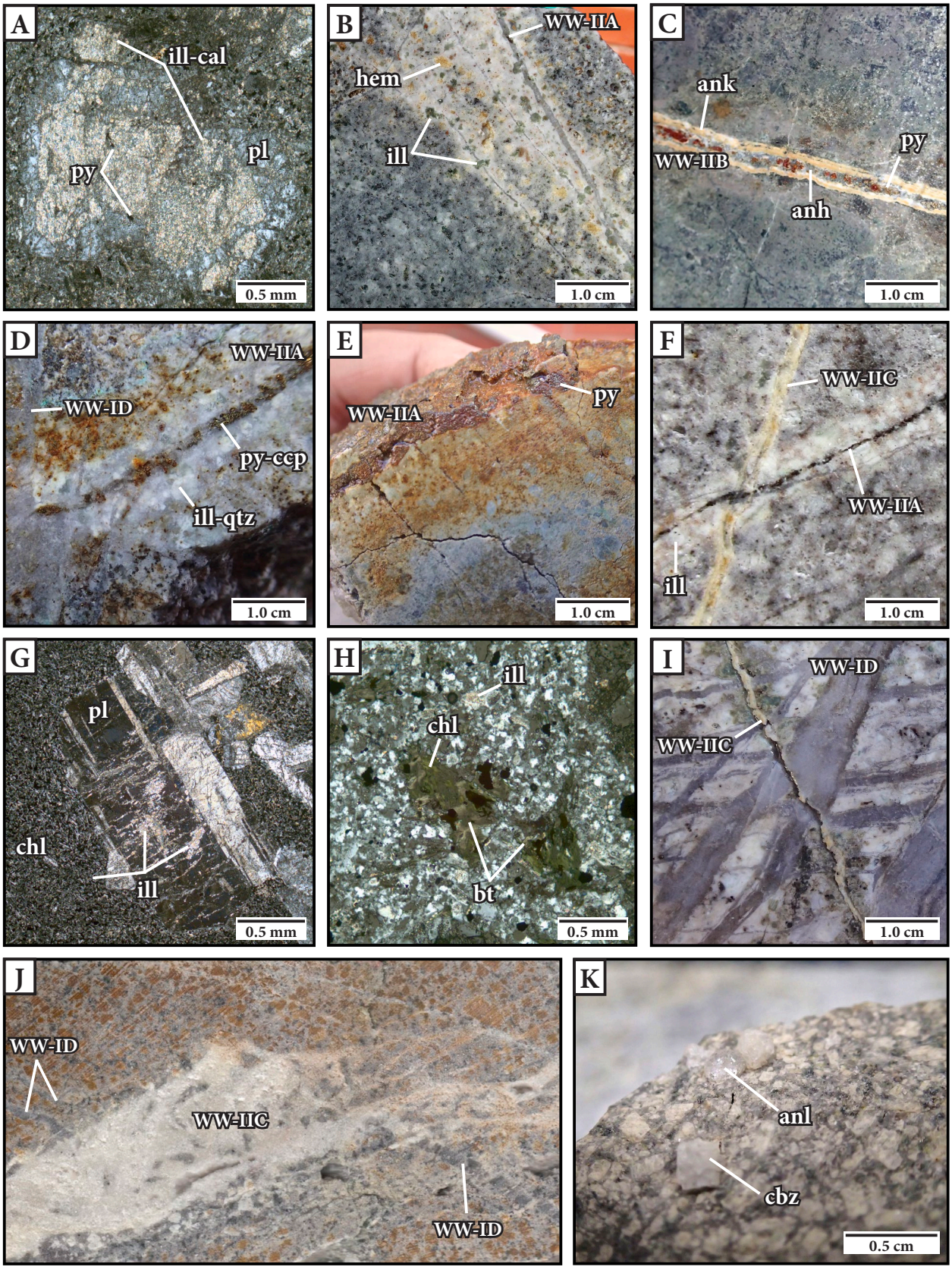
A
ill-cal
pl
py
0.5 mm
B
WW-IIA
hem
ill
1.0 cm
C
ank
WW-IIB
py
anh
1.0 cm
D
WW-IIA
WW-ID
py-ccp
ill-qtz
1.0 cm
E
WW-IIA
py
1.0 cm
F
WW-IIC
WW-IIA
ill
1.0 cm
G
pl
chl
ill
0.5 mm
H
ill
chl
bt
0.5 mm
I
WW-ID
WW-IIC
1.0 cm
J
WW-ID
WW-IIC
WW-ID
K
anl
cbz
0.5 cm

ting relationships with other vein stages have not been observed during this study. The occurrence of carbonate and pyrite has resulted in their classification as late-stage veins.

*Chlorite – illite alteration (WW6)*

Late-stage WW6 chlorite – illite alteration consists of a widespread, weak, selective alteration assemblage of illite, illite-smectite and chlorite that has overprinted all earlier alteration assemblages (WW1 to WW5) at Waisoi West (Table 5.5). Illite and illite-smectite occur as a subtle to weak dusting of plagioclase phenocrysts and groundmass components (Figs. 5.21G and H). Chlorite occurs as weak, selective alteration of Wainimala basaltic andesite-clast groundmass and as partial replacement of biotite-altered ferromagnesian minerals in both the WWIC and surrounding Wainimala host sequence. (Figs. 5.21G and H).

*Calcite ± montmorillonite ± gypsum ± zeolite veins (WW-IIC)*

Stage WW-IIC calcite-bearing veins (Table 5.6) are the youngest vein stage recognized at Waisoi West and have a widespread distribution throughout the deposit (Fig. 5.16). These veins are composed of calcite, gypsum, pyrite, hematite, montmorillonite, and zeolite. They occur as straight-walled, planar fracture coatings or as wispy, uneven veins up to 5 cm wide (Figs. 5.21I and J). Minor pyrite occurs locally, but no copper or gold mineralization has been observed. Stage WW-IIC veins have crosscut all alteration assemblages and all main-stage veins (Figs. 5.21I and J) and late-stage WW-IIA quartz – pyrite veins (Fig. 5.21F). No direct timing relationship with stage WW-IIB anhydrite – pyrite veins has been observed. Stage WW-IIC carbonate veins do not have significant alteration envelopes.

### 5.2.5 Waisoi East Cu-Au-Mo porphyry deposit

This section focuses on documenting the characteristics and paragenesis of copper, gold and molybdenum mineralization and hydrothermal alteration at the Waisoi East Cu-Au-Mo porphyry deposit. Waisoi East is located immediately east of Waisoi West and approximately 6.5 km north-northwest of Wainaulo (Fig. 3.1). The 0.3 wt % Cu grade shell is shallow (< 400 m from the present-day surface; Fig. 5.22A), elongate (3:2 aspect ratio; long axis = 1 km) and has a shallow plunge towards the north-northwest (Fig. 5.22A). Copper and gold mineralization is closely associated with multiple generations of quartz – sulfide veins and sulfide disseminations (Figs. 5.23 and 5.24). Significant molybdenum is hosted in quartz – molybdenite stockwork veins that have overprinted the early Cu-Au-bearing veins (Fig. 5.24C). Most of the Cu, Au and Mo occurs in the Wainimala Group host sequence, with a minor portion hosted in dacitic porphyry intrusions (Fig. 5.22A). The Waisoi East deposit is exposed at surface but has undergone limited weathering and oxidation. Although supergene enrichment occurs in some porphyry Cu deposits (e.g., Chuquicamata: Ossandón et al., 2001; Bayugo: Braxton and Mathur, 2011), no significant supergene copper mineralization has been noted at Waisoi East, probably due to the tropical weathering environment, where erosion rates are likely to out-strip accumulation (e.g., Chávez, 2000).

The dacitic intrusions at Waisoi East are composed of at least three medium-K, calc-alkaline, hornblende-bearing, quartz-feldspar-phyric stocks and pipes (DP1: quartz-eye dacite; DP2: quartz-bearing dacite and DP3: dacite porphyry). They intruded the Wainimala volcanics and are spatially coincident with Cu-Au-Mo mineralization (Fig. 5.22A). The intrusions are texturally and compositionally similar. Contact relationships between different intrusive phases have not been observed in this study. However, the intrusions can be distinguished based on quartz phenocryst abundance, copper-gold grades and presence of quartz-vein xenoliths (Fig. 5.25).

Ten hydrothermal alteration assemblages and eight vein types were documented from logging drill core on section NSE002 (Figs. 3.1, 5.22). The spatio-temporal distribution of hydrothermal alteration assemblages and their associated veins is illustrated in Figure 5.23 and summarized in Tables 5.7 and 5.8.

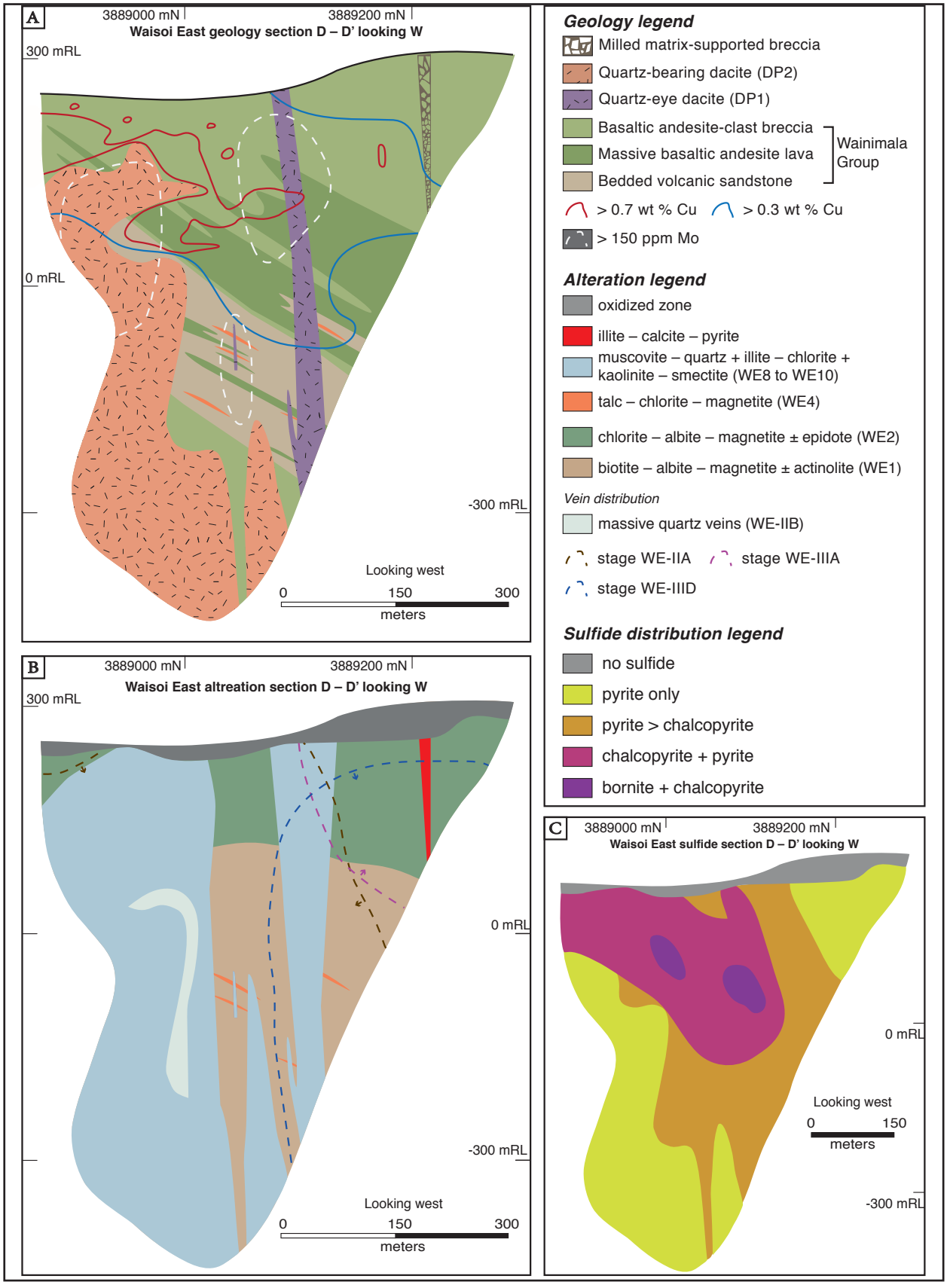


**Figure 5.22:** Section NSE002 (1937550 mE), Waisoi East. **A.** Geology of section NSE002, with distribution of copper and molybdenum mineralization. **B.** Alteration zonation of section NSE002 with distribution of selected vein stages relative to the Waisoi East dacitic intrusions. Muscovite – quartz (WE8), illite – chlorite (WE9) and kaolinite – smectite (WE10) have an ubiquitous distribution, however they are most intense and prominent overprinting the dacite porphyries. **C.** Distribution of sulfide species. Cross section location of D–D' on Fig. 3.6.

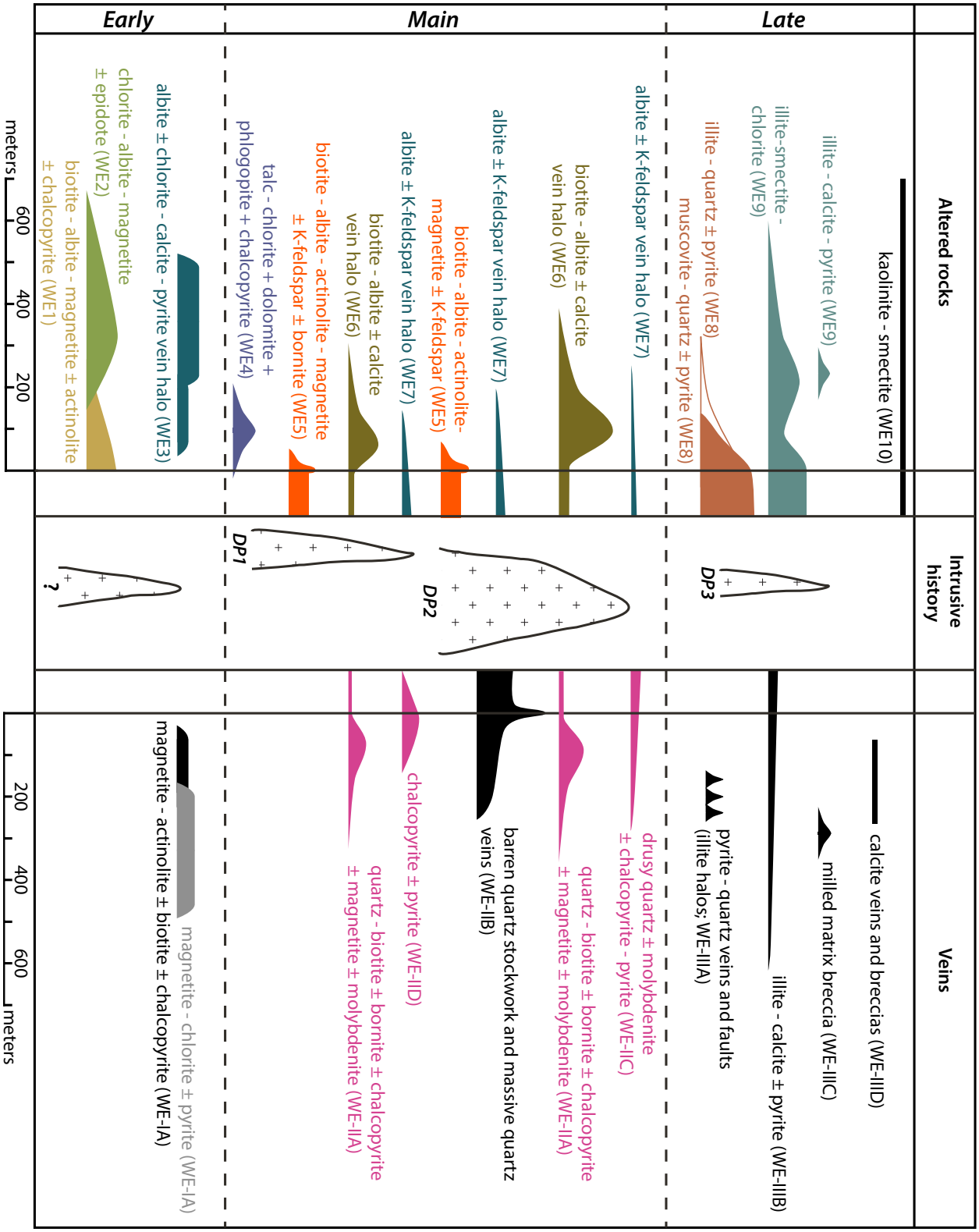


**Figure 5.23:** Schematic space-time diagram illustrating the hydrothermal alteration and vein paragenesis of the Waisoi East Cu-Au-Mo porphyry deposit. The relative age of the events are in order of oldest to youngest from the bottom to the top of the diagram. Hydrothermal alteration and veins observed within the mineralized intrusions are illustrated by the colored polygons within the columns immediately adjacent to the Intrusive history column. The distribution of each event relative to the mineralized intrusions is depicted by the horizontal component of its colored polygon. The relative intensity of each event is depicted by the vertical thickness of its respective colored polygon. Abbreviations: DP1 = quartz-eye dacite, DP2 = quartz-bearing dacite, DP3 = dacite porphyry, ? = possible hidden intrusion.

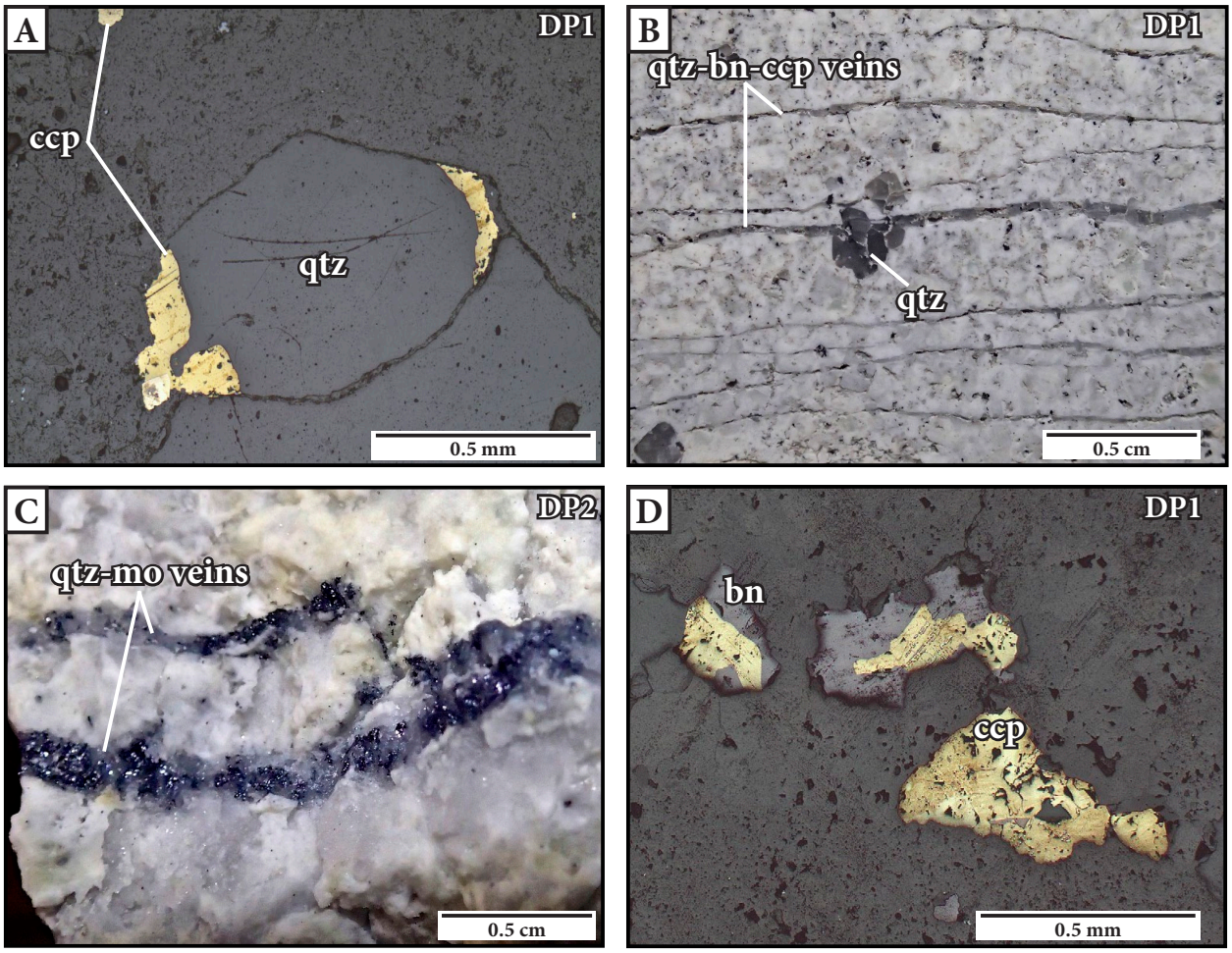


**Figure 5.24:** Examples of types and styles of mineralization at Waisoi East. **A.** Reflected light photomicrograph illustrating a quartz – chalcopyrite miarolitic cavity and disseminated chalcopyrite in the DP1 intrusion. Sample: NSE002 366 m. **B.** DP1 that has been crosscut by quartz – bornite – chalcopyrite veins. Sample: NSE002 366 m. **C.** Example of quartz vein-hosted molybdenite in the DP2 intrusion. Sample: NSE008 674 m. **D.** Reflected light photomicrograph of bornite replacing the edges of chalcopyrite in typical disseminations within the DP1 intrusion. Sample: NSE002 339 m. Abbreviations: bn = bornite, ccp = chalcopyrite, DP1 = quartz-eye dacite, DP2 = quartz-bearing dacite, mo = molybdenite, qtz = quartz.

### *5.2.5.1 Sulfide zonation at Waisoi East*

Bornite, chalcopyrite, and pyrite are the principal sulfide minerals at Waisoi East. The dominant sulfide species changes in a zonal arrangement outward from the core of the deposit to its periphery. At the core of Waisoi East is a small zone characterized by bornite + chalcopyrite (Fig. 5.22C). In this zone, bornite is interpreted to have precipitated after chalcopyrite, since it is typically observed having partially replaced the rims of chalcopyrite grains (Fig. 5.24D). Surrounding the bornite zone is a chalcopyrite > pyrite ± bornite domain that grades laterally outwards to a pyrite > chalcopyrite and then an annular pyrite-only domain (Fig. 5.22C). The sulfide zonation pattern is disrupted adjacent to the high-grade core by a pyrite-only domain associated with the DP2 intrusion (Fig. 5.22C).

**Table 5.7**: Styles and spatial and temporal distribution of alteration assemblages at Waisoi East

| Stage | Gangue minerals | Sulfide minerals | Alteration texture and intensity | Spatial and temporal distribution | Related veins |
|---|---|---|---|---|---|
| WE1 | Biotite, albite, magnetite, actinolite, rutile | ccp | Moderate intensity, selective alteration of plagioclase phenocrysts to albite and primary ferromagnesian minerals to biotite - magnetite - rutile ± actinolite ± chalcopyrite; patchy domains of intense biotite - albite ± rutile ± magnetite alteration occur in the Wainimala host sequence | Restricted to Wainimala host sequence and best preserved in the lava and sandstone units; occurs from the present-day surface to below -300 mRL and is > 500 m N-S (other dimensions are undefined); crosscut by DP1 and DP2; most likely associated with an early undocumented intrusion | None |
| WE2 | Chlorite, albite, magnetite, epidote, calcite, rutile | py, ccp | Moderate to strong intensity, selective alteration of plagioclase phenocrysts to albite and ferromagnesian minerals to chlorite - magnetite - rutile ± pyrite; intense, patchy aggregates of chlorite - magnetite - albite - calcite ± pyrite are rimmed by distinctive albite - calcite halos; intense albite - chlorite alteration of Wainimala basaltic andesite-clast breccia matrix and magnetite alteration of groundmass in clasts | Restricted to Wainimala basaltic andesite-clast breccia; occurs on the margins and outboard of WE1-altered rocks; extends beyond the limit of available drilling; formed prior to the emplacement of DP1 and DP2 | None |
| WE3 | Albite, chlorite, calcite | py, ccp | Strong intensity, pervasive, pale white to cream alteration halos; < 3 to 30 mm wide; vein halo is thinnest surrounding actinolite - magnetite veinlets (in WE1 domain) and thickest surrounding chlorite - magnetite veins (in WE2 domain) | Restricted to Wainimala host sequence; overprints WE1 and WE2 alteration; crosscut by DP1 and DP2 intrusions | WE-IA |
| WE4 | Talc, chlorite, magnetite, calcite phlogopite, dolomite | ccp, bn | Intense, pervasive talc - chlorite + phlogopite alteration surrounding fracture zones that contain quartz-vein stockworks | Most abundant in Wainimala host sequence; occurs rarely within DP1 intrusion; overprints WE1 alteration | None |
| WE5 | Biotite, albite, actinolite, magnetite, K-feldspar, rutile | bn, ccp | Moderate intensity, selective alteration of orthoclase phenocrysts to patchy biotite - K-feldspar, plagioclase phenocrysts and groundmass to albite ± calcite, and mafic minerals to biotite - actinolite - magnetite | Cyclically produced by DP1 and DP2 intrusions; occurs within both intrusions; overprinted and obscured by WE8, WE9, and WE10 alteration | None |
| WE6 | Biotite, albite, chlorite | ccp, bn | Moderate to strong intensity, selective to pervasive vein-halo alteration surrounding stage WE-IIA veins and fracture zones | Structurally controlled; occurs within the DP1 and DP2 intrusions as well as the Wainimala host sequence (< 400 m from intrusive contacts) | WE-IIA |
| WE7 | Albite, K-feldspar | | Weak intensity, selective to pervasive, white albite ± K-feldspar alteration halos surrounding stage WE-IIB and WE-IIC veins | Structurally controlled; occurs within DP1 and DP2 as well as the Wainimala host sequence (< 400 m from intrusive contacts); overprinted by WE8 illite alteration | WE-IIB WE-IIC |
| WE8 | Muscovite, quartz, illite, chlorite | py | Moderate to strong intensity, selective alteration of feldspar phenocrysts to muscovite or illite; patchy, pervasive muscovite alteration and disseminations of pyrite within the Wainimala basaltic andesite-clast breccia; pervasive muscovite - quartz - pyrite vein-halo alteration surrounding WE-IIIA veins and breccia zones | Best developed overprinting stage WE5 alteration in the DP1 and DP2 intrusions; weakly developed muscovite alteration has a widespread distribution throughout the Wainimala host sequence | WE-IIIA |
| WE9 | Illite, chlorite, illite-smectite, calcite | py, ccp | Weak to moderate intensity, partial replacement of ferromagnesian minerals by chlorite and feldspar phenocrysts by illite; strong to intense, pervasive, magnetite destructive alteration patches of fine-grained illite intergrown with chlorite ± sulfides | Ubiquitous alteration; best developed overprinting the DP1 and DP2 intrusions and is most intense overprinting the albite - chlorite-altered matrix of the Wainimala basaltic andesite-clast breccia in the WE2 alteration domain | WE-IIIB |
| WE10 | Kaolinite, montmorillonite, illite-smectite | | Moderate intensity, selective kaolinite - montmorillonite alteration of the outer edges of stage WE9 illite - chlorite alteration patches; weak, selective alteration of feldspar phenocrysts | Equivalent distribution to stage WE9 | None |

Abbreviations: bn = bornite, ccp = chalcopyrite, DP1 = quartz-eye dacite, DP2 = quartz-bearing dacite, py = pyrite.

**Table 5.8:** Vein stages of the Waisoi East deposit

| Vein Stage | Gangue minerals | Sulfide minerals | Form and texture | Spatial and temporal distribution | Alteration envelope |
|---|---|---|---|---|---|
| WE-IA | Magnetite, chlorite, actinolite, biotite, calcite | py, ccp | Discontinuous veinlets with diffuse, non-parallel vein walls and irregular vein shapes; occurs locally as fibrous bands and clots | Restricted to Wainimala host sequence; sparse distribution across Waisoi East; actinolite - magnetite - biotite veins occur in WE1 alteration domain and grade into magnetite - chlorite veins in the WE2 alteration domain | ab-chl-cal-py (WE3); φ < 30 mm |
| WE-IIA | Quartz, biotite, magnetite | bn, ccp, cv, mo | Discontinuous to continuous; irregular to straight-sided quartz veinlets and veins; gray to white quartz; locally occurs as fractured quartz-vein stockwork zones up to 1 m wide | Crosscuts DP1, DP2 and Wainimala host sequence; overprinted by barren quartz veins (WE-IIB) and quartz - molybdenite veins (WE-IIC); coincident with the highest Cu-Au grades at Waisoi East | bt-ab-cal (WE6); φ < 30 mm |
| WE-IIB | Quartz | py, ccp | Gray to white sugary quartz; continuous and undulose to straight-sided veins with sharp and parallel vein walls; locally occurs as massive coalesced stockworks (< 40 m wide) | Volumetrically the most significant vein stage at Waisoi East; most abundant on the margins of DP2 and adjacent Wainimala host sequence | ab (WE7); φ < 2 mm |
| WE-IIC | Quartz | mo, py, ccp | Continuous, sharp-walled and irregular to straight-sided quartz veins with euhedral molybdenite ± pyrite ± chalcopyrite partially infilling central cavities | Crosscuts DP1, DP2 and the Wainimala host sequence; crosscuts barren quartz veins (WE-IIB); coincident with the highest Mo grades at Waisoi East | ab (WE7); φ < 2 mm |
| WE-IID | | ccp, py | Discontinuous veins with diffuse, non-parallel vein walls and irregular vein shapes | Crosscuts WE-IIC veins and early biotite alteration; sparse; distribution is poorly constrained | ab (WE7); φ < 2 mm |
| WE-IIIA | Quartz | py, sp, gn | Continuous, straight to wavy, quartz - pyrite veins and < 3 m-wide polymict breccia zones with clasts of vein quartz and illite-altered lithic clasts; pyrite is typically coarse-grained, brassy, euhedral and intergrown with sugary-textured quartz | Crosscuts all rock types and previous vein stages at Waisoi East; sparse and widespread distribution throughout the deposit | ill-py-qtz-ms (WE8); φ = 1 – 50 cm |
| WE-IIIB | Illite, calcite | py | Discontinuous to continuous and irregular veins with diffuse vein walls | Distributed throughout Waisoi East and crosscuts all previous vein stages | ill (WE9); φ < 10 mm |
| WE-IIIC | Illite, calcite, biotite | py | Polymict, poorly sorted, chaotic, milled matrix-supported breccia with sub-rounded, granule- to pebble-sized clasts with possible illite - calcite - biotite - pyrite cement | Steeply inclined dike-like morphology; occurs in NSE008 from 176 – 181 m; no observed association with porphyry intrusions | None |
| WE-IIID | Calcite, quartz | py | White calcite ± quartz ± pyrite infill to brittle fracture zones; occurs locally as discontinuous to continuous, crenulated, irregular, branching veins and veinlets | Crosscuts all previous vein stages; most common in WE2 alteration domain | None |

Abbreviations: φ = vein-halo thickness, ab = albite, bn = bornite, bt = biotite, cal = calcite, ccp = chalcopyrite, chl = chlorite, cv = covellite, DP1 = quartz-eye dacite, DP2 = quartz-bearing dacite, gn = galena, ill = illite, mo = molybdenite, ms = muscovite, py = pyrite, qtz = quartz, sp = sphalerite.

### *5.2.5.2 Copper-molybdenum distribution*

A series of west-facing cross sections spaced at 100 m intervals illustrates the distribution of copper and molybdenum relative to mineralized dacites at Waisoi East (Fig. 3.6 and 5.26). The first frame at 1997600 mE (50 m east of the cross section in Fig. 5.22; Fig. 5.26A) shows that higher-grade copper (> 0.7 wt %) is superjacent to the DP2 intrusion and is entirely hosted by the Wainimala wall rocks from 200 – 250 mRL. The > 0.3 wt % Cu grade shell weakly drapes over the apical portion of the DP2 intrusion, as deep as -100 mRL. The > 0.01 wt % Mo grade

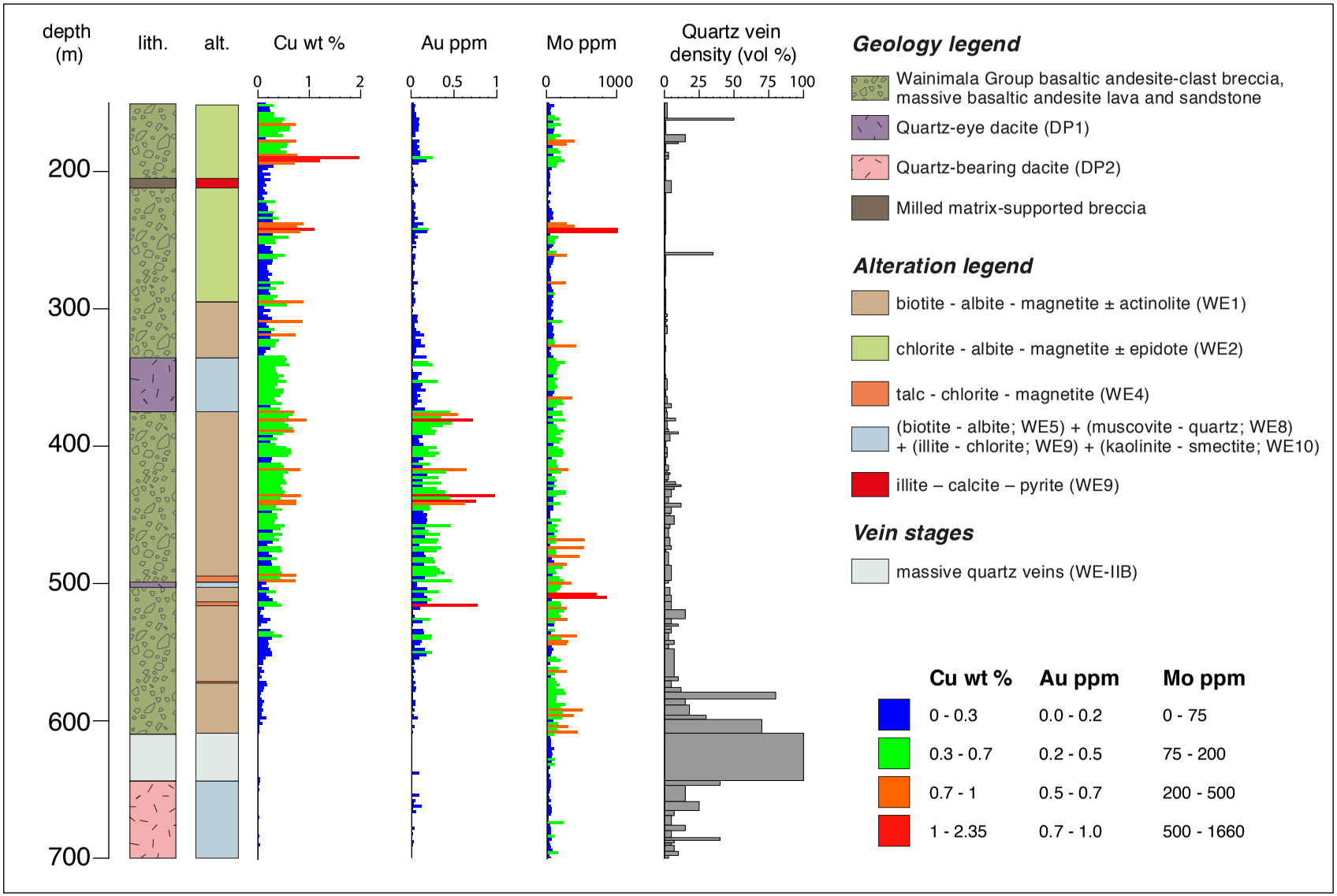


**Figure 5.25:** Simplified summary log of NSE002, which intersects two of the mineralized Waisoi East dacite porphyries. Significant changes in grade occur at the contact between the DP2 intrusion and the surrounding Wainimala wall rocks. At this boundary there is an inverse correlation between quartz vein density and copper-gold grade. The copper grades across the DP1 intrusion are fairly homogeneous. Spikes in the grade down hole are associated with stage WE-IIA structural zones and veins as well as talc – chlorite alteration zones.

shell forms a broad zone (> 500 m) across the cupola region of DP2 and extends downward to the north outside of the intrusion to a depth of -300 mRL. A small zone of > 0.02 wt % Mo and > 0.3 wt % Cu is coincident with the upper portion of the DP1 intrusion. In the next frame (100 m eastward; 1937700 mE; Fig. 5.26B) a similar pattern is illustrated, with the exception that the Cu grade shells cover a smaller area and the Mo grade shells cover a larger area (including new zones of > 0.03 wt % Mo). In the final frame at 1937800 mE (Fig. 5.26C), the higher-grade copper grade shell (> 0.7 wt % Cu) is gone and the low-grade Cu grade shell (> 0.3 wt % Cu) is strongly diminished. The Mo grade shells are still prominent and extend deep within the deposit. The Mo and Cu grade shells never intersect the DP3 dacite porphyry (Fig. 5.26).

*5.2.5.3 Early-stage mineralization, alteration and veins (WE-I)*

Three alteration assemblages are associated with early-stage mineralization at Waisoi East. The oldest alteration event produced a zone of biotite – albite – magnetite-altered rocks (WE1) in the core of the deposit that grades outward over hundreds of meters to a zone of chlorite – albite – magnetite-altered rocks (WE2). These alteration assemblages have been overprinted and crosscut by every alteration and vein type at Waisoi East, including an albite ± chlorite – calcite vein halo alteration assemblage (WE3) that surrounds early magnetite, biotite, and chlorite veins. Early-stage alteration and veins are restricted to the Wainimala host sequence (Fig. 5.27). It is difficult to determine the original distributions of early-stage alteration assemblages and veins, due to overprinting of biotite – albite and ubiquitous muscovite – pyrite, chlorite – illite and kaolinite – montmorillonite alteration assemblages. The early-stage alteration assemblages are best preserved in the peripheral areas of the deposit.

*Biotite – albite – magnetite ± actinolite ± chalcopyrite alteration (WE1)*

The earliest stage of alteration and mineralization at Waisoi East affected the Wainimala host sequence from 150 mRL to below -300 mRL in a broad zone (> 500 m wide; Fig. 5.22B), producing hydrothermal biotite, albite, magnetite, and lesser actinolite and rutile (Table 5.7). Stage

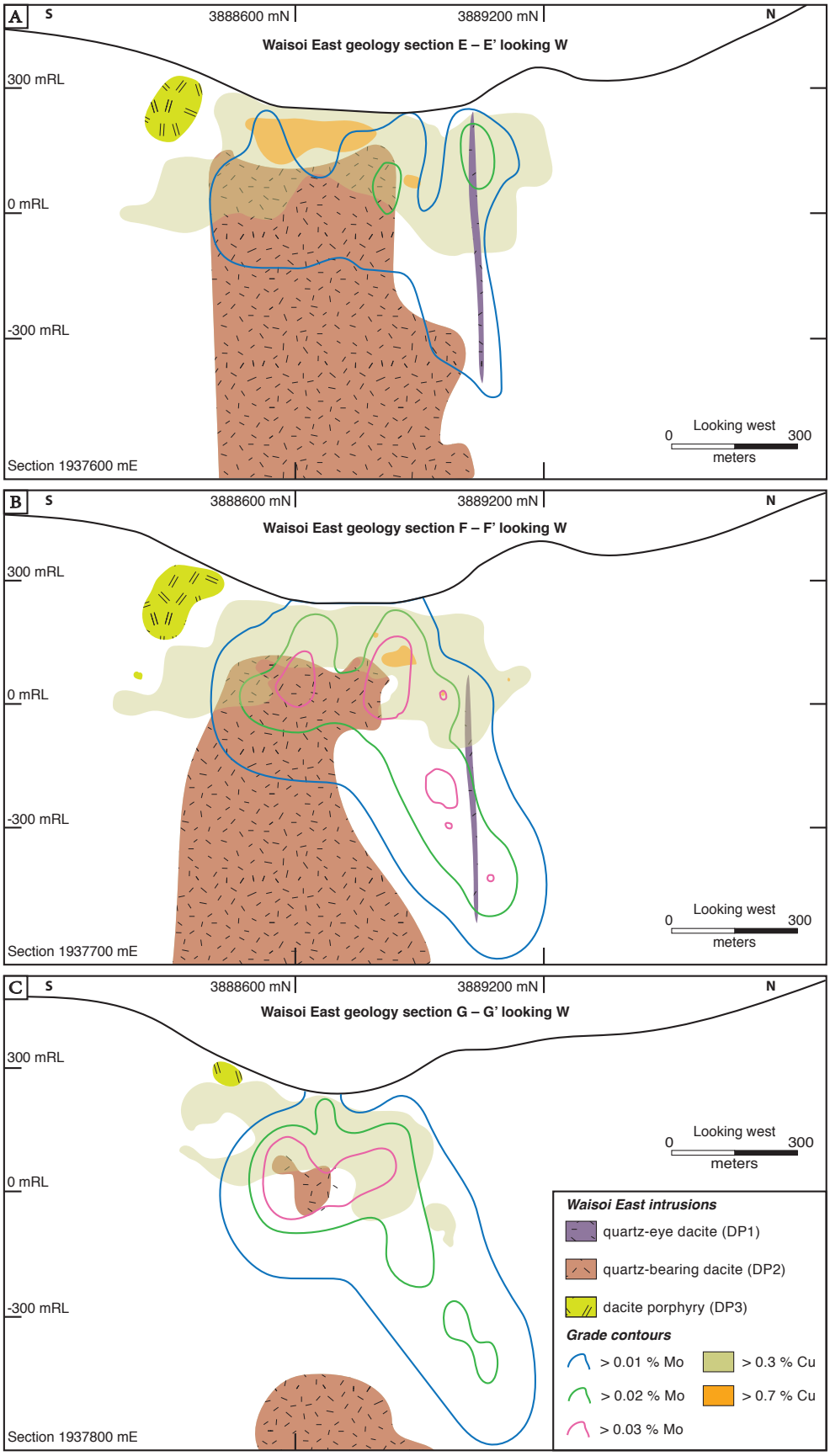


**Figure 5.26:** Waisoi East west-facing geology slices. Cross sections (0 m clips; looking west) spaced at 100 m across the Waisoi East deposit. Cross sections show distribution of Waisoi East dacite porphyries, copper and molybdenum grade shells and present-day surface. **A.** Cross section 1937600 mE. **B.** Cross section 1937700 mE. **C.** Cross section 1937800 mE. Cross section locations are shown on Figure 3.6.

WE1 alteration is preferentially developed and preserved in the massive basaltic andesite lava and sandstone units of the Wainimala Group (Figs. 5.22A, B and 5.27A). Biotite, magnetite, and actinolite occur as moderate to strong selective replacements of primary ferromagnesian minerals (Figs. 5.27A, B and D). Shreddy biotite and anhedral rutile, albite and magnetite pervasively altered the Wainimala sandstone unit and the groundmass of the basaltic andesite lava (Fig. 5.27B). Hydrothermal albite and rare K-feldspar selectively replaced primary feldspar phenocrysts and formed alteration rims to biotite – magnetite – actinolite alteration clots (Figs. 5.27A and C). Chalcopyrite is the principal sulfide associated with stage WE1 alteration and commonly occurs as fine-grained disseminations, along with magnetite, and are evenly distributed throughout the Wainimala host sequence (Fig. 5.27C). Stage WE1-altered rocks contain approximately four times the amount of disseminated magnetite (~ 4 vol %) than chalcopyrite (~ 1 vol %). Early-stage biotite alteration does not appear to be centered on any of the documented Waisoi East intrusions

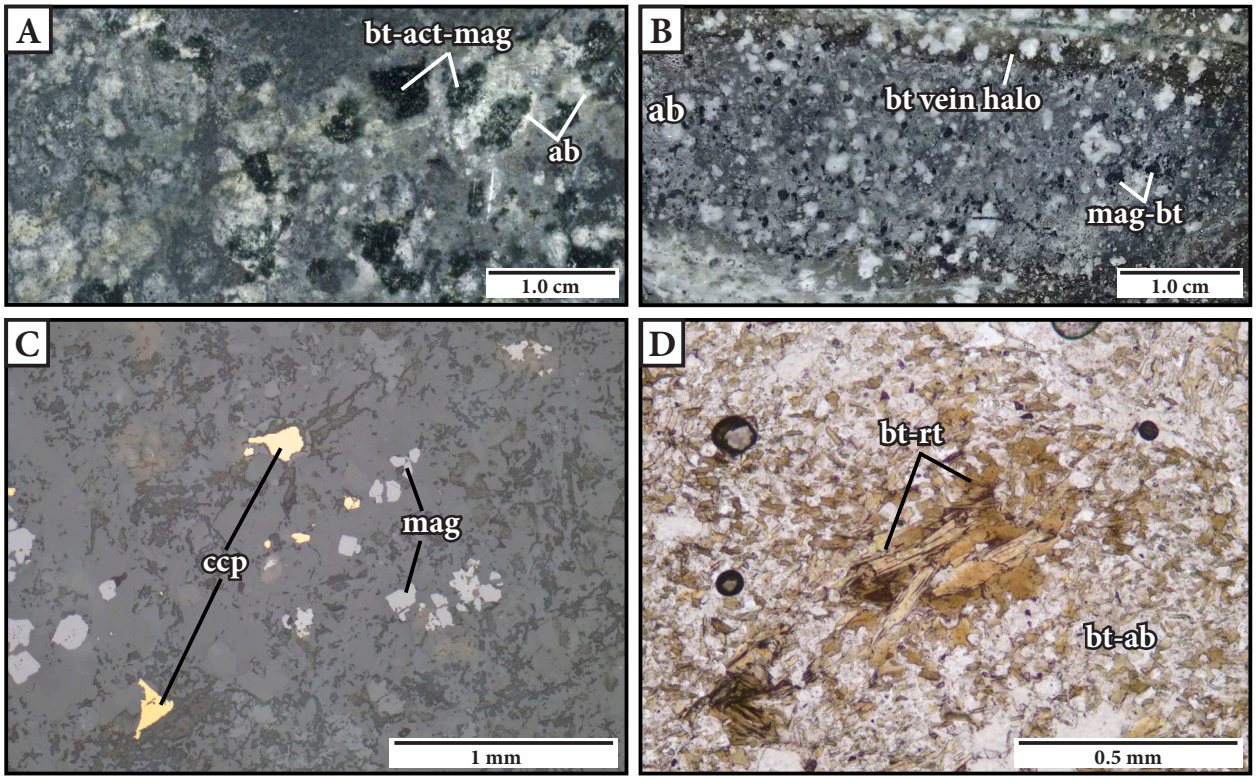


**Figure 5.27:** Examples of early-stage biotite (WE1) alteration at Waisoi East. **A.** Characteristic interval of massive basaltic andesite lava that did not react to chemical feldspar staining, showing that all plagioclase phenocrysts have been altered to albite. The image also shows selective alteration of ferromagnesian minerals to biotite – magnetite – actinolite with albite alteration rims and selective alteration of primary feldspar phenocrysts to albite. Sample: NSE002 529 m. **B.** Example of massive basaltic andesite lava with selective alteration of primary feldspar phenocrysts to albite and ferromagnesian minerals to magnetite ± biotite. Groundmass has been pervasively altered to albite ± biotite. This sample has been crosscut by later quartz veinlets with distinctive light brown biotite vein-halo alteration (WE6; top and bottom of photo). Sample: NSE008 356 m. **C.** Reflected light photomicrograph showing fine-grained disseminations of magnetite > pyrite in WE1-altered Wainimala host rocks. Sample: NSE002 528 m. **D.** Plane-polarized photomicrograph illustrating selective alteration of a ferromagnesian mineral to biotite – rutile and patchy domains of albite and shreddy biotite. Sample: NSE008 796 m. **C.** Sample: NSE008 356 m. Abbreviations: ab = albite, act = actinolite, bt = biotite, ccp = chalcopyrite, mag = magnetite, rt = rutile.

(Figs. 5.22 and 5.23). Ellis (1996) invoked an early regional greenschist facies burial metamorphism to account for observed biotite – albite – actinolite alteration that was overprinted by a quartz – biotite assemblage (Table 5.2). Stage WE1 likely corresponds to this pre-porphyry stage of Ellis (1996), but in the current study it is interpreted as early-stage hydrothermal alteration, rather than a metamorphic assemblage.

*Chlorite – albite – magnetite ± epidote ± calcite alteration (WE2)*

A chlorite – magnetite – albite ± epidote ± calcite alteration assemblage (Table 5.7) occurs outboard of the biotite-bearing WE1 assemblage and extends beyond the limit of available drilling (i.e., > 600 m from the margin of DP2; Figs. 5.22B and 5.23). WE2 alteration did not affect any of the Waisoi East intrusions (Fig. 5.22B and 5.23). Chlorite – magnetite – albite alteration is characterized by strong to intense, texturally destructive alteration of the Wainimala basaltic andesite-clast breccia (Fig. 5.28B). In this alteration domain, primary feldspar phenocrysts are altered to albite ± calcite, and ferromagnesian minerals are altered to chlorite – magnetite ± rutile ± pyrite (Fig. 5.28B). Rare epidote occurs as euhedral prisms in the cores of primary plagioclase minerals (Fig. 5.28A) and is intergrown with quartz, calcite and chlorite within amygdules (Fig. 5.28E). A characteristic feature of WE2 alteration is the occurrence of blotchy and irregular chlorite – magnetite – albite ± pyrite ± calcite spots rimmed by distinctive, cream to white albite – calcite + illite alteration halos (Figs. 5.28B, C and D). In more intensely altered domains, chlorite can make up to 30 vol % of the host rock (Appendix B), and the groundmass of amygdaloidal clasts within the Wainimala basaltic andesite-clast breccia can be completely altered to fine-grained magnetite (Figs. 5.28E and F). The matrix of the Wainimala basaltic andesite-clast breccia is indurated and has been pervasively replaced by white albite ± calcite (Fig. 5.28B). SWIR spectroscopy results are consistent with a Fe-Mg chlorite composition (i.e., the typical wavelength of the Fe-OH absorption feature is ca. 2250 nm; Appendix F) and chemical feldspar staining results show that albite is the principal feldspar in this alteration domain. The stage WE2 chlorite – albite alteration assemblage is localized in the Wainimala basaltic andesite-clast breccia (Figs. 5.22A and B). There is a strong lithological control on its distribution.

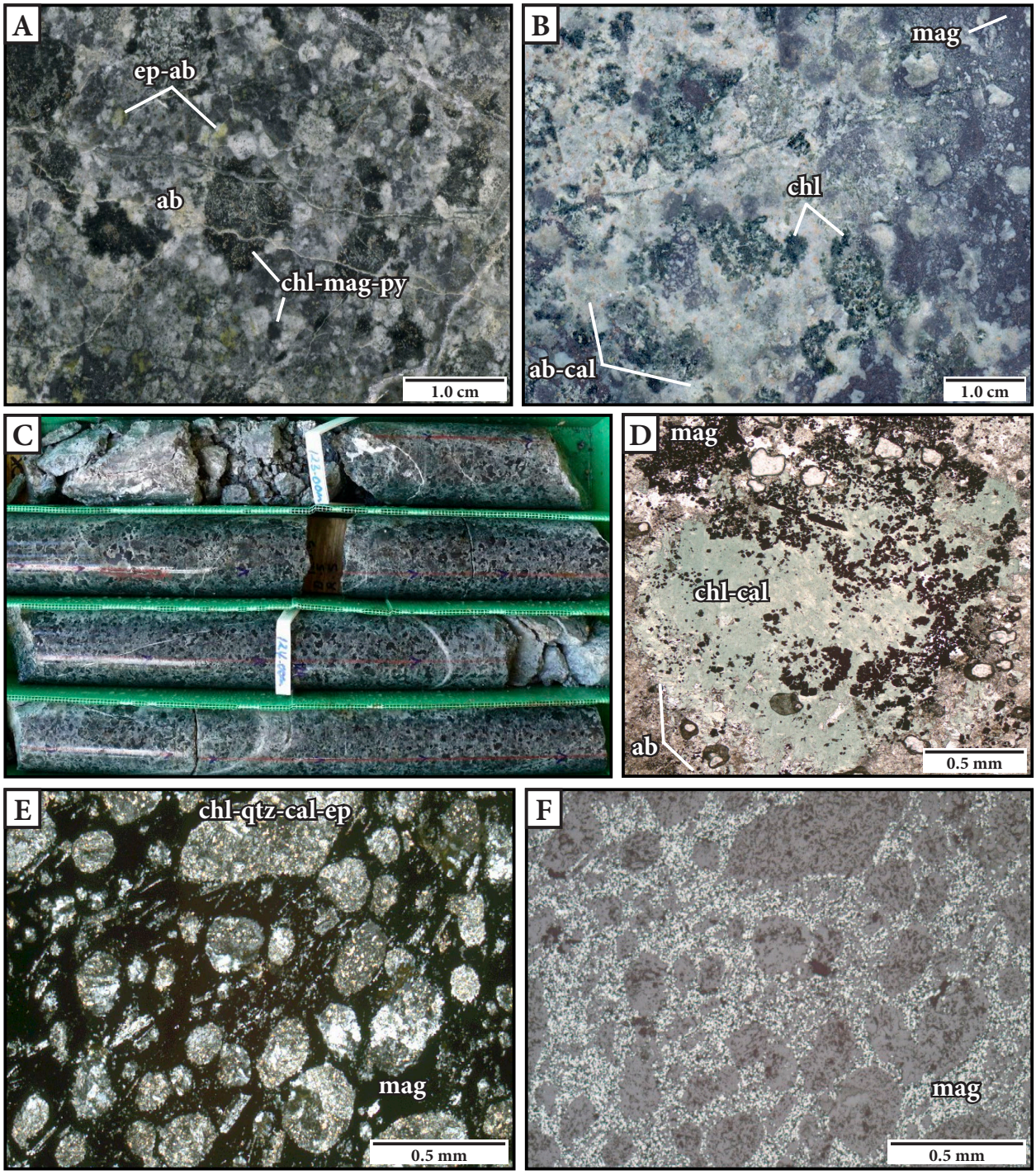


**Figure 5.28:** Examples of early-stage chlorite – albite – magnetite (WE2) alteration at Waisoi East. **A.** Interval of Wainimala basaltic andesite-clast breccia showing selective alteration of feldspar minerals to patchy epidote – albite. Chlorite – magnetite – pyrite alteration spots have distinctive rims of albite. Sample: NSE002 127 m. **B.** Interval of Wainimala basaltic andesite-clast breccia illustrating strong chlorite and magnetite alteration domains. The feldspar-rich matrix is indurated by strong albite ± calcite alteration. Sample: NSE008 80 m. **C.** Core box photograph illustrating the characteristic blotchy chlorite – magnetite alteration spots with white to cream-colored albite alteration halos (NSE002 122–125 m). **D.** Plane-polarized photomicrograph of a patchy chlorite – magnetite – albite – calcite alteration spot in the Wainimala basaltic andesite-clast breccia. Sample: NSE002 87.5 m. **E.** Cross-polarized photomicrograph of chlorite – quartz – calcite – epidote-filled amygdules surrounded by intense magnetite alteration of the matrix. Sample: NSE008 80 m. **F.** Reflected light photomicrograph illustrating that the opaque minerals in Fig. 5.28E are magnetite. Sample: NSE008 80 m. Abbreviations: ab = albite, cal = calcite, chl = chlorite, ep = epidote, mag = magnetite, py = pyrite, qtz = quartz.

*Magnetite veins (WE-IA) with albite – calcite ± chlorite vein-halo alteration (WE3)*

Stage WE-IA veins have a spatial association with both WE1 and WE2 alteration domains and consist of variable proportions of magnetite, chlorite, biotite, actinolite, calcite, pyrite and chalcopyrite (Table 5.8). WE-IA veins generally occur as discontinuous and irregular fibrous bands or clots with a variable vein aperture and diffuse vein walls (Figs. 5.39A, C and D). The veins and veinlets have narrow (< 3 mm) to thick (< 30 mm), distinctive, pale white to cream halos of albite – calcite ± chlorite ± pyrite alteration (WE3; Table 5.7; Fig. 5.29). In the WE2 alteration domain, the vein infill ranges from dominantly granular magnetite with lesser chlorite, calcite and pyrite (Figs. 5.29B and D) to dominantly chlorite that is intergrown with lesser magnetite and calcite (Fig. 5.29A). The WE-IA veins are typically thinner (< 5 mm wide) in the WE1 alteration domain, consisting of magnetite – actinolite ± biotite and lacking obvious vein-halo alteration (Fig. 5.29C). Stage WE-IA veins and veinlets have not been observed to crosscut any of the Waisoi East intrusions and are therefore interpreted to pre-date their emplacement (Fig. 5.23).

*5.2.5.4 Main-stage mineralization, alteration and veins (WE-II)*

Four distinct alteration assemblages and mineral associations are linked with main-stage mineralization at Waisoi East. The earliest alteration event is a structurally controlled, intense, pervasive talc – chlorite + phlogopite + calcite + dolomite mineral association (WE4). The second alteration event is composed of a selective biotite-bearing assemblage (WE5) that has overprinted both the DP1 and DP2 intrusions. The last two alteration events consist of selective and pervasive alteration halos surrounding multiple generations of quartz veins (WE6 and WE7). Main-stage mineralization is responsible for the bulk of Cu-Au and Mo grade at Waisoi East.

*Talc – chlorite + magnetite + phlogopite + calcite + dolomite alteration (WE4)*

Mineral associations of talc, chlorite, magnetite, phlogopite, calcite, dolomite and chalcopyrite occur as irregular, small (< 5 m-thick) domains of texturally destructive, intense, pervasive alteration of reactive lenses within the Wainimala bedded sandstone unit near its contact with

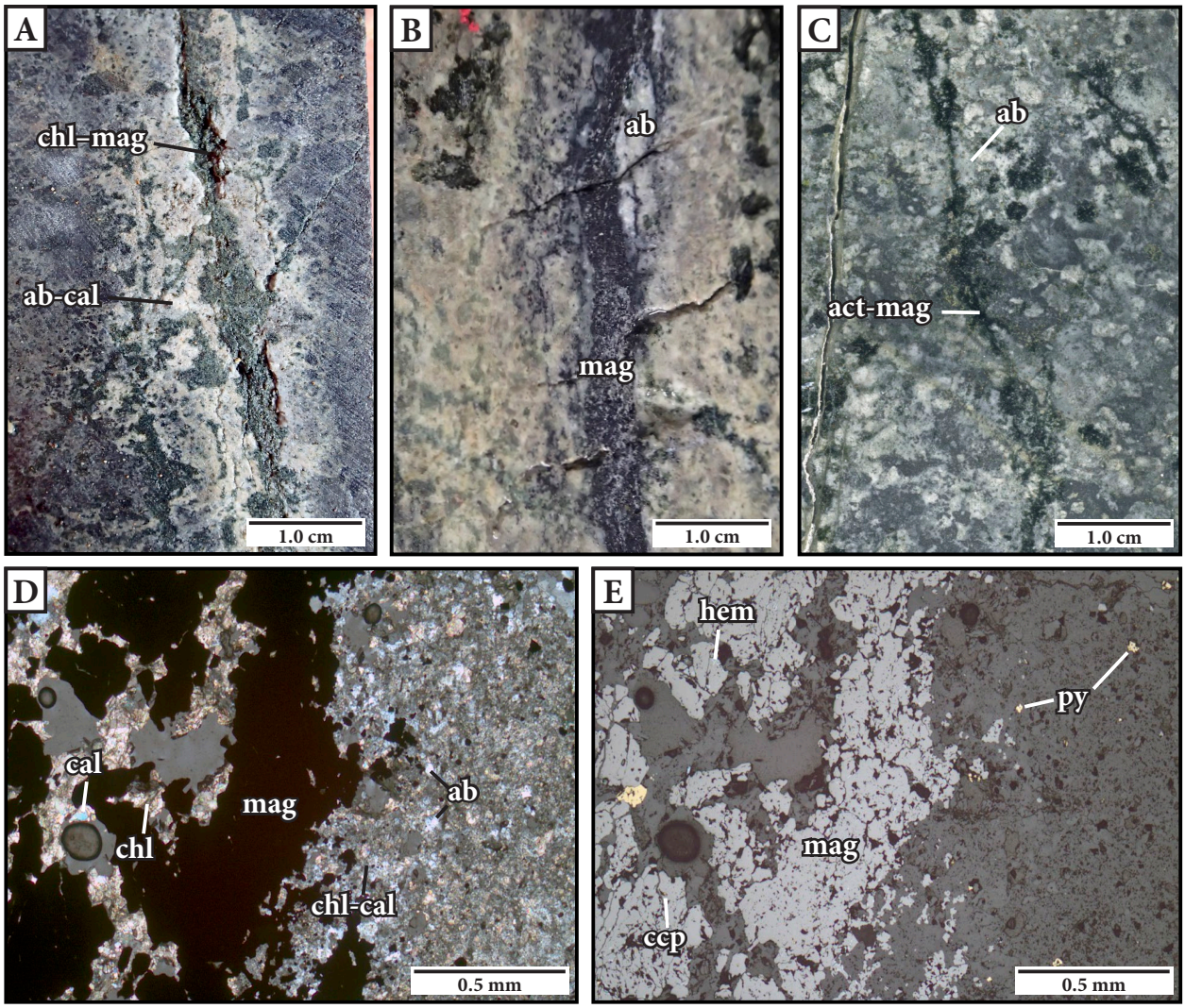


**Figure 5.29:** Examples of early-stage WE-IA veins with WE3 vein-halo alteration at Waisoi East. **A.** Interval of Wainimala basaltic andesite-clast breccia crosscut by chlorite – magnetite veins and clots with a pink and cream albite ± calcite alteration envelope within the WE2 alteration domain. Sample: NSE002 235 m. **B.** Interval of Wainimala basaltic andesite-clast breccia crosscut by a granular magnetite vein with white albite vein-halo alteration in the WE2 alteration domain. Sample: NSE008 200 m. **C.** Interval of massive basaltic andesite lava that has been crosscut by actinolite – magnetite – biotite veinlets and clots in the WE1 alteration domain. Sample: NSE002 529 m. **D.** Cross-polarized photomicrograph of a diffuse magnetite – chlorite – calcite – pyrite vein with pervasive albite – chlorite – calcite – pyrite alteration halos. Sample: NSE002 200 m. **E.** Reflected light photomicrograph illustrating that the opaque minerals in Fig. 5.29E are dominantly magnetite and pyrite. Hematite alteration has replaced magnetite along fractures within the vein. Magnetite contains fine inclusions of chalcopyrite > pyrite. Sample: NSE002 200 m. Abbreviations: ab = albite, act = actinolite, cal = calcite, ccp = chalcopyrite, chl = chlorite, hem = hematite, mag = magnetite, py = pyrite.

the DP1 intrusion (Table 5.7; Figs. 5.22B and 5.23). Talc also occurs in the DP1 intrusion (Fig. 5.23; Appendix B). The prograde assemblage of phlogopite – magnetite – dolomite ± quartz has been overprinted by talc – chlorite ± calcite ± chalcopyrite (Fig. 5.30B). WE4 alteration domains typically coincide with fracture zones defined by quartz-vein stockworks and have a beige to light gray talc – chlorite assemblage (locally up to 7.5 vol % talc and 6.8 vol % chlorite; Appendix B) that grades outwards over several meters to a brown phlogopite – magnetite alteration assemblage (Fig. 5.30A). Due to talc's low hardness, drill core with abundant talc-bearing retrograde alteration is typically incompetent (e.g., Chang and Meinert, 2008) and has a characteristic soapy feel.

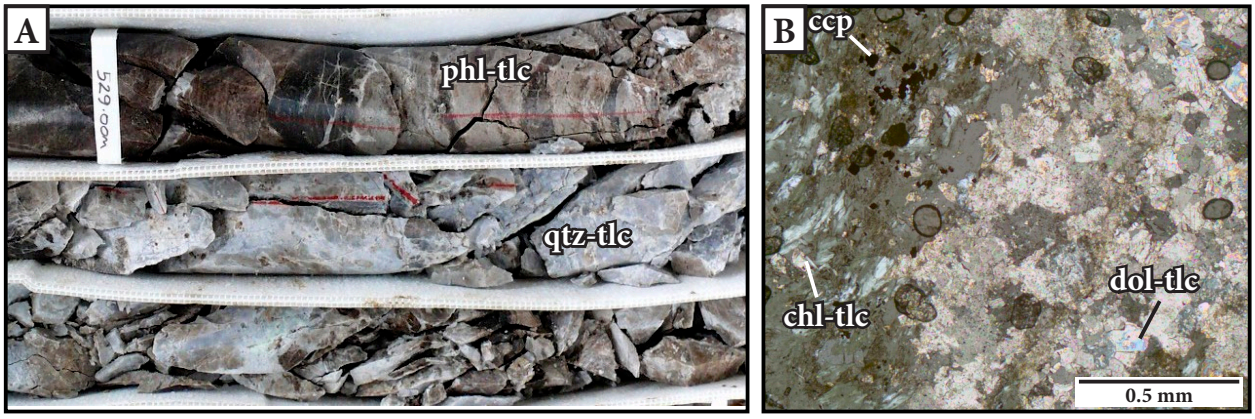


**Figure 5.30:** Examples of main-stage talc – chlorite + dolomite (WE4) alteration at Waisoi East. **A.** Core box photograph illustrating the characteristic lenticular, brown, beige and light gray chlorite – talc + phlogopite + dolomite alteration association. Drill core is highly fractured and has a characteristic soapy feel in talc-altered domains. Sample: NSE002 529–531 m. **B.** Cross-polarized photomicrograph of patchy chlorite – talc – chalcopyrite on the left. On the right are examples of polycrystalline talc replacing the edges of granoblastic dolomite. Sample: NSE002 529 m. Abbreviations: chl = chlorite, dol = dolomite, phl = phlogopite, qtz = quartz, tlc = talc.

Disseminated chalcopyrite and bornite occur close to the quartz-vein stockworks (Fig. 5.30A), and can have a positive affect on copper and gold grades at Waisoi East (locally up to 0.7 wt % Cu; assay value is from a two-meter composite interval; Fig. 5.25). SWIR spectroscopy results are consistent with Mg chlorite (i.e., the typical wavelength of the Fe-OH absorption feature is < 2248 nm; Appendix F), and QXRD results confirm the presence and abundance of talc (Appendix B).

*Albite – biotite – actinolite – magnetite ± K-feldspar ± sulfide alteration (WE5)*

The second main-stage alteration at Waisoi East (Table 5.7) affected the DP1 and DP2 intrusions and produced hydrothermal albite, biotite, actinolite, magnetite, and lesser K-feldspar and sulfide minerals. Stage WE5 alteration has been overprinted by several alteration events, which have obscured its characteristics and distribution within the Waisoi East intrusions. Rare examples of relict, moderate intensity, selective, shreddy biotite – actinolite – magnetite ± rutile alteration has replaced hornblende in both the DP1 and DP2 intrusions (Figs. 5.31A and B). Plagioclase phenocrysts have been altered to secondary albite ± calcite and orthoclase phenocrysts have been altered to fine-grained patchy K-feldspar – biotite (Fig. 5.31A). The quartzofeldspathic groundmass of the DP1 and DP2 intrusions has been strongly altered to albite ± K-feldspar – biotite. Albite can make up to 65 vol % of WE5-altered rocks (Appendix B). Fine-grained disseminated bornite after chalcopyrite is evenly distributed throughout WE5-altered DP1, but is rare to absent in the deeper portions of DP2 (Figs. 5.22 and 5.25).

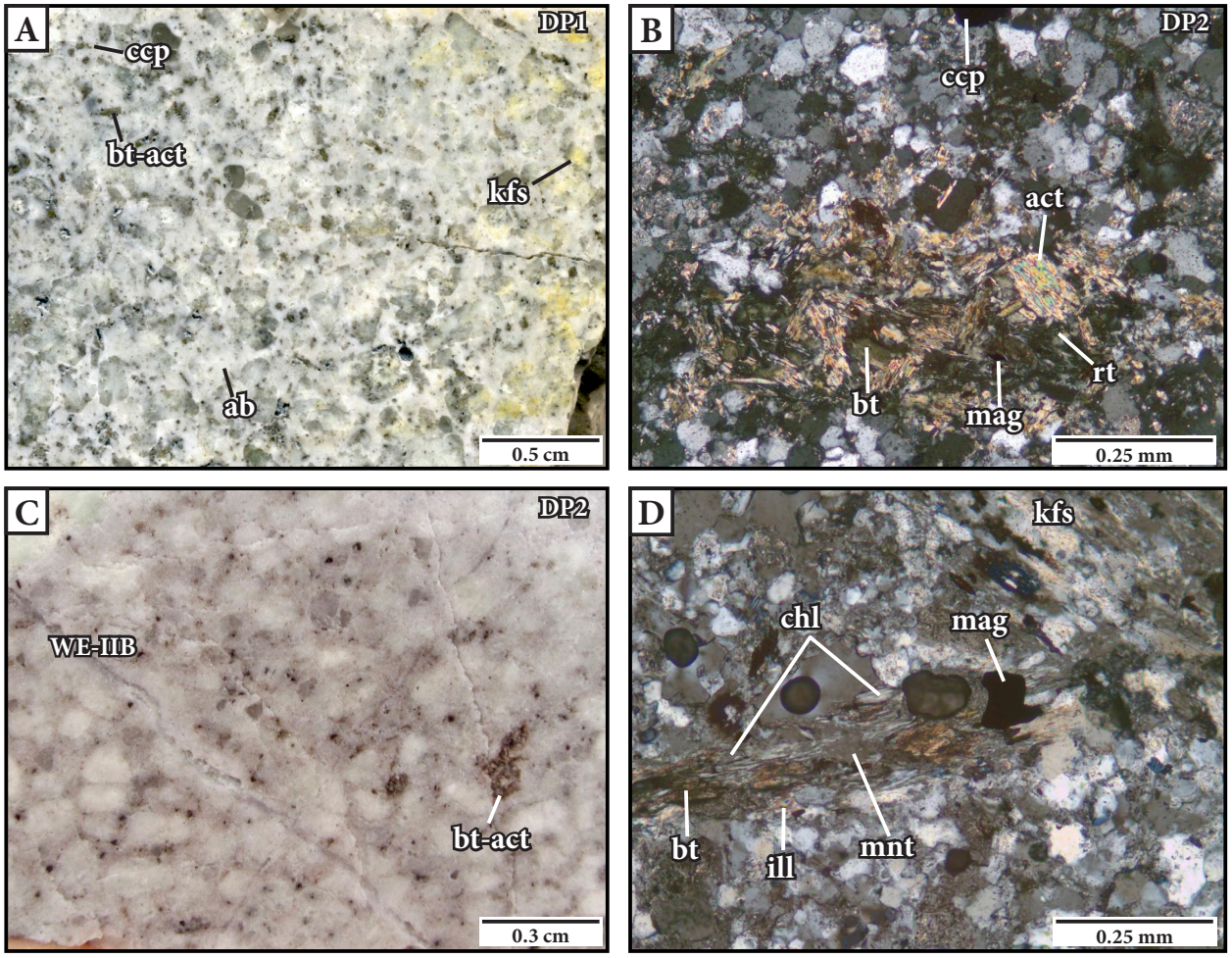


**Figure 5.31:** Examples of main-stage biotite – albite (WE5) alteration at Waisoi East. **A.** Characteristic interval of DP1 that has been treated with chemical feldspar staining, showing the distribution of albite (no stain) and K-feldspar (yellow stain) alteration. Selective alteration of ferromagnesian minerals to biotite – actinolite ± magnetite and primary feldspar phenocrysts and feldspathic groundmass to albite ± K-feldspar. Sample: NSE002 339 m. **B.** Cross-polarized photomicrograph of the DP2 intrusion illustrating selective alteration of a ferromagnesian mineral to actinolite – biotite – rutile – magnetite. Sample: NSE008 634 m. **C.** Interval of DP2 showing biotite – actinolite alteration of ferromagnesian minerals at the hand sample scale. Strong muscovite – quartz, illite – chlorite and kaolinite – montmorillonite overprinting alteration obscures stage WE5 alteration in the top right corner of the photograph. The sample is crosscut by barren quartz veins (WE-IIB). Sample: NSE008 641 m. **D.** Cross-polarized photomicrograph of an interval of DP2 illustrating selective alteration of a ferromagnesian mineral to biotite – magnetite and patchy alteration domains of K-feldspar in the groundmass (top right). Sample: NSE008 796 m. Abbreviations: ab = albite, act = actinolite, bt = biotite, ccp = chalcopyrite, chl = chlorite, DP1 = quartz-eye dacite, DP2 = quartz-bearing dacite, ill = illite, kfs = K-feldspar, mag = magnetite, mnt = montmorillonite, rt = rutile.

*Quartz – biotite ± sulfide veins (WE-IIA) with biotite – albite vein-halo alteration (WE6)*

Quartz veins and veinlets with variable amounts of biotite, bornite, and lesser amounts of chalcopyrite, covellite, and molybdenite are common in the DP1 intrusion as well as the surrounding Wainimala wall rocks (Table 5.8; Fig. 5.23). Stage WE-IIA veins that are found in the deeper portions of the deposit rarely contain sulfides (Figs. 5.25 and 5.32E). Locally, the biotite component of stage WE-IIA veins has undergone retrograde alteration to chlorite (Fig. 5.32C). These veins are typically discontinuous and have an irregular form, although continuous veins with sharp vein walls occur locally (Figs. 5.32A and C). Quartz crystals are anhedral and are typ-

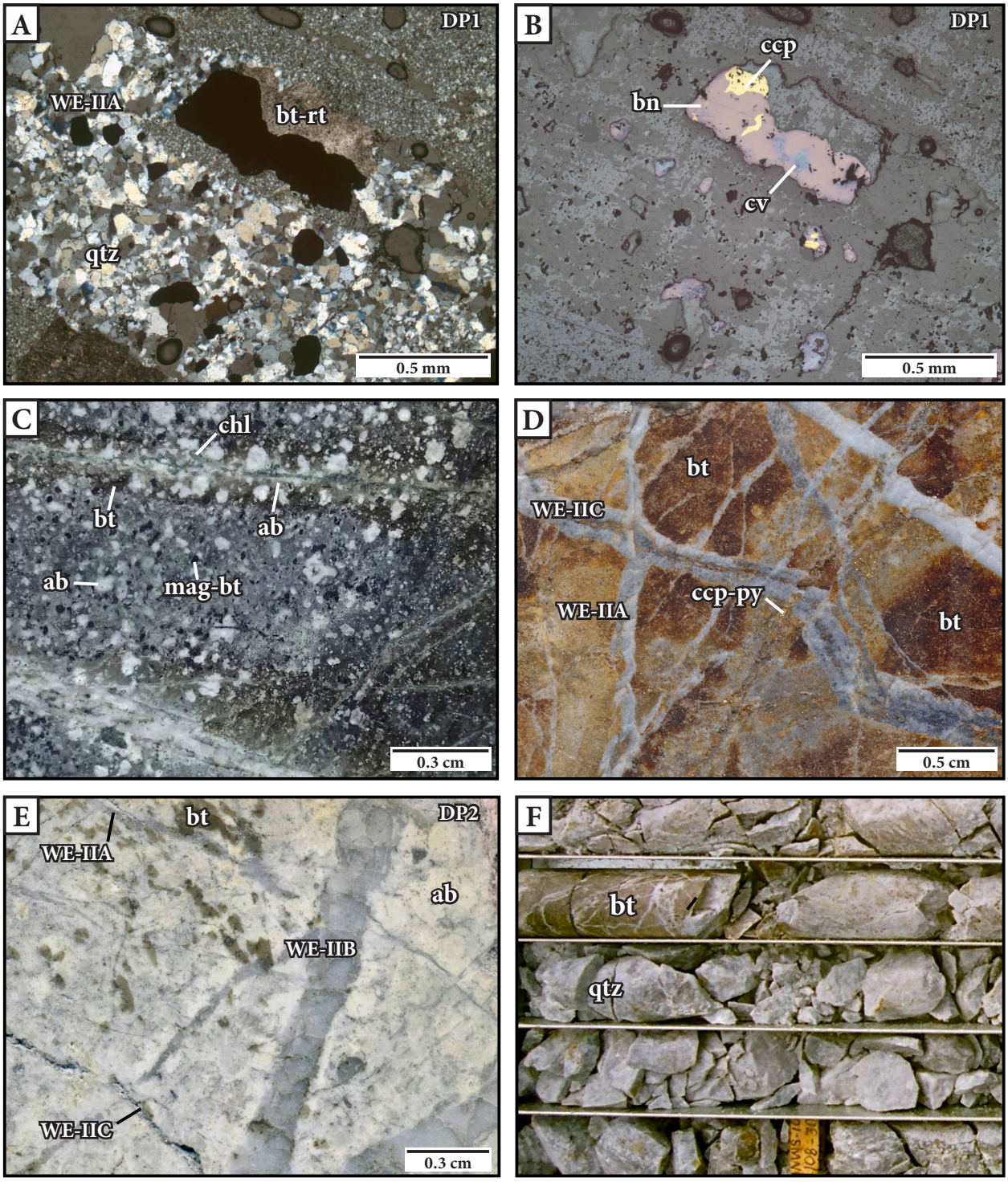


**Figure 5.32:** Examples of main-stage quartz – biotite – sulfide veins and fracture zones (WE-IIA) and their surrounding biotite – albite ± calcite alteration halos (WE6) at Waisoi East. **A.** Cross-polarized photomicrograph of the DP1 intrusion that is crosscut by a stage WE-IIA quartz – biotite – sulfide vein. Sample: NSE002 366 m. **B.** Reflected light photomicrograph illustrating that the opaque minerals in Fig. 5.32A are bornite replacing chalcopyrite with minor covellite. Sample: NSE002 366 m. **C.** Interval of Wainimala basaltic andesite lava that has been altered to biotite – albite – magnetite (WE1) and that has been crosscut by stage WE-IIA quartz – biotite veins with stage WE6 biotite – albite alteration halos. Sample: NSE008 335 m. **D.** Interval of Wainimala bedded sandstone that has been crosscut by stage WE-IIA quartz – biotite stockwork veins with coalesced WE6 biotite vein-halo alteration causing an apparent intense, pervasive biotite wash. Stage WE6 biotite alteration has been crosscut by stage WE-IIC quartz veins with centerline sulfides. Both quartz vein stages have been crosscut by a chalcopyrite – pyrite vein (stage WE-IID). Sample: NSE008 533 m. **E.** Interval of the DP2 intrusion that has been crosscut by stage WE-IIA quartz veins with stage WE6 biotite vein-halo alteration. Stage WE-IIB quartz veins have crosscut stage WE-IIA quartz – biotite veins. Stage WE-IIC drusy quartz veins have crosscut stage WE-IIB barren quartz veins. Sample: NSE002 697 m. **F.** Core box photograph illustrating a highly fractured zone of quartz – biotite – sulfide veins with an intense, pervasive biotite – albite – calcite alteration halo. Sample: NSE010 105.5 – 108.5 m. Abbreviations: ab = albite, bn = bornite, bt = biotite, ccp = chalcopyrite, chl = chlorite, cv = covellite, DP1 = quartz-eye dacite, DP2 = quartz-bearing dacite, mag = magnetite, py = pyrite, qtz = quartz.

ically intergrown with disseminated biotite and sulfide minerals (Figs. 5.32A and B). Stage WE-IIA veins are surrounded by moderate to strong intensity, pervasive halos of biotite, albite, and chalcopyrite (WE6; Tables 5.7 and 5.8; Figs. 5.32C and D). The vein halos have a variable thickness from 1 – 30 mm (Figs. 5.32C and E). Locally, vein halos have coalesced to produce intense, pervasive biotite alteration (Fig. 5.32D).

Highly fractured quartz – biotite – albite – sulfide zones are mineralogically and texturally similar to quartz – biotite – sulfide veins and have been grouped together in stage WE-IIA. These fracture zones contribute the bulk of copper and gold grade at Waisoi East (Figs. 5.22A, 5.23 and 5.25). Pale gray to white quartz intergrown with variable proportions of sulfides and biotite define the center of the fractured zones (Fig. 5.32F). The quartz component ranges from 5 mm to 1 m wide and is composed of either a singular vein or a quartz-vein stockwork (Fig. 5.32F). These fracture zones are surrounded by a biotite – albite ± calcite alteration halo up to 1 m wide. Where crosscutting relationships have been observed, stage WE6 biotite – albite vein-halo alteration has overprinted early-stage biotite – albite – magnetite (WE1; Fig. 5.32C) and chlorite – albite – magnetite (WE2) assemblages within the Wainimala wall rocks. Stage WE-IIC drusy quartz – sulfide veins have crosscut stage WE6 biotite alteration halos (Fig. 5.32D).

*Barren quartz veins (WE-IIB) with albite vein-halo alteration (WE7)*

Stage WE-IIB quartz veins are well developed within the DP2 intrusion and the Wainimala host sequence (Table 5.8). Volumetrically, they are the most significant vein stage at Waisoi East. The veins are composed of barren, gray to white, sugary quartz. Stage WE-IIB veins are undulose to straight-sided and have sharp vein walls. They have no internal symmetry. A massive (> 40 m across and > 300 m in vertical extent), barren quartz stockwork occurs on the margin of the DP2 intrusion (Fig. 5.22A and B). It has similar characteristics to the WE-IIB quartz-vein stockworks and is interpreted to be part of the same vein stage (Figs. 5.33A and B). Vein-halo alteration is generally absent, although weakly developed albite ± K-feldspar (WE7) alteration envelopes occur locally. Within these alteration envelopes primary magnetite has been preserved. Based on crosscutting relationships, stage WE-IIB veins pre-date stage WE-IIC veins (Figs. 5.33D and E).

*Drusy quartz – molybdenite veins (WE-IIC) with albite vein-halo alteration (WE7)*

Stage WE-IIC consists of irregular quartz veins with prominent, central open spaces that are lined with euhedral quartz and interstitial molybdenite, chalcopyrite and pyrite (Table 5.8; Figs. 5.24D, 5.32D and 5.33D). Much of the molybdenum at Waisoi East is spatially associated with the stage WE-IIC vein stockwork (Figs. 5.22A and 5.25). Cu-Fe sulfides are less prominent than molybdenite in stage WE-IIC veins but locally occur as fine concentrations along bands within the quartz veins (Fig. 5.32D). Veins are variable in width (1 to 30 mm), continuous and irregular in form, and have weakly developed albite ± K-feldspar (WE7) alteration halos. Stage WE-IIC veins have a broad distribution, occurring in both DP1 and DP2, as well as the surrounding Wainimala wall rocks (Fig. 5.23).

*Chalcopyrite ± pyrite veins (WE-IID) with albite vein-halo alteration (WE7)*

Stage WE-IID veins and veinlets with moderate to intense albite ± K-feldspar alteration halos (WE7) are the final vein stage associated with main-stage mineralization (Table 5.8; Fig. 5.23). At Waisoi East, stage WE-IID veins consist primarily of chalcopyrite with minor pyrite. These veins are sparse and crosscut stage WE-IIC quartz – sulfide veins (Fig. 5.32D). They are most abundant crosscutting the DP1 intrusion and occur up to 150 m from its intrusive margin (Fig. 5.23).

*5.2.5.5 Late-stage hydrothermal alteration and veins (WE-III)*

Late-stage hydrothermal features at Waisoi East consist of four distinct alteration assemblages that overprint the dacitic intrusions and surrounding Wainimala wall rocks at Waisoi East (Fig. 5.22). The oldest late-stage alteration assemblage is composed of fault-controlled and pervasive muscovite – pyrite – quartz ± illite alteration (WE8) associated with stage WE-IIIA pyrite – quartz veins. This alteration is overprinted by an ubiquitous selective to pervasive chlorite – illite alteration assemblage (WE9) that is spatially associated with a later kaolinite – montmorillonite assemblage (WE10). Crosscutting the stage WE8 alteration are illite – calcite ± pyrite veins (WE-IIIB) and a polymict, milled matrix-supported, quartz-vein-clast-bearing breccia (WE-IIIC). Pre-

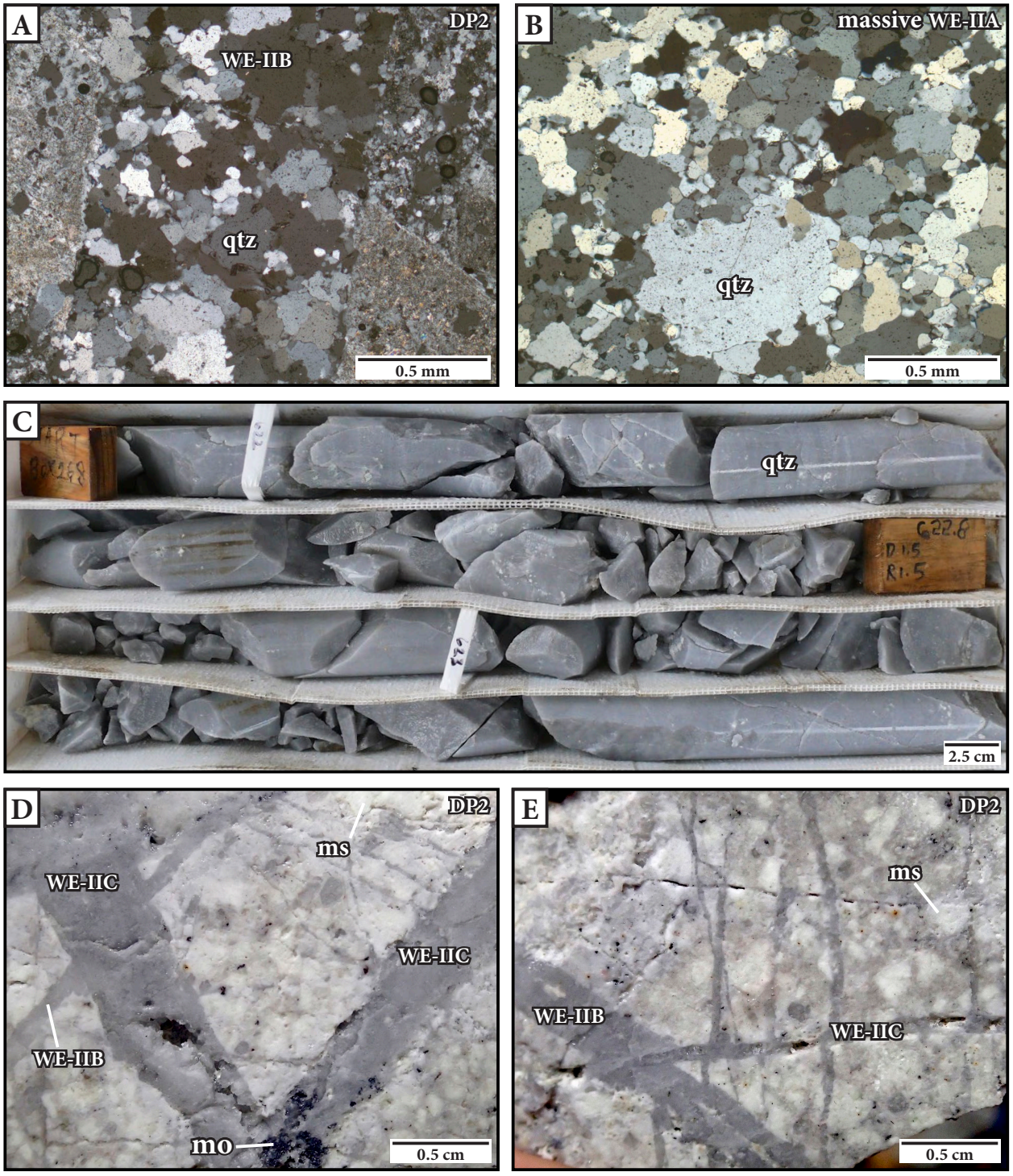


**Figure 5.33:** Examples of main-stage barren quartz veins (WE-IIB) and drusy quartz – molybdenite veins (WE-IIC). **A.** Cross-polarized photomicrograph of barren anhedral quartz vein within the DP2 intrusion. Sample: NSE002 697 m. **B.** Cross-polarized photomicrograph of massive barren stockwork at the margin of the DP2 intrusion. Quartz grains have very similar anhedral and granular textures and organization to the WE-IIB vein in Fig. 5.33A. Sample: NSE002 620 m. **C.** Core box photograph of an interval of massive barren quartz at the margin of the DP2 intrusion. Sample: NSE002 632 – 634 m. **D and E.** Intervals of the DP2 intrusion illustrating that stage WE-IIC crosscuts stage WE-IIB veins. Sample D: NSE008 725 m. Sample E: NSE002 710 m. Abbreviations: DP2 = quartz-bearing dacite, mo = molybdenite, ms = muscovite, qtz = quartz

vious workers have encountered limited zones of pink quartz + albite + pyrophyllite + corundum alteration (which cannot be an equilibrium mineral assemblage), but this was not observed in the current study.

*Muscovite – quartz – pyrite ± illite ± chlorite alteration (WE8)*

Two different styles of stage WE8 muscovite – pyrite – quartz alteration affected Waisoi East (Table 5.7). Selective, white muscovite ± illite alteration affected the feldspathic phenocrysts and groundmass components of the DP1 and DP2 intrusions (Fig. 5.34A). Outside of the intrusions, stage WE8 manifested as a patchy, pervasive, fine-grained and evenly distributed muscovite – pyrite alteration assemblage that has overprinted the groundmass of the Wainimala basaltic andesite-clast breccia (Fig. 5.34B). The second style presents as a pervasive muscovite – quartz – pyrite alteration halo to stage WE-IIIA veins and fault zones (Fig. 5.34D). Stage WE8 is best developed within the DP1 and DP2 intrusions (Fig. 5.22B); and elsewhere, it is difficult to map in terms of its intensity and distribution.

*Pyrite – quartz veins and associated fault zones (WE-IIIA)*

Stage WE-IIIA (Table 5.8) pyrite – quartz veins consist of crystalline aggregates of coarse, brassy pyrite and vuggy or sugary-textured quartz surrounded by intense, texturally destructive halos (< 1 m wide) of muscovite- or illite-altered rock with disseminated pyrite (Fig. 5.34C). These veins are typically associated with narrow (10 mm to 5 m wide), structurally-controlled polymict, breccia zones containing clasts of vein-quartz and angular, illite-altered lithic clasts in a fragmental matrix with up to 50 % disseminated pyrite (Fig. 5.34D). These breccia zones and veins have truncated all early- and main-stage veins and have been crosscut by the milled-matrix breccia (WE-IIIB) and calcite-cemented breccias and veins (WE-IIID). Stage WE-IIIA breccias and veins contain minor sphalerite and galena and commonly have an elevated Pb-Zn signature.

*Illite – chlorite ± illite-smectite alteration (WE9)*

A widespread, low-intensity assemblage consisting of illite – chlorite ± illite-smectite has partially replaced ferromagnesian minerals to chlorite, and feldspathic components have been partially dusted with illite ± illite-smectite (Table 5.8; Figs. 5.31D and 5.35B). Where WE9 chlorite – illite alteration has overprinted the WE3 chlorite – albite alteration assemblage, magnetite has

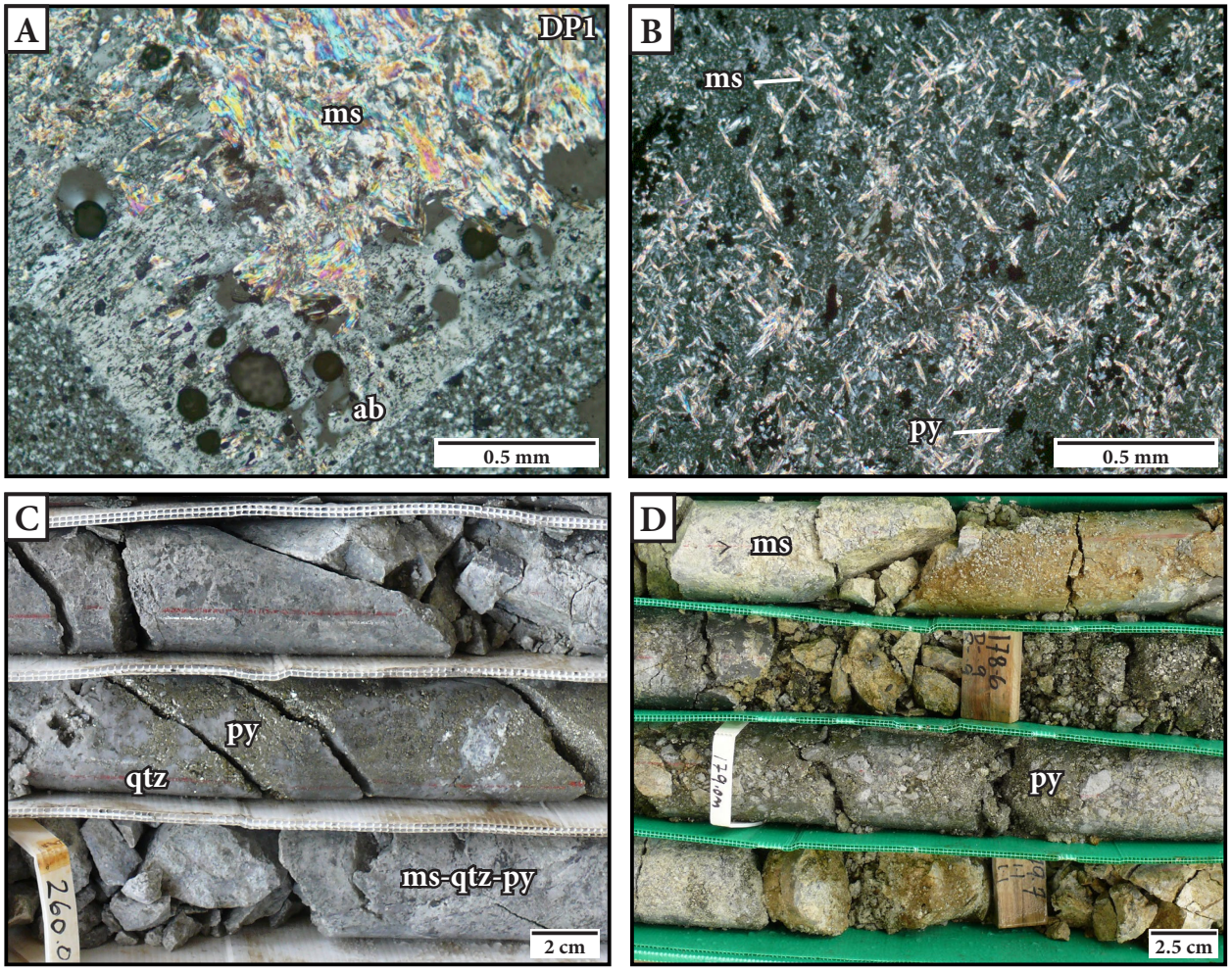


**Figure 5.34** Examples of muscovite – pyrite (WE8) alteration and pyrite – quartz (WE-IIIA) veins and breccias at Waisoi East. **A.** Cross-polarized photomicrograph of an albite-altered feldspar phenocryst in the DP1 intrusion that has been partially replaced by muscovite. Sample: NSE002 339. **B.** Cross-polarized photomicrograph of pervasive muscovite – pyrite alteration of the groundmass of Wainimala basaltic andesite-clast breccia. Sample: NSE002 214. **C.** Core box photograph of a central vein consisting of coarse-grained pyrite and vuggy quartz (WE-IIIA) that is surrounded by muscovite – quartz – pyrite alteration (WE8). Sample: NSE002 259 – 261 m. **D.** Core box photograph of a fractured pyrite – quartz breccia zone (WE-IIIA). Sample: NSE002 259 – 261 m. Abbreviations: ab = albite, DP1 = quartz eye dacite, ms = muscovite, py = pyrite, qtz = quartz.

been replaced by hematite along internal fractures (Fig. 5.29E) and domains of texturally destructive, intense, pervasive illite – chlorite ± chalcopyrite alteration has overprinted the albite – chlorite-altered groundmass of the Wainimala basaltic andesite-clast breccia (Fig. 5.35A). This has imparted a yellowish-beige hue to the matrix (Fig. 5.35C). Results from SWIR spectroscopy indicate that chlorite has a Fe-Mg composition (i.e., the typical wavelength of the Fe-OH absorption feature is between 2248 – 2252 nm; Appendix F).

*Illite – calcite ± pyrite veins (WE-IIIB)*

Stage WE-IIIB veins comprise intergrowths of illite, calcite and pyrite (Table 5.8). The illite has a milky white color and massive texture (Fig. 5.35D). These veins are irregularly shaped with

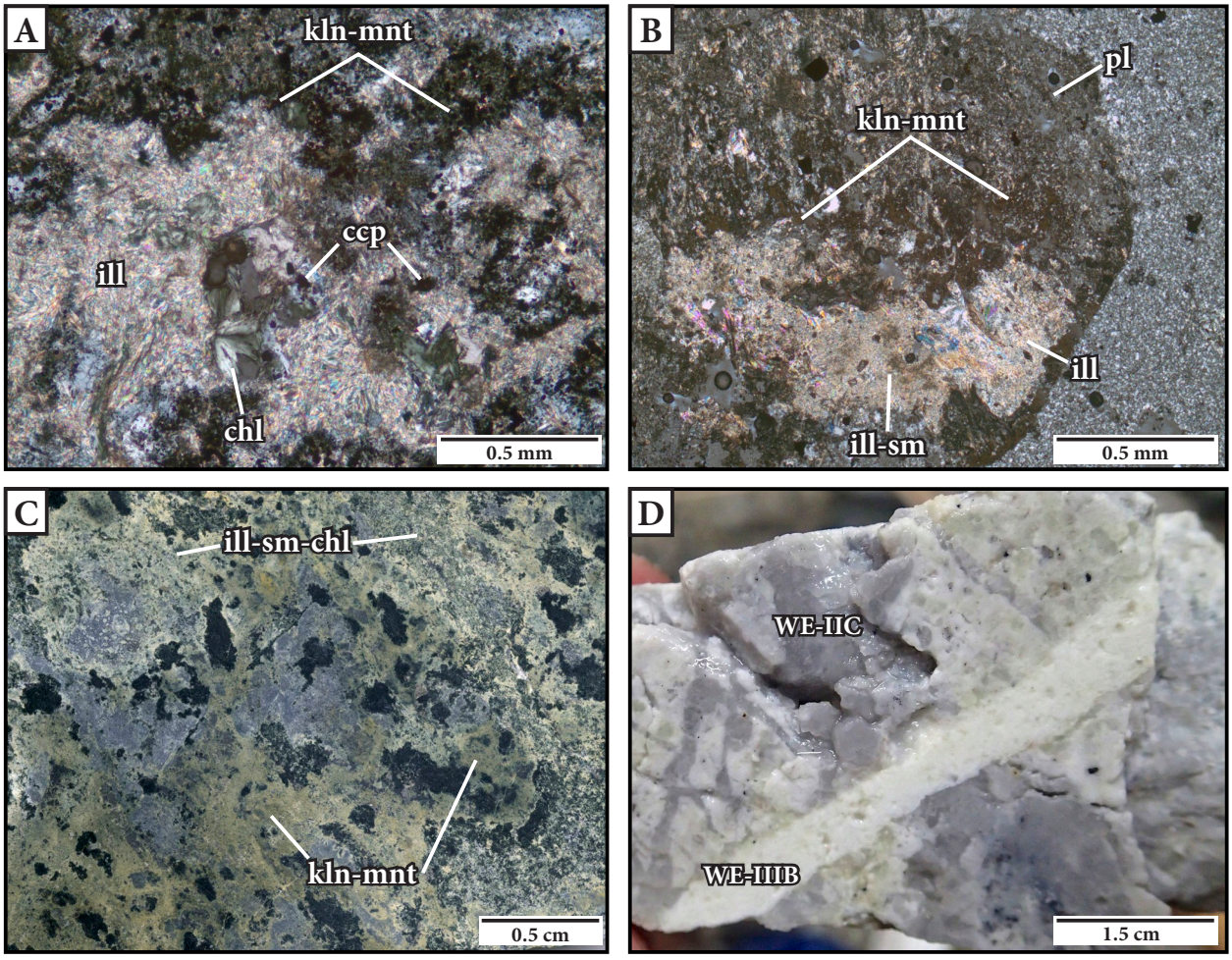


**Figure 5.35:** Examples of stage WE-IIIB illite – calcite veins, illite – chlorite (WE9) alteration and kaolinite – montmorillonite (WE10) alteration at Waisoi East. **A.** Cross-polarized photomicrograph of an intense illite – chlorite alteration spot within the Wainimala basaltic andesite-clast breccia matrix. The illite alteration is surrounded by a clay alteration rim. Sample: NSE002 226 m. **B.** Cross-polarized photomicrograph of selective illite – chlorite alteration patches partially replacing an albite-altered feldspar in the DP1 intrusion at Waisoi East. The edges of the alteration patch are replaced by kaolinite – montmorillonite alteration. Sample: NSE002 339 m. **C.** Interval of Wainimala basaltic andesite-clast breccia illustrating the strong illite-smectite – chlorite alteration, which has imparted a beige and green coloration to the groundmass. Murky brown color is kaolinite and montmorillonite alteration that has overprinted earlier chlorite – illite alteration. Sample: NSE002 103 m. **D.** Interval of quartz-bearing dacite containing vuggy quartz – molybdenite (WE-IIC) veins that have been crosscut by a late-stage illite – calcite – pyrite vein (WE-IIIB). Sample: NSE008 655 m. Abbreviations: ccp = chalcopyrite, chl = chlorite, ill = illite, ill-sm = illite-smectite, kln = kaolinite, mnt = montmorillonite, pl = plagioclase.

diffuse and non-parallel vein walls (Fig. 5.35D). These veins occur erratically throughout the Waisoi East deposit. Stage WE-IIIB veins have crosscut stage WE-IIC veins (Fig. 5.35D). Weakly developed, narrow (< 5 mm) illite alteration halos have been observed surrounding stage WE-IIIB veins locally, and may be associated with the chlorite – illite (WE9) alteration assemblage.

*Polymict, milled matrix-supported, quartz-vein-clast-bearing breccia (WE-IIIC)*

The polymict, milled matrix-supported, quartz-vein-clast-bearing breccia occupies a 5 to 10 m wide fracture zone in the northern portion of section NSE002 at 150 mRL (Table 5.8; Fig. 5.22A). The breccia consists of a main body with a narrow, dike-like geometry that has a transi-

tional contact with the adjacent host rock (Table 5.8). There is a network of smaller, finger-like (< 5 cm-wide) breccia dikes surrounding the main body that have sharp contacts with the host rocks (Fig. 5.36D). Clasts make up 50 to 70 % of the breccia and are poorly sorted (ranging from granule- to pebble-sized), polymict, sub-rounded to sub-angular, and have a chaotic clast organization. Clast types include vein-quartz, Waisoi East porphyry and Wainimala basaltic andesite clasts (Fig. 5.36A). The lithic clasts contain truncated quartz – sulfide veins (WE-IIC) that are crosscut by illite – calcite veins (WE-IIIB; Fig. 5.36A). The matrix consists of sand-sized aggregates of medium-brown biotite, illite, calcite and cubic pyrite (Fig. 5.36B). Clasts and matrix have been pervasively altered to illite – carbonate and disseminated pyrite and chalcopyrite (Fig. 5.36). Stage WE-IIIA pyrite veins have been truncated by this breccia (Fig. 5.36D). Slickenlines defined by the alignment of shreddy biotite suggest that this fault zone was tectonically active after the emplacement of the breccia (Fig. 5.36C).

The breccia is polymict, milled matrix-supported with sub-rounded clasts and formed late in the evolution of Waisoi East, based on crosscutting relationships and abundant vein-quartz clasts. No juvenile magmatic clasts or a spatial association with an intrusion were observed. These characteristics are consistent with the generation of this breccia via phreatic brecciation (cf. Sillitoe, 2010). The steeply dipping orientation of this breccia suggests a structural control on its formation. Faults, commonly localize phreatic breccias (e.g., Berger and Morrison, 1990; Tamas and Milesi, 2003). The polymict, milled matrix-supported, quartz-vein-clast-bearing breccia is interpreted to be a phreatic breccia dike occupying a steeply dipping fault. It was probably emplaced at a shallow depth in the upper levels of the hydrothermal system (i.e., probably 200 to 300 m depth and not > 1 km below the paleo-surface; cf. Sillitoe, 1985, Tamas and Milesi, 2003).

*Calcite-cemented breccias and calcite veins (WE-IIID)*

Subsequent to the development of selective illite – chlorite alteration (WE9), the Waisoi East deposit has been crosscut by barren calcite-rich veinlets that have no apparent vein-halo alteration (Table 5.8). Stage WE-IIID occurs as random, crenulated, irregular, branching veinlets and veins that have variable vein apertures (1 to 15 mm) and are most common in the chlorite – al-

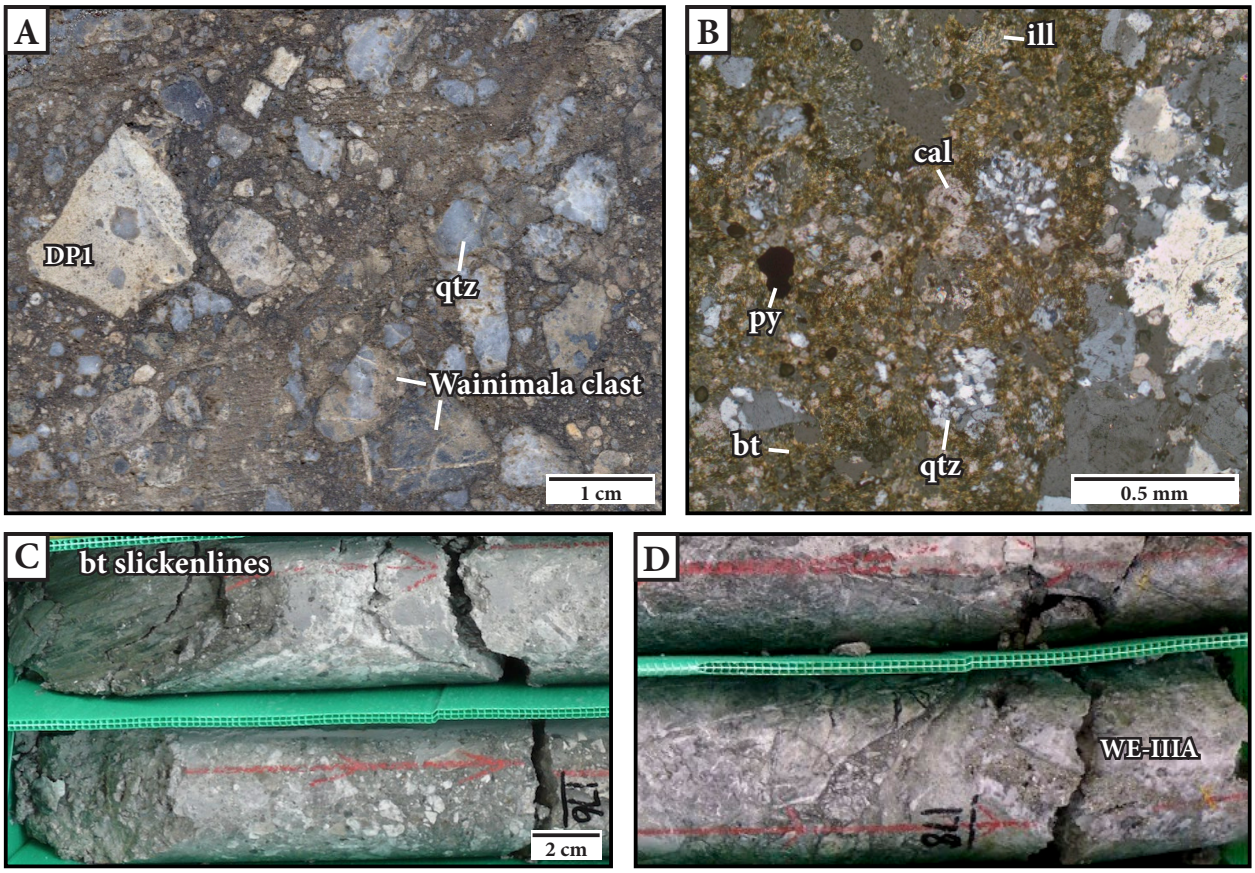


**Figure 5.36:** Examples of polymict, milled matrix-supported, quartz-vein-clast-bearing breccia (WE-IIIC). **A.** Interval of milled matrix breccia showing clasts of DP1 and Wainimala volcanics that have been crosscut by illite – calcite veins (WE-IIIB). There are abundant quartz vein clasts surrounded by a milled biotite matrix. Clasts have been altered to illite – calcite – pyrite. Sample: NSE008 177 m. **B.** Cross-polarized photomicrograph of the milled matrix breccia illustrating quartz-vein clasts surrounded by a milled biotite matrix that has been altered to calcite and pyrite. Sample: NSE002 177 m. **C.** Core box photograph of slickenlines defined by the alignment of biotite ± chlorite within the milled matrix breccia. Sample: NSE002 177 – 178 m. **D.** Core box photograph of finger-like breccia dikes at the margin of the main body of the milled matrix breccia. A quartz –pyrite vein (WE-IIIA) is truncated by one of the breccia fingers. Sample: NSE002 259 – 261 m. Abbreviations: bt = biotite, cal = calcite, DP1 = quartz-eye dacite, ill = illite, py = pyrite, qtz = quartz.

bite-altered domain (WE2). Where they occur as breccia cement, the drill core is typically soft and friable (Fig. 5.37). The breccia is monomict, composed of locally derived clasts (angular, blocky to splintery and not slabby), and have a jigsaw-fit to clast-rotated internal organization. The breccias are massive, with no obvious tectonic fabric. Based on crosscutting relationships, stage WE-IIID veinlets are younger than stage WE-IIIB and WE-IIIA (Fig. 5.36B).

*Kaolinite – montmorillonite alteration (WE10)*

The last hydrothermal event at Waisoi East is composed of kaolinite, montmorillonite, and illite-smectite (Table 5.7). Stage WE10 presents as weak to moderate intensity, selective kaolinite alteration of plagioclase phenocrysts and montmorillonite ± illite-smectite alteration of ferromag-


**Figure 5.37:** Core box photograph of calcite-cemented breccia illustrating the soft and friable nature of the drill core. The periphery of the breccia transitions into irregular and branching veins and veinlets of calcite. Sample: NSE008 590.5 – 598.2 m.

nesian minerals (Figs. 5.31D and 5.35B). Stage WE10 also occurs as moderate to strong intensity, selective kaolinite – montmorillonite ± illite-smectite alteration that overprints the outer edges of stage WE9 illite – chlorite alteration patches (Figs. 5.35A and B). Where this occurs, kaolinite and illite-smectite can make up over 12 vol % of the altered rock (Appendix B). Kaolinite – montmorillonite alteration imparts a characteristic pale to murky brown hue where it overprints earlier alteration stages (Fig. 5.35C). Locally, kaolinite – montmorillonite alteration is associated with faults and fracture zones. It has not been possible to link these faults between drill holes, therefore their orientation remains unclear. Stage WE10 alteration has a similar distribution to stage WE9, such that it overprints all Waisoi East dacitic intrusions and the surrounding Wainimala host sequence.

### *5.2.6 Discussion*

Using the classification scheme from McMillan and Panteleyev (1988), two contrasting styles of porphyry deposits can be recognized within the Namosi district. The first style is a variation on the plutonic-hosted porphyry deposit model (e.g., Wainaulo and Wainaulo West), consisting

of mineralizing dike swarms emplaced into porphyritic diorite plutons. The tabular, vertically attenuated orebodies are coincident with quartz- and epidote-vein stockworks that are localized around these dikes. The second type are volcanic-hosted porphyry deposits (e.g., Waisoi West and Waisoi East), consisting of multiphasic porphyritic stocks that intruded the volcanic host sequence. The orebodies are shallow and annular, occurring in and around the cupola of the porphyritic stocks, superjacent to high-volume, barren quartz-vein stockworks. Mineralization commonly occurs as disseminations and quartz-sulfide-veins that are most abundant within highly fractured zones surrounding the porphyritic stocks.

*5.2.6.1 Wainaulo*

Early-stage events were responsible for the introduction of medium-grade copper, low-grade Au and the bulk of Mo mineralization. Early-stage alteration occurs as a widespread concentric zonation surrounding dioritic intrusions and consists of a central zone of biotite – albite ± actinolite (sodic-potassic) alteration, a medial zone of actinolite – albite ± chlorite (calc-sodic or inner propylitic) alteration and a distal zone of chlorite – albite ± epidote (propylitic) alteration. Prograde chalcopyrite-bearing andradite – actinolite – magnetite (calcic exoskarn) alteration has locally replaced permeable, reactive carbonate-bearing horizons within the Namosi Andesite Formation. Fine-grained micas and clays with paragonitic compositions are commonly associated with these alteration assemblages.

Main-stage events produced high-grade copper and gold mineralization and are associated with the emplacement of quartz-diorite intrusions. The occurrence of bornite- and chalcopyrite-bearing USTs in the apical portion of the early-mineralization quartz-diorite porphyry dike implies the contemporaneous nature of magmatic and hydrothermal events at Wainaulo. Main-stage alteration and mineralization largely consists of a narrow zone of chlorite – albite – actinolite ± epidote (sodic to calc-sodic) alteration and spatially coincident quartz – sulfide vein stockworks (with albite vein halos) that occur within and surrounding the quartz-diorite intrusions. Crosscutting the quartz – sulfide vein stockworks are high-grade epidote – sulfide – anhydrite veins (with conspicuous K-feldspar – epidote vein halos, which are an unusual porphyry-related

vein style to contribute ore grade. Fine-grained micas with phengitic compositions are commonly associated with the K-feldspar vein halos. Main-stage mineralization, alteration and veins were emplaced cyclically with the intrusion of the EMQD, IMQD and LMQD dikes. However, the alteration intensity and vein and sulfide abundance decreased sequentially with each intrusion. The dominant sulfide species also changed associated with the emplacement of the EMQD (bornite), IMQD (chalcopyrite) and LMQD (pyrite) intrusions.

Late-stage events contributed minor amounts of lead and zinc and copper mineralization at Wainaulo. The bulk of this mineralization is associated with anhydrite – chlorite – pyrite veins with illite – pyrite (phyllic) vein-halo alteration. These veins have a sparse and widespread distribution at Wainaulo. A moderate intensity chlorite – illite ± illite-smectite (intermediate-argillic) alteration assemblage occurs in an upward-flaring alteration zone centered on and overprinting the quartz-diorite dike complex. The final alteration event at Wainaulo involved the development of fault-bounded zones of kaolinite – montmorillonite (argillic) alteration that has overprinted and partially destroyed main-stage alteration and mineralization within the core of the deposit.

The Wainaulo alteration zonation is similar to that described for porphyry Cu deposits in Sillitoe (2010) and for alkalic porphyry Au-Cu deposits in Wilson et al. (2003). Some key differences are that early and central calc-potassic alteration grades outward to calc-sodic (inner propylitic) and then propylitic alteration. The central calc-potassic alteration zone had then been overprinted by calc-sodic (or sodic) alteration (related to a later porphyritic intrusion). In contrast, Wilson et al (2003) and Wilson (2003) describe a pattern where calc-sodic alteration is overprinted by potassic and calc-potassic alteration. Several other porphyry systems have been documented to have an inner calc-sodic alteration assemblage (e.g., Koloula, Solomon Islands; Chivas, 1978). Another notable difference is that the intermediate-argillic (chlorite – sericite) alteration has an upward-flaring distribution centered on and overprinting the core of the calc-potassic and calc-sodic alteration zones. This alteration style had overprinted earlier developed, structurally controlled, phyllic alteration. In contrast, Sillitoe (2010) describes chlorite – sericite alteration to generally be overprinted by later phyllic alteration.

*5.2.6.2 Waisoi East and Waisoi West*

The first stage of alteration at the Waisoi deposits consists of a widespread zonation from biotite – albite – magnetite ± actinolite ± chalcopyrite (potassic to calc-potassic) alteration outward to chlorite – albite – magnetite ± calcite ± epidote (propylitic) alteration that is centered on quartz-dioritic to dacitic stocks. Locally, highly fractured zones with abundant quartz veins are altered to an assemblage of talc – Mg-chlorite + dolomite + phlogopite ± chalcopyrite (magnesian exoskarn) where early magmatic-hydrothermal fluids have reacted with magnesium-rich and carbonate-bearing horizons within the Wainimala Group host sequence. The majority of Cu-Au mineralization is associated with biotite-bearing quartz – sulfide ± magnetite stockworks that are overprinted by quartz – sulfide and then sulfide-only veins, all of which have albite ± K-feldspar vein-halo alteration. Fine-grained micas and clays with paragonitic compositions are commonly associated with these alteration assemblages. At Waisoi East, quartz – molybdenite ± pyrite ± chalcopyrite veins crosscut the earlier-formed quartz – sulfide and sulfide-only veins and stockworks and contribute significant molybdenum mineralization, even within the Cu-Au barren core of the dacitic stocks.

Late-stage alteration at the Waisoi deposits consists of a strong intensity, upwardly flaring, Pb-Zn-bearing paragonitic illite/muscovite – quartz – pyrite (phyllic) alteration zone that is centered on and best-developed within the quartz-diorite and dacite stocks. Overprinting and coincident with this alteration are zones of illite-smectite – chlorite (intermediate-argillic) and kaolinite – montmorillonite (argillic) alteration. The phyllic alteration at the Waisoi deposits is much more strongly developed than at Wainaulo. This is interpreted to indicate that the water to rock ratio was high during late-stage hydrothermal activity at the Waisoi deposits compared to at Wainaulo.

## 5.3 Re–Os geochronology

*5.3.1 Introduction*

Prior to this study, there had been no attempts to directly date the ages of mineralization in

the Namosi district. In the current study, Re–Os ages of molybdenite have been obtained from paragenetically constrained quartz – molybdenite veins from Wainaulo, Waisoi West and Waisoi East. These results are put in the context of the deposit-scale paragenesis to provide evidence for the rapid magmatic-hydrothermal evolution of the Namosi district.

### *5.3.2 Re–Os analytical methods*

Three molybdenite-bearing drill core samples (NVD037-188, NSE008-675 and NSW014-614; Table 5.9 and Figure 5.38) were sent to Dr. Robert Creaser at the University of Alberta Radiogenic Isotope Facility for mineral separation and Re–Os dating. For each sample, molybdenite mineral separates were produced by metal-free crushing, followed by gravity and then magnetic concentration separation techniques. The steps followed for molybdenite analysis are described in detail by Selby and Creaser (2004) and Markey et al. (2007). The $^{187}$Re and $^{187}$Os concentrations in molybdenite were determined by isotope dilution mass spectrometry using Carius-tube, solvent extraction, anion chromatography and negative thermal ionization mass spectrometry methods. A mixed double spike containing known amounts of isotopically enriched $^{185}$Re, $^{190}$Os, and $^{188}$Os analysis was used. Re–Os isotopic analysis was made using a ThermoScientific Triton mass spectrometer by Faraday collector. Total procedural blanks for Re and Os are < 3 picograms and 2 picograms, respectively, which are insignificant for the Re and Os concentrations in most molybdenite samples. The Chinese molybdenite powder HLP-5 (Markey et al., 1998) was analyzed as a standard. For this control sample over a period of two years, an average Re–Os date of 221.56 ± 0.40 Ma (1SD uncertainty, n = 10) has been obtained. This Re–Os age date is identical to that reported by Markey et al. (1998) of 221.0 ± 1.0 Ma.

**Table 5.9:** Re–Os data for molybdenite from Namosi district porphyry deposits

| Sample name | Deposit | Vein stage | Re (ppm) | $^{187}$Re (ppm) | $^{187}$Os (ppb) | Age (Ma) |
|---|---|---|---|---|---|---|
| NVD037-188 | Wainaulo | WO-IB | 402.3 (10) | 252.9 (7) | 23.97 (2) | 5.690 ± 0.023 |
| NSW014-614 | Waisoi West | WW-ID | 3400 (9) | 2137 (6) | 195.6 (19) | 5.494 ± 0.023 |
| NSW014-614 RPT | Waisoi West | WW-ID | 3506 (9) | 2203 (6) | 200.9 (15) | 5.473 ± 0.022 |
| NSE008-675 | Waisoi East | WE-IIC | 1941 (5) | 1220 (3) | 106.7 (8) | 5.248 ± 0.022 |

Abbreviations: ppb = parts per billion, ppm = parts per million, RPT = replicate,
Absolute uncertainties (in parentheses) are shown at the 2σ level for the last digit indicated.

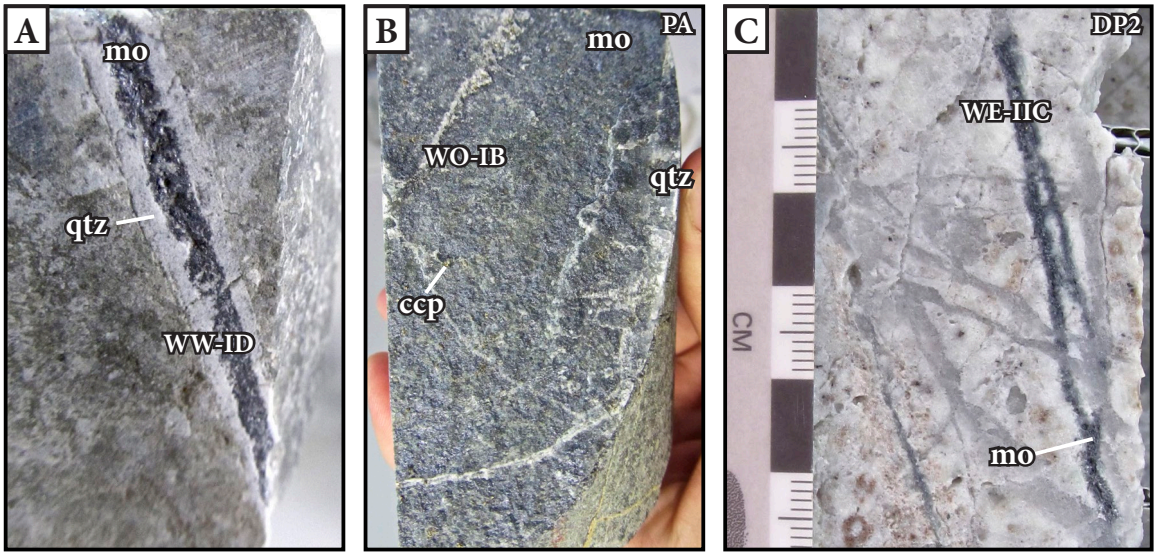


**Figure 5.38:** Hand sample photographs of the molybdenite-bearing quartz veins submitted for Re–Os age determinations. **A.** Wainimala sandstone from Waisoi West that has been crosscut by a stage WW-ID quartz – molybdenite vein. Sample: NSW014 614 m. **B.** Porphyritic andesite (PA) that has been crosscut by stage WO-IB quartz – molybdenite – chalcopyrite veins. Sample: NVD037 188 m. **C.** Quartz-bearing dacite (DP2) that has been crosscut by stage WE-IIC quartz – molybdenite veins. Sample: NSE008 675 m. Abbreviations: ccp = chalcopyrite, DP2 = quartz-bearing dacite, mo = molybdenite, PA = porphyritic andesite, qtz = quartz.

### *5.3.3 Results*

The results of the Re–Os age determinations are presented in Table 5.9. The age uncertainty is quoted at a 2σ level and includes all known analytical uncertainty. Analysis of a stage WO-IB quartz – molybdenite – chalcopyrite vein (Fig. 5.38B) from Wainaulo returned a $^{187}Re/^{187}Os$ age of 5.690 ± 0.023 Ma with a relatively low Re content (402.3 ppm Re; Table 5.9). Both analyses from a stage WW-ID quartz – molybdenite vein (Fig. 5.38A) from Waisoi West yielded Re–Os ages of ~ 5.5 Ma (specifically, 5.473 ± 0.022 and 5.494 ± 0.023 Ma), with high Re contents (up to 3506 ppm; Table 5.9). The stage WE-IIC quartz – molybdenite vein (Fig. 5.38C) from Waisoi East yielded an age of 5.248 ± 0.022 Ma with an intermediate Re content (1941 ppm; Table 5.9). These Re-Os ages constrain the timing of mineralization in relation to magmatism at the principal deposits within the Namosi district (Table 5.10).

### *5.3.4 Timing and duration of the Namosi magmatic-hydrothermal systems*

Bracketing the duration of the magmatic and mineralizing events within a porphyry district is an important step towards generating a genetic model (Chiaradia et al., 2013; e.g., Cadia district, Australia: Wilson et al., 2007; Baguio district, Philippines: Waters et al., 2011; Morococha district,

**Table 5.10**: Geochronology of Namosi district intrusions and molybdenite mineralization

| Material dated | Deposit | Sample ID | Age (± 2σ) | Dating method | Source |
|---|---|---|---|---|---|
| PD<br>Porphyritic diorite | Wainaulo | NVD019-583 | 5.99 ± 0.46 | U–Pb zircon<br>ELA-ICP-MS | This study |
| PA<br>Porphyritic andesite | Wainaulo | NWK-18 345.0 | 6.0 ± 0.3 | K–Ar<br>bulk | Tanaka et al. 2010 |
| EMD1 (stage WO-I)<br>Early-mineralization diorite 1 | Wainaulo | NVD040-550.6 | 5.654 ± 0.095 | U–Pb zircon<br>CA-TIMS | This study |
| | Wainaulo | NVD019-708.1 | 5.31 ± 0.43 | U–Pb zircon<br>ELA-ICP-MS | This study |
| Stage WO-IB quartz – molybdenite vein | Wainaulo | NVD037-188 | 5.690 ± 0.023 | Re–Os<br>molybdenite | This study |
| EMQD (stage WO-II)<br>Early-mineralization quartz-diorite | Wainaulo | NVD040-533 | 5.554 ± 0.054 | U–Pb zircon<br>CA-TIMS | This study |
| | Wainaulo | NVD037-640 | 5.46 ± 0.90 | U–Pb zircon<br>ELA-ICP-MS | This study |
| IMQD (stage WO-II)<br>Inter-mineralization quartz-diorite | Wainaulo | NVD | 5.4 ± 0.3 | U–Pb zircon<br>ELA-ICP-MS | Harris, 2009a |
| LMQD (stage WO-II)<br>Late-mineralization quartz-diorite | Wainaulo | NVD016-557.8 | 5.33 ± 0.22 | U–Pb zircon<br>ELA-ICP-MS | This study |
| QDP1 (stage WW-I)<br>Quartz-diorite porphyry 1 | Waisoi West | NSW006-406 | 5.492 ± 0.043 | U–Pb zircon<br>CA-TIMS | This study |
| Stage WW-ID quartz – molybdenite vein | Waisoi West | NSW014-614 | 5.494 ± 0.023 | Re–Os<br>molybdenite | This study |
| | Waisoi West | NSW014-614 RPT | 5.473 ± 0.022 | Re–Os<br>molybdenite | This study |
| DP1 (stage WE-II)<br>Quartz-eye dacite | Waisoi East | NSE002-360 | 5.432 ± 0.031 | U-Pb zircon<br>CA-TIMS | This study |
| DP2 (stage WE-II)<br>Quartz-bearing dacite | Waisoi East | NSE001W-633 | 5.297 ± 0.025 | U–Pb zircon<br>CA-TIMS | This study |
| Stage WE-IIC quartz – molybdenite vein | Waisoi East | NSE008-675 | 5.248 ± 0.022 | Re–Os<br>molybdenite | This study |

Peru: Catchpole et al., 2015). Several recent studies, using U–Pb dating of zircon and Re–Os dating of molybdenite (and other isotopic dating methods), have shown that the lifespan of porphyry copper systems can range from < 1 to > 4 Ma (e.g., Sillitoe and Mortensen, 2010; von Quadt et al., 2011; Deckart et al., 2013; Deckart et al., 2014; Catchpole et al., 2015). Geochronological results from this study provide a valuable contribution to the porphyry district model and indicate that the three principal deposits of the Namosi district formed over a span of about half a million years, separated by very short periods of magmatic quiescence.

The Namosi district is an ideal setting for the use of Re–Os on molybdenite and U–Pb on zircon to bracket the duration of the district-scale magmatic-hydrothermal system. Molybdenite occurs at each of the principal deposits. At the oldest deposit, Wainaulo, crosscutting relationships show that molybdenite was precipitated during the first mineralizing event. In the youngest deposit, Waisoi East, molybdenite has been paragenetically constrained to have been emplaced late

in the deposit history. The relative intrusive history at each deposit has been determined based on field relationships. Therefore, these results can bracket both the duration of mineralization and magmatic activity of the principal deposits within the district.

At Wainaulo, the U–Pb age for the precursor PD stock is within 2 – 3 % error of the U–Pb age that was determined for the earliest mineralized dike (EMD1; Table 5.10; Fig. 5.39). Due to the large errors associated with U–Pb ages analyzed using the ELA-ICP-MS method, the precise time gap between non-productive and productive diorite intrusions at Wainaulo has not been constrained reliably. However, bulk rock K–Ar ages for a hornblende diorite porphyry (interpreted here to be PA) were reported as 6.1 ± 0.5 Ma and two at 6.0 ± 0.3 Ma by Tanaka et al. (2010).

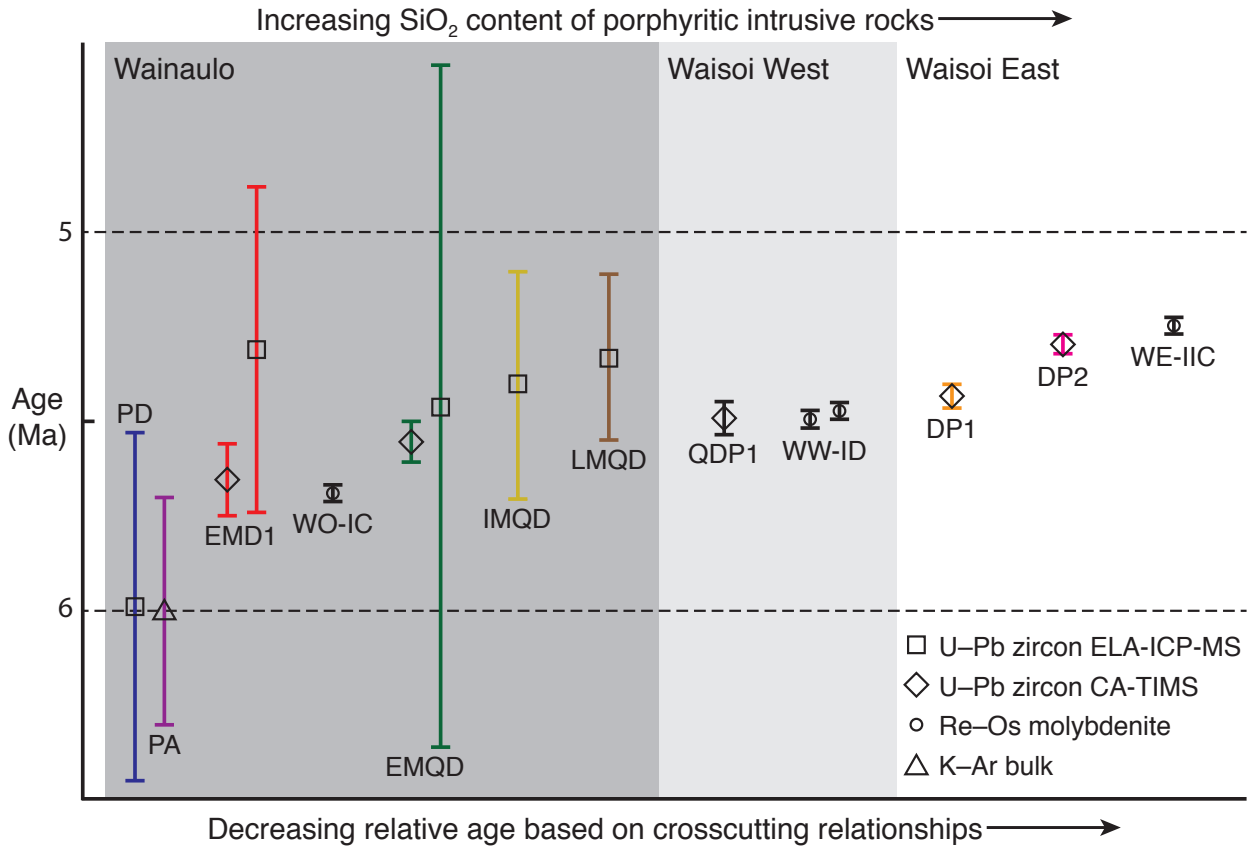


**Figure 5.39:** Summary of the geochronology of magmatic and mineralizing events in the Namosi district, illustrating the compositional evolution from dioritic (Wainaulo; 5.75 – 5.50 Ma; dark gray shaded area) to quartz-dioritic (Waisoi West; after 5.54 Ma; light gray shaded area) to dacitic (Waisoi East; 5.46 – 5.27 Ma; white area) magmatism. Stage WO-IC quartz – molybdenite – chalcopyrite veins were emplaced within error of the EMD1 dike at Wainaulo, stage WW-ID quartz – molybdenite veins were emplaced within error of the QDP1 stock at Waisoi West, and stage WE-IIC quartz – molybdenite veins were emplaced 2000 years outside of the 2σ confidence level for the DP2 stock at Waisoi East. This diagram also illustrates the deposit scale chronology of magmatic and mineralizing events at Wainaulo and Waisoi East. At Wainaulo, pre-mineralization magmatism occurred at ~ 6.0 Ma (PD and PA) and transitioned to early-stage magmatism and Cu-Au-Mo mineralization from 5.74 – 5.67 Ma. This early-stage mineralization was overprinted by high-grade main-stage Cu-Au mineralization associated with the EMQD dike from 5.60 – 5.50 Ma. At Waisoi East, magmatism associated with early Cu-Au mineralization was emplaced at 5.46 to 5.40 Ma and was overprinted by significant Mo mineralization associated with the DP2 stock from 5.27 – 5.23 Ma. Abbreviations: DP1 = quartz-eye dacite, DP2 = quartz-bearing dacite, EMD1 = early-mineralization diorite 1, EMQD = early-mineralization quartz-diorite, QDP1 = quartz-diorite porphyry 1, PA = porphyritic andesite, PD = porphyritic diorite.

An age of ~ 6.0 Ma for the pre-mineralization intrusions at Wainaulo is consistent with the age determinations for younger intrusions and is therefore considered to be reasonable. The tight gap in ages between the pre-mineralization porphyritic diorite (PD) and the oldest mineralized diorite (EMD1) suggests derivation from a common parental magma (e.g., Clark et al., 1990). The emplacement of the EMD1 dike at 5.654 ± 0.095 Ma overlaps with the age of molybdenite mineralization (5.690 ± 0.023 Ma) within stage WO-IB quartz – molybdenite – chalcopyrite veins (Table 5.10; Fig. 5.39). The EMD1 dike is interpreted to be the causative intrusion associated with early biotite – albite hydrothermal alteration and moderate Cu-Au-Mo mineralization at Wainaulo. On the other hand, the EMQD dike, which was emplaced at 5.554 ± 0.054 Ma, postdates the early molybdenum mineralization (Table 5.10; Fig. 5.39). EMQD is interpreted to be the causative intrusion associated with high-grade Cu-Au mineralization and albite – chlorite – epidote alteration at Wainaulo. The EMQD intrusion crosscuts the early biotite – albite alteration associated with EMD1. Therefore, the duration of biotite – albite alteration and the gap between successive mineralizing phases at Wainaulo could have been ~ 0.100 ± 0.149 m.y., i.e., the age for sample NVD040-550.6 minus the age for sample NVD040-533 ± the sum of the individual uncertainties.

At Waisoi West, one of the early phases of the QDP1 stock was emplaced at 5.492 ± 0.043 Ma, which overlaps with the ages determined for molybdenite mineralization in a stage WW-ID quartz – molybdenite vein (5.494 ± 0.023 and 5.473 ± 0.022 Ma; Table 5.10; Fig. 5.39). The time gap between early-stage magmatism at Wainaulo and Waisoi West is 0.062 ± 0.097 My.

At Waisoi East, DP1 was emplaced at 5.432 ± 0.031 Ma (Table 5.10; Fig. 5.39). This intrusion is associated with early Cu-Au mineralization. A distinct age was determined for DP2 at 5.297 ± 0.025 Ma, which is followed closely (~ 2,000 years later) by molybdenite mineralization (5.248 ± 0.022 Ma; Table 5.10; Fig. 5.39). Therefore, the time gap between early mineralization magmatism at Waisoi West and Waisoi East is 0.06 ± 0.074 My and for successive mineralized intrusions at Waisoi East is 0.184 ± 0.053 My. These geochronological results are consistent with crosscutting observations (Figs. 5.2, 5.16 and 5.23). The Re–Os and U–Pb results are consistent, suggesting that the dates reported in this study are reliable (cf. Chiaradia et al., 2013).

Magmatism within the Namosi porphyry copper district, including the pre-mineralization intrusions (PA and PD) at Wainaulo, developed over an interval of ≤ 750,000 years, whereas the duration of magmatic-hydrothermal activity lasted ≤ 500,000 years. This time period for the magmatic-hydrothermal evolution of the three principal deposits of the Namosi district is significantly shorter than the lifespan of typical porphyry copper systems of the central Andes (e.g., Chuquicamata, ≤ 3.9 Ma, Ballard et al., 2001; El Teniente, ≤ 3.4 Ma, Maksaev et al., 2004; Escondida, ≤ 5.2 Ma, Padilla-Garza et al., 2004; Los Pelambres, ≤ 3.83 Ma, Perelló et al., 2009; Quellaveco, ≤ 4.9 Ma, Sillitoe and Mortensen, 2010). The Namosi district life-cycle can be more closely compared with that of the Philippine Bayugo and Boyongan Cu-Au deposits (≤ 500,000 years; Braxton, 2007). However, this time frame does not take into account the other porphyry Cu-Au deposits and prospects of the Surigao district (i.e., Asiga River, Maraat, Suyoc and Madya). At Batu Hijau, Indonesia, Garwin (2002) showed that individual porphyry Cu-Au deposits formed quickly (i.e., 0.08 ± 0.08 My), but the district lifespan was much longer. Four distinct porphyry centers spanned 2.2 Ma, separated by 0.6 to 0.9 My amagmatic periods (Garwin, 2002). At Namosi the longest time gap between successive porphyry intrusions determined was 0.184 ± 0.053 My (with the exception of the time gap between the precursor pluton and early-mineralization dikes at Wainaulo). The ephemeral nature of magmatism within the Namosi district likely implies that the hypothesized underlying parental pluton may have had a much shorter lifespan than the porphyry deposit-related plutons of the central Andes and probably reflects a more dynamic and rapidly evolving tectonic environment.

## 5.4 Summary

Age determinations have constrained the genesis of productive Namosi district magmatism and mineralization to a period of less than 520 ky (from ~ 5.75 Ma to 5.23 Ma). The oldest porphyry deposit in the district is Wainaulo (5.749 – 5.500 Ma), which is a variation on the plutonic-hosted porphyry deposit and has a complex alteration and mineralization paragenesis. It has an early widespread potassic, inner propylitic and propylitic alteration zonation that is centered on a dioritic intrusive complex and is related to the bulk of Mo, medium-grade Cu and low-grade

Au mineralization. This is crosscut by a quartz-dioritic intrusive complex that is associated with high-grade Cu-Au mineralization, and sodic, calc-sodic and potassic alteration. The final stages of hydrothermal activity introduced structurally controlled phyllic and argillic alteration and widespread upwardly flaring intermediate argillic alteration.

Quartz-dioritic magmatism and related Cu-Au mineralization were emplaced at Waisoi West from 5.535 – 5.449 Ma, followed by dacitic magmatism and Cu-Au-Mo mineralization at Waisoi East from 5.463 – 5.226 Ma. Both Waisoi deposits are volcanic-hosted porphyry deposit types, and consist of intrusion concentric early potassic and propylitic alteration that is overprinted by a progression of sulfide bearing stockworks associated with sodic-potassic vein halos. Widespread, strong intensity, upward flaring phyllic alteration overprinted the intrusive complexes and overlying volcanic host sequence at each deposit. Molybdenite-bearing quartz – sulfide veins were emplaced late in the paragenesis of the Waisoi East deposit, and contributed significant molybdenum mineralization, even within the Cu-Au barren core of the dacitic stocks.

# CHAPTER 6

# Hydrothermal geochemistry

## 6.1 Introduction

This chapter presents new stable (S, O–D) and radiogenic (Sr) isotopic data for hydrothermal minerals from Wainaulo, Waisoi West and Waisoi East. These datasets are used to trace ore-forming fluid sources, as well as constrain evolutionary processes and depositional mechanisms for the Namosi district porphyry deposits.

## 6.2 Sulfur isotopes

### *6.2.1 Introduction*

In general, the sulfur isotopic compositions of sulfide minerals in porphyry Cu deposits range between -3 and +1 ‰ and sulfate values range from 8 – 15 ‰, suggesting a magmatic derivation (Field and Gustafson, 1976; Shelton and Rye, 1982; Rye, 2005). Diversions of $\delta^{34}S_{sulfide}$ below this range are more common in alkalic porphyry systems rather than calc-alkalic (e.g., Cadia: Wilson et al., 2007a; Galore Creek: Micko, 2010; Mount Polley: Pass et al., 2014). $\delta^{34}S$ values can provide intensive physicochemical information, such as temperature and oxidation potential of the ore-forming fluids, as well as possible sources of sulfur (Ohmoto and Rye, 1979). Sulfate – sulfide fractionation factors increase with decreasing temperature and are dependent on the oxidation state of the fluid (Ohmoto and Lasaga, 1982). Under more oxidizing conditions (e.g., $H_2S/SO_4 = 0.2$), magmatic fluids are depleted in $\delta^{34}S$ and tend to produce a wide range of $\delta^{34}S_{sulfide}$ values (e.g., Tintic: Hildreth and Hannah, 1996; Cadia: Wilson et al., 2007a). Homogeneous and positive $\delta^{34}S$ values are expected under more reducing conditions (e.g., Kerikil: Wurst, 2004; Kelian: Davies et al., 2008; Ampucao and Santo Tomas II: Cooke et al., 2011).

### *6.2.2 Previous work*

The only previous sulfur isotopic study of hydrothermal minerals in the Namosi district was by Egashira (2009), who performed sulfur isotope analyses on sulfide and sulfate minerals collected from deposits and prospects in the Waivaka Corridor (Wainivisowaqa, Wainaulo, Wainaulo West and Wainivuga; Fig. 1.2). Egashira (2009) reported values of $\delta^{34}S_{sulfide}$ from −8.6 to +3.8 ‰ and $\delta^{34}S_{sulfate}$ values between +10.0 and +17.0 ‰ (Table 6.1; Appendix G). No spatial zonation of $\delta^{34}S$ was identified. Egashira (2009) noted that over the duration of the mineralizing events (i.e., with progressively younger mineralizing vein stages) values of $\delta^{34}S_{sulfide}$ gradually decrease and values of $\delta^{34}S_{sulfate}$ increase, coinciding with a decreasing temperature of mineralization. The systematic variation in $\delta^{34}S$ was interpreted to result from fractionation of aqueous sulfate with respect to aqueous sulfide at lower temperature. Recalculated temperatures for hydrothermal fluids (using the sulfate – sulfide geothermometers from Ohmoto and Lasaga, Tables 6.2 and 6.5; Appendix G) range from 504 – 323°C. Egashira (2009) calculated a high bulk $\delta^{34}S$ of +7.0 ‰, which was

**Table 6.1:** $\delta^{34}S$ values of sulfides and sulfates from Waivaka Corridor deposits and prospects (data from Egashira, 2009)

| Deposit/prospect | Mineral | Number of analyses | Range of $\delta^{34}S$ (‰) | Mean $\delta^{34}S$ (‰) |
|---|---|---|---|---|
| Wainivisowaqa | Chalcopyrite | 5 | -3.3 to -0.4 | -1.9 |
| | Pyrite | 2 | -2.3 to -1.8 | -2.0 |
| Wainivuga | Bornite + chalcopyrite | 3 | -0.4 to +0.9 | +0.2 |
| | Chalcopyrite | 9 | -3.9 to +2.3 | 0 |
| | Pyrite | 1 | – | -2.0 |
| | Anhydrite | 2 | +11.5 to +17.3 | +14.4 |
| | Gypsum | 3 | +14.5 to +15.0 | +14.8 |
| | Anhydrite + gypsum | 1 | – | +15.6 |
| Wainaulo West | Sphalerite | 2 | -5.7 to +1.0 | -2.4 |
| | Bornite + chalcopyrite + pyrite | 1 | – | +1.1 |
| | Chalcopyrite | 7 | -5.7 to -0.2 | -1.6 |
| | Chalcopyrite + pyrite | 1 | – | -8.6 |
| | Pyrite | 5 | -1.8 to +0.6 | -0.4 |
| Wainaulo | Sphalerite | 1 | – | -1.3 |
| | Bornite + chalcopyrite | 2 | -0.7 to +0.7 | 0 |
| | Chalcopyrite | 26 | -4.1 to +3.8 | -0.5 |
| | Chalcopyrite + pyrite | 3 | -2.0 to 0 | -1.0 |
| | Pyrite | 7 | -5.0 to +0.2 | -2.3 |
| | Anhydrite | 10 | +10.7 to +16.8 | +13.3 |
| | Anhydrite + gypsum | 3 | +12.3 to +14.8 | +13.6 |
| | Gypsum | 6 | +10.2 to +14.6 | +13.0 |

Note that the deposit referred to here and elsewhere in this study as Wainaulo and the prospect referred to as Wainaulo West were termed Wainaulo-Southeast and Wainaulo, respectively, in Egashira (2009).

interpreted to indicate that the hydrothermal fluids were sourced from hydrous intermediate to silicic magmas in a subduction-related island arc setting (e.g., Sasaki and Ishihara, 1979).

### *6.2.3 Methods*

Seventy-four sulfur isotope compositions have been determined for sulfides and sulfates in Wainaulo (n = 49), Waisoi West (n = 15) and Waisoi East (n = 10). The analyzed samples were constrained paragenetically (Chapter 5) and comprise coarse crystalline pyrite and massive chalcopyrite and bornite encapsulated by silicate or sulfate vein material. The sulfate samples are coarse gypsum and anhydrite that were predominantly intergrown with pyrite or chalcopyrite. The coarse-grained nature of the minerals enabled 1 – 5 mg of monomineralic powders to be

**Table 6.2:** Sulfur isotope geothermometry of Waivaka Corridor sulfide – sulfate pairs (data from Egashira, 2009)

| Deposit/prospect | Drill hole ID | Depth (m) | Mineral | $\delta^{34}S$ (‰) | $\Delta\delta^{34}S$ [$SO_4^{2-}$ - $H_2S$] (‰) | T (°C) |
|---|---|---|---|---|---|---|
| Wainavuga | NWK008 | 259.8 | Anhydrite | +15.6 | 17.6 | 343 |
| | | | Pyrite | -2.0 | | |
| | NWK012 | 295.8 | Anhydrite | +11.5 | 11.2 | 509 |
| | | | Chalcopyrite | +0.3 | | |
| Wainaulo | NWK020 | 273.6 | Anhydrite | +12.3 | 13.6 | 434 |
| | | | Chalopyrite | -1.3 | | |
| | | 305.0 | Gypsum | +14.6 | 14.4 | 410 |
| | | | Pyrite | +0.2 | | |
| | | 393.6 | Anhydrite | +14.4 | 15.4 | 387 |
| | | | Pyrite | -1 | | |
| | | 445.5 | Gypsum | +13.6 | 15.1 | 368 |
| | | | Pyrite | -1.5 | | |
| | NWK027 | 225.7 | Anhydrite | 16.8 | 15.1 | 396 |
| | | | Chalcopyrite | 1.7 | | |
| | | 234.0 | Gypsum | 12.3 | 12.7 | 459 |
| | | | Chalcopyrite | -0.4 | | |
| | | 265.8 | Anhydrite | +15.1 | 11.3 | 506 |
| | | | Chalcopyrite | +3.8 | | |
| | | 306.8 | Anhydrite | +11.2 | 10.6 | 532 |
| | | | Chalcopyrite | +0.6 | | |
| | | 311.8 | Anhydrite | +12.1 | 14.5 | 410 |
| | | | Chalcopyrite | -2.4 | | |
| | | 358.8 | Anhydrite | +12.0 | 13.5 | 436 |
| | | | Chalcopyrite | -0.6 | | |

Temperature of precipitation estimates are based on the geothermometers (Table 6.5) of Ohmoto and Lasaga (1982). Note that the deposit referred to here and elsewhere in this study as Wainaulo and the prospect referred to as Wainaulo West were termed Wainaulo-Southeast and Wainaulo, respectively, in Egashira (2009).

hand drilled using a Dremel Multipro 225 T2 Flex-shaft drill. Careful examination of each powdered sample under a binocular microscope was carried out and any visible impurities were further separated and discarded. The powders were analyzed by Christine Cook at the University of Tasmania, Australia, by conventional methods using the techniques of Robinson and Kusakabe (1975). The samples were weighed on a Sartorius Microbalance SE2 in tin cups. Isotope measurements were performed on a VG Sira Series II mass spectrometer. There is an estimated analytical uncertainty of ± 0.1 ‰ for sulfide and of ± 0.4 ‰ for sulfate.

*6.2.4 Results*

Tables 6.3 and 6.4 present the results of the sulfur isotope study, with $\delta^{34}S$ reported relative to the Carbon Diablo Troilite (CDT). At Wainaulo, the sulfur isotope samples were selected from several vein stages and alteration assemblages that were interpreted to have sulfate – sulfide equilibrium textures (e.g., non-corroded mineral contacts). The sulfur isotopic signatures from all paragenetic stages sampled occupy a wide range of $\delta^{34}S$ values for sulfides and sulfates; although a few compositional trends were evident from the data. The Wainaulo sulfur isotopic compositions of sulfides and sulfates differ based on paragenetic stage and position within the Wainaulo hydrothermal system (Figs. 6.1, 6.2 and 6.3); however, there is not a significant variation of $\delta^{34}S$ values with respect to the different sulfide phases analyzed (Fig. 6.4). In broad terms, the $\delta^{34}S_{sulfide}$ values decrease from main-stage WO-IID veins to late-stage WO-IIIC veins, as well as from the porphyry center outwards to the distal part of the system (Fig. 6.2). The average $\delta^{34}S_{sulfate}$ values increase from main-stage to late-stage veins (Fig. 6.1) and decrease with increasing distance from the Wainaulo quartz-diorite porphyry complex (Fig. 6.3).

One stage WO2 anhydrite – chalcopyrite pair was analyzed; it has a $\delta^{34}S_{sulfide}$ value of +0.0 ‰ and a $\delta^{34}S_{sulfate}$ value of +11.2 ‰. Stage WO-IID pyrite, chalcopyrite and bornite have $\delta^{34}S$ values that range from -3.4 to +2.9 ‰ (n = 7) and anhydrite and gypsum $\delta^{34}S$ values that range from +5.4 to +12.0 ‰ (n = 5). Stage WO-IIIA veins have pyrite and chalcopyrite with $\delta^{34}S$ values ranging from -4.5 to +2.5 ‰ (n = 10) and gypsum and anhydrite values from +9.0 to +14.1 ‰ (n = 10). Stage WO-IIIC veins have the lowest average $\delta^{34}S_{sulfide}$ and the highest average $\delta^{34}S_{sulfate}$

**Table 6.3:** Sulfur isotope data and geothermometric results calculated from Wainaulo sulfide – sulfate pairs

| Sample ID | Stage | Occurrence | Mineral | $\delta^{34}S$ ‰ | T (°C) |
|---|---|---|---|---|---|
| NVD019-544 | WO2 | Anhydrite – chalcopyrite clot within andradite – actinolite – magnetite-altered rock | Anhydrite | +11.2 | 509 |
| | | | Chalcopyrite | +0.0 | |
| NVD018-732 | WO-IID | Epidote – anhydrite – pyrite vein with epidote – K-feldspar – phengite halo; crosscuts epidote – biotite-altered porphyritic andesite (PA) | Anhydrite | +10.6 | 477 |
| | | | Pyrite | -0.6 | |
| NVD040-476 | WO-IID | Epidote – anhydrite – tarnished-chalcopyrite vein; crosscut by illite-smectite – carbonate vein | Anhydrite | +12.0 | 429 |
| | | | Chalcopyrite | -1.8 | |
| NVD040-514 | WO-IID | Epidote – anhydrite – chalcopyrite – pyrite vein with epidote – K-feldspar – phengite halo; crosscuts biotite-altered porphyritic andesite (PA) | Anhydrite | +9.5 | 762 |
| | | | Pyrite | +2.9 | |
| NVD040-535 | WO-IID | Epidote – anhydrite – bornite vein with K-feldspar halo; crosscuts early mineralization quartz diorite (EMQD) | Anhydrite | – | |
| | | | Bornite | +1.0 | |
| NVD040-616 | WO-IID | Epidote – anhydrite – chalcopyrite vein with K-feldspar halo; crosscuts biotite-altered porphyritic andesite (PA) | Anhydrite | – | |
| | | | Chalcopyrite | -3.3 | |
| NVD047-956 | WO-IID | Epidote – anhydrite – pyrite vein with K-feldspar halo; crosscuts biotite-altered porphyritic andesite (PA) | Anhydrite | +9.5 | 502 |
| | | | Pyrite | -1.8 | |
| NVD047-1109 | WO-IID | Epidote – anhydrite – pyrite vein with K-feldspar halo; crosscuts biotite-altered rocks | Anhydrite | +5.4 | 614 |
| | | | Pyrite | -3.4 | |
| NVD008-211 | WO-IIIA | Gypsum – pyrite vein with chlorite selvage in actinolite – chlorite-altered Namosi Andesite Formation | Gypsum | +9.0 | 769 |
| | | | Pyrite | +2.5 | |
| NVD008-634 | WO-IIIA | Gypsum – pyrite vein with illite halo in biotite-altered Namosi Andesite Formation; cf. NWK020–281 | Gypsum | +12.4 | 395 |
| | | | Pyrite | -2.6 | |
| NVD040-305 | WO-IIIA | Gypsum – chalcopyrite – pyrite vein; crosscuts actinolite – chlorite-altered porphyritic andesite (PA) | Gypsum | +12.3 | 409 |
| | | | Chalcopyrite | -2.2 | |
| NVD047-251 | WO-IIIA | Anhydrite – pyrite vein with chlorite selvage; crosscut by calcite veins | Anhydrite | +9.6 | 517 |
| | | | Pyrite | -1.3 | |
| NVD047-741 | WO-IIIA | Anhydrite – pyrite – chalcopyrite vein; crosscut by calcite veins | Anhydrite | +9.6 | 419 |
| | | | Pyrite | -4.4 | |
| NVD047-991 | WO-IIIA | Anhydrite – pyrite vein with chlorite selvage | Anhydrite | +14.5 | 407 |
| | | | Pyrite | -2.4 | |
| NVD047-1050 | WO-IIIA | Anhydrite – pyrite vein with dark green chlorite selvage | Anhydrite | +12.7 | 380 |
| | | | Pyrite | -3.0 | |
| NVD047-1266 | WO-IIIA | Anhydrite – pyrite vein with dark green chlorite selvage | Anhydrite | +9.9 | 412 |
| | | | Pyrite | -4.5 | |
| NVD047-1371 | WO-IIIA | Anhydrite – chalcopyrite vein with chlorite selvage; crosscuts coarse-grained quartz vein | Anhydrite | +10.9 | 399 |
| | | | Chalcopyrite | -4.0 | |
| NWK020-281 | WO-IIIA | Gypsum – pyrite vein with illite halo in biotite-altered porphyritic andesite (PA); cf. NVD008–634 | Gypsum | +12.2 | 537 |
| | | | Pyrite | +1.8 | |
| NWK020-447 | WO-IIIA | Anhydrite – pyrite – sphalerite vein; crosscuts actinolite – magnetite – andradite-altered rock; crosscut by gypsum – pyrite vein | Anhydrite | +14.1 | 398 |
| | | | Pyrite | -0.9 | |
| NVD008-303 | WO-IIIC | Saccharoidal, opaque gypsum vein with coarse-grained pyrite; crosscuts quartz – anhydrite vein and biotite – actinolite-altered rock | Gypsum | +12.4 | 510 |
| | | | Pyrite | +1.3 | |
| NVD019-769 | WO-IIIC | Gypsum – pyrite vein with illite-smectite halo; crosscuts biotite-altered porphyritic andesite (PA) | Anhydrite | +12.9 | 373 |
| | | | Pyrite | -3.1 | |
| NVD019-774 | WO-IIIC | Gypsum – pyrite vein with illite-smectite halo that has crosscut biotite-altered porphyritic andesite (PA) | Gypsum | +13.1 | 359 |
| | | | Pyrite | -3.6 | |
| NVD047-1107 | WO-IIIC | Anhydrite – pyrite vein with illite-smectite halo; crosscut by < 0.01 mm–thick calcite veinlets | Anhydrite | +12.8 | 354 |
| | | | Pyrite | -4.1 | |

Temperature of precipitation estimates for sulfate – sulfide pairs are based on the geothermometers of Ohmoto and Lasaga (1982).

**Table 6.4:** Sulfur isotope data and geothermometric results from Waisoi West and Waisoi East

| Deposit | Sample ID | Stage | Occurrence | Mineral | $\delta^{34}S$ ‰ | T (°C) |
|---|---|---|---|---|---|---|
| Waisoi West | NSW001-650 | WW-IIB | Anhydrite – pyrite vein with ankerite selvage | Anhydrite | +12.4 | 488 |
| | | | | Pyrite | +0.7 | |
| | NSW001-854 | WW-IIB | Anhydrite – pyrite vein with ankerite selvage | Anhydrite | +12.4 | 475 |
| | | | | Pyrite | +0.2 | |
| | NSW006-226 | WW-IIA | Quartz – pyrite vein overprinted by kaolinite alteration | Pyrite | -0.6 | |
| | NSW006-316 | WW-IB | Biotite – chalcopyrite clot in albite-biotite-altered QDP1 | Chalcopyrite | -0.5 | |
| | NSW006-351 | WW-IE | Chalcopyrite stringer in albite-altered QDP1 | Chalcopyrite | -0.5 | |
| | NSW006-366 | WW-IIA | Quartz – pyrite vein with illite halo in albite-altered QDP1 | Pyrite | -1.5 | |
| | NSW006-432 | WW-IIA | Quartz – calcite – pyrite vein with illite halo in QDP1 | Pyrite | -2.9 | |
| | NSW006-463 | WW-IIA | Quartz – pyrite vein with illite halo in QDP2 | Pyrite | -2.7 | |
| | NSW006-487 | WW-IIA | Quartz – pyrite vein with illite halo in QDP2 | Pyrite | -2.0 | |
| | NSW006-953 | WW-IIA | Quartz – pyrite vein in magnetite-altered Wainimala Group | Pyrite | -1.9 | |
| | NSW010-404 | WW-IIA | Quartz – pyrite – chalcopyrite vein with illite halo | Pyrite | -2.7 | 444 |
| | | | | Chalcopyrite | -2.0 | |
| Waisoi East | NSE002-102 | WE-IIC | Quartz – pyrite – carbonate vein in Wainimala Group | Pyrite | +3.4 | |
| | NSE002-650 | WE-IIC | Pyrite – chalcopyrite vein with albite halo | Pyrite | +1.8 | |
| | NSE008-300 | WE-IIC | Quartz – pyrite – carbonate vein in Wainimala Group | Pyrite | +2.8 | |
| | NSE008-522 | WE-IIC | Quartz – pyrite – molybdenite vein with albite halo | Pyrite | +2.8 | |
| | NSE008-595 | WE-IIC | Quartz – pyrite vein with albite halo | Pyrite | +2.2 | |
| | NSE008-633 | WE-IIC | Quartz – pyrite vein with albite halo | Pyrite | +2.2 | |
| | NSE008-663 | WE-IIC | Quartz – pyrite – molybdenite vein with albite halo | Pyrite | +1.9 | |
| | NSE008-697 | WE-IIIB | Illite – calcite – pyrite vein | Pyrite | +2.0 | |
| | NSE008-710 | WE-IIC | Quartz – pyrite – molybdenite vein with albite halo | Pyrite | +2.0 | |
| | NSE008-787 | WE-IIIB | Illite – calcite – pyrite vein | Pyrite | +3.4 | |

Temperature of precipitation estimates for sulfate – pyrite pairs are based on the geothermometer of Ohmoto and Lasaga (1982). The temperature of precipitation estimate for the pyrite – chalcopyrite pair is based on the geothermometer of Ohmoto and Rye (1979). Abbreviations: QDP1 = quartz-diorite porphyry 1, QDP2 = quartz-diorite porphyry 2.

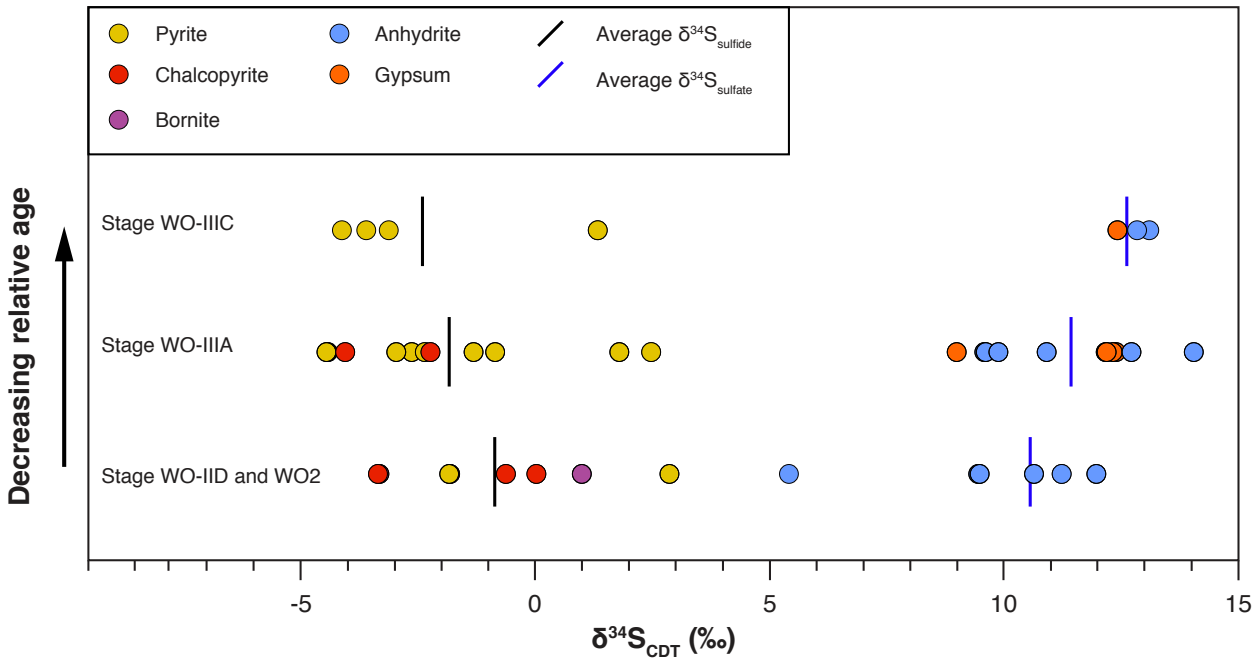


**Figure 6.1:** Distribution of $\delta^{34}S_{sulfide}$ and $\delta^{34}S_{sulfate}$ values from stage WO2, WO-IID, WO-IIIA and WO-IIIC veins and alteration stages at Wainaulo. There is a weak trend towards decreasing average values of sulfide and increasing average values of sulfate from the early stage WO2 (anhydrite – andradite – magnetite – actinolite alteration) and WO-IID (epidote – anhydrite – sulfide veins with K-feldspar – phengite vein halos) through to stage WO-IIIC (gypsum – pyrite veins with illite-smectite vein halos).

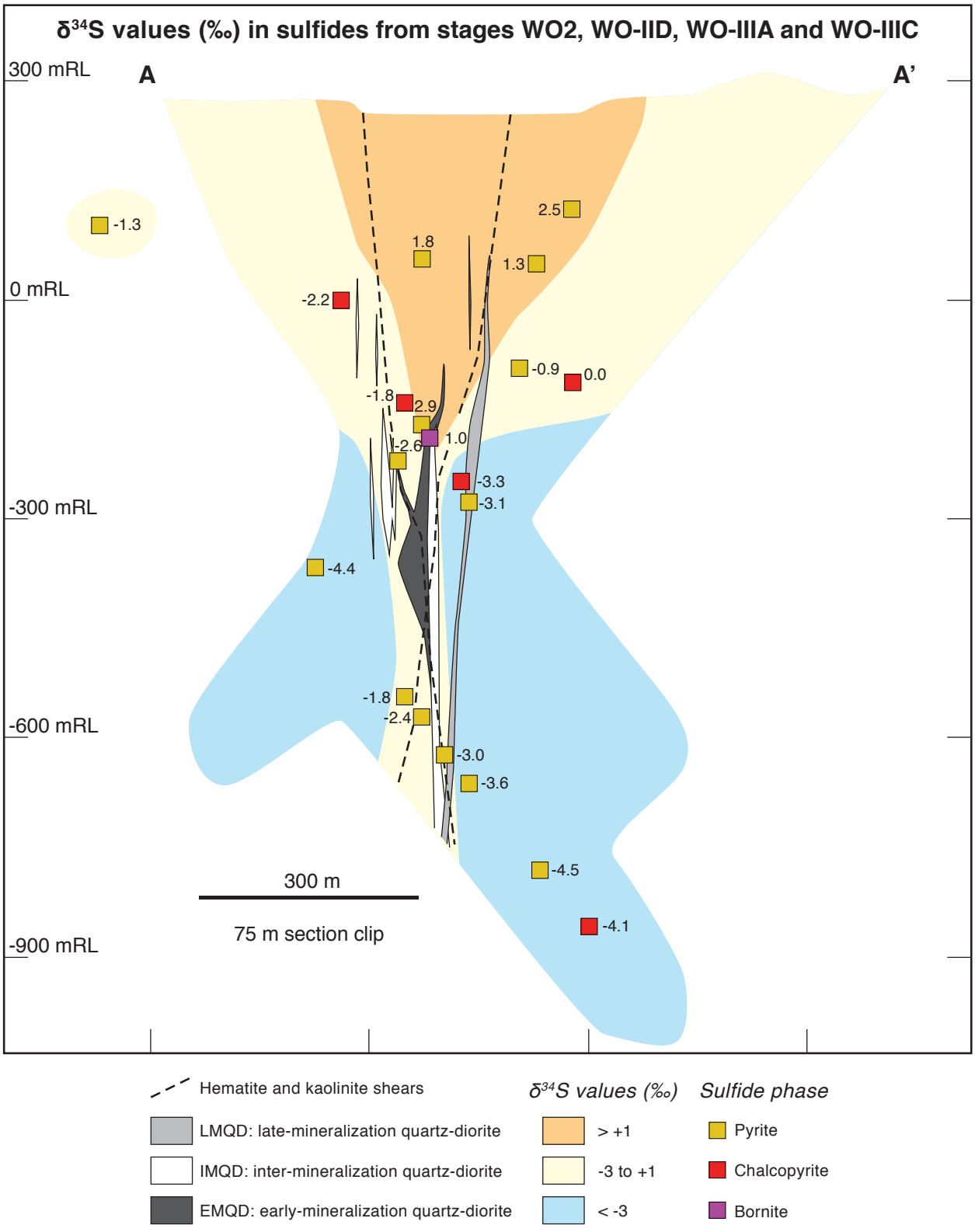


**Figure 6.2:** Distribution of $\delta^{34}S_{sulfide}$ values from stage WO2, WO-IID, WO-IIIA and WO-IIIC veins and alteration assemblages at Wainaulo. Samples are shown on section A – A' (NVD019). Heavy $\delta^{34}S$ values define an upwardly-flaring plume extending from the top of the early mineralization quartz diorite (EMQD) intrusion outward towards lower values at the deposit periphery.

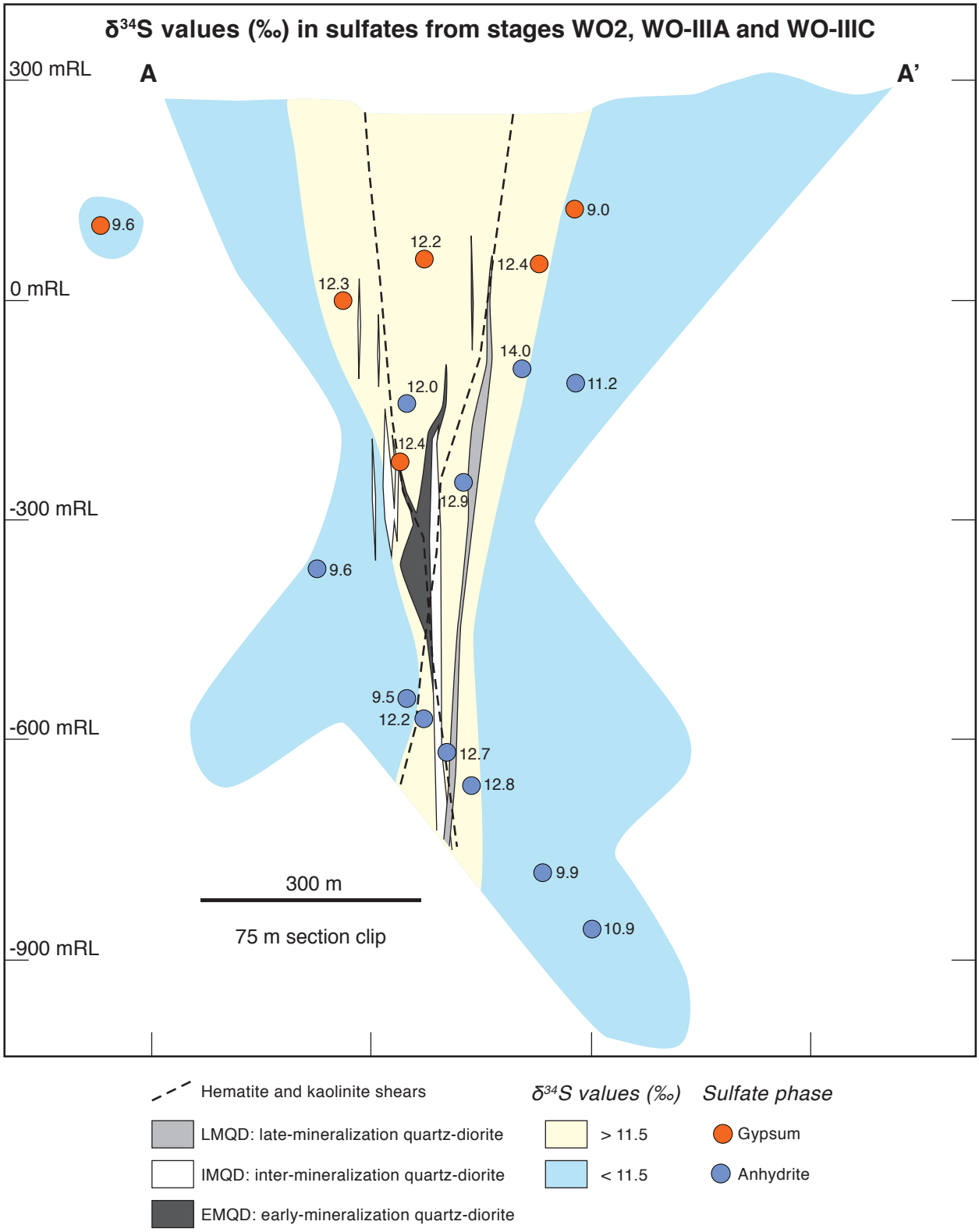


**Figure 6.3:** Distribution of $\delta^{34}S_{sulfate}$ values from stage WO2, WO-IIIA and WO-IIIC veins and alteration assemblages at Wainaulo. Samples are shown on section A – A' (NVD019). $\delta^{34}S$ values broadly decrease outwards from the Wainaulo intrusive complex and from the Hematite and Kaolinite shears.

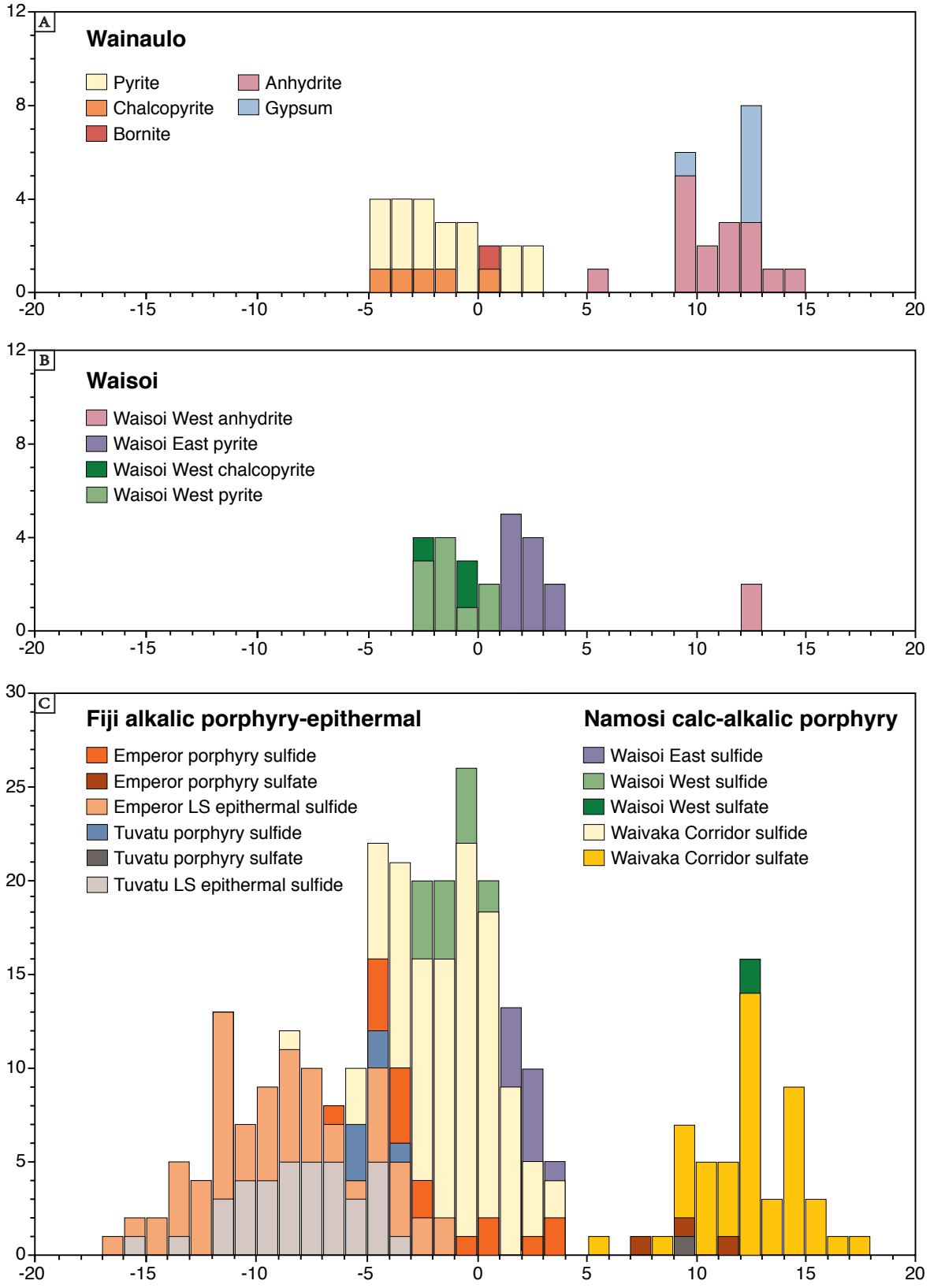


**Figure 6.4:** Cumulative frequency histogram of $\delta^{34}S$ values (‰, CDT) for ore deposits of the Namosi district. **A.** $\delta^{34}S$ values for stage WO2, WO-IID, WO-IIIA and WO-IIIC sulfides and sulfates from the Wainaulo Cu-Au porphyry deposit (Table 6.3). **B.** $\delta^{34}S$ values for stage WW-IB, WW-IE, WW-IIA and WW-IIB sulfides and sulfates from Waisoi West, and stage WE-IIC and WE-IIIB from Waisoi East (Table 6.4). **C.** Compilation of all data from the Namosi district (Appendix G), compared to data from the Emperor and Tuvatu alkalic porphyry-epithermal deposits. The Waivaka Corridor dataset incorporates data from Wainaulo (this study) as well as Wainaulo, Wainivisowaqa, Wainaulo West and Wainavuga (Egashira, 2009). Data for Emperor porphyry and epithermal stages are from Begg (1996), and data for Tuvatu porphyry and epithermal stages are from Scherbarth and Spry (2006).

values (Fig. 6.1). Pyrite and chalcopyrite (n = 4) $\delta^{34}S$ values range from -4.1 to +1.3 ‰. Stage WO-IIIC veins have the most narrow range of $\delta^{34}S_{sulfate}$ values for both anhydrite and gypsum at Wainaulo (+12.4 to +13.1 ‰; n = 4; Fig. 6.1).

At Waisoi West, the $\delta^{34}S$ values of pyrite (n = 9) and chalcopyrite (n = 2) range from -2.7 to +0.7 ‰, with a median value of -1.0 ‰. Specifically, two chalcopyrite samples from main-stage WW-IB and WW-IE veins have the same $\delta^{34}S$ value of -0.5 ‰; whereas, two pyrite samples from late-stage WW-IIB veins have values of +0.2 and +0.7 ‰. Pyrites from stage WW-IIA veins (n = 7) have the lightest $\delta^{34}S$ values (-2.9 to -0.6 ‰) at Waisoi West. Both anhydrite grains analyzed from stage WW-IIB veins have the same $\delta^{34}S$ value of +12.4 ‰. Further analyses are required to determine if there is zonation of $\delta^{34}S$ with respect to paragenetic stages at Waisoi West.

Sulfur isotopic compositions were determined for ten pyrites from two paragenetic stages at the Waisoi East Cu-Au-Mo porphyry deposit. Sulfur isotopic values for stage WE-IIIB (n = 2) are indistinguishable from and lie within the range of $\delta^{34}S$ values for pyrite samples from stage WE-IIC quartz – pyrite veins (n = 8). Data from both stages show a narrow range from +1.8 to +3.4 ‰, with a mean value of +2.4 ‰.

### *6.2.5 Geothermometry*

Fluid inclusion studies have shown that porphyry Cu-Au mineralization at Wainaulo was associated with high temperature (> 500 to 300°C) hypersaline brines (> 60 wt % NaCl equiv.) and low-density vapor (Nittetsu, 2007; Egashira, 2009). These temperature estimates are similar to the sulfur isotope geothermometric results from Egashira (2009) that have been recalculated to range from 532 to 368°C. In order to further constrain the temperatures of ore formation at Wainaulo, sulfur isotope geothermometry was conducted within the new paragenetic framework outlined in Chapter 5. Accurate sulfur isotope geothermometry requires that the sulfide and sulfate phases were formed in isotopic equilibrium, that no isotopic exchange took place after mineral deposition, and that pure mineral phases were separated for the analysis (Ohmoto and Rye, 1979). Only samples with textural evidence for mineral equilibrium (e.g., intergrowth textures) were selected

for this study. Great care was taken when separating the samples to ensure that the powders were free from visible impurities.

If the isotopic differences between sulfide and sulfate pairs are affected by primary equilibrium isotopic exchange reactions at the time of mineral precipitation, then temperature estimates may be determined from the $^{34}S$ fractionation between the cogenetic mineral pairs (Ohmoto and Rye, 1979; Field et al., 2005). For conditions of complete isotopic equilibrium, calculated sulfate – sulfide temperatures for magmatic hydrothermal deposits typically range from 600 to 450°C and are consistent with temperatures determined from other methods (Hoefs, 2009). Estimated temperatures for sulfide and sulfate precipitation were calculated using the sulfur isotope fractionation equations in Table 6.5 and are presented in Tables 6.3 and 6.4.

**Table 6.5:** Sulfur isotope geothermometry equations used in this study

| Mineral pair | Equation | Reference |
|---|---|---|
| Sulfate – pyrite | $1000\ ln\ \alpha = (6.463 \times 10^6)\ T^{-2} + 0.56$ | Ohmoto and Lasaga (1982) |
| Sulfate – chalcopyrite | $1000\ ln\ \alpha = (6.513 \times 10^6)\ T^{-2} + 0.56$ | Ohmoto and Lasaga (1982) |
| Pyrite – chalcopyrite | $1000\ ln\ \alpha = (0.45 \times 10^6)\ T^{-2}$ | Ohmoto and Rye (1979) |

At Wainaulo, sulfide – sulfate geothermometry was used to estimate temperatures from three different vein stages and one alteration stage. One anhydrite – chalcopyrite pair analyzed from stage WO2 yielded a temperature of 509°C, which is similar to the temperature that can be constrained based on the stage WO2 mineral assemblage, i.e., magnetite ± chalcopyrite ranges from 500 to 425°C (Simon et al., 2000) and actinolite and garnet are stable at temperatures greater than 300°C (Bird et al., 1984; Reyes, 1990). Eight sulfate – sulfide pairs analyzed from stage WO-IID veins at Wainaulo yielded a range of temperatures from 505 to 429°C, with two outliers of 762 and 614°C. Eight sulfide – sulfate pairs from stage WO-IIIA veins yielded temperatures ranging from 419 to 380°C, with three additional samples providing what are interpreted to be spurious temperatures above 517°C. Sulfur geothermometric calculations on four samples from the youngest sulfate-bearing vein stage at Wainaulo (WO-IIIC) yielded a temperature range from 373 to 354°C, with an outlier of 510°C.

At Waisoi West a pyrite – chalcopyrite pair from a main-stage WW-ID vein yielded a temperature of 444°C, using the pyrite – chalcopyrite geothermometer of Ohmoto and Rye (1979). Two anhydrite – pyrite pairs from Stage WW-IIB yielded similar temperatures of 488 and 475°C. There were no co-existing sulfate – sulfide pairs at Waisoi East observed in this study.

### *6.2.6 Sulfur isotope zonation*

The $\delta^{34}S$ values for stages WO2, WO-IID, WO-IIIA and WO-IIIC at Wainaulo define a spatial zonation wherein higher $\delta^{34}S_{sulfide}$ compositions occur in the core of the deposit and more negative values occur at the deposit periphery (Fig. 6.2). The opposite pattern exists for $\delta^{34}S_{sulfate}$ compositions (i.e., isotopically lower values grade outward to higher values with increasing distance from the deposit core; Fig. 6.3). The isotopically high $\delta^{34}S_{sulfide}$ (> +1.0 ‰) core has an upwardly-flaring morphology and occurs within and above the cupola zone of the Wainaulo quartz-diorite porphyry complex (Fig. 6.2). The spatial relationship between the positive $\delta^{34}S$ compositions and the mineralized quartz-diorite porphyries suggests that there may be a genetic link between the two. This pattern can be explained by a cooling, relatively reduced fluid emanating from the quartz-diorite porphyry complex and overprinting the relatively oxidized alteration associated with the early diorite intrusions (EMD1). Similar isotopic zonation to lower distal values has been described at Bingham, USA (Field, 1966), North Parkes, Australia (Heithersay and Walshe, 1995) and Dinkidi, Philippines (Wolfe and Cooke, 2011). No spatial or temporal variations in $\delta^{34}S$ were noted at Waisoi East or Waisoi West.

### *6.2.7 Sulfur isotopic compositions and sources*

The range of $\delta^{34}S$ values from the Namosi porphyry deposits ($\delta^{34}S_{sulfide}$ from -8.6 to +3.4 ‰ and $\delta^{34}S_{sulfate}$ from +5.4 to +17.3 ‰) is similar to the range typical for porphyry copper deposits worldwide ($\delta^{34}S_{sulfide}$: -3 to +1 ‰; $\delta^{34}S_{sulfate}$: +8 to +15 ‰; Ohmoto and Rye, 1979; Ohmoto and Goldhaber, 1997; Wilson et al., 2007). Their near-zero $\delta^{34}S_{sulfide}$ values indicate a predominantly magmatic sulfur source (Ohmoto and Rye, 1979; Field and Fifarek, 1985). There is a distinct difference between the populations of $\delta^{34}S$ values from the alkalic and calc-alkalic porphyry systems

of Viti Levu, Fiji. The Emperor (3.9 Ma; Begg, 1996) and Tuvatu (~ 4.9 Ma; Scherbarth and Spry, 2006) alkalic porphyry systems show a broader range of $\delta^{34}S$ values and have lighter average $\delta^{34}S$ overall, compared to the Namosi district porphyry systems (Fig. 6.4C).

Under oxidizing conditions (e.g., $SO_4/H_2S > 1$), a cooling magmatic fluid will result in a wide range of $\delta^{34}S_{sulfide}$ values that become increasingly more negative throughout the cooling history, whereas a narrow range of $\delta^{34}S_{sulfate}$ values will be produced. Under more reduced conditions $\delta^{34}S_{sulfide}$ values are expected to span a narrow range, while $\delta^{34}S_{sulfate}$ values occupy a relatively large range (Rye, 1993). There is a trend towards higher $\delta^{34}S_{sulfide}$ compositions throughout the evolution of the Namosi district (Figs. 6.4A and B). The wide range of negative to positive $\delta^{34}S_{sulfide}$ values and the narrow range of $\delta^{34}S_{sulfate}$ compositions for Wainaulo (Fig. 6.4) indicates mineral deposition from a relatively oxidized, sulfate dominant (i.e., $H_2S/SO_4^{2-} < 1$) magmatic-hydrothermal fluid (Ohmoto and Rye, 1979; Rye, 1993). This trend is also true for the Waisoi West porphyry system (Fig. 6.4). Conversely, pyrite from the younger Waisoi East Cu-Au-Mo porphyry deposit has a positive and narrow range of $\delta^{34}S_{sulfide}$ compositions (+1.8 to +3.4 ‰), consistent with a reduced magmatic-hydrothermal sulfur source (i.e., $H_2S/SO_4^{2-} > 1$; Ohmoto and Rye, 1979).

The bulk sulfur ($\delta^{34}S_{\Sigma S}$) must be between the average $\delta^{34}S$ values of sulfates and sulfides, i.e., between -1.1 (n = 59) and +12.3 ‰ (n = 40) for Wainaulo and between -1.4 (n = 13) and +12.4 ‰ (n = 2) for Waisoi West. A rough estimate for the bulk sulfur would be the midpoint between the average sulfide and sulfate $\delta^{34}S$ values. At both Wainaulo and Waisoi West the midpoint is ~ +5.5 ‰, which is at the upper end of the range for magmatic sulfur values (0 ± 5 ‰; Ohmoto and Rye, 1979). The absence of coexisting sulfate – sulfide pairs at Waisoi East prevents the $\delta^{34}S_{\Sigma S}$ value from being determined directly; however, it must have a bulk sulfur composition greater than that of the average $\delta^{34}S_{sulfide}$ value, i.e., greater than +2.4 ‰. More precise estimates of the bulk sulfur and redox state of the Wainaulo hydrothermal fluids can be obtained by plotting sulfide – sulfate mineral pair data on a $\delta^{34}S_{sulfate}$ vs. $\delta^{34}S_{sulfide}$ diagram (Fig. 6.5; Rye, 2005). In this plot, the $\delta^{34}S$ mineral data approximates for the $\delta^{34}S_{SO_4^{2-}}$ and $\delta^{34}S_{H_2S}$ values of the associated fluid. From the $\delta^{34}S_{sulfate}$ vs. $\delta^{34}S_{sulfide}$ plot for Wainaulo (Fig. 6.5) it can be shown that at a constant $\delta^{34}S_{\Sigma S} = 6.7$ ‰, the Wainaulo sulfate – sul-

fide pairs can be generated from hydrothermal fluids with a range of aqueous sulfate to sulfide ratios (i.e., R = 1.0, R = 1.6 and R = 2.9; Fig. 6.5). The shift in redox state occurred irrespective of temperature and paragenetic stage (Fig. 6.5). To test this observation, the $\delta^{34}S$ values for Wainaulo sulfate – sulfide pairs were also plotted on a $\delta^{34}S$ vs. temperature diagram and compared with sulfur fractionation curves modeled for fluids having a range of bulk sulfur (4 – 9 ‰) and a range of molar ratios of $SO_2$ (and $\Sigma SO_4^{2-}$) to $H_2S$ (1:1 to 2:1) in solution (Fig. 6.6). The temperatures for each mineral pair were obtained from sulfur isotope geothermometry and are reported in Table 6.3. The fluids were modeled assuming equilibrium conditions and temperatures ranging from 600 – 300°C. To allow for the effects of disproportionation of $SO_{2(g)}$ to $SO_4^{2-}$ (aq), all theoretical sulfide compositions were calculated using sulfide-$SO_2$ fractionation equations above 350°C, and sulfide-$SO_4^{2-}$ fractionation equations below 400°C (Rye, 1993; Ohmoto and Goldhaber, 1997); however, $\Sigma SO_4^{2-}$ values better approximate the measured data at all temperatures (Fig. 6.6). The modeled fractionation curves that best approximate the measured data have a constant bulk sul-

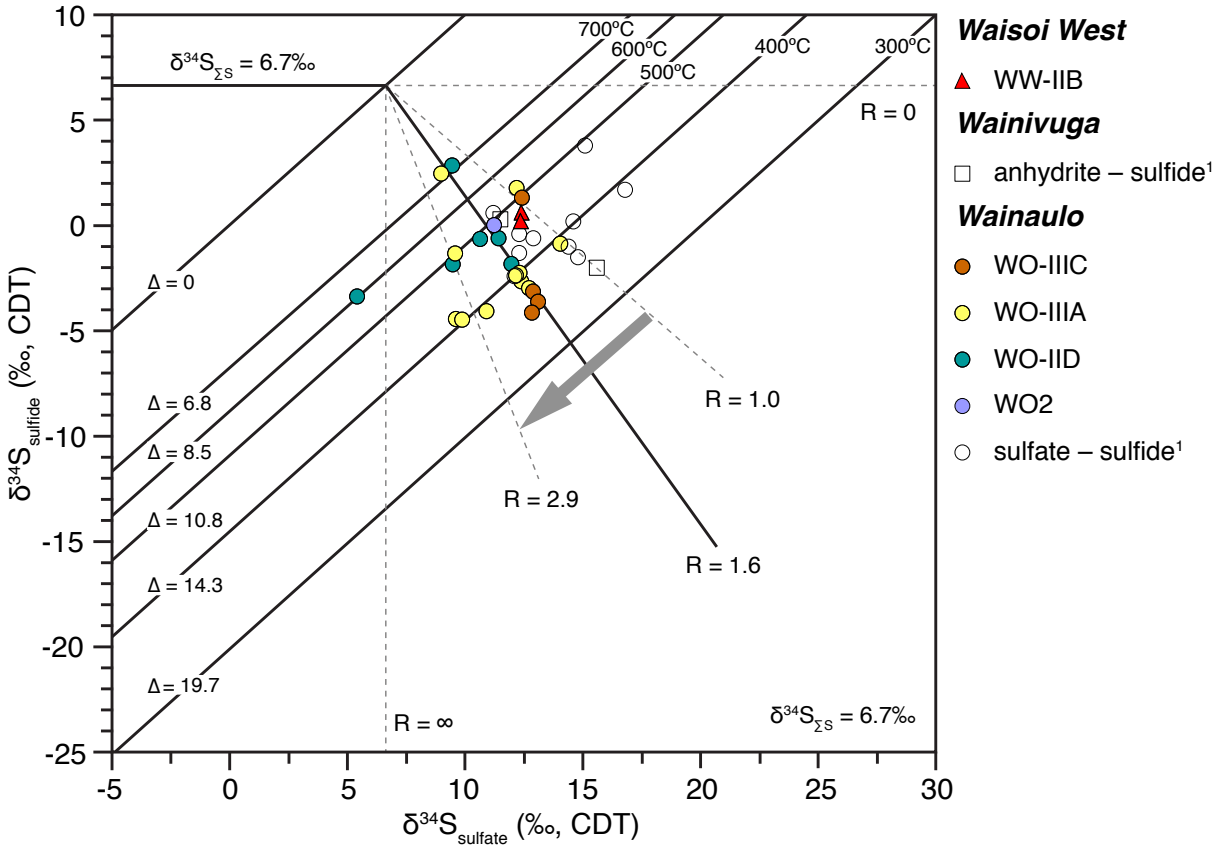


**Figure 6.5:** Plot of $\delta^{34}S_{SO_4^{2-}}$ versus $\delta^{34}S_{H_2S}$ for sulfate – sulfide pairs from Wainaulo, Wainivuga and Waisoi West. The spread in isotopic data from Wainaulo can be accounted for by three distinct best-fit lines that have slopes equivalent to the absolute value of the $SO_4^{2-}/H_2S$ ratios, or R, with values of R = 1.0, 1.6 and 2.9, and an intercept with the Δ = 0 fractionation line at $\delta^{34}S$ = 6.7 ‰ (which is equivalent to $\delta^{34}S_{\Sigma S}$ and is read from either the ordinate or the abscissa axis). The shift in redox state (R value) occurred irrespective of temperature and paragenetic stage. Values for anhydrite – sulfate from Wainivuga and stage WW-IIB from Waisoi West were plotted for comparative purposes. [1]Data from Egashira (2009).

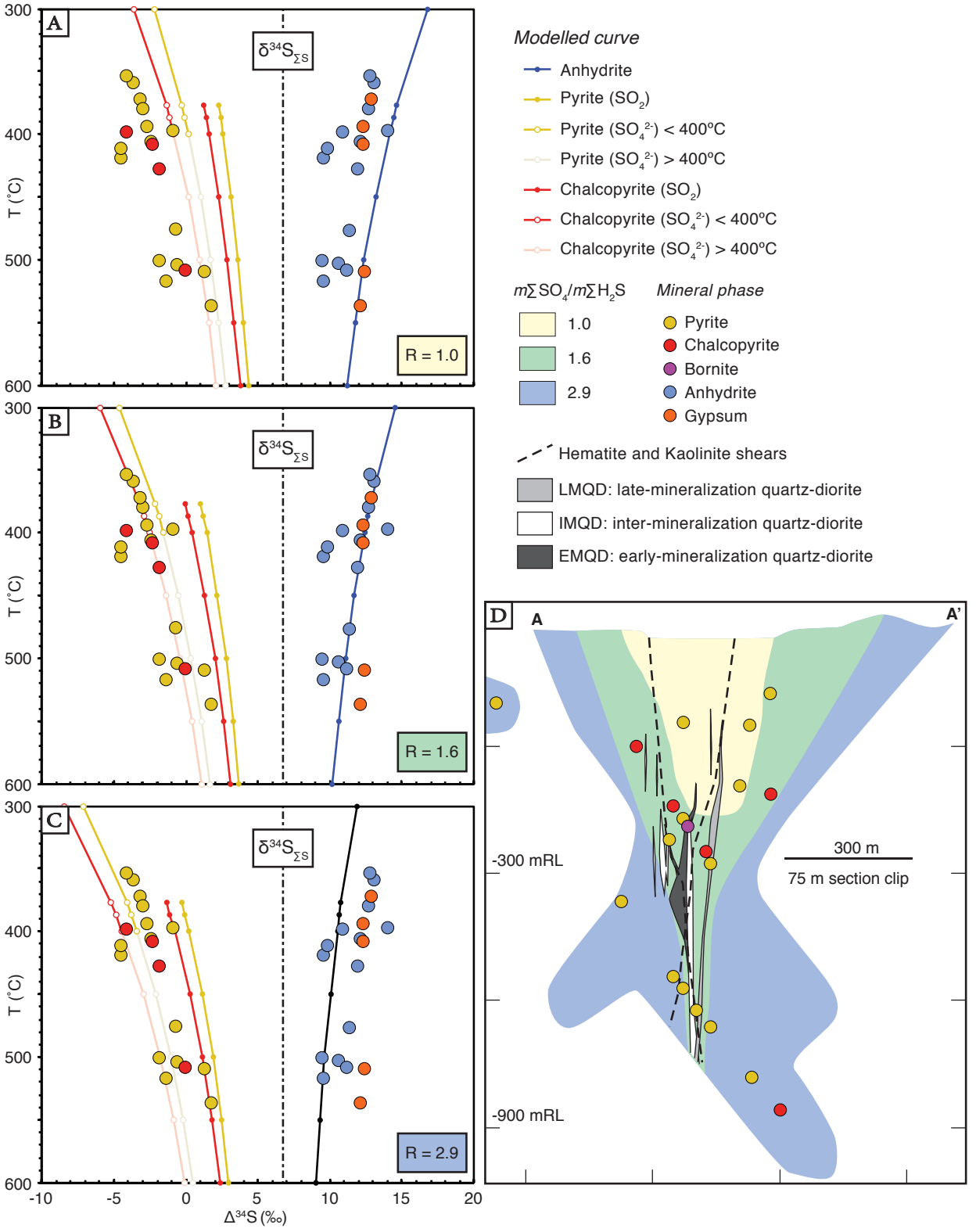


**Figure 6.6:** Measured and modeled $\delta^{34}S$ compositions from Wainaulo. Measured $\delta^{34}S$ values are for coexisting sulfate – sulfide pairs from four different paragenetic stages and the corresponding temperatures were calculated by sulfur isotope geothermometry (Table 6.3). Modeled $\delta^{34}S$ values are for theoretical sulfate – sulfide pairs that precipitated in equilibrium from a cooling fluid with a bulk sulfur composition of 6.7 ‰ and $m\Sigma SO_4/m\Sigma H_2S$ = 1.0 in Fig. 6.6A, $m\Sigma SO_4/m\Sigma H_2S$ = 1.6 in Fig. 6.6B and $m\Sigma SO_4/m\Sigma H_2S$ = 2.9 in Fig. 6.6C. **D.** NVD019 cross section with plotted $\delta^{34}S$ locations. Colored dots are the locations for sulfate – sulfide samples, and shaded yellow, green and blue areas represent domains of R = 1, R = 1.6 and R = 2.9, respectively. Modeling parameters are from an unpublished spreadsheet from G. Davidson.

fur of 6.7 ‰ and three different $m\Sigma H_2S/m\Sigma SO_2$ ratios (i.e., R = 1, R = 1.6 and R = 2.9), which is consistent with interpretations that can be made from the previous method (Figs. 6.5 and 6.6). The shift in redox state occurred irrespective of which sulfate and sulfide mineral phases were present (Fig. 6.6). The sulfate – sulfide pairs approximated by each modeled curve were plotted on section NVD019 and were tagged based on approximated redox state (yellow: R = 1.0; green: R = 1.6; blue: R = 2.9; Fig. 6.6D). The redox domains have a similar zonation to the sulfide distribution pattern illustrated in Figure 6.2, with an upward-flaring central zone defined by sulfur-bearing minerals that were precipitated from neutral fluids, grading outward to minerals precipitated from increasingly more oxidized fluids (Fig. 6.6D). This provides evidence that the zonation pattern cannot be explained by a cooling magmatic fluid alone (e.g., Rye, 1993). A more likely explanation is that a late, cooling, neutral fluid had emanated from the quartz-diorite intrusions and became more oxidized through wall-rock interaction as the fluid migrated away from the deposit core. The wall-rocks were previously oxidized due to the early biotite – albite – magnetite alteration associated with the EMD intrusions. This $\delta^{34}S_{sulfide}$ distribution is opposite to most documented porphyry systems (e.g., Cadia Valley deposits, New South Wales: Wilson et al., 2007; Golpu, Papua New Guinea; Rinne, 2015) where the high grade mineralized core of the deposits are characterized by the lowest $\delta^{34}S_{sulfide}$ values, and the highest $\delta^{34}S_{sulfide}$ values occur at the deposit peripheries (Wilson et al., 2007). Wall-rock reduction of magmatic sulfate was invoked to account for this opposite $\delta^{34}S_{sulfide}$ pattern (Wilson et al., 2007).

The bulk sulfur estimate of 6.7 ‰ is similar to the value determined by Egashira (2009) for the Waivaka Corridor ($\delta^{34}S_{\Sigma S}$ = 7 ‰). Egashira (2009) had estimated the $\delta^{34}S_{\Sigma S}$ of the Waivaka Corridor on a $\delta^{34}S$ vs. $\Delta\delta^{34}S_{sulfate - sulfide}$ plot by fitting two linear trend lines that converge to a point on the $\delta^{34}S$ axis ($\Delta\delta^{34}S_{sulfate - sulfide}$, $\delta^{34}S$) = (0, $\delta^{34}S_{\Sigma S}$). Both estimates are above the range for magmatic sulfur values (0 ± 5 ‰; Ohmoto and Rye, 1979). The high $\delta^{34}S_{\Sigma S}$ values for the Namosi district may imply contamination of magmatic sulfur by sedimentary sulfate due to assimilation or by seawater sulfate as a result of fluid mixing. Addition of seawater sulfate has been suggested as an explanation for elevated $\delta^{34}S_{\Sigma S}$ for hydrothermal fluids at several Philippine porphyry deposits (e.g., Sasaki et al., 1984) and is the preferred explanation for the high bulk sulfur values here.

## 6.3 Oxygen and deuterium isotopes

### *6.3.1 Introduction*

Oxygen and deuterium isotopic analyses have been conducted on hydrothermal minerals from Wainaulo, Waisoi West and Waisoi East in order to characterize potential fluid sources and to assess whether a seawater isotopic reservoir influenced their isotopic compositions. At Wainaulo, epidote occurs throughout the paragenesis, including as a gangue mineral in high-grade Cu-Au veins spatially associated with the core of the deposit. Therefore, analyzing the oxygen and deuterium isotopic composition of epidote can provide a method to evaluate the origin and evolution of the ore-forming hydrothermal fluids at Wainaulo. Mineral separates from the zeolite – calcite assemblage at Waisoi West and the illite – calcite – pyrite assemblage at Waisoi East provided a suite of oxygen – deuterium-bearing samples to characterize the evolution of hydrothermal fluids throughout the paragenetic history of the Namosi porphyry systems. Chivas et al. (1984) undertook an oxygen – deuterium isotope study of porphyry deposits in the southwest Pacific, which included several samples from Waisoi West. Their $\delta^{18}O_{fluid}$ and $\delta D_{fluid}$ data were recalculated and used in this section for comparative purposes (Table 6.6; Appendix G).

### *6.3.2 Methods*

The oxygen and deuterium isotopic compositions of epidote from three different vein and alteration stages at Wainaulo (n = 9), analcime from Waisoi West (n = 1) and illite from Waisoi East (n = 2) were determined by Jannine Cooper at GNS Science, Lower Hutt, New Zealand, between September and December 2014. In addition, anhydrite co-existing with epidote from one sample was analyzed for its oxygen isotopic composition. Drillcore samples containing epidote were crushed by hand and sieved through #16 and #32 mesh. Epidote was hand picked from the crushed fraction using tweezers. Analcime and illite were extracted directly out of veins using a tungsten carbide scribe. Illite and epidote chips were bathed in 10 mol HCl to remove carbonate contamination. Over 10 mg of mineral material for each sample were provided for oxygen isotopic analysis and over 90 mg were provided for each deuterium isotopic analysis.

Oxygen was extracted from epidote and illite chips using a $CO_2$-laser and $BrF_5$ according to the method of Sharp (1990). Samples and standards were heated overnight to 150°C prior to loading into a vacuum extraction line to remove any absorbed water. The samples were then evacuated for approximately six hours and left overnight in a vapor of $BrF_5$. Blank $BrF_5$ runs were then done until the yield was less than 0.2 μmoles oxygen. Oxygen was then passed through a fluorine-getter (in-line Hg diffusion pump) and converted to $CO_2$ by a graphite furnace. Yields were recorded and the gas was analyzed on a Geo20-20 mass spectrometer. Values for four NBS-28 standard analyses varied by less than 0.15‰, and the samples were normalized to the international quartz standard NBS-28 using a value of +9.6 ‰. Oxygen isotope values are reported in $\delta^{18}O$ notation, relative to Vienna Standard Mean Ocean Water (V-SMOW).

For determination of δD isotopic values, epidote, illite and analcime samples were analyzed on a HEKAtech high-temperature elemental analyzer coupled with a GV Instruments IsoPrime mass spectrometer. Samples were pyrolyzed at 1450°C in silver capsules. All samples were analyzed in triplicate. Results are reported with respect to V-SMOW and normalized to international standards IAEA-CH-7, NBS30 and NBS22 with reported δD values of -100 ‰, -66 ‰ and -118 ‰, respectively. The external precision for these measurements is better than 2‰.

### *6.3.3 Results*

A total of thirteen $\delta^{18}O$ and twelve δD measurements of epidote, illite, anhydrite and analcime were determined in the current study (Table 6.6). Detailed oxygen and deuterium isotopic results are provided in Appendix G.

#### *6.3.3.1 Oxygen isotopes*

At Wainaulo, the oxygen isotopic compositions of epidote from the stage WO4 alteration assemblage (epidote – albite – chlorite – illite ± calcite) ranges from +2.2 to +3.6 ‰ (n = 2), which is indistinguishable from the $\delta^{18}O$ value obtained for epidote from a stage WO-IE vein (epidote – biotite; +2.6 ‰) and $\delta^{18}O$ values obtained for epidote from stage WO-IID veins (epidote – an-

**Table 6.6:** Summary of hydrogen and oxygen isotopic determinations from this study and Chivas et al. (1984)

| Deposit | Sample | Mineral | Stage | Measured values | | Temperature (°C) | Calculated $\delta^{18}O$ (‰) | | Calculated $\delta D$ (‰) | |
|---|---|---|---|---|---|---|---|---|---|---|
| | | | | $\delta^{18}O$ (‰) | $\delta D$ (‰) | | $T_1$ (°C) | $T_2$ (°C) | $T_1$ (°C) | $T_2$ (°C) |
| Wainaulo | NVD040-514 | Epidote | WO-IID | +2.2 | -45.8 | 375 – 425 | +2.3 | +2.6 | -6.0 | -3.0 |
| | NVD040-530 | Epidote | WO-IID | +2.9 | -34.2 | 450 – 479 | +3.6 | +3.8 | +9.9 | +11.3 |
| | NVD008-534 | Epidote | WO-IID | +3.8 | -46.3 | 450 – 479 | +4.6 | +4.7 | -2.2 | -0.9 |
| | NVD037-651 | Epidote | WO-IID | +2.2 | -40.8 | 375 – 425 | +2.3 | +2.8 | -1.0 | +2.0 |
| | NVD047-1227 | Epidote | WO-IID | +2.2 | -38.2 | 375 – 425 | +2.3 | +2.8 | +1.6 | +4.6 |
| | NVD018-732 | Epidote | WO-IID | +3.3 | -44.2 | 375 – 425 | +3.4 | +3.9 | -4.4 | -1.4 |
| | NVD019-224 | Epidote | WO4 | +2.2 | -35.6 | 240 – 310 | -0.2 | +1.4 | -9.1 | -1.1 |
| | NVD008-072 | Epidote | WO4 | +3.6 | -35.4 | 240 – 310 | +1.1 | +2.8 | -8.8 | -0.8 |
| | NVD019-1045 | Epidote | WO-IE | +2.6 | -35.9 | 350 – 450 | +2.4 | +3.4 | +2.0 | +8.2 |
| | NVD019-1045 | Anhydrite | WO-IE | +4.7 | | 350 – 450 | +1.2 | +3.3 | | - |
| Waisoi West | WSD038-388 | Biotite | WW1? | | -42 | 450 – 550 | | | +1.5 | -7.8 |
| | WSD008-254 | Muscovite | WW4? | +11.6 | -19 | 250 – 350 | +6.6 | +9.2 | -3.3 | -5.6 |
| | WSD032-119 | Muscovite | WW4? | +7.9 | -23 | 250 – 350 | +2.9 | +5.5 | -7.3 | -9.6 |
| | WSD045-364 | Chlorite | WW2? | | -35 | 240 – 310 | | | -5.0 | |
| | WSD038-397 | Chlorite | WW2? | | -34 | 240 – 310 | | | -4.0 | |
| | WSD033-345 | Vein quartz | WW-ID? | +8.8 | | 350 – 500 | +3.5 | +6.5 | | |
| | WSD023-297 | Vein quartz | WW-ID? | +8.4 | | 350 – 500 | +3.1 | +6.1 | | |
| | WSD041-382 | Vein quartz | WW-ID? | +8.9 | | 350 – 500 | +3.6 | +6.6 | | |
| | NSW010-200 | Analcime | WW-IIC | +11.2 | -71.8 | 50 – 80 | -12.6 | -8.2 | | |
| Waisoi East | NSE008-633 | Illite | WE-IIIB | +9.4 | -53.6 | 220 – 310 | +3.4 | +6.2 | -36.9 | -39.4 |
| | NSE008-538 | Illite | WE-IIIB | +9.9 | -40.9 | 220 – 310 | +3.9 | +6.7 | -24.2 | -26.7 |

$\delta^{18}O$ and $\delta D$ are reported relative to V-SMOW. Refer to Appendix G for a more detailed description of the samples analyzed and representative sample photos, as well as an explanation for temperature ranges used and which fractionation factors were used.

hydrite – sulfide) ranging from +2.2 to +3.8 ‰ (n = 6). A single analysis of anhydrite from stage WO-IE has a slightly higher $\delta^{18}O$ composition of +4.7 ‰.

At Waisoi West a single oxygen isotope analysis on analcime from a late stage WW-IIC vein (analcime – chabazite – calcite – montmorillonite) yielded a high $\delta^{18}O$ value of +11.2 ‰, which is the highest value obtained during this study. At Waisoi East two illite mineral separates were analyzed for their $\delta^{18}O$ compositions from stage WE-IIIB veins (illite – calcite – pyrite) and they yielded relatively high $\delta^{18}O$ values of +9.4 and +9.9 ‰.

*6.3.3.2 Deuterium isotopes*

At Wainaulo, early stage WO4 and WO-IE epidotes have $\delta D$ values that are within error of each other (–35.4 to –35.9 ‰; n = 3); whereas epidote from stage WO-IID veins have lighter average $\delta D$ values and show a greater range (-34.2 to -46.3 ‰; n = 6).

Analcime from Waisoi West has the lowest measured hydrogen isotopic value of –71.8 ‰ (Table 6.6). The measured δD values for stage WE-IIIC illite are -40.9 and -53.6 ‰ (n = 2).

### *6.3.4 Discussion*

#### *6.3.4.1 Namosi meteoric water*

The composition of meteoric water at Namosi was not measured, but it is assumed here to be similar to that of modern day water from Wailevu River and groundwater from the Lambasa region of Vanua Levu, Fiji (Cox and Hulston, 1980; Fig. 6.7). Both of these waters occur at similar elevations and latitudes as the Namosi district porphyry deposits. The majority of the Fijian water data from Cox and Hulston (1980) lie close to the meteoric water line (MWL). Slight deviations of the δD values to the right of the MWL are interpreted to have resulted from evaporation. The Fijian waters measured by Cox and Hulston (1980) overlap with groundwater from the Emperor alkalic low-sulfidation epithermal Au deposit located approximately 60 km NW of the Namosi district (Ahmad et al., 1987a; Fig. 6.7).

#### *6.3.4.2 Oxygen and deuterium isotopic composition of hydrothermal fluids*

Fluids associated with main-stage WO-IID epidote precipitation at Wainaulo have higher $\delta^{18}O$ and δD compared to their analyzed mineral compositions (Table 6.6); whereas, the early-stage WO4 and WO-IE epidote have fluids with lower $\delta^{18}O$ and higher δD compared to their analyzed mineral compositions. The highest oxygen and hydrogen isotope fractionations are observed in stage WO4 epidote, stage WE-IIIC illite and stage WW-IIC analcime and this effect is interpreted to be as a result of their relatively low crystallization temperatures (< 310°C) compared to the main-stage WO-IID epidote (> 375°C; Fig. 6.7; Table 6.6).

#### *6.3.4.3 Potential fluid sources and fluid evolution*

The calculated $\delta^{18}O$ and δD results are interpreted to indicate that the fluids responsible for illite alteration at Waisoi East were principally of magmatic origin. The δD compositions of these

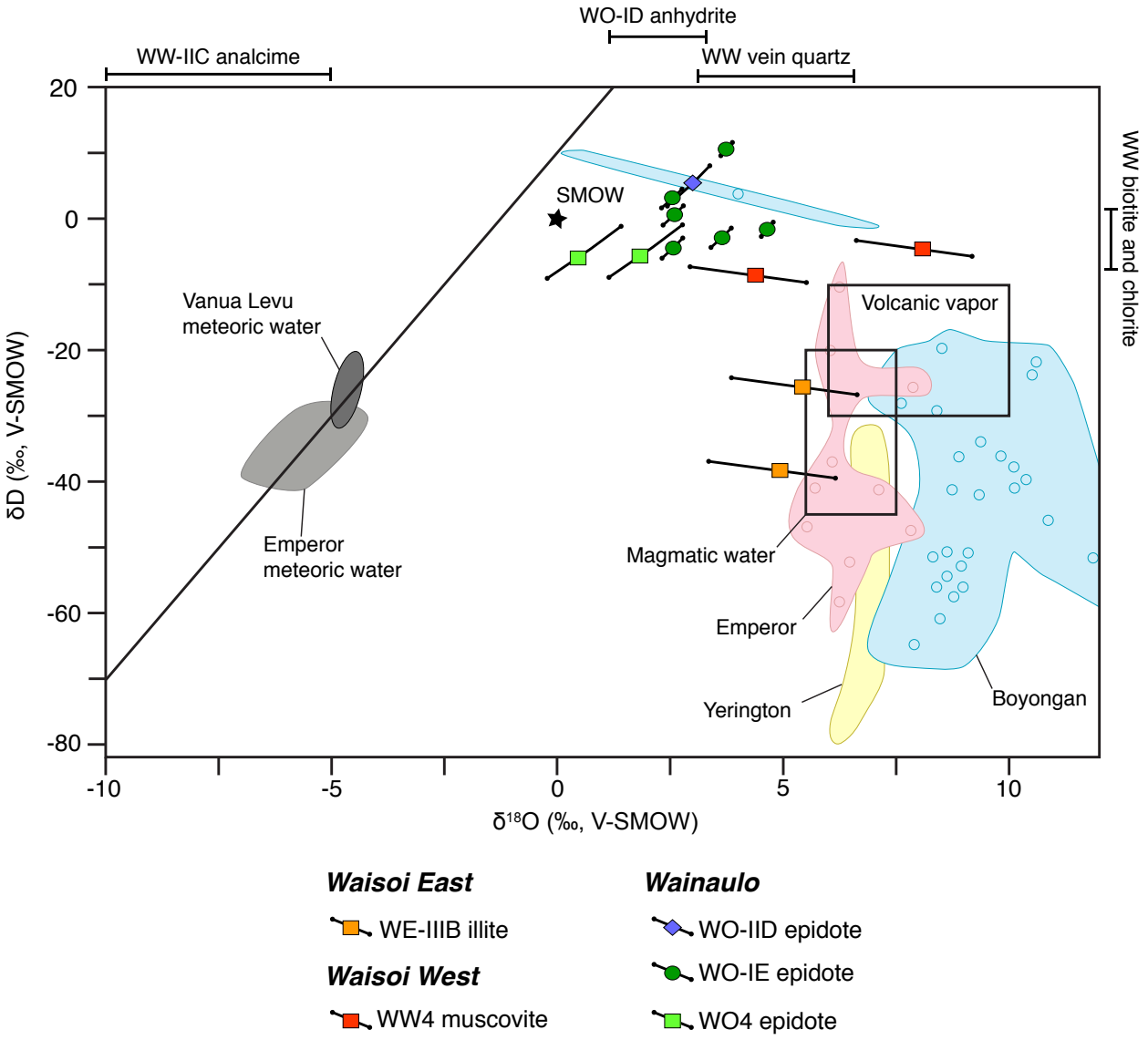


**Figure 6.7:** Calculated $\delta^{18}O$ and $\delta D$ composition of hydrothermal fluids in equilibrium with epidote from Wainaulo and illite from Waisoi East (this study) and muscovite from Waisoi West (Chivas et al., 1984; Table 6.5; Appendix G). The black lines associated with plotted data points represent the range of possible fluid compositions for that mineral at the temperatures specified in Table 6.5 and Appendix G. Shown for comparison are the range of fluid compositions from K-silicate stage alteration at Yerington (Dilles et al., 1992) and from various paragenetic stages at Boyongan (Braxton, 2007) and Emperor (Ahmad et al., 1987a). The field for volcanic vapor is from Giggenbach (1992) and the field for magmatic water is from Taylor (1997). Meteoric water at Namosi is probably similar to that from Vanua Levu (dark gray field: Cox and Hulston, 1980) and Emperor (light gray field: Ahmad et al., 1987a). The range of $\delta D$ compositions for biotite and chlorite formation waters from Waisoi West are shown on the right side of the diagram (values calculated from Chivas et al., 1984). The range of $\delta^{18}O$ compositions of vein quartz from Waisoi West are shown on the top of the diagram (values calculated from Chivas et al., 1984). Also shown are the range of $\delta^{18}O$ compositions for stage WO-ID anhydrite and stage WW-IIC analcime formation waters at Wainaulo and Waisoi West, respectively (Table 6.5; Appendix G).

waters is similar to those of magmatic waters from Taylor (1997) and waters that are actively discharging from high temperature volcanic fumaroles (Giggenbach, 1992; Fig. 6.6). Magmatic vapor and brine both appear to be the most likely fluids to have generated the illite alteration at Waisoi East (cf. Hedenquist and Richards, 1998; Harris and Golding, 2002). There is a slight depletion in $\delta^{18}O$ displayed in the data (Fig. 6.7), which indicates that meteoric water may have also been a small component involved during the precipitation of illite. The calculated $\delta^{18}O_{fluid}$

and $\delta D_{fluid}$ compositions of muscovite from Waisoi West plot well above the magmatic water field and slightly above the volcanic vapor field (Fig. 6.7). It is interpreted that volcanic vapor and another isotopically heavy water such as seawater were involved in the formation of muscovite at Waisoi West. Vapor-rich inclusions coexist with liquid-rich inclusions in late-stage quartz veins from the Waisoi deposits (Ellis, 1996), which indicates the occurrence of aqueous phase separation late in the paragenetic history of the deposits. This is consistent with the interpretation that both magmatic brine and vapor played a role in the deposition of late-stage illite and muscovite at Waisoi West and Waisoi East. The $\delta^{18}O$ and $\delta D$ data suggest that these magmatic components were mixed with external water at the Waisoi deposits.

The $\delta D_{fluid}$ values of epidote from stages WO4, WO-IE and WO-IID at Wainaulo are much higher than the range for magmatic water and volcanic vapor (Fig. 6.7). There is a significant depletion relative to magmatic values in $\delta^{18}O_{fluid}$ for epidote at Wainaulo. This enrichment in $\delta D_{fluid}$ and depletion in $\delta^{18}O_{fluid}$ requires the incorporation of an isotopically heavy water, most likely seawater, during the formation of epidote. This near-seawater signature for fluids associated with epidote at Wainaulo would exist irrespective of the temperatures chosen for mineral formation (Table 6.6; Fig. 6.7), and does not vary with respect to paragenetic stage. The $\delta D_{fluid}$ values for biotite and chlorite at Waisoi West are similar to the $\delta D_{fluid}$ values for epidote at Wainaulo, which suggests that fluids that formed early alteration at Waisoi West may also have had a significant seawater component (cf. Chivas et al., 1984). In contrast, the range of $\delta^{18}O_{fluid}$ values for late-stage WW-IIC analcime from Waisoi West falls within the range for Fijian meteoric waters.

## 6.4 Strontium isotopes

### *6.4.1 Introduction*

The submarine geological setting interpreted for the Namosi district host stratigraphy (Chapter 3), abundant Na-rich alteration assemblages (Chapter 5), high bulk sulfur ($\delta^{34}S_{\Sigma S}$ = 6.7 ‰) and elevated $\delta D_{fluid}$ values of hydrothermal minerals (this chapter), suggest that a seawater component may have been involved in the porphyry-related hydrothermal systems (cf. Margolis, 1993; Bat-

tles and Barton, 1995). The purpose of this strontium isotope study is to further assess if seawater was involved in porphyry or skarn mineralizing processes in the Namosi district. Since there is no temperature or mineral-dependent isotopic fractionation of strontium, the $^{87}Sr/^{86}Sr$ concentrations of hydrothermal minerals are interpreted to be representative of the fluids from which they precipitated, and therefore can be used to trace potential sources for hydrothermal fluids (e.g., Begg, 1996; Richards and Noble, 1998; Cooke et al., 2007; Cooke et al., 2011; Pass et al., 2014). Epidote and anhydrite typically have low Rb:Sr, allowing for reliable determination of initial strontium isotopic compositions (Nagasaki and Enami, 1998). At Namosi, epidote and anhydrite are cogenetic with copper-gold mineralization, and therefore, strontium isotope analysis on these minerals can help to constrain the Late Miocene to Early Pliocene copper-gold-bearing hydrothermal fluid sources. Volcanic and intrusive rocks from the Namosi district have $^{87}Sr/^{86}Sr$ ratios between 0.703418 and 0.703999 (Gill, 1984; Crawford, 2011; this study), whereas Miocene seawater $^{87}Sr/^{86}Sr$ ratios are substantially more radiogenic ($^{87}Sr/^{86}Sr$ = 0.7090; Faure, 1986). Therefore, a component of seawater Sr in the hydrothermal fluids would elevate the $^{87}Sr/^{86}Sr$ ratios for epidote and anhydrite to values above the range determined for Namosi district igneous rocks.

### *6.4.2 Previous work*

While there have not been any previous studies on the Sr isotopic characteristics of the Namosi district hydrothermal minerals, there has been one such study for the Emperor mine area in northern Viti Levu by Begg (1996), who presented fourteen Sr isotope analyses from various porphyry and epithermal stages at the deposit. The $^{87}Sr/^{86}Sr$ ratios were determined to range from 0.703726 – 0.703856. Begg (1996) concluded that the Sr in the ore fluids at Emperor were derived from a magmatic source and/or from circulating meteoric water that was in Sr isotopic equilibrium with the surrounding volcanic rocks. Seawater was excluded as a possible source of fluids in all stages of the Emperor porphyry-epithermal hydrothermal system (Begg, 1996). This interpretation is consistent with geological evidence for a subaerial setting at Emperor at the time of mineralization (e.g., host stratigraphy comprising subaerial lavas, caldera sediments deposited in a lacustrine environment; Setterfield, 1991; Setterfield et al., 1991; Begg, 1996).

### *6.4.3 Methods*

Five epidote, anhydrite and talc mineral separates from various alteration stages of the Wainaulo, Waisoi West and Waisoi East Cu-Au(-Mo) porphyry deposits were analyzed for their strontium isotopic compositions. The mineral separates were analyzed at the University of Melbourne by Dr. Roland Maas. Samples were hand-drilled, yielding powders that were then leached in cold 1M HCl for one hour (the talc sample was not included in this step), with the resulting supernatant solution extracted. The residue was then washed with water once, then leached and partially dissolved in HF-$NO_3$, except for the anhydrite residue, which was dissolved in 6M HCl. Part of each solution was loaded as phosphate onto single Ta filaments and analyzed in static multi-collection mode on a Finnigan-MAT 262 mass spectrometer. Mass fractionation was corrected by normalizing to $^{86}Sr/^{88}Sr = 0.1194$ and reported relative to SRM987 = 0.710230.

### *6.4.4 Results*

The initial strontium isotopic compositions of epidote from Wainaulo, anhydrite from Waisoi West and talc from Waisoi East range between 0.70364 and 0.70403 (Table 6.7). The $^{87}Sr/^{86}Sr$ ratio for the epidote separate from Wainaulo alteration stage WO4 (peripheral epidote – albite – chlorite – illite ± calcite; propylitic) is within error of the ratio for the later stage epidote from WO8 (epidote – garnet – magnetite – actinolite; calcic endoskarn). The epidote associated with high-

**Table 6.7:** Sr radiogenic isotope data for Namosi district epidote, anhydrite and talc mineral separates

| Mineral | Epidote | Epidote | Epidote | Anhydrite | Talc |
|---|---|---|---|---|---|
| Deposit | Wainaulo | Wainaulo | Wainaulo | Waisoi West | Waisoi East |
| Drill hole-depth (m) | NVD019-306 | NVD019-885 | NVD040-535 | NSW001-854 | NSE008-583 |
| Sample | EO 306 EP | EO 885 EP | EO 535 EP | EO ANH | EO SKA |
| Alteration/vein stage | WO4 | WO8 | WO-IIE | WW-IID | WE3 |
| Age (Ma) | ~ 5.7 | ~ 5.5 | ~ 5.5 | ~ 5.4 | ~ 5.3 |
| Rb ppm[1] | < 5 | < 5 | 22 | 10 | < 5 |
| Sr ppm[1] | 1382 | 194 | 207 | 505 | 1309 |
| $^{87}Rb/^{86}Sr$[1] | 0.010 | 0.074 | 0.307 | 0.057 | 0.011 |
| $^{87}Sr/^{86}Sr$ | 0.703778 (18) | 0.703808 (16) | 0.703664 (20) | 0.703963 (16) | 0.704035 (18) |
| $^{87}Sr/^{86}Sr_i$ | 0.70378 | 0.70380 | 0.70364 | 0.70396 | 0.70403 |
| % seawater[2] | 3.3 | 3.9 | 1.2 | 6.7 | 8.1 |

Absolute uncertainties (in parentheses) are shown at the 2σ level for the last digit indicated for $^{87}Sr/^{86}Sr$. Initial $^{87}Sr/^{86}Sr$ ratios have been calculated based on the ages reported in this table and using equations from DePaulo and Wasserburg (1976). Alteration and vein stages are described in Chapter 5. [1]Concentrations and parent/daughter ratios from portable XRF analyses. [2] % seawater calculated using average $^{87}Sr/^{86}Sr$ for Miocene seawater of 0.7090 (Faure, 1986) and average $^{87}Sr/^{86}Sr$ for Namosi district stratigraphy of 0.7036 (calculated from the range for $^{87}Sr/^{86}Sr$ as determined by Gill (1984), Crawford (2011) and this study).

grade WO-IID veins (epidote – sulfide – anhydrite with K-feldspar vein halos) has slightly less radiogenic strontium (Table 6.7). The anhydrite separate from Waisoi West vein stage WW-IID (anhydrite – sulfide veins) has more radiogenic strontium than the epidote samples from Wainaulo (Fig. 6.8). The talc separate from Waisoi East alteration stage WE3 (talc – phlogopite; magnesian exoskarn) has the most radiogenic strontium of any of the Namosi hydrothermal minerals analyzed in this study (Table 6.7; Fig. 6.8).

*6.4.5 Discussion*

Epidote separates from the Wainaulo porphyry Cu-Au deposit have similar initial Sr ratios (0.70364 – 0.70380; Table 6.7) to the carbonate and anhydrite Sr ratios determined for the Emperor porphyry-epithermal system (Fig. 6.8) and are within the upper range of data reported for Viti Levu igneous rocks (Fig. 6.7). The Waisoi anhydrite and talc $^{87}Sr/^{86}Sr$ ratios are slightly more radiogenic than the data reported for Emperor. The epidote, anhydrite and talc Sr data overlap with $^{87}Sr/^{86}Sr$ ratios obtained from other ocean island arc porphyry deposits (Fig. 6.8).

The Namosi hydrothermal gangue minerals have low $^{87}Sr/^{86}Sr$ ratios (Table 6.7; Fig. 6.7), consistent with a predominantly mantle-derived source of strontium (Kesler et al., 1975; Sillitoe, 1987). There is a general trend of increasing $^{87}Sr/^{86}Sr$ ratios from the early Wainaulo epidote samples to the late Waisoi East talc sample (Fig. 6.8). These hydrothermal minerals all have more radiogenic strontium than their related progenitor intrusions as well as more than the surrounding volcanic host sequence (Namosi Andesite Formation and Wainimala Group; Fig. 6.8). It is unlikely that the elevated strontium isotopic ratios have resulted from carbonate assimilation and incorporation into the Namosi magmatic-hydrothermal system, because there is no $^{87}Sr/^{86}Sr$ enrichment observed in the progenitor intrusions. It is possible that the elevated $^{87}Sr/^{86}Sr$ ratios resulted from fluid-rock interaction between magmatic-hydrothermal or meteoric water and thin calcareous horizons throughout the Namosi district stratigraphy (Chapter 3); however, no significant crustal sources of highly radiogenic Sr (e.g., thick limestone units or evaporite formations) have been documented in the district. The % seawater Sr component for a fossil hydrothermal fluid can be calculated based on $^{87}Sr/^{86}Sr$ ratios for hydrothermal minerals precipitated from those flu-

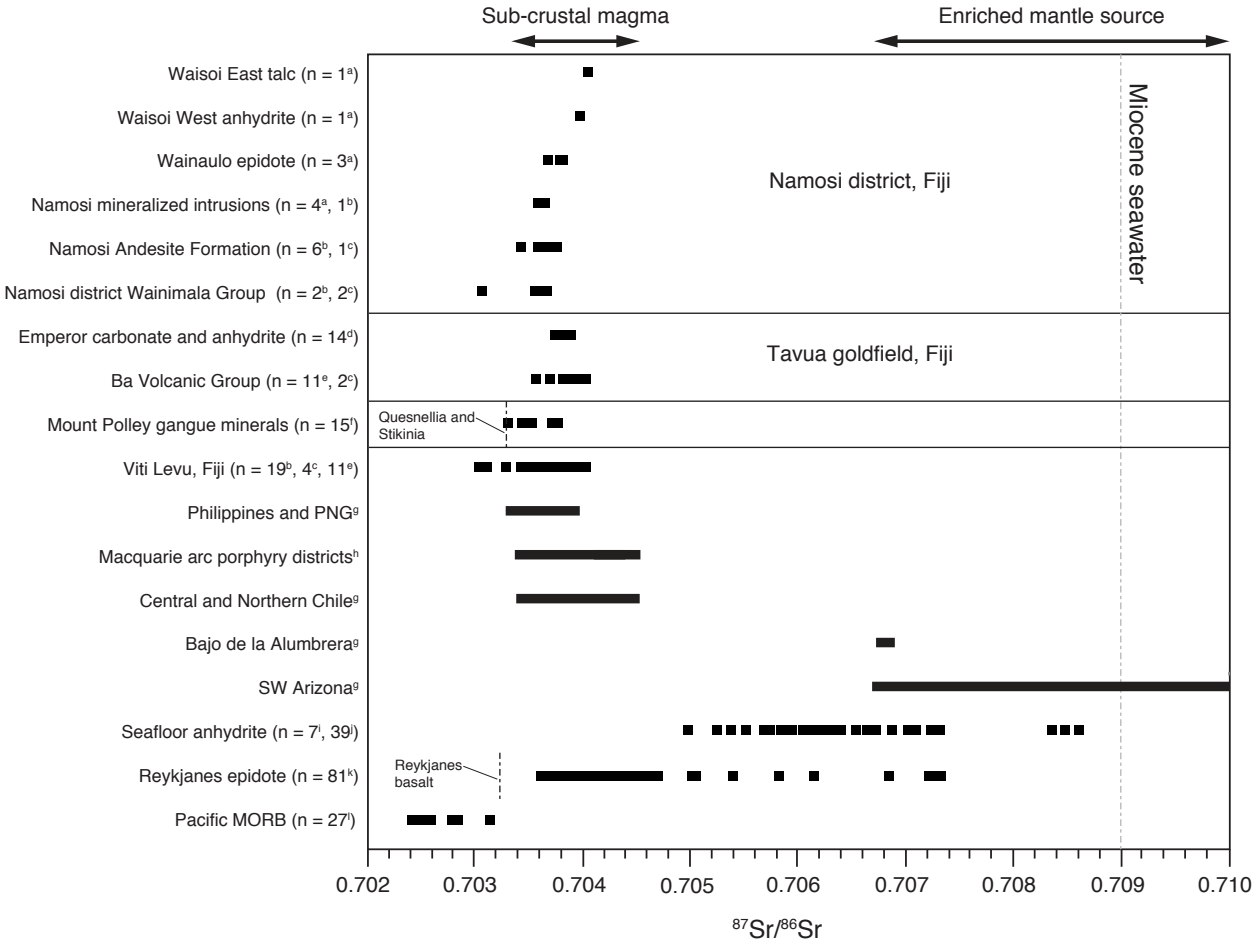


**Figure 6.8:** Strontium isotope data for epidote from Wainaulo, anhydrite from Waisoi West and talc from Waisoi East (Table 6.7), compared to Sr isotope analyses for carbonate and anhydrite from the Emperor alkalic Au deposit and host stratigraphy, as well as intrusions from calc-alkalic porphyry deposits from both island arc and continental settings and alkalic intrusions from NSW porphyry districts (Cadia and North Parkes). Also included are the range of Sr isotope compositions for Pacific MORB, anhydrite from TAG and PACMANUS seafloor hydrothermal systems, and epidote from the Reykjanes seawater-driven geothermal system. This diagram is modified after Cooke et al. (2011). Data sources: [a]this study, [b]Crawford (2011), [c]Gill (1984), [d]Begg (1996), [e]Rogers and Setterfield (1994), [f]Pass et al. (2014), [g]Sillitoe (1987), Sillitoe (1997), [h]Cooke et al. (2007), [i]Chiba et al. (1998), [j]Bach et al. (2005), [k]Marks et al. (2015), [l]Ito et al. (1987).

ids. The component of strontium derived from seawater in Namosi hydrothermal minerals were calculated to range from 1.2 – 8.1 % (Table 6.7), based on a Miocene seawater Sr ratio of 0.7090 and an average Sr ratio for the Namosi host rocks of 0.7036 (Table 6.7). It is suggested that at Waisoi West and Waisoi East there was likely an external component of Sr from seawater mixed with a dominant magmatic-hydrothermal (and possibly meteoric) Sr source component. These results are similar to those for the Mount Polley deposit, British Columbia (Pass et al., 2014). The initial Sr values for gangue minerals at Mount Polley were determined to be depleted; however, their initial Sr ratios are higher than that of the average Sr ratios for the surrounding Quesnellia and Stikinia host rocks (Lang et al., 1995; Pass et al., 2014; Fig. 6.8). Calculations to determine the

percentage of magmatically derived Sr in the source fluids revealed that seawater derived Sr in the Mount Polley ore zone minerals constituted up to 10.6 % of the total Sr.

The Reykjanes geothermal system is a modern, basalt-hosted hydrothermal system situated on the landward extension of the Mid-Atlantic Ridge in Iceland (Marks et al., 2015). The hydrothermal fluids at Reykjanes are a product of seawater that has been chemically modified through interaction with basaltic host rocks (Arnórsson et al., 1978; Ólafsson and Riley, 1978; Arnórsson, 1995; Bird and Spieler, 2004, Fridleifsson and Elders, 2005). The range of $^{87}Sr/^{86}Sr$ compositions of epidote grains from Reykjanes drill cuttings and drill core (0.70360 to 0.70731; Marks et al., 2015) is elevated in comparison to the average $^{87}Sr/^{86}Sr$ composition of the Reykjanes basalts (0.70322, Elderfield and Greaves, 1981; Fig. 6.7) and approaches the composition of modern seawater (0.70916); the mean $^{87}Sr/^{86}Sr$ composition (0.70437) is similar to that of the fluids from the Reykjanes geothermal system (0.70412 to 0.70421; Elderfield and Greaves, 1981; Millot et al., 2009). The component of strontium derived from seawater in Reykjanes epidotes was calculated using the data from Marks et al. (2015) to range from only 6 to 69 %, with a median of 14 % (Appendix H). Epidotes with the highest $^{87}Sr/^{86}Sr$ compositions and % seawater Sr were sampled superjacent to small feed zones (i.e., zones of high permeability), where seawater that was less isotopically exchanged with the host basalts was entering the hydrothermal system. This implies that in zones with higher fluid flow and a higher fluid to rock ratio, $^{87}Sr/^{86}Sr$ compositions of epidotes will more closely match the strontium values of the source fluid reservoir (e.g., seawater for the Reykjanes hydrothermal system). On the other hand, in areas with lower water to rock ratios, strontium in the fluid is able to isotopically equilibrate with the host rocks, resulting in $^{87}Sr/^{86}Sr$ compositions of epidote that more closely reflect the host rock composition. At Namosi, the calculated range of 1.2 – 8.1 % seawater Sr input may reflect low water to rock ratios and a resultant high degree of water-rock interaction that has modified circulating hydrothermal fluids, even if the source fluid was 100 % seawater.

Other hydrothermal systems with a submarine association have been shown to have minimal seawater strontium input. Venneman et al. (1993) used Sr, S, O and D isotopes to show that de-

spite a marine or near-marine geologic setting, high-sulfidation mineralization at Pueblo Veijo in the Dominican Republic was caused by magmatic fluids with relatively minor involvement of meteoric water. Venneman et al. (1993) concluded that the system was isolated from seawater due to mineral sealing caused by the retrograde solubility of calcite and/or anhydrite. Similar arguments have been made for the isolation of the White Island magmatic-hydrothermal system from seawater, with anhydrite precipitated on the fringe of the island due to heating of seawater to provide the hydrothermal seal (Hedenquist et al., 1993, Simmons et al., 2006).

## 6.5 Summary

Stable and radiogenic isotopes have provided constraints on fluid sources, composition and physicochemical conditions of ore formation and hydrothermal alteration for the Namosi district porphyry deposits. Sulfur isotopic compositions of stage WO2, WO-IID, WO-IIIA and WO-IIIC sulfides and sulfates are systematically zoned about the quartz-diorite intrusive complex at Wainaulo, with isotopically higher $\delta^{34}S_{sulfide}$ values occurring within and above the porphyry intrusions and lower values occurring at the deposit periphery. The opposite pattern has been observed for $\delta^{34}S_{sulfate}$, with isotopically lower values occurring at the core of the deposit and higher values at the deposit periphery. This spatial distribution of $\delta^{34}S$ values can be explained by a cooling fluid with a neutral redox state (R = 1.0) emanating from the quartz-diorite porphyry complex and overprinting the relatively oxidized alteration associated with the early diorite intrusions (EMD1). No spatial variation of $\delta^{34}S$ values were exhibited at the relatively more reduced Waisoi West and Waisoi East porphyry deposits.

Modeling of sulfur isotope values from co-existing sulfate – sulfide pairs from Wainaulo indicates that the fluid had a high bulk sulfur composition of +6.7 ‰ and was deposited under a range of aqueous sulfate:sulfide conditions (i.e., R = 1.0, R = 1.6 and R = 2.9). The $\delta^{34}S_{sulfide}$ values at Wainaulo range from -5.0 to +3.9 ‰ with an average of -1.5 ‰ (n = 53; this study and Egashira, 2009). The near-zero average $\delta^{34}S_{sulfide}$ value indicates a source fluid that was predominantly magmatic in origin; however, the high $\delta^{34}S_{\Sigma S}$ value may imply contamination of magmatic sulfur by sedimentary sulfate by assimilation or seawater sulfate as a result of fluid mixing.

Results from the oxygen and hydrogen stable isotope study indicate three different fluid sources were involved throughout the Namosi district paragenetic history: exsolved magmatic fluid, Late Miocene seawater and a local meteoric component. An influx of seawater mixed with magmatic fluids produced the epidote-bearing assemblages at Wainaulo, including the high-grade epidote – anhydrite – bornite veins that crosscut the early quartz – sulfide veins and albite – biotite and albite – chlorite – actinolite alteration assemblages in the core of the deposit. The calculated $\delta^{18}O$ and $\delta D$ composition of fluids in equilibrium with locally developed illite alteration at Waisoi East plot near the magmatic water field of Taylor (1997), suggesting that the late stage illite – calcite – pyrite assemblage at Waisoi East was probably precipitated from a non-boiling, primary magmatic fluid derived from arc magmas. A late stage ingress of meteoric fluids along fractures generated zeolite – calcite – montmorillonite alteration below 80°C at Waisoi West.

The Namosi district alteration minerals show a predominantly mantle-derived strontium isotopic signature with a minor input of seawater Sr or crustal Sr (up to 8.1 %). While this low percent seawater appears to be in disagreement with the near-seawater oxygen – deuterium isotopic signature of the Wainaulo epidotes, it can be reasoned that a high degree of water-rock interaction may have modified seawater-dominant hydrothermal fluids at Wainaulo to more closely reflect the Sr isotopic signature of the local host-rocks, as has occurred in the seawater-driven Reykjanes geothermal system in Iceland.

Overall, the S, O–D and Sr isotopic data confirm the importance of magmatic-hydrothermal fluids as well as an external seawater source to the mineralizing processes in the Namosi district porphyry deposits. This conclusion is consistent with the interpreted submarine setting for the Namosi district volcanic host sequence, which was interpreted to be comagmatic with the mineralized intrusions.

# CHAPTER 7

# Genetic model and conclusions

## 7.1 Introduction

This chapter presents a genetic model for the Namosi district porphyry deposits, based on the geological, geochemical and geochronological results discussed in previous chapters. The model proposes regional tectonic controls on the emplacement of the Namosi porphyry intrusions and summarizes their district-scale evolution. Key elements of the Namosi genetic model are illustrated in Figure 7.1.

## 7.2 Genetic model

### *7.2.1 Tectono-metallogenic model*

An important precursor to porphyry-epithermal mineralization in Fiji was a reversal of arc polarity at ~ 12 – 10 Ma (e.g., Solomon, 1990). The Melanesian Border Plateau collided with the Vitiaz Trench, choking west-southwest-directed subduction north of Fiji. After subduction terminated, north-directed subduction along the Matthew-Hunter Ridge was initiated (Fig. 2.1).

Rollback of the downgoing South Fiji Basin slab led to the opening of the North Fiji Basin. Due to the curvature of the Matthew-Hunter Trench and the resultant geometry of spreading centers in the North Fiji Basin, the Vanuatu Arc and Fiji Platform began to rotate inwardly in opposite directions (Fig. 2.1). Extensive oblique-slip fracture networks associated with arc rotation formed in Viti Levu (Fig. 2.4), preconditioning the Namosi region for localization of calc-alkalic magmatism.

By ~ 6 Ma the curvature of the Matthew-Hunter Trench had become more pronounced, caus-

ing the downgoing South Fiji Basin slab to develop a northwest-directed low-angle subduction component where it had rotated into contact with the west-dipping Pacific Plate (Fig. 2.3). This low-angle subduction geometry was critical to the formation of the Namosi district porphyry intrusions and associated Cu-Au(-Mo) mineralization (e.g., Cooke et al., 2005). Previous workers argued that Namosi magmatism was geographically separated from active subduction (e.g., Gill, 1984; Crawford, 2011) or that it was related to subduction along the Vitiaz Trench (Gill et al., 1984; Kroenke, 1984; Gill and Whelan, 1989a). However, Namosi district rocks have a subduction-related geochemical signature (e.g., Fig. 4.5), consistent with an Indo-Australian Plate (South Fiji Basin), rather than Pacific Plate (Vitiaz) source (Fig. 4.8).

From 5.5 to 3.0 Ma, slab rollback along the Matthew-Hunter Trench south of Fiji resulted in the south-southeast migration of backarc-related shoshonitic volcanism from Viti Levu to the Kadavu Islands (Fig. 2.5). A link between shoshonitic volcanic centers and alkalic porphyry-epithermal mineralization has been documented in northern Viti Levu (e.g., Emperor and Tuvatu Au deposits). Alkalic Au mineralization may occur elsewhere along this south-southeast shoshonitic trend.

### *7.2.2 Genetic model for Namosi district mineralization*

The chronology of geological and magmatic-hydrothermal events in the Namosi district is summarized in Figure 7.1. The oldest rocks of the Namosi district are low-K tholeiitic volcanics of the Nubuonaboto Formation (Mount Gordon sub-Group, Wainimala Group). These basement rocks were deposited in the Late Oligocene to Middle Miocene. The Nubuonaboto sequence is interpreted to have formed in a submarine intra-oceanic arc setting associated with west-directed subduction of the Pacific Plate (Rodda, 1994). These rocks are unconformably overlain by medium-K calc-alkalic andesite and volcaniclastic rocks of the Namosi Andesite Formation (Medrausucu Group). The foraminiferal assemblage (e.g., incomplete *Cycloclypeus indopacificus)* of the basal NAF calcareous sandstone facies suggest deposition at depths more than 200 m below sea level in a Late Miocene tropical environment (cf. Koba, 1978; Hallock and Glenn, 1986). The overlying andesitic hyaloclastite and lavas with perlitic fractures are also consistent with depo-

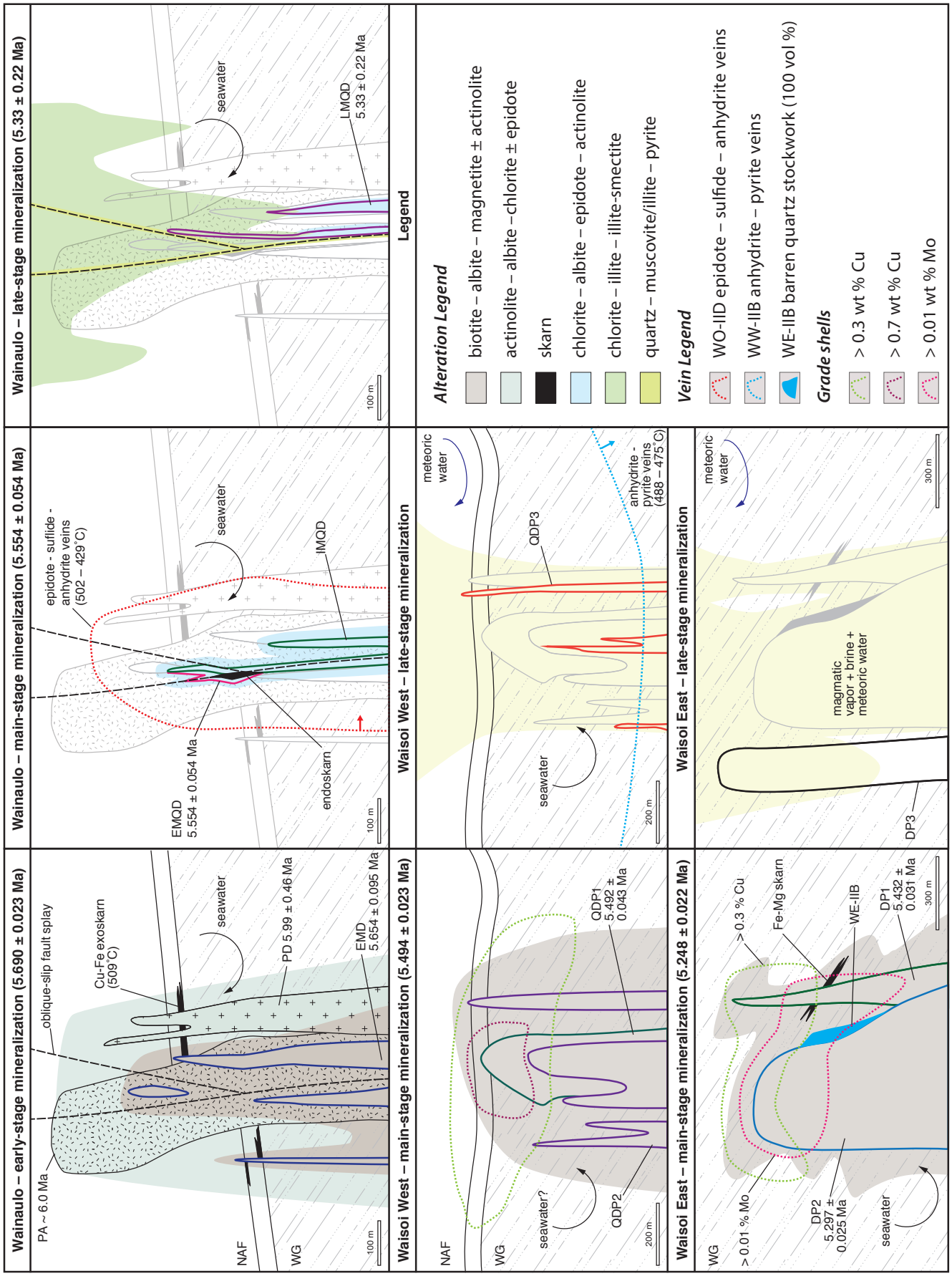
Wainaulo – early-stage mineralization (5.690 ± 0.023 Ma)
Wainaulo – main-stage mineralization (5.554 ± 0.054 Ma)
Wainaulo – late-stage mineralization (5.33 ± 0.22 Ma)
PA ~ 6.0 Ma
oblique-slip fault splay
Cu-Fe exoskarn (509°C)
seawater
PD 5.99 ± 0.46 Ma
EMD 5.654 ± 0.095 Ma
NAF
WG
100 m
epidote - suflide - anhydrite veins (502 – 429°C)
EMQD 5.554 ± 0.054 Ma
IMQD
endoskarn
LMQD 5.33 ± 0.22 Ma
Waisoi West – main-stage mineralization (5.494 ± 0.023 Ma)
Waisoi West – late-stage mineralization
Legend
seawater?
QDP1 5.492 ± 0.043 Ma
QDP2
200 m
meteoric water
QDP3
anhydrite - pyrite veins (488 – 475°C)
Alteration Legend
biotite – albite – magnetite ± actinolite
actinolite – albite –chlorite ± epidote
skarn
chlorite – albite – epidote – actinolite
chlorite – illite – illite-smectite
quartz – muscovite/illite – pyrite
Vein Legend
WO-IID epidote – sulfide – anhydrite veins
WW-IIB anhydrite – pyrite veins
WE-IIB barren quartz stockwork (100 vol %)
Grade shells
> 0.3 wt % Cu
> 0.7 wt % Cu
> 0.01 wt % Mo
Waisoi East – main-stage mineralization (5.248 ± 0.022 Ma)
Waisoi East – late-stage mineralization
> 0.01 % Mo
> 0.3 % Cu
Fe-Mg skarn
WE-IIB
DP1 5.432 ± 0.031 Ma
DP2 5.297 ± 0.025 Ma
magmatic vapor + brine + meteoric water
DP3
300 m

**Figure 7.1 (opposite):** Summary of a genetic model for the Namosi district Cu-Au(-Mo) porphyry deposits. This model highlights key elements from each of Wainaulo Cu-Au, Waisoi West Cu-Au and Waisoi East Cu-Au-Mo deposits. Abbreviations: DP1 = quartz-eye dacite, DP2 = quartz-bearing dacite, DP3 = dacite porphyry, EMD = early-mineralization diorite, EMQD = early-mineralization quartz-diorite, IMQD = inter-mineralization quartz-diorite, LMQD = late-mineralization quartz-diorite, NAF = Namosi Andesite Formation, PA = porphyritic andesite, PD = porphyritic diorite, QDP1 = quartz-diorite porphyry 1, QDP2 = quartz-diorite porphyry 2, QDP3 = quartz-diorite porphyry 3, WG = Wainimala Group.

sition in a subaqueous environment (e.g., McPhie et al., 1993). This volcanic sequence is interpreted to have formed as part of an arc associated with short-lived north-directed subduction of South Fiji Basin lithosphere along the Matthew-Hunter Trench in the Late Miocene.

The Wainimala Group basement and overlying Namosi Andesite Formation has been crosscut by a sequence of hypabyssal intrusions. The composition of Namosi district intrusions became increasingly more fractionated with each successive magmatic phase and ranges from early pre-mineralization diorite plutons to productive diorite, quartz-diorite and then dacite dikes and stocks over a timespan of ≤ 750,000 years (~ 6.00 – 5.25 Ma; Fig. 5.40; Table 5.10). A series of hydrothermal alteration systems developed in three principal porphyry centers and several smaller-scale centers over a time period of ~ 400,000 years (5.65 – 5.25 Ma; Fig. 5.40; Table 5.10). The Namosi district porphyry centers are interpreted as cupolas above a single large parental magma chamber, which became progressively more differentiated (e.g., Dilles, 1987; Sillitoe, 2010). In order of decreasing relative age, the three principal porphyry centers are the Wainaulo Cu-Au, Waisoi West Cu-Au and the Waisoi East Cu-Au-Mo deposits. The productive Namosi porphyry intrusions have a subduction-related geochemical signature (i.e., Nb, Ti, V and Sc depletion and LREE enrichment; Fig. 4.5), and are sourced from a primitive, depleted (e.g., $^{87}Sr/^{86}Sr$: 0.70358 – 0.70362; $^{143}Nd/^{144}Nd$: 0.513001 – 0.513058) hydrous parental magma (e.g., "saggy" convex HREE profiles; Fig. 4.5). There is a trend to increasing LREE concentrations prior to mineralization ($La/Sm_{cn}$; cf. Hollings et al., 2005; Table 4.5; Fig. 4.6B). The $La/Sm_{cn}$ ratios are highest for the Wainaulo early mineralization diorites (EMD: oldest of the Namosi mineralizing intrusions) and then decrease both with increasing $SiO_2$ and time (Figs. 4.6A and B). This is interpreted to reflect increasing crustal thickness up until the time of mineralization, and finally a change related to crustal thinning with initiation of backarc spreading in the Fiji Platform area. This model is consistent with the increasing $^{143}Nd/^{144}Nd$ values with decreasing age of Namosi mineralized intrusions (Fig. 4.7),

which records a shift towards a less contaminated and more primitive source.

Wainaulo is a variant of the plutonic-hosted porphyry class of deposits (cf. McMillan and Panteleyev, 1988). The Wainaulo orebody has an east-northeast-trending (080°), dike-like geometry (100 x 300 m; open at depth) defined by the 1.0 wt % Cu grade shell (Fig. 5.1). The orebody is parallel to east-northeast-trending faults of the WWW Fault Zone, which are interpreted to have localized Wainaulo copper-gold mineralization and porphyry emplacement (Fig. 2.4). Early stage porphyry mineralization (Stage WO-IB quartz molybdenite veins: 5.690 ± 0.023 Ma) is spatially and temporally associated with medium-K calc-alkalic diorite dikes (EMD: 5.654 ± 0.095 Ma) that have intruded both the submarine NAF and Wainimala Group host stratigraphy and comagmatic pre-mineralization plutons (PA and PD: 5.99 ± 0.46 Ma). The early stage alteration assemblages are characterized by the high abundance of albite ± oligoclase and paucity of K-feldspar, as well as moderate Cu, low Au, and sparse Mo mineralization. Hydrothermal alteration is broadly zoned about the EMD intrusions, from a central zone of biotite – albite (WO1), outward to medial actinolite – albite (WO3) and then distal epidote – albite – chlorite (WO4) alteration zones (Fig. 5.1A). There is also a zonation of sulfides about the EMD intrusions, from a chalcopyrite-rich core, through an intermediate zone of pyrite – chalcopyrite to a peripheral pyrite-only zone. Epidote from early alteration and vein stages (WO4 and WO-IE) has a mixed magmatic + seawater fluid source, which is interpreted to explain the abundance of albite in the hydrothermal mineral assemblages (cf. Battles and Barton, 1995). At Batu Hijau, the abundance of albite and oligoclase and lack of K-feldspar in its early-formed hydrothermal alteration assemblages is attributed to fluids derived from low-K calc-alkaline tonalites (Garwin, 2000; Idrus et al., 2009). The presence of anhydrite and epidote in early stage veins and alteration assemblages (Table 5.2 and 5.3) suggest precipitation from a sulfate-stable oxidized fluid. Cu-Fe mineralization and associated calc-silicate alteration (WO2) were generated where fluids sourced from the EMD intrusion reacted with calcareous horizons within basal NAF rocks.

Main-stage porphyry mineralization at Wainaulo is associated with quartz-diorite dikes (EMQD: 5.554 ± 0.054 Ma and IMQD) that have intruded along steeply dipping, deep, oblique-

slip faults (trending ~ 080°) and along the contacts of EMD dikes (Fig. 5.1). Adjacent to the steeply dipping faults, an andradite – epidote – magnetite endoskarn assemblage (WO8) has strongly altered the EMQD dike. A temporal relationship between magmatic and hydrothermal activity is evinced by abundant comb quartz layers (USTs) occurring in the apical portion of the EMQD dikes (cf. Shannon et al., 1982; Kirkham and Sinclair, 1988; Harris et al., 2005). The USTs at Wainaulo include fine-grained disseminations of bornite, chalcopyrite and magnetite, which is interpreted to suggest that the exsolved aqueous fluid phase contained dissolved metals. The EMQD dikes produced restricted zones of chlorite – albite – epidote – actinolite alteration (WO7) associated with sulfide-bearing quartz vein stockworks (WO-IIB and WO-IIC) that overprinted the early biotite – albite alteration (WO1). High-grade Cu- and Au-bearing epidote – anhydrite – sulfide veins with K-feldspar ± phengite vein halos (WO-IID) crosscut the quartz vein stockworks in the core of the deposit. Seawater was an important component of the source fluids responsible for these epidote – sulfide veins, which were an unusual ore contributor at Wainaulo. Main-stage sulfides define a zonation pattern from proximal chalcopyrite – bornite, to chalcopyrite > pyrite to distal pyrite > chalcopyrite (Fig. 5.2). Simon et al. 2000 determined that gold solubility in the Cu-Fe-S system between 400° and 700°C indicates that bornite will contain one order of magnitude more gold than coexisting chalcopyrite. This result may explain the gold-rich nature of the main-stage porphyry mineralization relative to the early-stage mineralization.

After the emplacement of the LMQD dike (5.33 ± 0.22 Ma), main stage mineralization was overprinted by anhydrite – pyrite ± sphalerite veins (WO-IIIA) and an upward-flaring domain of weak chlorite ± illite ± illite-smectite alteration (WO11) centered on the quartz-diorite complex. The final hydrothermal event at Wainaulo consisted of an intense, pervasive kaolinite – montmorillonite ± hematite ± ankerite ± gypsum assemblage (WO12) that was concentrated in and around steeply-dipping, east-northeast-trending faults and presented locally as banded veins of gypsum and ankerite with patches of montmorillonite and euhedral pyrite (WO-IIIC). Sulfur isotopic compositions from late-stage WO-IIIA and WO-IIIC sulfides and sulfates are systematically zoned about the quartz-diorite intrusive complex at Wainaulo. Isotopically higher $\delta^{34}S_{sulfide}$ values occur within and above the porphyry intrusions and lower values occur at the deposit periphery

(Fig. 6.2). The opposite pattern has been observed for $\delta^{34}S_{sulfate}$, with isotopically lower values occurring at the core of the deposit and higher values at the deposit periphery (Fig. 6.3). This spatial distribution of $\delta^{34}S$ values can be explained by a cooling fluid with a neutral redox state (R = 1.0) emanating from the quartz-diorite porphyry complex and overprinting the relatively oxidized alteration associated with the early diorite intrusions (EMD). The Wainaulo early-, main- and late-stage sulfides have $\delta^{34}S$ compositions (-4.5 to 2.9 ‰; $\delta^{34}S_{\Sigma S}$ = 6.7 ‰) that are typical of a predominantly magmatic source of sulfur mixed with a component of seawater sulfate.

Waisoi West is an example of a volcanic-hosted porphyry deposit (cf. McMillan and Panteleyev, 1988). The orebody can be defined by the > 0.7 wt % copper grade shell, which is elongate (3:2 aspect ratio; long axis = 400 m) and has a shallow plunge towards the north-northwest (25/050°). This trend is similar to that of the northwest-trending faults of the Mauivuso Fault Zone, which may be partly responsible for the localization of Waisoi West copper-gold mineralization and porphyry emplacement (Fig. 2.4). The Waisoi West intrusive complex is a composite stock comprising sub-vertical, steeply north-plunging quartz-diorite intrusions that have an unconstrained vertical continuity (at least 600 m; Fig. 5.16A). Most of the copper-gold mineralization at Waisoi West occurred in association with UST-bearing QDP1 intrusions (5.492 ± 0.043 Ma). Hydrothermal alteration consisting of a core of biotite – albite – magnetite (WW1) grading outward to chlorite – albite – magnetite (WW2) is concentrically zoned about the QDP1 intrusions. These alteration zones have been overprinted by albite ± K-feldspar vein-halo alteration (WW3) associated with main-stage saccharoidal-textured quartz ± sulfide veins (WW-ID) that were emplaced cyclically in response to successive intrusion of the QDP1, QDP2 and QDP3 quartz-diorite stocks. WW-ID veins associated with the QDP1 intrusion have been dated at 5.494 ± 0.023 Ma. Early biotite and chlorite may have a mixed magmatic + seawater source (i.e., $\delta D$ = -7.8 to +1.5 ‰; Table 6.6); however, further $\delta^{18}O$ and $\delta D$ isotopic testing is required to confirm this.

Late-stage pervasive and vein-style paragonite – quartz – pyrite ± calcite alteration (WW4) overprints main-stage alteration and veins. Stage WW4 alteration is preferentially developed in

the Waisoi West intrusive complex and becomes progressively more intense upwards and outwards. Widespread quartz – pyrite ± sphalerite ± galena ± chalcopyrite veins (WW-IIA) and deep (> -100 mRL) anhydrite – pyrite veins (WW-IIB; 488 – 475°C) are associated with this alteration assemblage. The calculated $\delta^{18}O_{fluid}$ and $\delta D_{fluid}$ compositions of stage WW4 muscovite from Waisoi West suggest that they were precipitated from mixed volcanic vapor and seawater (Fig. 6.6). The $^{87}Sr/^{86}Sr$ composition of stage WW-IIB anhydrite confirms the involvement of seawater (Table 6.7). The final hydrothermal event at Waisoi West was the emplacement of calcite ± montmorillonite ± gypsum ± chabazite ± analcime veins (WW-IIC). $\delta^{18}O_{fluid}$ and $\delta D_{fluid}$ isotopic values suggest that a late-stage ingress of meteoric fluids migrated along fractures, mixed with magmatic fluids and generated WW-IIC alteration below 80°C. No spatial variation of $\delta^{34}S$ values were exhibited at the relatively reduced Waisoi West deposit.

Waisoi East is another example of a volcanic-hosted porphyry deposit (e.g., McMillan and Panteleyev, 1988). The 0.3 wt % Cu grade shell is shallow (< 400 m from the present-day surface), elongate (3:2 aspect ratio; long axis = 1 km) and has a shallow plunge towards the north-northwest. Its emplacement has been controlled by the Mauivuso Fault Zone (Fig. 2.4). Copper-gold-molybdenum mineralization is associated with three texturally and compositionally similar hornblende-bearing, quartz-feldspar-phyric stocks and pipes (DP1: quartz-eye dacite; DP2: quartz-bearing dacite and DP3: dacite porphyry). DP1 was emplaced at 5.432 ± 0.031 Ma and is associated with early biotite – albite alteration (WE1) and Cu-Au mineralization. Chalcopyrite inclusions within DP1 quartz-eyes (Figs. 3.20B and 5.24A; inferred as miarolitic cavities) indicate that the magmatic fluid was metal bearing. A distinct age was determined for DP2 at 5.297 ± 0.025 Ma. DP2 is interpreted to be associated with the bulk of Mo mineralization (stage WE-IIC: 5.248 ± 0.022 Ma; Table 5.10; Fig. 5.40), and a zone of Cu-Au mineralization that weakly drapes over the apical portion of the DP2 intrusion. Biotite – albite (WE1) alteration, which is partly lithologically controlled, and chlorite – albite (WE2) alteration is broadly zoned about the DP2 intrusion. Discontinuous, small zones of Fe-Mg-Cu skarn alteration occurs adjacent to the DP1 and DP2 intrusions and is concordant with bedding within the Wainimala Group host stratigraphy. Both the DP1 and DP2 intrusions have barren (i.e., Cu-Au depleted) quartz-veined

cores, where temperatures may have been too high to permit appreciable Cu-Fe sulfide precipitation, resulting in the shallow cap-shaped 0.3 wt % Cu grade shell (e.g., Sillitoe, 2010). However, significant quantities of the higher-temperature mineral molybdenite occur within this same quartz-vein stockwork at deeper levels within the DP1 and DP2 intrusions (cf. Bingham: Landtwing et al., 2010; Seo et al., 2012).

The final stages of hydrothermal activity in the Waisoi East Cu-Au-Mo deposit are characterized by zones of intense, pervasive muscovite – pyrite – quartz (WE8) alteration that has overprinted and partially destroyed earlier formed biotite – albite (WE1) alteration within and above the mineralized dacite intrusions. Within the Wainimala Group host stratigraphy, structurally focused quartz – muscovite – pyrite ± sphalerite ± galena veins and fault zones (WE-II-IA) developed with intense, pervasive illite – muscovite – pyrite alteration envelopes. Widespread, low-intensity assemblages consisting of illite – chlorite ± illite-smectite (WE9) and kaolinite – montmorillonite (WE10) have overprinted the muscovite ± illite ± pyrite-altered rocks (WE8). Magnetite has been replaced by hematite along internal fractures (Fig. 5.30E) where stage WE9 alteration is present. This suggests that oxidation of iron occurred during this late-stage alteration. Accompanying chlorite – illite alteration are stage WE-IIIB illite – calcite ± pyrite veins that have an erratic distribution throughout the Waisoi East deposit. The calculated $\delta^{18}O_{fluid}$ and $\delta D_{fluid}$ values for stage WE-IIIB illite are interpreted to indicate that the fluids responsible for this alteration were a mix of volcanic vapor, magmatic brine and meteoric water (cf. Hedenquist and Richards, 1998; Harris and Golding, 2002).

Previous workers have speculated that the Waisoi magmatic-hydrothermal system might be older than Wainaulo (e.g., Ellis, 1996; Corbett, 2011). This hypothesis was based on K–Ar dates and the presence of host rocks from deeper levels in the local stratigraphy being exposed at Waisoi, whereas younger rocks are exposed at Wainaulo. The current study contradicts this hypothesis, and has presented high-resolution geochronology results that unequivocally show that Wainaulo is older than the Waisoi deposits. It is more likely that the deposits were emplaced at different stratigraphic levels. The diorite- to quartz-diorite-related Wainaulo Cu-Au deposit was

emplaced higher in the stratigraphy, the more felsic Waisoi West Cu-Au deposit was emplaced at an intermediate level, and the felsic dacite Waisoi East Cu-Au-Mo deposit was emplaced at the deepest relative level within the stratigraphic sequence.

### 7.3 Implications for exploration

Some of the outcomes from this thesis have implications for mineral exploration within the Namosi district and can be applied to other districts worldwide.

- At the regional tectonic scale, this study has shown that porphyry deposits can be generated from low-angle subduction associated with rotational tectonics. Identifying similar tectonic regimes elsewhere (e.g., West Mediterranean and Japan Sea) could lead to the discovery of new porphyry districts in greenfields environments.

- The distribution and characteristics of volcano-sedimentary rocks within the Namosi district reveal that the Namosi Cu-Au(-Mo) porphyry deposits were emplaced into the submarine flank of an emerging volcanic seamount. Exploration, alteration and fluid flow models for the Namosi district need to account for this geological setting and be open to a wide range of deposit styles and variability (e.g., shallow marine hydrothermal vents, skarn, porphyry and epithermal). More generally, this study highlights the possible juxtaposition in space and time of calc-alkalic porphyry Cu districts (e.g., Namosi district) with alkalic porphyry-epithermal Au districts (e.g., Tavua Goldfield) and shallow subaqueous VMS deposits (e.g., Wainivesi and Wainaleka). Exploration models for more ancient island arc porphyry belts (e.g., Stikine and Quesnel, British Columbia; Macquarie Arc, New South Wales) need to incorporate the possibility of such juxtapositions.

- Within the Waivaka Corridor, identifying sets of secondary faults (e.g., Hematite and Kaolinite shears at Wainaulo) can be used to predict the presence of deep basement faults within the Wainimala Group that localized porphyry-related mineralization at depth.

- At Wainaulo, simple field-based mineralogical and textural indicators and mobile hyperspectral analysis can be used to deconstruct the superimposed porphyry-hydrothermal signatures. The zonation from proximal albite – biotite to medial albite – actinolite to distal albite – chlorite – epidote mineral assemblages associated with the early diorite (EMD1) and low Au and moderate Cu grades can be used to vector into the early ore system. The increasing abundance of K-feldspar, which occurs as vein halos to epidote – sulfide veins, can be used to vector towards the high-grade Cu-Au ore associated with the quartz diorite complex (EMQD and IMQD). The K-feldspar within the vein halos is spatially associated with phengite and phengitic-illite, which are readily detected using hyperspectral analysis. Mapping the occurrence of phyllosilicate minerals with a phengitic composition may lead to the discovery of new high-grade ore zones at Wainaulo.

- Systematic sulfur isotopic determinations of paragenetically constrained sulfides and sulfates can be used as a vector to ore at Wainaulo-like deposits within the Waivaka Corridor (e.g., Holliday and Cooke, 2007; Wilson et al., 2007; Figs. 6.2 and 6.3). At Wainaulo $\delta^{34}S_{sulfide}$ values occurring within and above the porphyry intrusions are > +1.0 ‰ and $\delta^{34}S_{sulfate}$ values are > +11.5 ‰; whereas, $\delta^{34}S_{sulfide}$ values on the deposit periphery are < +1.0 ‰ and $\delta^{34}S_{sulfate}$ values are < +11.5 ‰. This zonation pattern, from positive $\delta^{34}S_{sulfide}$ values in the deposit core to more negative distal values, is similar to several other economic porphyry deposits (e.g., Bingham, USA: Field, 1966; North Parkes, Australia: Heithersay and Walshe, 1995; and Dinkidi, Philippines: Wolfe and Cooke, 2011).

## 7.4 Contributions to the porphyry district model

This study has improved upon the porphyry district model in the following ways:

- Several workers have previously related low-angle subduction with the occurrence of porphyry copper deposits (e.g., Kerrich et al., 2000; Cooke et al., 2005; Rinne, 2015). This thesis proposes a new tectono-metallogenic model that furthers this association and suggests that the Namosi district porphyry deposits are linked with a low-angle subduction compo-

nent that was active in the Fiji area during the Late Miocene to Early Pliocene. This model also demonstrates the importance of subduction zone geometry in generating incongruent deposit styles and geochemical signatures (e.g., calc-alkalic Namosi porphyry district and alkalic Emperor porphyry-low sulfidation Au district) within a close spatial arrangement.

- It is a common perception that porphyry deposits form beneath active stratovolcanos. However, recent studies have shown that porphyry formation can occur in a variety of geological settings (e.g., marine volcano-sedimentary basins; Harris et al., 2014). The Namosi district volcanic and plutonic rocks were emplaced in a submarine, purely oceanic arc environment and are probably associated with a single Late Miocene andesitic seamount. The lithofacies characteristics of the rocks in the vicinity of the Namosi porphyry deposits are consistent with formation within a few kilometers of a submarine dome complex. This outcome furthers the notion that a stratovolcano is not a necessary geological environment for porphyry ore formation.

- The combination of new whole-rock geochemistry and high-resolution geochronology provides an internally consistent story of a younging mineralizing porphyry system becoming more differentiated in the sequence from Wainaulo to Waisoi West to Waisoi East over a period of ~ 400 ky. These findings suggest that only a brief period in geological time is required to form a significant Cu-Au(-Mo) district, and that timescales of several My are not required to form high Sr/Y magmas with large mineralized systems (cf. Bellver-Baca and Chiaradia, 2015).

- This study highlights the importance of mantle-derived magmatic fluids in the development of porphyry copper districts that formed in a submarine environment. Other hydrothermal systems with a submarine association have been shown to have minimal seawater fluid input (e.g., Pueblo Veijo, Dominican Republic: Venneman et al., 1993; White Island, New Zealand: Hedenquist et al., 1993 and Simmons et al., 2006). This study also provides evidence for significant seawater involvement in the Namosi hydrothermal system, which may explain the abundance of albite in the alteration mineral assemblages.

## 7.5 Recommendations for future work

In order to better constrain the genetic model for porphyry mineralization throughout the Namosi district, additional studies further to the work conducted in this thesis should be considered:

- A geochronological investigation that includes the peripheral prospects would better constrain the regional evolution of the Namosi district. Most of the regional geochronology is based on whole-rock and hornblende K–Ar analyses as well as LA-ICP-MS zircon U–Pb age dates; both are problematic for reliable age dating in the Namosi district. K–Ar age determinations in many cases are likely to have been disturbed by later magmatic-hydrothermal events. The very low absolute concentrations of U and Pb within the Namosi district igneous rocks (i.e., zircon with < 80 ppm U; whole-rock with < 3 ppm Pb), precludes the possibility of reliable age determinations using laser-ablation methods. For example, the errors on most LA-ICP-MS U–Pb age dates determined as part of this study span the entire productive evolution of the Namosi district. ID-TIMS U–Pb zircon dating and Re–Os molybdenite dating methods are essential to overcome these aforementioned issues.

- A systematic and detailed study of the district-scale and deposit-scale structures should be undertaken to better understand the stress regimes that localized porphyry emplacement and related mineralization. It has been established that lineament orientations are consistent with bedrock fracture orientations in SE Viti Levu (e.g., Rahiman and Pettinga, 2008), therefore, an in-depth study using side-looking airborne radar (SLAR), digital terrain modeling, and magnetic and vertical aerial photography of Namosi district lineaments would help fill the gaps inherent in a field-based structural study as a result of poor surface exposure in the Namosi district area.

- To compliment the structural study, (U-Th)/He thermochronometry of rocks in the host sequence and mineralized intrusions, along with depth of emplacement estimates based on pressure-depth curves derived from fluid inclusion work, could help constrain the ex-

humation history as well as provide information to interpret the sense and magnitude of the vertical component of displacement in the district-scale faults.

- A regional study aimed at distinguishing between greenschist facies metamorphism and chlorite – albite – actinolite ± epidote hydrothermal alteration in the Wainimala Group rocks would help in determining the footprint of the Waisoi deposits and can be applied as a vector to ore (e.g., mineral chemistry of chlorite and epidote; Cooke et al., 2014; Wilkinson et al., 2015).

- Further $\delta^{18}O$ and $\delta D$ analyses on main-stage alteration minerals (e.g., biotite, muscovite chlorite and actinolite) at the Waisoi deposits and Wainaulo would improve constraints on the various types of hydrothermal fluids involved in alteration of the rocks and ore formation, and on the amount of mixing that occurred between the different fluids.

# REFERENCES

Ahmad, M., and Walshe, J.L., 1990, Wall-rock alteration at the Emperor gold-silver telluride deposit. Fiji: Australian Journal of Earth Sciences, v. 37, p. 189–199.

Ahmad, M., Solomon, M., and Walshe, J.L., 1987a, Mineralogical and geochemical studies of the Emperor gold telluride deposit, Fiji: Economic Geology, v. 82, p. 345–370.

Ahmad, M., Solomon, M., and Walshe, J.L., 1987b, The formation of the quartz-gold-telluride veins of the Emperor Mine, Fiji: Australasian Institute of Mining and Metallurgy, Pacific Rim Congress '87, Australia, Proceedings, p. 1–4.

Anderson, W.B., and Eaton, P.C., 1990, Gold mineralization at the Emperor mine, Vatukoula, Fiji: Journal of Geochemical Exploration, v. 36, p. 267–296.

Anderson, W.B., Antonio, M., Davis, B., Jones, G.F.P., Setterfield, T.N., and Tua, P., 1987, TheEmperor epithermal gold deposit, Vatukoula, Fiji: Australasian Institute of Mining and Metallurgy, Pacific Rim Congress '87, Australia, Proceedings, p. 9–12.

Arif, J., and Baker, T., 2004, Gold paragenesis and chemistry at Batu Hijau, Indoneisa: Implications for gold-rich porphyry copper deposits: Mineralium Deposita, v. 39, p. 523–535.

Auzende, J.-M., Pelletier, B., and Eissen, J.-P., 1995, The North Fiji Basin: geology, structure, and geodynamic evolution, *in* Taylor, B., ed., Back-arc basins: Tectonics and magmatism: New York, Plenum Press, p. 139–175.

Babcock, R.C., Jr., Ballantyne, G.H., and Phillips, C.H., 1995, Summary of the geology of the Bingham district, Utah, *in* Pierce, F.W., and Bolm, J.G., eds., Porphyry copper deposits of the American Cordillera: Tucson, The Arizona Geological Society Digest, v. 20, p. 316–335.

Bach, W., Roberts, S., and Binns, R.A., 2005, Data report: Chemical and isotopic (S, Sr) composition of anhydrite from ODP Leg 193, PACMANUS hydrothermal system, Manus Basin, Papua New Guinea: Proceedings of the Ocean Drilling Program, Scientific Results 193, p. 1–23.

Bailey, E.H., and Stevens, R.E., 1960, Selective staining of K-feldspar and plagioclase on rock slabs and thin sections: The American Mineralogist, v. 45, p. 1020–1025.

Ballard, J.R., Palin, J.M., Williams, I.S., Campbell, I.H., and Faunes, A., 2001, Two ages of porphyry intrusion resolved for the super-giant Chuquicamata copper deposit of northern Chile by ELA-ICP-MS and SHRIMP: Geology, v. 29, p. 383–386.

Band, R.B., 1967a, Geology of Korolevu Bay area, Viti Levu - Sheet 17, 1:50 000 geological series, Geological Survey of Fiji.

Band, R.B., 1967b, Geology of Navua River area, Viti Levu - Sheet 18, 1:50 000 geological series, Geological Survey of Fiji.

Band, R.B., 1967c, Geology of Mau area, Viti Levu - Sheet 19, 1:50 000 geological series, Geological Survey of Fiji.

Band, R.S., 1968, Geology of southern Viti Levu and Mbengga: Fiji Geological Survey Bulletin 15, 49 p.

Battles, D.A., and Barton, M.D., 1995, Arc-related sodic hydrothermal alteration in the western United States: Geology, v. 23, p. 913–916.

Begg, G., 1996, Genesis of the Emperor gold deposit, Fiji: Unpublished PhD thesis, Clayton, Australia, Monash University, 466 p.

Begg, G., and Gray, D.R., 2002, Arc dynamics and tectonic history of Fiji based on stress and kinematic analysis of dikes and faults of the Tavua Volcano, Viti Levu Island, Fiji: Tectonics, v. 21, p. 1–14.

Blichert-Toft, J., and Albarède, F., 1997, The Lu-Hf isotope geochemistry of chondrites and the evolution of the mantle-crust system: Earth and Planetary Science Letters, v. 148, p. 243–258.

Braxton, D., and Mathur, R., 2011, Exploration applications of copper isotopes in the supergene environment: A case study of the Bayugo porphyry copper-gold deposit, southern Philippines: Economic Geology, v. 106, p. 1447–1463.

Braxton, D.P., 2007, Boyongan and Bayugo porphyry copper gold deposits NE Mindanao, Philippines: Geology, geochemistry and tectonic evolution: Unpublished PhD thesis, Hobart, Australia, University of Tasmania, 277 p.

Brudzinski, M.R., and Chen, W.-P., 2003, A petrologic anomaly accompanying outboard earthquakes beneath Fiji-Tonga: corresponding evidence from broadband P and S waveforms: Journal of Geophysical Research, v. 108, 2299.

Bruns, T.R., Vedder, J.G., and Culotta, R.C., 1989, Structure and tectonics along the Kilinailau Trench, Bougainville -Buka island region, Papua New Guinea, *in* Vedder, J.G., and Bruns, T.R., eds., Geology and offshore resources of Pacific island arcs – Solomon Islands and Bougainville – PNG regions: Circum-Pacific Council for Energy and Mineral Resources, Houston, USA, Circum-Pacific Council for Energy and Mineral Resources Earth Science Series 12, p. 94–123.

Bull, K.F., and McPhie, J., 2007, Fiamme textures in volcanic successions: Flaming issues of definition and interpretation: Journal of Volcanology and Geothermal Research, v. 164, p. 205–216.

Burdekin Pacific Limited, 2005, Mineral resources statement Mount Kasi (http://www.asx.com.au/asxpdf/20050826/pdf/3s1y67trxxqnk.pdf).

Calmant, S., Lebellegard, P., Taylor, F., Bevis, M., Maillard, D., Recy, J., and Bonneau, J., 1995, Geodetic measurements of convergence across the New-Hebrides subduction zone: Geophysical Research Letters, v. 22, p. 2573–2576.

Calmant, S., Pelletier, B., Lebellegard, P., Bevis, M., Taylor, F.W., and Phillips, D.A., 2003, New insights on the tectonics along the New Hebrides subduction zone based on GPS results: Journal of Geophysical Research, v. 108, 2319.

Carney, J.N., and Macfarlane, A., 1978, Lower to middle Miocene sediments on Maewo, New Hebrides, and their relevance to the development of the Outer Melanesian arc system: Australian Society of Exploration Geophysicists Bulletin 9, p. 123–130.

Cas, R.A.F., and Wright, J.V., 1987, Volcanic successions: Modern and ancient: A geological approach to processes, products and successions: London, Allen & Unwin, 528 p.

Catchpole, H., Kouzmanov, K., Bendezú, A., Ovtcharova, M., Spikings, R., Stein, H., and Fontboté, L., 2015, Timing of porphyry (Cu-Mo) and base metal (Zn-Pb-Ag-Cu) mineralisation in a magmatic-hydrothermal system—Morococha district, Peru: Mineralium Deposita, v. 50, p. 895–922.

Chacko, T., Cole, L.R., and Horita, D.R., 1999, A new technique for determining equilibrium hydrogen isotope fractionation factors using the ion microprobe: application to the epidote-water system: Geochimica et Cosmochimica Acta, v. 63, p. 1–10.

Chang, Z., and Meinert, L.D., 2008, The Empire Cu-Zn mine, Idaho: Exploration implications of unusual skarn features related to high fluorine activity: Economic Geology, v. 103, p. 909–938.

Chávez, W.X., Jr., 2000, Supergene oxidation of copper deposits: Zoning and distribution of copper oxide minerals: Society of Economic Geologists Newsletter 41, p. 10–21.

Chen, W., and Brudzinski, M.R., 2001, Evidence for a large-scale remnant of subducted lithosphere beneath Fiji: Science, v. 292, p. 2475–2479.

Chiaradia, M., 2009, Adakite-like magmas from fractional crystallization and melting–assimilation of mafic lower crust (Eocene Macuchi arc, Western Cordillera, Ecuador): Chemical Geology, v. 265, p. 468–487.

Chiaradia, M., Müntener, O., Beate, B., and Fontignie, D., 2009, Adakite-like volcanism of Ecuador: lower crust magmatic evolution and recycling: Contributions to Mineralogy and Petrology, v. 158, p. 563–588.

Chiaradia, M., Schaltegger, U., Spikings, R., Wotzlaw, J.-F., and Ovtcharova, M., 2013, How accurately can we date the duration of magmatic-hydrothermal events in porphyry systems?—An invited paper: Economic Geology, v. 108, p. 565–584.

Chiba, H., Kusakabe, M., Matsuo, S., Hirano, S., and Somiya, S., 1981, Oxygen isotope fractionation factors between anhydrite and water from 100 to 550 °C: Earth and Planetary Science Letters, v. 53, p.55–62.

Chiba, H., Uchiyama, N., and Teagle, D.A.H., 1998, Stable isotope study of anhydrite and sulfide minerals at the TAG hydrothermal mound, Mid-Atlantic Ridge, 26°N: Ocean Drilling Program Scientific Results, Proceedings, v. 158, p. 85–90.

Chivas, A.R., 1978, Porphyry copper mineralization at the Koloula igneous complex, Guadalcanal, Solomon Islands: Economic Geology, v. 73, p. 645–677.

Chivas, A.R., O'Neil, J.R., and Katchan, G., 1984, Uplift and submarine formation of some Melanesian porphyry copper deposits: stable isotope evidence: Earth and Planetary Science Letters, v. 68, p. 326–334.

Clague, D.A., and Dalrymple, G.B., 1989, Tectonics, geochronology and origin of the Hawaii-Emperor Chain, *in* Winterer, E.L., Hussong, D.M., and Decker, R.W., eds., The geology of North America - The eastern Pacific and Hawaii: Boulder, Geological Society of America, v. N, p. 188–217.

Clark, A.H., Farrar, E., Kontak, D.J., Langridge, R.J., Arenas F., M.J., France, L.J., McBride, S.L., Woodman, P.L., Wasteneys, H.A., Sandeman, H.A., and Archibald, D.A., 1990, Geologic and geochronologic constraints on the metallogenic evolution of the Andes of southeastern Peru: Economic Geology, v. 85, p. 1520–1583.

Cole, J.W., Graham, I.J., and Gibson, I.L., 1990, Magmatic evolution of Late Cenozoic volcanic rocks of the Lau Ridge, Fiji: Contributions to Mineralogy and Petrology, v. 104, p. 540–554.

Coleman, P.J., 1997, Australia and the Melanesian arcs: a review of tectonic settings: AGSO Journal of Australian Geology and Geophysics, v. 17, p. 113–125.

Coleman, P.J., and Packham, G.H., 1976, The Melanesian Borderland and Indian-Pacific plate boundary: Earth Science Reviews, v. 12, p. 197–263.

Colley, H., and Flint, D.J., 1995, Metallic mineral deposits of Fiji: Government of Fiji Mineral Resources Department Memoir 4, 196 p.

Colley, H., and Greenbaum, D., 1980, The Mineral Deposits and Metallogenesis of the Fiji Platform: Economic Geology, v. 75, p. 807–809.

Collot, J.Y., Lallemand, S., Pelletier, B., Bissen, J.-P., Glaçon, G., Fisher, M.A., Green, H.G., Boulin, J., Daniel, J., and Monzier, M., 1992, Geology of the d'Entrecasteaux – New Hebrides arc collision zone: results from a deep submersible survey: Tectonophysics, v. 212, p. 213–241.

Conder, J.A., and Wiens, D.A., 2006, Seismic structure beneath the Tonga arc and Lau back-arc basin determined from joint Vp, Vp/Vs tomography: Geochemistry, Geophysics, Geosystems, v. 7, Q03018.

Cooke, D.R., and Bloom, M.S., 1990, Epithermal and subjacent porphyry mineralization, Acupan, Baguio district, Philippines: A fluid-inclusion and paragenetic study: Journal of Geochemical Exploration, v. 35, p. 297–340.

Cooke, D.R., Hollings, P., and Walshe, J.L., 2005, Giant porphyry deposits: Characteristics, distribution and tectonic controls: Economic Geology, v. 100, p. 801–818.

Cooke, D.R., Wilson, A.J., House, M.J., Wolfe R.C., Walshe, J.L., Lickfold, V., and Crawford, A.J., 2007, Alkalic porphyry Au-Cu and associated mineral deposits of the Ordovician to Early Silurian Macquarie arc, New South Wales: Australian Journal of Earth Sciences, v. 54, p. 445–463.

Cooke, D.R., Deyell, C.L., Waters, P.J., Gonzales, R.I., and Zaw, K., 2011, Evidence for magmatic-hydrothermal fluids and ore-forming processes in epithermal and porphyry deposits of the Baguio district, Philippines: Economic Geology, v. 106, p. 1399–1424.

Cooke, D.R., Baker, M., Hollings, P., Sweet, G., Chang, Z., Danyushevsky, L., Gilbert, S., Zhou, T., White, N., Gemmell, J.B., and Inglis, S., 2014, New advances in detecting the distal geochemical footprints of porphyry systems— epidote mineral chemistry as a tool for vectoring and fertility assessments, *in* Kelley, K.D., and Golden, H.C., eds., Building Exploration Capability for the 21st Century: Colorado, Colt Print Services, p. 127–152.

Cooper, P.A., and Kroenke, L.W., 1994, Deep seismicity in the North Fiji Basin, *in* Kroenke, L.W., and Eade, J.V., eds., Basin formation, ridge crest processes, and metallogenesis in the North Fiji Basin: Houston, Circum-Pacific Council for Energy and Mineral Resources, Circum-Pacific Council for Energy and Mineral Resources Earth Science Series 15, p. 33–39.

Cox, M.E., and Hulston, J.R., 1980, Stable isotope study of thermal and other waters in Fiji: New Zealand Journal of Science, v. 23, p. 237–249.

Crawford, A.J., 2011, Lithogeochemical discrimination of Cu-Au porphyry deposit-hosting igneous rocks suites, and application to the Namosi deposit, Fiji: Newcrest Mining Ltd. report (unpublished), 108 p.

Crawford, A.J., and Verbeeten, A.C., 2000, Adakite-high Nb basalt association, Kadavu-Hunter Ridge, SW Pacific: hot subduction and slab edge effects: State of the Arc Conference, Ruapehu, New Zealand, p. 39–40.

Crawford, A.J., Meffre, S., and Symonds, P.A., 2003, 120-0 Ma tectonic evolution of the southwest pacific and analogous geological evolution of the 600 to 220 Ma Tasman Fold Belt System. Geological Society of Australia Special Publication 22, p. 377–397.

Crawford, A.J., Meffre, S., Squire, R.J., Barron, L.M., and Falloon, T.J., 2007, Middle and Late Ordovician magmatic evolution of the Macquarie arc, Lachlan orogen, New South Wales: Australian Journal of Earth Sciences, v. 52, p. 181–214.

Cross, W., Iddings, J.P., Persson, L.V., and Washington, H.S., 1906, The texture of igneous rocks: The Journal of Geology, v. 14, p. 692–707.

Crowley, J.L., Schoene, B., and Bowring, S.A., 2007, U-Pb dating of zircon in the Bishop Tuff at the millennial scale: Geology, v. 35, p. 1123–1126.

Danyushevsky, L.V., Falloon, T.J., Crawford, A.J., Tetroeva, S.A., Leslie, R.L., and Verbeeten, A., 2008, High-Mg adakites from Kadavu Island Group, Fiji, southwest Pacific: Evidence for the mantle origin of adakite parental melts: Geology, v. 36, p. 499–502.

Davey, F.J., 1982, The structure of the South Fiji Basin: Tectonophysics, v. 87, p. 185–241.

Davies, A.G.S., Cooke, D.R., Gemmell, J.B., van Leeuwen, T., Cesare, P., and Hartshorn, G., 2008, Hydrothermal breccias and veins at the Kelian gold mine, Kalimantan, Indonesia: Genesis of a large epithermal gold deposit: Economic Geology, v. 103, p. 717–757.

DeBievre, P., and Taylor, P.D.P., 1993, Table of the isotopic composition of the elements: International Journal of Mass Spectrometry and Ion Processes, v. 123, p. 149.

Deckart, K., Clark, A.H., Cuadra, P., and Fanning, M., 2013, Refinement of the time-space evolution of the giant Mio-Pliocene Río Blanco-Los Bronces porphyry Cu–Mo cluster, Central Chile: new U–Pb (SHRIMP II) and Re–Os geochronology and $^{40}Ar/^{39}Ar$ thermochronology data: Mineralium Deposita, v. 48, p. 57–79.

Deckart, K., Silva, W., Spröhnle, C., and Vela, I., 2014, Timing and duration of hydrothermal activity at the Los Bronces porphyry cluster: an update: Mineralium Deposita, v. 49, p . 535–546.

Defant, M.J., and Drummond, M.S., 1990, Derivation of some modern arc magmas by melting of young subducted lithosphere: Nature, v. 347, p. 662–665.

Defant, M.J., and Drummond, M.S., 1993, Mount St. Helens: Potential example of the partial melting of the subducted lithosphere in a volcanic arc: Geology, v. 21, p. 547–550.

DePaolo, D.J., and Wasserburg, G.J., 1979, Petrogenetic mixing models and Nd-Sr isotopic patterns: Geochimica et Cosmochimica Acta, v. 43, p. 615–627.

Dilles, J.H., 1987, Petrology of the Yerington batholith, Nevada: Evidence for evolution of porphyry copper ore fluids: Economic Geology, v. 82, p. 1750–1789.

Dilles, J.H., and Einaudi, M.T., 1992, Wall-rock alteration and hydrothermal flow paths about the Ann-Mason porphyry copper deposit, Nevada—a 6-km vertical reconstruction: Economic Geology, v. 87, p. 1963–2001.

Dilles, J.H., and Proffett, J.M., 1995, Metallogenesis of the Yerington batholith, Nevada: Arizona Geological Society Digest 20, p. 306–315.

Dilles, J.H., Solomon, G.C., Taylor, H.P., and Einaudi, M.T., 1992, Oxygen and hydrogen isotope characteristics of hydrothermal alteration at the Ann-Mason porphyry copper deposit, Yerrington, Nevada: Economic Geology, v. 87, p. 44–63.

Dilles, J.H., Proffett, J.M., and Einaudi, M., 2000, Magmatic and hydrothermal features of the Yerington batholith with emphasis on the porphyry copper (Mo) deposit in the Ann-Mason area: Society of Economic Geologists Guidebook Series, v. 32, p. 67–89.

Dreher, S.T., Macpherson, C.G., Pearson, D.G., and Davidson, J.P., 2005, Re-Os isotope studies of Mindanao adakites: Implications for sources of metals and melts: Geology, v. 33, p. 957–960.

Dubois, J., Pascal, G., Barazangi, M., Isacks, B., and Oliver, J., 1973, Travel times of seismic waves between the New Hebrides and Fiji Islands: a zone of low velocity beneath the Fiji Plateau: Journal of Geophysical Research, v. 78, p. 3431–3436.

Eaton, P.C., and Setterfield, T.N., 1993, The relationship between epithermal and porphyry systems within the Tavua Caldera, Fiji: Economic Geology, v. 88, p. 1053–1083.

Egashira, S., 2009, Hydrothermal system of porphyry copper deposit at the Waivaka Corridor area, Namosi district, Viti Levu, Republic of the Fiji Islands: Unpublished MSc thesis, Fukuoka, Japan, Kyushu University, 54 p.

Einaudi, M.T., 1997, Mapping altered and mineralized rocks: An introduction to the Anaconda method: Stanford, CA, Stanford University.

Elliot, T., 1986, Siliclastic shorelines, *in* Reading, H.G., ed., Sedimentary Environments and Facies, 2nd ed.: Oxford, Blackwell Scientific Publications, p. 155–188.

Ellis, P.D., 1996, The geology and mineralisation of the Waisoi porphyry copper deposits, Namosi Province, Republic of Fiji: Unpublished MEconGeol thesis, Hobart, Australia, University of Tasmania, 219 p.

Ewart, A., 1982, The mineralogy and petrology of Tertiary-Recent orogenic volcanic rocks: with special reference to the andesitic-basaltic compositional range, *in* Thorpe, R.S., ed., Andesites: orogenic andesites and related rocks: New York, Wiley, p. 25–95.

Ewart, A., and Bryan, W.B., 1972, Petrography and Geochemistry of the Igneous Rocks from Eua, Tongan Islands: Geological Society of America Bulletin, v. 83, p. 3281–3298.

Ewart, A., Collerson, K.D., Regelous, M., Wendt, J.I., and Niu, Y., 1998, Geochemical evolution within the Tonga–Kermadec–Lau arc–back-arc systems: the role of varying mantle wedge composition in space and time: Journal of Petrology, v. 39, p. 331–368.

Falvey, D.A., 1978, Analysis of palaeomagnetic data from the New Hebrides: Australian Society of Exploration Geophysicists Bulletin, v. 9, p. 117–123.

Faure, G., 1986, Principles of isotope geology, 2nd ed.: Wiley, New York, USA, 589 p.

Field, C.W., 1966, Sulfur isotope abundance data, Bingham District, Utah: Economic Geology, v. 61, p. 850–871.

Field, C.W., Zhang, L., Dilles, J.H., Rye, R.O., and Reed, M.H., 2005, Sulfur and oxygen isotopic record in sulfate and sulfide minerals of early, deep, pre-Main stage porphyry Cu-Mo and late, shallow Main stage base-metal mineral deposits, Butte district, Montana: Chemical Geology, v. 215, p. 61–93.

Field, C.W., and Gustafson, L.B., 1976, Sulfur isotopes in the porphyry copper deposits at El Salvador: Economic Geology, v. 71, p. 1533–1548.

Field, C.W., and Fifarek, R.H., 1985, Light stable-isotope systematics in the epithermal environment: Reviews in Economic Geology, v. 2, p. 99–128.

Forsythe, D.L., 1971, Vertical zoning of gold-silver tellurides in the Emperor Gold Mine, Fiji: Proceedings of the Australian Institute of Mining and Metallurgy, v. 240, p. 25–31.

Gabriel, A. and Cox, E.P., 1929, A staining method for the quantitative determination of certain rock minerals: The American Mineralogist, v. 14, p. 290–292.

Garwin, S., 2000, The setting, geometry and timing of intrusion-related hydrothermal systems in the vicinity of the Batu Hijau porphyry copper-gold deposit, Sumbawa, Indonesia: Unpublished PhD thesis, Perth, Australia, University of Western Australia, 320 p.

Garwin, S., 2002, The geological setting of intrusion-related hydrothermal systems near the Batu Hijau porphyry copper-gold deposit, Sumbawa, Indonesia: Society of Economic Geologists Special Publication 9, p. 333–366.

Gerstenberger, H., and Haase, G., 1997, A highly effective emitter substance for mass spectrometric Pb isotope ratio determinations: Chemical Geology, v. 136, p. 309–312.

Gifkins, C.C., Herrmann, W., and Large, R., 2005, Altered volcanic rocks: A guide to description and interpretation: CODES, University of Tasmania, Hobart, Australia, 250 p.

Giggenbach, W.F., 1992, Isotopic shifts in waters from geothermal and volcanic systems along convergent plate boundaries and their origin: Earth and Planetary Science Letters, v. 133, p. 495–510.

Gill, J.B., 1970, Geochemistry of Viti Levu, Fiji, and its evolution as an island arc: Contributions to Mineralogy and Petrology, v. 27, p. 179–203.

Gill, J.B., 1974, Role of underthrust oceanic crust in the genesis of a Fijian Calc-alkaline suite: Contributions to Mineralogy and Petrology, v. 32, p. 29–45.

Gill, J.B., 1976, From island arc to oceanic islands: Fiji, southwestern Pacific: Geology, v. 4, p. 123–126.

Gill, J.B., 1981, Orogenic andesites and plate tectonics: Springer-Verlag, Berlin, Germany, 390 p.

Gill, J.B., 1984, Sr-Pb-Nd isotopic evidence that both MORB and OIB sources contribute to oceanic island arc magma in Fiji: Earth and Planetary Science Letters, v. 68, p. 443–458.

Gill, J.B., 1987, Early geochemical evolution of an oceanic island arc and back-arc: Fiji and the South Fiji Basin: Journal of Geology, v. 95, p. 589–615.

Gill, J.B., and Compston, W., 1973, Strontium isotopes in island arc volcanic rocks, in Coleman, P., ed., The Western Pacific-island arcs, marginal seas, geochemistry: Perth, Western Australia University Press, p. 483–496.

Gill, J.B., and McDougall, I., 1973, Biostratigraphic and geological significance of Miocene-Pliocene volcanism in Fiji: Nature, v. 241, p. 176–180.

Gill, J.B., and Stork, A.L., 1979, Miocene low-K dacites and trondhjemites of Fiji, *in* Barker, P., ed., Trondhjemites, dacites, and related rocks: Amsterdam, Elsevier, p. 629–649.

Gill, J.B., and Whelan, P., 1989a, Early rifting of an oceanic island arc (Fiji) produced shoshonitic to tholeiitic basalts: Journal of Geophysical Research, v. 94, p. 4561–4578.

Gill, J.B., and Whelan, P., 1989b, Postsubduction ocean island alkali basalts in Fiji: Journal of Geophysical Research, v. 94, p. 4579–4588.

Gill, J.B., Stork, A.L., and Whelan, P.W., 1984, Volcanism accompanying back-arc basin development in the Southwest Pacific: Tectonophysics. v. 102, p. 207–224.

Goolaerts, A., Mattielli, N., de Jong, J., Weis, D., and Scoates, J.S., 2004, Hf and Lu reference values for the zircon standard 91500 by MCICP-MS: Chemical Geology, v. 206, p. 1–9.

Govers, R., and Wortel, M.J.R., 2005, Lithosphere tearing at STEP faults: response to edges of subduction zones: Earth and Planetary Science Letters, v. 236, p. 505–523.

Green, T. H., 1972, Crystallization of calc-alkaline andesite under controlled high-pressure hydrous conditions: Contributions to Mineralogy and Petrology, v. 34, p. 150–166.

Green, T.H., and Ringwood, A.E., 1968, Genesis of the calc-alkaline igneous rock suite: Contributions to Mineralogy and Petrology, v. 18, p. 105–162.

Greene, H.G., and Collot, J.Y., 1994, Ridge – arc collision: Timing and deformation determined by Leg 134 drilling, central New Hebrides island arc, *in* Greene, H.G., Collot, J.Y., et al. eds., Proceedings of the Ocean Drilling Program, Scientific Results: College Station, Ocean Drilling Program, v. 134, p. 2841–2853.

Griffin, W.L., Belousova, E., Shee, S.R., Pearson, N.J., and O'Reilly, S., 2004, Archean crustal evolution in the northern Yilgarn Craton: U-Pb and Hf isotope evidence from detrital zircons: Precambrian Research, v. 131, p. 231–282.

Griffin, W.L., Pearson, N.J., Belousova, E.A., and Saeed, A., 2006, Comment: Hf-isotope heterogeneity in zircon 91500: Chemical Geology, v. 233, p. 358–363.

Gustafson, L., and Hunt, J., 1975, The porphyry copper deposit at El Salvador, Chile: Economic Geology, v. 70, p. 857–912.

Hall, R., and Spakman, W., 2002, Subducted slabs beneath the eastern Indonesia-Tonga region: insights from tomography: Earth and Planetary Science Letters, v. 201, p. 321–336.

Hallock, P., and Glenn, E.C., 1986, Large foraminifera: A tool for paleoenvironment analysis of Cenozoic carbonate depositional facies: Palaios, v. 1, p. 55–64.

Hamburger, M.W., and Isacks, B.L., 1987, Deep earthquakes in the southwest Pacific: a tectonic interpretation: Journal of Geophysical Research, v. 92, p. 13841–13854.

Hamburger, M.W., and Isacks, B.L., 1988, Diffuse back-arc deformation in the southwestern Pacific: Nature, v. 332, p. 599–604.

Hamburger, M.W., Everingham, I.B., Isacks, B.L., and Barazangi, M., 1988, Active tectonism within the Fiji platform, southwest Pacific: Geology, v. 16, p. 237–241.

Hampton, M.A., 1972, The role of subaqueous debris flow in generating turbidity currents: Journal of Sedimentary Petrology, v. 42, p. 775–793.

Hanus, V., and Vanek, J., 1981, Plate tectonic interpretation of deep earthquakes between the Tonga-Lau and New Hebrides subduction zones: Tectonophysics, v. 75, p. T19–T28.

Hanus, V., and Vanek, J., 1983, Deep structure of the Vanuatu (New Hebrides) island arc: intermediate depth collision of subducted lithospheric plates: New Zealand Journal of Geology and Geophysics, v. 26, p. 133–154.

Harris, A., 2009a, Report on 101125 Fiji (NWS+NVD): Newcrest Mining Ltd. report (unpublished), 1 p.

Harris, A., 2009b, Petrographic descriptions of altered rock samples from the Waisoi porphyry Cu-Au deposit, Namosi, Fiji: Newcrest Mining Ltd. report (unpublished), 34 p.

Harris, A., 2009c, Waivaka (Wainaulo) alteration and vein paragenesis, Namosi, Republic of the Fiji Islands: Newcrest Mining Ltd. report (unpublished), 9 p.

Harris, A., Carey, R., Holliday, J., Ackerman, B., MacCorquodale, F., Orovan, E., and Cooke, D., 2015, Mineral footprints to porphyry Cu-Au deposits: enhanced ore deposit models using high-resolution VNIR-SWIR core logging: PACRIM 2015 Congress, Hong Kong, China, March 18–21, Australian Institute of Mining and Metallurgy.

Harris, A.C., Cooke, D.R., Blackwell, J.L., Fox, N., and Orovan, E.A., 2013, Volcanotectonic setting of world-class alkalic porphyry and epithermal Au ± Cu deposits of the southwest Pacific: Society of Economic Geologists Special Publication 17, p. 337–359.

Harris, A.C., and Golding, S.D., 2002, New evidence of magmatic-fluid-related phyllic alteration: Implications for genesis of porphyry Cu deposits: Geology, v. 30, p. 335–338.

Harris, C., Pronost, J.J.M., Ashwal, L.D., and Cawthorn, R.G., 2005, Oxygen and hydrogen isotope stratigraphy of the Rustenburg Layered Suite, Bushveld Complex: Constraints on crustal contamination: Journal of Petrology, v. 46, p. 579–601.

Hatcher, R., 1998, Relation of structures, alteration and mineralization at the Tuvatu Gold Prospect, Viti Levu, Fiji Islands: Unpublished BASc (Honours) thesis, Brisbane, Australia, Queensland University of Technology, 151 p.

Hathway, B., 1993, The Nadi Basin: Neogene strike-slip faulting and sedimentation in a fragmented arc, western Viti Levu, Fiji: Journal of the Geological Society of London, v. 150, p. 563–581.

Hathway, B., 1994, Sedimentation and volcanism in an Oligocene-Miocene intra-oceanic arc and fore-arc, southwestern Viti Levu, Fiji: Journal of the Geological Society of London, v. 151, p. 499–514.

Hathway, B., and Colley, H., 1994, Eocene to Miocene geology of southwest Viti Levu, Fiji, *in* Stevenson, A.J., Herzer, R.J., and Ballance, P.F., eds., Geology and submarine resources of the Tonga Lau-Fiji region: SOPAC Technical Bulletin 8, p. 153–169.

Hawkins, J.W., 1995, The geology of the Lau Basin, *in* Taylor, B. ed., Back-arc basins: Tectonics and magmatism: New York, Plenum Press, p. 63–137.

Hedenquist, J.W., and Richards, J.P., 1998, The influence of geochemical techniques on the development of genetic models for porphyry copper deposits: Reviews in Economic Geology, v. 10, p. 235–256.

Hedenquist, J.W., Simmons, S.F., Giggenbach, W.F., and Eldridge, C.S., 1993, White Island, New Zealand, volcanic-hydrothermal system represents the geochemical environment of high-sulphidation Cu and Au ore deposition: Geology, v. 21, p. 731–734.

Hergt, J.M., and Woodhead, J.D., 2007, A critical evaluation of recent models for Lau–Tonga arc–backarc basin magmatic evolution: Chemical Geology, v. 245, p. 9–44.

Hilde, T.W.C., Uyeda, S., and Kroenke, L., 1977, Evolution of the western Pacific and its margin: present state of plate tectonics: Tectonophysics, v. 38, p. 145–165.

Hildreth, S.C., and Hannah, J.L., 1996, Fluid inclusion and sulfur isotope studies of the Tintic mining district, Utah: Implications for targeting fluid sources: Economic Geology, v. 91, p. 1270–1281.

Hirst, J.A., 1965, Geology of east and north-east Viti Levu: Fiji Geological Survey Bulletin 12, 51 p.

Hirst, J.A., 1967, Geology of Nanduruloulou area, Viti Levu - Sheet 14, 1:50 000 geological series, Geological Survey of Fiji.

Hoefs, J., 2009, Stable isotope geochemistry, 6th ed.: Springer-Verlag, Berlin, Germany, 285 p.

Holliday, J.R., and Cooke, D.R., 2007, Advances in geological models and exploration methods for copper ± gold porphyry deposits: Proceedings of the Fifth Decennial International Confer-

ence on Mineral Exploration: Toronto, Canada, Decennial Mineral Exploration Conferences, p. 791–809.

Hollings, P., Cooke, D.R., and Clark, A., 2005, Regional geochemistry of Tertiary volcanic rocks in Central Chile: Implications for the geodynamic environment of giant porphyry copper and epithermal gold mineralization: Economic Geology, v. 100, p. 887–904.

Hollings, P., Wolfe, R., Cooke, D.R., and Waters, P., 2011, Geochemistry of Tertiary igneous rocks of northern Luzon, Philippines: Evidence for a back-arc setting for alkalic porphyry copper-gold deposits and a case for slab rollback?: Economic Geology, v. 106, p. 1257–1277.

Houghton, B.F., and Landis, C.A., 1989, Sedimentation and volcanism in a Permain arc-related basin, southern New Zealand: Bulletin of Volcanology, vol. 51, p. 433–450.

Houtz, R.E.,1960, Geology of the Singatoka area, Viti Levu - Sheet 16, 1:50 000 geological series, Geological Survey of Fiji.

Houtz, R.E.,1962, Geology of Keiyasi, Viti Levu - Sheet 11, 1:50 000 geological series, Geological Survey of Fiji.

Ibbotson, P., 1960, Geology of Suva, Viti Levu - Sheet 20, 1:50 000 geological series, Geological Survey of Fiji.

Idrus, A., Kolb, J., Meyer, F.M., Arif, J., Setyandhaka, D. and Kepli, S., 2009, A preliminary study on skarn-related calc-silicate rocks associated with the Batu Hijau porphyry copper-gold deposit, Sumbawa Island, Indonesia: Resource Geology, v. 59, p. 295–306.

Imai, A., Ohbuchi, Y., Tanaka, T., Morita, S., and Yasunaga, K., 2007, Characteristics of porphyry Cu mineralization at Waisoi (Namosi District), Viti Levu, Fiji: Resource Geology, v. 57, p. 374–385.

Inokuchi, H., Yaskawa, K., and Rodda., P., 1992, Clockwise and anticlockwise rotation of Viti Levu, Fiji – in relation to the tectonic development of the North and South Fiji Basin: Journal International, v. 110, p. 225–237.

International Seismological Centre, 2009, Global seismic data from 1964 – 2009: Bulletin of the International Seismological Centre,Thatcham, United Kingdom, www.isc.ac.uk/iscgem

Ito, E., White, W.M., and Gopel, C., 1987, The O, Sr, Nd, and Pb isotope geochemistry of MORB: Chemical Geology, v. 62, p. 157–176.

Jaffey, A.H., Flynn, K.F., Glendenin, L.E., Bentley, W.C., and Essling, A.M., 1971, Precision measurement of half-lives and specific activities of $^{235}U$ and $^{238}U$: Physical Review, v. C4, p. 1889–1906.

Jenner, G.A., Cawood, P.A., Rautenschlein, M., and White, W.M., 1987, Composition of back-arc basin volcanics, Valu Fa Ridge, Lau Basin: evidence for a slab-derived component in their mantle source: Journal of Volcanology and Geothermal Research, v. 32, p. 209–222.

Jensen, E.P., and Barton, M.D., 2000, Gold deposits related to alkaline magmatism: Reviews in Economic Geology, v. 13, p. 279–314.

Johanssen, G., 2011, Geological mapping of the Waivaka Corridor: Namosi Joint Venture (unpublished), 17 p.

John, D.A., Ayuso, R.A., Barton, M.D., Blakely, R.J., Bodnar, R.J., Dilles, J.H., Floyd, G., Graybeal, F.T., Mars, J.C., McPhee, D.K., Seal, R.R., Taylor, R.D., and Vikre, P.G., 2010, Porphyry copper deposit model, Chapter B of Mineral deposit models for resource assessment: US Geological Survey Scientific Investigations Report 2010-5070-B, 169 p.

Johnson, H., 1994, Structure and petroleum geology of the Bligh Water and Bua Waters Basins, Fiji, *in* Stevenson, A.J., Herzer, R.J., and Ballance, P.F., eds., Geology and submarine resources of the Tonga Lau-Fiji region: SOPAC Technical Bulletin 8, p. 171–184.

Johnson, H.D., and Baldwin, C.T., 1996, Shallow clastic seas, *in* Reading, H.G., ed., Sedimentary environments: Processes, facies and stratigraphy, 3rd ed.: Oxford, Wiley-Blackwell, 704 p.

Jones, S., Herrmann, W., and Gemmell, J.B., 2005, Short wavelength infrared spectral characteristics of the HW Horizon: Implications for exploration in the Myra Falls volcanic-hosted massive sulfide camp, Vancouver Island, British Columbia, Canada: Economic Geology, v. 100, p. 273–294.

Kano, K.I., 1989, Interactions between andesitic magma and poorly consolidated sediments: Examples in the Neogene Shirahama Group, South Izu, Japan: Journal of Volcanology and Geothermal Research, v. 37, p. 59–75.

Karlsson, H.R., and Clayton, R.N., 1990, Oxygen isotope fractionation between analcime and water: an experimental study: Geochimica et Cosmochimica Acta, v. 54, p. 1359–1368.

Kesler, S.E., Jones, L.M., and Walker, R.L., 1975, Intrusive rocks associated with porphyry copper mineralization in island arc areas: Economic Geology, v. 70, p. 515–526.

Kesler, S.E., Sutter, J.F., Issigonis, M.J., Jones, L.M., and Walker, R.L., 1977, Evolution of porphyry copper mineralization in an oceanic island arc; Panama: Economic Geology, v. 72, p. 1142–1153.

Kirkham, R.V., and Sinclair, W.D., 1988, Comb quartz layers in felsic intrusions and their relationship to porphyry deposits, *in* Taylor, R.P., and Strong, D.F., eds., Recent advances in the geology of granite-related mineral deposits: Canadian Institute of Mining and Metallurgy Special Volume 39, p. 50–71.

Koba, M., 1978, Distribution and environment of recent Cycloclypeus: Science Reports of the Tohoku University, Series 7, p. 283–311.

Kroenke, L.W., 1972, Geology of the Ontong Java Plateau: Unpublished report No. 72-5, Hawaii Institute of Geophysics, Hawaii, USA, 119 p.

Kroenke, L.W., 1984, Cenozoic tectonic development of the southwest Pacific: U.N. ESCAP, CCOP/SOPAC Technical Bulletin 6, p. 111–122.

Kwak, T.A.P., 1990, Geochemical and temperature controls on ore mineralization at the Emperor Gold Mine,Vatukoula, Fiji: Journal of Geochemical Exploration, v. 36, p. 297–337.

Landtwing, M.R., Furrer, C., Pettke, T., Guillong, M., and Heinrich, C.A., 2010, The Bingham Canyon porphyry Cu-Mo-Au deposit: III. Zoned copper-gold ore deposition by magmatic vapor expansion: Economic Geology, v. 105, p. 91–118.

Lang, J.R., Stanley, C.R., Thompson, J.F.H., and Dunne, K.P.E., 1995, Na-K-Ca magmatic hydrothermal alteration in alkali porphyry Cu-Au deposits, British Columbia, *in* Thompson, J.F.H., ed., Magmas, fluids and ore deposits: Mineralogical Association of Canada, Short Course v. 23, p. 339–366.

Lang, J.R., and Titley, S.R., 1998, Isotopic and geochemical characteristics of Laramide magmatic systems in Arizona and implications for the genesis of porphyry copper deposits: Economic Geology, v. 93, p. 138–170.

Large, R.R., Gemmell, J.B., Paulick, H., and Huston, D.L., 2001, The alteration box plot: A simple approach to understanding the relationship between alteration mineralogy and lithogeochemistry associated with volcanic-hosted massive sulfide deposits: Economic Geology, v. 96, p. 957–971.

Lechler, P.J., and Desilets, M.O., 1987, A review of the use of loss on ignition as a measurement of total volatiles in whole-rock analysis: Chemical Geology, v. 63, p. 341–344.

Leggo, M.D., 1977, Contrasting geochemical expressions of copper mineralization at Namosi, Fiji: Journal of Geochemical Exploration, v. 8, p. 431–456.

Le Maitre, R.W., 1989, A classification of igneous rocks and glossary of terms: recommendations of the International Union of Geological Sciences Subcommission on the Systematics of Igneous Rocks: Blackwell Scientific Publications, Oxford, United Kingdom, 253 p.

Leslie, R.A.J., 2004, Primitive shoshonites from Fiji: mineralogy, melt inclusions and geochemistry: Unpublished PhD thesis, Hobart, Australia, University of Tasmania, 333 p.

Lickfold, V., Cooke, D.R., Smith, S.G., and Ullrich, T.D., 2003, Endeavour copper-gold porphyry deposits, Northparkes, New South Wales: Intrusive history and fluid evolution: Economic Geology, v. 98, p. 1607–1636.

Lowell, J.D., and Guilbert, J.M., 1970, Lateral and vertical alteration-mineralization zoning in porphyry ore deposits: Economic Geology, v. 65 , p. 373–408.

Ludwig, K.R., 2003, ISOPLOT 3.0: A geochronological toolkit for Microsoft Excel, 855: Berkeley Geochronology Center Special Publication 4, 71 p.

Lund, K., Aleinikoff, J., Kunk, M., Unruh, D., Zeihen, G., Hodges, W., Du Bray, E., and O'Neill, J., 2002, SHRIMP U-Pb and $^{40}Ar/^{39}Ar$ age contrasts for relating plutonism and mineralization in the Boulder batholith region, Montana: Economic Geology, v. 97, p. 241–267.

Maicher, D., White, J.D.L., and Batiza, R., Sheet hyaloclastite: density-current deposits of quench and bubble-burst fragments from thin, glassy sheet lava flows, Seamount Six, Eastern Pacific Ocean: Marine Geology, v. 171, p. 75–94.

Malahoff, A., Hammond, S.R., Naughton, J.J., Keeling, D.L., and Richmond, R.N., 1982, Geophysical evidence for post-Miocene rotation of the island of Viti Levu, Fiji, and its relationship to the tectonic development of the North Fiji Basin: Earth and Planetary Science Letters, v. 57, p. 398–414.

Margolis, J., 1993, Geology and intrusion-related copper-gold mineralization, Sulphurets, British Columbia, Canada: Unpublished PhD thesis, Eugene, USA, University of Oregon, 289 p.

Markey, R., Stein, H., and Morgan, J., 1998, Highly precise Re-Os dating for molybdenite using alkaline fusion and NTIMS: Talanta, v. 45, p. 935–946.

Markey, R., Stein, H.J., Hannah, J.L., Zimmerman, A., Selby, D., and Creaser, R.A., 2007, Standardizing Re-Os geochronology: A new molybdenite Reference Material (Henderson, USA) and the stoichiometry of Os salts: Chemical Geology, v. 244, p. 74–87.

Marsh, T.M., Einaudi, M.T., and McWilliams, M., 1997, $^{40}Ar/^{39}Ar$ geochronology of the Cu-Au and Au-Ag mineralization in the Potrerillos District, Chile: Economic Geology, v. 92, p. 784–806.

Martin, A.K., 2013, Double-saloon-door tectonics in the North Fiji Basin: Earth and Planetary Science Letters, v. 374, p. 191–203.

Martin, A.K., 2014, Concave slab out board of the Tonga subduction zone caused by opposite toroidal flows under the North Fiji Basin: Tectonophysics, v. 622, p. 56–61.

Martin, H., 1986, Effect of steeper Archean geothermal gradient on geochemistry of subduction-zone magmas: Geology, v. 14, p. 753–756.

Maksaev, V., Munizaga, F., McWilliams, M., Fanning, M., Mathur, R., Ruiz, J., and Zentilli, M., 2004, New chronology for El Teniente, Chilean Andes, from U-Pb, $^{40}Ar/^{39}Ar$, Re-Os and fis-

sion-track dating: Implications for the evolution of a supergiant porphyry Cu-Mo deposit: Society of Economic Geologists Special Publication 11, p. 15–54.

Mattinson, J.M., 2005, Zircon U-Pb chemical abrasion ("CA-TIMS") method: Combined annealing and multi-step partial dissolution analysis for improved precision and accuracy of zircon ages: Chemical Geology, v. 220, p. 47–66.

McDougall, I., 1963, Potassium-argon ages of some rocks from Viti Levu, Fiji: Nature, v. 198, p. 677.

McMillan, W.J., and Panteleyev, A., 1988, Porphyry copper deposits, *in* Roberts, R.G., and Sheahan, P.A., eds., Ore deposits models: Geological Association of Canada, Geoscience Canada, Reprint Series 3, p. 45–59.

McPhie, J., 1995, A Pliocene shoaling basaltic seamount: Ba Volcanic Group at Rakiraki, Fiji: Journal of Volcanology and Geothermal Research, v. 64, p. 193–210.

McPhie, J., and Orth, K., 1999, Peperite, pumice and perlite in submarine volcanic successions: implications for VHMS mineralisation: Australasian Institute of Mining and Metallurgy, Pacific Rim Congress '99, Indonesia, Proceedings, p. 643–648.

McPhie, J., Doyle, M., and Allen, R., 1993, Volcanic textures: A guide to the interpretation of textures in volcanic rocks: CODES, University of Tasmania, Hobart, Tasmania, 198 p.

Meffre, S., and Crawford, A.J., 2001, Collision tectonics in the New Hebrides arc (Vanuatu): Island Arc, v. 10, p. 33–50.

Meinert, L.D., 1997, Application of skarn deposit zonation models to mineral exploration: Exploration and Mining Geology, v. 6, p. 185–208.

Micko, J. , 2010, The geology and genesis of the Central zone alkalic copper-gold porphyry deposit, Galore Creek district, northwestern British Columbia, Canada: Unpublished PhD thesis, Vancouver, Canada, University of British Columbia, 359 p.

Morita, S., Tanaka, T., Nagane, M., Makuuchi, A., Takahata, H., Furuno, M., Takahashi, T., Yasunaga, K., and Murakami, H., 2002, Copper exploration project of Namosi Area in the Republic of Fiji Islands: Shigen Chishitsu, v. 52, p. 19–35.

Mundil, R., Ludwig, K.R., Metcalfe, I., and Renne, P.R., 2004, Age and timing of the Permian mass extinctions: U-Pb dating of closed-system zircons: Science, v. 305, p. 1760–1763.

Musgrave, R.J., and Firth, J.V., 1999, Magnitude and timing of New Hebrides Arc rotation: paleomagnetic evidence from Nendo, Solomon Islands: Journal of Geophysical Research: Solid Earth, v. 104, p. 2841–2853.

Mutschler, F.E., Ludington, S.D., and Bookstrom, A.A., 1999, Giant porphyry-related metal camps of the world; a database: U.S. Geological Survey Open File Report 99-556 (http://pubs.usgs.gov/of/1999/of99-556/).

Nagasaki, A, and Enami, M., 1998, Sr-bearing zoisite and epidote in ultra-high pressure (UHP) metamorphic rocks from the Su-Lu province, eastern China: an important Sr reservoir under UHP conditions: American Mineralogist, v. 83, p. 240–247.

Neall, V.E., and Trewick, S.A., 2008, The age and origin of the Pacific islands: a geological overview: Philosophical Transactions of the Royal Society B: Biological Sciences, v. 363, p. 3293–3308.

Newcrest Mining Ltd., 2010,Wainaulo mineral resource, June 2010: Newcrest Mining Ltd. report (unpublished), 93 p.

Newcrest Mining Ltd., 2013, Newcrest Mining Limited annual report 2013 (http://www.newcrest.com.au/media/annual_reports/FINAL_AR_2013_72dpi_web.pdf).

Newcrest Mining Ltd., 2015, Explanatory notes: Newcrest Mining (http://www.newcrest.com.au/media/resource_reserves/2015/Newcrest_-_Explanatory_Notes_-_December_2014_Resources_and_Reserves_Statement.pdf).

Nittetsu Mining Co., Ltd., 2007, Appendix 16: Data of Fluid Inclusion Study: Nittetsu Mining Co., Ltd. Excel spreadsheet (unpublished).

Nunn, P., 1998, Pacific Island Landscapes: Landscape and Geological Development of Southwest Pacific Islands, Especially Fiji, Samoa and Tonga: Suva, Fiji, Institute of Pacific Studies, University of the South Pacific, 318 p.

Ohmoto, H., and Goldhaber, M.B., 1997, Sulfur and carbon isotopes, *in* Barnes H.L., ed., Geochemistry of hydrothermal ore deposits, 3rd ed.: New York, Wiley, p. 517–612.

Ohmoto, H., and Lasaga, A.C. , 1982, Kinetics of reactions between aqueous sulfates and sulfides in hydrothermal systems: Geochimica et Cosmochimica Acta, v. 46, p. 1727–1745.

Ohmoto, H., and Rye, R.O., 1979, Isotopes of sulfur and carbon, *in* Barnes, H.L., ed., Geochemistry of hydrothermal ore deposits, 2nd ed.: New York, Wiley, p. 509–567.

Olson, S.F., 1984, The stratigraphic and structural setting of the Potrerillos porphyry copper district, northern Chile: Revista Geológica de Chile, v. 16, p. 3–29.

Orton, G.J., 1996, Volcanic environments, *in* Reading, H.G., ed., Sedimentary environments: Processes, facies and stratigraphy, 3rd ed.: Oxford, Wiley-Blackwell, 704 p.

Ossandón, G., Fréraut, R., Gustafson, L.B., Lindsay, D.D., and Zentilli, M., 2001, Geology of the Chuquicamata mine: A progress report: Economic Geology, v. 96, p. 351–366.

Oyarzun, R., Marquez, A., Lillo, J., Lopez, I., and Rivera, S., 2001, Giant versus small porphyry copper deposits of Cenozoic age in Northern Chile: adakite versus normal calc-alkaline magmatism: Mineralium Deposita, v. 36, p. 794–798.

Padilla-Garza, R.A., Titley, S.R., and Eastoe, C.J., 2004, Hypogene evolution of the Escondida porphyry copper deposit, Chile: Society of Economic Geologists Special Publication 11, p. 141–165.

Pals, D.W., Spry, P.G., and Chryssoulis, S.L., 2003, Invisible gold and tellurium in arsenic-rich pyrite from the Emperor gold deposit, Fiji: Implications for gold distribution and deposition: Economic Geology, v. 98, p. 479–493.

Pass, H.E., Cooke, D.R., Davidson, G., Maas, R., Dipple, G., Rees, C., Ferreira, L., Taylor, C. , and Deyell, C.L., 2014, Isotope geochemistry of the Northeast zone, Mount Polley alkalic Cu-Au-Ag porphyry deposit, British Columbia: A case for carbonate assimilation: Economic Geology, v. 109, p. 859–890.

Pearce, J.A., 1982, Trace element characteristics of lavas from destructive plate boundaries, *in* Thorpe, R.S., ed., Andesites: New York, Wiley, p. 525–548.

Pearce, J.A., Kempton, P.D., Nowell, G.M., and Noble, S.R., 1999, Hf-Nd element and isotope perspective on the nature and provenance of mantle and subduction components in Western Pacific arc-basin systems: Journal of Petrology, v. 40, p. 1579–1611.

Pearson, N.J., Griffin, W.L., and O'Reilly, S.Y., 2008, In-situ isotope ratio measurement: a decade of development of applications for mantle peridotites and kimberlites: 9th International Kimberlite Conference, Frankfurt, Germany, Extended Abstract no. 9IKC-A-00203.

Peccerillo, A., and Taylor, S.R., 1976, Geochemistry of Eocene calc-alkaline volcanic rocks from the Kastamonu area, northern Turkey: Contributions to Mineralogy and Petrology, v. 58, p. 63–81.

Pelletier, B., Lagabrielle, Y., Benoit, M., Cabioch, G., Calmant, S., Garel, E., and Guivel., C., 2001, Newly identifited segments of the Pacific–Australia plate boundary along the North Fiji transform zone: Earth and Planetary Science Letters, v. 193, p. 347–358.

Perelló, J., Sillitoe, R.H., Brockway, H., Posso, H., and Mpodozis, C., 2009, Contiguous porphyry Cu-Mo and Cu-Au mineralization at Los Pelambres, central Chile: Congreso Geológico Chileno, 12th, Santiago, 2009, Actas, Pendrive, 4 p.

Petterson, M.G., Neal, C.R., Mahoney, J.J., Kroenke, L.W., Saunders, A.D., Babbs, T.L., Duncan, R.A., Tolia, D., and McGrail, B., 1997, Structure and deformation of north and central Malaita, Solomon Islands: tectonic implications for the Ontong Java Plateau-Solomon arc collision, and for the fate of oceanic plateaus: Tectonophysics, v. 283, p. 1–33.

Pontual, S., Merry, N., and Gamson, P., 1997, Spectral interpretation field manual: Victoria, Australia, Auspec International Pty. Ltd., p. 1–169.

Pyle, D.G., Christie, D.M., and Mahoney, J.J., 1992, Resolving an isotopic boundary within the Australian–Antarctic Discordance: Earth and Planetary Science Letters, v. 112, p. 161–178.

Rahiman, T.I.H., and Pettinga, J.R., 2008, Analysis of lineaments and their relationship to Neogene fracturing, SE Viti Levu, Fiji: Geological Society of America Bulletin 120, p. 1544–1555.

Redmond, P.B., and Einaudi, M.T., 2010, The Bingham Canyon porphyry Cu-Mo-Au deposit: I. Sequence of intrusion, vein formation, and sulfide deposition: Economic Geology, v. 105, p. 43–68.

Richards, J.P., 2003, Tectono-magmatic precursors for porphyry Cu-(Mo-Au) deposit formation: Economic Geology, v. 96, p. 1515–1533.

Richards, J.P., 2011, Magmatic to hydrothermal metal fluxes in convergent and collided margins: Ore Geology Reviews, v. 40, p. 1–26.

Richards, J., and Kerrich, R., 2007, Adakite-like rocks: Their diverse origins and questionable role in metallogenesis: Economic Geology, v. 102, p. 537–576.

Richards, J.P., and Noble, S.R., 1998, Application of radiogenic isotope systems to the timing and origin of hydrothermal processes: Reviews in Economic Geology, v. 10, p. 195–234.

Rickwood, P.C., 1989, Boundary lines within petrologic diagrams which use oxides of major and minor elements: Lithos, v. 22, p. 247–263.

Rinne, M., 2015, Geology, alteration, and mineralisation of the Golpu porphyry and Wafi epithermal deposit, Morobe Province, Papua New Guinea: Unpublished PhD thesis, Hobart, Australia, University of Tasmania, 255 p.

Rodda, P., 1966, Economic geology of north and central Viti Levu: Fiji Geological Survey Note 21/66, 8 p.

Rodda, P., 1967, Outline of the geology of Viti Levu: New Zealand Journal of Geology and Geophysics, v. 10, p. 1260–1273.

Rodda, P., 1970, Geology of Namosi area, Viti Levu - Sheet 12, 1:50 000 geological series, Fiji Mineral Resources Department.

Rodda, P., 1976, An occurrence of orbicular gabbro in Fiji: New Zealand Journal of Geology and Geophysics, v. 19, p. 265–268.

Rodda, P., 1994, Geology in Fiji, *in* Stevenson, A.J., Herzer, R.H., and Balance, P.F., eds., Geology and submarine resources of Tonga-Lau-Fiji region: SOPAC Technical Bulletin 8, p. 131–151.

Rodda, P., and Band, R.B., 1966, Geology of Viti Levu, map-scale 1:250 000, Geological Survey of Fiji.

Rodda, P., and Band, R.B., 1967, Geology of Viti Levu: Fiji Geological Survey Annual Report 1966, p. 8–16.

Rogers, N.W., and Setterfield, T.N., 1994, Potassium and incompatible-element enrichment in shoshonitic lavas from the Tavua volcano, Fiji: Chemical Geology, v. 118, p. 43–62.

Rohrlach, B.D., and Loucks, R.R., 2005, Multi-million-year cyclic ramp-up of volatiles in a lower crustal magma reservoir trapped below the Tampakan copper-gold deposit by Mio-Pliocene crustal compression in the southern Philippines, *in* Porter, T.M., Super porphyry copper and gold deposits—A global perspective: Adelaide, Porter GeoConsultancy Publishing, v. 2, p. 369–407.

Rollinson, H., 1993, Using geochemical data: Evaluation, presentation, interpretation: Longman, Harlow, United Kingdom, 352 p.

Royle, D.Z., Taylor, G.P., and Inoke, F., 1979, Regional geology and re-assessment of the porphyry copper potential of SPL 1014, Viti Levu, Fiji: Fiji Mineral Resources Department Exploration Report 1014-61 (unpublished), 58 p.

Ruellan, E., and Lagabrielle, Y., 2005, Subductions et ouvertures océaniques dans le Sud-Oeste Pacific: Géomorphologie : relief, processus, environnement, v. 2, p. 121–142.

Ryan, W.B.F., Carbotte, S.M., Coplan, J.O., O'Hara, S., Melkonian, A., Arko, R., Weissel, R. A., Ferrini, V., Goodwillie, A., Nitsche, F., Bonczkowski, J., and Zemsky., R., 2009, Global Multi-Resolution Topography synthesis, Geochemistry, Geophysics, Geosystems, v. 10, Q03014.

Rye, R.O., 1993, The evolution of magmatic fluids in the epithermal environment: the stable isotope perspective: Economic Geology, v. 88, p. 733–753.

Rye, R.O., 2005, A review of the stable isotope geochemistry of sulfate minerals in selected igneous environments and related hydrothermal systems: Chemical Geology, v. 215, p. 5–36.

Salters, V.J.M., and Hart, S.R., 1991, The mantle source of ocean ridges, island arcs: the Hf-isotope connection: Earth and Planetary Science Letters: v. 104, p. 364–380.

Sasaki, A., and Ishihara, S., 1979, Sulfur isotope composition of the magnetite-series and ilmenite-series granitoids in Japan: Contributions to Mineralogy and Petrology, v. 68, p. 107–115.

Sasaki, A., Ulriksen, C.E., Sato, K., and Ishihara, S., 1984, Sulfur isotope reconnaissance of porphyry copper and manto-type deposits in Chile and the Philippines: Bulletin of the Geological Survey of Japan, v. 35 , p. 615–622.

Saunders, A., Norry, M., and Tarney, J., 1988, Origin of MORB and chemically-depleted mantle reservoirs: Trace element constraints: Journal of Petrology, v. 1, p. 415–445.

Schellart, W.P., Lister, G.S., and Jessell, M.W., 2002, Analogue modeling of arc and backarc deformation in the New Hebrides Arc and North Fiji Basin: Geology, v. 30, p. 311–314.

Schellart, W.P., Toy, V., and Lister, G., 2006, Late Cretaceous and Cenozoic reconstructions of the SW Pacific: tectonics controlled by subduction and slab rollback processes: Earth Science Reviews, v. 76, p. 191–233.

Scherbarth, N.L., and Spry, P.G., 2006, Mineralogical, petrological, stable isotope, and fluid inclusion characteristics of the Tuvatu Gold-Silver Telluride Deposit, Fiji: Comparisons with the Emperor Deposit: Economic Geology, v. 101, p. 135–158.

Schmitz, M.D., and Schoene, B., 2007, Derivation of isotope ratios, errors, and error correlations for U-Pb geochronology using $^{205}Pb$-$^{235}U$-($^{233}U$)-spiked isotope dilution thermal ionization mass spectrometric data: Geochemistry, Geophysics and Geosystems, v. 8, 8–20.

Scoates, J.S., and Friedman, R.M., 2008, Precise age of the platiniferous Merensky reef, Bushveld Complex, South Africa, by U-Pb zircon chemical abrasion ID-TIMS technique: Economic Geology, v. 103, p. 465–471.

Sdrolias, M., Mueller, R.D., and Gaina, C., 2003, Tectonic evolution of the Southwest Pacific using constraints from backarc basins: Geological Society of America Special Paper, v. 372, p. 343–359.

Seedorff, E., Dilles, J.H., Proffett, J.M., Einaudi, M.T., Zurcher, L., Stavast, W.J.A., Johnson, D.A., and Barton M.D., 2005, Porphyry deposits: Characteristics and origin of hypogene features: Economic Geology 100th Anniversary Volume, p. 251–298.

Selby, D., and Creaser, R.A., 2004, Macroscale NTIMS and microscale LA-MC-ICP-MS Re-Os isotopic analysis of molybdenite: Testing spatial restrictions for reliable Re-Os age determinations, and implications for the decoupling of Re and Os within molybdenite: Geochimica et Cosmochimica Acta, v. 68, p. 3897–3908.

Seo, J.H., Guillong, M., and Heinrich, C.A., 2012, Separation of molybdenum and copper in porphyry deposits: The roles of sulfur, redox, and pH in ore mineral deposition at Bingham Canyon: Economic Geology, v. 107, p. 333–356.

Setterfield, T.N., 1991, Evolution of the Tavua caldera and associated hydrothermal systems: Unpublished PhD thesis, Cambridge, United Kingdom, University of Cambridge, 231 p.

Setterfield, T.N., Eaton, P.C., Rose, W.J., and Sparks, R.S.J., 1991, The Tavua caldera, Fiji: A complex shoshonitic caldera formed by concurrent faulting and downsagging: Journal of the Geological Society, v. 148, p. 115–127.

Shannon, J.R., Walker, B.M., Carten, R.B., and Geraghty, E.P., 1982, Unidirectional solidification textures and their significance in determining relative ages of intrusions at the Henderson mine, Colorado: Geology, v. 10, p. 293–297.

Sharp, Z.D., 1990, Laser-based microanalytical method for in situ determination of oxygen isotope ratios of silicates and oxides: Geochimica et Cosmochimica Acta, v. 54, p. 1353–1357.

Shelton, K.L., and Rye, D.M., 1982, Sulfur isotopic composition of ores from Mines Gaspe, Quebec: An example of sulfate-sulfide disequilibria in ore-forming fluid with application to other porphyry-type deposit: Economic Geology, v. 77, p. 1688–1709.

Sheppard, S.M.F., and Gilg, H.A., 1996, Stable isotope geochemistry of clay minerals; the story of sloppy, sticky, lumpy and tough, Cairns-Smith (1971): Clay minerals, v. 31, p. 1–24.

Sillitoe, R.H., 1985, Ore-related breccias in volcanoplutonic arcs: Economic Geology, v. 80, p. 1467–1514.

Sillitoe, R.H., 1987, Copper, gold and subduction: A trans-Pacific perspective: Australasian Institute of Mining and Metallurgy, Pacific Rim Congress ‘87, Australia, Proceedings, p. 399–403.

Sillitoe, R.H., 1993, Gold-rich porphyry copper deposits: Geological model and exploration implications: Geological Association of Canada Special Paper 40, p. 465–478.

Sillitoe, R.H., 1997, Characteristics and controls of the largest porphyry copper-gold and epithermal gold deposits in the circum-Pacific region: Australian Journal of Earth Sciences, v. 44, p. 373–388.

Sillitoe, R.H., 2010, Porphyry copper systems: Economic Geology, v. 105, p. 3–41.

Sillitoe, R.H., and Gappe, I.M., Jr., 1984, Philippine porphyry copper deposits: Geologic setting and characteristics: Bangkok, Thailand, United Nations ESCAP, CCOP Technical Publication 14, 89 p.

Sillitoe, R.H., and Mortensen, J.K., 2010, Longevity of porphyry copper formation at Quellaveco, Peru: Economic Geology, v. 105, p. 1157–1162.

Simmons, S.F., Brown, K.L., and Browne, P.R.L., 2006, Precious metals in hydrothermal systems of the Taupo Volcanic Zone, *in* Christie, A.B., and Brathwaite, R.L., eds., Geology and Exploration of New Zealand Mineral Deposits: AusIMM Monograph 25, p. 203–211.

Singer, D.A., 1995, World-class base and precious metal deposits: A quantitative analysis: Economic Geology, v. 90, p. 88–104.

Skilling, I.P., White, J.D.L., and McPhie J., 2002, Peperite: A review of magma-sediment mingling: Journal of Volcanology and Geothermal Research, v. 114, p 1–17.

Smith, T.L, and Batiza, R., 1989, New field and laboratory evidence for the origin of hyaloclastite flows on seamount summits: Bulletin of Volcanology, v. 51, p. 96–114.

Snyder, G.L., and Fraser, G.D., 1963, Pillowed lavas, intrusive layered lava pods and pillowed lavas, Unalaska Island, Alaska, *in* Snyder, G.L., and Fraser, G.D., eds., Pillowed lavas, I: Intrusive layered lava pods and pillowed lavas, Unalaska Island, Alaska and, Pillowed lavas, II: A review of recent literature: U.S. Geological Survey Professional Paper 454-B,C, p. C1–C7.

Solomon, M., 1990, Subduction, arc reversal, and the origin of porphyry copper-gold deposits in island arcs: Geology, v. 18, p. 630–633.

Spry, P.G., and Scherbarth, N.L., 2006, The gold–vanadium–tellurium association at the Tuvatu gold–silver prospect, Fiji: conditions of ore deposition: Mineralogy and Petrology, v. 87, p. 171–186.

Stow, D.A.V., 2005, Sedimentary rocks in the field: A colour guide: London, Manson Publishing 320 p.

Sun, S., and McDonough, W.F., 1989, Chemical and isotopic systematics of oceanic basalts: Implications for mantle composition and processes: Geological Society Special Publication 42, p. 313–345.

Suzuoki, T., and Epstein, S., 1976, Hydrogen isotope fractionation between OH-bearing minerals and water: Geochimica et Cosmochimica Acta, v. 40, p. 1229–1240.

Swarbick, R.E., and Naylor, M.A., 1980, The Kathikas mélange, SW Cyprus: late Cretaceous submarine debris flows: Sedimentology, v. 27, p. 63–78.

Sykes, L.R., 1964, Deep-focus earthquakes in the New Hebrides region: Journal of Geophysical Research, v. 69, p. 5353–5355.

Sylvester, A.G., 1988, Strike-slip faults: Geological Society of America Bulletin 100, p. 1666–1703.

Tămaş, C.G., and Milési, J.-P., 2003, Hydrothermal breccia pipe structures – general features and genetic criteria – II. Phreatic breccias: Studia Universitatis Babeş-Bolyai Geologia, v. 48, p. 56–66.

Tanaka, T., Morita, S., Cho, H., Yamasawa, S., Miyoshi, M., and Murakami, H., 2003, Fracture survey at Waisoi copper deposits in Namosi area in the Republic of Fiji Islands: Shigen Chishitsu, v. 53, p. 1–18.

Tanaka, T., Morita, S., Takahata, H., Yasunaga, K., Imai, A., and Ishikawa, N., 2004, Copper exploration and its results of Waisoi deposits in Namosi area, Republic of Fiji Islands: Shigen Chishitsu, v. 54, p. 1–12.

Tanaka, T., Takahashi, T., Makuuchi, A., Yasunaga, K., and Maeda, K., 2006, Discovery of new copper mineralization zone in Namosi area, Republic of Fiji Islands: Shigen Chishitsu, v. 56, p. 1–10.

Tanaka, T., Imai, A., Egashira, S., Sakomoto, S., Yasunaga, K., and Maeda, K., 2010, Petrological and geochemical characteristics of intrusive rocks related to porphyry copper mineralization and the implications for the genesis of deposits in the Namosi area, Viti Levu, Republic of the Fiji Islands: Resource Geology, v. 60, p. 35–51.

Tappin, D.R., and Ballance, P.F., 1994, Contributions to the sedimentary geology of 'Eua Island, Kingdom of Tonga: reworking in an oceanic forearc, *in* Stevenson, A.J., Herzer, R.J., and Ballance, P.F., eds., Geology and submarine resources of the Tonga Lau-Fiji region: SOPAC Technical Bulletin 8, p. 1–20.

Taylor, S.R., Kaye, M., White, A.J.R., Duncan, A.R., and Ewart, A., 1969, Genetic significance of Co, Cr, Ni, Sc, and V in andesites: Geochimica Cosmochimica Acta, v. 8, p. 275–286.

Taylor, F.W., Bevis, M.G., Schutz, B.E., Kuang, D., Recy, J., Calmant, S., Charley, D., Regnier, M., Perin, B., Jackson, M., and Reichenfeld, C., 1995, Geodetic measurements of convergence at the New Hebrides island arc indicate arc fragmentation caused by an impinging aseismic ridge: Geology, v. 23, p. 1011–1014.

Taylor, G.K., Gascoyne, J., and Colley, H., 2000, Rapid rotation of Fiji: palaeomagnetic evidence and tectonic implications: Journal of Geophysical Research: Solid Earth, v. 105, p. 5771–5781.

Taylor, H.P., 1997, Oxygen and hydrogen isotope relationships in mineral deposits, *in* Barnes H.L., ed., Geochemistry of hydrothermal ore deposits, 3rd ed.: New York, Wiley, p. 229–302.

Thirlwall, M.F., 2000, Inter-laboratory and other errors in Pb isotope analyses investigated using a $^{207}Pb$-$^{204}Pb$ double spike: Chemical Geology, v. 163, p. 299–322.

Titley, S.R., 1982, The style and progress of mineralization and alteration in porphyry copper systems: American Southwest, *in* Titley, S.R., ed., Advances in geology of the porphyry copper deposits, southwestern North America: Tucson, University of Arizona Press, p. 93–116.

Todd, E., 2011, The youngest rocks from an old arc and the oldest rocks from a juvenile one: the memoirs of a SW Pacific subduction zone: Unpublished PhD thesis, Santa Cruz, USA, University of California, 275 p.

Tribble, G.W., 1991, Underwater observations of active lava flows from Kilauea volcano, Hawaii: Geology, v. 19, p. 633–636.

Turner, S.P., Hawkesworth, C.J., Rogers, N.W., Bartlett, J., Worthington, T., Hergt, J.M., Pearce, J. A., and Smith, I.E.M., 1997, $^{238}U$–$^{230}Th$ disequilibria, magma petrogenesis, and flux rates beneath the depleted Tonga–Kermadec island arc: Geochimica et Cosmochimica Acta, v. 61, p. 4855–4884.

Vennemann, T.W., Muntean, J.L., Kesler, S.E., O'Neil, J.R., Valley, J.W., and Russell, N., 1993, Stable isotope evidence for magmatic fluids in the Pueblo Viejo epithermal acid sulfate Au-Ag deposit, Dominican Republic: Economic Geology, v. 88, p. 55–71.

Verbeeten, A., 1996, Petrology, geochemistry and tectonic implications of magmatism along the northern Hunter Ridge and Kadavu Island group, Fiji: Unpublished PhD thesis, Hobart, Australia, University of Tasmania, 190 p.

von Quadt, A., Erni, M., Martinek, K., Moll, M., Peytcheva, I., and Heinrich, C.A., 2011, Zircon crystallization and the lifetimes of ore-forming magmatic hydrothermal systems: Geology, v. 39, p. 731–734.

Walker, R.G., 1984, Shelf and shallow marine sands, *in* Walker, R.G., ed., Facies models, 2nd ed.: Geoscience Canada Reprint Series 1, p. 141–170.

Waters, P.J., Cooke, D.R., Gonzales, R.I. and Phillips, D., 2011, Porphyry and epithermal deposits and $^{40}Ar/^{39}Ar$ geochronology of the Baguio district, Philippines: Economic Geology, v. 106, p. 1335–1363.

Weissel, J.K., 1981, Magnetic lineations in marginal basins of the western Pacific, *in* Extensional tectonics associated with convergent plate boundaries: Philosophical Transactions of the Royal Society of London, Series A: Mathematical and Physical Sciences, v. 300, p. 223–247.

Wessel, P., and Kroenke, L.W., 2000, Ontong Java Plateau and late Neogene changes in Pacific plate motion: Journal of Geophysical Research: Solid Earth, v. 105, p. 28255–28277.

Wharton, M.R., Hathway, B., and Colley, H., 1995, Volcanism associated with extension in an Oligocene-Miocene arc, southwestern Viti Levu, Fiji, *in* Smellie, J.L., ed., Volcanism Associated with Extension at Consuming Plate Margins: Geological Society London Special Publications, London, United Kingdom, v. 81, p. 95–114.

Whelan, P.M., Gill, J.B., Kolman, E., Duncan, R.A., and Drake, R.E., 1985, Radiometric dating of magmatic stages in Fiji, *in* Scholl, D.W., and Vallier, T.L., eds., Geology and offshore resources of Pacific island arcs—Tonga region: Circum-Pacific Council Energy Mineral Resources, Houston, Texas, USA, Council for Energy and Mineral Resources Earth Science Series 2, p. 415–440.

White, J.D.L., 2000, Subaqueous eruption-fed density currents and their deposits: Precambrian Research, v. 101, p. 87–109.

Wilkinson, J.J., Chang, Z., Cooke, D.R., Baker, M.J., Wilkinson, C.C., Inglis, S., Chen, H., Gemmell, J.B., 2015, The chlorite proximitor: a new tool for detecting porphyry ore deposits: Journal of Geochemical Exploration, v. 152, p. 10–26.

Wilson, A.J., 2003, The geology, genesis and exploration context of the Cadia gold-copper porphyry deposits, NSW, Australia: Unpublished PhD thesis, Hobart, Australia, University of Tasmania, 335 p.

Wilson, A.J., Cooke, D.R., and Harper, B.L., 2003, The Ridgeway gold-copper deposit: A high-grade alkalic porphyry deposit in the Lachlan fold belt, New South Wales, Australia: Economic Geology, v. 98, p. 1637–1666.

Wilson, A.J., Cooke, D.R., Stein, H.J., Fanning, C.M., Holliday, J.R., and Tedder, I.J., 2007, U-Pb and Re-Os geochronologic evidence for two alkalic porphyry ore-forming events in the Cadia district, New South Wales, Australia: Economic Geology, v. 102, p. 3–26.

Wilson, M.J., 1989, Igneous petrogenesis: London, United Kingdom, Unwin Hyman, 466 p.

Wolfe, R.C., and Cooke, D.R., 2011, Geology of the Didipio region and genesis of the Dinkidi alkalic porphyry Cu-Au deposit and related pegmatites, northern Luzon, Philippines: Economic Geology, v. 106, p. 1279–1315.

Wortel, R., Govers, R., and Spakman, W., 2009, Continental collision and the STEP-wise evolution of convergent plate boundaries: from structure to dynamics, *in* Lallemand, S., and Funiciello, F., eds., Subduction zone geodynamics: Springer-Verlag, Berlin, Germany, p. 47–59.

Wurst, A.T., 2004, Geology and genesis of the Permata-Batu Badinding-Hulubai, and Kerikil Au-Ag low sulfidation epithermal deposits, Mt. Muro, Kalimantan, Indonesia: Unpublished PhD thesis, Hobart, Australia, University of Tasmania, 423 p.

Zheng, Y.F., 1993, Calculation of oxygen isotope fractionation in hydroxyl-bearing silicates: Earth and Planetary Science Letters, v. 120, p. 247–263.

Zindler, A., and Hart, S.R., 1986, Chemical geodynamics: Annual Reviews of Earth and Planetary Sciences, v. 14, p. 493–571.